

nature

CLIMATE CLEAN-UP

The finance needed to phase out fossil fuels

Congo Basin
End the neglect of Earth's second largest rainforest

Something in the air
Assessing the possible climate impact of airborne microplastics

Fighting infection
A candidate antiviral drug for the treatment of dengue

PHOTOGRAPH BY GREGORY WATSON

Nature.2021.10.23

[Sat, 23 Oct 2021]

- [This Week](#)
- [News in Focus](#)
- [Books & Arts](#)
- [Opinion](#)
- [Work](#)
- [Research](#)
- [Amendments & Corrections](#)

This Week

- **[COVID, racism, China: three tests for the next NIH leader](#)**

[19 October 2021]

Editorial • The successor to Francis Collins will need to be steadfast, nimble and creative in how they run the world's largest biomedical research agency at a pivotal time.

- **[Young people will be key to climate justice at COP26](#)**

[20 October 2021]

Editorial • The world's youth movements are following the science of climate change. It's high time that world leaders did, too.

- **[Before making a mammoth, ask the public](#)**

[20 October 2021]

World View • I turned down the role of adviser to a de-extinction company — that task belongs to everyone.

- **[Climate change means thin ice for lakes worldwide](#)**

[18 October 2021]

Research Highlight • Study of lakes around the globe ties changes in ice coverage to human-induced warming.

- **[Our enormous fish catches have skewed ocean chemistry](#)**

[15 October 2021]

Research Highlight • Industrial fishing seems to have altered the processing of biomass in the ocean.

- **[Molecules that see the light embark on an epic trip](#)**

[14 October 2021]

Research Highlight • Illumination releases microscopic crawlers to follow a long, fibrous path.

- **[Cold-war spy pictures reveal a Soviet nuclear ‘cloud generator’](#)**

[11 October 2021]

Research Highlight • Declassified satellite pictures expose the catastrophic damage done by a plutonium complex in the Urals.

- **[Finicky no more: ancient snakes ate their way to success](#)**

[14 October 2021]

Research Highlight • The ancestor of living snakes lived on invertebrates, but its descendants colonized the planet by going gourmet.

- **Physicists ‘listen’ to sounds in a fluid of light** [11 October 2021]
Research Highlight • Light that flows through a device made of optical fibres behaves like the form of matter called a superfluid.
- **The ticking time bomb anchored off war-torn Yemen** [12 October 2021]
Research Highlight • A derelict oil tanker in the waters of the Middle Eastern nation is at high risk of rupturing, which would imperil millions of people already in crisis.

| [Next section](#) | [Main menu](#) |

- EDITORIAL
- 19 October 2021

COVID, racism, China: three tests for the next NIH leader

The successor to Francis Collins will need to be steadfast, nimble and creative in how they run the world's largest biomedical research agency at a pivotal time.



Departing NIH director Francis Collins works with leaders and staff at the agency's 27 institutes and centres. Credit: Andrew Harnik/Getty

Francis Collins will leave big shoes to fill when [he steps down](#) later this year, after 12 years as director of the world's biggest public funder of biomedical research. By then, he is expected to have obtained bipartisan

support for a funding increase that would bring the US National Institutes of Health (NIH) budget to US\$43 billion for the fiscal year 2021; when he took on the job, in 2009, it was \$30 billion. His scientific credentials as a physician and geneticist — which include heading up the public effort to sequence the human genome in the 1990s and early 2000s — positioned him to establish a number of [big-biology initiatives](#) at the agency. These have allowed the NIH to maintain its position as a global research powerhouse.

The challenge now comes in replacing him — a process that involves nomination by the president, followed by hearings and a vote in the Senate. Whoever takes on the role will need to be able to work with presidents and members of Congress, and to have the requisite scientific and administrative skills. The job also has a big diplomatic component, involving liaison with heads of international governments, as well as business leaders and those running philanthropic foundations, who are an increasing force across many research fields.

The agency's new leader will face myriad challenges, among them guiding biomedical research during and after the COVID-19 pandemic; dealing with systemic racism and inequity in science; and navigating scientific cooperation with China. That is in addition to the core role: securing the agency's budget, and being ever-more creative in making the case for supporting basic research. The choice of director must reflect [an increasingly diverse nation](#). For all but 2 years of its 134-year history, the NIH has been led by a man; cardiologist Bernadine Healy, who ran the NIH from 1991 to 1993, is the only woman to have led the agency. It's time for change.

COVID response

The NIH director oversees the agency's 27 institutes and centres, which together employ more than 20,000 people, including 1,200 principal investigators and over 4,000 postdocs. But the agency's reach extends well beyond its headquarters in Bethesda, Maryland. More than 80% of the NIH's funding supports hundreds of thousands of researchers in labs across the United States and around the world.



[US health agency will invest \\$1 billion to investigate ‘long COVID’](#)

The pandemic is an immediate priority. COVID-19 prompted the NIH, under Collins, to speed up some of its grant-distribution systems and to initiate rapid-response research into SARS-CoV-2 testing, vaccines and therapeutics. The success of mRNA vaccines against the virus stemmed, in part, from groundwork laid before the pandemic by NIH-funded research. The agency has also launched a \$1.15-billion research investigation over four years — one of the world’s most ambitious so far — into long COVID.

The next director must build on these initiatives and find the best way for the NIH to support basic research on efforts to bring the current pandemic to an end — and to prepare for the next one. One of the biggest challenges will be to balance this need with the other priorities and disease burdens that NIH is set up to address.

Racism and equity

As one of many organizations confronting discrimination, the NIH has had mixed results on its efforts to boost diversity, equity and inclusion in bioscience and its workforce. Under Collins, the agency announced that it will end its over-reliance on male animals and cells, and take sex into account in the design of biomedical studies. But the NIH was slower than

some other US federal agencies to adopt strict reporting guidelines when grant recipients are found to have violated an institution's sexual-harassment policies.

Anti-racism work needs to be a priority for Collins's successor. Black applicants received only 1.8% of NIH grant awards in 2020, a number that has barely budged since 2013 — and their success rate is lower than that for applicants from white, Hispanic and Asian communities. Earlier this year, the NIH embarked on an initiative called UNITE, intended to end structural racism in biomedical science. The agency plans to spend \$90 million on projects to reduce health disparities, and on studying how structural racism affects the health of minority communities. This work must also draw on the latest social science.

These are welcome moves, but much more funding and commitment are needed to tackle the persistent under-representation of Black researchers among the agency's grant recipients. It is imperative that the next director addresses real systemic barriers.

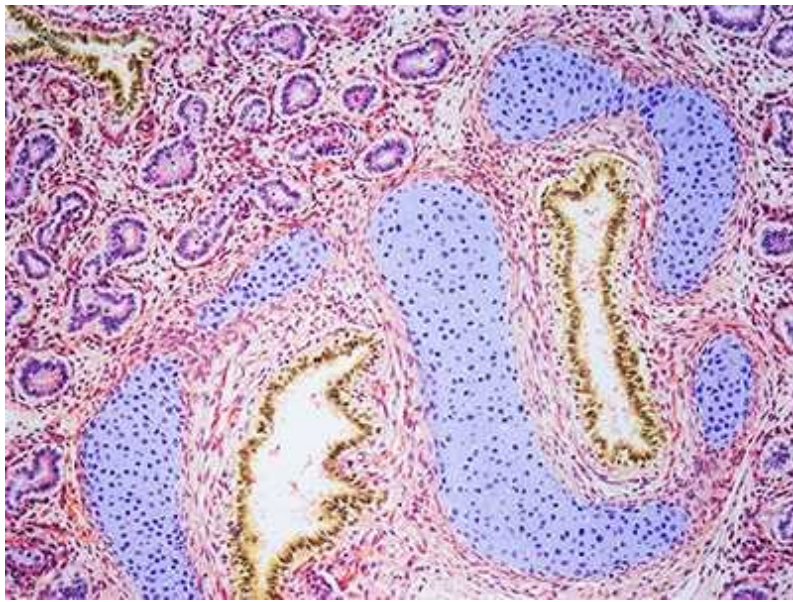
Diplomacy

The ability to work effectively with elected representatives is a crucial aspect of the NIH director's role — it involves responding to known and predictable diplomatic and political challenges, as well as reacting swiftly to new situations as they arise.

One such situation is US concerns that China's government might be using research collaborations as a means of spying on US research institutions. The NIH is among a number of science agencies caught up in allegations relating to these concerns, and some NIH-funded scientists with links to China have lost their jobs. Civil-rights groups say that many were targeted unfairly, partly as a result of relations between the United States and China taking a downward turn. The next NIH leader should advocate for clearer rules that enable US and Chinese researchers to be supported by each other's funding agencies — [as universities are calling for](#).

The president calls

The size and scale of the NIH, and its importance to US science, means that the NIH director works closely with the office of the president. President Joe Biden has a deep personal interest in biomedical research, having worked extensively with research advocates, particularly in cancer, when he served in the Senate and as vice-president under former president Barack Obama.



NIH reverses Trump-era restrictions on fetal-tissue research

The NIH will be expected to advance other priorities Biden has flagged, including an ambitious vision for redrawing the nation's science and technology enterprise, and the creation of an advanced research projects agency, or ARPA, [focused on health](#) (ARPA-H). This would follow the widely touted model of the defence ARPA, DARPA, in funding high-risk, innovative research projects.

Biden has proposed allocating \$6.5 billion to set up ARPA-H, although it's not yet clear to what extent Congress will go along with this request.

Questions facing the new NIH director will include whether ARPA-H should reside within the NIH — as Collins has advocated — or whether it should sit elsewhere within the US government. Wherever it finds a home, ARPA-H must be given enough authority and independence to avoid becoming bogged down by the slow gears typical of NIH operations.

Collins also served during the four years of the administration of Donald Trump, who reappointed him to the post. It's a reminder that the NIH chief must have a constructive working relationship with whichever party is in office. That relationship is often tested — especially when it comes to research priorities. Collins has backed the need for research involving fetal tissue, which comes from elective abortions. But this was not enough to stop the Trump administration drastically restricting research with fetal tissue. Although the Biden administration has reversed that decision, the next NIH director must prepare the case and build coalitions against future restrictions in this area.

The next NIH director will not be working alone — they will be able to draw on the expertise and wisdom of staff throughout the agency, as well as in the national and international research community. They must create opportunities and space to listen to diverse voices and perspectives. The pandemic has demonstrated the crucial importance of fundamental biomedical research in solving global problems and enhancing health. Now the world's leading biomedical research body must position itself to tackle many other problems — chronic disease, health inequality and the health dimensions of climate change — for which solutions have so far remained stubbornly out of reach.

Nature **598**, 385-386 (2021)

doi: <https://doi.org/10.1038/d41586-021-02842-7>

This article was downloaded by **calibre** from <https://www.nature.com/articles/d41586-021-02842-7>

- EDITORIAL
- 20 October 2021

Young people will be key to climate justice at COP26

The world's youth movements are following the science of climate change. It's high time that world leaders did, too.



Teenage climate activists are reading and quoting from reports of the Intergovernmental Panel on Climate Change. Credit: Ozan Kose/AFP/Getty

The teenage climate campaigner Greta Thunberg spoke for many *Nature* readers in August when she summed up the latest report from the Intergovernmental Panel on Climate Change (IPCC) as a “solid (but cautious) summary” of the best available science. “It confirms what we

already know from thousands of previous studies and reports,” she said. “It doesn’t tell us what to do. It is up to us to be brave and take decisions based on the scientific evidence provided in these reports.”

As world leaders prepare to travel to Glasgow, UK, for the 26th Conference of the Parties (COP26) to the United Nations climate convention, they would be wise to listen to the science-led youth movements, and to an emerging generation of young climate scientists.

Young people are reading and engaging with climate and biodiversity science and policy in a way that previous generations haven’t. They have good reason to: without action, their futures will be increasingly dominated by the heatwaves, storms and floods that have featured in climate projections since an early IPCC report in 1990 opened with a foreword calling global warming “potentially the greatest global environmental challenge facing mankind”.



[The broken \\$100-billion promise of climate finance – and how to fix it](#)

“People are suffering. People are dying. Entire ecosystems are collapsing,” Thunberg said at a UN climate-action summit in New York City in 2019. “We are in the beginning of a mass extinction, and all you can talk about is money and fairy tales of eternal economic growth.”

The Glasgow meeting, which takes place from 31 October to 12 November, is not about a new international agreement — that happened in Paris in 2015, when nations agreed to limit warming to between 1.5 and 2 °C above pre-industrial levels. Instead, it will see countries report their progress (or lack thereof) towards cutting emissions, and lay out their plans to become carbon neutral over the next decade. There are clear signs that some change is under way. Humanity's use of oil might already be levelling off — not because oil is running out, but because of the transition to electric vehicles, rising fuel efficiency and the falling costs of electricity from renewable sources. Support for new coal-fired power is falling in Europe and the United States, and [China has pledged to stop financing new coal plants abroad.](#)

Replacing fossil fuels is one section (although admittedly a large one) of a thousand-piece jigsaw. The scale of the net-zero challenge is like nothing that has come before. Tackling global warming requires a revolution in how economies are run, and in the choices world leaders must make. Energy and industry, agriculture, financial services, transport and much more must be transformed. Natural ecosystems that absorb carbon emissions need protection. But as of now, the prospects for Glasgow are anything but optimistic.



[Why fossil fuel subsidies are so hard to kill](#)

Many countries — especially those that have contributed the least to the world's carbon emissions, but stand to lose the most from a climate crisis — are rightly demanding action from rich nations. But leadership and resources are both in short supply. The Paris agreement requires countries to report on and update their climate pledges every five years. This timing allows emissions-reduction pledges to be adjusted to match the latest scientific assessments on what needs to be done to limit warming to 1.5–2 °C. Forty-eight countries — including major emitters — are yet to set new targets, and some clearly have no plans to accelerate their climate ambitions. In addition, the leaders of some of the largest nations — including Brazil, China, India and Russia — have not yet even committed to attending COP26.

At COP15 in Copenhagen in 2009, the richer countries agreed that by 2020, they would be providing US\$100 billion per year in financial assistance to less wealthy nations. What counts as climate finance was never defined, but even by their own — highly controversial — accounting, [they have yet to meet that requirement](#). Even if they do, the majority of pledges will be for loans, not grants.

This is where the new generation of climate researchers and campaigners can expect to make its mark. Glasgow marks the first time that countries must explain, in public, whether their actions will achieve climate targets, according to projections from research. Climate laggards, and countries that are not fulfilling their funding pledges, will be called out — regardless of whether their leaders attend.

For generations, world leaders have, in principle, accepted that the planet must be habitable for those that come after them. But this promise was never kept, perhaps because ‘future generations’ were not much more than words in a policy document. Now, that has changed. New generations are making themselves heard. Some of their representatives are being consulted as part of COP26; tens of millions more will be outside. They are reading climate science, and using that knowledge to argue for honesty and meaningful action from their leaders. Those attending COP26 would be wise to listen to their arguments, and involve them in decisions that will affect their futures more than anyone else’s.

doi: <https://doi.org/10.1038/d41586-021-02843-6>

This article was downloaded by **calibre** from <https://www.nature.com/articles/d41586-021-02843-6>

| [Section menu](#) | [Main menu](#) |

- WORLD VIEW
- 20 October 2021

Before making a mammoth, ask the public



I turned down the role of adviser to a de-extinction company — that task belongs to everyone.

- [Victoria Herridge](#) 9

Every few years for the past 20 or so, the story resurfaces, frozen in time like a permafrost carcass. At some future point, typically within the decade, scientists hope to ‘bring back the mammoth’. There have been a few tantalizing results — stirrings in mammoth nuclei transplanted into mouse eggs ([K. Yamagata et al. Sci. Rep. 9, 4050; 2019](#)) — but that’s it. Hence raised eyebrows at last month’s announcement by de-extinction champion and geneticist George Church, co-founder (with entrepreneur Ben Lamm) of biotechnology start-up Colossal: yet again, the world has about five years until a wobbly, woolly calf takes its first steps into the Anthropocene.

What Colossal actually aims to produce is less a mammoth than a new synthetic species, a chimaera of Asian elephant DNA and mitochondria, mammoth genetic code and, from the probable surrogate dam, African elephant epigenetics. The resulting cold-adapted elephants — Colossal hopes — will trample and graze northern Siberia to create something akin to the Ice Age grasslands of the woolly mammoth's heyday. Compacted, cooler soils and paler, more reflective foliage, will — the company says — help to avert climate disaster. De-extinction this is not. This is synthetic biology meets geoengineering.

Although I question the timeline, it was ethics, not feasibility, that was my main concern back in July, when Lamm asked if I, an outspoken critic of mammoth de-extinction, would join the advisory board.

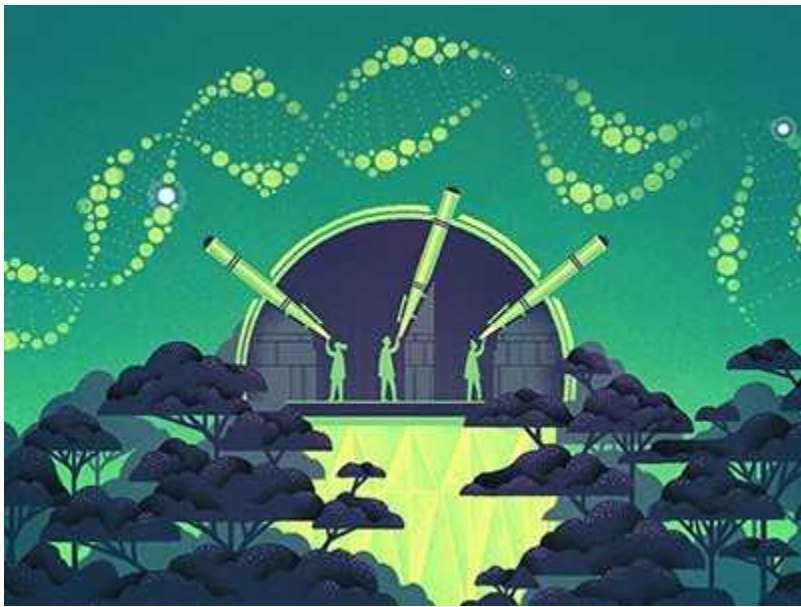


A behemoth revived

I said no. Not because I doubt Colossal's motives. Its founders are driven by a real desire to help the world, and have recruited expert advisers, including at least two excellent bioethicists. They are thoughtful and serious, and I wish them well. But reshaping the planet shouldn't be left to a chosen few, with insider advice from hand-picked experts. Instead, Colossal, and all companies like it, should do something as radical for business as its plans are for the planet: actively involve the public in its research decisions.

Colossal's plans push into ethically and politically fraught territory, operating on time scales that legislation can't keep pace with: gene editing; reproductive technology; animal welfare; conservation; and land management, to name a few. Both geoengineering and synthetic biology have a poor track record when it comes to people taking matters into their own hands. In 2012, the Haida Salmon Restoration Corporation, based in Vancouver, Canada, tipped 120 tonnes of iron sulfate and iron oxide into international waters off the coast of British Columbia as part of an ocean fertilization project, without the knowledge of national authorities. And there is Chinese researcher He Jiankui, sentenced to prison last year for his role in using CRISPR technology in at least two human embryos, resulting in the birth of gene-edited babies. These incidents have had a chilling effect on public trust and on research, and have destroyed the careers of at least three scientists. Open, public participation can rebuild that trust, and improve research outcomes.

Openness and public participation are core components of the Oxford Principles for geoengineering governance, which have underpinned international ethical and legal discourse on geoengineering since their endorsement by the UK government in 2010. These values are also central to the development of regulatory frameworks for genome engineering in humans, and to the potential requirement for free and informed consent from Indigenous and local communities before the implementation of engineered gene drives, in which altered genes propagate through an animal population. And they sit at the heart of the United Nations Research Roadmap for the COVID-19 Recovery.



A global observatory for gene editing

But they coexist uncomfortably with the business needs of confidentiality and the control of intellectual property. And consulting the public costs money. Colossal has committed to “radical” transparency, inclusion and community engagement, but has the chance to set the bar even higher, by empowering the public as part of its de-extinction journey.

There are tested ways to bring the public into research decisions. Groups such as Expert & Citizen Assessment of Science and Technology (ECAST) in the United States and Involve in the United Kingdom have pioneered public participatory research. For example, NASA’s Double Asteroid Redirection Test Mission, launching on 24 November, can be traced, in part, to public consultation run by ECAST in 2014, when planetary defence was flagged as a key public concern, shaping NASA’s long-term strategic focus.

True, this approach can act as a brake on research plans. In 2020, the solar geoengineering project SCoPEx, run by researchers at Harvard University in Cambridge, Massachusetts, suspended field experiments in Sweden in response to feedback gathered by its independent advisory committee. But for a business such as Colossal, as for NASA, this extra input could equally be a catalyst for innovation, and a way to remove the risk of derailment by protest and controversy. The gene-drive project Mice Against Ticks, for example, benefited when local involvement identified potential

unanticipated ecological consequences ([J. Buchthal et al. Phil. Trans. R. Soc. B 374, 20180105; 2019](#)).

The ethical road to de-extinction has to include informed citizen voices, alongside experts and activists. This might mean that the process takes longer than five years, but private enterprises working for the common good shouldn't shy away from the views of those they seek to serve. Let the people decide the future world they want to build.

Nature **598**, 387 (2021)

doi: <https://doi.org/10.1038/d41586-021-02844-5>

This article was downloaded by **calibre** from <https://www.nature.com/articles/d41586-021-02844-5>

| [Section menu](#) | [Main menu](#) |

- RESEARCH HIGHLIGHT
- 18 October 2021

Climate change means thin ice for lakes worldwide

Study of lakes around the globe ties changes in ice coverage to human-induced warming.



Global warming caused by human activity has led to thinner, less extensive ice on many lakes. Credit: Mehmet Emin Gurbuz/Anadolu Agency/Getty

Lakes throughout the world are getting warmer and freezing for fewer days per year because of global climate change¹.

Access options

Subscribe to Journal

Get full journal access for 1 year

\$199.00

only \$3.90 per issue

[Subscribe](#)

All prices are NET prices.

VAT will be added later in the checkout.

Tax calculation will be finalised during checkout.

Rent or Buy article

Get time limited or full article access on ReadCube.

from \$8.99

[Rent or Buy](#)

All prices are NET prices.

Additional access options:

- [Log in](#)
- [Learn about institutional subscriptions](#)

Nature **598**, 388 (2021)

doi: <https://doi.org/10.1038/d41586-021-02819-6>

References

1. 1.

Grant, L. *et al.* *Nature Geosci.* <https://doi.org/10.1038/s41561-021-00833-x> (2021).

This article was downloaded by **calibre** from <https://www.nature.com/articles/d41586-021-02819-6>

| [Section menu](#) | [Main menu](#) |

- RESEARCH HIGHLIGHT
- 15 October 2021

Our enormous fish catches have skewed ocean chemistry

Industrial fishing seems to have altered the processing of biomass in the ocean.



Industrial-scale fishing since the late nineteenth century has sharply reduced the biomass processed by ocean-going fish. Credit: Shen Lei/VCG/Getty

Industrial fishing might have disrupted some of the chemical flows in the ocean as much as human-induced climate change has¹.

Access options

Subscribe to Journal

Get full journal access for 1 year

\$199.00

only \$3.90 per issue

[Subscribe](#)

All prices are NET prices.

VAT will be added later in the checkout.

Tax calculation will be finalised during checkout.

Rent or Buy article

Get time limited or full article access on ReadCube.

from \$8.99

[Rent or Buy](#)

All prices are NET prices.

Additional access options:

- [Log in](#)
- [Learn about institutional subscriptions](#)

Nature **598**, 388 (2021)

doi: <https://doi.org/10.1038/d41586-021-02801-2>

References

1. 1.

Bianchi, D., Carozza, D. A., Galbraith, E. D., Guiet, J. & DeVries, T. *Sci. Adv.* **7**, eabd7554 (2021).

This article was downloaded by **calibre** from <https://www.nature.com/articles/d41586-021-02801-2>

| [Section menu](#) | [Main menu](#) |

- RESEARCH HIGHLIGHT
- 14 October 2021

Molecules that see the light embark on an epic trip

Illumination releases microscopic crawlers to follow a long, fibrous path.



Light unleashes ‘traveller’ molecules (shown here moving faster than actual speed) to scoot along track-like fibres. Credit: M. Samperi *et al.*/*Nature Chem.*

As a violet-blue light washes over a newly created gel, the glow prompts ‘traveller’ molecules embedded within to begin their march — a journey that could lead to the development of new molecular-scale machines¹.

Access options

Subscribe to Journal

Get full journal access for 1 year

\$199.00

only \$3.90 per issue

[Subscribe](#)

All prices are NET prices.

VAT will be added later in the checkout.

Tax calculation will be finalised during checkout.

Rent or Buy article

Get time limited or full article access on ReadCube.

from \$8.99

[Rent or Buy](#)

All prices are NET prices.

Additional access options:

- [Log in](#)
- [Learn about institutional subscriptions](#)

Nature **598**, 388 (2021)

doi: <https://doi.org/10.1038/d41586-021-02800-3>

References

1. 1.

Samperi, M. *et al.* *Nature Chem.* <https://doi.org/10.1038/s41557-021-00791-2> (2021).

This article was downloaded by **calibre** from <https://www.nature.com/articles/d41586-021-02800-3>

- RESEARCH HIGHLIGHT
- 11 October 2021

Cold-war spy pictures reveal a Soviet nuclear ‘cloud generator’

Declassified satellite pictures expose the catastrophic damage done by a plutonium complex in the Urals.

 Satellite image of the partially frozen Lake Kyzyltash with a thick cloud of steam

A 1966 satellite picture shows a plume of steam rising from a partially frozen lake in the Soviet Union, an indicator that plutonium was being produced there. Credit: G. Kiarszys/United States Geological Survey

The operation of a notorious Soviet plutonium-making facility decades ago caused ecological devastation in the Southern Urals¹.

Access options

Subscribe to Journal

Get full journal access for 1 year

\$199.00

only \$3.90 per issue

[Subscribe](#)

All prices are NET prices.

VAT will be added later in the checkout.

Tax calculation will be finalised during checkout.

Rent or Buy article

Get time limited or full article access on ReadCube.

from \$8.99

[Rent or Buy](#)

All prices are NET prices.

Additional access options:

- [Log in](#)
- [Learn about institutional subscriptions](#)

Nature **598**, 388 (2021)

doi: <https://doi.org/10.1038/d41586-021-02756-4>

References

1. 1.

Kiarszys, G. *Camb. Archaeol. J.*
<https://doi.org/10.1017/S0959774321000494> (2021).

This article was downloaded by **calibre** from <https://www.nature.com/articles/d41586-021-02756-4>

- RESEARCH HIGHLIGHT
- 14 October 2021

Finicky no more: ancient snakes ate their way to success

The ancestor of living snakes lived on invertebrates, but its descendants colonized the planet by going gourmet.



A yellow blunt-headed tree snake (*Imantodes inornatus*) dines on frog eggs, one of the many epicurean delights of modern snakes. Credit: John David Curlis ([CC BY 4.0](#))

After the devastating mass extinction that wiped out the dinosaurs, snakes quickly developed a taste for a bountiful array of creatures — helping to give rise to the nearly 4,000 modern-day snake species¹.

Access options

Subscribe to Journal

Get full journal access for 1 year

\$199.00

only \$3.90 per issue

[Subscribe](#)

All prices are NET prices.

VAT will be added later in the checkout.

Tax calculation will be finalised during checkout.

Rent or Buy article

Get time limited or full article access on ReadCube.

from \$8.99

[Rent or Buy](#)

All prices are NET prices.

Additional access options:

- [Log in](#)
- [Learn about institutional subscriptions](#)

Nature **598**, 389 (2021)

doi: <https://doi.org/10.1038/d41586-021-02790-2>

References

1. 1.

Grundler, M. C. & Rabosky, D. L. *PLoS Biol.* **19**, e3001414 (2021).

This article was downloaded by **calibre** from <https://www.nature.com/articles/d41586-021-02790-2>

- RESEARCH HIGHLIGHT
- 11 October 2021

Physicists ‘listen’ to sounds in a fluid of light

Light that flows through a device made of optical fibres behaves like the form of matter called a superfluid.



Optical fibres formed into a mesh (schematic diagram) can induce light to form a superfluid. Credit: M. Wimmer *et al./Phys. Rev. Lett.*

Physicists have built a new kind of device for coaxing light to act like a superfluid — a fluid at very low temperatures that can flow without any internal friction¹.

Access options

Subscribe to Journal

Get full journal access for 1 year

\$199.00

only \$3.90 per issue

[Subscribe](#)

All prices are NET prices.

VAT will be added later in the checkout.

Tax calculation will be finalised during checkout.

Rent or Buy article

Get time limited or full article access on ReadCube.

from \$8.99

[Rent or Buy](#)

All prices are NET prices.

Additional access options:

- [Log in](#)
- [Learn about institutional subscriptions](#)

Nature **598**, 389 (2021)

doi: <https://doi.org/10.1038/d41586-021-02643-y>

References

1. 1.

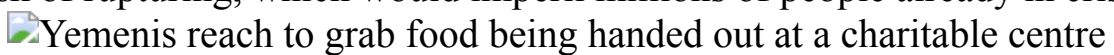
Wimmer, W., Monika, M., Carusotto, I., Peschel, U. & Price, H. M.
Phys. Rev. Lett. **127**, 163901 (2021).

This article was downloaded by **calibre** from <https://www.nature.com/articles/d41586-021-02643-y>

- RESEARCH HIGHLIGHT
- 12 October 2021

The ticking time bomb anchored off war-torn Yemen

A derelict oil tanker in the waters of the Middle Eastern nation is at high risk of rupturing, which would imperil millions of people already in crisis.



Food aid in Yemen, where millions live on the brink of starvation, could be severely curtailed if a rusting tanker anchored off the coast spills its cargo.
Credit: Mohammed Hamoud/Getty

A few kilometres off the Yemeni coast lies an abandoned oil tanker that has long aroused fears of a catastrophe: it could crack or explode at any time, and would release more than four times the amount of oil leaked by the *Exxon Valdez* in 1989. Modelling work shows that such a spill would endanger the lives of millions¹.

Access options

Subscribe to Journal

Get full journal access for 1 year

\$199.00

only \$3.90 per issue

[Subscribe](#)

All prices are NET prices.
VAT will be added later in the checkout.
Tax calculation will be finalised during checkout.

Rent or Buy article

Get time limited or full article access on ReadCube.

from \$8.99

[Rent or Buy](#)

All prices are NET prices.

Additional access options:

- [Log in](#)
- [Learn about institutional subscriptions](#)

Nature **598**, 389 (2021)

doi: <https://doi.org/10.1038/d41586-021-02784-0>

References

1. 1.

Huynh, B. Q. *et al.* *Nature Sustain.* <https://doi.org/10.1038/s41893-021-00774-8> (2021).

This article was downloaded by **calibre** from <https://www.nature.com/articles/d41586-021-02784-0>

News in Focus

- **[Viral filter, outbreak investigation reboot and the Economics Nobel](#)** [20 October 2021]
News Round-Up • The latest science news, in brief.
- **[COVID super-immunity: one of the pandemic's great puzzles](#)** [14 October 2021]
News • People who have previously recovered from COVID-19 have a stronger immune response after being vaccinated than those who have never been infected. Scientists are trying to find out why.
- **[Why easing COVID restrictions could prompt a fierce flu rebound](#)** [07 October 2021]
News • As pandemic restrictions ease, other respiratory viruses are returning in unexpected ways.
- **[Chilean researchers unhappy following investigation of star neuroscientist](#)** [13 October 2021]
News • Committee found that University of Chile neuroscientist Claudio Hetz did not deliberately alter published images — but some researchers fear his practices set a poor precedent.
- **[Burnt seeds show people used tobacco 12,000 years ago](#)** [13 October 2021]
News • The earliest evidence that Stone Age hunter-gatherers chewed or smoked the plant have been discovered among the remains of an ancient fire.
- **[China's COVID vaccines have been crucial — now immunity is waning](#)** [14 October 2021]
News • Billions of shots of China's CoronaVac and Sinopharm vaccines have been given globally, but studies have questioned the length of protection they offer.
- **[The broken \\$100-billion promise of climate finance — and how to fix it](#)** [20 October 2021]
News Feature • At Glasgow's COP26 summit, countries will argue for more money to mitigate and adapt to the effects of climate change.
- **[Why fossil fuel subsidies are so hard to kill](#)** [20 October 2021]

News Feature • Behind the struggle to stop governments propping up the coal, oil and gas industries.

| [Next section](#) | [Main menu](#) | [Previous section](#) |

- NEWS ROUND-UP
- 20 October 2021

Viral filter, outbreak investigation reboot and the Economics Nobel

The latest science news, in brief.



Highly efficient devices called HEPA filters (right) successfully remove coronavirus particles from the air.Credit: Getty

Real-world data show filters clean SARS-CoV-2 from air

Research at a UK hospital suggests that [portable filters effectively remove SARS-CoV-2 virus particles from the air](#) — the first such evidence from a real-world setting ([A. Conway-Morris et al. Preprint at medRxiv https://doi.org/gm3hkf; 2021](#)).

Earlier experiments that tested air filters' performance assessed their ability to remove inactive particles in carefully controlled environments. As a result, "what was not known was how effective they would be in a real-world ward setting for clearing SARS-CoV-2", says study co-author Vilas Navapurkar, a physician at Addenbrooke's Hospital in Cambridge, UK.

To determine how high-efficiency particulate air (HEPA) filters stand up to real-world conditions, Navapurkar and his co-authors installed them in two fully occupied COVID-19 wards. They collected air samples from the wards during a week when the filters were switched on and two weeks when they were off.

In one ward, the team found SARS-CoV-2 particles in the air when the filter was off, but not when it was on. And on both wards, the filters removed other pathogens, such as *Staphylococcus aureus* and *Escherichia coli*. The results, which have not been peer reviewed, indicate that HEPA filters might be an affordable way to reduce COVID-19 transmission in hospitals.



Outbreak investigations often involve sampling bats and other animals for deadly viruses that spillover into humans. Credit: Andre

Malerba/Bloomberg/Getty

WHO names researchers to reboot outbreak origin investigations

The World Health Organization (WHO) has selected [26 scientists to oversee a fresh investigation into the origins of the COVID-19 pandemic](#), and into future outbreaks of emerging diseases. The organization plans to officially appoint all or most of them soon after a two-week period of public review.

With the launch of its Scientific Advisory Group for the Origins of Novel Pathogens (SAGO), the WHO has revamped its approach to outbreaks, which previously involved researchers unravelling the origins of epidemics as the need arises. Shortcomings in that approach have become clear as the origin of the COVID-19 pandemic remains unknown nearly two years after it began.

“This topic requires a lot of technical expertise, so I’m glad to see that the WHO has selected serious people with enough research background to understand the work that may be required to investigate the origins of outbreaks,” says Gigi Gronvall, a biosecurity researcher at Johns Hopkins University in Baltimore, Maryland, who is not involved with SAGO.

The WHO says the group will advise on further information required to uncover where the coronavirus SARS-CoV-2 came from. Some SAGO members might be involved in the next phase of the COVID-19 origins investigation in China, and perhaps in other countries — indeed, 6 of them were part of the first team of 34 researchers on a WHO-organized mission that wrapped up in March. SAGO is also tasked with developing a framework to guide investigations into the start of epidemics more generally, such as defining what data to collect (for instance, from animals such as bats, pictured above).

Maria Van Kerkhove, who heads the WHO’s emerging-diseases unit and helped to design SAGO, says the organization selected the 26 unpaid advisers from more than 700 applicants. They all hail from different countries, and have expertise ranging from biosafety to wildlife biology.

“Next time an outbreak is declared, the secretariat can pull this committee together,” she says, and ask for advice on what information researchers should collect immediately.

Once the panel’s membership is confirmed, the group will take stock of what’s already known about the origins of COVID-19, and outline next steps.

Economics Nobel rewards ‘credibility revolution’

The ‘natural experiments’ approach to economics that won three researchers the 2021 Sveriges Riksbank Prize in Economic Sciences has helped to make the field more robust, say economists.

Joshua Angrist at the Massachusetts Institute of Technology in Cambridge, Guido Imbens at Stanford University in California and David Card at the University of California, Berkeley, [received the award](#) for work that shows how causation can be inferred from observational data in real-world natural experiments. Their work has been used to examine, for example, how differences in the minimum wage affect jobs and businesses; and the economic impacts of immigration.

The award came as a “complete surprise”, Card told *Nature*. “I thought that there are many very deserving alternatives.”

Understanding cause and effect in social science is hampered because controlled experiments — such as randomized controlled trials — are not always practically or ethically possible. But economics has undergone “a credibility revolution”, says macroeconomist Lisa Cook at Michigan State University in East Lansing, “and these folks were central to it”.

Nature **598**, 391 (2021)

doi: <https://doi.org/10.1038/d41586-021-02845-4>

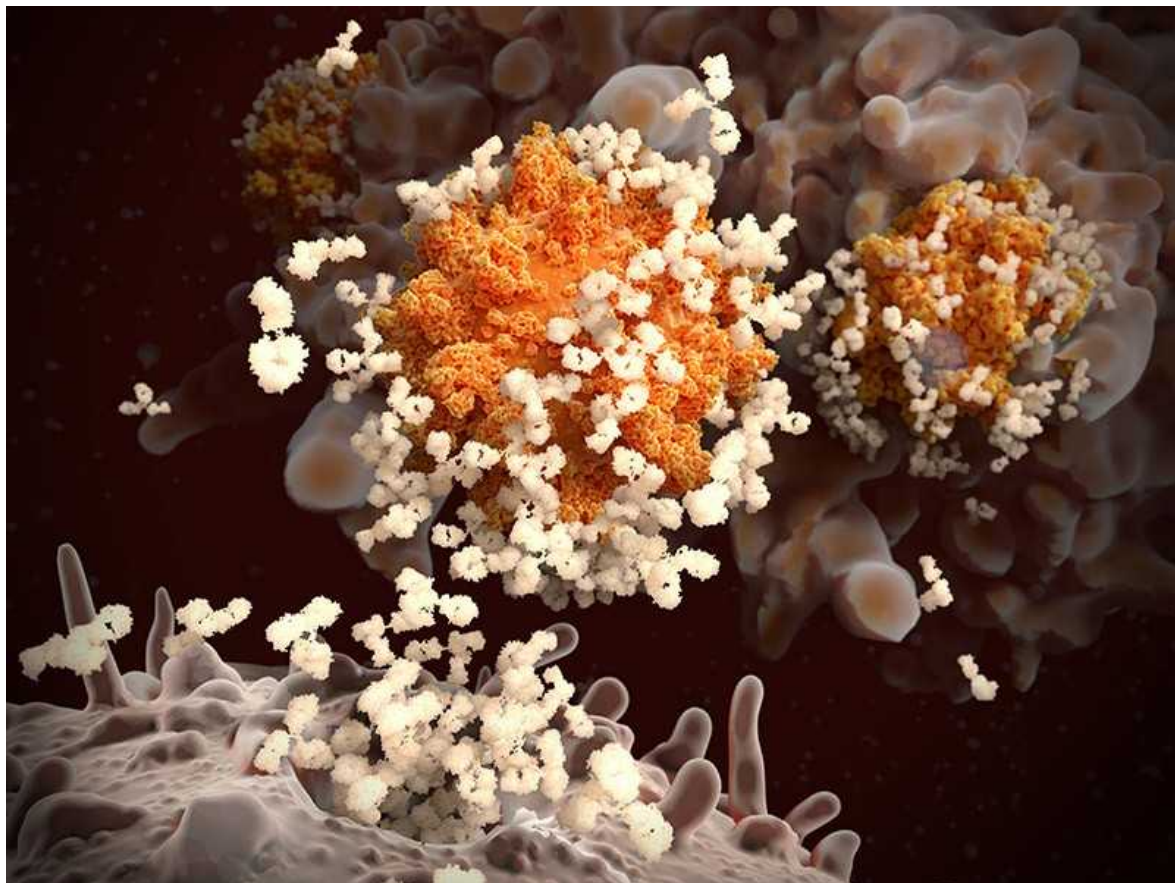
| [Section menu](#) | [Main menu](#) |

- NEWS
- 14 October 2021

COVID super-immunity: one of the pandemic's great puzzles

People who have previously recovered from COVID-19 have a stronger immune response after being vaccinated than those who have never been infected. Scientists are trying to find out why.

- [Ewen Callaway](#)



Antibodies responding to SARS-CoV-2 particles (illustration). Researchers are investigating heightened immune responses in people who are vaccinated after recovering from COVID-19. Credit: Juan Gaertner/Science Photo Library

Around a year ago — before Delta and other variants entered the COVID-19 lexicon — virologists Theodora Hatzioannou and Paul Bieniasz, both at the Rockefeller University in New York City, set out to make a version of a key SARS-CoV-2 protein with the ability to dodge all the infection-blocking antibodies our body makes.

The goal was to identify the parts of spike — the protein SARS-CoV-2 uses to infect cells — that are targeted by these neutralizing antibodies in order to map a key part of our body's attack on the virus. So the researchers mixed and matched potentially concerning mutations identified in lab experiments and circulating viruses, and tested their Franken-spikes in harmless ‘pseudotype’ viruses incapable of causing COVID-19. In a study published this September in *Nature*¹, they reported that a spike mutant containing 20 changes was fully resistant to neutralizing antibodies made by most of the people tested who had been either infected or vaccinated — but not to everyone’s.



[Kids and COVID: why young immune systems are still on top](#)

Those who had recovered from COVID-19 months before receiving their jabs harboured antibodies capable of defanging the mutant spike, which displays much more resistance to immune attack than any known naturally occurring variant. These peoples' antibodies even blocked other types of coronaviruses. "It's very likely they will be effective against any future variant that SARS-CoV-2 throws against them," says Hatzioannou.

As the world watches out for new coronavirus variants, the basis of such 'super-immunity' has become one of the pandemic's great mysteries. Researchers hope that, by mapping the differences between the immune protection that comes from infection compared with that from vaccination, they can chart a safer path to this higher level of protection.

"It has implications on boosters and how our immune responses are primed for the next variant that emerges," says Mehul Suthar, a virologist at Emory University in Atlanta, Georgia. "We're flying by the seat of our pants trying to figure this stuff out."

Hybrid immunity

Not long after countries began rolling out vaccines, researchers started noticing unique properties of the vaccine responses of people who had previously caught and recovered from COVID-19. "We saw that the antibodies come up to these astronomical levels that outpace what you get from two doses of vaccine alone," says Rishi Goel, an immunologist at the University of Pennsylvania in Philadelphia who is part of a team studying super-immunity — or 'hybrid immunity', as most scientists call it.

Initial studies of people with hybrid immunity found that their serum — the antibody-containing portion of blood — was far better able to neutralize immune-evading strains, such as the Beta variant identified in South Africa, and other coronaviruses, compared with 'naive' vaccinated individuals who had never encountered SARS-CoV-2². It wasn't clear whether this was just due to the high levels of neutralizing antibodies, or to other properties.

The most recent studies suggest that hybrid immunity is, at least partly, due to immune players called memory B cells. The bulk of antibodies made after

infection or vaccination come from short-lived cells called plasmablasts, and antibody levels fall when these cells inevitably die off. Once plasmablasts are gone, the main source of antibodies becomes much rarer memory B cells that are triggered by either infection or vaccination.



[International COVID-19 trial to restart with focus on immune responses](#)

Some of these long-lived cells make higher-quality antibodies than plasmablasts, says Michel Nussenzweig, an immunologist at the Rockefeller. That's because they evolve in organs called lymph nodes, gaining mutations that help them to bind more tightly to the spike protein over time. When people who recovered from COVID-19 are re-exposed to SARS-CoV-2's spike, these cells multiply and churn out more of these highly potent antibodies.

“You get a sniff of antigen, in this case of mRNA vaccine, and those cells just explode,” says Goel. In this way, a first vaccine dose in someone who has previously been infected is doing the same job as a second dose in someone who has never had COVID-19.

Potent antibodies

Differences between the memory B cells triggered by infection and those triggered by vaccination — as well as the antibodies they make — might also underlie the heightened responses of hybrid immunity. Infection and vaccination expose the spike protein to the immune system in vastly different ways, Nussenzweig says.

In a series of studies^{3,4,5}, Nussenzweig's team, which includes Hatzioannou and Bieniasz, compared the antibody responses of infected and vaccinated people. Both lead to the establishment of memory B cells that make antibodies that have evolved to become more potent, but the researchers suggest this occurs to a greater extent after infection.

The team isolated hundreds of memory B cells — each making a unique antibody — from people at various time points after infection and vaccination. Natural infection triggered antibodies that continued to grow in potency and their breadth against variants for a year after infection, whereas most of those elicited by vaccination seemed to stop changing in the weeks after a second dose. Memory B cells that evolved after infection were also more likely than those from vaccination to make antibodies that block immune-evading variants such as Beta and Delta.



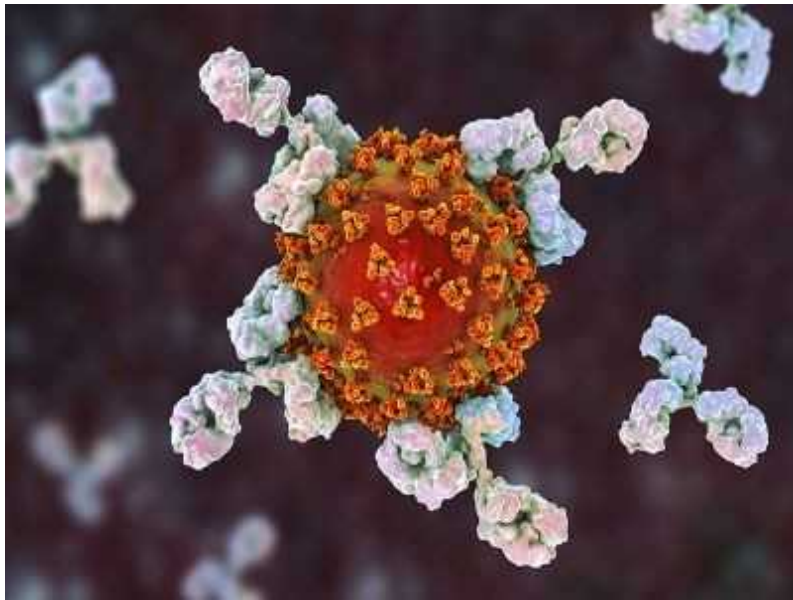
Health-care workers receiving the Pfizer–BioNTech COVID-19 vaccine. People who get the vaccine after infection are less likely to test positive for COVID-19 than individuals with no history of infection. Credit: Paula Bronstein/Getty

A separate study found that, compared with mRNA vaccination, infection leads to a pool of antibodies that recognize variants more evenly by targeting diverse regions of spike⁶. The researchers also found that people with hybrid immunity produced consistently higher levels of antibodies, compared with never-infected vaccinated people, for up to seven months. Antibody levels were also more stable in people with hybrid immunity, reports the team led by immunologist Duane Wesemann at Harvard Medical School in Boston, Massachusetts.

‘Not surprising’

Many studies of hybrid immunity haven’t followed naive vaccine recipients for as long as those who recovered from COVID-19, and it’s possible their B cells will make antibodies that gain potency and breadth with more time, additional vaccine doses, or both, researchers say. It can take months for a stable pool of memory B cells to establish itself and mature.

“It’s not surprising that people infected and vaccinated are getting a nice response,” says Ali Ellebedy, a B-cell immunologist at Washington University in St. Louis, Missouri. “We are comparing someone who started the race three to four months ago to someone who started the race now.”



COVID vaccine immunity is waning — how much does that matter?

There is some evidence that people who received both jabs without previously being infected seem to be catching up. Ellebedy's team collected lymph-node samples from mRNA-vaccinated individuals and found signs that some of their memory B cells triggered by the vaccination were gaining mutations, up to 12 weeks after the second dose, that enabled them to recognize diverse coronaviruses, including some that cause common colds⁷.

Goel, University of Pennsylvania immunologist John Wherry and their colleagues found signs that six months after vaccination, memory B cells from naive individuals were continuing to grow in number and evolve greater capacity to neutralize variants⁸. Antibody levels fell after vaccination, but these cells should start cranking out antibodies if they encounter SARS-CoV-2 again. “The reality is you have a pool of high-quality memory B cells that are there to protect you if you ever see this antigen again,” Goel says.

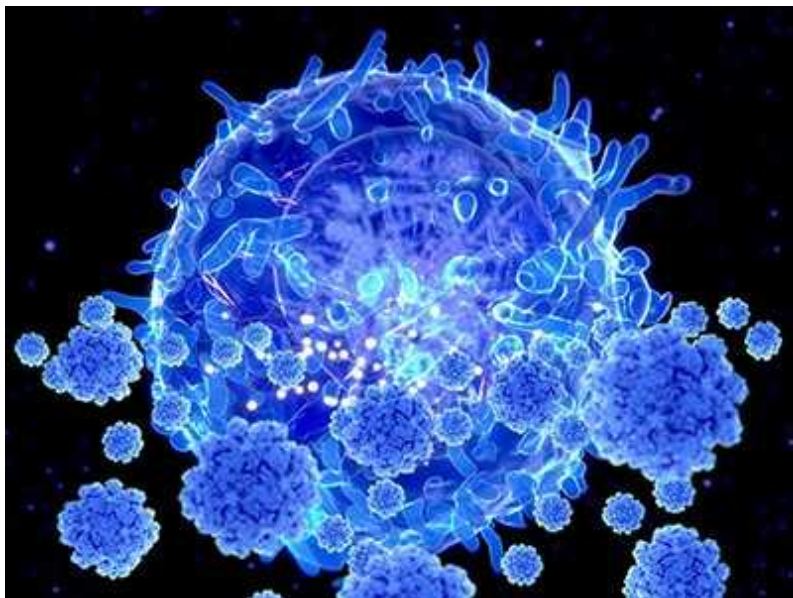
Booster benefits

A third vaccine dose might allow people who haven't been infected to achieve the benefits of hybrid immunity, says Matthieu Mahévas, an immunologist at the Necker Institute for Sick Children in Paris. His team

found that some of the memory B cells from naive vaccine recipients could recognize Beta and Delta, two months after vaccination⁹. “When you boost this pool, you can clearly imagine you will generate potent neutralizing antibodies against variants,” Mahévas says.

Extending the interval between vaccine doses could also mimic aspects of hybrid immunity. In 2021, amid scarce vaccine supplies and a surge in cases, officials in the Canadian province of Quebec recommended a 16-week interval between first and second doses (since reduced to 8 weeks).

A team co-led by Andrés Finzi, a virologist at the University of Montreal, Canada, found that people who received this regimen had SARS-CoV-2 antibody levels similar to those in people with hybrid immunity¹⁰. These antibodies could neutralize a swathe of SARS-CoV-2 variants — as well as the virus behind the 2002–04 SARS epidemic. “We are able to bring naive people to almost the same level as previously infected and vaccinated, which is our gold standard,” says Finzi.



How ‘killer’ T cells could boost COVID immunity in face of new variants

Understanding the mechanism behind hybrid immunity will be key to emulating it, say scientists. The latest studies focus on antibody responses made by B cells, and it’s likely that T-cell responses to vaccination and infection behave differently. Natural infection also triggers responses against

viral proteins other than spike — the target of most vaccines. Nussenzweig wonders whether other factors unique to natural infection are crucial. During infection, hundreds of millions of viral particles populate the airways, encountering immune cells that regularly visit nearby lymph nodes, where memory B cells mature. Viral proteins stick around in the gut of some people months after recovery, and it's possible that this persistence helps B cells hone their responses to SARS-CoV-2.

Researchers say that it is also important to determine the real-world effects of hybrid immunity. A study from Qatar suggests that people who get Pfizer–BioNTech's mRNA vaccine after infection are less likely to test positive for COVID-19 than are individuals with no history of infection¹¹. Hybrid immunity might also be responsible for falling case numbers across South America, says Gonzalo Bello Bentancor, a virologist at the Oswaldo Cruz Institute in Rio de Janeiro, Brazil. Many South American countries experienced very high infection rates earlier in the pandemic, but have now vaccinated a large proportion of their populations. It's possible that hybrid immunity is better than the immunity from vaccination alone at blocking transmission, says Bello Bentancor.

As breakthrough infections caused by the Delta variant stack up, researchers including Nussenzweig are keen to study the immunity in people who were infected after their COVID-19 vaccinations, rather than before. An individual's first exposure to influenza virus biases their responses to subsequent exposures and vaccinations — a phenomenon called original antigenic sin — and researchers want to know if this occurs with SARS-CoV-2.

Those studying hybrid immunity stress that — whatever the potential benefits — the risks of a SARS-CoV-2 infection mean that it should be avoided. “We are not inviting anybody to get infected and then vaccinated to have a good response,” says Finzi. “Because some of them will not make it through.”

Nature **598**, 393–394 (2021)

doi: <https://doi.org/10.1038/d41586-021-02795-x>

References

1. 1.
Schmidt, F. *et al.* *Nature* <https://doi.org/10.1038/s41586-021-04005-0> (2021).
2. 2.
Stamatatos, L. *et al.* *Science* **372**, 1413–1418 (2021).
3. 3.
Gaebler, C. *et al.* *Nature* **591**, 639–644 (2021).
4. 4.
Wang, Z. *et al.* *Nature* **595**, 426–431 (2021).
5. 5.
Cho, A. *et al.* *Nature* <https://doi.org/10.1038/s41586-021-04060-7> (2021).
6. 6.
Chen, Y. *et al.* Preprint at bioRxiv
<https://doi.org/10.1101/2021.09.09.459504> (2021).
7. 7.
Turner, J. S. *et al.* *Nature* **596**, 109–113 (2021).
8. 8.
Goel, R. R. *et al.* *Science* <https://doi.org/10.1126/science.abm0829> (2021).
9. 9.

Sokal, A. *et al.* *Immunity* <https://doi.org/10.1016/j.immuni.2021.09.011> (2021).

10. 10.

Tauzin, A. *et al.* Preprint at medRxiv
<https://doi.org/10.1101/2021.09.17.21263532> (2021).

11. 11.

Abu-Raddad, L. J. *et al.* Preprint at medRxiv
<https://doi.org/10.1101/2021.07.25.21261093> (2021).

This article was downloaded by **calibre** from <https://www.nature.com/articles/d41586-021-02795-x>

| [Section menu](#) | [Main menu](#) |

- NEWS
- 07 October 2021

Why easing COVID restrictions could prompt a fierce flu rebound

As pandemic restrictions ease, other respiratory viruses are returning in unexpected ways.

- [Nicola Jones](#) ⁰



Influenza and other respiratory viruses were suppressed by measures intended to curb COVID. Credit: Shutterstock

The COVID-19 pandemic is continuing to have unusual and unexpected effects on a number of respiratory diseases — some have been quashed, others have ploughed through and still more are rebounding off-season. These fluxes are complicating medical responses to the pandemic, but also providing scientists with an opportunity to study how these viruses spread.

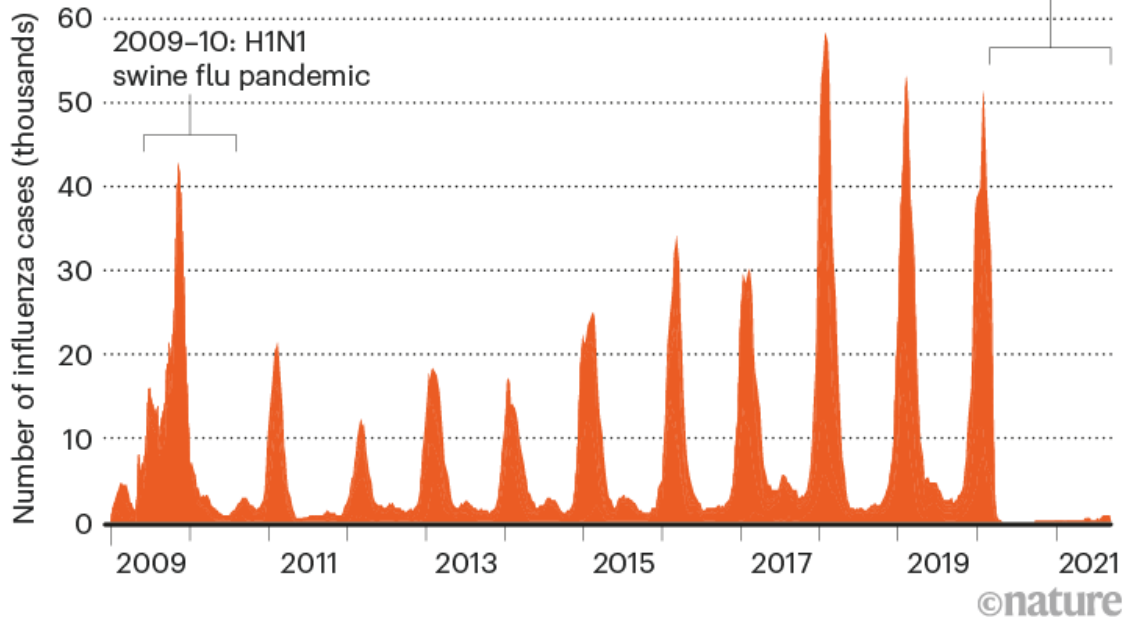
As cold-and-flu season ostensibly starts in the Northern Hemisphere, researchers warn to expect the unexpected. “If anyone tells you they know, they don’t know,” says epidemiologist John Paget at the Netherlands Institute for Health Services Research in Utrecht. Most agree that influenza will eventually rebound, possibly fiercely, as travel restrictions and societal interventions designed to curb the coronavirus, such as mask wearing, wane. “Once we let our good health practices lapse, then flu is likely to hit hard,” says Robert Ware, a clinical epidemiologist at Griffith University in Queensland, Australia.

Seasonal flu typically kills 290,000–650,000 people a year worldwide. But for most of 2020 and 2021, it practically vanished from much of the globe. FluNet, a tool for tracking global virological data on influenza maintained by the World Health Organization, shows that the proportion of positive flu tests has remained roughly flat since April 2020, despite increased surveillance (see ‘Viral shift’).

VIRAL SHIFT

Measures to curb the spread of COVID-19 sharply reduced cases of influenza, but researchers expect it to rebound eventually.

2020–21:
COVID-19
pandemic



Source: World Health Organization

Flu break

The United States recorded just 646 flu deaths in the 2020–21 season — the annual average is in the tens of thousands — and there was only one paediatric flu death. Australia has had no seasonal influenza deaths so far in 2021, compared with between 100 and 1,200 in previous years.

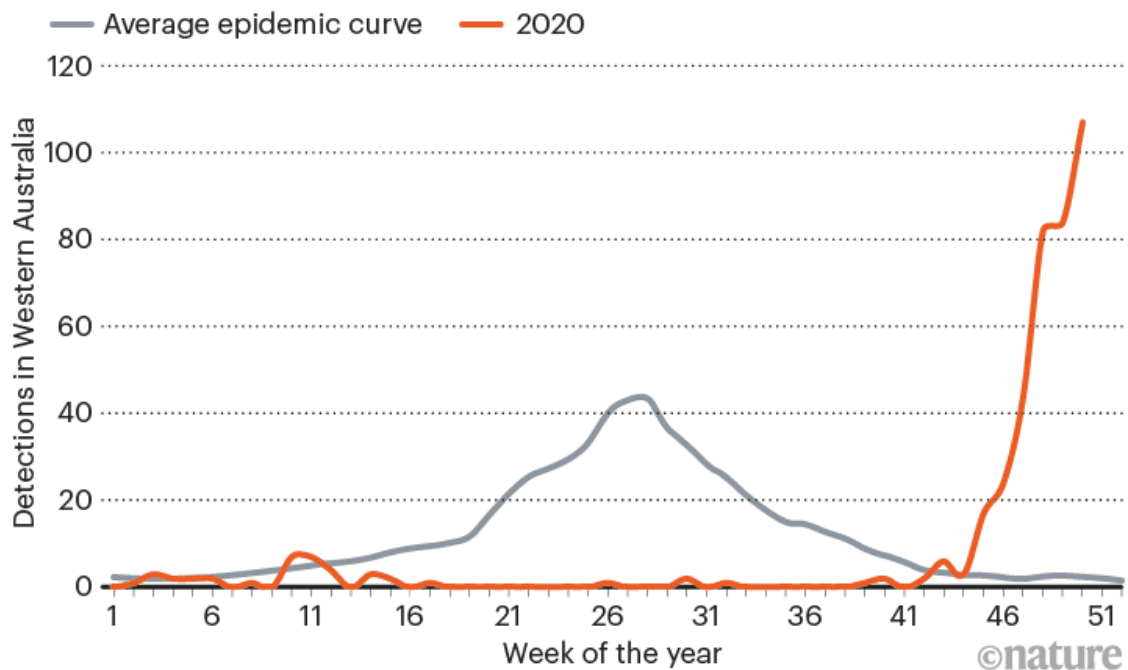
The decline in flu has persisted despite the variable lifting of social interventions to curb coronavirus. This hammers home the importance of international travel in bringing flu to any given country, says Richard Webby at St. Jude Children's Research Hospital in Memphis, Tennessee. "It says a lot about seeding events and how important they are," he says. Flu has continued to circulate at low levels in the tropics, researchers note, so will probably spread from there once borders reopen.

Pandemic response measures also seem to have suppressed some bacterial infections, including those that cause pneumonia and meningitis and are associated with sepsis¹. But some viruses [have behaved differently](#). Rhinoviruses, for example, a major cause of the common cold, continued to spread throughout the pandemic, and infections even shot up in some countries², possibly because these viruses aren't as susceptible as many others to measures such as surface cleaning and hand washing, and because they faced little competition from other respiratory viruses. There is emerging evidence that these mild viruses might protect people from more serious diseases during infection^{3,4}.

And some typical winter viruses have bounced back out of season. Infections caused by common human coronaviruses (another major common-cold culprit) and parainfluenza viruses were at very low levels in the United States in 2020 but started to rise to pre-pandemic levels in spring 2021 — an unusual time for colds to hit. Likewise, infections with respiratory syncytial virus (RSV), which usually causes mild cold symptoms but is also responsible for about 5% of deaths in children under 5 worldwide, were at a historic low for a year and then started rising months later than usual, in April 2021. RSV infections were [still climbing at the end of August](#) (see 'Strong rebound').

STRONG REBOUND

Infections with respiratory syncytial virus (RSV) reached historic lows in 2020 amid COVID restrictions. But they rebounded intensely in countries including Australia when these measures were eased.



Source: Foley, D. A. *et al. Clin. Infect. Dis.* <http://doi.org/10.1093/cid/ciaa1906> (2021).

Off-season peaks

The strangely timed bumps might be related to school reopenings, according to a report from the US Centers for Disease Control and Prevention (CDC)⁵, along with a build-up of susceptible, unexposed infants in the absence of a vaccine ([RSV vaccines](#) are under development).

Off-season RSV peaks have been seen elsewhere, too, in countries including South Africa, Japan, Australia and the Netherlands. In Western Australia, an RSV peak in December 2020 was 2.5 times larger than the July peak for 2019⁶. A steep onset of disease doesn't necessarily translate to more cases overall, however: the total number of RSV cases in Queensland was lower

than usual, Ware notes, “but because all the cases came close together it was much more intense”, putting strain on health resources.

It would be worrying to see rebound effects caused by a build-up of immunologically naive people in seasonal flu, researchers caution. Around the world, there are signs of circulating H3N2, H1N1 and B influenza viruses, says Amber Winn, an epidemiologist in the CDC’s Division of Viral Diseases in Atlanta, Georgia. A wave of influenza B infections in winter 2019–20, she notes, contributed to a record number of paediatric flu deaths that season. “That’s why getting your flu vaccine this season may be especially important,” she says.

Nature **598**, 395 (2021)

doi: <https://doi.org/10.1038/d41586-021-02558-8>

References

1. 1.

Brueggemann, A. B. *et al.* *Lancet Digital Health* **3**, E360–E370 (2021).

2. 2.

Takashita, E. *et al.* *Influenza Other Respir. Viruses* **15**, 488–494 (2021).

3. 3.

Van Leuven, J. T. *et al.* Preprint at bioRxiv
<https://doi.org/10.1101/2020.11.06.371005> (2021).

4. 4.

Dee, K. *et al.* *J. Infect. Dis.* **224**, 31–38 (2021).

5. 5.

Olsen, S. J. *et al.* *Morbid. Mortal. Weekly Rep.* **70**, 1013–1019 (2021).

6. 6.

Foley, D. A. *et al. Arch. Dis. Child.*
<https://doi.org/10.1136/archdischild-2021-322507> (2021).

This article was downloaded by **calibre** from <https://www.nature.com/articles/d41586-021-02558-8>

| [Section menu](#) | [Main menu](#) |

- NEWS
- 13 October 2021
- Update [13 October 2021](#)

Chilean researchers unhappy following investigation of star neuroscientist

Committee found that University of Chile neuroscientist Claudio Hetz did not deliberately alter published images — but some researchers fear his practices set a poor precedent.

- [Emiliano Rodríguez Mega](#)



Claudio Hetz has been cleared of scientific fraud but will implement measures to improve the quality of his group's research. Credit: CONICYT

A high-profile neuroscientist at the University of Chile in Santiago has been found not guilty of scientific fraud — although an investigation revealed that there were altered images in a number of his research publications. Some members of Chile's research community say, in their opinion, that the scientist's actions set a poor example for researchers in the country, and question why his punishment wasn't harsher.



Publishers unite to tackle doctored images in research papers

A committee investigating the case detected “patterns of behaviour that were objectionable and contrary to scientific ethics”, but concluded that there was no evidence that the scientist, Claudio Hetz, had deliberately falsified data to change the conclusions of experiments — a distinction that cleared him of fraud. He's been allowed to keep his job and will continue to run a research group, although it will be downsized and his publications monitored.

The case comes as Chile attempts to correct ethics lapses within its government and society, and [reconcile inequality](#) among its people, including academics, through social and political change. The country is in the process of [rewriting its constitution](#), which dates from the military dictatorship that ended in 1990.

Hetz, whose laboratory studies neurological diseases such as Alzheimer's, is one of the most cited researchers in his field. He is also director of the Biomedical Neuroscience Institute at the University of Chile; he was deputy director from 2011 to 2018 under Andrés Couve Correa, the country's current science minister. Hetz tells *Nature* he accepts full responsibility, but points out that any image manipulations did not ultimately affect his results. "There is no fraud," he says. "The papers are valid."

Manipulations uncovered

The altered images came to light when commenters discussed them on PubPeer, a website for post-publication review. In January this year, science blogger Leonid Schneider wrote about images in more than 20 articles published between 2002 and 2021, some of them when Hetz was a junior scientist in Chile, Switzerland and the United States, and others after he set up his own lab in 2008.



[Meet this super-spotter of duplicated images in science papers](#)

In March, the University of Chile commissioned an advisory committee to investigate his work. The four-person panel, made up of scientists either from Hetz's university, but outside his department, or from independent institutions, analysed 18 of Hetz's papers. [In a ten-page report](#), the committee says that no fraud occurred, but Hetz's actions reveal "an enormous carelessness and lack of rigor". In at least two of his early papers,

Hetz altered images to add or remove cells “for aesthetic reasons”. Committee members also found that images in several recent papers contained “undeclared manipulations”, such as bands or lanes in western blots and electrophoresis gels that were cropped and pasted into different positions.

The committee declined to comment on its findings to *Nature*. “The report speaks for us,” said Patricio Aceituno, an emeritus member of the university’s physical sciences and mathematics department who coordinated the committee, in an e-mail.

The months-long investigation — and the media attention it received in Chile — has personally affected Hetz and his lab members, he says, noting that some of them are still on medical leave owing to mental-health problems that stem from the public exposure and criticism. He acknowledges that the image manipulations shouldn’t have happened, and even though he notes that he did not personally perform some of the experiments in question, he says that, as group leader, he should have noticed and flagged the problems.

Improving lab standards

Some members of Chile’s research community take issue with the investigation’s conclusions, because this isn’t the first time Hetz has been accused of altering published images. In 2012, the University of Chile carried out an investigation after a now-extinct blog suggested that there was evidence of image manipulation in at least six of his papers. That investigation, too, found that Hetz was not guilty of scientific fraud, but that he had committed an abnormally high number of “unintentional” errors. As a result of that incident, Hetz implemented measures to improve lab standards, including a policy to regulate how team members used their research logbooks, and the creation of a lab-wide repository where members could back up each paper’s raw data.



[Chinese ministry investigates duplications in papers by university president](#)

Looking back, however, Hetz sees that these actions “were not enough”. “It’s been super frustrating,” he adds.

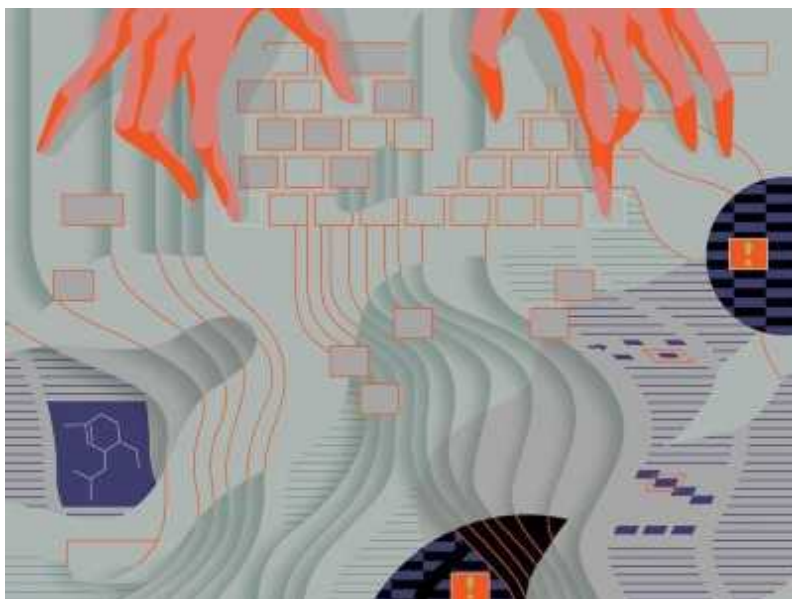
In response to the latest investigation, Hetz says: “Our attitude is to be transparent.” On his [lab website](#) and on PubPeer, he and his co-authors have addressed image modifications in at least 16 papers, providing original data for several more and apologizing for mistakes. He has also requested image corrections at various journals; most editors have accepted them, although some deemed them unnecessary, according to screenshots of e-mails posted on the lab website. Only one image has been retracted.

Hetz tells *Nature* he plans to make changes to his lab, aimed at ensuring his science is “bullet proof”. One measure is to reduce his lab from 21 people to 18 by March next year. The university has put in place an external team of researchers that will review the lab’s results and make sure they’re consistent with the raw data before permitting the team to submit them for publication. The university’s school of medicine, with which Hetz is affiliated, will institute scientific-integrity training for its researchers and students.

A time of transformation

But some Chilean researchers are upset about the outcome. They say Hetz's actions go against scientific practice and ethics, and that the consequences are not harsh enough. "I think he should receive an exemplary sanction" such as temporarily being barred from mentoring new students, says Ximena Báez, a biotechnologist at the Federico Santa María Technical University in Valparaíso, Chile, who is also president of the National Association of Postgraduate Researchers in the country.

For Adriana Bastías, a plant geneticist at the Autonomous University of Chile in Santiago who is also the president of the Chilean Network of Women Researchers, the fact that Hetz was investigated twice and not punished in any significant way, in her view, "means that when you have power, publications, and you are a great scientist, you are not investigated or sanctioned in the same way" as early-career scientists or less prestigious researchers might be. She thinks these people would probably be expelled or suspended.



[The science institutions hiring integrity inspectors to vet their papers](#)

Flavio Salazar, an immunologist and vice-rector for research and development at the University of Chile, who co-commissioned the investigation, acknowledges that the case has caused a fierce debate. He condemns Hetz's actions. But he says the committee's findings must be

upheld, and thinks that having made the report public “generates a kind of moral sanction, which is not minor”.

Others think the case sets a poor precedent, particularly at a time when [journal publishers are trying to rein in the growing problem](#) of image manipulation by issuing guidelines on how to deal with incidents ranging from data “beautification” to fabrication with an intent to mislead. C. K. Gunsalus, a research-integrity specialist at the University of Illinois at Urbana-Champaign, thinks Hetz’s actions damage the education of early-career scientists and undermine trust and accountability in the scientific process. “When someone persists with a pattern of behaviour over a long period of time that results in untrustworthy work, even after an intervention, it is hard from a distance to see that as other than a deliberate set of choices or a reckless disregard for scientific integrity,” says Gunsalus, who read a translated version of the 2021 committee findings at *Nature*’s request.

“I think these are very unfair opinions,” Hetz says. “I actively take action to improve Chilean science.” He says that his lab probably has some of the highest quality standards in the country, and adds that as director of the Biomedical Neuroscience Institute, he has promoted initiatives to improve the use of logbooks and create systems to back up data.



[Science journals crack down on image manipulation](#)

Some scientists worry that the case is emblematic of Chile's current struggles. "What [Hetz] did is absolutely questionable," says Mercedes López Nitsche, a clinical immunologist at the University of Chile. "But we must not forget that this was enabled because, in Chile, we built a society and a culture where ethics is no longer the rule."

For now, Hetz says he's ready to move on. "I'm really tired," he says. "I consider this a closed chapter; now comes a process of learning and improvement."

Nature **598**, 396-397 (2021)

doi: <https://doi.org/10.1038/d41586-021-02682-5>

Updates & Corrections

- **Update 13 October 2021:** This story was updated to include the information that Adriana Bastias is the president of the Chilean Network of Women Researchers.

This article was downloaded by **calibre** from <https://www.nature.com/articles/d41586-021-02682-5>

| [Section menu](#) | [Main menu](#) |

- NEWS
- 13 October 2021

Burnt seeds show people used tobacco 12,000 years ago

The earliest evidence that Stone Age hunter-gatherers chewed or smoked the plant have been discovered among the remains of an ancient fire.

- [Tosin Thompson](#)



Excavations at the site in Utah, where charred tobacco seeds were found among the contents of a 12,300-year-old hearth. Credit: D. Duke *et al.*/*Nat. Hum. Behav.*

Archaeologists have uncovered evidence that hunter-gatherers in North America were using tobacco around 12,300 years ago — 9,000 years earlier than was previously documented.

Tobacco use spread worldwide after contact between European explorers and Indigenous people in North America in the fifteenth century. But researchers debate precisely how and when tobacco plants (*Nicotiana* spp.) were first domesticated.

Now, Daron Duke and his colleagues at the Far Western Anthropological Research Group in Davis, California, have discovered the oldest direct evidence of tobacco use at a hunter-gatherer camp in Utah's West Desert. They published the findings on 11 October in *Nature Human Behaviour*¹.



Ancient genomics is recasting the story of the Americas' first residents

The site lies alongside the now-dry channel of a prehistoric river called the Old River Bed, where people camped 13,000 to 9,500 years ago. While excavating a historical site located within the US Air Force's Utah Test and Training Range, the team found an ancient hearth containing four burnt tobacco-plant seeds.

The researchers used radiocarbon dating to determine how old the hearth and its contents were. The tobacco seeds themselves were too small and fragile to be dated, but the team determined that other burned woody material in the hearth was around 12,300 years old. The charred seeds were presumed to be of a similar age.

Although the team cannot say for certain how the tobacco was used, the fact that only seeds remain implies that the leaves and stems of the tobacco plant — the parts with the intoxicant effect — were consumed. The seeds, which

are small and easily caught in the sticky hairs of the plant, could've been picked up and when the flowering parts were harvested. "People in the Pleistocene likely smoked tobacco or chewed tobacco in a similar fashion to how it's used today," says Jaime Kennedy, an archaeologist at the University of Oregon in Eugene.

Duck bones

Artefacts found in and around the hearth provide context for the find. These include fragments of a Haskett, a spear tip commonly used by roaming hunter-gatherers in North America during the Pleistocene. In this case, the researchers say, it seems to have been used to hunt various species of duck: a large number of waterfowl bones were uncovered at the site.



The scientist-gardener who is harnessing tobacco's power to heal

Duke's team also found charred seeds from other plants traditionally eaten by Native American communities: goosefoot (*Chenopodium* spp.), red maids (*Calandrina* spp.) and hairgrass (*Deschampsia* spp.).

The tobacco seeds were unlikely to have been deposited into the hearth naturally, the researchers say, but they investigated this possibility. The seeds could have come from the hunted ducks' stomachs, or from plants growing

in the vicinity of the hearth. But tobacco grows upland — away from wetlands and typical waterfowl foods. “The birds would have to be away from their natural habitat and eating something that is basically toxic and not palatable,” says Duke. He and his team examined sediments from the area around the time of human occupation. “We found only common wetland plants, not tobacco,” he says.

It is especially interesting that tobacco was found along with seeds from edible plants such as goosefoot, says Kennedy. “This discovery highlights the ancient symbiotic relationship between people and plants like tobacco that flourish in anthropogenically disturbed soils,” she says.

Nature **598**, 397-398 (2021)

doi: <https://doi.org/10.1038/d41586-021-02789-9>

References

1. 1.

Duke, D. *et al.* *Nature Hum. Behav.* <https://doi.org/10.1038/s41562-021-01202-9> (2021).

This article was downloaded by **calibre** from <https://www.nature.com/articles/d41586-021-02789-9>

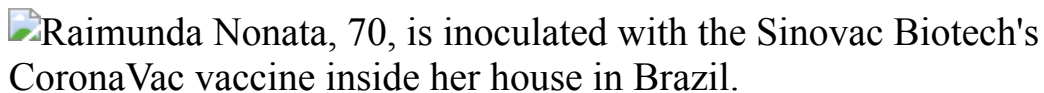
| [Section menu](#) | [Main menu](#) |

- NEWS
- 14 October 2021

China's COVID vaccines have been crucial — now immunity is waning

Billions of shots of China's CoronaVac and Sinopharm vaccines have been given globally, but studies have questioned the length of protection they offer.

- [Smriti Mallapaty](#)



A woman receives a dose of Sinovac's CoronaVac COVID-19 vaccine in Cachoeira do Piriá, Brazil, in January. Credit: Tarso Sarraf/AFP via Getty

China's CoronaVac and Sinopharm vaccines account for almost half of the 7.3 billion COVID-19 vaccine doses delivered globally, and have been enormously important in fighting the pandemic, particularly in less wealthy nations.

But as the doses mount, so have the data, with studies suggesting that the immunity from two doses of either vaccine wanes rapidly, and the protection offered to older people is limited. This week the World Health Organization [announced advice](#) from its Strategic Advisory Group of Experts on Immunization (SAGE) that people over 60 should receive a third dose of the same or another vaccine to ensure sufficient protection.



China's COVID vaccines are going global — but questions remain

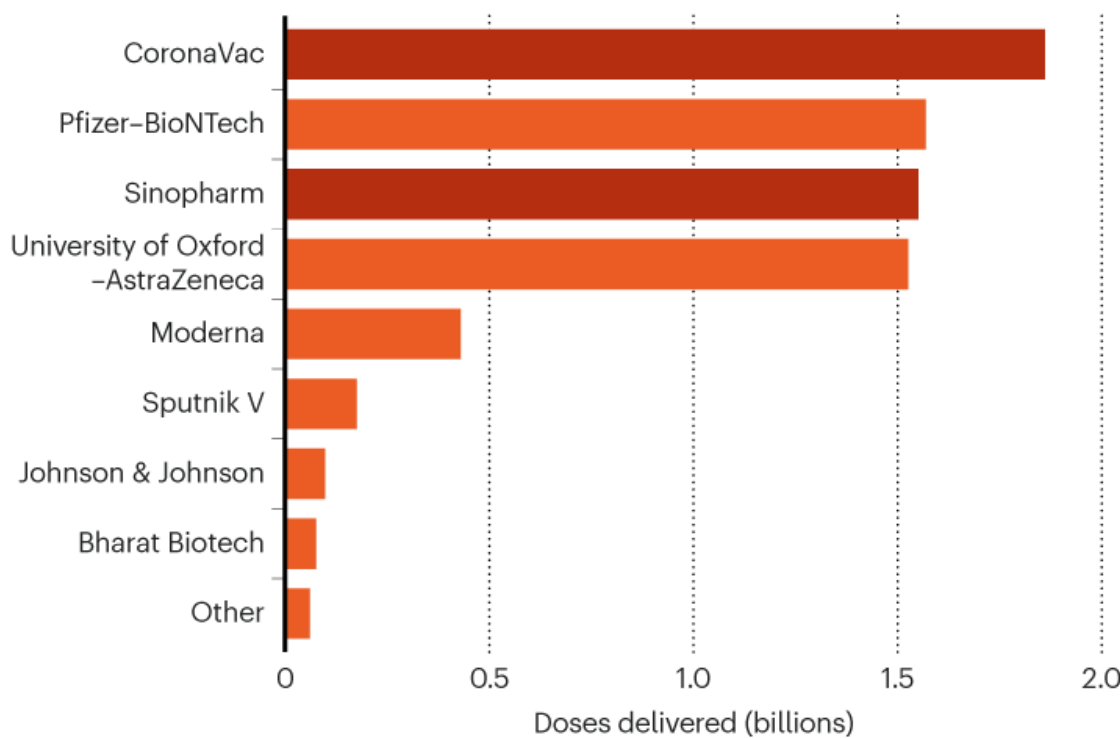
The recommendation is “sensible and necessary”, says Manoel Barral-Netto, an immunologist at the Oswaldo Cruz Foundation in Salvador, Brazil.

A number of countries are already offering [third doses](#) to all adults or are trying [mix-and-match](#) approaches. Some experts are even questioning whether China’s jabs — based on inactivated virus — should continue to be used at all when other options are available.

But others say that the vaccines still have a major part to play. “These are not bad vaccines. They’re just vaccines that haven’t been optimized yet,” says Gagandeep Kang, a virologist at the Christian Medical College in Vellore, India, who advises SAGE.

THE RACE TO VACCINATE

Out of the eight vaccines that account for the vast majority of COVID-19 vaccine doses delivered globally, China's CoronaVac and Sinopharm jabs account for nearly half of all doses.



©nature

Source: Data from Airfinity.

Inactivated vaccines

CoronaVac, produced by Beijing-based company Sinovac, is the world's most widely used COVID-19 vaccine. Not far behind is the vaccine developed in Beijing by state-owned Sinopharm (see 'The race to vaccinate').

In mid-2021, the World Health Organization (WHO) [approved the shots](#) for emergency use, on the basis of limited clinical-trial data suggesting that [CoronaVac](#) was 51% and Sinopharm 79% effective at preventing symptomatic disease. This was on a par with the 63% efficacy reported for the University of Oxford–AstraZeneca's viral-vector vaccine at the time of

its WHO listing, but lower than the 90% and higher efficacies of the mRNA vaccines developed by Pfizer–BioNTech and Moderna.

Both the Chinese vaccines are inactivated vaccines, which use killed SARS-CoV-2 virus. Researchers say this type of vaccine seems to be less potent because it triggers an immune response against many viral proteins. By contrast, mRNA and viral-vector vaccines target the response to the spike protein, which is what the virus uses to enter human cells.

“You don’t choose the target with inactivated vaccines, you just throw in all these different antigens,” explains Jorge Kalil, a physician and immunologist at the University of São Paulo Medical School, Brazil.

About 2.4 billion doses of the Chinese vaccines have been administered in China, but almost 1 billion doses have gone to 110 other countries (see 'Biggest takers for China's vaccines'). Reports earlier this year of COVID-19 surges in several countries that had vaccinated many people with these vaccines — such as the Seychelles and Indonesia — prompted questions about the protection they offered.

Numerous studies have now been undertaken in nations including Brazil, Chile and Thailand, to understand waning immunity and protection in different groups.



Vials of China's CoronaVac vaccine, ready to be administered in Bangkok. Credit: Lillian Suwanrumpha/AFP via Getty

Lower antibody responses

Some studies have found that compared with vaccines made using other technologies, China's inactivated vaccines initially generate lower levels of 'neutralizing' or virus-blocking antibodies — considered a proxy for protection — and that these levels drop quickly over time.

One study of 185 health-care workers in Thailand¹, not yet peer-reviewed, found that 60% had high levels of neutralizing antibodies one month after receiving a second dose of CoronaVac, compared with 86% of those who had received two shots of the Oxford–AstraZeneca vaccine.

Co-author Opas Putcharoen, an infectious-diseases specialist at the Thai Red Cross Emerging Infectious Diseases Clinical Center in Bangkok, says the team also found that three months after receiving the second CoronaVac shot, the antibody prevalence dropped to just 12%.

But “waning of antibodies isn’t necessarily the same as waning of immune protection”, says Ben Cowling, an epidemiologist at the University of Hong Kong. He says that vaccines induce complex immune responses, including B cells and T cells, which might be more long lived than neutralizing antibodies.

One study from Hong Kong², which has not been peer-reviewed, showed that CoronaVac induces a significantly lower antibody response compared with Pfizer–BioNTech’s mRNA jab one month after two doses, but that the T-cell response was comparable.



[WHO approval of Chinese CoronaVac COVID vaccine will be crucial to curbing pandemic](#)

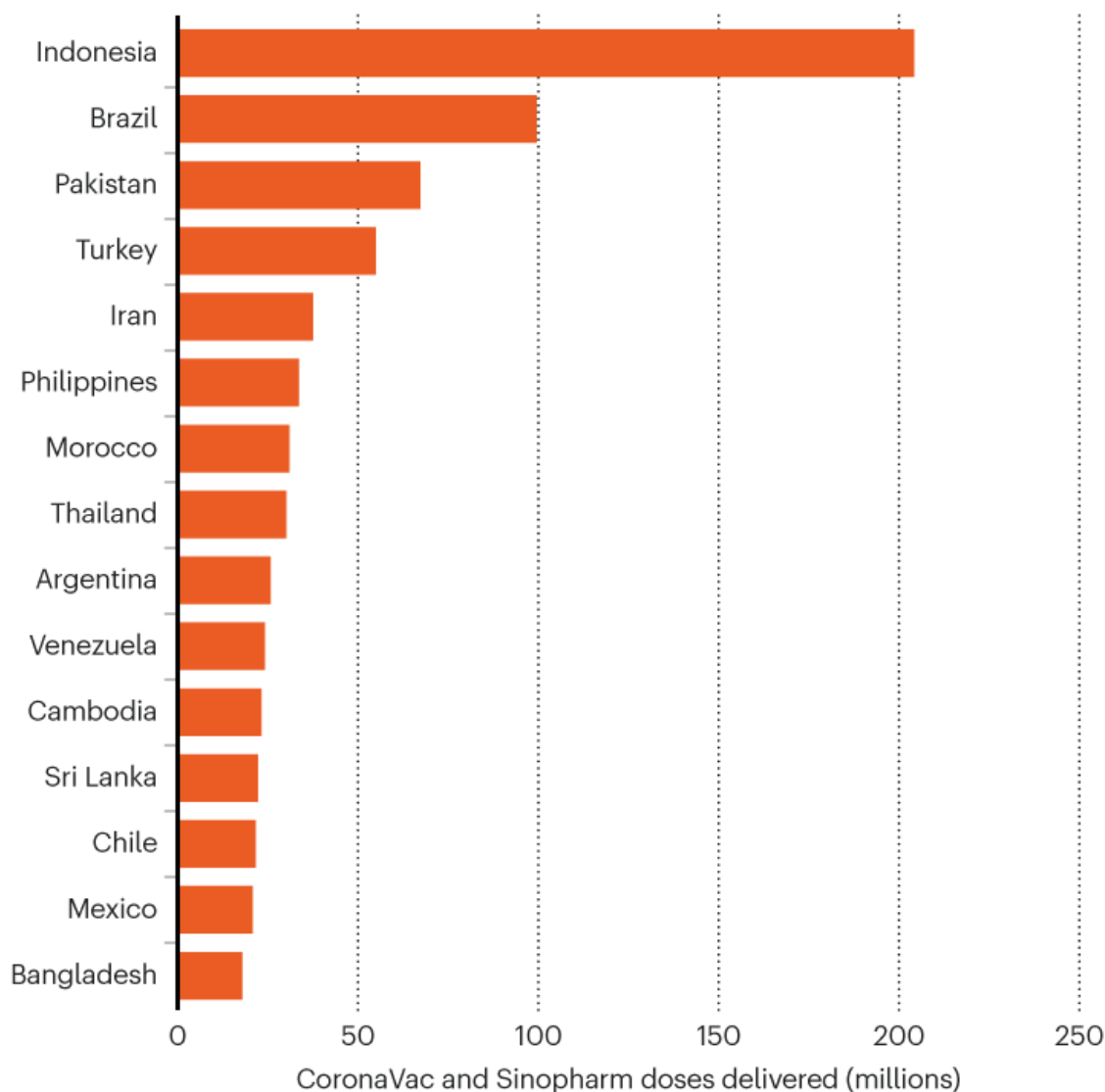
Another non-peer-reviewed study, of health-care workers in China³, also found that B cells and T cells specific for SARS-CoV-2 could be detected five months after two doses of the Sinopharm vaccine.

So far, studies assessing protection over time are limited. But preliminary analysis of a mass-vaccination campaign with CoronaVac in Chile suggests a small but significant decline in efficacy against symptomatic disease, although protection against hospitalization remains high, says Eduardo Undurraga, a public-health researcher at the Pontifical Catholic University of Chile in Santiago.

Vaccines made using other technologies have seen a similar trend of waning antibodies and protection against infection, but more-robust protection against severe disease and death. But researchers say that because the Chinese inactivated vaccines start at a lower base of neutralizing antibodies, the protection they offer could drop faster than those with a stronger head start.

BIGGEST TAKERS FOR CHINA'S VACCINES

More than two billion doses of China's CoronaVac and Sinopharm vaccines have been administered in China, but nearly one billion doses have gone to 110 other nations.



Source: Data from Airfinity.

To boost, or not to boost

The less-potent immune response from inactivated vaccines also has implications for the protection they offer to older people. The immune system weakens with age and vaccines are generally less effective in older people, says Kang, but the effect seems to be more pronounced with the inactivated vaccines.

A massive analysis of some one million people who were hospitalized with COVID-19 in Brazil⁴ found that CoronaVac offered up to 60% protection against severe disease up to the age of 79 — not far off the 76% protection offered by the Oxford–AstraZeneca vaccine.

But the picture changes drastically in people over 80, says co-author Daniel Villela, an epidemiologist at the Oswaldo Cruz Foundation at Rio de Janeiro, Brazil. In that group, CoronaVac was only 30% effective at preventing severe disease and 45% effective against death, compared with 67% and 85%, respectively, for the Oxford–AstraZeneca jab.

Research by Barral-Netto and his colleagues⁵ found that CoronaVac prevented only 33% of deaths due to COVID-19 in people 90 and older. Neither study has been peer-reviewed, but Villela says they influenced Brazil's government to start giving people older than 70 a third shot of an mRNA or viral-vector vaccine in August — that decision has now been extended to people older than 60.

“It was better to receive CoronaVac than nothing,” says Barral-Netto, but now that other vaccines are flowing into Brazil “it is probably not very wise to keep vaccinating people with this vaccine”, he says, adding that the Brazilian government has said it will stop purchasing CoronaVac.

Other countries, including Chile, Abu Dhabi in the United Arab Emirates and China, are also giving booster jabs to those who received the CoronaVac or Sinopharm vaccines.

Clinical-trial data from China⁶, not yet peer-reviewed, suggest that a third dose of CoronaVac increases neutralizing antibody levels, and a similar boost has been observed in studies of third doses of Sinopharm's vaccine.

And earlier this month, the Chilean government reported preliminary results on the effectiveness of booster shots, based on data from some two million people who had received two shots of CoronaVac, and a third shot of the CoronaVac, Pfizer–BioNTech or Oxford–AstraZeneca vaccines. Protection against COVID-19 jumped from 56% after two shots to 80% or higher after a third shot of any vaccine, with protection against hospitalization rising from 84% to 87%.



Health-care workers prepare to give doses of either the CoronaVac or the Oxford–AstraZeneca vaccine at a mass vaccination hub in Bangkok. Credit: Lillian Suwanrumpha/AFP via Getty

Mix and match

Some researchers say an alternative to a three-dose schedule might be to mix and match with just two doses.

Sompong Vongpunsawad, a virologist at Chulalongkorn University in Bangkok, led a team that looked at antibody levels in 54 people who received one dose of CoronaVac and one of Oxford–AstraZeneca. The results⁷, not yet peer-reviewed, suggested that the immune response was similar to two doses of AstraZeneca, and higher than two doses of CoronaVac.

Vongpunsawad says the finding is useful in places where doses of some vaccines are in short supply. “It was like bingo — we can actually solve the vaccine limitation crisis,” he says. The result spurred the Thai government to recommend mix-and-match schedules, he says.



Mix-and-match COVID vaccines: the case is growing, but questions remain

A trial in China also found that using an adenovirus-vector vaccine produced by the Tianjin-based company CanSino Biologics, in addition to one or two doses of CoronaVac, induced higher neutralizing antibody levels, compared with two doses of CoronaVac alone⁸.

It is not yet clear how long that protection will last, and how these antibody levels translate to actual protection, but researchers say such mixing has merit.

“For all vaccines, it’s very much an evolving situation,” says Kang.
“Inactivated vaccines are a big part of our portfolio. So we really need to figure out how to use them.”

Nature **598**, 398-399 (2021)

doi: <https://doi.org/10.1038/d41586-021-02796-w>

References

1. 1.

Jantarabenjakul, W. *et al.* Preprint at medRxiv
<https://doi.org/10.1101/2021.08.27.21262721> (2021).

2. 2.

Ka Pun Mok, C. *et al.* Preprint at SSRN
<https://doi.org/10.2139/ssrn.3884943> (2021).

3. 3.

Liu, Y. *et al.* Preprint at medRxiv
<https://doi.org/10.1101/2021.09.12.21263373> (2021).

4. 4.

Villela, D. A. M. *et al.* Preprint at medRxiv
<https://doi.org/10.1101/2021.09.10.21263084> (2021).

5. 5.

Cerquiera-Silva, T. *et al.* Preprint at medRxiv
<https://doi.org/10.1101/2021.08.21.21261501> (2021).

6. 6.

Li, M. *et al.* Preprint at medRxiv
<https://doi.org/10.1101/2021.08.03.21261544> (2021).

7. 7.

Yorsaeng, R. *et al.* Preprint at medRxiv
<https://doi.org/10.1101/2021.09.01.21262955> (2021).

8. 8.

Li, J. *et al.* Preprint at medRxiv
<https://doi.org/10.1101/2021.09.03.21263062> (2021).

This article was downloaded by **calibre** from <https://www.nature.com/articles/d41586-021-02796-w>

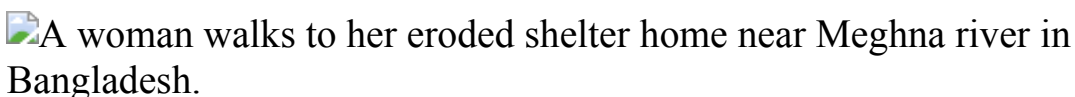
| [Section menu](#) | [Main menu](#) |

- NEWS FEATURE
- 20 October 2021

The broken \$100-billion promise of climate finance — and how to fix it

At Glasgow's COP26 summit, countries will argue for more money to mitigate and adapt to the effects of climate change.

- [Jocelyn Timperley](#)⁰



A damaged temporary home near the Meghna River in Bangladesh, in a coastal area threatened by erosion and rising saltwater levels in soil. Credit: Zakir Hossain Chowdhury/Barcroft Media/Getty

Twelve years ago, at a United Nations climate summit in Copenhagen, rich nations made a significant pledge. They promised to channel US\$100 billion a year to less wealthy nations by 2020, to help them adapt to climate change and mitigate further rises in temperature.

That promise was broken. Figures for 2020 are not yet in, and those who negotiated the pledge don't agree on accounting methods, but a report last year for the UN¹ concluded that "the only realistic scenarios" showed the \$100-billion target was out of reach. "We are not there yet," conceded UN secretary-general António Guterres.

Frustrations at this failure are contributing to rising tensions ahead of next month's crucial COP26 climate summit in Glasgow, UK. "By the time we get to Glasgow, if they haven't given us another \$100 billion [for 2021], then they are completely unable to meet their obligations," says Saleemul Huq,

director of the International Centre for Climate Change and Development in Dhaka.



[Global climate action needs trusted finance data](#)

Compared with the investment required to avoid dangerous levels of climate change, the \$100-billion pledge is minuscule. Trillions of dollars will be needed each year to meet the 2015 Paris agreement goal of restricting global warming to “well below” 2 °C, if not 1.5 °C, above pre-industrial temperatures. And developing nations (as they are termed in the Copenhagen pledge) will need hundreds of billions of dollars annually to adapt to the warming that is already inevitable. “But the \$100 billion is iconic in terms of the good faith of the countries that promised it,” Huq says.

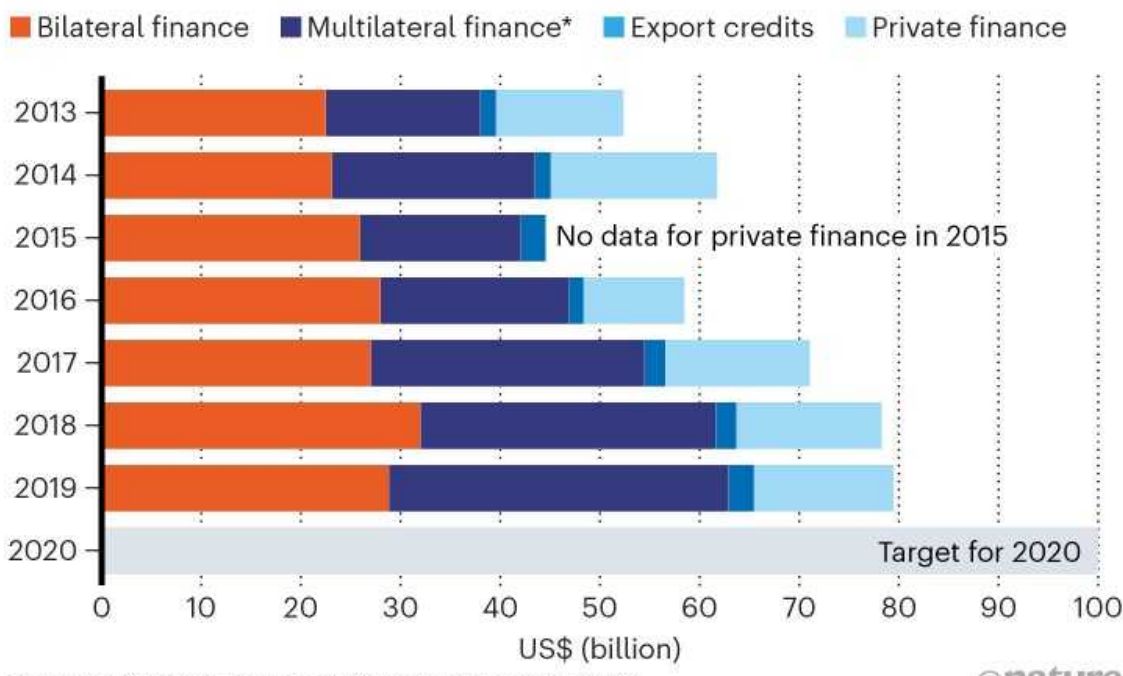
A flurry of pledges just before the Glasgow meeting have led to hopes that, by 2022, rich nations will manage to transfer \$100 billion annually. But negotiators are already looking further ahead: at COP26, discussions will begin on a new climate-finance pledge for the mid-2020s. *Nature* lays out how the \$100-billion pledge failed, which countries are most to blame — and how climate finance might be transformed in the future.

How badly did rich countries fall short?

Negotiators never agreed on precisely how to measure countries' pledges. The Organisation for Economic Co-operation and Development (OECD), an intergovernmental body made up mostly of rich countries, bases its assessment on reports from the wealthy nations themselves. They contributed \$80 billion in climate finance to developing countries in 2019, it announced in September², up from \$78 billion in 2018. Most of this money came from public grants or loans, transferred either from one country to another directly, or through funds from multilateral development banks (MDBs). A smaller amount is private finance that the public money is said to have mobilized, such as loan guarantees and loans given alongside public funds (see 'Missed target').

MISSED TARGET

Rich countries promised developing nations US\$100 billion a year in climate finance by 2020.



©nature

Source: Ref. 2

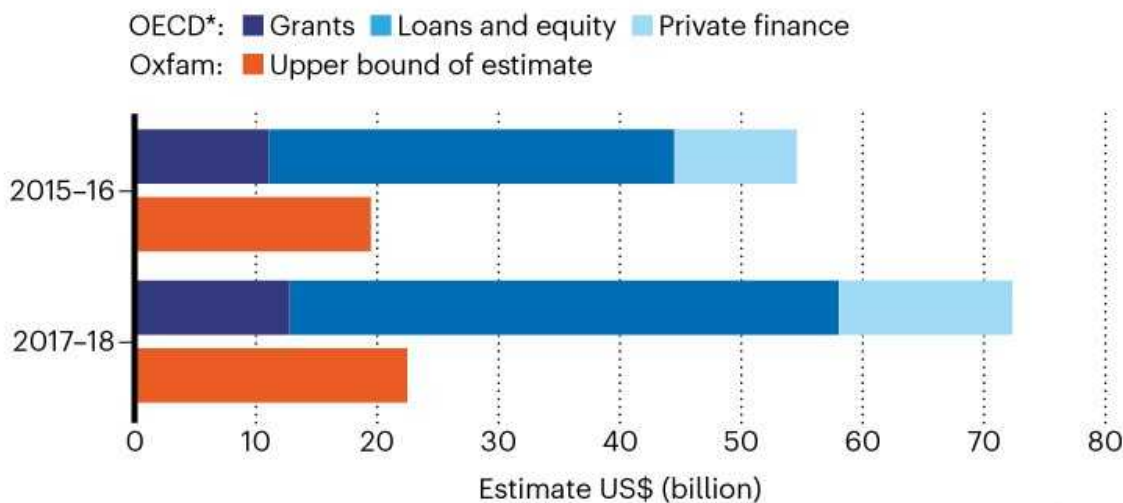
The figures are unlikely to have risen much in 2020: a June 2021 report from MDBs³ suggests that the climate finance they provided to developing countries fell last year. "It isn't a great sign," says Joe Thwaites, who

specializes in climate finance at the World Resources Institute (WRI) in Washington DC. International climate finance has probably stalled, he says, in part owing to the COVID-19 pandemic.

But some analysts say the OECD's numbers are vastly inflated. In a 2020 report⁴, the international-aid charity Oxfam estimated public climate financing at only \$19 billion–\$22.5 billion in 2017–18, around one-third of the OECD's estimate (see 'Inflated figures?'). That is largely because Oxfam argues that, besides grants, only the benefit accrued from lending at below-market rates should be counted, not the full value of loans. It also says that some countries incorrectly count development aid as going towards climate projects. Japan, for instance, treats the full value of some aid projects as 'climate relevant' even when they don't exclusively target climate action, says Tracy Carty, a senior policy adviser on climate change at Oxfam. As another example, some road construction projects are reported as climate aid, with most or all of their costs included in OECD estimates, says Romain Weikmans, a climate-finance specialist at the Finnish Institute of International Affairs in Helsinki.

INFLATED FIGURES?

Charities such as Oxfam say that climate aid is worth much less than its face value, in part because a lot of it comes as loans, not grants.



*Organisation for Economic Co-operation and Development

©nature

Sources: Refs 2 & 4

Many low- and middle-income countries agree with Oxfam, and some go further: in 2015, India's ministry of finance disputed the OECD's estimate of \$62 billion of climate finance in 2014, saying that the real figure was \$1 billion. Diann Black-Layne, Antigua and Barbuda's climate-change ambassador and formerly the lead climate negotiator for a group of low-lying coastal and island nations called the Alliance of Small Island States, says rich nations have intentionally inflated their climate aid.

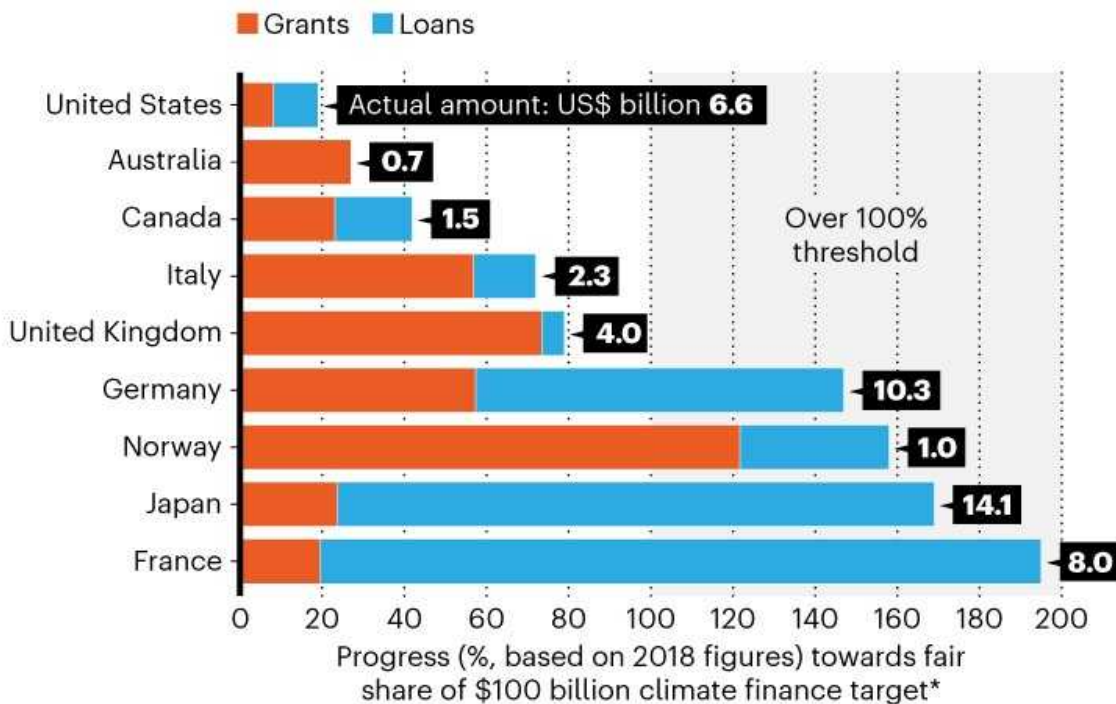
Who is not paying enough?

Although rich nations collectively agreed to the \$100-billion goal, they made no formal deal on what each should pay. Instead, countries announce pledges in the hope that others will follow. Multiple analyses of a notional fair share for these payments reach the same conclusion: the United States has fallen far short.

An October report from the WRI⁵ reckoned that the US should contribute 40–47% of the \$100 billion, depending on whether the calculation takes into account wealth, past emissions or population. But its average annual contribution from 2016 to 2018 was only around \$7.6 billion, the WRI estimates. Australia, Canada and Greece also fell far short of what they should have contributed. Japan and France, on the other hand, have transferred more than their fair share — although almost all of their funding came in the form of repayable loans, not grants (see 'Fair share').

FAIR SHARE

The United States has not paid enough in climate finance to developing nations, considering the size of its economy. Japan and France have paid more than their fair share, but much of it in loans, not grants.



*Estimates include both bilateral and multilateral development bank financing, and incorporates European Union climate financing, apportioned to relevant nations

©nature

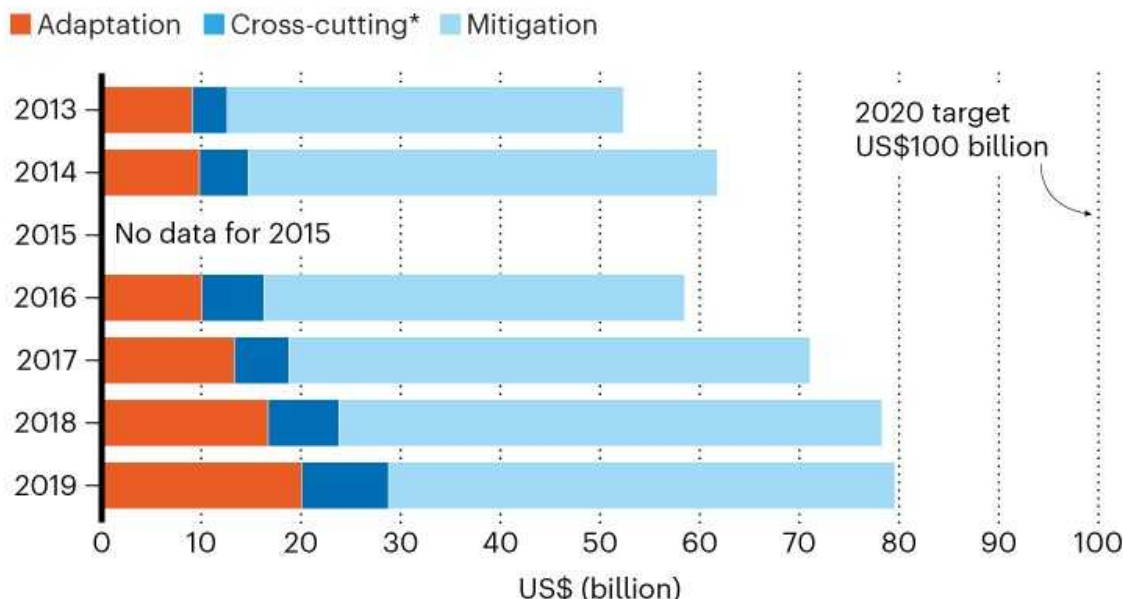
Source: Ref. 5

Where has the money gone?

Most of the climate finance has gone to projects to reduce greenhouse-gas emissions. The Paris agreement aimed for a balance between these ‘mitigation’ projects and those that help people adapt to the effects of climate change. But just \$20 billion went to adaptation projects in 2019, less than half of the funds for mitigation projects, the OECD found² (see ‘Adaptation lagging’). The UN estimates⁶ that developing countries already need \$70 billion per year to cover adaptation costs, and will need \$140 billion–\$300 billion in 2030.

ADAPTATION LAGGING

Most public climate financing to developing nations has gone to projects that reduce carbon emissions, rather than helping people adapt to climate change.



*Relevant to adaptation and mitigation.

©nature

Source: Ref. 2

Donors might favour mitigation projects because success is clear and measurable — it can be quantified by the avoided or captured carbon emissions — whereas it's less easy to define successful adaptation, says climate-finance researcher Jessica Omukuti at the University of Oxford, UK, who works on equitable ways for the world to reach net zero carbon emissions. "A person or group is never fully adapted to climate change, because new climate risks and vulnerabilities emerge," she says. Politicians in developed countries also perceive that they get more praise from other nations, and from domestic voters, for spending to reduce emissions, she adds, whereas adaptation aid is seen as only helping specific recipient countries.



Why fossil fuel subsidies are so hard to kill

Another reason for the imbalance between mitigation and adaptation is that money is increasingly provided as loans rather than grants. “Adaptation almost never is a loan-giving situation,” says Huq. “If you’re giving poor people money to help them deal with the impacts of climate change, that doesn’t generate money.” Private finance, in particular, almost always seems to go to mitigation projects that can generate returns on investment, such as solar farms and electric cars.

Most of the climate finance is also going to middle-income countries, not the poorest, most-vulnerable countries. “Many, many African countries are lamenting that they are not able to jump through the hoops [to access climate finance] because of the complexity and the technicality,” says Chukwumerije Okereke, an economist at Alex-Ekwueme Federal University Ndifu-Alike in Ikwo, Nigeria. “And they’re not receiving sufficient capacity-building exercises and training in this.”

Even the money that does go to the neediest countries might not be reaching its target. In July, the International Institute for Environment and Development in London reported that it had tried to track funding for adaptation projects in the UN’s 46 ‘least developed countries’, and could account for only \$5.9 billion between 2014 and 2018, less than 20% of the

amount developed countries said they had given. “How much actually goes to the most vulnerable people on the planet?” asks Huq.

What do developing countries want now?

The \$100 billion pledge has long been seen as a minimum, to increase over time. But some recipient countries have said they are willing to accept a static target for now, if wealthy countries clearly set out how it will be met.

“The demand at the moment is since you failed to deliver the \$100 billion in 2020, give us a plan for \$500 billion over five years,” says Huq. In July, the ‘V20’, a group of finance ministers from 48 climate-vulnerable countries, called for that plan, including more grant-based finance, and at least 50% of funding to go to adaptation. Huq notes that countries are allocating their own budgets to climate change, too. Bangladesh’s government, for instance, says its climate-related spending totals about \$3 billion: that’s some 7% of the government’s overall budget, or 0.73% of the country’s gross domestic product (GDP). And poor families in rural Bangladesh spend \$2 billion a year themselves on preventing climate-related disasters or repairing the damage they cause, notes an Oxfam analysis (see go.nature.com/2yuycvn).



A woman stands amid the debris of her house damaged by cyclone Amphan in Satkhira, Bangladesh, in May 2020. The cyclone, the strongest in the area in decades, was fuelled by sea-surface heating intensified by climate change. Credit: Munir Uz Zaman/AFP/Getty

New pledges have been pouring in: Canada, Japan and Germany announced theirs at a meeting of the G7 group of wealthy nations in June, at which countries also reaffirmed their commitment to contribute \$100 billion annually through to 2025. In September, the European Union pledged an extra \$5 billion by 2027, and US President Joe Biden promised that the United States would provide \$11.4 billion in annual financing by 2024, which would make it the largest single climate-finance contributor. But much of that funding requires US Congressional approval, and many other countries will be contributing much more as a proportion of their economy. “The EU and its member states are already providing roughly double the amount the US has pledged, even with a combined economy just three-quarters the size of America’s,” says Thwaites.



Young people will be key to climate justice at COP26

The question remains of whether rich nations can convince less wealthy ones that they are serious about meeting their pledges. Some people argue that promises should exclude private finance, to avoid confusion. Still, the extra pledges should enable wealthy nations to reach the \$100 billion target for 2022, according to climate economist Nicholas Stern at the London School of Economics.

Some governments are addressing the call for more adaptation funding. In August, Denmark said it would allocate 60% of its climate finance to adaptation, and other countries, including the Netherlands and the United Kingdom, have committed to ramping up adaptation finance.

At COP26, formal negotiations will also begin on a post-2025 goal. A specific climate-finance target is unlikely to be set this year, although in July, South African environment minister Barbara Creecy suggested a figure of \$750 billion a year by 2030. Many countries also want extra finance for ‘loss and damage’, to help people experiencing irreversible climate-related losses that cannot be adapted to.

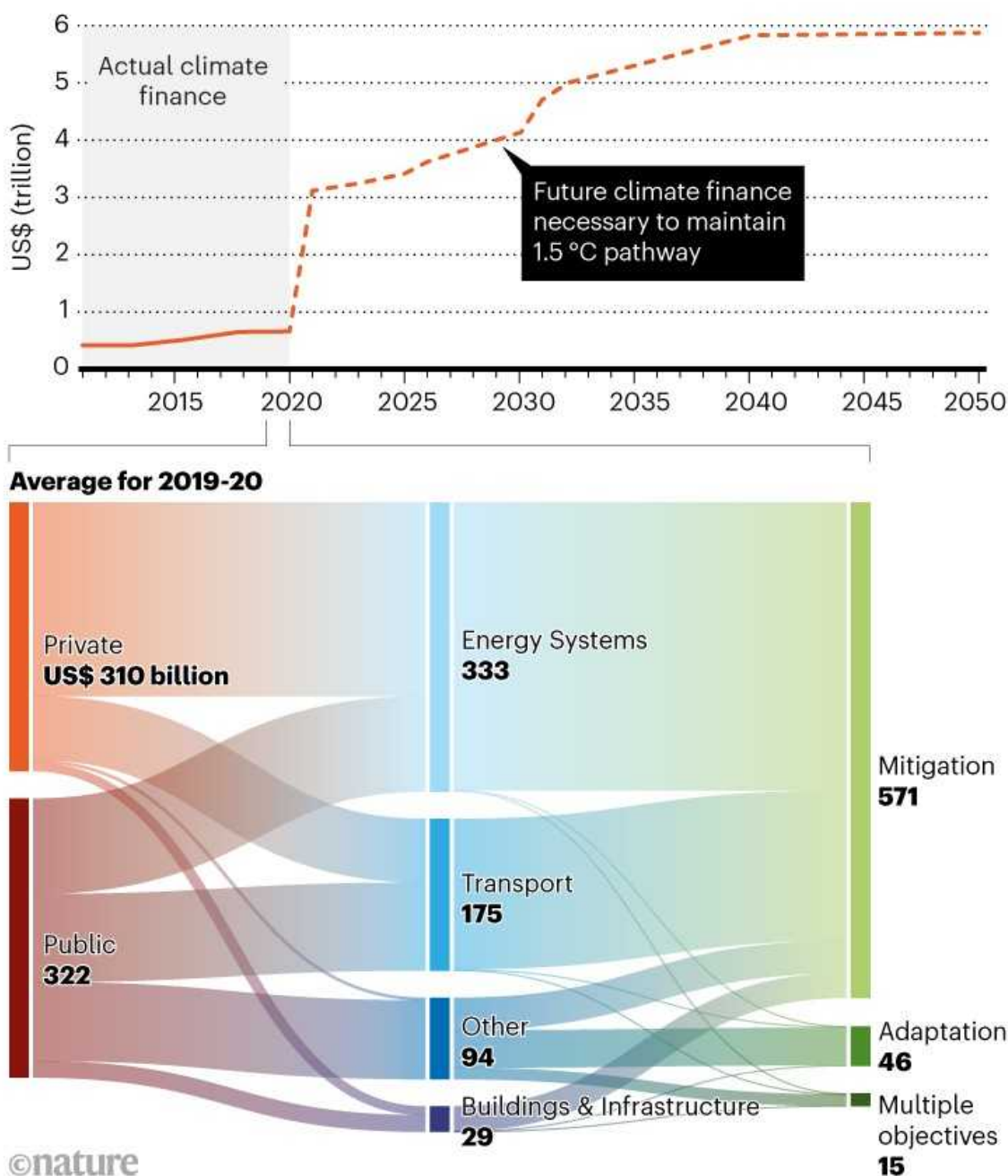
How much climate finance is enough?

Increasingly, the concept of climate finance is becoming redundant, Huq argues. “Every dollar spent is climate money spent,” he says. “You either spend it wisely or you spend it unwisely.”

However, the Climate Policy Initiative (CPI), a non-profit research group based in San Francisco, California, estimates⁷ that flows of climate-related finance in and between countries amounted to \$632 billion per year in 2019–20, or about 0.7% of the world’s GDP. Around half of this was private funding, much of it for renewable-energy generation (see ‘The climate-finance universe’).

THE CLIMATE-FINANCE UNIVERSE

Climate financing already exceeds US\$600 billion, but a steep rise is needed to avoid warming in excess of 1.5 °C. Around half of climate-related financing is private; much of it goes to mitigation projects in energy systems (such as solar and wind farms).



Source: Ref. 7

That is far below the UN Intergovernmental Panel on Climate Change's estimate that \$1.6 trillion–\$3.8 trillion is required annually to avoid warming exceeding 1.5 °C. Frustratingly, fossil fuels are still being subsidized, receiving some \$554 billion per year between 2017 and 2019, by one estimate. And in 2020, annual global military spending reached \$2 trillion.

The CPI warns that the pandemic and its economic effects have put an emphasis on spending in areas such as public health (developed nations spent trillions last year to deal with the COVID-19 pandemic), making the mid-to-long-term prospects of climate finance uncertain. The real challenge now is how to ensure that the wider universe of private finance is spent on projects that address the problems of climate change, says Sarah Colenbrander, director of the climate and sustainability programme at the Overseas Development Institute, a think tank based in London. “If we don’t do that, we are going to fail on climate even more catastrophically than we’ve already done,” she says.

Nature **598**, 400-402 (2021)

doi: <https://doi.org/10.1038/d41586-021-02846-3>

References

1. 1.

Independent Expert Group on Climate Finance. *Delivering on the \$100 Billion Climate Finance Commitment and Transforming Climate Finance* (Independent Expert Group on Climate Finance, 2020).

2. 2.

Organisation for Economic Co-operation and Development. *Climate Finance Provided and Mobilised by Developed Countries: Aggregate Trends Updated with 2019 Data* (OECD, 2021).

3. 3.

Multilateral Development Banks. *2020 Joint Report on Multilateral Development Banks' Climate Finance* (Multilateral Development Banks, 2020).

4. 4.

Carty, T., Kowalzig J. & Zagema, B. *Climate Finance Shadow Report 2020* (Oxfam, 2020).

5. 5.

Bos, J. & Thwaites, J. *A Breakdown of Developed Countries' Public Climate Finance Contributions Towards the \$100 Billion Goal* (World Resources Institute, 2021).

6. 6.

United Nations Environment Programme. *Adaptation Gap Report 2020* (UNEP, 2020).

7. 7.

Naran, B. *et al. Global Landscape of Climate Finance 2021* (Climate Policy Initiative, 2021).

This article was downloaded by **calibre** from <https://www.nature.com/articles/d41586-021-02846-3>

- NEWS FEATURE
- 20 October 2021

Why fossil fuel subsidies are so hard to kill

Behind the struggle to stop governments propping up the coal, oil and gas industries.

- [Jocelyn Timperley](#) 0



A machine sprays water to dampen coal dust at an open pit mine in Russia. Credit: Andrey Rudakov/Bloomberg/Getty

Fossil-fuel subsidies are one of the biggest financial barriers hampering the world's shift to renewable energy sources. Each year, governments around the world pour around half a trillion dollars into artificially lowering the price of fossil fuels — more than triple what renewables receive. This is despite repeated pledges by politicians to end this kind of support, including statements from the G7 and G20 groups of nations.

"I think everyone seems to be basically on the same page that something needs to be done about fossil-fuel subsidies," says Harro van Asselt, a specialist in climate law and policy at the University of Eastern Finland in Joensuu. "It's the discrepancy between the rhetoric and the reality that is starting to bite a little bit. We're figuring out that it's incredibly challenging to actually make it happen."

Change is possible. At least 53 countries reformed their fossil-fuel subsidies between 2015 and 2020, [according to the Global Subsidies Initiative](#) (GSI), a research group in Geneva, Switzerland. And US President Joe Biden is the latest high-profile politician to vow to eliminate them. But much more needs to be done. "In the next few years, all governments need to eliminate fossil fuel subsidies," the International Energy Agency (IEA) says in a 2021 report¹ laying out a road map to a world with net-zero carbon emissions.

How are fossil fuels subsidized?

Fossil-fuel subsidies generally take two forms. Production subsidies are tax breaks or direct payments that reduce the cost of producing coal, oil or gas. These are common in Western countries and are often influential in locking in infrastructure such as oil pipelines and gas fields, says Bronwen Tucker, an analyst in Edmonton, Canada, at Oil Change International, a non-profit research organization headquartered in Washington DC that works to reveal the costs of fossil fuels.



Young people will be key to climate justice at COP26

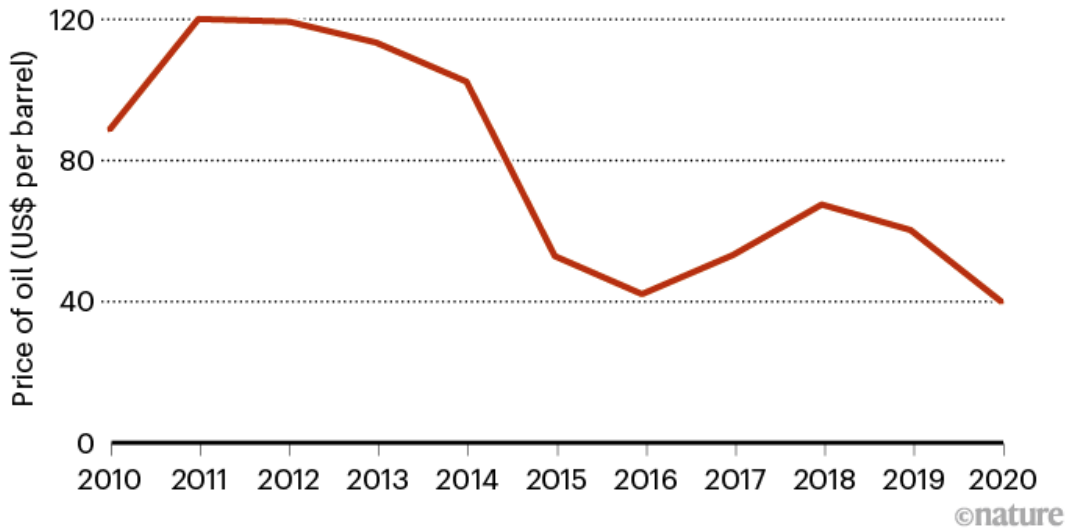
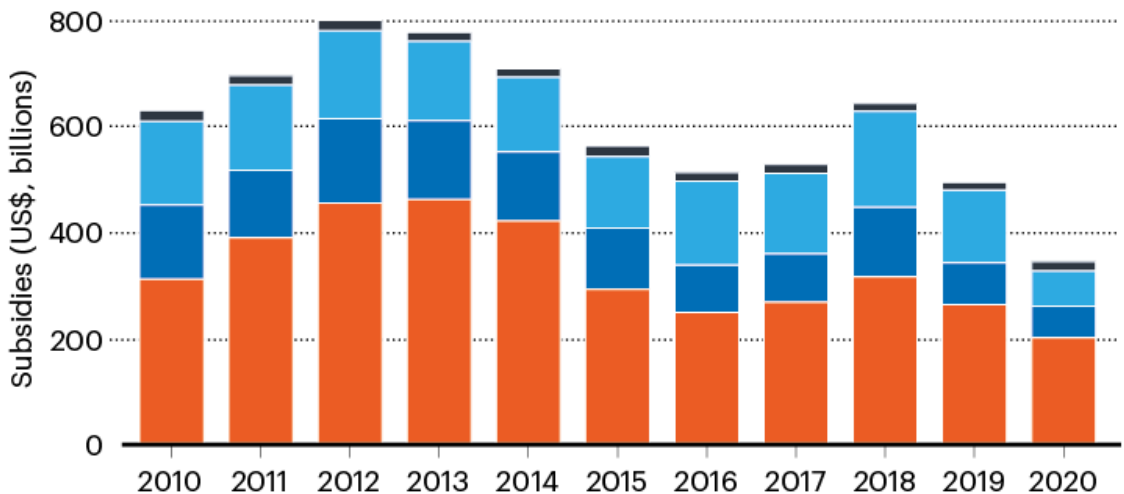
Consumption subsidies, meanwhile, cut fuel prices for the end user, such as by fixing the price at the petrol pump so that it is less than the market rate. These are more common in lower-income countries — in some, they help people to get clean cooking fuel they couldn't otherwise afford. In others, such as the Middle East, the subsidies are sometimes regarded as helping citizens to benefit from a country's endowment of natural resources, says Michael Taylor, an energy analyst in Bonn, Germany, who works at the International Renewable Energy Agency (IRENA), headquartered in Abu Dhabi.

The IEA and the Organisation for Economic Co-operation and Development (OECD), an intergovernmental body in Paris, estimate that 52 advanced and emerging economies — representing about 90% of global fossil-fuel supplies — gave subsidies worth an average of US\$555 billion each year from 2017 to 2019. This dipped to \$345 billion in 2020 only because of lower fuel consumption and declining fuel prices during the COVID-19 pandemic (see 'Fluctuating fossil-fuel subsidies').

FLUCTUATING FOSSIL-FUEL SUBSIDIES

Annual figures for fossil-fuel subsidies are heavily influenced by the price of oil. Subsidies fell in 2020 because of reduced fuel consumption during the COVID-19 pandemic and a drop in the oil price.

■ Petroleum ■ Natural gas ■ Electricity ■ Coal



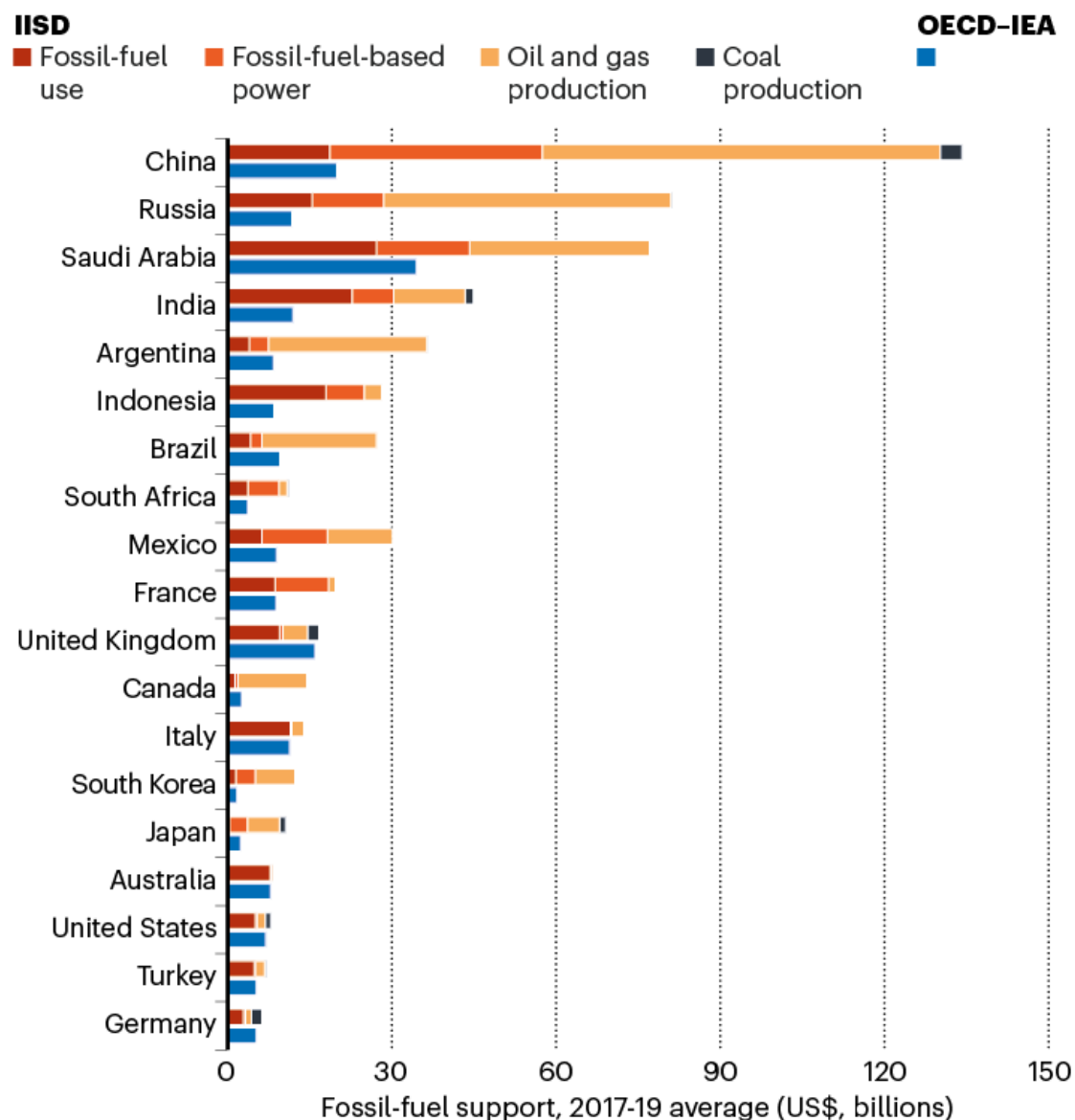
Source: [OECD–IEA](#)

But organizations disagree about how to estimate subsidies. A complication is that some of the public financing of fossil fuels (such as that from state-owned enterprises) mingles both subsidy and non-subsidy elements, points out the International Institute for Sustainable Development (IISD), a non-profit organization in Winnipeg, Canada. In a report published last November², the IISD incorporates all of this public finance into what it calls

“support” for fossil fuels, and estimates that the G20 group of countries alone gave an average of \$584 billion per year between 2017 and 2019, higher than the OECD–IEA analysis. The biggest providers of support were listed as China, Russia, Saudi Arabia and India (see ‘Differing estimates’).

DIFFERING ESTIMATES

An IISD* report gives larger estimates of fossil-fuel support for some countries because it includes public financing such as that from state-owned firms, unlike OECD-IEA† estimates of subsidies.



*IISD, International Institute for Sustainable Development.

†OECD-IEA, Organisation for Economic Co-operation and Development-International Energy Agency.

Some analysts argue that the hidden costs of fossil fuels — such as their impacts on air pollution and global warming — are, in effect, a kind of subsidy, because polluters are not paying for the damage they cause. Last month, the International Monetary Fund calculated³ total fossil-fuel subsidies in 2020 at \$5.9 trillion, or almost 7% of global gross domestic product (GDP), largely as a result of these external costs. But some disagree with this approach. “The damage caused by fossil fuels is massive, but I would not call it a subsidy,” says Johannes Urpelainen, who specializes in energy policy at the Johns Hopkins School of Advanced International Studies in Washington DC.

Why are they so hard to get rid of?

One problem is definitions. The G7 and G20 countries have vowed to eliminate “inefficient fossil fuel subsidies”, although they haven’t clearly defined what this phrase means. “It’s a very vague commitment,” says Ludovic Subran, chief economist at the multinational insurance firm Allianz, which published a report on eliminating subsidies in May⁴.



The broken \$100-billion promise of climate finance – and how to fix it

Some countries don’t agree that they have any subsidies to remove. The UK government, for example, says it has none, although the IISD rates it as

among the worst of the OECD-member nations, calculating that it gave \$16 billion a year to support fossil fuels in 2017–19, on average². In large part, this is because the United Kingdom forgoes some tax revenue from the use of fossil fuels and directly funds its oil and gas industry. (Other analysts agree with the IISD; a 2019 European Commission report⁵ came to similar conclusions.)

“They reject the idea that they have any inefficient fossil-fuel subsidies,” says Angela Picciariello, senior research officer in climate and sustainability at the Overseas Development Institute in London. So “it’s quite hard to engage with them on this”. (The UK government did not reply to *Nature*’s request for comment.) The country did announce in 2020 that it would end support for fossil-fuel energy overseas.

What’s more, each nation has its own reasons for subsidizing fossil fuels, often intertwined with its industrial policies. There are three main barriers to removing production subsidies, Urpelainen says. First, fossil-fuel companies are powerful political groups. Second, there are legitimate concerns about job losses in communities that have few alternative employment options. And third, people often worry that rising energy prices might depress economic growth or trigger inflation.



An aerial view of the coal yard that supports a steel plant in Nanjing, eastern China. Credit: Feature China/Barcroft Media/Getty

However, these barriers are surmountable, as some countries have demonstrated. Money not given to fossil-fuel firms can be redistributed to offset the effects of rising energy prices. According to the GSI, the Philippines, Indonesia, Ghana and Morocco each introduced cash transfers and social support, such as education funds and health insurance for poor families, to compensate for the removal of subsidies. Governments also need a plan to help fossil-fuel workers find different employment, adds Subran.

One way to overcome political hesitancy to remove energy subsidies is to maintain support but simply make it contingent on a move to greener energy, Subran says. State-owned enterprises that support fossil fuels can diversify into renewables, adds Picciariello, citing Ørsted, the Danish state enterprise that converted from a fossil-fuel firm into one of the world's biggest renewable producers.

Periods of low oil prices are generally thought of as good times to remove consumption subsidies, because retail prices can be kept stable. According to the IISD, subsidy reform in India — an oil importer — significantly reduced its support for oil and gas between 2014 and 2019 while taking advantage of low oil prices (see go.nature.com/3ae5uff). (Despite this, the IISD counts overall support in India as rising², because of growing investments from state-owned enterprises and public financing institutions.)



A female worker in India's Jharia coalfield, where a large amount of the country's coal is mined. Credit: Jonas Gratzer/LightRocket/Getty

Low oil prices also helped Saudi Arabia to begin increasing its heavily subsidized domestic fossil-fuel and electricity prices, which are among the cheapest in the world, says Glada Lahn, an environment and energy-resources specialist at the Chatham House policy institute in London. The country has made “significant progress” by gradually increasing fuel prices since 2016, she says. It has cushioned the impacts of the price hikes

somewhat by offering cash transfers to lower-income families — although it has now capped fuel prices again to stimulate the economy in the wake of the COVID-19 pandemic.

It is important that countries are careful to ensure that climate policies don't hurt the lowest-income communities, notes Tucker: when Ecuador introduced a rapid fuel-tax hike in 2019, widespread protests by citizens prompted the government to reintroduce subsidies. When India decreased its subsidies for liquefied petroleum gas (LPG), it hoped that giving free LPG cylinders to rural populations for use as cooking fuel, a plan it had announced in response to COVID-19, would compensate for higher prices. But it didn't give them enough, says Vibhuti Garg, a senior energy specialist at the IISD in New Delhi. This means that people instead burn wood and other biofuels — which can ultimately lead to higher carbon emissions.

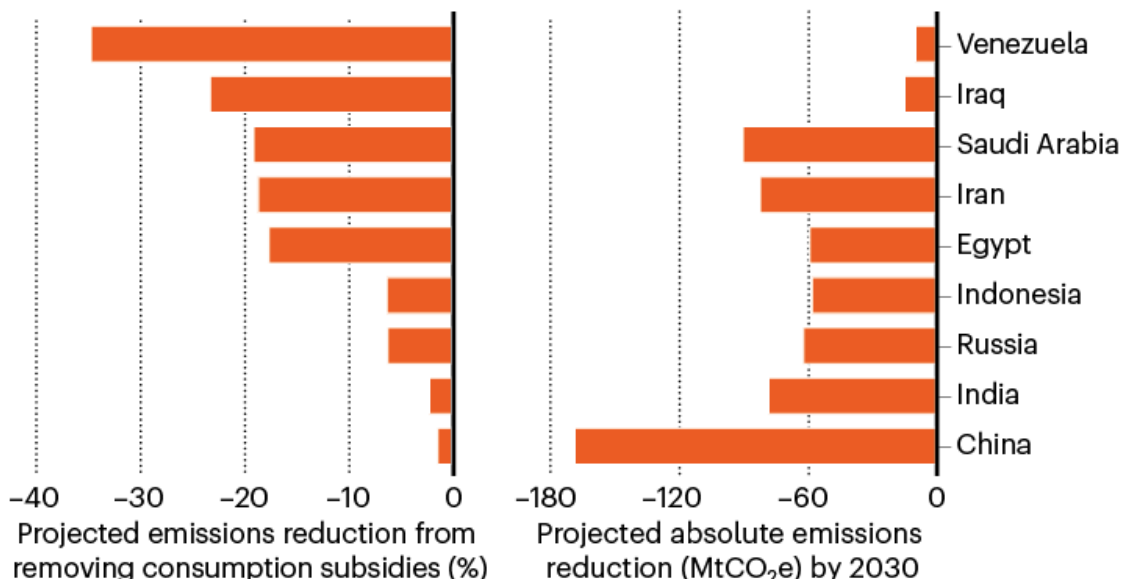
The GSI highlights Egypt as an example of how to remove subsidies well. In 2013, the country spent around 7% of its GDP on fossil-fuel subsidies, more than its spending on health and education combined, according to a World Bank report⁶. But then it rolled back the financing, reducing it to 2.7% in the 2016–17 budget. The government communicated with citizens throughout the changes, and used the money to support health and education. However, some commentators said insufficient support was given to poor households.

What effect would reducing subsidies have on climate change?

Removing consumption subsidies in 32 countries would cut their greenhouse-gas emissions by an average of 6% by 2025, according to an IISD July report⁷. This chimes with a 2018 United Nations report⁸ suggesting that phasing out fossil-fuel support could reduce global emissions by between 1% and 11% from 2020 to 2030, with the largest effect occurring in the Middle East and North Africa (see 'Carbon cuts'). That reduction could be amplified if the money that would have subsidized fossil fuels was instead used to support renewable energy.

CARBON CUTS

Countries could cut their carbon emissions by removing fossil-fuel subsidies.



Analysis from the IISD only models the removal of consumption subsidies (those that reduce price for end users). ©nature

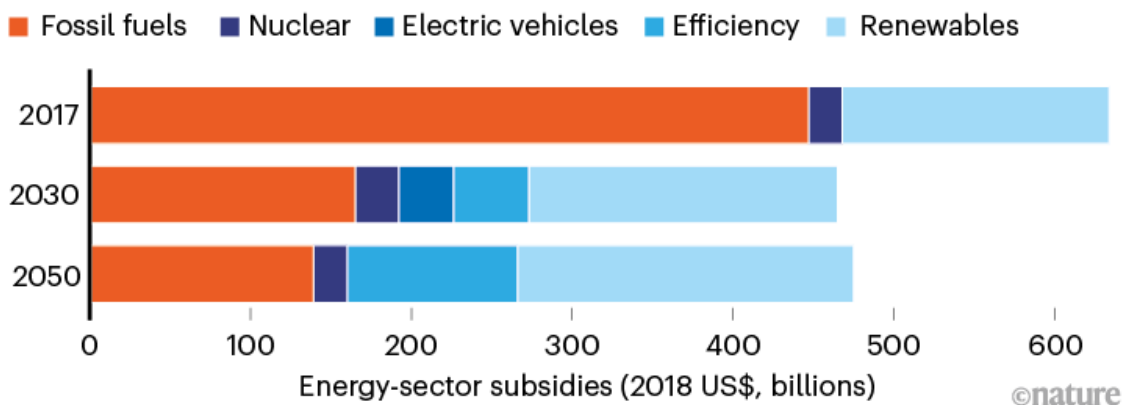
Source: [Ref. 7](#)

A 2020 report by IRENA⁹ tracked some \$634 billion in energy-sector subsidies in 2020, and found that around 70% went to fossil fuels. Only 20% went to renewable power generation, 6% to biofuels and just over 3% to nuclear. “This overwhelming imbalance of subsidies between fossil fuels and clean energy is a drag on us achieving the Paris climate goals,” says Taylor, who wrote the report. The balance of these numbers varies from year to year, because fossil-fuel subsidies swing around depending largely on the price of oil, he adds.

The IRENA report also mapped out a scenario of how global energy subsidies might change by 2050 to help limit global temperature rises to below 2 °C, compared with pre-industrial levels. It sees subsidies for fossil fuels and renewable electricity falling and moving to renewable energy in transport and buildings, and to energy-efficiency measures (see ‘Changing future’). However, some fossil-fuel support is retained, almost all of which would bolster carbon capture and storage for industrial processes such as cement and steel production.

CHANGING FUTURE

In one scenario for ramping up clean energy, energy subsidies fall and move from fossil fuels to renewables and energy efficiency.



Source: [Ref. 9](#)

What are the short-term prospects for reform?

Ahead of November's COP26 climate summit in Glasgow, UK, the G20's Italian presidency has said it will push for more progress on phasing out fossil-fuel subsidies. This January, Biden issued an executive order telling federal agencies to cut fossil-fuel subsidies under their direct control. However, legislative approval by Congress would be needed to end most of the tax breaks and financial incentives for the US oil and gas industry.

Meanwhile, Russia's President Vladimir Putin has said the country will try to be carbon neutral by 2060 — yet its economy is still very dependent on fossil fuels, with plans to develop new oil and gas fields, says Vasily Yablokov, head of climate and energy at the Russia branch of environmental campaigning group Greenpeace, in St Petersburg. "The withdrawal of subsidies would be perceived as a shock that will also affect consumers," he says.

Some climate advocates also warn against new subsidies to fossil fuels being developed in the name of emissions reductions. Tucker is wary, for example, of subsidies for 'blue' hydrogen — a term used for the process in which hydrogen is made from fossil fuels and the carbon dioxide emitted as a by-product is captured and stored. The chair of a leading UK hydrogen industry

association quit his post in August, saying fossil-fuel companies were promoting projects that were “not sustainable”, to access billions in taxpayer subsidies.

At the fringes of G20 and G7 summits, groups of small countries have long been working together to try to build a consensus on subsidy reform. An initiative on trade and climate change launched by Costa Rica, Fiji, Iceland, New Zealand and Norway in 2019 aims to set up a member-based agreement in which countries would phase out fossil-fuel subsidies and remove barriers to trade in environmental goods and services. These countries are not the biggest subsidy providers, but this could set a “precedent on developing binding rules on limiting fossil-fuel subsidies, which otherwise do not exist”, says van Asselt.

It’s not enough to phase out only subsidies, says Tucker: ultimately, the goal should be to stop governments giving companies licences to extract fossil fuels altogether. Nevertheless, she’s heartened by the active debates on subsidy reform in countries such as Canada, the United States and the United Kingdom. “Ending subsidies is something that can be won right now,” she says.

Nature **598**, 403-405 (2021)

doi: <https://doi.org/10.1038/d41586-021-02847-2>

References

1. 1.

International Energy Agency. *Net Zero by 2050: A Roadmap for the Global Energy Sector* (IEA, 2021).

2. 2.

Geddes, A. *et al. Doubling Back and Doubling Down: G20 Scorecard on Fossil Fuel Funding* (International Institute for Sustainable Development, 2020).

3. 3.

Parry, I., Black, S. & Vernon, N. *Still Not Getting Energy Prices Right: A Global and Country Update of Fossil Fuel Subsidies*. IMF Working Paper WP/21/236 (International Monetary Fund, 2021).

4. 4.

Zimmer, M., Kuhanathan, A. & Badre, A. *Abolishing Fuel Subsidies in a Green and Just Transition* (Allianz, 2021).

5. 5.

European Commission. *Energy Prices and Costs in Europe* (EC, 2109).

6. 6.

Energy Sector Management Assistance Program. *Energy Subsidy Reform Facility Country Brief: Egypt* (World Bank, 2017).

7. 7.

Kuehl, J. et al. *Cutting Emissions Through Fossil Fuel Subsidy Reform and Taxation* (International Institute for Sustainable Development, 2021).

8. 8.

UN Environment Programme. *Emissions Gap Report 2018* (UN, 2018).

9. 9.

Taylor, M. *Energy Subsidies: Evolution in the Global Energy Transformation to 2050* (International Renewable Energy Agency, 2020).

| [Section menu](#) | [Main menu](#) |

Books & Arts

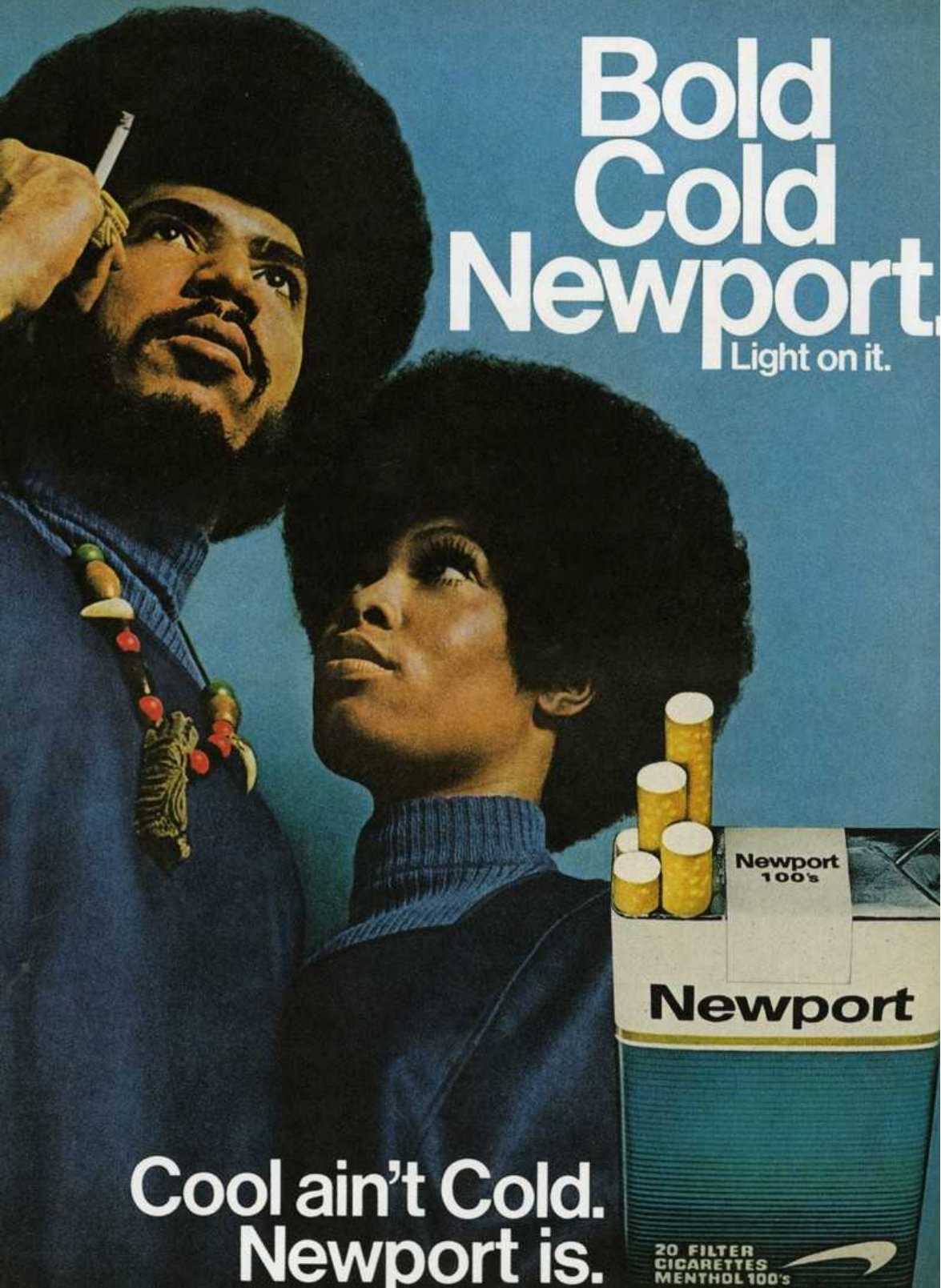
- **[How cigarettes became a civil-rights issue](#)** [18 October 2021]
Book Review • Tobacco companies still profit from decades of marketing to Black Americans.
- **[Synthetic biology — a call to meddle better](#)** [19 October 2021]
Book Review • An expansive survey of the hopes and fears, hypes and fails of genetic manipulation.
- **[Transformative hydrogen and wrestling with testosterone: Books in brief](#)** [30 September 2021]
Book Review • Andrew Robinson reviews five of the week's best science picks.

- BOOK REVIEW
- 18 October 2021

How cigarettes became a civil-rights issue

Tobacco companies still profit from decades of marketing to Black Americans.

- [Nidhi Subbaraman](#)



Bold Cold Newport.

Light on it.

Cool ain't Cold.
Newport is.

20 FILTER
CIGARETTES
MENTHOL 100's

Credit: Alamy

Pushing Cool: Big Tobacco, Racial Marketing, and the Untold Story of the Menthol Cigarette *Keith Wailoo* Univ. Chicago Press (2021)

In 2019, when the New York City Council proposed a ban on menthol cigarettes, health advocates noted their popularity among Black Americans, and the disproportionate harm they brought to the community. But the move had a vocal critic.

Civil-rights icon Al Sharpton opposed the ban, arguing that sales would go underground, drawing unwanted police attention to Black people as a result. The proposal was dropped.

In this incident, medical historian Keith Wailoo saw a pattern repeating: civil-rights champions have frequently opposed restrictions on sales of menthol cigarette in defence of Black consumers' choices. Wailoo's book *Pushing Cool* documents how, starting in the 1960s, the US tobacco industry methodically and deliberately brought about this cruel irony, by tailoring its marketing and branding to drive up menthol sales among Black smokers. The corporations drew in Black cultural figures, civil-rights leaders and politicians in their bid to keep selling flavoured cigarettes.



[Big Tobacco, war and politics](#)

Wailoo makes a case that tobacco companies strategically cultivated preferences for menthol cigarettes in Black communities over decades, to keep sales rising and deflect concerns about health risks.

His takeaway is this: Black Americans today smoke menthols at higher rates than any other group because of the ‘push’ from cigarette companies and their savvy advertisers rather than the ‘pull’ of consumer preferences. The health impacts are stark: Black Americans are more likely than white ones to die from diseases linked to smoking.

Wailoo mines press reports through the decades, along with posters, billboards and troves of internal industry documentation that cigarette companies were forced to make public after a spate of lawsuits that ended in 1998. With deadly repetition, menthols have been silent players on the stage of US history, witnesses to epic flashpoints at which health and politics collide. The case is stronger for the specificity and rich detail that Wailoo weaves into it, although occasionally the vast cast of characters makes it difficult to follow the plot.

‘Healthy’ profits

From the 1930s to the 1950s, tobacco companies marketed menthols as healthier alternatives to normal smokes, falsely touting the cooling sensation from the minty flavour as a salve for sore throats or colds. Market research indicated that people worried about health risks could be pacified with suggestions of medicinal effects from a menthol brand.

Two events shifted that dynamic. First, the US government began shutting down false advertising claims about health benefits, prompting companies to cast around for other aspects of their customers’ tastes, preferences or identity that influenced how they shopped.



Truth decay: when uncertainty is weaponized

Second, the strongest evidence yet of the health harms of cigarettes arrived in 1964, when a pivotal report from the US surgeon-general linked smoking to lung cancer. No longer able to hook people on health, cigarette companies looked to target customers on the basis of race, gender and class. As the civil-rights movement reached a crescendo that decade, market-research firms identified Black Americans as a vast untapped market for menthol sales.

Billboards went up in cities with a majority of Black residents; many fewer turned up in suburbs that white people were moving to. “Racial marketing” began to define advertising of menthol brands. A 1964 ad by Brown & Williamson for its Kool brand of menthol cigarettes marked such a shift: a smiling young man and woman lean over a rock parapet by a waterfall. Each holds a cigarette; the woman reaches past a palm frond and trails one hand in the stream. The tagline: “Feel extra coolness in your throat.” Black news media ran a version featuring a Black couple, a rare early inclusion of Black models in advertising. A white couple posed in the version that reached white readers.

In the 1970s, tobacco branding was endemic at cultural and sporting events; for a time, Brown & Williamson was a major sponsor of jazz concerts. And in the 1980s, dollars flowed from tobacco companies to social and political

causes: Brown & Williamson partnered with civil-rights group the NAACP to fund a business incubator; RJR supported *Ebony*, the Black culture magazine; Philip Morris sponsored a meeting of the Congressional Black Caucus that drew 8,000 attendees.

Wronging rights

These moves paid dividends over the next decades, as the US government and health leaders tried to curb Big Tobacco, Wailoo argues.

In the 1990s, when US health secretary Louis Sullivan opposed an upcoming menthol brand called Uptown, aimed at Black smokers, one of his chief adversaries was NAACP executive director Benjamin Hooks.

Uptown never made it to the shelves, but menthol burned on. In 2009, US legislators elected to regulate tobacco as a drug, and flavoured cigarettes were banned — all except menthols, after opposition from powerful Black lawmakers. In 2018, when US Food and Drug Administration (FDA) commissioner Scott Gottlieb tried to enact a menthol-cigarette ban, he failed. Two years later, the FDA proposed bans on vape flavours because of their appeal to young people, but exempted menthol. This April, the regulator announced that it was working on another proposal to ban menthol cigarettes; what shape that will take remains to be seen.

In a grim coda, Wailoo observes that before they were killed in police custody, Eric Garner used to sell cigarettes, and George Floyd was buying some. Their deaths, in 2014 and 2020, sparked resurgences in the Black Lives Matter movement and global calls to end racism. Yet again, he notes, tobacco companies' pervasive legacies linger on, colliding with the defining social movements of our day.

Nature **598**, 407-408 (2021)

doi: <https://doi.org/10.1038/d41586-021-02849-0>

| [Section menu](#) | [Main menu](#) |

- BOOK REVIEW
- 19 October 2021

Synthetic biology — a call to meddle better

An expansive survey of the hopes and fears, hypes and fails of genetic manipulation.

- [Gaia Vince](#) ⁰



Enviropigs are genetically engineered to excrete low levels of phosphorus. Credit: Jim Ross/NYT/Redux/eyevine

Life as We Made It: How 50,000 Years of Human Innovation Refined — and Redefined — Nature Beth Shapiro Basic (2021)

Pigs need phosphorus in their diet. But most of the phosphorus in their grain feed is in the form of phytic acid, which they cannot digest. As a result, they excrete it into the environment, badly polluting the watersheds around pig farms and, farther afield, causing oceanic dead zones. Farmers can add a costly enzyme to the feed to help the animals break down phytic acid, but this often gets destroyed in the feed mix before the pigs can use it.

Enter Enviropig. Researchers inserted two genes, one from a strain of the bacterium *Escherichia coli* and one from a mouse, into a pig genome to enable the animal to produce the enzyme in its saliva. These farmyard chimaeras can't breathe fire, but they can excrete up to 65% less phosphorus than normal pigs — without the need for costly supplements.

We've made a mess of the planet with our meddling. Now, thanks to biotechnology, we have tools — witness Enviropig — to repair it. Should we use them? Molecular biologist Beth Shapiro thinks so. For instance, we could engineer species' genomes "to help them adapt to drier soils, more acidic oceans, and more polluted streams"; to create 'gene drives', systems that override natural selection in invasive species to wipe them out; and even to resurrect extinct species. Synthetic biology could help to solve some of our biggest problems, from hunger to the climate crisis, and look after other species, too. We are the planet's caretakers, Shapiro argues in her book *Life as We Made It*, and "it's time to embrace this role".



[Timely book tells the CRISPR story so far](#)

Her expansive survey of the hopes and fears — and the hypes and fails — of genetic manipulation is an enjoyable tour of ‘impossible’ species created to solve pressing human problems. We visit hornless cattle, flavour-saving tomatoes, golden rice, malarial mosquitoes gene-edited to spread sterility, yeast genetically engineered to produce a synthetic ‘blood’ for tasty veggie burgers, endangered ferrets cloned to help save the species from extinction, and more.

Shapiro looks over the horizon to possibilities scientists are working towards — from the recreation of extinct mammoths to the common crops that have been engineered to store more carbon in their roots, helping to combat climate change.

Her enthusiasm doesn’t blind her to the pitfalls and ethical dilemmas of synthetic biology. She provides thoughtful accounts of hubristic endeavours that have gone wrong. A lack of transparency and public consultation — sometimes simply due to naivety — has damaged the field and enabled conspiracy theorists and anti-genetic-modification extremists to dominate the political narrative and spread disinformation on risks for decades. Now, she says, “if we want enough food to feed 9 or 10 billion people as well as breathable air, drinkable water, and biodiverse habitats, then we need more control over evolution” — we need to direct it.



[Outstanding reportage from the front lines of geoengineering](#)

Shapiro is calling for greater acceptance of genetic modification, with a clearer and less hostile route through the regulatory framework. No one has been allowed to try an Enviropig. And that's the problem: synthetic biology's potential is huge, but only a handful of creations have ever made it out of the laboratory. Golden rice has been under development since the 1990s, yet it couldn't be used anywhere until this July, when the Philippines became the first country to approve it for planting. Whether farmers do so remains to be seen.

To some degree, the argument against synthetic biology is irrelevant. We have been creating new life through unnatural means for decades. Cattle are routinely bred using artificial insemination and embryo transfer, enabling a cow to produce as many as ten calves a year instead of just one, which can be lifesaving in parts of the world that suffer from food insecurity, Shapiro writes. And, of course, humanity's long quest to tame and improve the natural world for our survival and profit goes back millennia.

The cautionary tale is that, in many cases, it was this quest that caused today's biggest environmental problems. For instance, oceanic dead zones are the result of humans creating (through breeding) a domestic version of wild boar, and keeping hundreds of millions of them in artificial landscapes (farms) while relying on the biosphere to deal with the resultant effluent.



A biographer and a bioethicist take on the CRISPR revolution

Fully one-third of the book documents our prehistoric modifications to the environment, following the evolution of humans and the extinction of megafauna through a combination of climate change and human impacts. Shapiro, who works on ancient DNA, personalizes this familiar story with her own research anecdotes. She focuses on her pet study subject, the American bison, and its near-misses with extinction. The latest reprieve came courtesy of conservation measures rolled out by ex-hunter and former US president Theodore Roosevelt. The animals that had once numbered in the tens of millions bounced back from a surviving population of fewer than 300 at the beginning of the twentieth century to more than 500,000 today.

Shapiro's point, throughout the book, is that we've always meddled with nature; the answer is not to stop meddling, but to meddle better. She builds a convincing case, despite the occasional troubling assertion, such as that "there are more of us today than we can feed using existing technologies", with which many would take issue. However, there is no doubt that synthetic biology has the potential to help solve some of our biggest global problems. With this clear-eyed account of its humanitarian potential, Shapiro has done the field a great service.

Nature **598**, 408-409 (2021)

doi: <https://doi.org/10.1038/d41586-021-02848-1>

This article was downloaded by **calibre** from <https://www.nature.com/articles/d41586-021-02848-1>

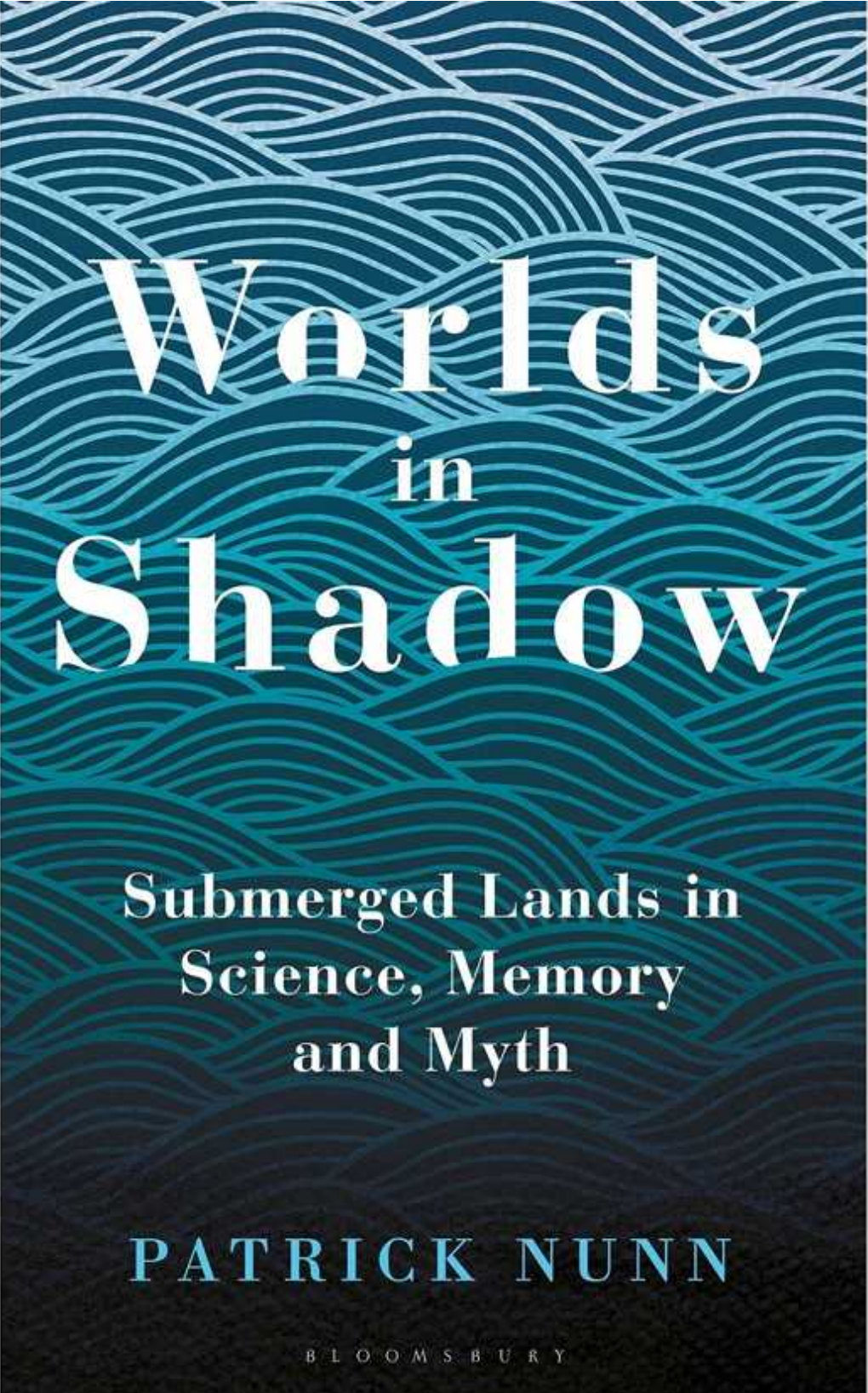
| [Section menu](#) | [Main menu](#) |

- BOOK REVIEW
- 30 September 2021

Transformative hydrogen and wrestling with testosterone: Books in brief

Andrew Robinson reviews five of the week's best science picks.

- [Andrew Robinson](#) 0



Worlds in Shadow

Submerged Lands in
Science, Memory
and Myth

PATRICK NUNN

BLOOMSBURY

Worlds in Shadow

Patrick Nunn *Bloomsbury Sigma* (2021)

Our rising sea levels are often said to be unprecedented and to require new solutions, implying that the past has nothing to teach us. This is wrong, argues oceanic geoscientist Patrick Nunn, who is part of the Intergovernmental Panel on Climate Change. His realistic but hopeful history of submerged lands across millennia and around the globe mixes “science, memory and myth” — including the legend of Atlantis — to show how our ancestors learnt to live in challenging coastal environments and to manage adversity in many forms and places.

*'Engaging, authoritative
and very timely.'*

MIKE BERNERS-LEE

Marco
Alverà

The Hydrogen Revolution

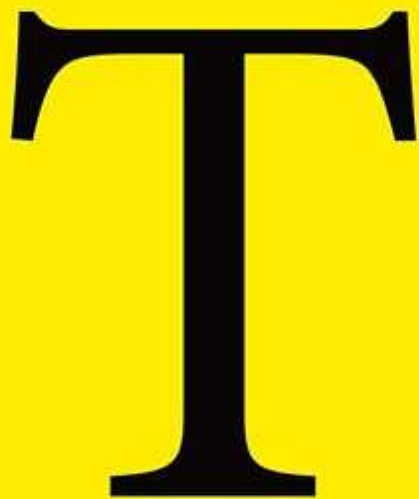
A Blueprint
for the
Future
of Clean
Energy

The Hydrogen Revolution

Marco Alverà *Hodder Studio* (2021)

“We are on the cusp of a hydrogen revolution,” writes Marco Alverà, head of Europe’s largest gas-infrastructure company. In 1874, science-fiction writer Jules Verne predicted water would become a fuel, through electrolysis into hydrogen and oxygen. In the 1890s, a Danish windmill with a dynamo was used to store hydrogen as a fuel for illumination. Since the 1930s, fuel cells have reversed electrolysis to make electricity and water from hydrogen. Now they are almost competitive with fossil fuels, argues Alverà in his urgent call to action.

The Story of TESTOSTERONE,
the HORMONE that
DOMINATES and DIVIDES US

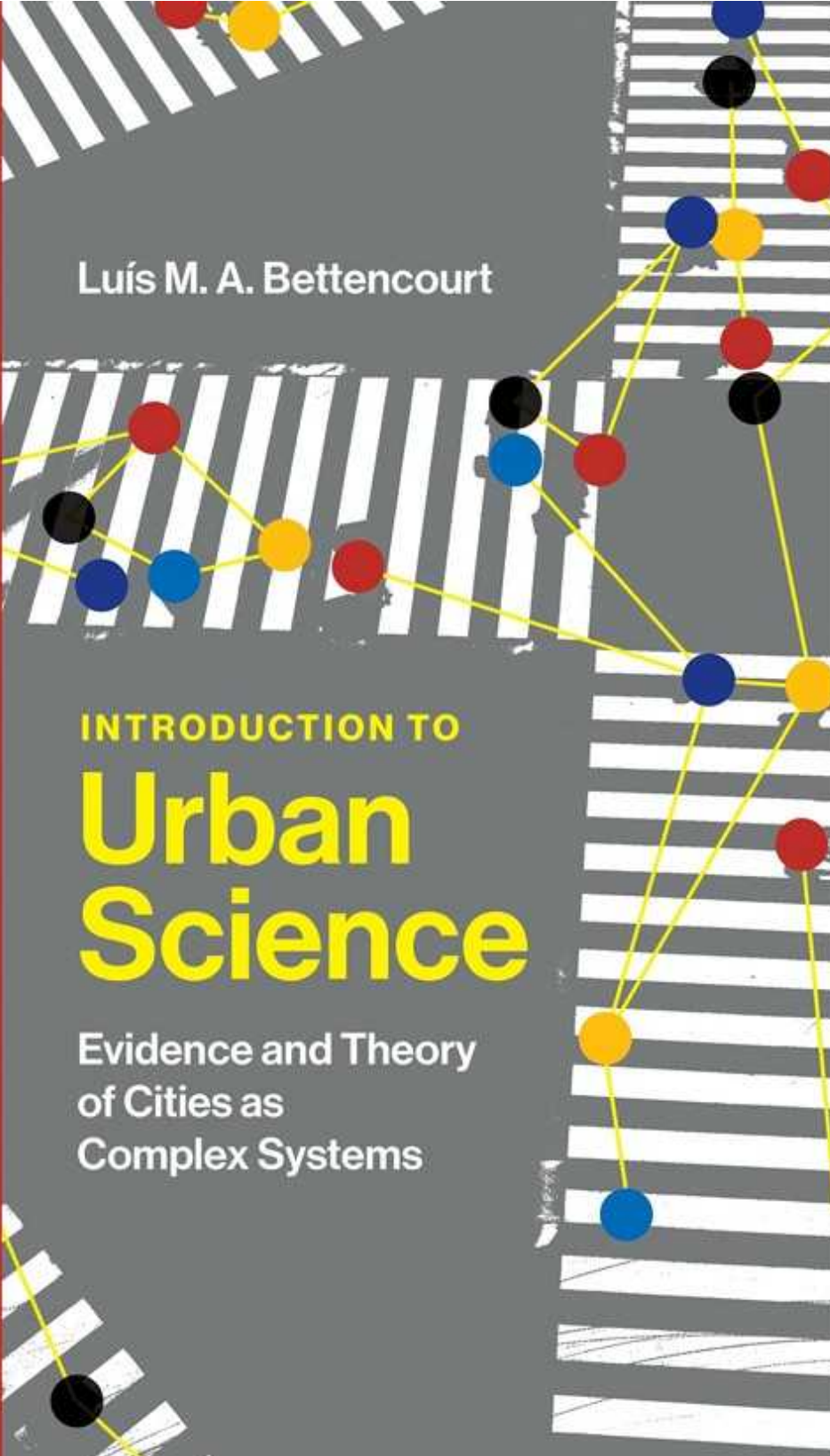


CAROLE HOOVEN

Testosterone

Carole Hooven *Cassell* (2021)

Testosterone has been controversial since its naming in 1935. Men typically produce 10–20 times more than women, but how does it affect society? Biologist Carole Hooven's fascination began in Africa, after seeing a male chimpanzee savagely beat a female beside her offspring with a stick, for no apparent reason. Her vivid study wrestles with whether sex hormones create pronounced mental differences. She concludes: "In a number of important ways, testosterone pushes the psychology and behaviour of the sexes apart."



Luis M. A. Bettencourt

INTRODUCTION TO

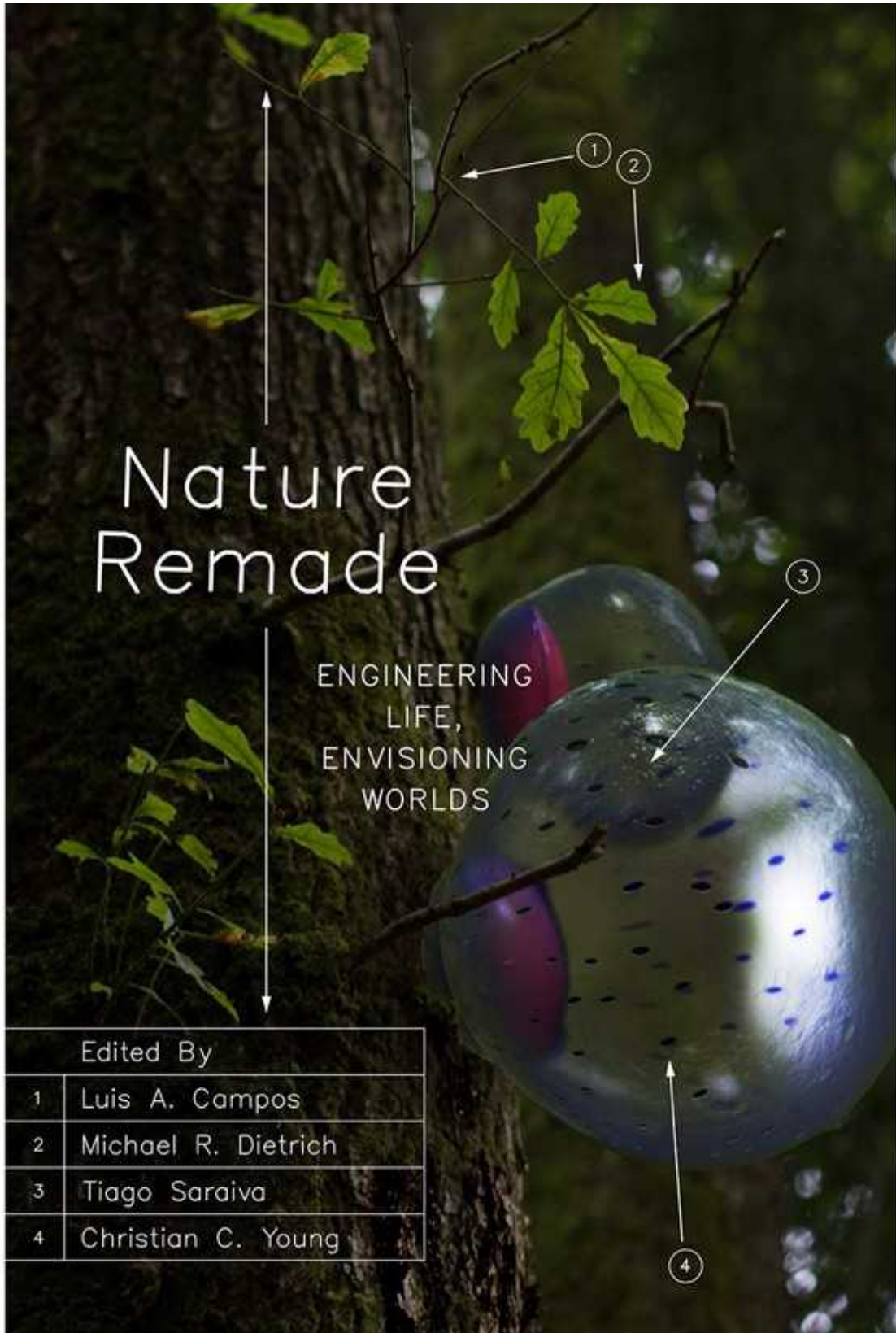
Urban Science

Evidence and Theory
of Cities as
Complex Systems

Introduction to Urban Science

Luís M. A. Bettencourt *MIT Press* (2021)

Two aerial photographs preface this detailed statistical study. In one photo, Tokyo has been almost flattened by 1940s bombing; in the other, it is rebuilt as the world's largest city, with nearly 40 million inhabitants. These illustrate, says physicist-turned-urban ecologist Luis Bettencourt, that "knowledge, human cooperation and collective action" can build a better urban future. His brand of modelling treats cities as complex adaptive systems, to make useful and falsifiable predictions about crime, economic output, migration and more.



Nature Remade

Eds Luis A. Campos *et al.* *Univ. Chicago Press* (2021)

Engineering applied to biology provokes fascination and apprehension. This essay collection explores that tension on scales ranging from molecules to people to planet, across eras and cultures. The editors — three historians and a biologist — aim to show that every effort at remaking nature “inescapably occurs in a particular social and political milieu”. Original examples include orange cultivation in Palestinian identity and the African American scholars who explored “black eugenics”.

Nature **598**, 409 (2021)

doi: <https://doi.org/10.1038/d41586-021-02676-3>

This article was downloaded by **calibre** from <https://www.nature.com/articles/d41586-021-02676-3>

| [Section menu](#) | [Main menu](#) |

Opinion

- **Congo Basin rainforest — invest US\$150 million in science**
[20 October 2021]
Comment • The world's second-largest rainforest is key to limiting climate change — it needs urgent study and protection.
- **Countries of the Indo-Gangetic Plain must unite against air pollution** [19 October 2021]
Correspondence •
- **The lesson of talk over tea and cakes? Local research matters** [19 October 2021]
Correspondence •
- **United States has several programmes for early-career leaders** [19 October 2021]
Correspondence •
- **Credit local authors fairly on international research papers**
[19 October 2021]
Correspondence •

- COMMENT
- 20 October 2021

Congo Basin rainforest — invest US\$150 million in science

The world's second-largest rainforest is key to limiting climate change — it needs urgent study and protection.

- [Lee J. T. White](#) ⁰,
- [Eve Bazaiba Masudi](#) ¹,
- [Jules Doret Ndongo](#) ²,
- [Rosalie Matondo](#) ³,
- [Arlette Soudan-Nonault](#) ⁴,
- [Alfred Ngomanda](#) ⁵,
- [Ifo Suspense Averti](#) ⁶,
- [Corneille E. N. Ewango](#) ⁷,
- [Bonaventure Sonké](#) ⁸ &
- [Simon L. Lewis](#) ⁹



A warden with an orphaned mountain gorilla in the Virunga National Park sanctuary in the Democratic Republic of the Congo. Credit: Phil Moore/AFP/Getty

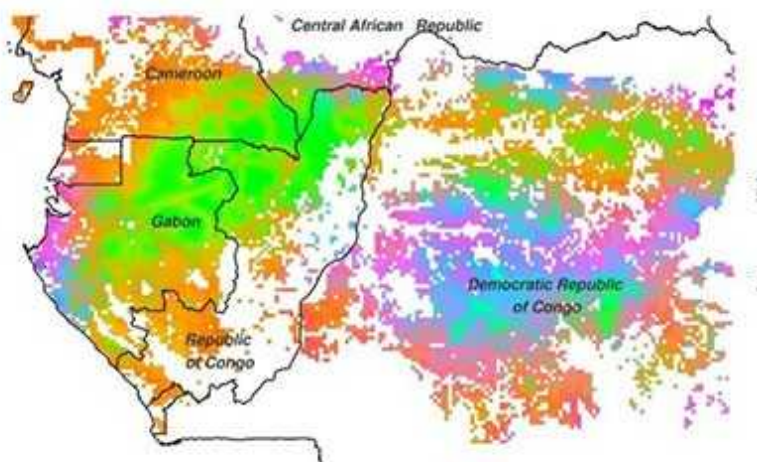
Earth's second-largest expanse of tropical forest lies in central Africa, in the Congo Basin. The region supports the livelihoods of 80 million people. The rainfall that the forest generates as far away as the Sahel and the Ethiopian highlands supports a further 300 million rural Africans. These forests are crucial to regulating Earth's climate, and are home to forest elephants, gorillas and humans' closest relatives, chimpanzees and bonobos.

Such services to people and the planet are not guaranteed, given rapid climate change and ongoing development in the region. The forest's ability to absorb carbon dioxide is slowing as temperatures rise¹. Deforestation, although lower than elsewhere in the tropics over recent decades, has led to the loss of more than 500,000 hectares of forest in 2019 alone (see go.nature.com/3dnxm9e). Without new policies, this is expected to increase.

Yet, too often, central Africa's rainforests are ignored or downplayed. The Congo Basin forests receive much less academic and public attention than do those in the Amazon and southeast Asia. Between 2008 and 2017, the Congo Basin received just 11.5% of international financial flows for forest protection and sustainable management in tropical areas, compared with 55% for southeast Asia and 34% for the Amazon region².

The area is neglected even by comparison with the rest of Africa. For example, a key UK-funded programme of climate research, called Future Climate for Africa, invested £20 million (US\$27 million) in modelling and four projects focused on eastern, western and southern Africa. None focused on the Congo Basin or central Africa.

The result of this neglect is clear in high-level climate assessments. Central Africa was one of only two regions worldwide without enough data for the Intergovernmental Panel on Climate Change to assess past trends in extreme heat in its 2021 Working Group I report (the other was the southern tip of South America).



A collaborative look at the Congo Basin

We are a group of ministers who have responsibility for forests in the region, and scientists who work on the ground and advise governments. Together we call for a Congo Basin Climate Science Initiative. This should comprise a

\$100-million, decade-long programme of research, tied to a separate \$50-million fund to train Congo Basin nationals to become PhD-level scientists. Such funding would transform our understanding of these majestic forests, providing crucial input for policymakers to help them enact policies to avoid the region's looming environmental crises.

There is precedent for such a transformation. In the mid-1990s, rainforest science in the Amazon region was limited and was largely conducted by overseas scientists. Formally beginning in 1998 and led by Brazilians, the Large-Scale Biosphere-Atmosphere Experiment in Amazonia programme, known as the LBA, was a 10-year, \$100-million effort. It revolutionized understanding of the Amazon rainforest and its role in the Earth system.

The LBA involved 6 years of intensive measurements and covered climatology, hydrology, ecology and biogeochemistry across an area of 550 million hectares. It comprised 120 projects and 1,700 participants, 990 of whom were Brazilians³. One of its greatest legacies was the creation of a new cadre of Brazilian researchers. Two decades on, Brazil is now widely acknowledged as the world's leading nation for tropical forest monitoring, and is at the forefront of rainforest science.

We should — we must — do the same for central Africa.

Known unknowns

The Greater Congo Basin covers some 240 million hectares of contiguous forests, straddling 8 nations (see ‘Earth’s second green lung’). Merely sampling this vast area is daunting. Access often requires days of travel in dugout canoes and long treks through the humid jungle, punctuated by wading through swamps. There is also a pervasive prejudice: too many people think working in the Congo Basin region is perilous, whether the hazards are political instability, unfamiliar diseases or dangerous animals. In reality, for the vast majority of central Africa, the risks are similar to working in the Amazon rainforest or east African savannah ecosystems.

EARTH'S SECOND GREEN LUNG

The Congo Basin rainforest covers about 240 million hectares across 8 nations. Crucial to the climate, it absorbs the same annual amount of carbon as Africa emitted from fossil-fuel use each year in the 2010s. The forest supports hundreds of millions of people across Africa.



Source: Ref. 1

These various challenges can be surmounted. Papers from the past few years, co-authored by many of us, highlight how important and understudied the region is. In 2017, the world's largest tropical peatland complex was mapped for the first time — an area spanning 14.6 million hectares in the heart of the Congo basin⁴. This work radically shifted our understanding of carbon stores in the region. In March 2020, an international consortium showed that Africa's rainforests annually absorb the same amount of carbon¹

as was emitted each year by fossil-fuel use across the entire African continent in the 2010s⁵.

In December 2020, a striking 81% decline in fruit production over 3 decades in an area of forest in Gabon was shown to coincide with climate warming and an 11% decline in the body condition of forest elephants (they rely on fruit for part of their diet)⁶. And in April, the first region-wide assessment of tree community composition in central Africa was published⁷, mapping areas that are vulnerable to climate change and human pressures.



Biodiversity needs every tool in the box: use OECMs

Overall, the strikingly recent (although somewhat limited) data suggest that the tropical forests of the Congo Basin are more carbon-dense⁸, more efficient at slowing climate change¹ and more resistant to our changing climate⁹ than are Amazon tropical forests. But we do not know how increasing droughts, higher temperatures, selective logging and deforestation might interact — including the possibility of reduced rainfall in the Sahel¹⁰ and Ethiopian highlands¹¹. Some 2,500 years ago, vast swathes of the Congo Basin forests were lost during a period of climate stress, but researchers do not understand the historic context of that event, nor the likelihood of a repeat¹².

Little is known about the region because not enough science is done in central Africa. Remarkably, researchers still do not understand the basic principles of why different types of forest occur where they do in the Congo Basin. Climate models for this region are poor, both because of the complex interplay of Atlantic, Indian and Southern ocean influences and because of a lack of local climate data. Without more data and more specialists, it is impossible to make reliable predictions of these forests' responses to changes in climate and land use.

Next steps

Investment in basic science is urgently needed to fill these gaps. A Congo Basin Climate Science Initiative should focus on three important overarching questions: how does the Congo Basin currently operate as an integrated system? How will changes in land use and climate affect its function? And how sustainable are different options for development?

Within these broad topics are more specific questions that politicians will need answers to if nations are to achieve net-zero CO₂ emissions by 2050. One such question is how much carbon is stored in vegetation and soils. These and other quantities must be reported as part of countries' commitments to the 2015 Paris climate agreement. At present, most central African countries rely on default values, which could be way off the mark. A recent paper¹³ on African montane forests largely near the edges of the basin, for example, showed that measured carbon storage values were 67% higher than the default values.



A child on the Mongala River in the dense forest of the Democratic Republic of the Congo. Credit: Pascal Maitre/Panos

A science initiative will work only if there is enthusiasm and leadership from researchers and active support from key Congo Basin countries, alongside buy-in from funders. We envision three steps to achieve these aims.

First, scientists from the Congo region should hold a workshop with the LBA architects and participants to assess lessons from the Amazon region. This south–south cooperation would build a scientist-led framework to address the crucial research questions.

Second, a meeting of politicians and advisers from the region would facilitate discussions of the policy-relevant questions that scientists should investigate. This would be led by Cameroon, the Democratic Republic of the Congo, Gabon and the Republic of the Congo — the four nations conducting the most research in the region. The meeting will help to lock in political

support across ministries responsible for forests, environment, water, climate, science and universities.



Nature-based solutions can help cool the planet — if we act now

Third, partners will need to develop an overarching science programme that is acceptable to funders. Such a programme will probably include scaling up many efforts that are already under way, but which are currently insufficient in scope or unreliably funded. This would speed up scientific progress.

For example, a handful of established, long-term field sites already exist in the Greater Congo Basin, including in Lopé National Park in Gabon and in the Yangambi Biosphere Reserve in the Democratic Republic of the Congo. These ‘supersites’ are sophisticated field stations with full-time staff who collect reliable, long-term data sets on vegetation, animals and the physical environment, including greenhouse-gas fluxes at Yangambi. But the sites are too few in number, and they rely on the heroic efforts of local champions. There should be a dozen or so locations across the region, with consistent funding to support complex research projects.

Similarly, the African Tropical Rainforest Observation Network (AfriTRON), established in 2009, tracks every tree in permanent sample plots to estimate the carbon balance of undisturbed forests. Although this observatory has ramped up from its original 40 sites in central Africa to

more than 200 today, these cover just 250 hectares of the roughly 240-million-hectare total. That is very sparse sampling from which to draw regional conclusions.

Meanwhile, the Forest Global Earth Observatory (ForestGEO), established in 1990 to understand how tropical forests maintain such a diverse number of tree species, has established just 4 sites in central Africa in 30 years, with none in the centre of the basin. There is an obvious need for expansion.



African forest elephants in Ivindo National Park, Gabon. Credit: Amaury Hauchard/AFP/Getty

Finally, the 2016 AfriSAR airborne field campaign, a collaboration between NASA, the European Space Agency and the Gabonese Agency for Space Studies and Observation, showed how to combine different data sets to carefully map forest types and their carbon stocks in Lopé National Park in Gabon. This model could be replicated elsewhere in the basin.

All of this work will require linking theory, observations, experiments and modelling. It should attract a diversity of leading international experts to focus on Africa and provide training to Congo Basin nationals. A \$100-million research programme would provide new opportunities and much-needed career options for African scientists. The tied investment of \$50 million, focused on building talent, could produce approximately 200 PhDs awarded by leading universities worldwide. This would create a new generation of scientists, including future leaders, from central Africa. The training programme would ensure the necessary step-change in science capacity, and provide opportunities for young African researchers who currently find it hard to compete for international scholarships, which are often won by students from Asia or South America.

Agreeing on open access for all the data collected, as in the LBA programme, will significantly boost the initiative's science impact.

Money well spent

This \$150-million science programme over 10 years needs investors. One option would be to combine funds from governments that have made large forest- and science-related investments in the Congo Basin in the past, notably Belgium, France, Germany, Norway, the United Kingdom, the United States and the European Union. Alternatives include United Nations agencies, international climate funds and private philanthropy organizations. Such a programme should be high on funders' agendas, given the UN Sustainable Development Goals (SDGs). These include raising capacity for effective climate-change-related planning and management (SDG13), increasing financial resources to conserve and sustainably use biodiversity and ecosystems (SDG15), boosting the number of researchers in lower-income countries, and increasing research and development (R&D) funding (SDG9), all before 2030.

Global R&D funding was \$2.2 trillion in 2019¹⁴. Thus, investing \$150 million over a decade to better understand and protect the world's second-largest extent of tropical forest is modest. To put this sum in context, the US government's total projected cost for the Human Genome Project was \$2.7 billion, and the European Space Agency spends approximately \$500 million

on its larger, long-lasting scientific satellites. The \$100 million that the LBA brought to the Amazon in the 1990s is equivalent to about \$160 million in today's terms.



Ethiopia, Somalia and Kenya face devastating drought

The investment in science will pay for itself many times over. Consider just the role of forests as reservoirs of zoonotic diseases. Better forest management lowers the risk of disease outbreaks, let alone a pandemic¹⁵.

Critics might argue that direct interventions in development aid are more urgent than investing in climate and ecological science. However, these funds are usually independent and do not compete. Furthermore, the old division between ending poverty and protecting the environment no longer applies: Africans will suffer disproportionately if temperatures are not limited as per the Paris agreement. That must include protection of the forests of the Congo Basin.

Further efforts could help to support the goals of the Congo Basin science programme. For example, there is a lack of economic models that show how standing forests can become more valuable than converted landscapes. Developing these would support policy decisions to maintain forest cover.

There are also several efforts under way to improve forest management that aim to empower local people, increase income and protect the environment. These include the transfer of land-management decisions to local populations, such as through community forestry, and creating high-value end products from selective logging rather than relying on the export of raw, unprocessed timber. A new science initiative could assess various approaches to understand what works best.

We know so little about the majestic forests of central Africa. A Congo Basin Climate Science Initiative would curb our collective ignorance. A lack of investment is the barrier to safeguarding these precious ecosystems. Surmount this, and the future of Earth's second 'great green lung' will be brighter.

Nature **598**, 411–414 (2021)

doi: <https://doi.org/10.1038/d41586-021-02818-7>

References

1. 1.

Hubau, W. *et al. Nature* **579**, 80–87 (2020).

2. 2.

Atyi, R. E. *et al. International Financial Flows to Support Nature Protection and Sustainable Forest Management in Central Africa* (Central Africa Forest Observatory, 2019).

3. 3.

Lahsen, M. & Nobre, C. A. *Environ. Sci. Policy* **10**, 62–74 (2007).

4. 4.

Dargie, G. C. *et al. Nature* **542**, 86–90 (2017).

5. 5.

Ayompe, L. M., Davis, S. J. & Egoh, B. N. *Environ. Res. Lett.* **15**, 124039 (2020).

6. 6.

Bush, E. R. *et al.* *Science* **370**, 1219–1222 (2020).

7. 7.

Réjou-Méchain, M. *et al.* *Nature* **593**, 90–94 (2021).

8. 8.

Lewis, S. L. *et al.* *Phil. Trans. R. Soc. B* **368**, 20120295 (2013).

9. 9.

Bennett, A. C. *et al.* *Proc. Natl Acad. Sci. USA* **118**, e2003169118 (2021).

10. 10.

Salih, A. A. M., Zhang, Q. & Tjernström, M. *J. Geophys. Res. Atmospheres* **120**, 6793–6808 (2015).

11. 11.

Gebrehiwot, S. G. *et al.* *WIREs Water* **6**, e1317 (2019).

12. 12.

Malhi, Y. *Proc. Natl Acad. Sci. USA* **115**, 3202–3204 (2018).

13. 13.

Cuni-Zanchez, A. *et al.* *Nature* **596**, 536–542 (2021).

14. 14.

Sargent, J. F. *Global Research and Development Expenditures: Fact Sheet R44283* (Congressional Research Service, 2021).

15. 15.

Everard, M., Johnston, P., Santillo, D. & Staddon, C. *Environ. Sci. Policy* **111**, 7–17 (2020).

This article was downloaded by **calibre** from <https://www.nature.com/articles/d41586-021-02818-7>

| [Section menu](#) | [Main menu](#) |

- CORRESPONDENCE
- 19 October 2021

Countries of the Indo-Gangetic Plain must unite against air pollution

- [Muhammad Fahim Khokhar](#) ORCID: <http://orcid.org/0000-0003-4489-6593>⁰,
- [Muhammad Shehzaib Anjum](#) ORCID: <http://orcid.org/0000-0002-2873-5741>¹,
- [Abdus Salam](#) ORCID: <http://orcid.org/0000-0002-5609-6828>²,
- [Vinayak Sinha](#) ORCID: <http://orcid.org/0000-0002-5508-0779>³,
- [Manish Naja](#) ORCID: <http://orcid.org/0000-0002-4597-1690>⁴,
- [Hiroshi Tanimoto](#) ORCID: <http://orcid.org/0000-0002-5424-9923>⁵,
- [James H. Crawford](#) ORCID: <http://orcid.org/0000-0002-6982-0934>⁶&
- [Mohammed Iqbal Mead](#) ORCID: <http://orcid.org/0000-0003-0436-4074>⁷

Pakistan, India, Nepal and Bangladesh share a global air-pollution hotspot spanning the Indo-Gangetic Plain. It accounts for almost 30% of global deaths from poor air quality (<https://stateofglobalair.org>). We call for expanded collaboration across the region to increase monitoring and data sharing.

Access options

Subscribe to Journal

Get full journal access for 1 year

\$199.00

only \$3.90 per issue

[Subscribe](#)

All prices are NET prices.

VAT will be added later in the checkout.

Tax calculation will be finalised during checkout.

Rent or Buy article

Get time limited or full article access on ReadCube.

from \$8.99

[Rent or Buy](#)

All prices are NET prices.

Additional access options:

- [Log in](#)
- [Learn about institutional subscriptions](#)

Nature **598**, 415 (2021)

doi: <https://doi.org/10.1038/d41586-021-02829-4>

This article was downloaded by **calibre** from <https://www.nature.com/articles/d41586-021-02829-4>

- CORRESPONDENCE
- 19 October 2021

The lesson of talk over tea and cakes? Local research matters

- [Sandersan Onie](#) ⁰ &
- [Ashra Daswin](#) ¹

One of us, A.D., has been part of a national effort to establish support groups for mental health across Indonesia. These groups used formal meetings to discuss people's problems, in line with research published in leading scientific journals. All except one failed. That one was much less formal and more compatible with the local culture. People gossiped (*ghibah*) and casually chatted about their lives over tea and *kueh* (cakes) while doing handicrafts. The benefits were remarkable.

Access options

Subscribe to Journal

Get full journal access for 1 year

\$199.00

only \$3.90 per issue

[Subscribe](#)

All prices are NET prices.

VAT will be added later in the checkout.

Tax calculation will be finalised during checkout.

Rent or Buy article

Get time limited or full article access on ReadCube.

from \$8.99

[Rent or Buy](#)

All prices are NET prices.

Additional access options:

- [Log in](#)
- [Learn about institutional subscriptions](#)

Nature **598**, 415 (2021)

doi: <https://doi.org/10.1038/d41586-021-02832-9>

This article was downloaded by **calibre** from <https://www.nature.com/articles/d41586-021-02832-9>

| [Section menu](#) | [Main menu](#) |

- CORRESPONDENCE
- 19 October 2021

United States has several programmes for early-career leaders

- [Dalal Najib](#)⁰,
- [John Boright](#)¹ &
- [John Hildebrand](#)²

Your Editorial misleadingly claims that the United States is among the countries that do not have a Young Academy ([Nature 594, 474; 2021](#)). The goals of national programmes for early-career science leaders can vary: some choose not to call themselves academies. The United States has had such a programme since 2018, entitled New Voices in Sciences, Engineering, and Medicine.

Access options

Subscribe to Journal

Get full journal access for 1 year

\$199.00

only \$3.90 per issue

[Subscribe](#)

All prices are NET prices.
VAT will be added later in the checkout.

Tax calculation will be finalised during checkout.

Rent or Buy article

Get time limited or full article access on ReadCube.

from \$8.99

[Rent or Buy](#)

All prices are NET prices.

Additional access options:

- [Log in](#)
- [Learn about institutional subscriptions](#)

Nature **598**, 415 (2021)

doi: <https://doi.org/10.1038/d41586-021-02830-x>

This article was downloaded by **calibre** from <https://www.nature.com/articles/d41586-021-02830-x>

| [Section menu](#) | [Main menu](#) |

- CORRESPONDENCE
- 19 October 2021

Credit local authors fairly on international research papers

- [Angela I. N. Obasi](#) ORCID: <http://orcid.org/0000-0001-6801-8889>⁰,
- [Seye Abimbola](#) ORCID: <http://orcid.org/0000-0003-1294-3850>¹,
- [Ndekya Oriyo](#) ORCID: <http://orcid.org/0000-0001-6336-9911>²,
- [Ben Morton](#) ORCID: <http://orcid.org/0000-0002-6164-2854>³,
- [André Vercueil](#) ORCID: <http://orcid.org/0000-0003-1591-4131>⁴ &
- [Refiloe Masekela](#) ORCID: <http://orcid.org/0000-0001-9665-2035>⁵

As co-signatories on a consensus statement released this month (see [B. Morton et al. *Anaesthesia* https://doi.org/10.1111/anae.15597; 2021](#)), we call on all scientific journals to adopt a system that promotes fairness in author-contribution assessments for research done in low-to-middle-income countries by teams that include authors from institutions in high-income countries.

Our system consists of a structured reflexivity statement that asks authors a series of open-ended questions that broadly follow established authorship criteria (see go.nature.com/3aed2). These help to ensure that researchers from low- to middle income countries and other disadvantaged groups, such as women and early-career researchers, are properly represented.

Progress in addressing such imbalances has been slow ([A. I. Obasi *Lancet* 396, 651–653; 2020](#)). For example, one-fifth of the papers describing COVID-19 in Africa contain no African authors and, of those that do, the first and last authors are almost always from high-income nations ([A. V. Naidoo et al. *BMJ Glob. Health* 6, e004612; 2021](#)).

Such reflexivity statements (see also *Cell* **184**, 1–2; 2021 and [go.nature.com/3degzc2](https://doi.org/10.1016/j.cell.2020.10.032)) will encourage inclusive and open discussion of issues affecting equity, including capacity strengthening and research legacy in host countries.

Nature **598**, 415 (2021)

doi: <https://doi.org/10.1038/d41586-021-02831-w>

This article was downloaded by **calibre** from <https://www.nature.com/articles/d41586-021-02831-w>

| [Section menu](#) | [Main menu](#) |

Work

- **How three refugee scientists kept their research hopes alive**

[19 October 2021]

Career Feature • Two organizations that support at-risk academics offered funding, fellowship and language support at a critical time.

- **Saving hawksbill sea turtles from rats, cats and Hurricane**

Ida [18 October 2021]

Where I Work • Hatching season on the Caribbean island of Barbados is a busy time for Carla Daniel.

- CAREER FEATURE
- 19 October 2021

How three refugee scientists kept their research hopes alive

Two organizations that support at-risk academics offered funding, fellowship and language support at a critical time.

- [Virginia Gewin](#) ⁰

[Find a new job](#)



Bombed buildings in Aden, Yemen, in November 2018.Credit: Giles Clarke/UNOCHA/Getty

The Institute of International Education (IIE), a non-profit organization based in New York City that supports international researchers, estimates that thousands of displaced scientists from nations such as Syria, Iraq and Yemen are now living as refugees elsewhere. Its figures are based on refugee counts, pre-war higher-education data from the countries of origin, applications for assistance and personal anecdotes.

It's unclear how many scientists will be able to leave Afghanistan, but a *Nature* editorial last month called on the international scientific community to help support those who become refugees as well as researchers who must remain in the unstable country (see [*Nature* 597, 8; 2021](#)).

Refugee scientists who have escaped nations that are riven by war or other conflicts can struggle to continue their research in their new countries of residence.

The IIE's Scholar Rescue Fund (IIE-SRF) offers fellowships and is one of a small number of sources of support for refugee scientists' efforts to keep their research going. Another is the Council for At Risk Academics (CARA), a London-based charity that helps academics to continue their work at one of 124 partner universities and institutions in the United Kingdom, or in other safe locations.

CARA launched a Syria programme in 2016 following a huge increase in the number of academics seeking help after fleeing the country, where civil war broke out in 2011. Kate Robertson, CARA's Syria programme adviser, says the programme requires applicants to have held a paid post as a lecturer or researcher at a higher-education institution or an equivalent.

Unsurprisingly, female refugee scientists can face extra challenges — including gendered, cultural and socio-political barriers to academia (see [*R. Ibesh et al. Int. J. Educ. Res. Open* 2, 100027; 2021](#)). At CARA, for example, there is a 6:1 ratio of men to women among programme participants. "There's always been a gender imbalance," says Robertson. But she says that more women are now applying for research grants and leading teams.

Nature spoke to two CARA-supported refugee scientists from Syria (one of whom requested anonymity) and an IIE-supported researcher from Yemen about their trials and triumphs as they continue their research despite extraordinary conditions.



Adnan Almohamad and archaeologist Jen Baird at Senate House Library, University of London. Credit: Adnan Almohamad

ADNAN ALMOHAMAD: Improving my English would change everything

Adnan Almohamad is an archaeologist from Syria, who is now based in Istanbul, Turkey.

I came back to Syria in 2008 with my wife and three children, after earning a master's degree in social sciences in France that focused on archaeological antiquities. When the war started, I was working in the Syrian government's

Directorate-General of Antiquities and Museums, and was a lecturer in the Department of Antiquities at the University of Aleppo. In 2012, the Free Syrian Army took control of eastern Aleppo, and my family and I fled the city after government forces began randomly bombing the area where we were living. I went to Manbij, my hometown, which is about 90 kilometres east of Aleppo and was then under control of the Free Syria Army. In 2014, once violence escalated as Islamic State rebels took control, I sent my family to Osmaniye, a small city in southern Turkey, but I came back to Manbij and formed a small, secret team to document the destruction of Syrian cultural heritage.

In 2016, I was forced to flee to Turkey, joining my family in Osmaniye. When I first arrived, I worked at least 12 hours a day in a factory, for US\$3–5 per day. It was just enough to buy food. I was always worried about how to pay rent and other bills. I was lost. I had no time to think about my academic future.

In December 2018, I left my family to seek work in Istanbul. I met a friend who told me about CARA's Syria programme. It was a turning point in my life: in 2019, I e-mailed CARA and got a reply 20 minutes later. They invited me to attend a workshop in Istanbul a month later, about how to write high-quality academic papers.

CARA then awarded me a grant to conduct research on the destruction and looting of Syrian cultural heritage sites, particularly in Manbij and surrounding areas. It also gave me funding for a research visit to Birkbeck, University of London and Durham University, UK. I travelled there in mid-2019, and shared my knowledge of what's happening on the ground regarding Syrian heritage and cultural resources. We had collected photos, videos and reports documenting destruction and looting of archaeological and cultural heritage sites. We shared these with foreign academics who had been able to access only satellite imagery, and we were able to compare my information with theirs to understand the scale of the damage.



Shash Hamdan, a Roman tomb near the upper Euphrates river, Syria, in 2010.Credit: Adnan Almohamad

I don't speak Turkish. I speak some French and know some words in English. If I could improve my English or study English in the United Kingdom for six months, it would change everything for me. My goal is to attain a PhD in archaeology and, one day, to write a book on the archaeological history of the countryside east of Aleppo, spanning the earliest beginnings of agrarian civilization, the Bronze and Iron ages, and the Roman and Ottoman empires.

CARA's Syria programme has helped me return to my academic life. It gave me the opportunity to connect with Syrian and foreign academics, to acquire academic research skills and to improve my English. I have produced five articles; two have been accepted, two are under review and I am still working on the fifth.

ANONYMOUS FEMALE CHEMIST: Don't wait for the situation to get better

The interviewee, who requested anonymity, is a Syrian who is now based in Turkey.

In 2012, I had just finished my master's degree in chemistry at a university in Syria when fighting broke out in the country.

My husband, children and I didn't leave Syria right away, because we expected the war to end soon. We moved to the northern suburbs of Aleppo, but once the shelling reached those areas, we felt we had to move to Turkey. When we arrived there we had little money, so we stayed in a refugee camp, which I estimate held around 1,000 people. We were allowed to set up temporary Syrian schools to teach our children, and to work in the camp's schools for nominal wages. After a year, we were able to rent a modest house in a town in southern Turkey.



[Biochemistry in a conflict zone](#)

Hoping our stay would be temporary, I found work as a chemistry teacher rather than continuing my own education. But I didn't speak Turkish or have Turkish citizenship, so my employment options were limited. It was really

difficult when we first moved to Turkey because we couldn't communicate with others, which also made sharing my CV or presenting myself or my work so much harder.

My husband, too, studied chemistry and worked as a teacher in Syria. Three years on from our arrival in Turkey, we realized that we would be living there as refugees for quite a while. We decided to think of ways to continue with our academic goals.

In 2016, I started learning Turkish and made contact with CARA. I was invited to a round-table discussion involving academics and Turkish officials; I was one of only two female academics. CARA provided us with English-language courses and tutors. These weekly sessions helped me and fellow Syrian academics to improve our language competency; we are now familiar with English grammar and how to read, but conversation is still difficult.

Ultimately, I decided to pursue a research scholarship from the Turkish government to conduct my PhD, and was awarded one in 2016 after an initial rejection. I started my PhD in chemistry the following year. Many Syrians have been granted Turkish citizenship. Employment options are very different depending on whether you have citizenship or not. If you don't, you can teach foreigners or international students as long as you can speak either Turkish or English, but contracts are temporary.

To get a job in academia, immigrants must get an equivalence certificate, a document stating that your degree is equivalent to the corresponding Turkish degree. These certificates are issued only by the Turkish Ministry of Education. It's difficult to get one: I took the required exam last month for my master's degree, but I did not pass. A group of colleagues are signing a petition to have this requirement reviewed, because so few people have passed.



Afghanistan's terrified scientists predict huge research losses

I experience more equity in Turkey as an educated woman in academia than I did in Syria. But, as a refugee here, I've been on a path that's full of challenges: I've had to travel long distances every week, produce research in a foreign language, collaborate with people I didn't know and live in a world of uncertainties.

There are very few female Syrian academics compared with male ones; I know only about ten other female researchers. I hope that women can be provided with more support to increase those numbers.

I know I will achieve something; I am meant to be here in Turkey. In May, I published a review paper, and I plan to finish my PhD in three months' time.

My advice to other refugee scientists is not to waste any time once you move to a new country. Start learning the native language as soon as possible. And don't make the mistake we did: don't wait for the situation to get better. Find ways to continue on an academic path. If the situation improves in Syria and we can go back, we will be going back stronger than before.



Residency battles: Hasan Maridi
Credit: Hasan Maridi

HASAN MARIDI: Securing residency is my biggest challenge

Hasan Maridi is a Yemeni nuclear physicist, now based in Jordan and Poland.

I'm from a village on the Red Sea coast of Yemen. I got my PhD in nuclear physics in November 2014 from Cairo University, and returned to Yemen the following year to build a life there with my wife and three children. By then, the country's civil war had escalated, and on 26 March 2015, there were air strikes led by Saudi Arabian forces that were intervening on behalf of the Yemeni government. Soon after, there was no water, no Internet, no anything.

I focused on how to support my family, and found work teaching in the Faculty of Engineering at the University of Hodeida, based in the Red Sea port city of that name, earning about US\$90 monthly. I worked there half-time for about two years. Sometimes I taught courses far from my speciality to keep my family fed. We lived in a single room without beds, water and electricity. I remember trying to find a street lamp so that I could write lectures and correct the exam papers of my students. In the summer, when there was no teaching work, I drove a taxi and worked in a sweet factory.

I am a theoretical nuclear physicist. When I heard about the IIE-SRF scholarship, I applied and got a grant in 2018. In August, I travelled to Jordan. It was a difficult and terrifying trip, on which I was interrogated at dozens of security checkpoints. In February 2019, my family joined me in Amman. I found work as an assistant professor in alternative energy technology at Philadelphia University in Amman, the institution that hosted my scholarship. I then applied for a scholarship from the Polish National Agency for Academic Exchange, an organization set up in 2017 to foster academic mobility between Poland and other countries.

I joined the Heavy Ion Laboratory at the University of Warsaw for two weeks in early 2020. I had met its principal investigator several years earlier at an international conference, so he knew my situation in Yemen and sponsored me. Then, COVID-19 emerged, and I returned to Jordan for six months. In September 2020, I returned to Warsaw to continue my research with a mini-scholarship from the IIE-SRF — about five months of funding.

The biggest challenge lately has been securing residency for my family in Jordan. In April 2021, I returned to Jordan to resolve their residency status. It's been a long, convoluted process. I now have to pay fees to receive residence cards for my family. Hopefully these will allow my family to receive visas to enter Poland, and join me there next year.

I have worked hard. In 2021, I published an article in the *International Journal of Modern Physics E*, and I am a co-author and first author on two papers published by *Physical Review C*, a nuclear-physics journal and the best in my field. I forgot about visa and residency problems when I'm working.

In 2020, I co-founded the Association of Yemeni Academics and Professionals to assist Yemeni academics abroad. We have a Facebook group and a YouTube channel. We share information on grant or job opportunities, and we write recommendation letters. I'm confident in myself, and confident that I will reach my career goal of one day working at top US research laboratories.

Nature **598**, 527-529 (2021)

doi: <https://doi.org/10.1038/d41586-021-02850-7>

These interviews have been edited for length and clarity.

This article was downloaded by **calibre** from <https://www.nature.com/articles/d41586-021-02850-7>

- WHERE I WORK
- 18 October 2021

Saving hawksbill sea turtles from rats, cats and Hurricane Ida

Hatching season on the Caribbean island of Barbados is a busy time for Carla Daniel.

- [Natasha Gilbert](#) ⁰



Carla Daniel is field director of the Barbados Sea Turtle Project, based at the University of the West Indies, Cave Hill, Barbados. Micah B. Rubin for *Nature*

It was turtle-nesting season when this photograph was taken one night in June. I am on Needham's Point beach measuring a critically endangered female hawksbill turtle (*Eretmochelys imbricata*). As field director of the Barbados Sea Turtle Project, I run the day-to-day conservation activities and train and manage volunteers.

We also run research projects that inform our conservation activities. We collect data such as shell length, which can tell us the age at which females become sexually mature and can indicate growth rates. These data help us to keep track of turtle health and survival. For example, if we start seeing smaller turtles, this could indicate that they are maturing faster, or that food is scarce and the turtles are growing more slowly.

In August, the baby turtles hatch. I was on call 7 days a week for around 8 hours a day, responding to emergencies. These included hatchlings

wandering off in the wrong direction, putting them at risk of being hit by a car or eaten by predators such as rats and cats. We took the hatchlings to a safe spot on the beach and released them. I also had to prepare for the expected swells as Hurricane Ida passed us by: when beaches flood, nests can wash away. We took rescued eggs and premature hatchlings to a makeshift intensive-care unit until they were ready for release. We aim to leave no turtle behind.

I have worked at the project for 15 years. I recently finished a master's degree on the coloration of the Barbados bullfinch (*Loxigilla barbadensis*) at the University of the West Indies, which hosts the turtle project. Next year I hope to start a PhD, part of which will look at the conflict between tourism and sea-turtle survival in Barbados. Here, interactions between sea turtles and humans occur at every stage of the turtles' lives and can affect their survival. After my doctorate, I will continue to focus on helping sea turtles in the Caribbean. There is something addictive about making a real-time, tangible difference to their lives.

Nature **598**, 532 (2021)

doi: <https://doi.org/10.1038/d41586-021-02851-6>

This article was downloaded by **calibre** from <https://www.nature.com/articles/d41586-021-02851-6>

Research

- **[The genetic symphony underlying evolution of the brain's prefrontal cortex](#)** [01 October 2021]

News & Views • The prefrontal cortex of the human brain is larger than that of other species. Comparisons of mouse, macaque and human brains uncover some of the genetic and molecular factors behind these differences.

- **[Untwisted trilayer graphene hosts superconductivity and magnetism](#)** [19 October 2021]

News & Views • Superconductivity and magnetism have been observed in layered graphene in which the sheets are twisted with respect to each other. But a simpler, more stable graphene system also exhibits these phases.

- **[A step towards therapeutics for dengue](#)** [06 October 2021]

News & Views • Finding a treatment for dengue, the most prevalent mosquito-borne viral disease in humans, has been difficult. A compound called JNJ-A07 displays promising activity against dengue virus in mouse models of infection.

- **[Non-magnetic objects induced to move by electromagnets](#)**

[20 October 2021]

News & Views • A set of electromagnets has been used to move metal objects without touching them, even though the objects are not magnetic. This method could potentially be used like a ‘tractor beam’ to move hazardous objects in space.

- **[Flies sense the world while sleeping](#)** [29 September 2021]

News & Views • High-throughput analyses of how sleeping fruit flies respond to a variety of odours show that the brains of these insects continue to process the value of the signals conveyed by sensory information during sleep.

- **[Carbon monoxide gas produced by a giant impact in the inner region of a young system](#)** [20 October 2021]

Article • A carbon monoxide gas ring co-orbiting with dusty debris is observed in the outer terrestrial planet region of the star HD 172555, which indicates that a planetary-scale impact took place.

- **[Half- and quarter-metals in rhombohedral trilayer graphene](#)** [01 September 2021]

Article • A study shows that rhombohedral graphene is an ideal platform for well-controlled tests of many-body theory and reveals that magnetism in moiré materials is fundamentally itinerant in nature.

- **Superconductivity in rhombohedral trilayer graphene** [01

September 2021]

Article • Superconductivity is observed in rhombohedral trilayer graphene in the absence of a moiré superlattice, with two distinct superconducting states both occurring at a symmetry-breaking transition where the Fermi surface degeneracy changes.

- **Dexterous magnetic manipulation of conductive non-magnetic objects** [20 October 2021]

Article • Time-varying magnetic fields can be used to manipulate the position and orientation of conductive non-magnetic objects.

- **Perovskite solar cells with atomically coherent interlayers on SnO₂ electrodes** [20 October 2021]

Article • An atomically coherent interlayer between the electron-transporting and perovskite layers in perovskite solar cells enhances charge extraction and transport from the perovskite, enabling high power conversion efficiency.

- **Metallaphotoredox-enabled deoxygenative arylation of alcohols** [31 August 2021]

Article • A metallaphotoredox-based cross-coupling platform is capable of activating a wide range of free alcohols using N-heterocyclic carbene salts, cleaving C–O bonds to form free carbon radicals that are then used to form new C–C bonds.

- **Pliocene decoupling of equatorial Pacific temperature and pH gradients** [20 October 2021]

Article • New proxy data for ocean pH and an ocean–atmosphere model show that a radically different ocean circulation led to decoupling of ocean productivity and upwelling in the equatorial Pacific Ocean 3–6 million years ago.

- **Direct radiative effects of airborne microplastics** [20 October 2021]

Article • Preliminary modelling of airborne microplastics suggests that they may be exerting a minor cooling influence on the present-day atmosphere, and continued production could have increasing effects on the climate system in future.

- **The three major axes of terrestrial ecosystem function** [22 September 2021]

Article • Three key axes of variation of ecosystem functional changes and their underlying causes are identified from a dataset of surface gas exchange measurements across major terrestrial biomes and climate zones.

- **Convergent somatic mutations in metabolism genes in chronic liver disease** [13 October 2021]

Article • Whole-genome sequencing analysis of somatic mutations in liver samples from patients with chronic liver disease identifies driver mutations in metabolism-related genes such

as FOXO1, and shows that these variants frequently exhibit convergent evolution.

- **Sensory processing during sleep in *Drosophila melanogaster*** [29 September 2021]

Article • The authors develop a paradigm to study sensory discrimination during sleep in *Drosophila melanogaster*.

- **Regulation of prefrontal patterning and connectivity by retinoic acid** [01 October 2021]

Article • Studies in mice, humans and macaques show that retinoic acid signalling has an important role in the development of the prefrontal cortex (PFC) in primates and may also underlie the evolutionary diversification of the PFC.

- **Hominini-specific regulation of CBLN2 increases prefrontal spinogenesis** [01 October 2021]

Article • The authors identify deletions in a retinoic acid signalling responsive genetic element that leads to disproportionate increase of dendritic spines on neurons of the human prefrontal cortex.

- **The EDS1–PAD4–ADR1 node mediates *Arabidopsis* pattern-triggered immunity** [08 September 2021]

Article • The authors provide mechanistic insights into the crosstalk between signalling components of pattern-triggered immunity and effector-triggered immunity and their molecular linkers.

- **Activation of TIR signalling boosts pattern-triggered immunity** [20 September 2021]

Article • A study reveals that activation of Toll/interleukin-1 receptor signalling is an important mechanism for boosting plant defence during pattern-triggered immunity.

- **A pan-serotype dengue virus inhibitor targeting the NS3–NS4B interaction** [06 October 2021]

Article • The small molecule JNJ-A07 interferes with the interaction between the NS3 and NS4B proteins of dengue virus and reduces the viral load in mice even when first administered at peak viraemia.

- **Mutant clones in normal epithelium outcompete and eliminate emerging tumours** [13 October 2021]

Article • The rarity of tumour formation despite the high proportion of cancer-driver mutations in epithelia is explained by the competitive fitness of tumour cells relative to that of surrounding mutant epithelial cells.

- **Mechanism for Cas4-assisted directional spacer acquisition in CRISPR–Cas** [29 September 2021]

Article • Structures of the Cas4–Cas1–Cas2 complex from *Geobacter sulfurreducens* show that a 3'-overhang in the protospacer adjacent motif is required for complex assembly and spacer insertion into the CRISPR array.

- **Structural insights into hepatitis C virus receptor binding and entry** [15 September 2021]

Article • Crystal structures of the hepatitis C virus (HCV) glycoprotein E2 in complex with CD81 reveal the conformational changes that occur in E2 after binding of CD81 and the effects of pH on binding affinity.

- NEWS AND VIEWS
- 01 October 2021

The genetic symphony underlying evolution of the brain's prefrontal cortex

The prefrontal cortex of the human brain is larger than that of other species. Comparisons of mouse, macaque and human brains uncover some of the genetic and molecular factors behind these differences.

- [Jenelle L. Wallace](#) [ORCID: http://orcid.org/0000-0002-9565-2751](http://orcid.org/0000-0002-9565-2751)⁰
&
- [Alex A. Pollen](#) [ORCID: http://orcid.org/0000-0003-3263-8634](http://orcid.org/0000-0003-3263-8634)¹

A symphony arises from the careful coordination of many musical instruments in an orchestra. Similarly, gene expression is controlled by proteins and other molecules known as *trans*-acting regulators that behave like conductors to drive the expression of multiple genes at distant sites. Further control is exerted by stretches of DNA called *cis*-regulatory elements (CREs) that act like musicians to control the expression of individual genes nearby on the chromosome. Changes in CREs have been proposed to underlie evolutionary changes across populations, because these elements have highly specific effects on an organism's characteristics. By contrast, changes in *trans*-regulatory factors coordinate the activity of large suites of genes to influence multiple traits¹. In two studies in *Nature*, Shibata *et al.*^{2,3} explore the interplay between *cis*- and *trans*-regulatory changes in a hallmark of human evolution — the large size and highly connected nature of a brain region called the prefrontal cortex (PFC).

Access options

[Subscribe to Journal](#)

Get full journal access for 1 year

\$199.00

only \$3.90 per issue

[Subscribe](#)

All prices are NET prices.

VAT will be added later in the checkout.

Tax calculation will be finalised during checkout.

Rent or Buy article

Get time limited or full article access on ReadCube.

from \$8.99

[Rent or Buy](#)

All prices are NET prices.

Additional access options:

- [Log in](#)
- [Learn about institutional subscriptions](#)

Nature **598**, 417-418 (2021)

doi: <https://doi.org/10.1038/d41586-021-02460-3>

References

1. 1.

Carroll, S. B. *Cell* **134**, 25–36 (2008).

2. 2.

Shibata, M. *et al. Nature* **598**, 483–488 (2021).

3. 3.

Shibata, M. *et al. Nature* **598**, 489–494 (2021).

4. 4.

Buckner, R. L. & Krienen, F. M. *Trends Cogn. Sci.* **17**, 648–665 (2013).

5. 5.

Striedter, G. F. in *Principles of Brain Evolution* Ch. 9 (Sinauer, 2005).

6. 6.

Elston, G. N. *et al. Anat. Rec.* **288A**, 26–35 (2006).

7. 7.

Cadwell, C. R., Bhaduri, A., Mostajo-Radji, M. A., Keefe, M. G. & Nowakowski, T. J. *Neuron* **103**, 980–1004 (2019).

8. 8.

Miller, J. A. *et al. Nature* **508**, 199–206 (2014).

9. 9.

Carlén, M. *Science* **358**, 478–482 (2017).

- NEWS AND VIEWS
- 19 October 2021

Untwisted trilayer graphene hosts superconductivity and magnetism

Superconductivity and magnetism have been observed in layered graphene in which the sheets are twisted with respect to each other. But a simpler, more stable graphene system also exhibits these phases.

- [Thiti Taychatanapat](#) ⁰

Electrons typically propagate without interacting in graphene, a single layer of carbon atoms arranged in a honeycomb lattice. But when three sheets of graphene are stacked on top of one another so that their lattices are aligned but offset — forming rhombohedral trilayer graphene — an electric field can be used to induce interactions between the electrons. In two papers in *Nature*, Zhou *et al.* report that these interactions give [rise to ferromagnetism](#)¹, the type of magnetism found in iron magnets, and [superconductivity](#)² (zero electrical resistance). These states have already been observed in other trilayer configurations, in which the graphene sheets are slightly rotated out of alignment with each other or with a substrate, but rhombohedral trilayer graphene is more structurally stable than these materials.

Access options

Subscribe to Journal

Get full journal access for 1 year

\$199.00

only \$3.90 per issue

Subscribe

All prices are NET prices.

VAT will be added later in the checkout.

Tax calculation will be finalised during checkout.

Rent or Buy article

Get time limited or full article access on ReadCube.

from \$8.99

Rent or Buy

All prices are NET prices.

Additional access options:

- [Log in](#)
- [Learn about institutional subscriptions](#)

Nature **598**, 418-420 (2021)

doi: <https://doi.org/10.1038/d41586-021-02773-3>

References

1. 1.

Zhou, H. *et al.* *Nature* **598**, 429–433 (2021).

2. 2.

Zhou, H., Xie, T., Taniguchi, T., Watanabe, K. & Young, A. F. *Nature* **598**, 434–438 (2021).

3. 3.

Zhang, F., Sahu, B., Min, H. & MacDonald, A. H. *Phys. Rev. B* **82**, 035409 (2010).

4. 4.

Eisenstein, J. P., Pfeiffer, L. N. & West, K. W. *Phys. Rev. Lett.* **68**, 674–677 (1992).

5. 5.

Scalapino, D. J. *Rev. Mod. Phys.* **84**, 1383–1417 (2012).

6. 6.

Chen, G. *et al.* *Nature* **579**, 56–61 (2020).

7. 7.

Chen, G. *et al.* *Nature* **572**, 215–219 (2019).

8. 8.

Cao, Y., Park, J. M., Watanabe, K., Taniguchi, T. & Jarillo-Herrero, P. *Nature* **595**, 526–531 (2021).

9. 9.

Soulen, R. J. Jr *et al.* *Science* **282**, 85–88 (1998).

This article was downloaded by **calibre** from <https://www.nature.com/articles/d41586-021-02773-3>

- NEWS AND VIEWS
- 06 October 2021

A step towards therapeutics for dengue

Finding a treatment for dengue, the most prevalent mosquito-borne viral disease in humans, has been difficult. A compound called JNJ-A07 displays promising activity against dengue virus in mouse models of infection.

- [Scott B. Biering](#)⁰ &
- [Eva Harris](#)¹

Despite immense effort spent in pursuit of a therapeutic for dengue, no treatment is currently available. An effective drug against dengue virus (DENV) is urgently needed, because this mosquito-transmitted virus represents a tremendous public-health burden, with about 3.9 billion people at risk of infection (see go.nature.com/3fbf9xz) and an estimated 51 million cases of dengue annually worldwide¹. Several challenges have precluded the development of such a therapeutic: it must be administered orally, must rapidly lower the amount of virus in the bloodstream to stem progression to severe dengue, and must be similarly potent against all four main types of DENV (dubbed serotypes DENV-1 to DENV-4), all while exhibiting an acceptable safety profile. Excitingly, [writing in Nature](#), Kaptein *et al.*² describe a compound that targets the dengue virus protein NS4B and ticks all of these boxes.

Access options

Subscribe to Journal

Get full journal access for 1 year

\$199.00

only \$3.90 per issue

[Subscribe](#)

All prices are NET prices.

VAT will be added later in the checkout.

Tax calculation will be finalised during checkout.

Rent or Buy article

Get time limited or full article access on ReadCube.

from \$8.99

[Rent or Buy](#)

All prices are NET prices.

Additional access options:

- [Log in](#)
- [Learn about institutional subscriptions](#)

Nature **598**, 420-421 (2021)

doi: <https://doi.org/10.1038/d41586-021-02638-9>

References

1. 1.

Cattarino, L., Rodriguez-Barraquer, I., Imai, N., Cummings, D. A. T. & Ferguson, N. M. *Sci. Transl. Med.* **12**, aax4144 (2020).

2. 2.

Kaptein, S. J. F. *et al.* *Nature* **598**, 504–509 (2021).

3. 3.

Bardiot, D. *et al.* *J. Med. Chem.* **61**, 8390–8401 (2018).

4. 4.

Xie, X., Zou, J., Wang, Q.-Y. & Shi, P.-Y. *Antivir. Res.* **118**, 39–45 (2015).

5. 5.

Katzelnick, L. C. *et al.* *Science* **358**, 929–932 (2017).

6. 6.

Low, J. G. H., Ooi, E. E. & Vasudevan, S. G. *J. Infect. Dis.* **215**, S96–S102 (2017).

7. 7.

Nguyen, N. M. *et al.* *J. Infect. Dis.* **207**, 1442–1450 (2013).

8. 8.

Moquin, S. A. *et al.* *Sci. Transl. Med.* **13**, eabb2181 (2021).

9. 9.

Wang, Q.-Y. *et al.* *J. Virol.* **89**, 8233–8244 (2015).

10. 10.

Xie, X. *et al.* *J. Virol.* **85**, 11183–11195 (2011).

11. 11.

Hernandez-Morales, I. *et al.* *Antivir. Res.* **147**, 149–158 (2017).

12. 12.

Simmons, C. P. *et al.* *PLoS Negl. Trop. Dis.* **6**, e1752 (2012).

This article was downloaded by **calibre** from <https://www.nature.com/articles/d41586-021-02638-9>

| [Section menu](#) | [Main menu](#) |

- NEWS AND VIEWS
- 20 October 2021

Non-magnetic objects induced to move by electromagnets

A set of electromagnets has been used to move metal objects without touching them, even though the objects are not magnetic. This method could potentially be used like a ‘tractor beam’ to move hazardous objects in space.

- [Eric Diller](#) 

Imagine trying to catch a fragment of a rocket nozzle in orbit above Earth’s atmosphere. The fragment is travelling faster than a bullet, and tumbling rapidly end over end. Around 27,000 orbiting pieces of such debris are large enough to be tracked by the US Space Surveillance Network, and they constantly threaten active spacecraft and satellites. If the debris were magnetic, then magnets could be used to safely grab hold of the objects and dispose of them — but orbital debris tends to contain little or no magnetic material. In [a paper in *Nature*](#), Pham *et al.*¹ report a method that allows magnets to grab non-magnetic objects from a distance, which could potentially be used by clean-up satellites for debris capture and disposal.

Access options

Subscribe to Journal

Get full journal access for 1 year

\$199.00

only \$3.90 per issue

Subscribe

All prices are NET prices.
VAT will be added later in the checkout.
Tax calculation will be finalised during checkout.

Rent or Buy article

Get time limited or full article access on ReadCube.

from \$8.99

Rent or Buy

All prices are NET prices.

Additional access options:

- [Log in](#)
- [Learn about institutional subscriptions](#)

Nature **598**, 421–423 (2021)

doi: <https://doi.org/10.1038/d41586-021-02771-5>

References

1. 1.

Pham, L. N. *et al.* *Nature* **598**, 439–443 (2021).

2. 2.

Kummer, M. P. *et al.* *IEEE Trans. Robot.* **26**, 1006–1017 (2010).

3. 3.

Liu, X., Lu, Y., Zhou, Y. & Yin, Y. *Adv. Space Res.* **61**, 2147–2158 (2018).

4. 4.

Reinhardt, B. Z. & Peck, M. A. *J. Spacecr. Rockets* **53**, 241–248 (2016).

5. 5.

Witze, A. *Nature* **561**, 24–26 (2018).

This article was downloaded by **calibre** from <https://www.nature.com/articles/d41586-021-02771-5>

| [Section menu](#) | [Main menu](#) |

- NEWS AND VIEWS
- 29 September 2021

Flies sense the world while sleeping

High-throughput analyses of how sleeping fruit flies respond to a variety of odours show that the brains of these insects continue to process the value of the signals conveyed by sensory information during sleep.

- [Wanhe Li](#) ⁰ &
- [Alex C. Keene](#) ¹

Sleep is a complex behaviour nearly ubiquitous among animal species^{1,2}. Many animals, including humans, are less responsive to sensory stimuli during sleep than when they are awake. However, human sleep is unlikely to involve a complete loss of consciousness, because people respond to salient stimuli — such as the sound of names³ or a baby crying — during sleep, while filtering out more-trivial sensory cues. But whether other animals can evaluate the importance or value signalled by different sensory stimuli during sleep is not clear. [Writing in Nature](#), French *et al.*⁴ show that the fruit fly *Drosophila melanogaster* also actively processes sensory information during sleep, and that the salience of different sensory stimuli can be affected by whether it is fed or starved.

Access options

Subscribe to Journal

Get full journal access for 1 year

\$199.00

only \$3.90 per issue

Subscribe

All prices are NET prices.
VAT will be added later in the checkout.
Tax calculation will be finalised during checkout.

Rent or Buy article

Get time limited or full article access on ReadCube.

from \$8.99

Rent or Buy

All prices are NET prices.

Additional access options:

- [Log in](#)
- [Learn about institutional subscriptions](#)

Nature **598**, 423-424 (2021)

doi: <https://doi.org/10.1038/d41586-021-02441-6>

References

1. 1.

Keene, A. C. & Duboue, E. R. *J. Exp. Biol.* **221**, jeb159533 (2018).

2. 2.

Joiner, W. J. *Curr. Biol.* **26**, R1073–R1087 (2016).

3. 3.

Oswald, I., Taylor, A. M. & Treisman, M. *Brain* **83**, 440–453 (1960).

4. 4.

French, A., Geissmann, Q., Beckwith, E. J. & Gilestro, G. F. *Nature* **598**, 479–482 (2021).

5. 5.

Siclari, F., Larocque, J. J., Postle, B. R. & Tononi, G. *Front. Psychol.* **4**, 542 (2013).

6. 6.

Geissmann, Q. *et al.* *PLoS Biol.* **15**, e2003026 (2017).

7. 7.

Joiner, W. J., Crocker, A., White, B. H. & Sehgal, A. *Nature* **441**, 757–760 (2006).

8. 8.

Donlea, J. M. *et al.* *Neuron* **97**, 378–389 (2018).

9. 9.

Sitaraman, D. *et al.* *Curr. Biol.* **25**, 2915–2927 (2015).

10. 10.

Aso, Y. *et al.* *eLife* **3**, e04580 (2014).

11. 11.

Berry, J. A., Cervantes-Sandoval, I., Chakraborty, M. & Davis, R. L. *Cell* **161**, 1656–1667 (2015).

12. 12.

Chouhan, N. S., Griffith, L. C., Haynes, P. & Sehgal, A. *Nature* **589**, 582–585 (2021).

13. 13.

Chiu, C. N. & Prober, D. A. *Front. Neural Circuits* **7**, 58 (2013).

14. 14.

Trojanowski, N. F. & Raizen, D. M. *Trends Neurosci.* **39**, 54–62 (2016).

This article was downloaded by **calibre** from <https://www.nature.com/articles/d41586-021-02441-6>

| [Section menu](#) | [Main menu](#) |

- Article
- [Published: 20 October 2021](#)

Carbon monoxide gas produced by a giant impact in the inner region of a young system

- [Tajana Schneiderman](#) ORCID: [orcid.org/0000-0003-2082-3488¹](https://orcid.org/0000-0003-2082-3488),
- [Luca Matrà](#) ORCID: [orcid.org/0000-0003-4705-3188²](https://orcid.org/0000-0003-4705-3188),
- [Alan P. Jackson](#) ORCID: [orcid.org/0000-0003-4393-9520^{3,4}](https://orcid.org/0000-0003-4393-9520),
- [Grant M. Kennedy](#) ORCID: [orcid.org/0000-0001-6831-7547^{5,6}](https://orcid.org/0000-0001-6831-7547),
- [Quentin Kral](#) ORCID: [orcid.org/0000-0001-6527-4684⁷](https://orcid.org/0000-0001-6527-4684),
- [Sebastián Marino](#) ORCID: [orcid.org/0000-0002-5352-2924^{8,9}](https://orcid.org/0000-0002-5352-2924),
- [Karin I. Öberg](#) ORCID: [orcid.org/0000-0001-8798-1347¹⁰](https://orcid.org/0000-0001-8798-1347),
- [Kate Y. L. Su](#) ORCID: [orcid.org/0000-0002-3532-5580¹¹](https://orcid.org/0000-0002-3532-5580),
- [David J. Wilner](#) ORCID: [orcid.org/0000-0003-1526-7587¹⁰](https://orcid.org/0000-0003-1526-7587) &
- [Mark C. Wyatt⁸](#)

Nature volume **598**, pages 425–428 (2021)

- 687 Accesses
- 399 Altmetric
- [Metrics details](#)

Subjects

- [Exoplanets](#)
- [Inner planets](#)

Abstract

Models of terrestrial planet formation predict that the final stages of planetary assembly—lasting tens of millions of years beyond the dispersal of young protoplanetary disks—are dominated by planetary collisions. It is through these giant impacts that planets like the young Earth grow to their final mass and achieve long-term stable orbital configurations¹. A key prediction is that these impacts produce debris. So far, the most compelling observational evidence for post-impact debris comes from the planetary system around the nearby 23-million-year-old A-type star HD 172555. This system shows large amounts of fine dust with an unusually steep size distribution and atypical dust composition, previously attributed to either a hypervelocity impact^{2,3} or a massive asteroid belt⁴. Here we report the spectrally resolved detection of a carbon monoxide gas ring co-orbiting with dusty debris around HD 172555 between about six and nine astronomical units—a region analogous to the outer terrestrial planet region of our Solar System. Taken together, the dust and carbon monoxide detections favour a giant impact between large, volatile-rich bodies. This suggests that planetary-scale collisions, analogous to the Moon-forming impact, can release large amounts of gas as well as debris, and that this gas is observable, providing a window into the composition of young planets.

Access options

Subscribe to Journal

Get full journal access for 1 year

\$199.00

only \$3.90 per issue

[Subscribe](#)

All prices are NET prices.

VAT will be added later in the checkout.

Tax calculation will be finalised during checkout.

Rent or Buy article

Get time limited or full article access on ReadCube.

from \$8.99

[Rent or Buy](#)

All prices are NET prices.

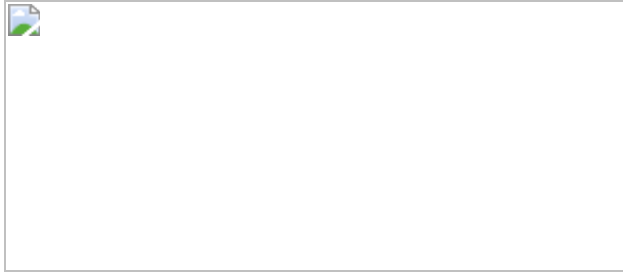
Additional access options:

- [Log in](#)
- [Access through your institution](#)
- [Learn about institutional subscriptions](#)

Fig. 1: Cleaned emission maps of the HD 172555 system.



Fig. 2: Mass–temperature degeneracy of the CO data.



Data availability

The ALMA programme number for the presented data is 2012.1.00437.S and data can be found in the online ALMA archive. The cleaned .fits files

are available upon request from the corresponding author.

Code availability

RADMC-3D is available at <https://github.com/dullemond/radmc3d-2.0> and emcee is available at <https://emcee.readthedocs.io/en/stable/>. Custom code, including the ring model and non-LTE code, is available at https://github.com/tmschneiderhd172555_CO_2021.

References

1. 1.

Morbidelli, A., Lunine, J. I., O'Brien, D. P., Raymond, S. N. & Walsh, K. J. Building terrestrial planets. *Annu. Rev. Earth Planet. Sci.* **40**, 251–275 (2012).

2. 2.

Lisse, C. M. et al. Abundant circumstellar silica dust and SiO gas created by a giant hypervelocity collision in the 12 Myr HD 172555 system. *Astrophys. J.* **701**, 2019–2032 (2009).

3. 3.

Johnson, B. C. et al. A self-consistent model of the circumstellar debris created by a giant hypervelocity impact in the HD 172555 system. *Astrophys. J.* **761**, 45 (2012).

4. 4.

Wyatt, M. C. et al. Steady state evolution of debris disks around A stars. *Astrophys. J.* **663**, 365–382 (2007).

5. 5.

Mamajek, E. E. & Bell, C. P. M. On the age of the β Pictoris moving group. *Mon. Not. R. Astron. Soc.* **445**, 2169–2180 (2014).

6. 6.

David, T. J. & Hillenbrand, L. A. The ages of early-type stars: Strömgren photometric methods calibrated, validated, tested, and applied to hosts and prospective hosts of directly imaged exoplanets. *Astrophys. J.* **804**, 146 (2015).

7. 7.

Prusti, T. et al. The Gaia mission. *Astron. Astrophys.* **595**, A1 (2016).

8. 8.

Gaia Collaboration et al. Gaia Data Release 2: summary of the contents and survey properties. *Astron. Astrophys.* **616**, A1 (2018).

9. 9.

Zuckerman, B., Song, I., Bessell, M. S. & Webb, R. A. The β Pictoris moving group. *Astrophys. J.* **562**, L87–L90 (2001).

10. 10.

Cote, J. B and A type stars with unexpectedly large colour excesses at IRAS wavelengths. *Astron. Astrophys.* **181**, 77–84 (1987).

11. 11.

Smith, R., Wyatt, M. C. & Haniff, C. A. Resolving the terrestrial planet forming regions of HD113766 and HD172555 with MIDI. *Mon. Not. R. Astron. Soc.* **422**, 2560–2580 (2012).

12. 12.

Engler, N., Schmid, H. M., Quanz, S. P., Avenhaus, H. & Bazzon, A. Detection of scattered light from the hot dust in HD 172555. *Astron.*

Astrophys. **618**, 1–15 (2018).

13. 13.

Chen, C. H. et al. Spitzer IRS spectroscopy of IRAS-discovered debris disks. *Astrophys. J. Suppl. Ser.* **166**, 351–377 (2006).

14. 14.

Gontcharov, G. A. Pulkovo compilation of radial velocities for 35 495 Hipparcos stars in a common system. *Astron. Lett.* **32**, 759–771 (2006).

15. 15.

Kral, Q., Marino, S., Wyatt, M. C., Kama, M. & Matrà, L. Imaging [CI] around HD 131835: reinterpreting young debris discs with protoplanetary disc levels of CO gas as shielded secondary discs. *Mon. Not. R. Astron. Soc.* **489**, 3670–3691 (2019).

16. 16.

Kennedy, G. M. & Kenyon, S. J. Stellar mass dependent disk dispersal. *Astrophys. J.* **695**, 1210–1226 (2009).

17. 17.

Ribas, Á., Bouy, H. & Merín, B. Protoplanetary disk lifetimes vs. stellar mass and possible implications for giant planet populations. *Astron. Astrophys.* **576**, A52 (2015).

18. 18.

Wyatt, M. C., Panić, O., Kennedy, G. M. & Matrà, L. Five steps in the evolution from protoplanetary to debris disk. *Astrophys. Space Sci.* **357**, 103 (2015).

19. 19.

Isella, A. et al. The Disk Substructures at High Angular Resolution Project (DSHARP) - IX: a high definition study of the HD 163296 planet forming disk. *Astrophys. J. Lett.* **869**, L49 (2018).

20. 20.

Boehler, Y. et al. The complex morphology of the young disk MWC 758: spirals and dust clumps around a large cavity. *Astrophys. J.* **853**, 162 (2017).

21. 21.

Morris, M. A. & Desch, S. J. Thermal histories of chondrules in solar nebula shocks. *Astrophys. J.* **722**, 1474–1494 (2010).

22. 22.

Su, K. Y. L. et al. Mid-infrared studies of HD 113766 and HD 172555: assessing variability in the terrestrial zone of young exoplanetary systems. *Astrophys. J.* **898**, 21 (2020).

23. 23.

Matrà, L., Öberg, K. I., Wilner, D. J., Olofsson, J. & Bayo, A. On the ubiquity and stellar luminosity dependence of exocometary CO gas: detection around M dwarf TWA 7. *Astron. J.* **157**, 117 (2019).

24. 24.

Matrà, L., Panić, O., Wyatt, M. C. & Dent, W. R. F. CO mass upper limits in the Fomalhaut ring—the importance of NLTE excitation in debris discs and future prospects with ALMA. *Mon. Not. R. Astron. Soc.* **447**, 3936–3947 (2015).

25. 25.

Marino, S. et al. Exocometary gas in the HD 181327 debris ring. *Mon. Not. R. Astron. Soc.* **460**, 2933–2944 (2016).

26. 26.

Matrà, L. et al. Detection of exocometary CO within the 440 Myr-old Fomalhaut belt: a similar CO+CO₂ ice abundance in exocomets and Solar System comets. *Astrophys. J.* **842**, 9 (2017).

27. 27.

Kral, Q., Matrà, L., Wyatt, M. C. & Kennedy, G. M. Predictions for the secondary CO, C and O gas content of debris discs from the destruction of volatile-rich planetesimals. *Mon. Not. R. Astron. Soc.* **469**, 521–550 (2017).

28. 28.

Zuckerman, B. & Song, I. A 40Myr old gaseous circumstellar disk at 49 CETI: massive CO-rich comet clouds at young A-type stars. *Astrophys. J.* **758**, 77 (2012).

29. 29.

Prialnik, D. & Rosenberg, E. D. Can ice survive in main-belt comets? Long-term evolution models of comet 133P/Elst-Pizarro. *Mon. Not. R. Astron. Soc. Lett.* **399**, L79–L83 (2009).

30. 30.

Snodgrass, C. et al. The Main Belt comets and ice in the Solar System. *Astron. Astrophys. Rev.* **25**, 5 (2017).

31. 31.

Marino, S. et al. ALMA observations of the η Corvi debris disc: inward scattering of CO-rich exocomets by a chain of 3-30 M_{\oplus} planets? *Mon. Not. R. Astron. Soc.* **465**, 2595–2615 (2017).

32. 32.

Benz, W., Anic, A., Horner, J. & Whitby, J. A. The origin of Mercury. *Space Sci. Rev.* **132**, 189–202 (2007).

33. 33.

Chau, A., Reinhardt, C., Helled, R. & Stadel, J. Forming Mercury by giant impacts. *Astrophys. J.* **865**, 35 (2018).

34. 34.

Canup, R. M. Simulations of a late lunar-forming impact. *Icarus* **168**, 433–456 (2004).

35. 35.

Canup, R. M. Forming a moon with an Earth-like composition via a giant impact. *Science* **338**, 1052-1055 (2012).

36. 36.

Mastrobuono-Battisti, A., Perets, H. B. & Raymond, S. N. A primordial origin for the compositional similarity between the Earth and the Moon. *Nature* **520**, 212–215 (2015).

37. 37.

Marinova, M. M., Aharonson, O. & Asphaug, E. Mega-impact formation of the Mars hemispheric dichotomy. *Nature* **453**, 1216–1219 (2008).

38. 38.

Nimmo, F., Hart, S. D., Korycansky, D. G. & Agnor, C. B. Implications of an impact origin for the Martian hemispheric dichotomy. *Nature* **453**, 1220–1223 (2008).

39. 39.

Davies, J. H. Did a mega-collision dry Venus' interior? *Earth Planet. Sci. Lett.* **268**, 376–383 (2008).

40. 40.

Wyatt, M. C. & Jackson, A. P. Insights into planet formation from debris disks: II. giant impacts in extrasolar planetary systems. *Space Sci. Rev.* **205**, 231–265 (2016).

41. 41.

Heays, A. N., Bosman, A. D. & van Dishoeck, E. F. Photodissociation and photoionisation of atoms and molecules of astrophysical interest. *Astron. Astrophys.* **602**, A105 (2017).

42. 42.

Schlichting, H. E. & Mukhopadhyay, S. Atmosphere impact losses. *Space Sci. Rev.* **214**, 34 (2018).

43. 43.

Kegerreis, J. A. et al. Atmospheric erosion by giant impacts onto terrestrial planets: a scaling law for any speed, angle, mass, and density. *Astrophys. J. Lett.* **901**, L31 (2020).

44. 44.

Lammer, H. et al. Origin and evolution of the atmospheres of early Venus, Earth and Mars. *Astron. Astrophys. Rev.* **26**, 2 (2018).

45. 45.

Biersteker, J. B. & Schlichting, H. E. Atmospheric mass-loss due to giant impacts: the importance of the thermal component for hydrogen–helium envelopes. *Mon. Not. R. Astron. Soc.* **485**, 4454–4463 (2019).

46. 46.

Högbom, J. & Cornwell, T. Aperture synthesis with a non-regular distribution of interferometer baselines. Commentary. *Astron. Astrophys.* **500**, 55–66 (2009).

47. 47.

White, J. A. et al. The MESAS Project: long-wavelength follow-up observations of Sirius A. *Astrophys. J.* **875**, 55 (2019).

48. 48.

Beckwith, S. V. W., Sargent, A. I., Chini, R. S. & Guesten, R. A survey for circumstellar disks around young stellar objects. *Astron. J.* **99**, 924 (1990).

49. 49.

Foreman-Mackey, D., Hogg, D. W., Lang, D. & Goodman, J. emcee: the MCMC hammer. *Publ. Astron. Soc. Pac.* **125**, 306–312 (2013).

50. 50.

Matrà, L. et al. Molecular reconnaissance of the β Pictoris gas disk with the SMA: a low HCN/(CO+CO₂) outgassing ratio and predictions for future surveys. *Astrophys. J.* **853**, 147 (2018).

51. 51.

Husser, T. O. et al. A new extensive library of PHOENIX stellar atmospheres and synthetic spectra. *Astron. Astrophys.* **553**, A6 (2013).

52. 52.

Feroz, F., Hobson, M. P. & Bridges, M. MultiNest: an efficient and robust Bayesian inference tool for cosmology and particle physics. *Mon. Not. R. Astron. Soc.* **398**, 1601–1614 (2009).

53. 53.

Sepulveda, A. G. et al. The REASONS Survey: resolved millimeter observations of a large debris disk around the nearby F star HD 170773. *Astrophys. J.* **881**, 84 (2019).

54. 54.

Yelverton, B., Kennedy, G. M., Su, K. Y. L. & Wyatt, M. C. A statistically significant lack of debris discs in medium separation binary systems. *Mon. Not. R. Astron. Soc.* **488**, 3588–3606 (2019).

55. 55.

Marboeuf, U., Bonsor, A. & Augereau, J. C. Extrasolar comets: the origin of dust in exozodiacal disks? *Planet. Space Sci.* **133**, 47–62 (2016).

56. 56.

Matrà, L. et al. An empirical planetesimal belt radius–stellar luminosity relation. *Astrophys. J.* **859**, 72 (2018).

57. 57.

Marino, S., Bonsor, A., Wyatt, M. C. & Kral, Q. Scattering of exocomets by a planet chain: exozodi levels and the delivery of cometary material to inner planets. *Mon. Not. R. Astron. Soc.* **479**, 1651–1671 (2018).

58. 58.

Biver, N. et al. The 1995–2002 long-term monitoring of comet C/1995 O1 (Hale-Bopp) at radio wavelength. *Earth Moon Planets* **90**, 5–14 (2002).

59. 59.

Wyatt, M. C. et al. How observations of circumstellar disk asymmetries can reveal hidden planets: pericenter glow and its application to the HR 4796 disk. *Astrophys. J.* **527**, 918–944 (1999).

60. 60.

Wyatt, M. C., Bonsor, A., Jackson, A. P., Marino, S. & Shannon, A. How to design a planetary system for different scattering outcomes: giant impact sweet spot, maximizing exocomets, scattered discs. *Mon. Not. R. Astron. Soc.* **464**, 3385–3407 (2017).

Acknowledgements

We are grateful to J. Biersteker for discussions on the liberation of atmospheres in the aftermath of giant impacts. This paper makes use of ALMA data ADS/JAO.ALMA\#2012.1.00437.S. ALMA is a partnership of ESO (representing its member states), NSF (USA) and NINS (Japan), together with NRC (Canada), NSC and ASIAA (Taiwan) and KASI (Republic of Korea), in cooperation with the Republic of Chile. The Joint ALMA Observatory is operated by ESO, AUI/NRAO and NAOJ. K.I.Ö. acknowledges support from the Simons Foundation (SCOL \#321183). G.M.K. is supported by the Royal Society as a Royal Society University Research Fellow.

Author information

Affiliations

1. Department of Earth, Atmospheric and Planetary Sciences,
Massachusetts Institute of Technology, Cambridge, MA, USA

Tajana Schneiderman

2. Centre for Astronomy, School of Physics, National University of Ireland Galway, Galway, Ireland

Luca Matrà

3. Centre for Planetary Sciences, University of Toronto at Scarborough, Toronto, Ontario, Canada

Alan P. Jackson

4. School of Earth and Space Exploration, Arizona State University, Tempe, AZ, USA

Alan P. Jackson

5. Department of Physics, University of Warwick, Coventry, UK

Grant M. Kennedy

6. Centre for Exoplanets and Habitability, University of Warwick, Coventry, UK

Grant M. Kennedy

7. LESIA, Observatoire de Paris, Université PSL, CNRS, Sorbonne Université, Université Paris Diderot, Sorbonne Paris Cité, Meudon, France

Quentin Kral

8. Institute of Astronomy, University of Cambridge, Cambridge, UK

Sebastián Marino & Mark C. Wyatt

9. Jesus College, University of Cambridge, Cambridge, UK

Sebastián Marino

10. Center for Astrophysics | Harvard & Smithsonian, Cambridge, MA, USA

Karin I. Öberg & David J. Wilner

11. Steward Observatory, University of Arizona, Tucson, AZ, USA

Kate Y. L. Su

Contributions

T.S. led the optically thin modelling and discussion. L.M. led the radiative transfer modelling. T.S. and L.M. were involved in data reduction, processing and writing of the manuscript. All authors contributed to discussions of the results and commented on the manuscript.

Corresponding author

Correspondence to Tajana Schneiderman.

Ethics declarations

Competing interests

The authors declare no competing interests.

Additional information

Peer review information *Nature* thanks Inseok Song and the other, anonymous, reviewer(s) for their contribution to the peer review of this work. Peer reviewer reports are available.

Publisher's note Springer Nature remains neutral with regard to jurisdictional claims in published maps and institutional affiliations.

Extended data figures and tables

[Extended Data Fig. 1 Posterior probability distributions for the model parameters obtained from the emcee fitting process.](#)

All parameters are well constrained, with best-fit values listed in Extended Data Table 1. This model was fitted to spectral data retaining original channel widths, assumed a Gaussian prior on the inclination, and assumed a stellar mass of $1.76 M_{\odot}$.

Extended Data Table 1 Best fit values (50 ± 34 percentile) to the optically thin model of gas emission. Left column indicates values derived from the MCMC run where a Gaussian prior was applied to the inclination. Right column indicates values derived from the MCMC run where flat priors were applied to all model parameters

Supplementary information

Peer Review File

Rights and permissions

Reprints and Permissions

About this article

Cite this article

Schneiderman, T., Matrà, L., Jackson, A.P. *et al.* Carbon monoxide gas produced by a giant impact in the inner region of a young system. *Nature* **598**, 425–428 (2021). <https://doi.org/10.1038/s41586-021-03872-x>

- Received: 12 April 2021
- Accepted: 01 August 2021
- Published: 20 October 2021
- Issue Date: 21 October 2021
- DOI: <https://doi.org/10.1038/s41586-021-03872-x>

Share this article

Anyone you share the following link with will be able to read this content:

[Get shareable link](#)

Sorry, a shareable link is not currently available for this article.

[Copy to clipboard](#)

Provided by the Springer Nature SharedIt content-sharing initiative

This article was downloaded by **calibre** from <https://www.nature.com/articles/s41586-021-03872-x>

| [Section menu](#) | [Main menu](#) |

- Article
- [Published: 01 September 2021](#)

Half- and quarter-metals in rhombohedral trilayer graphene

- [Haoxin Zhou](#) ORCID: [orcid.org/0000-0003-1235-0035](#)¹ na1,
- [Tian Xie](#) ORCID: [orcid.org/0000-0002-6406-0403](#)¹ na1,
- [Areg Ghazaryan](#)²,
- [Tobias Holder](#) ORCID: [orcid.org/0000-0003-1365-4276](#)³,
- [James R. Ehrets](#)¹,
- [Eric M. Spanton](#)¹,
- [Takashi Taniguchi](#) ORCID: [orcid.org/0000-0002-1467-3105](#)⁴,
- [Kenji Watanabe](#) ORCID: [orcid.org/0000-0003-3701-8119](#)⁵,
- [Erez Berg](#) ORCID: [orcid.org/0000-0001-8956-3384](#)¹,
- [Maksym Serbyn](#) ORCID: [orcid.org/0000-0002-2399-5827](#)¹ &
- [Andrea F. Young](#) ORCID: [orcid.org/0000-0001-5954-8028](#)¹

Nature volume **598**, pages 429–433 (2021)

- 7846 Accesses
- 20 Altmetric
- [Metrics details](#)

Subjects

- [Electronic and spintronic devices](#)
- [Electronic properties and devices](#)
- [Ferromagnetism](#)

Abstract

Ferromagnetism is most common in transition metal compounds where electrons occupy highly localized *d* orbitals. However, ferromagnetic order may also arise in low-density two-dimensional electron systems^{1,2,3,4,5}. Here we show that gate-tuned van Hove singularities in rhombohedral trilayer graphene⁶ drive spontaneous ferromagnetic polarization of the electron system into one or more spin and valley flavours. Using capacitance and transport measurements, we observe a cascade of transitions tuned to the density and electronic displacement field between phases in which quantum oscillations have fourfold, twofold or onefold degeneracy, associated with a spin- and valley-degenerate normal metal, spin-polarized ‘half-metal’, and spin- and valley-polarized ‘quarter-metal’, respectively. For electron doping, the salient features of the data are well captured by a phenomenological Stoner model⁷ that includes valley-anisotropic interactions. For hole filling, we observe a richer phase diagram featuring a delicate interplay of broken symmetries and transitions in the Fermi surface topology. Finally, we introduce a moiré superlattice using a rotationally aligned hexagonal boron nitride substrate^{5,8}. Remarkably, we find that the isospin order is only weakly perturbed, with the moiré potential catalysing the formation of topologically nontrivial gapped states whenever itinerant half- or quarter-metal states occur at half- or quarter-superlattice band filling. Our results show that rhombohedral graphene is an ideal platform for well-controlled tests of many-body theory, and reveal magnetism in moiré materials^{4,5,9,10} to be fundamentally itinerant in nature.

Access options

Subscribe to Journal

Get full journal access for 1 year

\$199.00

only \$3.90 per issue

Subscribe

All prices are NET prices.
VAT will be added later in the checkout.
Tax calculation will be finalised during checkout.

Rent or Buy article

Get time limited or full article access on ReadCube.

from \$8.99

Rent or Buy

All prices are NET prices.

Additional access options:

- [Log in](#)
- [Access through your institution](#)
- [Learn about institutional subscriptions](#)

Fig. 1: Spontaneous symmetry breaking in rhombohedral trilayer graphene.

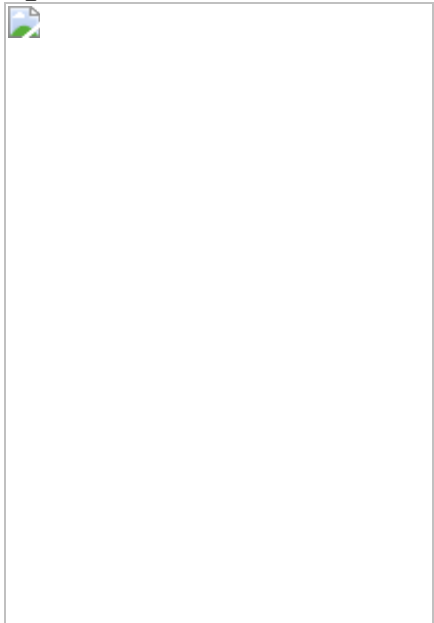


Fig. 2: Stoner ferromagnetism in the conduction band.



Fig. 3: Ferromagnetism and Fermi surface topology in the valence band.

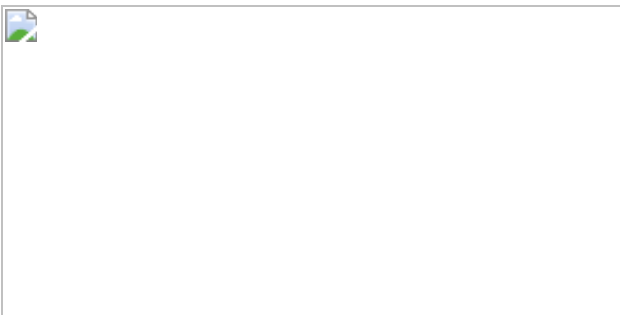
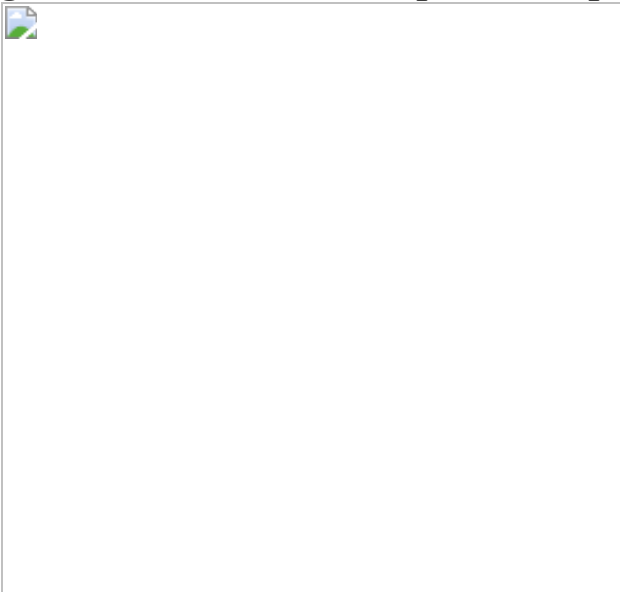


Fig. 4: Effect of a moiré superlattice potential.



Data availability

The data that support the findings of this study are available from the corresponding author on reasonable request.

References

1. 1.

Tanatar, B. & Ceperley, D. M. Ground state of the two-dimensional electron gas. *Phys. Rev. B* **39**, 5005–5016 (1989).

2. 2.

Pudalov, V. M., Kuntsevich, A. Y., Burmistrov, I. S. & Reznikov, M. Thermodynamic studies of two-dimensional correlated electron systems. *J. Low Temp. Phys.* **181**, 99–111 (2015).

3. 3.

Hossain, M. S. et al. Observation of spontaneous ferromagnetism in a two-dimensional electron system. *Proc. Natl Acad. Sci. USA* **117**, 32244–32250 (2020).

4. 4.

Sharpe, A. L. et al. Emergent ferromagnetism near three-quarters filling in twisted bilayer graphene. *Science* **365**, 605–608 (2019).

5. 5.

Chen, G. et al. Tunable correlated Chern insulator and ferromagnetism in a moiré superlattice. *Nature* **579**, 56–61 (2020).

6. 6.

Zhang, F., Sahu, B., Min, H. & MacDonald, A. H. Band structure of ABC-stacked graphene trilayers. *Phys. Rev. B* **82**, 035409 (2010).

7. 7.

Stoner, E. C. Collective electron ferromagnetism. *Proc. R. Soc. A* **165**, 372–414 (1938).

8. 8.

Chen, G. et al. Evidence of a gate-tunable Mott insulator in a trilayer graphene moiré superlattice. *Nat. Phys.* **15**, 237–241 (2019).

9. 9.

Serlin, M. et al. Intrinsic quantized anomalous Hall effect in a moiré heterostructure. *Science* **367**, 900–903 (2020).

10. 10.

Polshyn, H. et al. Electrical switching of magnetic order in an orbital Chern insulator. *Nature* **588**, 66–70 (2020).

11. 11.

Castro, E. V., Peres, N. M. R., Stauber, T. & Silva, N. A. P. Low-density ferromagnetism in biased bilayer graphene. *Phys. Rev. Lett.* **100**, 186803 (2008).

12. 12.

Lee, Y. et al. Gate tunable magnetism and giant magnetoresistance in ABC-stacked few-layer graphene. Preprint at <https://arxiv.org/abs/1911.04450> (2019).

13. 13.

Kerelsky, A. et al. Moiréless correlations in ABCA graphene. *Proc. Natl Acad. Sci. USA* **118**, 4 (2021).

14. 14.

Shi, Y. et al. Electronic phase separation in multilayer rhombohedral graphite. *Nature* **584**, 210–214 (2020).

15. 15.

Chen, G. et al. Signatures of tunable superconductivity in a trilayer graphene moiré superlattice. *Nature* **572**, 215–219 (2019).

16. 16.

Eisenstein, J. P., Pfeiffer, L. N. & West, K. W. Negative compressibility of interacting two-dimensional electron and quasiparticle gases. *Phys. Rev. Lett.* **68**, 674–677 (1992).

17. 17.

Varlet, A. et al. Anomalous sequence of quantum Hall liquids revealing a tunable Lifshitz transition in bilayer graphene. *Phys. Rev. Lett.* **113**, 116602 (2014).

18. 18.

Zibrov, A. A. et al. Emergent Dirac gullies and gully-symmetry-breaking quantum Hall states in ABA trilayer graphene. *Phys. Rev. Lett.* **121**, 167601 (2018).

19. 19.

Zondiner, U. et al. Cascade of phase transitions and Dirac revivals in magic-angle graphene. *Nature* **582**, 203–208 (2020).

20. 20.

Xiao, D., Chang, M.-C. & Niu, Q. Berry phase effects on electronic properties. *Rev. Mod. Phys.* **82**, 1959–2007 (2010).

21. 21.

Dean, C., Kim, P., Li, J. I. A. & Young, A. F. in *Fractional Quantum Hall Effects: New Developments* (eds Halperin, B. I. & Jain, J. K.) 317–375 (World Scientific, 2020).

22. 22.

Zhang, Y.-H., Mao, D., Cao, Y., Jarillo-Herrero, P. & Senthil, T. Nearly flat Chern bands in moiré superlattices. *Phys. Rev. B* **99**, 075127 (2019).

23. 23.

Regan, E. C. et al. Mott and generalized Wigner crystal states in WSe₂/WS₂ moiré superlattices. *Nature* **579**, 359–363 (2020).

24. 24.

Xu, Y. et al. Correlated insulating states at fractional fillings of moiré superlattices. *Nature* **587**, 214–218 (2020).

25. 25.

Balents, L., Dean, C. R., Efetov, D. K. & Young, A. F. Superconductivity and strong correlations in moiré flat bands. *Nat. Phys.* **16**, 725–733 (2020).

26. 26.

Masubuchi, S., Ono, M., Yoshida, K., Hirakawa, K. & Machida, T. Fabrication of graphene nanoribbon by local anodic oxidation lithography using atomic force microscope. *Appl. Phys. Lett.* **94** 082107 (2009).

27. 27.

Li, H. et al. Electrode-free anodic oxidation nanolithography of low-dimensional materials. *Nano Lett.* **18**, 8011–8015 (2018).

28. 28.

Wang, L. et al. One-dimensional electrical contact to a two-dimensional material. *Science* **342**, 614–617 (2013).

29. 29.

Zibrov, A. A. et al. Tunable interacting composite fermion phases in a half-filled bilayer-graphene Landau level. *Nature* **549**, 360–364 (2017).

30. 30.

Alicea, J. & Fisher, M. P. A. Interplay between lattice-scale physics and the quantum Hall effect in graphene. *Solid State Commun.* **143**, 504–509 (2007).

31. 31.

Kharitonov, M. Phase diagram for the $v = 0$ quantum Hall state in monolayer graphene. *Phys. Rev. B* **85**, 155439 (2012).

32. 32.

Cong, C. et al. Raman characterization of ABA- and ABC-stacked trilayer graphene. *ACS Nano* **5**, 8760–8768 (2011).

33. 33.

Polshyn, H. et al. Quantitative transport measurements of fractional quantum Hall energy gaps in edgeless graphene devices. *Phys. Rev. Lett.* **121**, 226801 (2018).

Acknowledgements

We acknowledge discussions with A. MacDonald, L. Fu, F. Wang and M. Zaletel. A.F.Y. acknowledges support from the National Science Foundation under DMR-1654186, and the Gordon and Betty Moore Foundation under award GBMF9471. We acknowledge the use of the research facilities within the California NanoSystems Institute, supported by the University of California, Santa Barbara and the University of California, Office of the President. K.W. and T.T. acknowledge support from the Elemental Strategy Initiative conducted by the MEXT, Japan (grant number JPMXP0112101001) and JSPS KAKENHI (grant numbers 19H05790 and JP20H00354). E.B. and T.H. were supported by the European Research

Council under grant HQMAT (grant agreement number 817799). A.G. acknowledges support by the European Unions Horizon 2020 research and innovation programme under the Marie Skłodowska-Curie grant agreement number 754411.

Author information

Author notes

1. These authors contributed equally: Haoxin Zhou, Tian Xie

Affiliations

1. Department of Physics, University of California, Santa Barbara, CA, USA

Haoxin Zhou, Tian Xie, James R. Ehrets, Eric M. Spanton, Erez Berg, Maksym Serbyn & Andrea F. Young

2. Institute of Science and Technology, Klosterneuburg, Austria

Areg Ghazaryan

3. Department of Condensed Matter Physics, Weizmann Institute of Science, Rehovot, Israel

Tobias Holder

4. International Center for Materials Nanoarchitectonics, National Institute for Materials Science, Tsukuba, Japan

Takashi Taniguchi

5. Research Center for Functional Materials, National Institute for Materials Science, Tsukuba, Japan

Kenji Watanabe

Contributions

H.Z. and T.X. fabricated the device with assistance from E.M.S. and J.R.E. H.Z. performed the measurements, advised by A.F.Y. K.W. and T.T. grew the hBN crystals. A.G., T.H., E.B. and M.S. contributed to the theoretical interpretation and performed the numerical simulations. H.Z., A.G., M.S., E.B. and A.F.Y. wrote the manuscript with input from all authors.

Corresponding author

Correspondence to Andrea F. Young.

Ethics declarations

Competing interests

The authors declare no competing interests.

Additional information

Peer review information *Nature* thanks Mikito Koshino and the other, anonymous, reviewer(s) for their contribution to the peer review of this work. Peer reviewer reports are available.

Publisher's note Springer Nature remains neutral with regard to jurisdictional claims in published maps and institutional affiliations.

Extended data figures and tables

Extended Data Fig. 1 Sample fabrication procedure.

a, ABC-stacked domains in mechanically exfoliated trilayer graphene flakes are identified by taking the Raman spectra and extracting the peak maximum corresponding to the 2D mode³². **b**, ABC-stacked domains are isolated using atomic force microscope based anodic oxidation

lithography²⁷. **c**, The lower part of the heterostructure is assembled on a polypropylene carbonate (PPC) film which is then **d**, flipped as it is deposited onto the target substrate³³. **e**, The sample is then vacuum annealed at 375 °C to remove the PPC film under the heterostructure. **f**, The upper part of the heterostructure, which contains the top graphite gate, trilayer graphene and hBN, is assembled separately and deposited onto the lower part of the heterostructure. **g**, The top hBN and top graphite gate are etched with XeF₂ followed by O₂ plasma to open windows on the heterostructure, allowing the stacking order to be confirmed after the manipulations of step f. **h**, The heterostructure is etched with CHF₃ and O₂ plasma and metal is deposited to form electrical contacts. **i**, Typical Raman spectra of ABA- and ABC-stacked trilayer graphene, centered on the 2D mode. **j**, Optical micrograph of the trilayer graphene flake used to fabricate Sample A. Scale bar represents 20μm. **k**, Raman spectrum map of the trilayer graphene flake in panel j. The color represents the peak position of the 2D mode. The scan range is indicated in black dashed line in panel j. The scale bar represents 10μm. **l**, Optical micrograph of partially processed Sample A. The cyan regions are where the top graphite gate and the hBN on top of it has been etched. Since the bottom gate does not overlap with the etched window, this allows inspection with Raman spectroscopy of the stacking order of the trilayer graphene. The sale bar represents 10μm. The rough location of the actual device is indicated by black dashed line. **m**, Raman spectrum map of the partially processed Sample A. The region surrounded by a red boundary box remains in ABC-stacking order, which later became the active device region for sample A. **n**, Optical micrograph of Sample A after fabrication. Scale bar represents 3μm. **o**, Optical micrograph of Sample B. Scale bar represents 3μm.

Extended Data Fig. 2 Measurements at low carrier density and displacement field.

a, Inverse compressibility versus carrier density and out-of-plane magnetic field near the charge neutrality point at $\langle D=0 \rangle$. **b**, Zoom-in of a. **c**, Line-cuts of b along the direction indicated by the arrows in b. **d**, $\langle \{R\}_{xx} \rangle$ versus carrier density and out-of-plane magnetic field near the charge neutrality point at $\langle D=0 \rangle$. **e**, Zoom-in of d. **f**, Line-cuts of e along the

direction indicated by the arrows in e. g, $\langle R \rangle_{xy}$ versus carrier density and out-of-plane magnetic field near the charge neutrality point at $(D=0)$. h, Zoom-in of g. i, Line-cuts of h along the direction indicated by the arrows in h.

Extended Data Fig. 3 Shubnikov de Haas oscillation at $D = 0$ in Sample A.

a, $\langle R \rangle_{xx}$ vs n_e and $\langle B \rangle_{\perp}$ measured at $(D=0)$. b, Fast Fourier transform of data in a, the range of $\langle B \rangle_{\perp}$ chosen is 0.02T to 1T. The multiple phases are schematically represented by the Fermi contours on the top.

Extended Data Fig. 4 Shubnikov de Haas oscillation at $D = 0$ in Sample A.

a, b, Inverse compressibility as function of carrier density and displacement measured at $(T=5.6)K$. c, d, Inverse compressibility as a function of carrier density measured at various temperatures at $(D=0.46) V/nm$ (c) and $(-0.46) V/nm$ (d). Each curve is offset by $50eV \cdot (A) \cdot \{u\} \cdot \{c\}$ for clarity.

Extended Data Fig. 5 Shubnikov de Haas oscillations in Sample A.

a, c, $\langle R \rangle_{xx}$ vs $\langle B \rangle_{\perp}$ at electron doping. The measurements are performed at $(D=-0.43)V/nm$ at $\{n\}_{\{e\}} = 0.27 \times 10^{12} \{cm\}^{-2}$ in a, $(0.54 \times 10^{12} \{cm\}^{-2})$ in b and $(1.09 \times 10^{12} \{cm\}^{-2})$ in c. The fast Fourier transform in Fig. 2b was calculated from these results. d, e, $\langle R \rangle_{xx}$ vs n_e and $\langle B \rangle_{\perp}$ at hole doping. Data in panel d are measured at $(D=0.23) V/nm$. Data in panel e are measured at $(D=0.4) V/nm$. The fast Fourier transforms in Fig. 3c, d are calculated from these results.

Extended Data Fig. 6 Quantum capacitance magneto-oscillations.

a–f, Inverse compressibility as a function of the out-of-plane magnetic field at fixed n_e and D . **g, h**, Inverse compressibility versus the out-of-plane magnetic field and the carrier density at $(D=)$ 0.34V/nm. The range of carrier density is chosen to lie within the one-fold degenerate phase in panel **g** and two-fold degenerate phase in panel **h**; in both cases no change in the degeneracy is observed in the low- (B_{\perp}) limit.

Extended Data Fig. 7 In-plane magnetic field dependence of the phase boundaries.

a, κ vs n_e and (B_{\parallel}) at $(D=)$ 0.37V/nm, which covers the phase boundary between a 4-fold degenerate phase and a 1-fold degenerate phase. **b**, Same as **a**, measured at $(D=)$ 0.33V/nm, which covers a phase boundary between a 1-fold degenerate phase with a simple Fermi surface and a 1-fold degenerate phase with annular Fermi surface. **c**, (R_{xx}) vs n_e and (B_{\parallel}) at $(D=)$ 0.37V/nm, which covers a phase boundary between a 4-fold degenerate phase and a 2-fold degenerate phase.

Extended Data Fig. 8 Anomalous Hall effect and Magnetic hysteresis.

a, Hall resistance (R_{xy}) as a function of the out-of-plane magnetic field (B_{\perp}) measured at $(n_{\rm e}) = 0.19 \times 10^{12} \text{ cm}^{-2}$, $(D = -0.4)$ V/nm. **b**, Same measurement at $(n_{\rm e}) = 0.43 \times 10^{12} \text{ cm}^{-2}$, $(D = 0.38)$ V/nm with a 0.1T in-plane magnetic field applied. The curves measured at different temperatures are offset by 200Ω for clarity. The Hall resistance was obtained by measuring the four-terminal resistance in two configurations and applying the Onsager reciprocal relation⁹.

Extended Data Fig. 9 Magnetic field response of the insulating states in Sample B.

a, Inverse compressibility versus carrier density and out-of-plane magnetic field at $(D=)$ 0.52 V/nm measured in sample B. **b**, Same as **a**, measured at $(D=)$ -0.57 V/nm. **c**, $\langle\{R\}_{xy}\rangle$ versus $\langle\{B\}_{\perp}\rangle$ measured at $\langle\{n\}_{\{\rm e\}}\rangle = -0.52 \times 10^{12} \text{ cm}^{-2}$, $(D=)$ -0.47 V/nm.

Extended Data Fig. 10 Extended κ vs n_e and D data at $B = 0$.

The contact resistance increases at $\langle\{n\}_{\{\rm e\}}\rangle > 0$, $(D > 0)$ and at $\langle\{n\}_{\{\rm e\}}\rangle < 0$, $(D < 0)$ due to the formation of a pn-junction near the contact, producing the defect features near the charge neutrality point.

Supplementary information

Supplementary Information

This file contains theoretical modelling, and includes Supplementary Table 1, Figs. 1–3 and additional references.

Peer Review File

Rights and permissions

Reprints and Permissions

About this article

Cite this article

Zhou, H., Xie, T., Ghazaryan, A. *et al.* Half- and quarter-metals in rhombohedral trilayer graphene. *Nature* **598**, 429–433 (2021).
<https://doi.org/10.1038/s41586-021-03938-w>

- Received: 08 April 2021

- Accepted: 20 August 2021
- Published: 01 September 2021
- Issue Date: 21 October 2021
- DOI: <https://doi.org/10.1038/s41586-021-03938-w>

Share this article

Anyone you share the following link with will be able to read this content:

[Get shareable link](#)

Sorry, a shareable link is not currently available for this article.

[Copy to clipboard](#)

Provided by the Springer Nature SharedIt content-sharing initiative

[Superconductivity in rhombohedral trilayer graphene](#)

- Haoxin Zhou
- Tian Xie
- Andrea F. Young

Article 01 Sept 2021

[Untwisted trilayer graphene hosts superconductivity and magnetism](#)

- Thiti Taychatanapat

News & Views 19 Oct 2021

| [Section menu](#) | [Main menu](#) |

- Article
- [Published: 01 September 2021](#)

Superconductivity in rhombohedral trilayer graphene

- [Haoxin Zhou¹](#),
- [Tian Xie ORCID: orcid.org/0000-0002-6406-0403¹](#),
- [Takashi Taniguchi ORCID: orcid.org/0000-0002-1467-3105²](#),
- [Kenji Watanabe ORCID: orcid.org/0000-0003-3701-8119³](#) &
- [Andrea F. Young ORCID: orcid.org/0000-0001-5954-8028¹](#)

Nature volume **598**, pages 434–438 (2021)

- 10k Accesses
- 23 Altmetric
- [Metrics details](#)

Subjects

- [Electronic properties and devices](#)
- [Superconducting properties and materials](#)

Abstract

To access superconductivity via the electric field effect in a clean, two-dimensional device is a central goal of nanoelectronics. Recently, superconductivity has been realized in graphene moiré heterostructures^{1,2,3,4}; however, many of these structures are not mechanically stable, and experiments show signatures of strong disorder.

Here we report the observation of superconductivity—manifesting as low or vanishing resistivity at sub-kelvin temperatures—in crystalline rhombohedral trilayer graphene^{5,6}, a structurally metastable carbon allotrope. Superconductivity occurs in two distinct gate-tuned regions (SC1 and SC2), and is deep in the clean limit defined by the ratio of mean free path and superconducting coherence length. Mapping of the normal state Fermi surfaces by quantum oscillations reveals that both superconductors emerge from an annular Fermi sea, and are proximal to an isospin-symmetry-breaking transition where the Fermi surface degeneracy changes⁷. SC1 emerges from a paramagnetic normal state, whereas SC2 emerges from a spin-polarized, valley-unpolarized half-metal¹⁷ and violates the Pauli limit for in-plane magnetic fields by at least one order of magnitude^{8,9}. We discuss our results in view of several mechanisms, including conventional phonon-mediated pairing^{10,11}, pairing due to fluctuations of the proximal isospin order¹², and intrinsic instabilities of the annular Fermi liquid^{13,14}. Our observation of superconductivity in a clean and structurally simple two-dimensional metal provides a model system to test competing theoretical models of superconductivity without the complication of modelling disorder, while enabling new classes of field-effect controlled electronic devices based on correlated electron phenomena and ballistic electron transport.

Access options

Subscribe to Journal

Get full journal access for 1 year

\$199.00

only \$3.90 per issue

[Subscribe](#)

All prices are NET prices.

VAT will be added later in the checkout.

Tax calculation will be finalised during checkout.

Rent or Buy article

Get time limited or full article access on ReadCube.

from \$8.99

[Rent or Buy](#)

All prices are NET prices.

Additional access options:

- [Log in](#)
- [Access through your institution](#)
- [Learn about institutional subscriptions](#)

Fig. 1: Superconductivity in RTG.



Fig. 2: Fermiology of SC1.

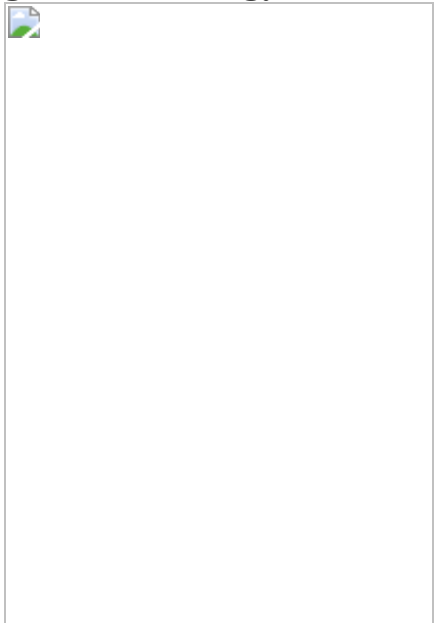


Fig. 3: Magnetic field dependence of SC1.

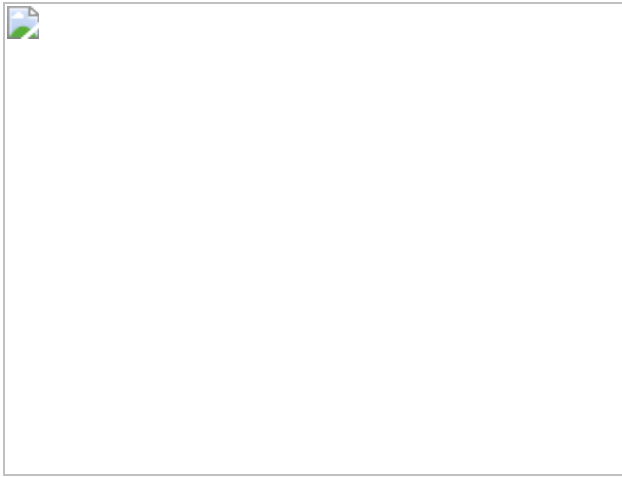
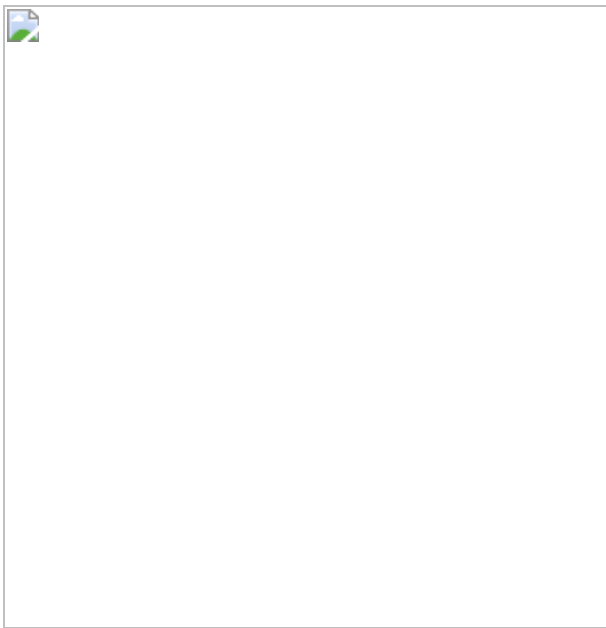


Fig. 4: Fermiology and $\langle \langle \boldsymbol{B} \rangle \rangle_{\parallel}$ dependence of SC2.



Data availability

The data that support the findings of this study are available from the corresponding authors on reasonable request.

References

1. 1.

Cao, Y. et al. Unconventional superconductivity in magic-angle graphene superlattices. *Nature* **556**, 43–50 (2018).

2. 2.

Chen, G. et al. Signatures of tunable superconductivity in a trilayer graphene moiré superlattice. *Nature* **572**, 215–219 (2019).

3. 3.

Park, J. M., Cao, Y., Watanabe, K., Taniguchi, T. & Jarillo-Herrero, P. Tunable strongly coupled superconductivity in magic-angle twisted trilayer graphene. *Nature* **590**, 249–255 (2021).

4. 4.

Hao, Z. et al. Electric field-tunable superconductivity in alternating-twist magic-angle trilayer graphene. *Science* **371**, 1133 (2021).

5. 5.

Koshino, M. & McCann, E. Trigonal warping and Berry's phase $N\pi$ in ABC-stacked multilayer graphene. *Phys. Rev. B* **80**, 165409 (2009).

6. 6.

Zhang, F., Sahu, B., Min, H. & MacDonald, A. H. Band structure of ABC-stacked graphene trilayers. *Phys. Rev. B* **82**, 035409 (2010).

7. 7.

Zhou, H. et al. Half and quarter metals in rhombohedral trilayer graphene. Preprint at <https://arxiv.org/abs/2104.00653> (2021).

8. 8.

Clogston, A. M. Upper limit for the critical field in hard superconductors. *Phys. Rev. Lett.* **9**, 266–267 (1962).

9. 9.

Chandrasekhar, B. S. A note on the maximum critical field of high-field superconductors. *Appl. Phys. Lett.* **1**, 7–8, (1962).

10. 10.

Bardeen, J., Cooper, L. N. & Schrieffer, J. R. Theory of superconductivity. *Phys. Rev.* **108**, 1175–1204 (1957).

11. 11.

Gor'kov, L. P. Superconducting transition temperature: interacting Fermi gas and phonon mechanisms in the nonadiabatic regime. *Phys. Rev. B* **93**, 054517 (2016).

12. 12.

Scalapino, D. J. A common thread: the pairing interaction for unconventional superconductors. *Rev. Mod. Phys.* **84**, 1383–1417 (2012).

13. 13.

Kohn, W. & Luttinger, J. M. New mechanism for superconductivity. *Phys. Rev. Lett.* **15**, 524–526 (1965).

14. 14.

Chubukov, A. V. & Kivelson, S. A. Superconductivity in engineered two-dimensional electron gases. *Phys. Rev. B* **96**, 174514 (2017).

15. 15.

Cooper, L. N. Bound electron pairs in a degenerate Fermi gas. *Phys. Rev.* **104**, 1189–1190 (1956).

16. 16.

Stoner, E. C. Collective electron ferromagnetism. *Proc. R. Soc. A* **165**, 372–414 (1938).

17. 17.

Mathur, N. D. et al. Magnetically mediated superconductivity in heavy fermion compounds. *Nature* **394**, 39–43 (1998).

18. 18.

Lee, Y. et al. Gate tunable magnetism and giant magnetoresistance in ABC-stacked few-layer graphene. Preprint at <https://arxiv.org/abs/1911.04450> (2019).

19. 19.

Shi, Y. et al. Electronic phase separation in multilayer rhombohedral graphite. *Nature* **584**, 210–214 (2020).

20. 20.

Castro, E. V., Peres, N. M. R., Stauber, T. & Silva, N. A. P. Low-density ferromagnetism in biased bilayer graphene. *Phys. Rev. Lett.* **100**, 186803 (2008).

21. 21.

Berezinsky, V. L. Destruction of long range order in one-dimensional and two-dimensional systems having a continuous symmetry group. I. Classical systems. *Sov. Phys. JETP* **32**, 493–500 (1971).

22. 22.

Kosterlitz, J. M. & Thouless, D. J. Ordering, metastability and phase transitions in two-dimensional systems. *J. Phys. C* **6**, 1181–1203 (1973).

23. 23.

Anderson, P. W. Theory of dirty superconductors. *J. Phys. Chem. Solids* **11**, 26–30 (1959).

24. 24.

Abrikosov, A. A. & Gor'kov, L. P. Contribution to the theory of superconducting alloys with paramagnetic impurities. *Zhur. Eksptl. i Teoret. Fiz.* **39**, 1782–1796 (1960).

25. 25.

Tinkham, M. *Introduction to Superconductivity* 2nd edn (McGraw-Hill, New York, 1975).

26. 26.

Wang, L. et al. One-dimensional electrical contact to a two-dimensional material. *Science* **342**, 614–617 (2013).

27. 27.

Taychatanapat, T., Watanabe, K., Taniguchi, T. & Jarillo-Herrero, P. Electrically tunable transverse magnetic focusing in graphene. *Nat. Phys.* **9**, 225–229 (2013).

28. 28.

Lee, M., Wallbank, J. R., Gallagher, P., Watanabe, K., Taniguchi, T., Fal'ko, V. I. & Goldhaber-Gordon, D. Ballistic miniband conduction in a graphene superlattice. *Science* **353**, 1526–1529 (2016).

29. 29.

Lee, J. Y. et al. Theory of correlated insulating behaviour and spin-triplet superconductivity in twisted double bilayer graphene. *Nat. Comm.* **10**, 5333 (2019).

30. 30.

Cornfeld, E., Rudner, M. S. & Berg, E. Spin-polarized superconductivity: order parameter topology, current dissipation, and multiple-period Josephson effect. *Phys. Rev. Research* **3**, 013051 (2021).

31. 31.

Löthman, T. & Black-Schaffer, A. M. Universal phase diagrams with superconducting domes for electronic flat bands. *Phys. Rev. B* **96**, 064505 (2017).

32. 32.

Ojajärvi, R., Hyart, T., Silaev, M. A. & Heikkilä, T. T. Competition of electron-phonon mediated superconductivity and Stoner magnetism on a flat band. *Phys. Rev. B* **98**, 054515 (2018).

33. 33.

Gor'kov, L. P. Phonon mechanism in the most dilute superconductor SrTiO₃. *Proc. Natl. Acad. Sci. USA* **113**, 4646 (2016).

34. 34.

Kopnin, N. B., Heikkilä, T. T. & Volovik, G. E. High-temperature surface superconductivity in topological flat-band systems. *Phys. Rev. B* **83**, 220503 (2011).

35. 35.

McMillan, W. L. Transition temperature of strong-coupled superconductors. *Phys. Rev.* **167**, 331–344 (1968).

36. 36.

Poole C. P. Jr., Zasadzinski, J. F., Zasadzinski, R. K., & Allen, P. B., *Handbook of Superconductivity* Ch. 9, 433-489, edited by Poole, C. P. Jr (Academic Press, 2000).

37. 37.

Masubuchi, S., Ono, M., Yoshida, K., Hirakawa, K. & Machida, T. Fabrication of graphene nanoribbon by local anodic oxidation lithography using atomic force microscope. *Appl. Phys. Lett.* **94**, 082107 (2009).

38. 38.

Li, H. et al. Electrode-free anodic oxidation nanolithography of low-dimensional materials. *Nano Lett.* **18**, 8011–8015 (2018).

Acknowledgements

The authors acknowledge extensive discussions with E. Berg and M. Zaletel and thank them for their comments on the completed manuscript. The authors also acknowledge discussions with S. Kivelson, S. Das Sarma, A. Bernevig and A. H. Macdonald. We acknowledge experimental assistance from L. Cohen, who installed the dilution refrigerator. This project was primarily funded by the United States Department of Energy under DE-SC0020043. A.F.Y. acknowledges the support of the Gordon and Betty Moore Foundation under award GBMF9471. K.W. and T.T. acknowledge support from the Elemental Strategy Initiative conducted by the MEXT, Japan (grant number JPMXP0112101001) and JSPS KAKENHI (grant numbers 19H05790 and JP20H00354).

Author information

Affiliations

1. Department of Physics, University of California, Santa Barbara, CA, USA

Haoxin Zhou, Tian Xie & Andrea F. Young

2. International Center for Materials Nanoarchitectonics, National Institute for Materials Science, Tsukuba, Japan

Takashi Taniguchi

3. Research Center for Functional Materials, National Institute for Materials Science, Tsukuba, Japan

Kenji Watanabe

Contributions

H.Z. fabricated the device with assistance from T.X. H.Z. performed the measurements, advised by A.F.Y. K.W. and T.T. grew the hexagonal boron nitride crystals. H.Z. and A.F.Y. wrote the manuscript with input from all authors.

Corresponding author

Correspondence to Andrea F. Young.

Ethics declarations

Competing interests

The authors declare no competing interests.

Additional information

Peer review information *Nature* thanks Mikito Koshino, Folkert de Vries and the other, anonymous, reviewer(s) for their contribution to the peer review of this work. Peer reviewer reports are available.

Publisher's note Springer Nature remains neutral with regard to jurisdictional claims in published maps and institutional affiliations.

Publisher's note Springer Nature remains neutral with regard to jurisdictional claims in published maps and institutional affiliations.

Extended data figures and tables

Extended Data Fig. 1 Displacement field dependence of SC1.

a, $\langle R \rangle_{xx}$ as a function of $\langle n \rangle_{\rm e}$ and T at $D=0.46$ V/nm. **b**, at $(D=0.4)$ V/nm. **c**, at $(D=0.34)$ V/nm.

Extended Data Fig. 2 Temperature dependent data for SC1 and SC2.

a, Temperature dependent $\langle dV/dI \rangle$ measurements of SC1. Measurements were performed at $\langle n \rangle_{\rm e} = -1.8 \times 10^{12} \text{ cm}^{-2}$, $(D=0.46)$ V/nm. **b**, $\langle V(I) \rangle$ for SC1. The dashed line shows $\langle V \rangle \propto I^3$; we take $\langle T \rangle_{\rm BKT}$ as the highest temperature where the $\langle V(I) \rangle$ curve shows I^3 scaling. **c**, $\langle R \rangle_{xx}(T)$ for SC1 with $\langle T \rangle_{\rm BKT}$ indicated. **d**, Same as panel **a**, but for SC2. Measurements were performed at $\langle n \rangle_{\rm e} = -0.55 \times 10^{12} \text{ cm}^{-2}$, $(D=0.33)$ V/nm. **e**, Same as panel **b**, but for SC2. **f**, Same as panel **c**, but for SC2.

Extended Data Fig. 3 Comparison of quantum oscillations and transverse magnetic electron focusing at $\langle \boldsymbol{D} \rangle = 0$.

a, $\langle R \rangle_{xx}$ vs $\langle n \rangle_{\rm e}$ and B_{\perp} measured at $D=0$. **b**, Fourier transform of $\langle R \rangle_{xx}(B_{\perp})$ for data in panel **a**. **c**, Non-local resistance measured in the configuration in Fig. 3c as a function of $\langle n \rangle_{\rm e}$ and B_{\perp} .

Extended Data Fig. 4 $\langle R \rangle_{\parallel}$ -dependence of SC1.

a, Temperature dependent $\langle dV/dI \rangle$ measurements of SC1. Measurements were performed at $\langle n \rangle_{\rm e} = -1.8 \times 10^{12}$

$\{\{\rm cm\}\}^{\{-2\}}$, $(D=0.46)V/\text{nm}$. **b**, $\langle R_{xx}(T) \rangle$ for SC1 with $\langle T \rangle_{\{\rm BKT\}}$ indicated. **c**, $\langle V(I) \rangle$ for SC1. The dashed line shows $\langle V \rangle \propto I^3$ we take $\langle T \rangle_{\{\rm BKT\}}$ as the highest temperature where the $\langle V(I) \rangle$ curve shows I^3 scaling. **d-f**, Same as panel **a-c** measured at $\langle B \rangle_{\parallel} = 50\text{mT}$. **g-i**, Same as panels **a-c** measured at $\langle B \rangle_{\parallel} = 100\text{mT}$. **j-l**, Same as panels **a-c** measured at $\langle B \rangle_{\parallel} = 150\text{mT}$. **m-o**, Same as panels **a-c** measured at $\langle B \rangle_{\parallel} = 175\text{mT}$.

Extended Data Fig. 5 Magnetic field dependence of SC2.

a, $\langle R_{xx} \rangle$ vs $\langle n_e \rangle$ measured at $(D=0.33)V/\text{nm}$ and various $\langle B_{\perp} \rangle$ with $\langle B_{\parallel} \rangle = 0$. **b**, Same as **a**, measured at various $\langle B_{\parallel} \rangle$ with $\langle B_{\perp} \rangle = 0$.

Extended Data Fig. 6 Temperature dependence of $\langle R_{xx} \rangle$ measured at $(D=0.4V/\text{nm}$ and $\langle n_e \rangle < 0$.

Bottom panel shows $\langle R_{xx} \rangle$ as a function of $\langle n_e \rangle$ at different temperature. Top panels show $\langle R_{xx} \rangle$ vs (T) at fixed $\langle n_e \rangle$ extracted from the bottom panel.

Extended Data Fig. 7 In-plane magnetic field dependence of the PIP phase near SC1.

a, $\langle B_{\parallel} \rangle$ - dependence of $\langle R_{xx} \rangle$ near SC1 at $D=0.228V/\text{nm}$. **b**, Zoom-in of panel **a**. **c**, Same as panel **b** but measured with an out-of-plane field applied instead of in-plane field. **d**, Schematic phase diagram extracted from panel **a**. Insets are schematic Fermi contours of the isospin polarized and unpolarized phases.

Supplementary information

Peer Review File

Rights and permissions

Reprints and Permissions

About this article

Cite this article

Zhou, H., Xie, T., Taniguchi, T. *et al.* Superconductivity in rhombohedral trilayer graphene. *Nature* **598**, 434–438 (2021).

<https://doi.org/10.1038/s41586-021-03926-0>

- Received: 14 June 2021
- Accepted: 18 August 2021
- Published: 01 September 2021
- Issue Date: 21 October 2021
- DOI: <https://doi.org/10.1038/s41586-021-03926-0>

Share this article

Anyone you share the following link with will be able to read this content:

[Get shareable link](#)

Sorry, a shareable link is not currently available for this article.

[Copy to clipboard](#)

Provided by the Springer Nature SharedIt content-sharing initiative

[Half- and quarter-metals in rhombohedral trilayer graphene](#)

- Haoxin Zhou
- Tian Xie
- Andrea F. Young

Article 01 Sept 2021

Double superconductivity

- David Abergel

Research Highlight 06 Oct 2021

Untwisted trilayer graphene hosts superconductivity and magnetism

- Thiti Taychatanapat

News & Views 19 Oct 2021

This article was downloaded by **calibre** from <https://www.nature.com/articles/s41586-021-03926-0>

| [Section menu](#) | [Main menu](#) |

- Article
- [Published: 20 October 2021](#)

Dexterous magnetic manipulation of conductive non-magnetic objects

- [Lan N. Pham](#) [ORCID: orcid.org/0000-0001-8766-1167](#)¹,
- [Griffin F. Tabor](#) [ORCID: orcid.org/0000-0003-3992-7391](#)²,
- [Ashkan Pourkand](#)²,
- [Jacob L. B. Aman](#) [ORCID: orcid.org/0000-0003-3191-5521](#)³,
- [Tucker Hermans](#) [ORCID: orcid.org/0000-0003-2496-2768](#)^{2,4} &
- [Jake J. Abbott](#) [ORCID: orcid.org/0000-0002-0665-1934](#)¹

[Nature](#) volume **598**, pages 439–443 (2021)

- 1633 Accesses
- 25 Altmetric
- [Metrics details](#)

Subjects

- [Applied physics](#)
- [Mechanical engineering](#)
- [Techniques and instrumentation](#)

Abstract

Dexterous magnetic manipulation of ferromagnetic objects is well established, with three to six degrees of freedom possible depending on object geometry¹. There are objects for which non-contact dexterous

manipulation is desirable that do not contain an appreciable amount of ferromagnetic material but do contain electrically conductive material. Time-varying magnetic fields generate eddy currents in conductive materials^{2,3,4}, with resulting forces and torques due to the interaction of the eddy currents with the magnetic field. This phenomenon has previously been used to induce drag to reduce the motion of objects as they pass through a static field^{5,6,7,8}, or to apply force on an object in a single direction using a dynamic field^{9,10,11}, but has not been used to perform the type of dexterous manipulation of conductive objects that has been demonstrated with ferromagnetic objects. Here we show that manipulation, with six degrees of freedom, of conductive objects is possible by using multiple rotating magnetic dipole fields. Using dimensional analysis¹², combined with multiphysics numerical simulations and experimental verification, we characterize the forces and torques generated on a conductive sphere in a rotating magnetic dipole field. With the resulting model, we perform dexterous manipulation in simulations and physical experiments.

Access options

Subscribe to Journal

Get full journal access for 1 year

\$199.00

only \$3.90 per issue

[Subscribe](#)

All prices are NET prices.

VAT will be added later in the checkout.

Tax calculation will be finalised during checkout.

Rent or Buy article

Get time limited or full article access on ReadCube.

from \$8.99

[Rent or Buy](#)

All prices are NET prices.

Additional access options:

- [Log in](#)
- [Access through your institution](#)
- [Learn about institutional subscriptions](#)

Fig. 1: Induced forces and torques on a conductive sphere in three canonical positions relative to a rotating magnetic dipole.



Fig. 2: Typical numerical and experimental results for force-torque characterization.



Fig. 3: Dexterous manipulation of a copper sphere in simulated microgravity.



Data availability

All data generated and scripts for analyses during this study are included in the published article and can be found using the following link:

<https://osf.io/uk3rx/>.

References

1. 1.

Abbott, J. J., Diller, E. & Petruska, A. J. Magnetic methods in robotics. *Annu. Rev. Control Robot. Auton. Syst.* **3**, 57–90 (2020).

2. 2.

Hertz, H. *Miscellaneous Papers* Chapter 2 [transl. Jones, D. E. & Schott, G. A.] (Macmillan, 1896).

3. 3.

Griffiths, D. J. *Introduction to Electrodynamics* 4th edition (Cambridge Univ. Press, 2017).

4. 4.

Nagel, J. R. Induced eddy currents in simple conductive geometries: mathematical formalism describes the excitation of electrical eddy currents in a time-varying magnetic field. *IEEE Antennas Propag. Mag.* **3**, 81–88 (2018).

5. 5.

Youngquist, R. C., Nurge, M. A., Starr, S. O., Leve, F. A. & Peck, M. A. A slowly rotating hollow sphere in a magnetic field: first steps to de-spin a space object. *Am. J. Phys.* **84**, 181–191 (2016).

6. 6.

Nurge, M. A., Youngquist, R. C. & Starr, S. O. A thick-walled sphere rotating in a uniform magnetic field: the next step to de-spin a space object. *Am. J. Phys.* **85**, 596–610 (2017).

7. 7.

Nurge, M. A., Youngquist, R. C. & Starr, S. O. Drag and lift forces between a rotating conductive sphere and a cylindrical magnet. *Am. J. Phys.* **86**, 443–452 (2018).

8. 8.

Sharma, K. K. et al. Space debris reduction using eddy currents. In *2018 Atmospheric Flight Mechanics Conf.*, 3161 (American Institute of Aeronautics and Astronautics, 2018).

9. 9.

Reinhardt, B. Z. & Peck, M. A. New electromagnetic actuator for on-orbit inspection. *J. Spacecraft Rockets* **53**, 241–248 (2016).

10. 10.

Liu, X., Lu, Y., Zhou, Y. & Yin, Y. Prospects of using a permanent magnetic end effector to despin and detumble an uncooperative target. *Adv. Space Res.* **61**, 2147–2158 (2018).

11. 11.

Smith, Y. R., Nagel, J. R. & Rajamani, R. K. Eddy current separation for recovery of non-ferrous metallic particles: a comprehensive review. *Miner. Eng.* **133**, 149–159 (2019).

12. 12.

Buckingham, E. On physically similar systems; illustrations of the use of dimensional equations. *Phys. Rev.* **4**, 345 (1914).

13. 13.

Shan, M., Guo, J. & Gill, E. Review and comparison of active space debris capturing and removal methods. *Prog. Aerosp. Sci.* **80**, 18–32 (2016).

14. 14.

Mark, C. P. & Kamath, S. Review of active space debris removal methods. *Space Policy* **47**, 194–206 (2019).

15. 15.

Kessler, D. J., Johnson, N. L., Liou J. C. & Matney, M. The Kessler syndrome: implications to future space operations. *Adv. Astronaut. Sci.* **137**, AAS 10-016 (2010).

16. 16.

Opiela, J. N. A study of the material density distribution of space debris. *Adv. Space Res.* **43**, 1058–1064 (2009).

17. 17.

Pelrine, R. et al. Diamagnetically levitated robots: an approach to massively parallel robotic systems with unusual motion properties. *IEEE Int. Conf. Robotics and Automation*, 739–744 (2012).

18. 18.

Mirica, K. A., Ilievski, F., Ellerbee, A. K., Shevkoplyas, S. S. & Whitesides, G. M. Using magnetic levitation for three dimensional self-assembly. *Adv. Mater.* **23**, 4134–4140 (2011).

19. 19.

Petruska, A. J. & Abbott, J. J. Omnimagnet: an omnidirectional electromagnet for controlled dipole-field generation. *IEEE Trans. Magn.* **50**, 8400410 (2014).

20. 20.

Wright, S. E., Mahoney, A. W., Popek, K. M. & Abbott, J. J. The spherical-actuator-magnet manipulator: a permanent-magnet robotic end-effector. *IEEE Trans. Robot.* **33**, 1013–2924 (2017).

21. 21.

Petruska, A. J. & Abbott, J. J. Optimal permanent-magnet geometries for dipole field approximation. *IEEE Trans. Magn.* **49**, 811–819 (2013).

22. 22.

Lynch, K. M. & Park, F. C. *Modern Robotics: Mechanics, Planning, and Control* (Cambridge Univ. Press, 2017).

23. 23.

Diller, E., Giltinan, J., Lum, G. Z., Ye, Z. & Sitti, M. Six-degree-of-freedom magnetic actuation for wireless microrobotics. *Int. J. Robot. Res.* **35**, 114–128 (2016).

24. 24.

Kummer, M. P. et al. OctoMag: an electromagnetic system for 5-DOF wireless micromanipulation. *IEEE Trans. Robot.* **26**, 1006–1017

(2010).

25. 25.

Petruska, A. J. & Nelson, B. J. Minimum bounds on the number of electromagnets required for remote magnetic manipulation. *IEEE Trans. Robot.* **31**, 714–722 (2015).

26. 26.

Ryan, P. & Diller, E. Magnetic actuation for full dexterity microrobotic control using rotating permanent magnets. *IEEE Trans. Robot.* **33**, 1398–1409 (2017).

Acknowledgements

This work was supported by the National Science Foundation under grants 1841845 and 1846341.

Author information

Affiliations

1. Department of Mechanical Engineering, University of Utah, Salt Lake City, UT, USA

Lan N. Pham & Jake J. Abbott

2. School of Computing, University of Utah, Salt Lake City, UT, USA

Griffin F. Tabor, Ashkan Pourkand & Tucker Hermans

3. Lawrence Livermore National Laboratory, Livermore, CA, USA

Jacob L. B. Aman

4. NVIDIA, Seattle, WA, USA

Tucker Hermans

Contributions

J.J.A. and T.H. proposed the research. All authors participated in the planning of the article. L.N.P. and J.J.A. performed the dimensional analysis and designed the experiments to characterize force-torque. L.N.P. and J.L.B.A. performed the numerical simulations to characterize force-torque. G.F.T. and T.H. designed the numerical microgravity manipulation simulator and control scheme, and integrated the controller into the experimental manipulation system. L.N.P., G.F.T. and A.P. designed and performed the manipulation experiments. L.N.P., G.F.T. and J.J.A drafted the manuscript. All other authors performed a critical revision.

Corresponding author

Correspondence to Jake J. Abbott.

Ethics declarations

Competing interests

J.J.A. has patents and patents pending on electromagnet and permanent-magnet devices designed to generate rotating magnetic dipole fields. The other authors declare no competing interests.

Additional information

Peer review information *Nature* thanks Eric Diller and the other, anonymous, reviewer(s) for their contribution to the peer review of this work.

Publisher's note Springer Nature remains neutral with regard to jurisdictional claims in published maps and institutional affiliations.

Supplementary information

Supplementary Information

This document comprises the complete supplementary information associated with the article, organized in eight sections, ordered as the respective topics are introduced in the article: 1. Dimensional analysis. 2. Characterization of force and torque. 3. Model derivation. 4. Experimental verification of force and torque. 5. Comparison of numerical and experimental results. 6. Manipulation numerical simulations. 7. Manipulation experiments. 8. Discussion.

Supplementary Video 1

Numerical simulation of dexterous manipulation of a copper sphere in microgravity, with 3-DOF position control along the edges of a cube and uncontrolled orientation, using six dipole-field sources surrounding the sphere. The black line is the path taken, and an orthonormal frame depicts the sphere's orientation. Highlighting indicates which single dipole-field source is activated at any given instant.

Supplementary Video 2

Numerical simulation of dexterous manipulation of a copper sphere in microgravity, with 3-DOF position control along the edges of a cube and 3-DOF constant-orientation control, using six dipole-field sources surrounding the sphere. The black line is the path taken, and an orthonormal frame depicts the sphere's orientation. Highlighting indicates which single dipole-field source is activated at any given instant.

Supplementary Video 3

Dexterous manipulation of a copper sphere floating in a raft on the surface of water, with 2-DOF position control along the edges of a square in the horizontal plane and uncontrolled orientation about the vertical axis, using four electromagnetic dipole-field sources located below the sphere. The

yellow line is the path taken, and a red arrow depicts the sphere's orientation, which is logged over time. Highlighting indicates which single dipole-field source is activated at any given instant, with a blue arrow depicting the axis of rotation of the rotating magnetic dipole.

Supplementary Video 4

Dexterous manipulation of a copper sphere floating in a raft on the surface of water, with 2-DOF position control along the edges of a square in the horizontal plane and 1-DOF orientation control about the vertical axis, using four electromagnetic dipole-field sources located below the sphere. The yellow line is the path taken, and a red arrow depicts the sphere's orientation, which is logged over time. Highlighting indicates which single dipole-field source is activated at any given instant, with a blue arrow depicting the axis of rotation of the rotating magnetic dipole.

Rights and permissions

Reprints and Permissions

About this article

Pham, L.N., Tabor, G.F., Pourkand, A. *et al.* Dexterous magnetic manipulation of conductive non-magnetic objects. *Nature* **598**, 439–443 (2021). <https://doi.org/10.1038/s41586-021-03966-6>

- Received: 11 March 2021
- Accepted: 26 August 2021
- Published: 20 October 2021
- Issue Date: 21 October 2021

- DOI: <https://doi.org/10.1038/s41586-021-03966-6>

Share this article

Anyone you share the following link with will be able to read this content:

[Get shareable link](#)

Sorry, a shareable link is not currently available for this article.

[Copy to clipboard](#)

Provided by the Springer Nature SharedIt content-sharing initiative

[**Non-magnetic objects induced to move by electromagnets**](#)

- Eric Diller

News & Views 20 Oct 2021

This article was downloaded by **calibre** from <https://www.nature.com/articles/s41586-021-03966-6>

| [Section menu](#) | [Main menu](#) |

- Article
- [Published: 20 October 2021](#)

Perovskite solar cells with atomically coherent interlayers on SnO₂ electrodes

- [Hanul Min](#)¹ na1,
- [Do Yoon Lee](#)¹ na1,
- [Junu Kim](#)²,
- [Gwisu Kim](#)¹,
- [Kyoung Su Lee](#)¹,
- [Jongbeom Kim](#)¹,
- [Min Jae Paik](#)¹,
- [Young Ki Kim](#)³,
- [Kwang S. Kim](#) [ORCID: orcid.org/0000-0002-6929-5359](#)²,
- [Min Gyu Kim](#) [ORCID: orcid.org/0000-0002-2366-6898](#)⁴,
- [Tae Joo Shin](#) [ORCID: orcid.org/0000-0002-1438-3298](#)³ &
- [Sang Il Seok](#) [ORCID: orcid.org/0000-0001-9976-6628](#)¹

Nature volume **598**, pages 444–450 (2021)

- 3405 Accesses
- 16 Altmetric
- [Metrics details](#)

Subjects

- [Devices for energy harvesting](#)

- [Solar cells](#)

Abstract

In perovskite solar cells, the interfaces between the perovskite and charge-transporting layers contain high concentrations of defects (about 100 times that within the perovskite layer), specifically, deep-level defects, which substantially reduce the power conversion efficiency of the devices^{1,2,3}. Recent efforts to reduce these interfacial defects have focused mainly on surface passivation^{4,5,6}. However, passivating the perovskite surface that interfaces with the electron-transporting layer is difficult, because the surface-treatment agents on the electron-transporting layer may dissolve while coating the perovskite thin film. Alternatively, interfacial defects may not be a concern if a coherent interface could be formed between the electron-transporting and perovskite layers. Here we report the formation of an interlayer between a SnO_2 electron-transporting layer and a halide perovskite light-absorbing layer, achieved by coupling Cl-bonded SnO_2 with a Cl-containing perovskite precursor. This interlayer has atomically coherent features, which enhance charge extraction and transport from the perovskite layer, and fewer interfacial defects. The existence of such a coherent interlayer allowed us to fabricate perovskite solar cells with a power conversion efficiency of 25.8 per cent (certified 25.5 per cent) under standard illumination. Furthermore, unencapsulated devices maintained about 90 per cent of their initial efficiency even after continuous light exposure for 500 hours. Our findings provide guidelines for designing defect-minimizing interfaces between metal halide perovskites and electron-transporting layers.

Access options

Subscribe to Journal

Get full journal access for 1 year

\$199.00

only \$3.90 per issue

[Subscribe](#)

All prices are NET prices.

VAT will be added later in the checkout.

Tax calculation will be finalised during checkout.

Rent or Buy article

Get time limited or full article access on ReadCube.

from \$8.99

[Rent or Buy](#)

All prices are NET prices.

Additional access options:

- [Log in](#)
- [Access through your institution](#)
- [Learn about institutional subscriptions](#)

Fig. 1: Interlayer formation from Cl-bSO and Cl-cPP.

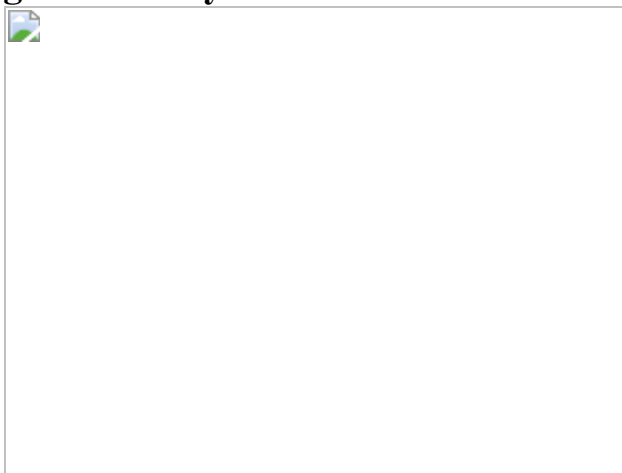


Fig. 2: Local geometric environments around the Sn atoms in the SnO₂ electrodes, before and after applying the perovskite precursor solution.

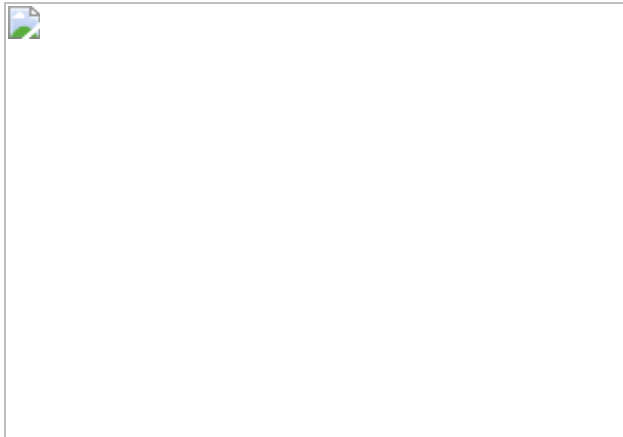


Fig. 3: Two-dimensional GI-WAXD patterns, HR-TEM and photoluminescence after applying Cl-cPP on Cl-bSO and SnO₂.

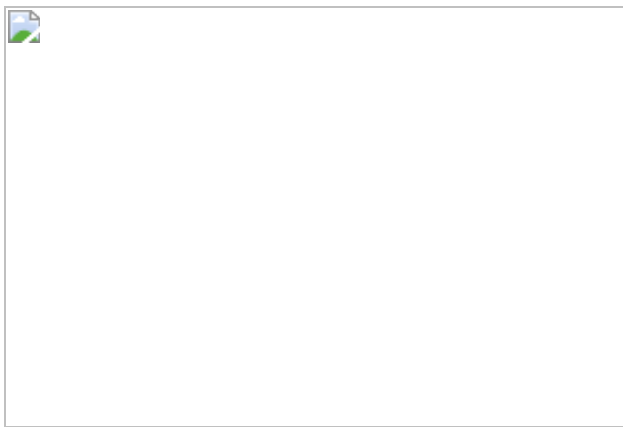


Fig. 4: Performance of PSCs based on various electrodes.

Data availability

The data that support the findings of this study are available from the corresponding authors on reasonable request.

Code availability

The code used for this study is available from the corresponding authors on reasonable request.

References

1. 1.

Ni, Z. et al. Resolving spatial and energetic distributions of trap states in metal halide perovskite solar cells. *Science* **367**, 1352–1358 (2020).

2. 2.

Ono, L. K., Liu, S. & Qi, Y. Reducing detrimental defects for high-performance metal halide perovskite solar cells. *Angew. Chem. Int. Ed.* **59**, 6676–6698 (2020).

3. 3.

Schulz, P., Cahen, D. & Kahn, A. Halide perovskites: is it all about the interfaces? *Chem. Rev.* **119**, 3349–3417 (2019).

4. 4.

Jiang, Q. et al. Surface passivation of perovskite film for efficient solar cells. *Nat. Photon.* **13**, 460–466 (2019).

5. 5.

Jung, E. H. et al. Efficient, stable and scalable perovskite solar cells using poly(3-hexylthiophene). *Nature* **567**, 511–515 (2019).

6. 6.

Azmi, R. et al. Shallow and deep trap state passivation for low-temperature processed perovskite solar cells. *ACS Energy Lett.* **5**, 1396–1403 (2020).

7. 7.

Jeon, N. J. et al. Compositional engineering of perovskite materials for high-performance solar cells. *Nature* **517**, 476–480 (2015).

8. 8.

Hui, W. et al. Stabilizing black-phase formamidinium perovskite formation at room temperature and high humidity. *Science* **371**, 1359–1364 (2021).

9. 9.

Jeong, M. J., Yeom, K. M., Kim, S. J., Jung, E. H. & Noh, J. H. Spontaneous interface engineering for dopant-free poly(3-hexylthiophene) perovskite solar cells with efficiency over 24%. *Energy Environ. Sci.* (2021).

10. 10.

Yoo, J. J. et al. Efficient perovskite solar cells via improved carrier management. *Nature* **590**, 587–593 (2021).

11. 11.

Jeong, J. et al. Pseudo-halide anion engineering for α -FAPbI₃ perovskite solar cells. *Nature* **592**, 381–385 (2021).

12. 12.

Tan, H. et al. Efficient and stable solution-processed planar perovskite solar cells via contact passivation. *Science* **355**, 722–726 (2017).

13. 13.

Jiang, Q. et al. Enhanced electron extraction using SnO₂ for high-efficiency planar-structure HC(NH₂)₂PbI₃-based perovskite solar cells. *Nat. Energy* **2**, 16177 (2017).

14. 14.

Jung, K.-H., Seo, J.-Y., Lee, S., Shin, H. & Park, N.-G. Solution-processed SnO₂ thin film for a hysteresis-free planar perovskite solar cell with a power conversion efficiency of 19.2%. *J. Mater. Chem. A* **5**, 24790–24803 (2017).

15. 15.

Jeong, S., Seo, S., Park, H. & Shin, H. Atomic layer deposition of a SnO₂ electron-transporting layer for planar perovskite solar cells with a power conversion efficiency of 18.3%. *Chem. Commun.* **55**, 2433–2436 (2019).

16. 16.

Anaraki, E. H. et al. Highly efficient and stable planar perovskite solar cells by solution-processed tin oxide. *Energy Environ. Sci.* **9**, 3128–3134 (2016).

17. 17.

McGott, D. L. et al. 3D/2D passivation as a secret to success for polycrystalline thin-film solar cells. *Joule* **5**, 1057–1073 (2021).

18. 18.

Aydin, E., De Bastiani, M. & De Wolf, S. Defect and contact passivation for perovskite solar cells. *Adv. Mater.* **31**, e1900428 (2019).

19. 19.

Li, Z. et al. Spontaneous interface ion exchange: passivating surface defects of perovskite solar cells with enhanced photovoltage. *Adv.*

Energy Mater. **9**, 1902142 (2019).

20. 20.

Min, H. et al. Efficient, stable solar cells by using inherent bandgap of α -phase formamidinium lead iodide. *Science* **366**, 749–753 (2019).

21. 21.

Yoon, S. M. et al. Surface engineering of ambient-air-processed cesium lead triiodide layers for efficient solar cells. *Joule* **5**, 183–196 (2021).

22. 22.

Tao, S. et al. Absolute energy level positions in tin- and lead-based halide perovskites. *Nat. Commun.* **10**, 2560 (2019).

23. 23.

Khan, J. et al. Low-temperature-processed SnO_2 –Cl for efficient PbS quantum-dot solar cells via defect passivation. *J. Mater. Chem. A* **5**, 17240–17247 (2017).

24. 24.

Ke, W. et al. Low-temperature solution-processed tin oxide as an alternative electron transporting layer for efficient perovskite solar cells. *J. Am. Chem. Soc.* **137**, 6730–6733 (2015).

25. 25.

Dong, Q., Shi, Y., Zhang, C., Wu, Y. & Wang, L. Energetically favored formation of SnO_2 nanocrystals as electron transfer layer in perovskite solar cells with high efficiency exceeding 19%. *Nano Energy* **40**, 336–344 (2017).

26. 26.

Kılıç, Ç. & Zunger, A. Origins of coexistence of conductivity and transparency in SnO₂. *Phys. Rev. Lett.* **88**, 095501 (2002).

27. 27.

Kim, M. et al. Methylammonium chloride induces intermediate phase stabilization for efficient perovskite solar cells. *Joule* **3**, 2179–2192 (2019).

28. 28.

Hao, F., Stoumpos, C. C., Cao, D. H., Chang, R. P. H. & Kanatzidis, M. G. Lead-free solid-state organic–inorganic halide perovskite solar cells. *Nat. Photon.* **8**, 489–494 (2014).

29. 29.

Kamat, P. V., Bisquert, J. & Buriak, J. Lead-free perovskite solar cells. *ACS Energy Lett.* **2**, 904–905 (2017).

30. 30.

Hailey, A. K., Hiszpanski, A. M., Smilgies, D.-M. & Loo, Y.-L. The diffraction pattern calculator (DPC) toolkit: a user-friendly approach to unit-cell lattice parameter identification of two-dimensional grazing-incidence wide-angle X-ray scattering data. *J. Appl. Cryst.* **47**, 2090–2099 (2014).

31. 31.

Weller, M. T., Weber, O. J., Frost, J. M. & Walsh, A. Cubic perovskite structure of black formamidinium lead iodide, α -[HC(NH₂)₂]PbI₃, at 298 K. *J. Phys. Chem. Lett.* **6**, 3209–3212 (2015).

32. 32.

Alberti, A. et al. Pb clustering and PbI₂ nanofragmentation during methylammonium lead iodide perovskite degradation. *Nat. Commun.*

10, 2196 (2019).

33. 33.

Yang, G. et al. Effective carrier-concentration tuning of SnO₂ quantum dot electron-selective layers for high-performance planar perovskite solar cells. *Adv. Mater.* **30**, 1706023 (2018).

34. 34.

Lee, J.-W. et al. Solid-phase hetero epitaxial growth of α -phase formamidinium perovskite. *Nat. Commun.* **11**, 5514 (2020).

35. 35.

Krückemeier, L., Krogmeier, B., Liu, Z., Rau, U. & Kirchartz, T. Understanding transient photoluminescence in halide perovskite layer stacks and solar cells. *Adv. Energy Mater.* **11**, 2003489 (2021).

36. 36.

Kim, G., Min, H., Lee, K. S., Yoon, S. M. & Seok, S. I. Impact of strain relaxation on performance of α -formamidinium lead iodide perovskite solar cells. *Science* **370**, 108–112 (2020).

37. 37.

Chen, S. et al. Spatial distribution of lead iodide and local passivation on organo-lead halide perovskite. *ACS Appl. Mater. Interfaces* **9**, 6072–6078 (2017).

38. 38.

Khenkin, M. V. et al. Consensus statement for stability assessment and reporting for perovskite photovoltaics based on ISOS procedures. *Nat. Energy* **5**, 35–49(2020).

39. 39.

Perdew, J. P., Burke, K. & Ernzerhof, M. Generalized gradient approximation made simple. *Phys. Rev. Lett.* **77**, 3865–3868 (1996).

40. 40.

Tkatchenko, A. & Scheffler, M. Accurate molecular van der Waals interactions from ground-state electron density and free-atom reference data. *Phys. Rev. Lett.* **102**, 073005 (2009).

41. 41.

Kresse, G. & Furthmüller, J. Efficiency of ab-initio total energy calculations for metals and semiconductors using a plane-wave basis set. *Comput. Mater. Sci.* **6**, 15–50 (1996).

Acknowledgements

This work was supported by the Basic Science Research Program (NRF-2018R1A3B1052820) through the National Research Foundation of Korea (NRF) funded by the Ministry of Science, ICT & Future Planning (MSIP). This work was also supported by the Defense Challengeable Future Technology Program of the Agency for Defense Development, Republic of Korea, a brand project (1.200030.01) of UNIST, and Alchemist Project (2019309101046). We thank UCRF (UNIST central research facilities) for use of equipment and the beamline staff at Pohang Accelerator Laboratory.

Author information

Author notes

1. These authors contributed equally: Hanul Min, Do Yoon Lee

Affiliations

1. Department of Energy and Chemical Engineering, Ulsan National Institute of Science and Technology, Ulsan, South Korea

Hanul Min, Do Yoon Lee, Gwisu Kim, Kyoung Su Lee, Jongbeom Kim, Min Jae Paik & Sang Il Seok

2. Department of Chemistry, Ulsan National Institute of Science and Technology, Ulsan, South Korea

Junu Kim & Kwang S. Kim

3. UNIST Central Research Facilities, Ulsan National Institute of Science and Technology, Ulsan, South Korea

Young Ki Kim & Tae Joo Shin

4. Beamline Research Division, Pohang Accelerator Laboratory, Pohang University of Science and Technology, Pohang, South Korea

Min Gyu Kim

Contributions

S.I.S., H.M. and D.Y.L. conceived the work and designed the experiment. H.M. and D.Y.L. fabricated the PSCs with various electrodes and characterized the perovskite films. Junu Kim conducted the theoretical simulations, with supervision from K.S.K. K.S.L. measured the thermally stimulated current. Jongbeom Kim and G.K. carried out the model PSC fabrication and SEM measurements. M.J.P. prepared the SnO₂ colloids. Y.K.K. conducted HR-TEM. T.J.S. conducted and interpreted the GI-WAXD. M.G.K. measured and interpreted the XAFS. S.I.S. and H.M. wrote the manuscript, with all authors contributing feedback and comments. S.I.S. directed and supervised the study.

Corresponding authors

Correspondence to Min Gyu Kim, Tae Joo Shin or Sang Il Seok.

Ethics declarations

Competing interests

The authors declare no competing interests.

Additional information

Peer review information *Nature* thanks the anonymous reviewers for their contribution to the peer review of this work.

Publisher's note Springer Nature remains neutral with regard to jurisdictional claims in published maps and institutional affiliations.

Extended data figures and tables

[Extended Data Fig. 1 Cl⁻ ion contents analysed by ToF-SIMS.](#)

The black line is the analysis result for the Cl ions on the thin film obtained after spin coating with the $\text{SnCl}_2 \cdot 2\text{H}_2\text{O}$ solution dissolved in ethanol and then heat treatment at 190 °C for 1 h. The blue line is the result of Cl⁻ion analysis on a thin film obtained by spin coating a SnO_2 colloid generated by heat treatment at 70 °C for 30 min after dissolving 0.1 mol of SnCl_4 in deionised water.

[Extended Data Fig. 2 Depth profiles analysed by ToF-SIMS with a PSC fabricated using a commercial \$\text{SnO}_2\$ colloids as electron-transporting layer.](#)

[Extended Data Fig. 3 DFT simulation of the formation of the interlayer between the perovskite and \$\text{SnO}_2\$.](#)

a, back side view, **b**, right side view, and **c**, left side view of Fig. 1d in (a) 3-dimensional and (b) 2-dimensional shapes. [Pb (black), I (purple), Cl

(green), C (brown), N (light blue), H (white), Sn (dark blue), and O (red)].

Extended Data Fig. 4 Theoretical simulation for the formation of an interlayer between Cl-TiO₂ and Cl-cPP.

Extended Data Fig. 5 Wavelet transform of correlation between the Fourier-transformed peaks with *k*-space data for local geometric environments around Sn of SnO₂, which was annealed at 120 °C for 1 h using a perovskite precursor without Cl⁻ ions coated on a Cl-bSO electrode.

Extended Data Fig. 6 Simulation of the diffraction peaks by a, FAPbI₃ ($a = 6.351 \text{ \AA}$, Pm-3m (#221) space group) and b, PbI₂ ($a = b = 4.555 \text{ \AA}$, $c = 6.964 \text{ \AA}$, P-3m1 (#164) space group) using the Diffraction Pattern Calculator (DPC) toolkit.

Extended Data Fig. 7 1D GI-WAXD profiles for the out-of-plane (q_z -cut; along $q_{xy} = 0$) and in-plane (q_{xy} -cut; along $q_z = 0$).

Extended Data Fig. 8 2D GI-WAXD image focused on the interlayer structure.

Crystallographic information was empirically derived from the diffraction patterns. The crystal structure of this interlayer can be assumed to be

tetragonal with $a = b = 5.56 \text{ \AA}$, $c = 5.29 \text{ \AA}$. If the (001) crystal plane is oriented parallel to the substrate, the observed characteristic diffraction peaks belong to ($11l$) and ($22l$) families.

Extended Data Fig. 9 Steady-state PLs of perovskites with and without the SnO₂ or TiO₂ electrode on the glass substrate.

Extended Data Fig. 10 Time-resolved photoluminescence (TRPL) spectra after excitation at 520 nm (P-C-520M) with repetition rate of 200 kHz and a fluence of 34 nJ cm⁻² per pulse for perovskite films on various ETLs coated on FTO substrates and perovskite without ETL on glass.

Extended Data Table 1 All parameters determined from the J-V curve of Fig. 4c.

Supplementary information

Supplementary Information

This file contains Supplementary Figs. 19 and Supplementary Table 1.

Rights and permissions

Reprints and Permissions

About this article

Cite this article

Min, H., Lee, D.Y., Kim, J. *et al.* Perovskite solar cells with atomically coherent interlayers on SnO₂ electrodes. *Nature* **598**, 444–450 (2021). <https://doi.org/10.1038/s41586-021-03964-8>

- Received: 30 March 2021
- Accepted: 26 August 2021
- Published: 20 October 2021
- Issue Date: 21 October 2021
- DOI: <https://doi.org/10.1038/s41586-021-03964-8>

Share this article

Anyone you share the following link with will be able to read this content:

[Get shareable link](#)

Sorry, a shareable link is not currently available for this article.

[Copy to clipboard](#)

Provided by the Springer Nature SharedIt content-sharing initiative

This article was downloaded by **calibre** from <https://www.nature.com/articles/s41586-021-03964-8>

- Article
- [Published: 31 August 2021](#)

Metallaphotoredox-enabled deoxygenative arylation of alcohols

- [Zhe Dong ORCID: orcid.org/0000-0001-9714-1069¹](#) &
- [David W. C. MacMillan ORCID: orcid.org/0000-0003-3352-4532¹](#)

Nature volume **598**, pages 451–456 (2021)

- 17k Accesses
- 48 Altmetric
- [Metrics details](#)

Subjects

- [Synthetic chemistry methodology](#)
- [Photocatalysis](#)

Abstract

Metal-catalysed cross-couplings are a mainstay of organic synthesis and are widely used for the formation of C–C bonds, particularly in the production of unsaturated scaffolds¹. However, alkyl cross-couplings using native *sp*³-hybridized functional groups such as alcohols remain relatively underdeveloped². In particular, a robust and general method for the direct deoxygenative coupling of alcohols would have major implications for the field of organic synthesis. A general method for the direct deoxygenative cross-coupling of free alcohols must overcome several challenges, most

notably the *in situ* cleavage of strong C–O bonds³, but would allow access to the vast collection of commercially available, structurally diverse alcohols as coupling partners⁴. We report herein a metallaphotoredox-based cross-coupling platform in which free alcohols are activated *in situ* by N-heterocyclic carbene salts for carbon–carbon bond formation with aryl halide coupling partners. This method is mild, robust, selective and most importantly, capable of accommodating a wide range of primary, secondary and tertiary alcohols as well as pharmaceutically relevant aryl and heteroaryl bromides and chlorides. The power of the transformation has been demonstrated in a number of complex settings, including the late-stage functionalization of Taxol and a modular synthesis of Januvia, an antidiabetic medication. This technology represents a general strategy for the merger of *in situ* alcohol activation with transition metal catalysis.

Access options

Subscribe to Journal

Get full journal access for 1 year

\$199.00

only \$3.90 per issue

[Subscribe](#)

All prices are NET prices.

VAT will be added later in the checkout.

Tax calculation will be finalised during checkout.

Rent or Buy article

Get time limited or full article access on ReadCube.

from \$8.99

[Rent or Buy](#)

All prices are NET prices.

Additional access options:

- [Log in](#)
- [Access through your institution](#)
- [Learn about institutional subscriptions](#)

Fig. 1: Direct deoxygenative arylation of alcohols.

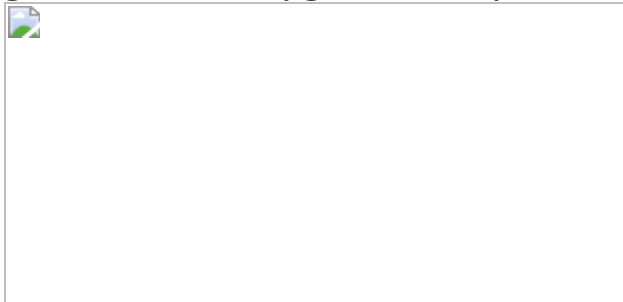


Fig. 2: Proposed mechanism and nitrogen-heterocyclic carbene evaluation for deoxygenative arylation.

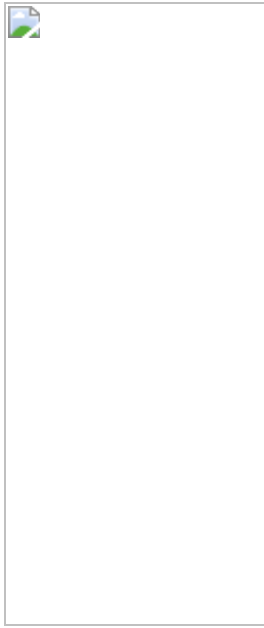


Fig. 3: Alcohol scope for deoxygenative arylation.

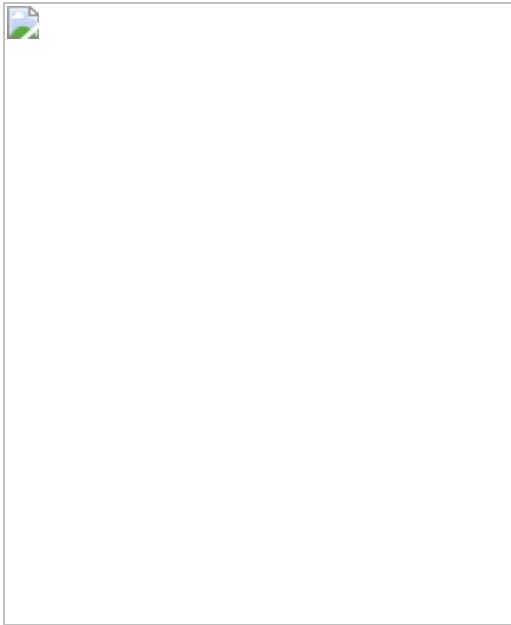
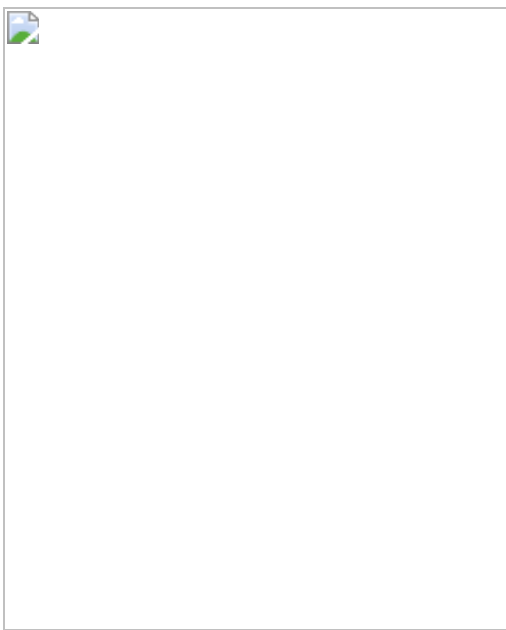


Fig. 4: Chirality transfer from chiral diol and late-stage drug molecule functionalization.



Data availability

The data supporting the findings of this study are available within the paper and its [Supplementary Information](#).

References

1. 1.

Corbet, J.-P. & Mignani, G. Selected patented cross-coupling reaction technologies. *Chem. Rev.* **106**, 2651–2710 (2006).

2. 2.

Choi, J. & Fu, G. C. Transition metal-catalyzed alkyl-alkyl bond formation: another dimension in cross-coupling chemistry. *Science* **356**, eaaf7230 (2017).

3. 3.

Herrmann, J. M. & König, B. Reductive deoxygenation of alcohols: catalytic methods beyond Barton–McCombie deoxygenation. *Eur. J. Org. Chem.* **2013**, 7017–7027 (2013).

4. 4.

Blakemore, D. C. et al. Organic synthesis provides opportunities to transform drug discovery. *Nat. Chem.* **10**, 383–394 (2018).

5. 5.

Ruiz-Castillo, P. & Buchwald, S. L. Applications of palladium-catalyzed C–N cross-coupling reactions. *Chem. Rev.* **116**, 12564–12649 (2016).

6. 6.

Walters, W. P., Green, J., Weiss, J. R. & Murcko, M. A. What do medicinal chemists actually make? a 50-year retrospective. *J. Med. Chem.* **54**, 6405–6416 (2011).

7. 7.

Zuo, Z. et al. Merging photoredox with nickel catalysis: coupling of α -carboxyl sp^3 -carbons with aryl halides. *Science* **345**, 437–440 (2014).

8. 8.

Everson, D. A., Jones, B. A. & Weix, D. J. Replacing conventional carbon nucleophiles with electrophiles: nickel-catalyzed reductive alkylation of aryl bromides and chlorides. *J. Am. Chem. Soc.* **134**, 6146–6159 (2012).

9. 9.

Sakai, H. A., Liu, W., Le, C. & MacMillan, D. W. C. Cross-electrophile coupling of unactivated alkyl chlorides. *J. Am. Chem. Soc.* **142**, 11691–11697 (2020).

10. 10.

Suga, T. & Ukaji, Y. Nickel-catalyzed cross-electrophile coupling between benzyl alcohols and aryl halides assisted by titanium co-reductant. *Org. Lett.* **20**, 7846–7850 (2018).

11. 11.

Ertl, P. & Schuhmann, T. A systematic cheminformatics analysis of functional groups occurring in natural products. *J. Nat. Prod.* **82**, 1258–1263 (2019).

12. 12.

Jia, X.-G., Guo, P., Duan, J. & Shu, X.-Z. Dual nickel and Lewis acid catalysis for cross-electrophile coupling: the allylation of aryl halides with allylic alcohols. *Chem. Sci.* **9**, 640–645 (2018).

13. 13.

Guo, P. et al. Dynamic kinetic cross-electrophile arylation of benzyl alcohols by nickel catalysis. *J. Am. Chem. Soc.* **143**, 513–523 (2021).

14. 14.

Li, Z. et al. Electrochemically enabled, nickel-catalyzed dehydroxylative cross-coupling of alcohols with aryl halides. *J. Am. Chem. Soc.* **143**, 3536–3543 (2021).

15. 15.

Barton, D. H. R. & McCombie, S. W. A new method for the deoxygenation of secondary alcohols. *J. Chem. Soc. Perkin Trans. 1* **16**, 1574–1585. (1975).

16. 16.

Zhang, L. & Koreeda, M. Radical deoxygenation of hydroxyl groups via phosphites. *J. Am. Chem. Soc.* **126**, 13190–13191 (2004).

17. 17.

Vara, B. A., Patel, N. R. & Molander, G. A. *O*-benzyl xanthate esters under Ni/photoredox dual catalysis: selective radical generation and Csp³ –Csp² cross-coupling. *ACS Catal.* **7**, 3955–3959 (2017).

18. 18.

Yang, C.-T. et al. Copper-catalyzed cross-coupling of nonactivated secondary alkyl halides and tosylates with secondary alkyl grignard reagents. *J. Am. Chem. Soc.* **134**, 11124–11127 (2012).

19. 19.

Zhang, X. & MacMillan, D. W. C. Alcohols as latent coupling fragments for metallaphotoredox catalysis: sp³ –sp² cross-coupling of oxalates with aryl halides. *J. Am. Chem. Soc.* **138**, 13862–13865 (2016).

20. 20.

Ye, Y., Chen, H., Sessler, J. L. & Gong, H. Zn-mediated fragmentation of tertiary alkyl oxalates enabling formation of alkylated and arylated

quaternary carbon centers. *J. Am. Chem. Soc.* **141**, 820–824 (2019).

21. 21.

Coulembier, O. et al. Alcohol adducts of *N*-heterocyclic carbenes: latent catalysts for the thermally-controlled living polymerization of cyclic esters. *Macromolecules* **39**, 5617–5628 (2006).

22. 22.

McNally, A., Prier, C. K. & MacMillan, D. W. C. Discovery of an α -amino C–H arylation reaction using the strategy of accelerated serendipity. *Science* **334**, 1114–1117 (2011).

23. 23.

Joe, C. L. & Doyle, A. G. Direct acylation of $\text{C}(\text{sp}^3)$ –H bonds enabled by nickel and photoredox catalysis. *Angew. Chem. Int. Ed.* **55**, 4040–4043 (2016).

24. 24.

Slinker, J. D. et al. Efficient yellow electroluminescence from a single layer of a cyclometalated iridium complex. *J. Am. Chem. Soc.* **126**, 2763–2767 (2004).

25. 25.

Dinnocenzo, J. P. & Banach, T. E. Deprotonation of tertiary amine cation radicals. A direct experimental approach. *J. Am. Chem. Soc.* **111**, 8646–8653 (1989).

26. 26.

Kochi, J. K. Chemistry of alkoxy radicals: cleavage reactions. *J. Am. Chem. Soc.* **84**, 1193–1197 (1962).

27. 27.

Zhao, L., Zhang, C., Zhuo, L., Zhang, Y. & Ying, J. Y. Imidazolium salts: a mild reducing and antioxidative reagent. *J. Am. Chem. Soc.* **130**, 12586–12587 (2008).

28. 28.

Trnka, T. M. et al. Synthesis and activity of ruthenium alkylidene complexes coordinated with phosphine and N-heterocyclic carbene ligands. *J. Am. Chem. Soc.* **125**, 2546–2558 (2003).

29. 29.

Bellemin-Laponnaz, S. Synthesis of *N,O*-heterocyclic carbene and coordination to rhodium(I) and copper(I). *Polyhedron* **29**, 30–33 (2010).

30. 30.

Sladojevich, F., Arlow, S. I., Tang, P. & Ritter, T. Late-stage deoxyfluorination of alcohols with PhenoFluor. *J. Am. Chem. Soc.* **135**, 2470–2473 (2013).

31. 31.

Kato, T., Matsuoka, S. & Suzuki, M. N-heterocyclic carbene-mediated redox condensation of alcohols. *Chem. Commun.* **52**, 8569–8572 (2016).

32. 32.

Gusev, D. G. Electronic and steric parameters of 76 N-heterocyclic carbenes in Ni(CO)₃(NHC). *Organometallics* **28**, 6458–6461 (2009).

33. 33.

Yuan, M., Song, Z., Badir, S. O., Molander, G. A. & Gutierrez, O. On the nature of C(sp³)–C(sp²) bond formation in nickel-catalyzed tertiary radical cross-couplings: a case study of Ni/photoredox catalytic cross-

coupling of alkyl radicals and aryl halides. *J. Am. Chem. Soc.* **142**, 7225–7234 (2020).

34. 34.

Gonnard, L., Guérinot, A. & Cossy, J. Cobalt-catalyzed cross-coupling of 3- and 4-iodopiperidines with grignard reagents. *Chem. Eur. J.* **21**, 12797–12803 (2015).

35. 35.

Kutchukian, P. S. et al. Chemistry informer libraries: a chemoinformatics enabled approach to evaluate and advance synthetic methods. *Chem. Sci.* **7**, 2604–2613 (2016).

36. 36.

Zhang, R. et al. Profiling and application of photoredox C(sp³)–C(sp²) cross-coupling in medicinal chemistry. *ACS Med. Chem. Lett.* **9**, 773–777 (2018).

Acknowledgements

Research reported in this publication was supported by the NIH National Institute of General Medical Sciences (R35 GM134897-02) and gifts from Merck, Bristol-Myers Squibb, Eli Lilly, and Janssen Research and Development LLC. The authors thank C. Liu and R. Lambert for assistance in preparing this manuscript.

Author information

Affiliations

1. Merck Center for Catalysis at Princeton University, Princeton, NJ, USA

Zhe Dong & David W. C. MacMillan

Contributions

Z.D. performed and analysed the experiments. Z.D. and D.W.C.M. designed the experiments. Z.D. and D.W.C.M. prepared this manuscript.

Corresponding author

Correspondence to David W. C. MacMillan.

Ethics declarations

Competing interests

The authors declare no competing interests.

Additional information

Peer review information *Nature* thanks the anonymous reviewer(s) for their contribution to the peer review of this work.

Publisher's note Springer Nature remains neutral with regard to jurisdictional claims in published maps and institutional affiliations.

Extended data figures and tables

[Extended Data Fig. 1 Aryl halide scope for deoxygenative arylation.](#)

Both (hetero)aryl bromides and chlorides can be utilized under same reaction conditions. All yields are isolated. Experiments typically run with 1.0 equivalent of aryl halide, 1.7 equivalent of alcohol and 1.6 equivalent of NHC on 0.5 mmol scale. *See [Supplementary Information](#) for experimental details.

Supplementary information

Supplementary Information

Supplementary Figs. 1–15, Tables 1–8and supplementary text.

Rights and permissions

Reprints and Permissions

About this article

Cite this article

Dong, Z., MacMillan, D.W.C. Metallaphotoredox-enabled deoxygenative arylation of alcohols. *Nature* **598**, 451–456 (2021).
<https://doi.org/10.1038/s41586-021-03920-6>

- Received: 17 May 2021
- Accepted: 17 August 2021
- Published: 31 August 2021
- Issue Date: 21 October 2021
- DOI: <https://doi.org/10.1038/s41586-021-03920-6>

Share this article

Anyone you share the following link with will be able to read this content:

[Get shareable link](#)

Sorry, a shareable link is not currently available for this article.

[Copy to clipboard](#)

Provided by the Springer Nature SharedIt content-sharing initiative

This article was downloaded by **calibre** from <https://www.nature.com/articles/s41586-021-03920-6>

| [Section menu](#) | [Main menu](#) |

- Article
- [Published: 20 October 2021](#)

Pliocene decoupling of equatorial Pacific temperature and pH gradients

- [Madison G. Shankle](#) ORCID: [orcid.org/0000-0002-8052-9136^{1,2}](https://orcid.org/0000-0002-8052-9136),
- [Natalie J. Burls](#) ORCID: [orcid.org/0000-0002-6950-3808³](https://orcid.org/0000-0002-6950-3808),
- [Alexey V. Fedorov](#) ORCID: [orcid.org/0000-0001-5428-1117^{1,4}](https://orcid.org/0000-0001-5428-1117),
- [Matthew D. Thomas^{1,5}](#),
- [Wei Liu⁶](#),
- [Donald E. Penman^{1,7}](#),
- [Heather L. Ford](#) ORCID: [orcid.org/0000-0002-8081-7023⁸](https://orcid.org/0000-0002-8081-7023),
- [Peter H. Jacobs](#) ORCID: [orcid.org/0000-0002-6951-7126^{9,10}](https://orcid.org/0000-0002-6951-7126),
- [Noah J. Planavsky](#) ORCID: [orcid.org/0000-0001-5849-8508¹](https://orcid.org/0000-0001-5849-8508) &
- [Pincelli M. Hull](#) ORCID: [orcid.org/0000-0001-8607-4817¹](https://orcid.org/0000-0001-8607-4817)

Nature volume **598**, pages 457–461 (2021)

- 779 Accesses
- 63 Altmetric
- [Metrics details](#)

Subjects

- [Palaeoceanography](#)
- [Palaeoclimate](#)
- [Physical oceanography](#)

Abstract

Ocean dynamics in the equatorial Pacific drive tropical climate patterns that affect marine and terrestrial ecosystems worldwide. How this region will respond to global warming has profound implications for global climate, economic stability and ecosystem health. As a result, numerous studies have investigated equatorial Pacific dynamics during the Pliocene (5.3–2.6 million years ago) and late Miocene (around 6 million years ago) as an analogue for the future behaviour of the region under global warming^{1,2,3,4,5,6,7,8,9,10,11,12}. Palaeoceanographic records from this time present an apparent paradox with proxy evidence of a reduced east–west sea surface temperature gradient along the equatorial Pacific^{1,3,7,8}—indicative of reduced wind-driven upwelling—conflicting with evidence of enhanced biological productivity in the east Pacific^{13,14,15} that typically results from stronger upwelling. Here we reconcile these observations by providing new evidence for a radically different-from-modern circulation regime in the early Pliocene/late Miocene¹⁶ that results in older, more acidic and more nutrient-rich water reaching the equatorial Pacific. These results provide a mechanism for enhanced productivity in the early Pliocene/late Miocene east Pacific even in the presence of weaker wind-driven upwelling. Our findings shed new light on equatorial Pacific dynamics and help to constrain the potential changes they will undergo in the near future, given that the Earth is expected to reach Pliocene-like levels of warming in the next century.

Access options

Subscribe to Journal

Get full journal access for 1 year

\$199.00

only \$3.90 per issue

[Subscribe](#)

All prices are NET prices.
VAT will be added later in the checkout.
Tax calculation will be finalised during checkout.

Rent or Buy article

Get time limited or full article access on ReadCube.

from \$8.99

[Rent or Buy](#)

All prices are NET prices.

Additional access options:

- [Log in](#)
- [Access through your institution](#)
- [Learn about institutional subscriptions](#)

Fig. 1: Different paradigms of Pliocene climate (degree of reduction in the zonal sea surface temperature gradient) predict different changes in zonal pH gradient.

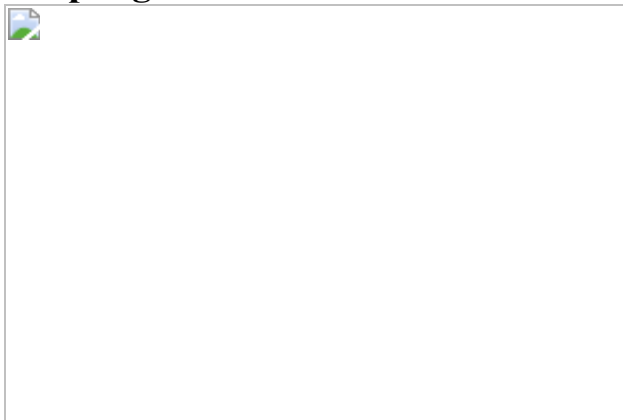


Fig. 2: $\delta^{11}\text{B}$ -reconstructed pH shows an enhanced zonal pH gradient relative to modern at around 3 Ma and around 6 Ma.



Fig. 3: Model output shows similar results in pH and pH-anomaly relative to modern.

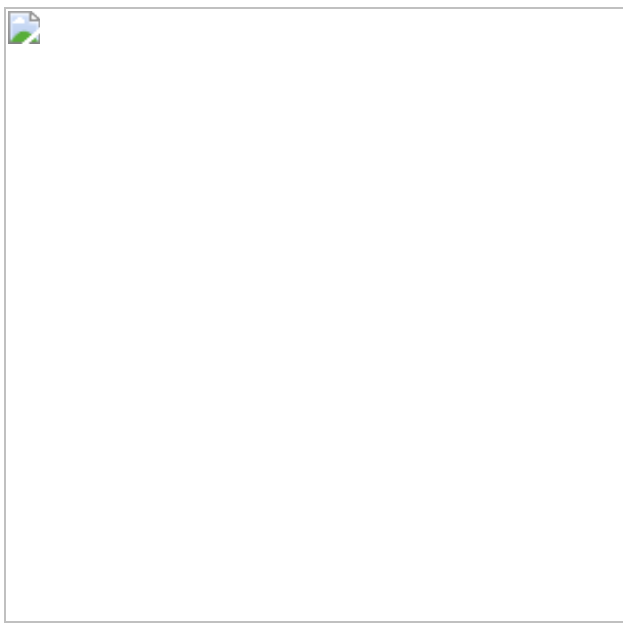
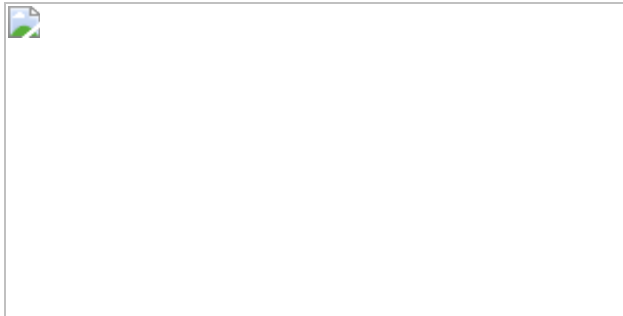


Fig. 4: Model output (pH, ventilation age and water mass transport) evinces a Pacific meridional overturning circulation in which water parcels spend a prolonged time at depth.



Data availability

The proxy data and model output produced in this study are available as .xslm and .nc files in NOAA's paleoclimate data repository (<https://www.ncdc.noaa.gov/paleo/study/33252>) (<https://doi.org/10.25921/A-MPV-J413>). [Source data](#) are provided with this paper.

Code availability

The code used in this paper to produce pH from $d^{11}B$ (and to produce all the proxy-related figures) is publicly available as Matlab scripts on GitHub (https://github.com/Maddie-Sh/ShankleEtAl2021_Pliocene-pH). The CESM 1.2.2.1 code is available from https://svn-ccsm-models.cgd.ucar.edu/cesm1/release_tags/cesm1_2_2_1. The Python code used to create select model figures is available at <https://github.com/nburlis/ShankleEtAl2021>. [Source data](#) are provided with this paper.

References

1. 1.

Wara, M. W., Ravelo, A. C. & Delaney, M. L. Permanent El Niño-like conditions during the Pliocene warm period. *Science* **309**, 758–761 (2005).

2. 2.

Fedorov, A. V. et al. The Pliocene paradox (mechanisms for a permanent El Niño). *Science* **312**, 1485–1490 (2006).

3. 3.

Zhang, Y. G., Pagani, M. & Liu, Z. A 12-million-year temperature history of the tropical Pacific Ocean. *Science* **344**, 84–88 (2014).

4. 4.

Fedorov, A. V., Burls, N. J., Lawrence, K. T. & Peterson, L. C. Tightly linked zonal and meridional sea surface temperature gradients over the past five million years. *Nat. Geosci.* **8**, 975–980 (2015).

5. 5.

Ford, H. L., Ravelo, A. C., Dekens, P. S., LaRiviere, J. P. & Wara, M. W. The evolution of the equatorial thermocline and the early Pliocene El Padre mean state. *Geophys. Res. Lett.* **42**, 4878–4887 (2015).

6. 6.

Tierney, J. E., Haywood, A. M., Feng, R., Bhattacharya, T. & Otto-Bliesner, B. L. Pliocene warmth consistent with greenhouse gas forcing. *Geophys. Res. Lett.* **46**, 9136–9144 (2019).

7. 7.

Lawrence, K. T., Liu, Z. & Herbert, T. D. Evolution of the eastern tropical Pacific through Plio-Pleistocene glaciation. *Science* **312**, 79–83 (2006).

8. 8.

Dekens, P. S., Ravelo, A. C. & McCarthy, M. D. Warm upwelling regions in the Pliocene warm period. *Paleoceanography* **22**, PA3211 (2007).

9. 9.

Ford, H. L., Ravelo, A. C. & Hovan, S. A deep Eastern Equatorial Pacific thermocline during the early Pliocene warm period. *Earth Planet. Sci. Lett.* **355**, 152–161 (2012).

10. 10.

Fedorov, A. V. et al. Patterns and mechanisms of early Pliocene warmth. *Nature* **496**, 43–49 (2013).

11. 11.

O'Brien, C. L. et al. High sea surface temperatures in tropical warm pools during the Pliocene. *Nat. Geosci.* **7**, 606–611 (2014).

12. 12.

Ravelo, A. C., Lawrence, K. T., Fedorov, A. & Ford, H. L. Comment on “A 12-million-year temperature history of the tropical Pacific Ocean”. *Science* **346**, 1467 (2014).

13. 13.

Lyle, M. Neogene carbonate burial in the Pacific Ocean. *Paleoceanography* **18**, 1059 (2003).

14. 14.

Lyle, M. & Baldauf, J. Biogenic sediment regimes in the Neogene equatorial Pacific, IODP Site U1338: burial, production, and diatom community. *Palaeogeogr. Palaeoclimatol. Palaeoecol.* **433**, 106–128 (2015).

15. 15.

Ma, Z., Ravelo, A. C., Liu, Z., Zhou, L. & Paytan, A. Export production fluctuations in the eastern equatorial Pacific during the Pliocene-Pleistocene: reconstruction using barite accumulation rates. *Paleoceanography* **30**, 1455–1469 (2015).

16. 16.

Burls, N. J. et al. Active Pacific meridional overturning circulation (PMOC) during the warm Pliocene. *Sci. Adv.* **3**, e1700156 (2017).

17. 17.

Bjerknes, J. Atmospheric teleconnections from the equatorial Pacific. *Mon. Wea. Rev.* **97**, 163–172 (1969).

18. 18.

Philander, S. G. El Niño, La Niña, and the southern oscillation. *Int. Geophys. Ser.* **46**, 289 (1989).

19. 19.

Iizumi, T. et al. Impacts of El Niño SOUTHERN OSCILLATION on the global yields of major crops. *Nat. Commun.* **5**, 3712 (2014).

20. 20.

Anderson, W., Seager, R., Baethgen, W. & Cane, M. Crop production variability in North and South America forced by life-cycles of the El Niño Southern Oscillation. *Agric. For. Meteorol.* **239**, 151–165 (2017).

21. 21.

Heede, U. K., Fedorov, A. V. & Burls, N. J. Time scales and mechanisms for the tropical Pacific response to global warming: a tug of war between the ocean thermostat and weaker Walker. *J. Clim.* **33**, 6101–6118 (2020).

22. 22.

Foster, G. L., Royer, D. L. & Lunt, D. J. Future climate forcing potentially without precedent in the last 420 million years. *Nat. Commun.* **8**, 14845 (2017).

23. 23.

Haywood, A. M. et al. Large-scale features of Pliocene climate: results from the Pliocene Model Intercomparison Project. *Clim. Past* **9**, 191–209 (2013).

24. 24.

Haywood, A. M., Dowsett, H. J. & Dolan, A. M. Integrating geological archives and climate models for the mid-Pliocene warm period. *Nat. Commun.* **7**, 10646 (2016).

25. 25.

Prescott, C. L. et al. Assessing orbitally-forced interglacial climate variability during the mid-Pliocene warm period. *Earth Planet. Sci. Lett.* **400**, 261–271 (2014).

26. 26.

Haywood, A. M. et al. The Pliocene Model Intercomparison Project Phase 2: large-scale climate features and climate sensitivity. *Clim. Past* **16**, 2095–2123 (2020).

27. 27.

Brierley, C. M. & Fedorov, A. V. Relative importance of meridional and zonal sea surface temperature gradients for the onset of the ice ages and Pliocene-Pleistocene climate evolution. *Paleoceanography* **25**, PA2214 (2010).

28. 28.

McClymont, E. L. et al. Lessons from a high-CO₂ world: an ocean view from ∼3 million years ago. *Clim. Past* **16**, 1599–1615 (2020).

29. 29.

Burls, N. J. et al. Simulating Miocene warmth: insights from an opportunistic multi-model ensemble (MioMIP1). *Paleoceanogr. Paleoclimatology* **36**, e2020PA004054 (2021).

30. 30.

Ravelo, A. C., Dekens, P. S. & McCarthy, M. Evidence for El Niño-like conditions during the Pliocene. *GSA Today* **16**, 4–11 (2006).

31. 31.

Liu, J. et al. Eastern equatorial Pacific cold tongue evolution since the late Miocene linked to extratropical climate. *Sci. Adv.* **5**, eaau6060 (2019).

32. 32.

Wycech, J. B., Gill, E., Rajagopalan, B., Marchitto, T. M. Jr & Molnar, P. H. Multiproxy reduced-dimension reconstruction of Pliocene equatorial Pacific sea surface temperatures. *Paleoceanogr. Paleoclimatology* **35**, e2019PA003685 (2020).

33. 33.

White, S. M. & Ravelo, A. C. The benthic B/Ca record at Site 806: new constraints on the temperature of the West Pacific Warm Pool and the “El Padre” state in the Pliocene. *Paleoceanogr. Paleoclimatology* **35**, e2019PA003812 (2020).

34. 34.

Rae, J. W. B., Foster, G. L., Schmidt, D. N. & Elliott, T. Boron isotopes and B/Ca in benthic foraminifera: proxies for the deep ocean carbonate system. *Earth Planet. Sci. Lett.* **302**, 403–413 (2011).

35. 35.

Rae, J. W. B. in *Boron Isotopes* (eds. Marschall, H. & Foster, G.) 107–143 (Springer, 2018).

36. 36.

Henehan, M. J. et al. A new boron isotope-pH calibration for *Orbulina universa*, with implications for understanding and accounting for ‘vital effects’. *Earth Planet. Sci. Lett.* **454**, 282–292 (2016).

37. 37.

Takahashi, T. et al. Climatological mean and decadal change in surface ocean pCO₂, and net sea–air CO₂ flux over the global oceans. *Deep Sea Res. Part II Top. Stud. Oceanogr.* **56**, 554–577 (2009).

38. 38.

Burls, N. J. & Fedorov, A. V. Simulating Pliocene warmth and a permanent El Niño-like state: the role of cloud albedo. *Paleoceanography* **29**, 893–910 (2014).

39. 39.

Burls, N. J. & Fedorov, A. V. What controls the mean east–west sea surface temperature gradient in the equatorial Pacific: the role of cloud albedo. *J. Clim.* **27**, 2757–2778 (2014).

40. 40.

Dowsett, H. J. et al. Sea surface temperature of the mid-Piacenzian ocean: a data-model comparison. *Sci. Rep.* **3**, 2013 (2013).

41. 41.

Brierley, C., Burls, N., Ravelo, C. & Fedorov, A. Pliocene warmth and gradients. *Nat. Geosci.* **8**, 419–420 (2015).

42. 42.

Sautter, L. R. & Thunell, R. C. Planktonic foraminiferal response to upwelling and seasonal hydrographic conditions; sediment trap results

from San Pedro Basin, Southern California Bight. *J. Foraminifer. Res.* **21**, 347–363 (1991).

43. 43.

Rebotim, A. et al. Factors controlling the depth habitat of planktonic foraminifera in the subtropical eastern North Atlantic. *Biogeosciences* **14**, 827–859 (2017).

44. 44.

Buckley, M. W. & Marshall, J. Observations, inferences, and mechanisms of the Atlantic Meridional Overturning Circulation: a review. *Rev. Geophys.* **54**, 5–63 (2016).

45. 45.

Thomas, M. D. & Fedorov, A. V. The eastern subtropical Pacific origin of the equatorial cold bias in climate models: a Lagrangian perspective. *J. Clim.* **30**, 5885–5900 (2017).

46. 46.

Sarmiento, J. L., Hughes, T. M. C., Stouffer, R. J. & Manabe, S. Simulated response of the ocean carbon cycle to anthropogenic climate warming. *Nature* **393**, 245–249 (1998).

47. 47.

Fedorov, A. V., Brierley, C. M. & Emanuel, K. Tropical cyclones and permanent El Niño in the early Pliocene epoch. *Nature* **463**, 1066–1070 (2010).

48. 48.

Christensen, V., De la Puente, S., Sueiro, J. C., Steenbeek, J. & Majluf, P. Valuing seafood: the Peruvian fisheries sector. *Mar. Policy* **44**, 302–311 (2014).

49. 49.

Gutierrez, D., Akester, M. & Naranjo, L. Productivity and sustainable management of the Humboldt Current large marine ecosystem under climate change. *Environ. Dev.* **17**, 126–144 (2016).

50. 50.

Clark, P. U. et al. Consequences of twenty-first-century policy for multi-millennial climate and sea-level change. *Nat. Clim. Chang.* **6**, 360–369 (2016).

51. 51.

Martínez-Botí, M. A. et al. Plio-Pleistocene climate sensitivity evaluated using high-resolution CO₂ records. *Nature* **518**, 49–54 (2015).

52. 52.

Mayer, L. A. et al. *Proceedings of the Ocean Drilling Program: Initial Reports* Vol. 138 (Ocean Drilling Program, 1992).

53. 53.

Kroenke, L. W. et al. *Proceedings of the Ocean Drilling Program: Initial Reports* Vol. 130 (Ocean Drilling Program, 1991).

54. 54.

Edgar, K. M., Anagnostou, E., Pearson, P. N. & Foster, G. L. Assessing the impact of diagenesis on δ¹¹B, δ¹³C, δ¹⁸O, Sr/Ca and B/Ca values in fossil planktic foraminiferal calcite. *Geochim. Cosmochim. Acta* **166**, 189–209 (2015).

55. 55.

Foster, G. L., Lear, C. H. & Rae, J. W. B. The evolution of pCO₂, ice volume and climate during the middle Miocene. *Earth Planet. Sci. Lett.* **341**, 243–254 (2012).

56. 56.

Penman, D. E., Höönsch, B., Zeebe, R. E., Thomas, E. & Zachos, J. C. Rapid and sustained surface ocean acidification during the Paleocene-Eocene thermal maximum. *Paleoceanography* **29**, 357–369 (2014).

57. 57.

Höönsch, B. & Hemming, N. G. Ground-truthing the boron isotope-paleo-pH proxy in planktonic foraminifera shells: partial dissolution and shell size effects. *Paleoceanography* **19**, PA4010 (2004).

58. 58.

Chaisson, W. P. & Ravelo, A. C. Pliocene development of the east-west hydrographic gradient in the equatorial Pacific. *Paleoceanography* **15**, 497–505 (2000).

59. 59.

Karnauskas, K. B., Mittelstaedt, E. & Murtugudde, R. Paleoceanography of the eastern equatorial Pacific over the past 4 million years and the geologic origins of modern Galapagos upwelling. *Earth Planet. Sci. Lett.* **460**, 22–28 (2017).

60. 60.

Lisiecki, L. E. & Raymo, M. E. A Pliocene-Pleistocene stack of 57 globally distributed benthic δ¹⁸O records. *Paleoceanography* **20**, (2005).

61. 61.

Zhang, Y. G., Pagani, M., Henderiks, J. & Ren, H. A long history of equatorial deep-water upwelling in the Pacific Ocean. *Earth Planet. Sci. Lett.* **467**, 1–9 (2017).

62. 62.

Ogg, J. G., Gradstein, F. M. & Smith, A. G. (eds.) *A Geologic Time Scale 2004* (Cambridge Univ. Press, 2004).

63. 63.

Spezzaferri, S. et al. Fossil and genetic evidence for the polyphyletic nature of the planktonic foraminifera "*Globigerinoides*", and description of the new genus *Trilobatus*. *PLoS ONE* **10**, e0128108 (2015).

64. 64.

Martínez-Botí, M. A. et al. Boron isotope evidence for oceanic carbon dioxide leakage during the last deglaciation. *Nature* **518**, 219–222 (2015).

65. 65.

Key, R. M. et al. A global ocean carbon climatology: results from Global Data Analysis Project (GLODAP). *Global Biogeochem. Cycles* **18**, GB4031 (2004).

66. 66.

Olsen, A. et al. GLODAPv2. 2020—the second update of GLODAPv2. *Earth Syst. Sci. Data* **12**, 3653–3678 (2020).

67. 67.

Suzuki, T. et al. *PACIFICA Data Synthesis Project* (Carbon Dioxide Information Analysis Center, 2013).

68. 68.

Schlitzer, R. Electronic atlas of WOCE hydrographic and tracer data now available. *Eos Trans.* **81**, 45 (2000).

69. 69.

Schlitzer, R. Ocean Data View. (2018). Available at: <https://www.odv.awi.de>.

70. 70.

Dickson, A. G., Sabine, C. L. & Christian, J. R. *Guide to Best Practices for Ocean CO₂ Measurements* (North Pacific Marine Science Organization, 2007).

71. 71.

Lewis, E. R. & Wallace, D. W. R. *Program Developed for CO₂ System Calculations* (Environmental System Science Data Infrastructure for a Virtual Ecosystem, 1998).

72. 72.

Huang, B. et al. Extended reconstructed sea surface temperature, version 5 (ERSSTv5): upgrades, validations, and intercomparisons. *J. Clim.* **30**, 8179–8205 (2017).

73. 73.

NOAA Climate Prediction Center Internet Team. Cold and Warm Episodes by Season. (2021). Available at: https://origin.cpc.ncep.noaa.gov/products/analysis_monitoring/ensostuff/ONI_v5.php. (Accessed: 22 March 2021)

74. 74.

Zeebe, R. E. & Tyrrell, T. History of carbonate ion concentration over the last 100 million years II: revised calculations and new data. *Geochim. Cosmochim. Acta* **257**, 373–392 (2019).

75. 75.

Foster, G. L. Seawater pH, pCO₂ and [CO^{2−}₃] variations in the Caribbean Sea over the last 130 kyr: a boron isotope and B/Ca study of planktic foraminifera. *Earth Planet. Sci. Lett.* **271**, 254–266 (2008).

76. 76.

Kiss, E. Ion-exchange separation and spectrophotometric determination of boron in geological materials. *Anal. Chim. Acta* **211**, 243–256 (1988).

77. 77.

Okai, T., Suzuki, A., Kawahata, H., Terashima, S. & Imai, N. Preparation of a new Geological Survey of Japan geochemical reference material: Coral JCp-1. *Geostand. Newslet.* **26**, 95–99 (2002).

78. 78.

Al-Ammar, A. S., Gupta, R. K. & Barnes, R. M. Elimination of boron memory effect in inductively coupled plasma-mass spectrometry by ammonia gas injection into the spray chamber during analysis. *Spectrochim. Acta Part B At. Spectrosc.* **55**, 629–635 (2000).

79. 79.

Berner, E. K. & Berner, R. A. *Global Environment: Water, Air, and Geochemical Cycles* (Prentice-Hall, 1996).

80. 80.

Broecker, W. S. & Peng, T. S. *Tracers in the Sea* (Eldigio, 1982).

81. 81.

Fantle, M. S. & DePaolo, D. J. Sr isotopes and pore fluid chemistry in carbonate sediment of the Ontong Java Plateau: calcite

recrystallization rates and evidence for a rapid rise in seawater Mg over the last 10 million years. *Geochim. Cosmochim. Acta* **70**, 3883–3904 (2006).

82. 82.

Lowenstein, T. K., Timofeeff, M. N., Brennan, S. T., Hardie, L. A. & Demicco, R. V. Oscillations in Phanerozoic seawater chemistry: evidence from fluid inclusions. *Science* **294**, 1086–1088 (2001).

83. 83.

Horita, J., Zimmermann, H. & Holland, H. D. Chemical evolution of seawater during the Phanerozoic: implications from the record of marine evaporites. *Geochim. Cosmochim. Acta* **66**, 3733–3756 (2002).

84. 84.

Chalk, T. B. et al. Causes of ice age intensification across the mid-Pleistocene transition. *Proc. Natl Acad. Sci. USA* **114**, 13114–13119 (2017).

85. 85.

Greenop, R. et al. Orbital forcing, ice volume, and CO₂ across the Oligocene-Miocene transition. *Paleoceanogr. Paleoclimatology* **34**, 316–328 (2019).

86. 86.

Sosdian, S. M., Babilia, T. L., Greenop, R., Foster, G. L. & Lear, C. H. Ocean carbon storage across the middle Miocene: a new interpretation for the Monterey event. *Nat. Commun.* **11**, 134 (2020).

87. 87.

Evans, D. & Müller, W. Deep time foraminifera Mg/Ca paleothermometry: nonlinear correction for secular change in seawater

Mg/Ca. *Paleoceanography* **27**, PA4205 (2012).

88. 88.

Tierney, J. E., Malevich, S. B., Gray, W., Vetter, L. & Thirumalai, K. Bayesian calibration of the Mg/Ca paleothermometer in planktic foraminifera. *Paleoceanogr. Paleoclimatology* **34**, 2005–2030 (2019).

89. 89.

Anand, P., Elderfield, H. & Conte, M. H. Calibration of Mg/Ca thermometry in planktonic foraminifera from a sediment trap time series. *Paleoceanography* **18**, 1050 (2003).

90. 90.

Gray, W. R. et al. Deglacial upwelling, productivity and CO₂ outgassing in the North Pacific Ocean. *Nat. Geosci.* **11**, 340–344 (2018).

91. 91.

Lemarchand, D., Gaillardet, J., Lewin, E. & Allegre, C. J. Boron isotope systematics in large rivers: implications for the marine boron budget and paleo-pH reconstruction over the Cenozoic. *Chem. Geol.* **190**, 123–140 (2002).

92. 92.

Simon, L., Lécuyer, C., Maréchal, C. & Coltice, N. Modelling the geochemical cycle of boron: implications for the long-term δ¹¹B evolution of seawater and oceanic crust. *Chem. Geol.* **225**, 61–76 (2006).

93. 93.

Greenop, R. et al. A record of Neogene seawater δ¹¹B reconstructed from paired δ¹¹B analyses on benthic and planktic foraminifera. *Clim.*

Past **13**, 149–170 (2017).

94. 94.

Foster, G. L., Pogge von Strandmann, P. A. E. & Rae, J. W. B. Boron and magnesium isotopic composition of seawater. *Geochem. Geophys. Geosystems* **11**, Q08015 (2010).

95. 95.

Shields, C. A. et al. The low-resolution CCSM4. *J. Clim.* **25**, 3993–4014 (2012).

96. 96.

Moore, J. K., Doney, S. C. & Lindsay, K. Upper ocean ecosystem dynamics and iron cycling in a global three-dimensional model. *Global Biogeochem. Cycles* **18**, GB4028 (2004).

97. 97.

Tan, I., Storelvmo, T. & Zelinka, M. D. Observational constraints on mixed-phase clouds imply higher climate sensitivity. *Science* **352**, 224–227 (2016).

98. 98.

Erfani, E. & Burls, N. J. The strength of low-cloud feedbacks and tropical climate: a CESM sensitivity study. *J. Clim.* **32**, 2497–2516 (2019).

99. 99.

Li, R. L., Storelvmo, T., Fedorov, A. V. & Choi, Y.-S. A positive IRIS feedback: insights from climate simulations with temperature-sensitive cloud–rain conversion. *J. Clim.* **32**, 5305–5324 (2019).

100. 100.

Mauritsen, T. & Stevens, B. Missing iris effect as a possible cause of muted hydrological change and high climate sensitivity in models. *Nat. Geosci.* **8**, 346–351 (2015).

101. 101.

Williams, I. N. & Pierrehumbert, R. T. Observational evidence against strongly stabilizing tropical cloud feedbacks. *Geophys. Res. Lett.* **44**, 1503–1510 (2017).

102. 102.

Sahoo, N. & Storelvmo, T. Testing the sensitivity of past climates to the indirect effects of dust. *Geophys. Res. Lett.* **44**, 5807–5817 (2017).

103. 103.

Thomas, M. D., Fedorov, A. V., Burls, N. J. & Liu, W. Oceanic pathways of an active Pacific meridional overturning circulation (PMOC). *Geophys. Res. Lett.* **48**, e2020GL091935 (2021).

104. 104.

Blanke, B. & Raynaud, S. Kinematics of the Pacific equatorial undercurrent: an Eulerian and Lagrangian approach from GCM results. *J. Phys. Oceanogr.* **27**, 1038–1053 (1997).

105. 105.

Gent, P. R. & Mcwilliams, J. C. Isopycnal mixing in ocean circulation models. *J. Phys. Oceanogr.* **20**, 150–155 (1990).

106. 106.

Van Sebille, E. et al. Lagrangian ocean analysis: fundamentals and practices. *Ocean Model.* **121**, 49–75 (2018).

107. 107.

Arakawa, A. & Lamb, V. R. Computational design of the basic dynamical processes of the UCLA general circulation model. *Gen. Circ. Model. Atmos.* **17**, 173–265 (1977).

108. 108.

Marshall, B. J. et al. Morphometric and stable isotopic differentiation of *Orbulina universa* morphotypes from the Cariaco Basin, Venezuela. *Mar. Micropaleontol.* **120**, 46–64 (2015).

109. 109.

Raitzsch, M. et al. Boron isotope-based seasonal paleo-pH reconstruction for the Southeast Atlantic – a multispecies approach using habitat preference of planktonic foraminifera. *Earth Planet. Sci. Lett.* **487**, 138–150 (2018).

110. 110.

Guillermic, M. et al. Seawater pH reconstruction using boron isotopes in multiple planktonic foraminifera species with different depth habitats and their potential to constrain pH and pCO₂ gradients. *Biogeosciences* **17**, 3487–3510 (2020).

111. 111.

Bartoli, G., Hönisch, B. & Zeebe, R. E. Atmospheric CO₂ decline during the Pliocene intensification of Northern Hemisphere glaciations. *Paleoceanography* **26**, PA4213 (2011).

112. 112.

Hönisch, B., Hemming, N. G., Archer, D., Siddall, M. & McManus, J. F. Atmospheric carbon dioxide concentration across the mid-Pleistocene transition. *Science* **324**, 1551–1554 (2009).

113. 113.

Seki, O. et al. Alkenone and boron-based Pliocene pCO₂ records. *Earth Planet. Sci. Lett.* **292**, 201–211 (2010).

114. 114.

Sosdian, S. M. et al. Constraining the evolution of Neogene ocean carbonate chemistry using the boron isotope pH proxy. *Earth Planet. Sci. Lett.* **498**, 362–376 (2018).

115. 115.

de la Vega, E., Chalk, T. B., Wilson, P. A., Bysani, R. P. & Foster, G. L. Atmospheric CO₂ during the mid-Piacenzian warm period and the M2 glaciation. *Sci. Rep.* **10**, 11002 (2020).

116. 116.

Medina-Elizalde, M. & Lea, D. W. The mid-Pleistocene transition in the tropical Pacific. *Science* **310**, 1009–1012 (2005).

117. 117.

Liu, Z. & Herbert, T. D. High-latitude influence on the eastern equatorial Pacific climate in the early Pleistocene epoch. *Nature* **427**, 720–723 (2004).

118. 118.

Regenberg, M. et al. Global dissolution effects on planktonic foraminiferal Mg/Ca ratios controlled by the calcite-saturation state of bottom waters. *Paleoceanography* **29**, 127–142 (2014).

119. 119.

Pagani, M., Liu, Z., LaRiviere, J. & Ravelo, A. C. High Earth-system climate sensitivity determined from Pliocene carbon dioxide concentrations. *Nat. Geosci.* **3**, 27–30 (2010).

120. 120.

Conte, M. H. et al. Global temperature calibration of the alkenone unsaturation index (UK' 37) in surface waters and comparison with surface sediments. *Geochem. Geophys. Geosystems* **7**, Q02005 (2006).

121. 121.

Kim, J.-H. et al. New indices and calibrations derived from the distribution of crenarchaeal isoprenoid tetraether lipids: implications for past sea surface temperature reconstructions. *Geochim. Cosmochim. Acta* **74**, 4639–4654 (2010).

122. 122.

Evans, D., Brierley, C., Raymo, M. E., Erez, J. & Müller, W. Planktic foraminifera shell chemistry response to seawater chemistry: Pliocene–Pleistocene seawater Mg/Ca, temperature and sea level change. *Earth Planet. Sci. Lett.* **438**, 139–148 (2016).

123. 123.

Coggon, R. M., Teagle, D. A. H., Smith-Duque, C. E., Alt, J. C. & Cooper, M. J. Reconstructing past seawater Mg/Ca and Sr/Ca from mid-ocean ridge flank calcium carbonate veins. *Science* **327**, 1114–1117 (2010).

124. 124.

Rausch, S., Böhm, F., Bach, W., Klügel, A. & Eisenhauer, A. Calcium carbonate veins in ocean crust record a threefold increase of seawater Mg/Ca in the past 30 million years. *Earth Planet. Sci. Lett.* **362**, 215–224 (2013).

125. 125.

Dekens, P. S., Lea, D. W., Pak, D. K. & Spero, H. J. Core top calibration of Mg/Ca in tropical foraminifera: refining

paleotemperature estimation. *Geochemistry, Geophys. Geosystems* **3**, 1–29 (2002).

126. 126.

Müller, P. J., Kirst, G., Ruhland, G., Von Storch, I. & Rosell-Melé, A. Calibration of the alkenone paleotemperature index U37K' based on core-tops from the eastern South Atlantic and the global ocean (60° N–60° S). *Geochim. Cosmochim. Acta* **62**, 1757–1772 (1998).

Acknowledgements

The authors acknowledge and appreciate the aid of J. Robbins, W. Strojje, D. Asael and S. Zhang in supervising clean lab chemistry, boron and trace element analysis, and data processing. The authors also appreciate discussion with J. Rae. This work was supported by NSF Award 1602557 and 170251 to P.M.H., NSF Award 1844380 and 2002448 to N.J.B. and Sloan Ocean Fellowships to P.M.H. and N.J.B. Additional funding to A.V.F. was provided by the Guggenheim Fellowship and the ARCHANGE project (ANR-18-MPGA-0001, France). We acknowledge high-performance computing support from Cheyenne (<https://doi.org/10.5065/D6RX99HX>) provided by NCAR’s Computational and Information Systems Laboratory, sponsored by the NSF.

Author information

Affiliations

1. Department of Earth and Planetary Sciences, Yale University, New Haven, CT, USA

Madison G. Shankle, Alexey V. Fedorov, Matthew D. Thomas, Donald E. Penman, Noah J. Planavsky & Pincelli M. Hull

2. School of Earth and Environmental Sciences, University of St Andrews, St Andrews, UK

Madison G. Shankle

3. Department of Atmospheric, Oceanic and Earth Sciences, George Mason University, Fairfax, VA, USA

Natalie J. Burls

4. LOCEAN/IPSL, Sorbonne University, Paris, France

Alexey V. Fedorov

5. University Corporation for Atmospheric Research, Boulder, CO, USA

Matthew D. Thomas

6. Department of Earth and Planetary Sciences, University of California, Riverside, CA, USA

Wei Liu

7. Department of Geosciences, Utah State University, Logan, UT, USA

Donald E. Penman

8. School of Geography, Queen Mary University of London, London, UK

Heather L. Ford

9. Department of Environmental Science and Policy, George Mason University, Fairfax, VA, USA

Peter H. Jacobs

10. NASA Goddard Space Flight Center, Greenbelt, MD, USA

Peter H. Jacobs

Contributions

M.S. contributed: study design, boron and trace element data collection, data analysis, writing, editing. N.B. contributed: study design, model simulations, writing, editing. A.F. contributed: supervision, writing, editing. M.T. contributed: model simulations, Lagrangian analysis, editing. W.L. contributed: Lagrangian analysis. D.P. contributed: data analysis, supervision, editing. HF contributed: BAYMAG SST data processing, editing. P.J. contributed: model simulations. N.P. contributed: study design, supervision, writing, editing. P.H. contributed: study design, supervision, writing, editing.

Corresponding authors

Correspondence to Madison G. Shankle or Pincelli M. Hull.

Ethics declarations

Competing interests

The authors declare no competing interests.

Additional information

Peer review information *Nature* thanks Kelsey Dyez, Julia Tindall and the other, anonymous, reviewer(s) for their contribution to the peer review of this work. Peer reviewer reports are available.

Publisher's note Springer Nature remains neutral with regard to jurisdictional claims in published maps and institutional affiliations.

Extended data figures and tables

[Extended Data Fig. 1 pCO₂ from this study's western equatorial Pacific \(WEP\) pH values match previous δ¹¹B-derived studies.](#)

a, b, $p\text{CO}_2$ estimates (blue markers and shaded areas showing 68% and 95% confidence intervals) from this study's pH data from the WEP, a region in equilibrium with the atmosphere³⁷, assuming a modern-like alkalinity of $2,275 \pm 200 \mu\text{mol kg}^{-1}$ (**a**) versus a modern-like calcite saturation state ($\Omega = 5 \pm 2$ (error bars), $\Omega = 4$ (lower black squares) and $\Omega = 6$ (upper black squares); **b**). Grey data points show $\delta^{11}\text{B}$ -derived estimates of $p\text{CO}_2$ from previously published studies, with shading showing reported confidence intervals^{51,84,111,112,113,114,115}.

[Source data](#)

Extended Data Fig. 2 $\delta^{11}\text{B}$ -reconstructed pH matches model output over 25–75 m depth (top left, bottom); reconstructed pH data from ~3 Ma compared to model output also provided for reference (top right).

a, Modelled pH along the equator (at 55 m depth (red solid and blue dashed lines) and across the 25–75 m depth range (shaded areas)) and $\delta^{11}\text{B}$ -derived pH (circles with 2σ uncertainty from a Monte Carlo simulation, as in Fig. 2b). Markers placed at their approximate longitudes (159.362°E for western ODP Site 806 and 269.182°E for eastern ODP Site 846). The observed (see [Methods](#)) modern gradient in surface pH averaged across the 25–50 m depth range is included for reference (yellow crosses), as well as the range of pH from available modern observations (vertical yellow bars on crosses). **b–g**, Climatological model output of pH and $\delta^{11}\text{B}$ -reconstructed pH with proxy data (circles) from ~3 Ma instead of ~6 Ma (**b, c**) and model output (contours) at distinct depths of 25 m ad 55 m (bracketing *O. universa*'s depth habitat) instead of averaged over the 25–55 m range (**d–g**). In all panels, more acidic waters (or more acidic waters in the past) are shown in yellow-green colours.

[Source data](#)

Extended Data Fig. 3 Extended physical oceanographic model output links pH changes to a Pacific meridional overturning

circulation.

a–d, Timeseries of PMOC strength (blue lines), zonal Pacific pH gradient (ΔpH , black lines), and zonal Pacific SST gradient (ΔSST , red lines) for the model control run (**a, b**) and early Pliocene/late Miocene run (**c, d**). PMOC strength (Max PMOC Streamfunction) is defined as the maximum streamfunction north of 25°N and below 500 m depth in sverdrups (1 Sv = $10^6 \text{ m}^3 \text{ s}^{-1}$). The pH gradient is defined as the pH difference between a western (5°S–5°N, 150–170°E) and eastern Pacific box (5°S–5°N, 260–280°E), taken at 55 m depth. The SST gradient is defined as the SST difference between the same boxes taken at the surface. Note that while the zonal SST gradient equilibrates within ~500 years in the early Pliocene/late Miocene experiment (**d**) and is hardly influenced by the appearance of the PMOC between ~800–1,600 years, the zonal pH gradient increases in phase with the PMOC (**c**). **e–h**, Zonally averaged streamfunction over the Pacific (**e, g**) and Atlantic (**f, h**) basins for the control run (**e, f**) and early Pliocene/late Miocene (**g, h**) runs of the model Positive (green values) denote clockwise circulation, and negative (pink) values denote counterclockwise rotation. Panel **g** is the same as Fig. 4b in the main text.

Source data

Extended Data Fig. 4 This study's ~1 Ma samples fall in different stages of the glacial–interglacial cycles, and $\delta^{11}\text{B}$ -pH core top calibration used in this study recreates observed ambient pH.

a, b, High-resolution sea surface temperature records from western equatorial Pacific site ODP 806 *G. ruber*-derived Mg/Ca data¹¹⁶ (**a**) and eastern equatorial Pacific ODP Site 846 alkenone ($\text{U}^{13}\text{C}_{37}$) data¹¹⁷ (**b**). In both panels the ages of the ~1 Ma samples in this study are overlain as green lines, falling at different points in the glacial–interglacial cycles. **c**, Core top, net tow, and sediment trap $\delta^{11}\text{B}$ data^{36,109,110} converted to pH using the calibration of Henehan et al.³⁶ shows good agreement with reported in situ pH. For the odd point to the far right (dark orange, *x*),

Raitzsch et al¹⁰⁹, calculated in situ pH using an anomalous low value of alkalinity ($\sim 200 \mu\text{mol kg}^{-1}$ lower than alkalinity for the location reported in datasets such as GLODAPv2⁶⁶. Recalculating pH using the same in situ temperature and salinity as Raitzsch et al. but an alkalinity value derived from GLODAPv2 ($2,325 \mu\text{mol kg}^{-1}$) brings the point in agreement with the other data (empty dark orange circle). For the odd point in the lower part of the figure (dark green, *x*), Guillermic and colleagues¹¹⁰, report an unrealistic value for temperature at this site: $\sim 18^\circ\text{C}$ whereas the same site (in the central Indian Ocean) appears to be closer to $\sim 26^\circ\text{C}$ on average according to GLODAPv2. When we re-calculate $\delta^{11}\text{B}$ -pH derived pH using GLODAPv2's 26°C , this brings the point into better agreement with the other data (empty dark green circle). The line of best fit and 2σ shading was calculated with the original odd data points, however, and note that the core top data is still in good agreement with reported in situ pH following this calibration.

[Source data](#)

[**Extended Data Fig. 5 Modern observational pH shows modest zonal pH gradients.**](#)

a–d, Observed pH (or pH calculated from alkalinity and total dissolved inorganic carbon (DIC)) from all cruises within 5° latitude and longitude of our study sites (pale profiles) during neutral-ENSO (**a**), El Niño (**b**) and La Niña conditions (**c**). Thick lines in panels **a–c** show average profiles from all stations on a given cruise. **d**, Average pH-depth profiles from all neutral-ENSO observations. Modern reference values of pH (that is, diamonds on the *y* axis in Fig. 2) were derived from averaging panel **d**'s profiles over 25–50 m depth (approximate depth habitat of *O. universa*). **e–g**, Modern pH derived from cruise-based observations of alkalinity and total DIC. Data compiled from the GLODAPv2 dataset⁶⁶ and plotted using the Ocean Data View software (R. Schlitzer, Ocean Data View, <https://www.osv.awi.de>, 2018). Overlain are this study's sites (black diamonds) as well as the site of the additional 3 Ma pH values⁵¹ included in Fig. 2 (blue square).

[Source data](#)

Extended Data Fig. 6 An enhanced early Pliocene/late Miocene zonal pH gradient is observed under different treatments of the data.

$\delta^{11}\text{B}$ -derived pH from *O. universa* from the east (blue) and west (red) with 2σ uncertainty from a Monte Carlo simulation (empty circles; averages at ~ 1 Ma, ~ 3 Ma and ~ 6 Ma in filled circles) showing: all observations of modern pH used in producing average modern pH reference values (diamonds) given as individual dashes (**a**), the range of pH from using varied SST records in the pH calculation (grey bars) (**b**), pH as calculated using the SST record derived from calibrating this study's Mg/Ca data with the BAYMAG calibration⁸⁸ (**c**), and pH as calculated using dissolution-corrected¹¹⁸ Mg/Ca SSTs from this study (yellow squares) (**d**). In panel **b**, pH ranges cover pH calculated using: TEX86-derived³ SSTs, Mg/Ca-derived SSTs (this study) using a linear correction for Mg/Ca_{SW}, and Mg/Ca-derived SSTs (this study) using a power-law correction⁸⁷ for Mg/Ca_{SW}. Both Mg/Ca-SST calibrations were done using the Mg/Ca_{SW} record of Fantle and DePaolo⁸¹.

Source data

Extended Data Fig. 7 Choice of Mg/Ca calibration or even SST proxy has little effect on pH.

a–c, Mg/Ca-derived SSTs for eastern (blue) and western (red) equatorial Pacific at ~ 1 Ma, ~ 3 Ma and ~ 6 Ma calculated using the *O. universa* calibration of Anand et al.⁸⁹, using a linear (dark squares) and power-law (light squares) relationship between Mg/Ca_{SW} and Mg/Ca_{test}, and using the Bayesian calibration BAYMAG⁸⁸, also corrected for Mg/Ca_{SW}. Error bars denote calibration errors on *O. universa* calibration (squares) and 95% confidence intervals on the BAYMAG-calibrated data (circles). Dark squares are plotted at correct ages; other markers are offset for ease of viewing. **d–f**, $\delta^{11}\text{B}$ -derived pH at the time points calculated using SST records from UK'₃₇^{7,119} (crosses, using the SST calibration of Conte et

al.¹²⁰), TEX_{86}^3 (asterisks, using the SST calibration of Kim et al.¹²⁰), and Mg/Ca data (this study, using the *O. universa* SST calibration of Anand et al.⁸⁹) (assuming a linear (circles) and power-law⁸⁷ (triangles) relationship between Mg/Ca_{SW} and Mg/Ca_{test}). Note that because the western-site U^{K'}₃₇ record¹¹⁹ (red crosses, bottom panels) only extends back to ~5.3 Ma, we assume the maximum temperature calculable by this calibration (~28.5 °C¹²¹) for our western points at ~6 Ma (red crosses, panel **f**), towards which the record of Pagani et al.¹¹⁹ was trending and had nearly approached even by ~5.3 Ma (~28.3–28.4 °C)). All error bars on pH depict uncertainty (2σ) returned from a Monte Carlo simulation.

Source data

Extended Data Fig. 8 Different Mg/Ca_{seawater} records influence sea surface temperatures but have only a modest impact on pH.

a, Various published Mg/Ca_{SW} reconstructions^{11,81,88,122} (lines) plotted alongside proxy-based estimates (orange points) from carbonate veins^{123,124} (orange triangle and diamond) and fluid inclusions^{82,83} (orange circle and square) with error reported in those studies (where there are error bars). **b–d**, Using different Mg/Ca_{SW} records only slightly affect SSTs and even less so pH results. **b**, SSTs calculated from *T. sacculifer* Mg/Ca data¹ using the species-specific calibration of Dekens et al.¹²⁵ and various Mg/Ca_{SW} reconstructions^{11,81,88,122}. **c**, SSTs calculated from *O. universa* Mg/Ca data (this study) using the species-specific calibration of Anand et al.⁸⁹ **a** and various Mg/Ca_{SW} reconstructions^{11,81,88,122}. **d**, $\delta^{11}\text{B}$ -derived pH (this study) using the various SST reconstructions in panel **c**. Note that the Mg/Ca_{SW} records of O'Brien et al.¹¹ and Evans et al.¹²² (blue and purple lines in panel **a**) do not extend back far enough to apply to the ~6 Ma data, ending at ~4.8 Ma and ~5 Ma, respectively.

Source data

Extended Data Fig. 9 Different sea surface temperature proxies record varying reductions in the zonal sea surface temperature gradient, and a dissolution correction and different Mg/Ca_{SW} record is applied to this study's data.

a, b, SST records from the eastern (blue) and western (red) equatorial Pacific. **a**, SST records which evince a collapse of the modern zonal SST gradient include: *T. sacculifer* Mg/Ca data¹ calibrated and corrected for Mg/Ca_{SW} with the Bayesian BAYMAG calibration⁸⁸ with 95% confidence intervals (pale blue and red bands); U^{K'}₃₇ data^{7,119} using a global ocean annual-mean calibration¹²⁶ with its associated 1 s.e. ($\pm 1.1^\circ\text{C}$) (dark blue and red bands, dashed line shows upper saturation limit of the proxy); *T. sacculifer* Mg/Ca data¹ using a species-specific calibration¹²⁵ and corrected for Mg/Ca_{SW} by O'Brien et al.¹¹ (bright blue and red lines, no uncertainty reported); and *O. universa* Mg/Ca data (this study) using a species-specific calibration⁸⁹ and the Mg/Ca_{SW} record of Fantle and DePaolo⁸¹, assuming a linear relationship between Mg/Ca_{SW} and Mg/Ca_{test} (square markers with calibration error in error bars). Note that the three Mg/Ca records in this panel all use different Mg/Ca_{SW} records^{11,81,88}. As the goal of this figure is to depict the range of temperature (and temperature gradient) reconstructions from the literature, we have not standardized them all to the same Mg/Ca_{SW} record. **b**, SST records which evince the modern zonal SST gradient being roughly maintained back into the early Pliocene/late Miocene, derived from TEX₈₆ data³ using the calibration of Kim et al.¹²¹, with its associated calibration error ($\pm 2.5^\circ\text{C}$) (blue and red bands). **c**, SSTs calculated from *O. universa* Mg/Ca data in this study both with (solid squares) and without (empty squares) applying the dissolution correction of Regenberg and colleagues¹¹⁸. **d**, Western equatorial Pacific (WEP) SSTs according to *T. sacculifer* Mg/Ca data¹ (lines) versus *O. universa* (this study, points). Depending on choice of Mg/Ca_{SW} record (light versus darker colours), even *T. sacculifer* may record cooler-than-modern temperatures in the WEP. Average annual modern WEP SST (from GLODAPv2⁶⁶) given in the dashed line.

Source data

Extended Data Table 1 Past literature categorizes *O. universa* as a mixed layer-dwelling species

Supplementary information

Supplementary Information

Supplementary Discussion and additional references.

Peer Review File

Source data

Source Data Fig. 1

Source Data Fig. 2

Source Data Fig. 3

Source Data Fig. 4

Source Data Extended Data Fig. 1

Source Data Extended Data Fig. 2

Source Data Extended Data Fig. 3

Source Data Extended Data Fig. 4

Source Data Extended Data Fig. 5

Source Data Extended Data Fig. 6

[**Source Data Extended Data Fig. 7**](#)

[**Source Data Extended Data Fig. 8**](#)

[**Source Data Extended Data Fig. 9**](#)

Rights and permissions

[Reprints and Permissions](#)

About this article

Cite this article

Shankle, M.G., Burls, N.J., Fedorov, A.V. *et al.* Pliocene decoupling of equatorial Pacific temperature and pH gradients. *Nature* **598**, 457–461 (2021). <https://doi.org/10.1038/s41586-021-03884-7>

- Received: 29 November 2020
- Accepted: 06 August 2021
- Published: 20 October 2021
- Issue Date: 21 October 2021
- DOI: <https://doi.org/10.1038/s41586-021-03884-7>

Share this article

Anyone you share the following link with will be able to read this content:

[Get shareable link](#)

Sorry, a shareable link is not currently available for this article.

[Copy to clipboard](#)

Provided by the Springer Nature SharedIt content-sharing initiative

This article was downloaded by **calibre** from <https://www.nature.com/articles/s41586-021-03884-7>

| [Section menu](#) | [Main menu](#) |

- Article
- [Published: 20 October 2021](#)

Direct radiative effects of airborne microplastics

- [Laura E. Revell](#) [ORCID: orcid.org/0000-0002-8974-7703¹](#),
- [Peter Kuma](#) [ORCID: orcid.org/0000-0002-0910-8646¹](#) nAff³,
- [Eric C. Le Ru](#) [ORCID: orcid.org/0000-0002-3052-9947²](#),
- [Walter R. C. Somerville](#) [ORCID: orcid.org/0000-0002-9965-4324²](#) &
- [Sally Gaw](#) [ORCID: orcid.org/0000-0002-9556-3089¹](#)

Nature volume **598**, pages 462–467 (2021)

- 1387 Accesses
- 355 Altmetric
- [Metrics details](#)

Subjects

- [Atmospheric science](#)
- [Climate and Earth system modelling](#)
- [Environmental monitoring](#)
- [Optical physics](#)

Abstract

Microplastics are now recognized as widespread contaminants in the atmosphere, where, due to their small size and low density, they can be transported with winds around the

Earth^{1,2,3,4,5,6,7,8,9,10,11,12,13,14,15,16,17,18,19,20,21,22,23,24,25}. Atmospheric aerosols, such as mineral dust and other types of airborne particulate matter, influence Earth's climate by absorbing and scattering radiation (direct radiative effects) and their impacts are commonly quantified with the effective radiative forcing (ERF) metric²⁶. However, the radiative effects of airborne microplastics and associated implications for global climate are unknown. Here we present calculations of the optical properties and direct radiative effects of airborne microplastics (excluding aerosol–cloud interactions). The ERF of airborne microplastics is computed to be 0.044 ± 0.399 milliwatts per square metre in the present-day atmosphere assuming a uniform surface concentration of 1 microplastic particle per cubic metre and a vertical distribution up to 10 kilometres altitude. However, there are large uncertainties in the geographical and vertical distribution of microplastics. Assuming that they are confined to the boundary layer, shortwave effects dominate and the microplastic ERF is approximately -0.746 ± 0.553 milliwatts per square metre. Compared with the total ERF due to aerosol–radiation interactions²⁷ (-0.71 to -0.14 watts per square metre), the microplastic ERF is small. However, plastic production has increased rapidly over the past 70 years²⁸; without serious attempts to overhaul plastic production and waste-management practices, the abundance and ERF of airborne microplastics will continue to increase.

Access options

Subscribe to Journal

Get full journal access for 1 year

\$199.00

only \$3.90 per issue

[Subscribe](#)

All prices are NET prices.

VAT will be added later in the checkout.

Tax calculation will be finalised during checkout.

Rent or Buy article

Get time limited or full article access on ReadCube.

from \$8.99

[Rent or Buy](#)

All prices are NET prices.

Additional access options:

- [Log in](#)
- [Access through your institution](#)
- [Learn about institutional subscriptions](#)

Fig. 1: Concentrations of airborne microplastics reported by previous studies.

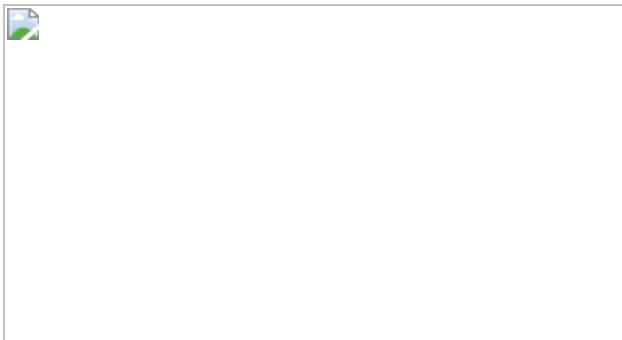
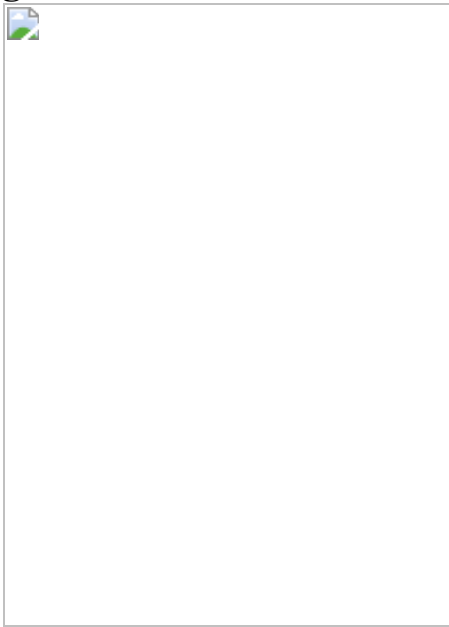


Fig. 2: Optical properties of microplastic fragments and fibres.



Fig. 3: ERF of airborne microplastics.



Data availability

GCM data that support the findings of this study are available at <https://doi.org/10.5281/zenodo.5093843>. Source data are provided with this paper.

Code availability

Custom code generated in this study is available at
<https://doi.org/10.5281/zenodo.5093843>.

References

1. 1. Akhbarizadeh, R. et al. Suspended fine particulate matter (PM_{2.5}), microplastics (MPs), and polycyclic aromatic hydrocarbons (PAHs) in air: Their possible relationships and health implications. *Environ. Res.* **192**, 110339 (2021).
2. 2. Allen, S. et al. Atmospheric transport and deposition of microplastics in a remote mountain catchment. *Nat. Geosci.* **12**, 339–344 (2019).
3. 3. Allen, S. et al. Examination of the ocean as a source for atmospheric microplastics. *PLoS ONE* **15**, e0232746 (2020).
4. 4. Bergmann, M. et al. White and wonderful? Microplastics prevail in snow from the Alps to the Arctic. *Sci. Adv.* **5**, eaax1157 (2019).
5. 5. Brahney, J., Hallerud, M., Heim, E., Hahnenberger, M. & Sukumaran, S. Plastic rain in protected areas of the United States. *Science* **368**, 1257–1260 (2020).
6. 6. Cai, L. et al. Characteristic of microplastics in the atmospheric fallout from Dongguan city, China: preliminary research and first evidence. *Environ. Sci. Pollut. Res. Int.* **24**, 24928–24935 (2017).

7. 7.

Dris, R., Gasperi, J., Saad, M., Mirande, C. & Tassin, B. Synthetic fibers in atmospheric fallout: a source of microplastics in the environment? *Mar. Pollut. Bull.* **104**, 290–293 (2016).

8. 8.

Dris, R. et al. A first overview of textile fibers, including microplastics, in indoor and outdoor environments. *Environ. Pollut.* **221**, 453–458 (2017).

9. 9.

Gaston, E., Woo, M., Steele, C., Sukumaran, S. & Anderson, S. Microplastics differ between indoor and outdoor air masses: insights from multiple microscopy methodologies. *Appl. Spectrosc.* **74**, 1079–1098 (2020).

10. 10.

Klein, M. & Fischer, E. K. Microplastic abundance in atmospheric deposition within the metropolitan area of Hamburg, Germany. *Sci. Total Environ.* **685**, 96–103 (2019).

11. 11.

Knobloch, E. et al. Comparison of deposition sampling methods to collect airborne microplastics in Christchurch, New Zealand. *Wat. Air Soil Pollut.* **232**, 133 (2021).

12. 12.

Levermore, J. M., Smith, T. E. L., Kelly, F. J. & Wright, S. L. Detection of microplastics in ambient particulate matter using Raman spectral imaging and chemometric analysis. *Anal. Chem.* **92**, 8732–8740 (2020).

13. 13.

Li, Y. et al. Airborne fiber particles: types, size and concentration observed in Beijing. *Sci. Total Environ.* **705**, 135967 (2020).

14. 14.

Liu, K. et al. Source and potential risk assessment of suspended atmospheric microplastics in Shanghai. *Sci. Total Environ.* **675**, 462–471 (2019).

15. 15.

Liu, K. et al. Consistent transport of terrestrial microplastics to the ocean through atmosphere. *Environ. Sci. Technol.* **53**, 10612–10619 (2019).

16. 16.

Liu, C. et al. Widespread distribution of PET and PC microplastics in dust in urban China and their estimated human exposure. *Environ. Int.* **128**, 116–124 (2019).

17. 17.

Liu, K. et al. Global inventory of atmospheric fibrous microplastics input into the ocean: an implication from the indoor origin. *J. Hazard. Mater.* **400**, 123223 (2020).

18. 18.

Materić, D. et al. Micro- and nanoplastics in Alpine snow: a new method for chemical identification and (semi)quantification in the nanogram range. *Environ. Sci. Technol.* **54**, 2353–2359 (2020).

19. 19.

Su, L., Nan, B., Craig, N. J. & Pettigrove, V. Temporal and spatial variations of microplastics in roadside dust from rural and urban Victoria, Australia: implications for diffuse pollution. *Chemosphere* **252**, 126567 (2020).

20. 20.

Syafei, A. D., Nurasin, N. R., Assomadi, A. F. & Boedisantoso, R. Microplastic pollution in the ambient air of Surabaya, Indonesia. *Curr. World Environ.* **61**, 290–298 (2019).

21. 21.

Wang, X. et al. Atmospheric microplastic over the South China Sea and East Indian Ocean: abundance, distribution and source. *J. Hazard. Mater.* **389**, 121846 (2020).

22. 22.

Wright, S. L., Ulke, J., Font, A., Chan, K. L. A. & Kelly, F. J. Atmospheric microplastic deposition in an urban environment and an evaluation of transport. *Environ. Int.* **136**, 105411 (2020).

23. 23.

Zhang, Y. et al. Microplastics in glaciers of the Tibetan Plateau: evidence for the long-range transport of microplastics. *Sci. Total Environ.* **758**, 143634 (2021).

24. 24.

Brahney, J. et al. Constraining the atmospheric limb of the plastic cycle. *Proc. Natl Acad. Sci. USA* **118**, e2020719118 (2021).

25. 25.

Evangelou, N. et al. Atmospheric transport is a major pathway of microplastics to remote regions. *Nat. Commun.* **11**, 3381 (2020).

26. 26.

Myhre, G. et al. in *Climate Change 2013: The Physical Science Basis* (eds Stocker, T. F. et al.) Ch. 8 (IPCC, Cambridge Univ. Press, 2013).

27. 27.

Bellouin, N. et al. Bounding global aerosol radiative forcing of climate change. *Rev. Geophys.* **58**, e2019RG000660 (2020).

28. 28.

Geyer, R., Jambeck, J. R. & Law, K. L. Production, use, and fate of all plastics ever made. *Sci. Adv.* **3**, e1700782 (2017).

29. 29.

Andrady, A. L. Microplastics in the marine environment. *Mar. Pollut. Bull.* **62**, 1596–1605 (2011).

30. 30.

de Souza Machado, A. A., Kloas, W., Zarfl, C., Hempel, S. & Rillig, M. C. Microplastics as an emerging threat to terrestrial ecosystems. *Glob. Change Biol.* **24**, 1405–1416 (2018).

31. 31.

Rochman, C. M. Microplastics research—from sink to source. *Science* **360**, 28–29 (2018).

32. 32.

Goodman, K. E., Hare, J. T., Khamis, Z. I., Hua, T. & Sang, Q.-X. A. Exposure of human lung cells to polystyrene microplastics significantly retards cell proliferation and triggers morphological changes. *Chem. Res. Toxicol.* **34**, 1069–1081 (2021).

33. 33.

Spracklen, D. V. et al. Explaining global surface aerosol number concentrations in terms of primary emissions and particle formation. *Atmos. Chem. Phys.* **10**, 4775–4793 (2010).

34. 34.

Bullard, J. E., Ockelford, A., O'Brien, P. & McKenna Neuman, C. Preferential transport of microplastics by wind. *Atmos. Environ.* **245**, 118038 (2021).

35. 35.

Tsigaridis, K. & Kanakidou, M. The Present and future of secondary organic aerosol direct forcing on climate. *Curr. Clim. Change Rep.* **4**, 84–98 (2018).

36. 36.

González-Pleiter, M. et al. Occurrence and transport of microplastics sampled within and above the planetary boundary layer. *Sci. Total Environ.* **761**, 143213 (2020).

37. 37.

Mishra, A. K., Koren, I. & Rudich, Y. Effect of aerosol vertical distribution on aerosol-radiation interaction: a theoretical prospect. *Heliyon* **1**, e00036 (2015).

38. 38.

Lohmann, U. et al. Total aerosol effect: radiative forcing or radiative flux perturbation? *Atmos. Chem. Phys.* **10**, 3235–3246 (2010).

39. 39.

Bellouin, N. et al. Aerosol forcing in the Climate Model Intercomparison Project (CMIP5) simulations by HadGEM2-ES and the role of ammonium nitrate. *J. Geophys. Res.* **116**, D20206 (2011).

40. 40.

Jervis, D. A. Optical brighteners: improving the colour of plastics. *Plast. Addit. Compd* **5**, 42–46 (2003).

41. 41.

Twomey, S. The influence of pollution on the shortwave albedo of clouds. *J. Atmos. Sci.* **34**, 1149–1152 (1977).

42. 42.

Albrecht, B. A. Aerosols, cloud microphysics, and fractional cloudiness. *Science* **245**, 1227–1230 (1989).

43. 43.

Ganguly, M. & Ariya, P. A. Ice Nucleation of model nanoplastics and microplastics: a novel synthetic protocol and the influence of particle capping at diverse atmospheric environments. *ACS Earth Space Chem.* **3**, 1729–1739 (2019).

44. 44.

Vergara-Temprado, J. et al. Strong control of Southern Ocean cloud reflectivity by ice-nucleating particles. *Proc. Natl Acad. Sci. USA* **115**, 2687–2692 (2018).

45. 45.

Eriksen, M. et al. Plastic pollution in the world's oceans: more than 5 trillion plastic pieces weighing over 250,000 tons afloat at sea. *PLoS ONE* **9**, e111913 (2014).

46. 46.

Boé, J., Somot, S., Corre, L. & Nabat, P. Large discrepancies in summer climate change over Europe as projected by global and regional climate models: causes and consequences. *Clim. Dyn.* **54**, 2981–3002 (2020).

47. 47.

Wessel, P. & Smith, W. H. F. A global self-consistent, hierarchical, high-resolution shoreline database. *J. Geophys. Res. Solid Earth* **101**, 8741–8743 (1996).

48. 48.

Python Language Reference, Version 3.6
<https://www.python.org/downloads/release/python-360/> (Python Software Foundation).

49. 49.

Horwitz, J. W. Infrared refractive index of polyethylene and a polyethylene-based material. *Opt. Eng.* **50**, 093603 (2011).

50. 50.

Smith, D. R. & Loewenstein, E. V. Optical constants of far infrared materials. 3: plastics. *Appl. Opt.* **14**, 1335–1341 (1975).

51. 51.

Sultanova, N., Kasarova, S. & Nikolov, I. Dispersion Properties of Optical Polymers. *Acta Phys. Pol. A* **116**, 585–587 (2009).

52. 52.

Zhang, X., Qiu, J., Zhao, J., Li, X. & Liu, L. Complex refractive indices measurements of polymers in infrared bands. *J. Quant. Spectrosc. Radiat. Transf.* **252**, 107063 (2020).

53. 53.

Zhang, X., Qiu, J., Li, X., Zhao, J. & Liu, L. Complex refractive indices measurements of polymers in visible and near-infrared bands. *Appl. Opt.* **59**, 2337–2344 (2020).

54. 54.

Flores-Mijangos, J. & Beltrán-López, V. Far-infrared laser measurement of the refractive index of polypropylene. *Appl. Opt.* **42**, 592–596 (2003).

55. 55.

Myers, T. L. et al. Accurate measurement of the optical constants n and k for a series of 57 inorganic and organic liquids for optical modeling and detection. *Appl. Spectrosc.* **72**, 535–550 (2018).

56. 56.

Sellmeier, W. Ueber die durch die Aetherschwingungen erregten Mitschwingungen der Körpertheilchen und deren Rückwirkung auf die ersteren, besonders zur Erklärung der Dispersion und ihrer Anomalien. *Ann. Phys.* **223**, 386–403 (1872).

57. 57.

Kroon, F. J., Motti, C. E., Jensen, L. H. & Berry, K. L. E. Classification of marine microdebris: a review and case study on fish from the Great Barrier Reef, Australia. *Sci. Rep.* **8**, 16422 (2018).

58. 58.

Plastics—The Facts 2018: An Analysis of European Plastics Production, Demand and Waste Data (PlasticsEurope, 2018);
<http://www.plasticseurope.org>

59. 59.

China Leads in Growth of Polymers & Plastic Products, (Plastemart, 2006);
www.plastemart.com/upload/Literature/chineseplasticandpolymergrowth.asp

60. 60.

Edwards, J. M. & Slingo, A. Studies with a flexible new radiation code. I: choosing a configuration for a large-scale model. *Q. J. R. Meteorol. Soc.* **122**, 689–719 (1996).

61. 61.

Lean, J. L. & DeLand, M. T. How does the Sun's spectrum vary? *J. Clim.* **25**, 2555–2560 (2012).

62. 62.

Kokhanovsky, A. A. & Zege, E. P. Local optical parameters of spherical polydispersions: simple approximations. *Appl. Opt.* **34**, 5513–5519 (1995).

63. 63.

van de Hulst, H. C. *Light Scattering by Small Particles* (Wiley, 1957).

64. 64.

Kokhanovsky, A. A. & Macke, A. Integral light-scattering and absorption characteristics of large, nonspherical particles. *Appl. Opt.* **36**, 8785–8790 (1997).

65. 65.

Bohren, C. F. & Huffman, D. R. *Absorption and Scattering of Light by Small Particles* (John Wiley & Sons Inc., 1983).

66. 66.

Duntley, S. Q. The optical properties of diffusing materials. *J. Opt. Soc. Am.* **32**, 61–70 (1942).

67. 67.

Walters, D. et al. The Met Office Unified Model Global Atmosphere 7.0/7.1 and JULES Global Land 7.0 configurations. *Geosci. Model*

Dev. **12**, 1909–1963 (2019).

68. 68.

Edwards, J. M., Manners, J., Thelen, J.-C., Ingram, W. J. & Hill, P. G. *Unified Model Documentation Paper 023: The Radiation Code (UM Version 11.4)* (Met Office, 2018).

69. 69.

Lamarque, J. F. et al. Historical (1850–2000) gridded anthropogenic and biomass burning emissions of reactive gases and aerosols: methodology and application. *Atmos. Chem. Phys.* **10**, 7017–7039 (2010).

70. 70.

Forster, P. M. et al. Recommendations for diagnosing effective radiative forcing from climate models for CMIP6. *J. Geophys. Res. Atmos.* **121**, 12460–12475, (2016).

71. 71.

Oreopoulos, L. & Mlawer, E. Modeling: the Continual Intercomparison of Radiation Codes (CIRC). *Bull. Am. Meteorol. Soc.* **91**, 305–310 (2010).

Acknowledgements

This research was supported by the Royal Society of New Zealand Marsden Fund (contract number MFP-UOC1903). We acknowledge the UK Met Office for the use of the MetUM, SOCRATES and the Continual Intercomparison of Radiation Codes (CIRC). We acknowledge the contribution of New Zealand eScience Infrastructure (NeSI) high-performance computing facilities to the results of this research. New Zealand's national facilities are provided by NeSI and funded jointly by NeSI's collaborator institutions and through the Ministry of Business, Innovation and Employment's Research Infrastructure programme

(<https://www.nesi.org.nz>, last access: 20 April 2021). We also acknowledge the use of the Rāpoi computing facility at Victoria University of Wellington, along with the open source software used in the analysis: Devuan GNU+Linux, Python, numpy, scipy and matplotlib. L.E.R. thanks Jonny Williams for technical assistance. L.E.R. and P.K. acknowledge R. Martinez Gazoni for helpful discussions.

Author information

Author notes

1. Peter Kuma

Present address: Department of Meteorology, Stockholm University, Stockholm, Sweden

Affiliations

1. School of Physical and Chemical Sciences, University of Canterbury, Christchurch, New Zealand

Laura E. Revell, Peter Kuma & Sally Gaw

2. The MacDiarmid Institute for Advanced Materials and Nanotechnology, School of Chemical and Physical Sciences, Victoria University of Wellington, Wellington, New Zealand

Eric C. Le Ru & Walter R. C. Somerville

Contributions

L.E.R. Conceptualized the study, acquired funding, supervised the study, wrote the original draft and conducted the analysis together with P.K. and W.R.C.S. . P.K. contributed to the methodology, software, validation, and writing of the original draft. E.C.L.R. contributed to the methodology, validation, funding acquisition, supervision and review and editing of the manuscript. W.R.C.S. contributed to the methodology and validation, and

writing of the original draft. S.G. reviewed and edited the manuscript and contributed to funding acquisition.

Corresponding author

Correspondence to Laura E. Revell.

Ethics declarations

Competing interests

The authors declare no competing interests.

Additional information

Peer review information *Nature* thanks Ben Booth, Steven Allen, Rachid Dris and the other, anonymous, reviewer(s) for their contribution to the peer review of this work.

Publisher's note Springer Nature remains neutral with regard to jurisdictional claims in published maps and institutional affiliations.

Extended data figures and tables

[Extended Data Fig. 1 Composition of airborne microplastics collected in previous studies compared with reported plastic production data.](#)

The studies included disaggregated composition by morphotype and are presented for **(a)** fragments; **(b)** fibres. Polymer compositions include acrylic (ACR, including polyacrylonitrile and poly(N-methyl acrylamide)), polyamide (PA, including nylon), polyethylene and polypropylene (PE-PP), polyester (PES, including polyethylene terephthalate), polystyrene (PS), polyurethane (PUR), polyvinyl acetate (PVA), polyvinyl chloride (PVC),

resins (RES, including epoxy, phenoxy and alkyd resins), and various other types (OTH)

[Source data](#).

Extended Data Fig. 2 Size distributions of microplastic fragments reported by previous studies.

A gamma distribution was fitted to match the majority of the empirical distributions. The distributions are normalized to unity and approximated by a gamma distribution with the shape parameter of 2 and scale parameter 15 μm

[Source data](#).

Extended Data Fig. 3 Size distributions of microplastic fibre lengths reported by previous studies.

A gamma distribution was fitted to match the majority of the empirical distributions. The distributions are normalized to unity and approximated by a gamma distribution with the shape parameter of 2.5 and scale parameter 250 μm

[Source data](#).

Extended Data Fig. 4

Morphotypes of airborne microplastic collected in previous studies

[Source data](#).

Extended Data Fig. 5 Refractive index of polymers based on a literature survey.

Polymer compositions include high-density polyethylene (HDPE), polyacrylic acid (PAA), polyethylene terephthalate (PET), polypropylene (PP), polystyrene (PS) and polyvinyl chloride (PVC). The mean calculated

over regular wavelength intervals on a \log_{10} scale is shown by the dashed black lines. In (a) equation (2) was fitted to the mean. In (b) equation (3) was used to fit a 4th degree polynomial to the \log_{10} of the mean using the least squares method. The solid black lines represent the fits given by equations (2) and 3, and these fits were used in the calculations of microplastic optical properties

[Source data.](#)

Extended Data Fig. 6 Colours of airborne microplastics collected in previous studies, where colour was reported.

Black includes grey; blue includes turquoise; green includes lime; red includes pink, purple, brown and orange; white includes transparent

[Source data.](#)

Extended Data Fig. 7 The empirical aspect ratio of fibres collected in European and Arctic snow (the only study to date to report fibre aspect ratio).

A least squares fit of the form $(D=A)\log\left(1+\frac{L}{B}\right)$ is also shown, where D is the fibre diameter, L is the fibre length and A and B are fitted coefficients, rounded to the nearest integer

[Source data.](#)

Extended Data Table 1 Prescribed microplastic surface concentrations in GCM simulations

Extended Data Table 2 Optical properties of microplastic fragments and fibres supplied to the GCM in the shortwave and longwave bands

Source data

Source Data Fig. 1

[**Source Data Fig. 2**](#)

[**Source Data Fig. 3**](#)

[**Source Data Extended Data Fig. 1**](#)

[**Source Data Extended Data Fig. 2**](#)

[**Source Data Extended Data Fig. 3**](#)

[**Source Data Extended Data Fig. 4**](#)

[**Source Data Extended Data Fig. 5**](#)

[**Source Data Extended Data Fig. 6**](#)

[**Source Data Extended Data Fig. 7**](#)

Rights and permissions

[**Reprints and Permissions**](#)

About this article

Cite this article

Revell, L.E., Kuma, P., Le Ru, E.C. *et al.* Direct radiative effects of airborne microplastics. *Nature* **598**, 462–467 (2021). <https://doi.org/10.1038/s41586-021-03864-x>

- Received: 24 January 2021
- Accepted: 29 July 2021
- Published: 20 October 2021

- Issue Date: 21 October 2021
- DOI: <https://doi.org/10.1038/s41586-021-03864-x>

Share this article

Anyone you share the following link with will be able to read this content:

[Get shareable link](#)

Sorry, a shareable link is not currently available for this article.

[Copy to clipboard](#)

Provided by the Springer Nature SharedIt content-sharing initiative

This article was downloaded by **calibre** from <https://www.nature.com/articles/s41586-021-03864-x>

| [Section menu](#) | [Main menu](#) |

- Article
- Open Access
- [Published: 22 September 2021](#)

The three major axes of terrestrial ecosystem function

- [Mirco Migliavacca](#) [ORCID: orcid.org/0000-0003-3546-8407^{1,2}](#) [nAff55](#),
- [Talie Musavi¹](#),
- [Miguel D. Mahecha](#) [ORCID: orcid.org/0000-0003-3031-613X^{1,2,3,4}](#),
- [Jacob A. Nelson¹](#),
- [Jürgen Knauer⁵](#) [nAff56](#),
- [Dennis D. Baldocchi⁶](#),
- [Oscar Perez-Priego⁷](#),
- [Rune Christiansen⁸](#),
- [Jonas Peters⁸](#),
- [Karen Anderson](#) [ORCID: orcid.org/0000-0002-3289-2598⁹](#),
- [Michael Bahn](#) [ORCID: orcid.org/0000-0001-7482-9776¹⁰](#),
- [T. Andrew Black¹¹](#),
- [Peter D. Blanken](#) [ORCID: orcid.org/0000-0002-7405-2220¹²](#),
- [Damien Bonal](#) [ORCID: orcid.org/0000-0001-9602-8603¹³](#),
- [Nina Buchmann](#) [ORCID: orcid.org/0000-0003-0826-2980¹⁴](#),
- [Silvia Calderaru](#) [ORCID: orcid.org/0000-0001-5839-6480¹](#),
- [Arnaud Carrara¹⁵](#),
- [Nuno Carvalhais^{1,16}](#),
- [Alessandro Cescatti¹⁷](#),
- [Jiquan Chen](#) [ORCID: orcid.org/0000-0003-0761-9458¹⁸](#),
- [Jamie Cleverly](#) [ORCID: orcid.org/0000-0002-2731-7150^{19,20}](#),
- [Edoardo Cremonese](#) [ORCID: orcid.org/0000-0002-6708-8532²¹](#),
- [Ankur R. Desai](#) [ORCID: orcid.org/0000-0002-5226-6041²²](#),
- [Tarek S. El-Madany](#) [ORCID: orcid.org/0000-0002-0726-7141¹](#),
- [Martha M. Farella](#) [ORCID: orcid.org/0000-0002-2925-4093²³](#),
- [Marcos Fernández-Martínez](#) [ORCID: orcid.org/0000-0002-5661-3610²⁴](#),
- [Gianluca Filippa²¹](#),
- [Matthias Forkel²⁵](#),

- [Marta Galvagno](#)²¹,
- [Ulisse Gomarasca](#) ORCID: [orcid.org/0000-0001-7389-7793](#)¹,
- [Christopher M. Gough](#) ORCID: [orcid.org/0000-0002-1227-7731](#)²⁶,
- [Mathias Göckede](#) ORCID: [orcid.org/0000-0003-2833-8401](#)¹,
- [Andreas Ibrom](#) ORCID: [orcid.org/0000-0002-1341-921X](#)²⁷,
- [Hiroki Ikawa](#)²⁸,
- [Ivan A. Janssens](#) ORCID: [orcid.org/0000-0002-5705-1787](#)²⁴,
- [Martin Jung](#) ORCID: [orcid.org/0000-0002-7588-1004](#)¹,
- [Jens Kattge](#) ORCID: [orcid.org/0000-0002-1022-8469](#)^{1,2},
- [Trevor F. Keenan](#) ORCID: [orcid.org/0000-0002-3347-0258](#)^{6,29},
- [Alexander Knohl](#) ORCID: [orcid.org/0000-0002-7615-8870](#)^{30,31},
- [Hideki Kobayashi](#) ORCID: [orcid.org/0000-0001-9319-0621](#)³²,
- [Guido Kraemer](#) ORCID: [orcid.org/0000-0003-4865-5041](#)^{3,33},
- [Beverly E. Law](#) ORCID: [orcid.org/0000-0002-1605-1203](#)³⁴,
- [Michael J. Liddell](#)³⁵,
- [Xuanlong Ma](#)³⁶,
- [Ivan Mammarella](#) ORCID: [orcid.org/0000-0002-8516-3356](#)³⁷,
- [David Martini](#) ORCID: [orcid.org/0000-0003-2180-5126](#)¹,
- [Craig Macfarlane](#)³⁸,
- [Giorgio Matteucci](#)³⁹,
- [Leonardo Montagnani](#) ORCID: [orcid.org/0000-0003-2957-9071](#)^{40,41},
- [Daniel E. Pabon-Moreno](#)¹,
- [Cinzia Panigada](#)⁴²,
- [Dario Papale](#) ORCID: [orcid.org/0000-0001-5170-8648](#)⁴³,
- [Elise Pendall](#) ORCID: [orcid.org/0000-0002-1651-8969](#)⁴⁴,
- [Josep Penuelas](#) ORCID: [orcid.org/0000-0002-7215-0150](#)^{45,46},
- [Richard P. Phillips](#) ORCID: [orcid.org/0000-0002-1345-4138](#)⁴⁷,
- [Peter B. Reich](#) ORCID: [orcid.org/0000-0003-4424-662X](#)^{44,48,49},
- [Micol Rossini](#) ORCID: [orcid.org/0000-0002-6052-3140](#)⁴²,
- [Eyal Rotenberg](#)⁵⁰,
- [Russell L. Scott](#) ORCID: [orcid.org/0000-0003-2987-5380](#)⁵¹,
- [Clement Stahl](#)⁵²,
- [Ulrich Weber](#) ORCID: [orcid.org/0000-0001-7116-035X](#)¹,
- [Georg Wohlfahrt](#) ORCID: [orcid.org/0000-0003-3080-6702](#)¹⁰,
- [Sebastian Wolf](#) ORCID: [orcid.org/0000-0001-7717-6993](#)¹⁴,
- [Ian J. Wright](#) ORCID: [orcid.org/0000-0001-8338-9143](#)^{44,53},
- [Dan Yakir](#) ORCID: [orcid.org/0000-0003-3381-1398](#)⁵⁰,
- [Sönke Zaehle](#) ORCID: [orcid.org/0000-0001-5602-7956](#)¹ &
- [Markus Reichstein](#) ORCID: [orcid.org/0000-0001-5736-1112](#)^{1,2,54}

Nature volume 598, pages 468–472 (2021)

- 22k Accesses
- 232 Altmetric
- [Metrics details](#)

Subjects

- [Biogeography](#)
- [Ecosystem ecology](#)

Abstract

The leaf economics spectrum^{1,2} and the global spectrum of plant forms and functions³ revealed fundamental axes of variation in plant traits, which represent different ecological strategies that are shaped by the evolutionary development of plant species². Ecosystem functions depend on environmental conditions and the traits of species that comprise the ecological communities⁴. However, the axes of variation of ecosystem functions are largely unknown, which limits our understanding of how ecosystems respond as a whole to anthropogenic drivers, climate and environmental variability^{4,5}. Here we derive a set of ecosystem functions⁶ from a dataset of surface gas exchange measurements across major terrestrial biomes. We find that most of the variability within ecosystem functions (71.8%) is captured by three key axes. The first axis reflects maximum ecosystem productivity and is mostly explained by vegetation structure. The second axis reflects ecosystem water-use strategies and is jointly explained by variation in vegetation height and climate. The third axis, which represents ecosystem carbon-use efficiency, features a gradient related to aridity, and is explained primarily by variation in vegetation structure. We show that two state-of-the-art land surface models reproduce the first and most important axis of ecosystem functions. However, the models tend to simulate more strongly correlated functions than those observed, which limits their ability to accurately predict the full range of responses to environmental changes in carbon, water and energy cycling in terrestrial ecosystems^{7,8}.

[Download PDF](#)

Main

Terrestrial ecosystems provide multiple functions (for example, resource use and potential uptake of carbon dioxide, among others) and ecosystem services on which society depends⁵. To understand and predict the response mechanisms of ecosystems as a whole to climatic and other environmental changes, it is crucial to establish how many and which functions need to be measured to obtain a good representation of overall ecosystem functioning. So far, the key functional axes that control the behaviour of terrestrial ecosystems have not yet been quantified⁵. This can be achieved by identifying associations between a comprehensive set of ecosystem functions measured consistently across major terrestrial biomes and a range of climatic conditions.

Here, we identify and quantify the major axes of terrestrial ecosystem functions and sources of variation along these axes. First, we characterize multiple ecosystem functions across major terrestrial biomes. Second, we identify the most important axes of variation of ecosystem functions using an exploratory analysis similar to that used for the global spectrum of plant forms and functions³. Third, we analyse which variables drive the variation along these axes, from a suite of climatic variables, and the structural and chemical properties of the vegetation. Fourth, we analyse the extent to which two state-of-the-art land surface models (models that simulate the states and exchange of matter and energy between the Earth's surface and the atmosphere) reproduce the key axes of ecosystem functions. Understanding and quantifying the main axes of variation of the multi-dimensional space of ecosystem functions, their drivers and the degree to which land surface models are able to correctly represent the axes is a crucial prerequisite for predicting which terrestrial functions are the most vulnerable to climate and environmental changes.

We use carbon dioxide (CO_2), water vapour (H_2O), and energy flux data from 203 sites (1,484 site years) from FLUXNET datasets^{9,10}. These sites cover a wide variety of climate zones and vegetation types (Extended Data Figs. 1–3, Supplementary Table 1). A previous report⁶ suggested a series of core ecosystem functional properties that can be derived from carbon, water and energy flux observations related to efficiencies or potential rates of key physiological and ecohydrological processes (for example, evapotranspiration, photosynthesis energy partitioning and so on) that control land surface–atmosphere interactions. For each site, we calculated a single set of functional properties (see ‘Calculation of ecosystem functions from FLUXNET’ in Methods for details on the calculation and definition of abbreviations): maximum gross CO_2 uptake at light saturation (GPP_{sat}), maximum net ecosystem productivity (NEP_{max}), maximum evapotranspiration (ET_{max}), evaporative fraction (EF) (that is, the ratio between latent heat flux and available energy, indicative of energy partitioning), EF amplitude (EF_{ampl}), maximum dry canopy surface conductance (G_{smax}), maximum and mean basal ecosystem respiration (Rb_{max} and Rb , respectively), and apparent carbon-use

efficiency (aCUE) (that is, the remaining fraction of carbon entering the ecosystem). We also computed several metrics of growing season water-use efficiency (WUE) that account in different ways for physical evaporation and stomatal regulation effects: underlying WUE (uWUE), stomatal slope at ecosystem scale (G1), and WUE_t , a second variant of WUE, but based on transpiration estimates¹¹ (see [Methods](#)). We calculated average climate and soil water availability variables for each site, encompassing the following: cumulative soil water availability index (CSWI), mean annual precipitation (P), mean shortwave incoming radiation (SW_{in}), mean air temperature (T_{air}), and mean vapour pressure deficit during the growing season (VPD). In addition, we compiled information on canopy-scale structural variables such as foliar nitrogen concentration (N%), maximum leaf area index (LAI_{max}), maximum canopy height (H_c), and above-ground biomass (AGB), when available (Methods, [Supplementary Table 1](#)).

The key axes of the multi-dimensional space of terrestrial ecosystem functions were identified using principal component analysis (PCA; see [Methods](#)). We find that the first three axes of variation (the principal components; PCs) explain 71.8% of the multi-dimensional functional space variation (Fig. [1a,b](#), [Supplementary Information 2](#)). The first axis (PC1) explains 39.3% of the variance and is dominated by maximum ecosystem productivity properties, as indicated by the loadings of GPP_{sat} and NEP_{max} , and maximum evapotranspiration (ET_{max}) (Fig. [1c,d](#)). Also, Rb contributes with positive loadings to PC1 (Fig. [1d](#)), indicating the coupling between productivity and ecosystem respiration (both autotrophic and heterotrophic)¹². The first axis runs from sites with low productivity and evapotranspiration to sites with high photosynthesis, high net productivity, and high maximum evapotranspiration; that is, from cold and arid shrublands and wetlands, to forests in continental, tropical and temperate climates (Fig. [2a,b](#)). The second axis (PC2) explains 21.4% of the variance and refers to water-use strategies as shown by the loadings of water-use efficiency metrics (uWUE, WUE_t , and G1), evaporative fraction and maximum surface conductance (Fig. [1c,d](#)). Plant functional types do not explain clearly the variability of the second axis, with the exception of the evergreen and mixed forest, and the wetlands that are at the opposite extremes of the range (Fig. [2c](#)). This axis runs (Fig. [2c,d](#)) from temperate forests, dry and subtropical sites with a low average evaporative fraction (that is, available energy is mainly dissipated by sensible heat) but higher water-use efficiency (Fig. [2d](#)), to sites in cold or tropical climates, as well as wetlands with a high evaporative fraction (that is, available energy is used for evapotranspiration), high surface conductance and low water-use efficiency (Fig. [2c,d](#)). The third axis (PC3) explains 11.1% of the variance and includes key attributes that reflect the carbon-use efficiency of ecosystems. PC3 is dominated by apparent carbon-use efficiency (aCUE), basal ecosystem respiration (Rb and Rb_{max}) and the amplitude

of EF (EF_{amp1}) (Fig. 1c, d). Rb and aCUE contribute to PC3 with opposite loadings, indicating that the PC3 ranges from sites with high aCUE and low Rb to sites with low aCUE and high Rb. The third axis runs from Arctic and boreal sites with low PC values to hot and dry climates (Fig. 2f), potentially indicating the imprint of aridity and temperature over the efficiency of ecosystems to use the assimilated carbon. We find no clear relation to plant functional types, with the exception of deciduous and evergreen forests that are at the extremes of the PC3 range (Fig. 2e).

Fig. 1: Key dimensions of multivariate space of terrestrial ecosystem functions.

 figure1



a, Biplot resulting from the PCA. Different colours of the points represent different plant functional types (PFTs): CSH (closed shrublands); DBF (deciduous broadleaved forest); DNF (deciduous needleleaf forests); EBF (evergreen broadleaved forest); ENF (evergreen needleleaf forest); GRA (grasslands); MF (mixed forest); OSH (open shrublands); SAV (savannah); and WET (wetlands). Bigger points represent the centroid of the distribution for each PFT. **b**, Explained variance for each principal component. **c, d**, Bar plots of the contribution (c) and loading (d) of each ecosystem functional property (EFP) to each principal component. Orange bars represent the loadings and the contributions that are considered significant (Supplementary Information 2).

Fig. 2: Distribution of plant functional types and climate types along the principal components (PC1–PC3).

 figure2

a, c, e, Plant functional types (PFTs). **b, d, f**, Climate types. Letters represent statistically significant differences in the average PCs (Tukey's HSD test, $P < 0.05$), such that groups not containing the same letter are different. The effect size of the one-way ANOVA (η^2) is reported ($n = 203$ sites). In the box plots the central line represents the mean; the lower and upper box limits correspond to the 25th and 75th percentiles and the upper (lower) whiskers extend to 1.5 (-1.5) times the interquartile range, respectively. Colours indicate different climate types and PFTs (cont, continental; subtrop, subtropical; temp, temperate; trop, tropical; PFT definitions are as in Fig. 1).

We analyse the predictive relative importance of five climatic variables (T_{air} , VPD, CSWI, P , and SW_{in}) and four vegetation structural characteristics (LAI_{max} , AGB, H_c and N%) on the predictability of the principal components using random forests (see ‘Predictive variable importance’ in Methods). We find that the maximum productivity axis (PC1) is largely explained by vegetation structure (LAI_{max} , AGB, H_c and N%) and VPD (Fig. 3a, Extended Data Fig. 4a–e). The water-use strategies axis (PC2) is mostly explained by maximum canopy height (H_c), followed by climate variables (Fig. 3b, Extended Data Fig. 4i–l). Structural and climate variables jointly explain the variability of the carbon-use efficiency axis (PC3). The most important structural

predictors of PC3 are AGB and N%, whereas VPD, T_{air} and SW_{in} are the most important climate drivers (Fig. 3c, Extended Data Fig. 4m–q).

Fig. 3: Importance of climate and vegetation properties.



a–c, Predictive relative importance for PC1 (**a**), PC2 (**b**) and PC3 (**c**). Numbers in the circles represent the percentage increase in mean squared error (MSE). Yellow circles represent vegetation structural variables; light blue circles represent climate variables.

The dependencies described above can only be interpreted causally if the regression models are in fact causal regression models (see Supplementary Information 3 for a formal definition). In many situations, this fails to be the case owing to the existence of hidden confounders; that is, unmeasured variables that influence both the principal components and the covariates (here climate and structural variables)¹³. Using an invariance-based analysis (see ‘Invariant causal regression models and causal variable importance’ in Methods), we find evidence that the full regression model including all the selected structural and climatic variables might be causal (Supplementary Information 3.2.1, Supplementary Fig. 3.3). If this is indeed the case, we can make the following statements. When considering groupwise causal variable importance, we can conclude that vegetation structure is a stronger causal driver than climate of the spatial (that is, across sites) variability of the maximum realized productivity axis (PC1) (Supplementary Fig. 3.7), and both are significant (Supplementary Table 3.2). Consider two contiguous plots of forest experiencing the same climate conditions, one disturbed and the other not. The undisturbed forest, which is likely to be taller, with higher LAI and carbon stocks, would probably have higher maximum photosynthetic rates and net ecosystem production, which are the most important variables loading on the first axis. Although, in time, the variability of climate controls the variability of gross and net CO₂ uptake and productivity^{14,15}, which are variables related to the maximum productivity axis (PC1), in space (that is, across sites) we find only a marginal control in very cold and radiation-limited sites (Extended Data Fig. 5a for a PC1 map), or for very warm and high atmospheric aridity (high VPD) conditions (Extended Data Fig. 4d based on predictive variable importance). Both vegetation structure and climate variables seem to have a joint direct causal effect on PC2 (Supplementary Fig 3.7). Although vegetation canopy height is constrained by

resource availability¹⁶, particularly water, our results suggest that it acts itself as a control on the water-use strategies axis (PC2) and that it has a stronger causal effect on PC2 than each of the climate variables (Supplementary Fig. 3.6). The importance of vegetation height for ecosystem water-use strategies is manifold. First, vegetation height controls the coupling between stomata and atmosphere by influencing surface roughness and then aerodynamic resistance¹⁷, which modulates leaf-to-air VPD and water use efficiency. Second, vegetation height reflects variation in water-use efficiency that decreases as a consequence of progressive hydraulic constraints on stomatal conductance to water vapour and growth in taller vegetation¹⁶. Third, canopy height might reflect stand age and it is influenced by disturbances. Studies on forest chronosequence show a more conservative use of water in younger forests, which results in higher water-use efficiency¹⁸. We cannot exclude that our results are indirectly affected by the gradient from grass to forests, but postulate that these effects are likely to be minimal (Extended Data Fig. 6). Vegetation structure has a direct causal effect on the carbon-use efficiency axis (PC3; Supplementary Fig 3.7). Previous studies show that vegetation structure reflects climatic constraints but also the successional stage of an ecosystem after disturbance¹⁹. Increasing stand age—which is typically associated with higher above-ground biomass—is also associated with reduced forest production efficiency²⁰. The negative partial dependence of PC3 on above-ground biomass (Extended Data Fig. 4n, based on predictive variable importance) is likely to be related to higher autotrophic and heterotrophic respiration rates per unit of CO₂ taken up by photosynthesis as biomass increases²¹. The positive dependence of PC3 on N% (Extended Data Fig. 4q, based on predictive variable importance) supports previous findings that carbon-use efficiency might be controlled by the nutrient status of the vegetation²².

The two representative—yet complementary—land surface models examined here (OCN and JSBACH) partially reproduce the main axes of terrestrial ecosystem functions (Extended Data Fig. 7). This is shown when comparing the PCA calculated from FLUXNET data with simulated ecosystem functional properties from 48 site-level runs, mostly in temperate and boreal sites (Extended Data Fig. 7). The models are broadly consistent with the FLUXNET observations in the description of the potential productivity axis (PC1), but diverge in the description of the water-use strategies (PC2) and the carbon-use efficiency (PC3) axes. Despite the overall good agreement between observed and modelled fluxes at a half-hourly timescale (Supplementary Table 4), we show that, first, models are limited in simulating the relationships between ecosystem functions (Extended Data Fig. 8); and, second, models tend to overstate observed correlation strengths among ecosystem functions, as shown by the larger variance explained by the PC1 in models compared to observations (Extended Data Fig 7h, i). As a result, the ecosystem functional space that can be simulated by the models, represented by the area shown in Extended Data Fig. 9, is smaller than that expected from observations, particularly in the plane

spanned by the PC2 and PC3 (Extended Data Fig. 9d–f). The limited variability of the model output points to an insufficient representation of the actual variability of the vegetation properties by the average parameterization of plant functional types. Uncertain implementation of plant hydraulics and water acquisition or conservation strategies in land surface models is a key limitation²³ that explains the observed discrepancy in PC2. With regard to PC3, one limitation is that models lack flexibility in representing the response of respiration rates and carbon-use efficiency to climate, nutrients, disturbances and substrate availability (including biomass and stand age)^{20,24}.

The identification of the key axes of terrestrial ecosystem function and their relationships with climate and vegetation structure will help to support the development of the next generation of land surface models and complement their benchmarking²⁵. By comparing the contributions of the functions and their loadings to the principal components, we can assess whether the representations of ecosystem functions in the models and in the ‘real world’ are coherent, and if not, which key processes or model formulations need improvement. For example, we show that vegetation height controls the water-use strategies axis (PC2), which is not well reproduced by the land surface models²³. This suggests that future land surface models need to include a representation of water-use strategies that explicitly accounts for hydraulic limitations to growth, vegetation stature, vertical and horizontal structures and microenvironments of the canopy, and a refined parameterization of stomatal control. Likewise, the inclusion of a flexible representation of carbon-use efficiency would enable models to reproduce the third axis of ecosystem functions²⁴. The comparison of the variances explained by functional axes and the loadings of the functions in simulated and observed data will indicate whether simulated ecosystem functions are appropriately coordinated. The overly tight coupling of ecosystem functions by models indicates a lack of flexibility in ecosystem responses to environmental drivers, such as adaptive carbon and water couplings.

In summary, by analysing a consistent set of ecosystem functions across major terrestrial biomes and climate zones, we show that three key axes capture the terrestrial ecosystem functions. The first and most important axis represents maximum productivity and is driven primarily by vegetation structure, followed by mean climate. The second axis is related to water-use strategies, and is driven by vegetation height. The third axis is related to ecosystem carbon-use efficiency; it is controlled by vegetation structure, but shows a gradient related to aridity. We find that the plant functional type concept does not necessarily capture the variability of ecosystem functions, because the majority of plant functional types are evenly distributed along the water-use strategies (PC2) and carbon-use efficiency (PC3) axes. Our approach allows the overall functioning of terrestrial ecosystems to be summarized and offers a way towards the development of metrics of ecosystem multifunctionality⁵—a measure

of ecosystem functions as a whole, which is crucial to achieving a comprehensive assessment of the responses of ecosystems to climate and environmental variability, as well as biodiversity losses⁵. The analysis focuses on relatively few critical functions related to carbon, water and energy cycling of ecosystems. To attain a fully comprehensive characterization of the key axes of terrestrial ecosystem functions, more parameters related to nutrient cycling, seed dispersal and chemical defences—among others—should be included. The concept of the key axes of ecosystem functions could be used as a backdrop for the development of land surface models, which might help to improve the predictability of the terrestrial carbon and water cycle in response to future changing climatic and environmental conditions.

Methods

FLUXNET data

The data used in this study belong to the FLUXNET LaThuile⁹ and FLUXNET2015 Tier 1 and Tier 2 datasets¹⁰, which make up the global network of CO₂, water vapour and energy flux measurements. We merged the two FLUXNET releases and retained the FLUXNET2015 (the most recent and with a robust quality check) version of the data when the site was present in both datasets. Croplands were removed to avoid the inclusion of sites that are heavily managed in the analysis (for example, fertilization and irrigation).

The sites used cover a wide variety of climate zones (from tropical to Mediterranean to Arctic) and vegetation types (wetlands, shrublands, grasslands, savanna, evergreen and deciduous forests). It should be noted though that tropical forests are underrepresented in the FLUXNET database (Extended Data Figs. [1](#), [3](#)).

Sites were excluded in cases in which: (i) data on precipitation or radiation were not available or completely gap-filled; (ii) the calculation of functional properties failed because of low availability of measured data (see ‘Calculation of ecosystem functions from FLUXNET’); and (iii) fluxes showed clear discontinuities in time series indicating a change of instrumentation set-up (for example, changes in the height of the ultrasonic anemometer or gas analyser).

The final number of sites selected was 203 (1,484 site years). The geographical distribution is shown in Extended Data Fig. [1](#), the distribution in the climate space is shown in Extended Data Fig. [2](#) and the fraction of sites for each climate classes is reported in Extended Data Fig. [3](#).

For each site, we downloaded the following variables at half-hourly temporal resolution: (i) gross primary productivity (GPP, $\mu\text{mol CO}_2 \text{ m}^{-2} \text{ s}^{-1}$) derived from the night-time flux partitioning²⁶ (GPP_NT_VUT_50 in FLUXNET 2015 and GPP_f in LaThuile), (ii) net ecosystem exchange (NEE, $\mu\text{mol CO}_2 \text{ m}^{-2} \text{ s}^{-1}$) measurements filtered using annual friction velocity (u^* , m s^{-1}) threshold (NEE_VUT_50 in FLUXNET 2015; NEE in LaThuile); (iii) latent heat (LE, W m^{-2}) fluxes, which were converted to evapotranspiration (ET, mm); (iv) sensible heat (H , W m^{-2}) fluxes; (v) air temperature (T_{air} , $^{\circ}\text{C}$); (vi) vapour pressure deficit (VPD, hPa); (vii) global shortwave incoming radiation (SW_{in} , W m^{-2}); (viii) net radiation (R_n , W m^{-2}); (ix) ground heat flux (G , W m^{-2}); (x) friction velocity u^* (m s^{-1}); and (xi) wind speed (u , m s^{-1}). For the energy fluxes (H , LE) we selected the fluxes not corrected for the energy balance closure to guarantee consistency between the two FLUXNET datasets (in the LaThuile dataset energy fluxes were not corrected).

The cumulative soil water index (CSWI, mm) was computed as a measure of water availability according to a previous report²⁷. Half-hourly values of transpiration estimates (T , mm) were calculated with the transpiration estimation algorithm (TEA)²⁸. The TEA has been shown to perform well against both model simulations and independent sap flow data²⁸.

For 101 sites, ecosystem scale foliar N content (N%, gN 100 g⁻¹) was computed as the community weighted average of foliar N% of the major species at the site sampled at the peak of the growing season or gathered from the literature^{29,30,31,32}. Foliar N% for additional sites was derived from the FLUXNET Biological Ancillary Data Management (BADM) product and/or provided by site principal investigators (Supplementary Table 1, Extended Data Fig. 1). It should be noted that this compilation of N% data might suffer from uncertainties resulting from the scaling from leaves to the eddy covariance footprint, the sampling strategy (including the position along the vertical canopy profile), the species selection and the timing of sampling. About 30% of the data comes from a coordinated effort that minimized these uncertainties^{29,30}, and for the others we collected N% data that were representative for the eddy covariance footprint^{31,32}.

Maximum leaf area index (LAI_{max}, $\text{m}^2 \text{ m}^{-2}$) and maximum canopy height (H_c , m) were also collected for 153 and 199 sites, respectively, from the literature^{32,33}, the BADM product, and/or site principal investigators.

Earth observation retrievals of above-ground biomass (AGB, tons of dry matter per hectare (t DM ha^{-1})) were extracted from the GlobBiomass dataset³⁴ at its original resolution (grid cell 100×100 m) for each site location. All the grid cells in a $300 \times$

300 m and 500×500 m window around each location were selected to estimate the median and 95th percentiles of AGB for each site. The median of AGB was selected to avoid the contribution of potential outliers to the expected value of AGB. The analysis further explored the contribution of higher percentiles in the local variation of AGB as previous studies have highlighted the contribution of older and larger trees in uneven stand age plots to ecosystem functioning³⁵. According to the evaluation against AGB measured at 71 FLUXNET sites (Extended Data Fig. 10), we decided to use the product with median AGB values extracted from the 500×500 m window.

A total of 94 sites have all the data on vegetation structure (N%, LAI_{max}, H_c, and AGB).

The list of sites is reported in Supplementary Table 1 along with the plant functional type (PFT), Köppen-Geiger classification, coordinates, and when available N%, LAI_{max}, H_c and AGB.

In this study we did not make use of satellite information, with the exception of the AGB data product. Future studies will benefit from new missions such as the ECOsystem Spaceborne Thermal Radiometer Experiment on Space Station (ECOSTRESS), the fluorescence explorer (FLEX), hyperspectral, and radar and laser detection and ranging (LiDAR) missions (for example, Global Ecosystem Dynamics Investigation (GEDI)), to characterize a multivariate space of structural and functional properties.

Calculation of ecosystem functions from FLUXNET

Starting from half-hourly data, we calculated at each site a single value for each of the ecosystem functions listed below. For the calculations of functional properties we used, unless otherwise indicated, good-quality data: quality flag 0 (measured data) and 1 (good-quality gap-filled data) in the FLUXNET dataset.

Gross primary productivity at light saturation (GPP_{sat})

GPP at light saturation using photosynthetically active radiation as driving radiation and $2,000 \mu\text{mol m}^{-2} \text{s}^{-1}$ as saturating light. GPP_{sat} represents the ecosystem-scale maximum photosynthetic CO₂ uptake^{15,30,36}. The GPP_{sat} was estimated from half-hourly data by fitting the hyperbolic light response curves with a moving window of 5 days and assigned at the centre of the moving window^{30,37}. For each site the 90th percentile from the GPP_{sat} estimates was then extracted.

Maximum net ecosystem productivity (NEP_{max})

This was computed as the 90th percentile of the half-hourly net ecosystem production ($\text{NEP} = -\text{NEE}$) in the growing season (that is, when daily GPP is higher than 30% of the GPP amplitude). This metric represents the maximum net CO_2 uptake of the ecosystem.

Basal ecosystem respiration (R_b and $R_{b\max}$)

Basal ecosystem respiration at reference temperature of 15 °C was derived from night-time NEE measurements²⁶. Daily basal ecosystem respiration (R_{b_d}) was derived by fitting an Arrhenius type equation over a five-day moving window and by keeping the sensitivity to temperature parameter (E_0) fixed as in the night-time partitioning algorithms^{26,38}. R_{b_d} varies across seasons because it is affected by short-term variations in productivity^{33,39}, phenology⁴⁰ and water stress⁴¹. For each site, the mean of the R_{b_d} (R_b) and the 95th percentile ($R_{b\max}$) were computed. The calculations were conducted with the REddyProc R package v.1.2.2 (ref. ³⁸).

Apparent carbon-use efficiency (aCUE)

The aCUE as defined in this study is the efficiency of an ecosystem to sequester the carbon assimilated with photosynthesis³⁹. aCUE is an indication of the proportion of respired carbon with respect to assimilated carbon within one season. A previous report⁶ showed that little of the variability in aCUE can be explained by climate or conventional site characteristics, and suggested an underlying control by plant, faunal and microbial traits, in addition to site disturbance history. Daily aCUE ($a\text{CUE}_d$) is defined as $a\text{CUE}_d = 1 - (R_{b_d}/GPP_d)$, where GPP_d is daily mean GPP and R_{b_d} is derived as described above. For each site, aCUE was computed as the median of $a\text{CUE}_d$.

Metrics of water-use efficiency (WUE)

Various metrics of WUE are described below: stomatal slope or slope coefficient (G1), underlying water-use efficiency (uWUE), and water-use efficiency based on transpiration (WUE_t). The three metrics were used because they are complementary, as shown in previous studies^{11,42}.

Stomatal slope or slope coefficient (G1)

This is the marginal carbon cost of water to the plant carbon uptake. G1 is the key parameter of the optimal stomatal model derived previously⁴³. G1 is inversely related

to leaf-level WUE. At leaf level, G1 is calculated using nonlinear regression and can be interpreted as the slope between stomatal conductance and net CO₂ assimilation, normalized for VPD and CO₂ concentration⁴³. A previous report⁴² showed the potential of the use of G1 at ecosystem scale, where stomatal conductance is replaced by surface conductance (G_s), and net assimilation by GPP. The methodology is implemented in the bigleaf R package⁴⁴. The metric was computed in the following situations: (i) incoming shortwave radiation (SW_{in}) greater than 200 W m⁻²; (ii) no precipitation event for the last 24 h⁴⁵, when precipitation data are available; and (iii) during the growing season: daily GPP > 30% of its seasonal amplitude⁴⁴.

Underlying water-use efficiency (uWUE)

The underlying WUE was computed following a previous method⁴⁶. uWUE is a metric of water-use efficiency that is negatively correlated to G1 at canopy scale⁴⁴:

$$\$ \$ \{ \text{\rm uWUE} \} = \text{frac} \{ \{ \text{\rm GPP} \} / \sqrt{ \{ \{ \text{\rm VPD} \} \} } \} / \{ \{ \text{\rm ET} \} \} . \$ \$$$

uWUE was calculated using the same filtering that was applied for the calculation of G1. The median of the half-hourly retained uWUE values was computed for each site and used as a functional property.

Water-use efficiency based on transpiration (WUE_t)

The WUE based on transpiration (T) was computed to reduce the confounding effect resulting from soil evaporation^{11,28}:

$$\$ \$ \{ \{ \text{\rm WUE} \} \} _t = \text{frac} \{ \{ \text{\rm GPP} \} \} / T , \$ \$$$

where T is the mean annual transpiration calculated with the transpiration estimation algorithm (TEA) developed by in a previous study²⁸ and GPP is the mean annual GPP.

Maximum surface conductance ($G_{s\max}$)

Surface conductance (G_s) was computed by inverting the Penman–Monteith equation after calculating the aerodynamic conductance (G_a).

Among the different formulations of G_a (m s⁻¹) in the literature, we chose to use here the calculation of the canopy (quasi-laminar) boundary layer conductance to heat transfer, which ranges from empirical to physically based (for example, ref. ⁴⁷). Other

studies^{48,49} suggested an empirical relationship between G_a , the horizontal wind speed (u) and the friction velocity, u^* :

$$\$ \$ \{ G \} _{\{ \{ \backslash rm\{ a \} \} \}} = \backslash frac\{ 1 \} \{ (\backslash frac\{ u \} \{ \{ u \} ^\{ * 2 \} \} + 6.2u\{ * \} ^\{ -0.67 \}) \} \$ \$$$

G_s (m s^{-1}) is computed by inverting the Penman–Monteith equation:

$$\$ \$ \{ G \} _{\{ \{ \backslash rm\{ s \} \} \}} = \backslash frac\{ \{ \{ \backslash rm\{ LEG \} \} \} _{\{ \{ \backslash rm\{ a \} \} \}} \backslash gamma \} \{ \backslash Delta \\ (\{ R \} _{\{ \{ \backslash rm\{ n \} \} } - G - S) + \rho \{ C \} _{\{ \{ \backslash rm\{ p \} \} \}} \{ G \} _{\{ \{ \backslash rm\{ a \} \} \}} \{ \backslash rm\{ VPD \} \} - \\ \{ \backslash rm\{ LE \} \} (\Delta + \gamma) \} \$ \$$$

where Δ is the slope of the saturation vapour pressure curve (kPa K^{-1}), ρ is the air density (kg m^{-3}), C_p is the specific heat of the air ($\text{J K}^{-1} \text{kg}^{-1}$), γ is the psychrometric constant (kPa K^{-1}), VPD (kPa), R_n (W m^{-2}), G (W m^{-2}) and S is the sum of all energy storage fluxes (W m^{-2}) and set to 0 as not available in the dataset. When not available, G also was set to 0.

G_s represents the combined conductance of the vegetation and the soil to water vapour transfer. To retain the values with a clear physiological interpretation, we filtered the data as we did for the calculation of G1.

For each site, the 90th percentile of the half-hourly G_s was calculated and retained as the maximum surface conductance of each site (G_{smax}). G_s was computed using the bigleaf R package⁴⁴.

Maximum evapotranspiration in the growing season (ET_{max})

This metric represents the maximum evapotranspiration computed as the 95th percentile of ET in the growing season and using the data retained after the same filtering applied for the G1 calculation.

Evaporative fraction (EF)

EF is the ratio between LE and the available energy, here calculated as the sum of $H + LE$ (ref. ⁵⁰). For the calculation of EF, we used the same filtering strategy as for G1. We first calculated mean daytime EF. We then computed the EF per site as the growing season average of daytime EF. We also computed the amplitude of the EF in the growing season by calculating the interquartile distance of the distribution of mean daytime EF (EF_{amp}).

Principal component analysis

A PCA was conducted on the multivariate space of the ecosystem functions. Each variable (ecosystem functional property, EFP) was standardized using z -transformation (that is, by subtracting its mean value and then dividing by its standard deviation). From the PCA results we extracted the explained variance of each component and the loadings of the EFPs, indicating the contribution of each variable to the component. We performed the PCA using the function `PCA()` implemented in the R package `FactoMineR`⁵¹.

We justify using PCA over nonlinear methods because it is an exploratory technique that is highly suited to the analysis of the data volume used in this study, whereas other nonlinear methods applied to such data would be over-parameterized. For the same reason, PCA was used in previous work concerning the global spectrum of leaf and plant traits, and fluxes^{1,3,52}.

To test the significance of dimensionality of the PCA, we used a previously described methodology⁵³. We used the R package `ade4` (ref. ⁵⁴) and evaluated the number of significant components of the PCA to be retained to minimize both redundancy and loss of information (Supplementary Information ²). We tested the significance of the PCA loadings using a combination of the bootstrapped eigenvector method⁵⁵ and a threshold selected using the number of dimensions⁵⁶ (Supplementary Information ²).

Predictive variable importance

A random forests (RF) analysis was used to identify the vegetation structure and climate variables that contribute the most to the variability of the significant principal components, which were identified with the PCA analysis (see ‘Principal component analysis’). In the main text we refer to the results of this analysis as ‘predictive variable importance’ to distinguish this to the ‘causal variable importance’ described below.

The analysis was conducted using the following predictor variables: as structural variables, N% ($\text{gN } 100 \text{ g}^{-1}$), LAI_{\max} ($\text{m}_2 \text{ m}^{-2}$), AGB (t DM ha^{-1}) and H_c (m); as climatic variables, mean annual precipitation (P , mm), mean VPD during the growing season (VPD, hPa), mean shortwave radiation (SW_{in} , W m^{-2}), mean air temperature (T_{air} , $^{\circ}\text{C}$); and the cumulative soil water index (CSWI, –), as indicator of site water availability.

We used partial dependencies of variables to assess the relationship between individual predictors and the response variable (that is, PC1, PC2 and PC3).

The results from the partial dependency analysis can be used to determine the effects of individual variables on the response, without the influence of the other variables. The partial dependence function was calculated using the `pdp` R package^{[57](#)}.

The partial dependencies were calculated restricted to the values that lie within the convex hull of their training values to reduce the risk of interpreting the partial dependence plot outside the range of the data (extrapolation).

Invariant causal regression models and causal variable importance

We have quantified the dependence of the principal components on the different structural and climatic variables using nonlinear regression. Such dependencies can only be interpreted causally if the regression models are in fact causal regression models (see Supplementary Information [3](#) for a formal definition), which may not be the case if there are hidden confounders. To see whether the regression models allow for a causal interpretation, we use invariant causal prediction^{[58](#)}. This method investigates whether the regression models are stable with respect to different patterns of heterogeneity in the data, encoded by different environments (that is, subsets of the original dataset). The rationale is that a causal model, describing the full causal mechanism for the response variable, should be invariant with respect to changes in the environment if the latter does not directly influence the response variable^{[13,59](#)}. Other non-causal models may be invariant, too, but a non-invariant model cannot be considered causal.

How to choose the environments is a modelling choice that must satisfy the following criteria. First, it should be possible to assign each data point to exactly one environment. Second, the environments should induce heterogeneity in the data, so that, for example, the predictor variables have different distributions across environments. Third, the environments must not directly affect the response variable, only via predictors, although the distribution of the response may still change between environments. The third criterion can be verified by expert knowledge and is assumed to hold for our analysis. In addition, if it is violated, then, usually, no set is invariant^{[58](#)}, which can be detected from data.

In our analysis, we assigned each data point (that is, each site) to one of two environments (two subsets of the original dataset): the first includes forest sites in North America, Europe or Asia; and the second includes non-forest and forest ecosystems from South America, Africa or Oceania, and non-forest ecosystems from North America, Europe or Asia (see Supplementary Information [3.1.3.1](#) for details). Our choice satisfies the method's assumption that the distribution of the predictors is different between the two environments (that is, they induce heterogeneity in the data; see Supplementary Fig. [3.1](#)). Environments that are too small or too homogeneous do

not provide any evidence against the full set of covariates being a candidate for the set of causal predictors. Other choices of environments than the one presented here yield consistent results (Supplementary Information [3.2.1](#), Supplementary Fig. [3.4](#)).

For each subset of predictors, we test whether the corresponding regression model is invariant (yielding the same model fit in each environment). Although many models were rejected and considered non-invariant, the full model (with all the nine predictors and used in the predictive variable importance analysis) was accepted as invariant, establishing the full set of covariates as a reasonable candidate for the set of direct causal predictors. We used both RF (randomForest package in R⁶⁰) and generalized additive models, GAM⁶¹ (mgcv package⁶² in R) to fit the models. Both methods lead to comparable results but with a better average performance of the RF: GAM led to slightly better results than RF for PC1, whereas for PC2 and PC3 RF showed a much better model performance (Supplementary Table [3.1](#), Supplementary Information [3.2.2](#)). Therefore, in the main text we showed only the results from the RF (except for PC1).

If, indeed, the considered regression models are causal, this allows us to make several statements. First, we can test for the existence of causal effects by testing for statistical significance of the respective predictors in the fitted models. Second, we can use the response curves of the fitted model to define a variable importance measure with a causal interpretation. In the main text we refer to this variable importance as ‘causal variable importance’. For details, see Supplementary Information [3.1.2](#). More formally, we considered the expected value of the predicted variables (the principal components) under joint interventions on all covariates (AGB , H_c , LAI_{max} , $N\%$, T_{air} , VPD , SW_{in} , $CSWI$ and P) at once, and then, to define the importance, we quantified how this expected value depends on the different covariates. We applied the same analysis to groups of vegetation structural and climate covariates (see ‘Groupwise variable importance’ in Supplementary Information [3.1.2.3](#), [3.2.3](#)).

The details of the methodology and the results are described in Supplementary Information [3](#), in which we also provide further details on the choice of environment variable and on the statistical tests that we use to test for invariance. An overview of the invariance-based methodology is shown in Supplementary Fig. [3.1](#).

Land surface model runs

We run two widely used land surface models: Orchidee-CN (OCN) and Jena Scheme for Biosphere Atmosphere Coupling in Hamburg (JSBACH):

OCN

The dynamic global vegetation model OCN is a model of the coupled terrestrial carbon and nitrogen cycles^{63,64}, derived from the ORCHIDEE land surface model. It operates at a half-hourly timescale and simulates diurnal net carbon, heat and water exchanges, as well as nitrogen trace gas emissions, which jointly affect the daily changes in leaf area index, foliar nitrogen, and vegetation structure and growth. The main purpose of the model is to analyse the longer-term (interannual to decadal) implication of nutrient cycling for the modelling of land–climate interactions^{64,65}. The model can run offline, driven by observed meteorological parameters, or coupled to the global circulation model.

JSBACH

JSBACH v.3 is the land surface model of the MPI Earth System Model^{66,67}. The model operates at a half-hourly time step and simulates the diurnal net exchange of momentum, heat, water and carbon with the atmosphere. Daily changes in leaf area index and leaf photosynthetic capacity are derived from a prognostic scheme assuming a PFT-specific set maximum leaf area index and a set of climate responses modulating the seasonal course of leaf area index. Carbon pools are prognostic allowing for simulating the seasonal course of net land–atmosphere carbon exchanges.

We selected OCN and JSBACH because they are widely used land surface models with different structures. JSBACH is a parsimonious representation of the terrestrial energy, water and carbon exchanges used to study the coupling of land and atmosphere processes in an Earth system model⁶⁷. OCN has also been derived from the land surface model ORCHIDEE⁶⁸, but it includes a more comprehensive representation of plant physiology, including a detailed representation of the tight coupling of the C and N cycling⁶³. Both models contribute to the annual global carbon budget of the Global Carbon Project⁶⁹ and have shown good performance compared to a number of global benchmarks. OCN was further used in several model syntheses focused on the interaction between changing N deposition and CO₂ fertilization^{70,71,72}. Both OCN and JSBACH can operate at a half-hourly timescale and simulate net and gross carbon exchanges, water and energy fluxes, and therefore are ideal for the extraction of ecosystem functional properties, as done with the eddy covariance data.

The models were driven by half-hourly meteorological variables (shortwave and longwave downward flux, air temperature and humidity, precipitation, wind speed and atmospheric CO₂ concentrations) observed at the eddy covariance sites. OCN was furthermore driven by N deposition fields⁷³. Vegetation type, soil texture and plant available water were prescribed on the basis of site observations, but no additional site-specific parameterization was used. Both models were brought into equilibrium with respect to their ecosystem water storage and biogeochemical pools by repeatedly

looping over the available site years. We added random noise (mean equal to 0 and standard deviation of 5% of the flux value) to the fluxes simulated by the models to mimic the random noise of the eddy covariance flux observations. An additional test conducted without noise addition showed only a marginal effect on the calculations of the functional properties and the ecosystem functional space.

We used runs of the JSBACH and OCN model for 48 FLUXNET sites (Supplementary Table 1). The simulated fluxes were evaluated against the observation to assess the performance of the models at the selected sites. From the model outputs and from each site we derived the ecosystem functions using the same methodology described above. Then the PCA analysis was performed on the three datasets (FLUXNET, OCN and JSBACH) and restricted to the 48 sites used to run the models. We ran the models only on the subset of sites for which the information for the parameterization and high-quality forcing was available. However, the different ecosystem functions emerge from the model structure and climatological conditions. Therefore, even with a smaller set of site we can evaluate whether models reproduce the key dimensions of terrestrial ecosystem function by comparing the PCA results from FLUXNET and the model runs.

Reporting summary

Further information on research design is available in the [Nature Research Reporting Summary](#) linked to this paper.

Data availability

Data used for this study are the FLUXNET dataset LaThuile (<https://fluxnet.fluxdata.org/data/la-thuile-dataset/>) and FLUXNET2015 (<https://fluxnet.fluxdata.org/data/fluxnet2015-dataset/>). Biological, ancillary, disturbance and metadata information for the sites were collected from databases and the literature and are available at the following address together with the reproducible workflow (<https://doi.org/10.5281/zenodo.5153538>). OCN and JSBACH model runs are available in the reproducible workflow (<https://doi.org/10.5281/zenodo.5153538>).

Code availability

The R codes used for this analysis are available at: <https://doi.org/10.5281/zenodo.5153538>. The R codes for the causality analysis are available at: <https://doi.org/10.5281/zenodo.5153534>. The TEA algorithm is available at <https://doi.org/10.5281/zenodo.3921923>.

References

1. 1.

Wright, I. J. et al. The worldwide leaf economics spectrum. *Nature* **428**, 821–827 (2004).

2. 2.

Reich, P. B., Walters, M. B. & Ellsworth, D. S. From tropics to tundra: global convergence in plant functioning. *Proc. Natl Acad. Sci. USA* **94**, 13730–13734 (1997).

3. 3.

Díaz, S. et al. The global spectrum of plant form and function. *Nature* **529**, 167–171 (2016).

4. 4.

Bruelheide, H. et al. Global trait–environment relationships of plant communities. *Nat. Ecol. Evol.* **2**, 1906–1917 (2018).

5. 5.

Manning, P. et al. Redefining ecosystem multifunctionality. *Nat. Ecol. Evol.* **2**, 427–436 (2018).

6. 6.

Reichstein, M., Bahn, M., Mahecha, M. D., Kattge, J. & Baldocchi, D. D. Linking plant and ecosystem functional biogeography. *Proc. Natl Acad. Sci. USA* **111**, 13697–13702 (2014).

7. 7.

Anderegg, W. R. L. et al. Climate-driven risks to the climate mitigation potential of forests. *Science* **368**, eaaz7005 (2020).

8. 8.

Bonan, G. B. Forests and climate change: forcings, feedbacks, and the climate benefits of forests. *Science* **320**, 1444–1449 (2008).

9. 9.

Baldocchi, D. ‘Breathing’ of the terrestrial biosphere: lessons learned from a global network of carbon dioxide flux measurement systems. *Aust. J. Bot.* **56**, 1–26 (2008).

10. 10.

Pastorello, G. et al. The FLUXNET2015 dataset and the ONEFlux processing pipeline for eddy covariance data. *Sci. Data* **7**, 225 (2020).

11. 11.

Nelson, J. A. et al. Ecosystem transpiration and evaporation: insights from three water flux partitioning methods across FLUXNET sites. *Global Change Biol.* **26**, 6916–6930 (2020).

12. 12.

Janssens, I. A. et al. Productivity overshadows temperature in determining soil and ecosystem respiration across European forests. *Global Change Biol.* **7**, 269–278 (2001).

13. 13.

Pearl, J. *Causality* (Cambridge University Press, 2009).

14. 14.

Krich, C. et al. Functional convergence of biosphere–atmosphere interactions in response to meteorological conditions. *Biogeosciences* **18**, 2379–2404 (2021).

15. 15.

Musavi, T. et al. Stand age and species richness dampen interannual variation of ecosystem-level photosynthetic capacity. *Nat. Ecol. Evol.* **1**, 0048 (2017).

16. 16.

Ryan, M. G., Phillips, N. & Bond, B. J. The hydraulic limitation hypothesis revisited. *Plant Cell Environ.* **29**, 367–381 (2006).

17. 17.

De Kauwe, M. G., Medlyn, B. E., Knauer, J. & Williams, C. A. Ideas and perspectives: how coupled is the vegetation to the boundary layer? *Biogeosciences* **14**, 4435–4453 (2017).

18. 18.

Skubel, R. et al. Age effects on the water-use efficiency and water-use dynamics of temperate pine plantation forests. *Hydrol. Processes* **29**, 4100–4113 (2015).

19. 19.

Law, B. E., Thornton, P. E., Irvine, J., Anthoni, P. M. & Van Tuyl, S. Carbon storage and fluxes in ponderosa pine forests at different developmental stages. *Global Change Biol.* **7**, 755–777 (2001).

20. 20.

Collalti, A. et al. Forest production efficiency increases with growth temperature. *Nat. Commun.* **11**, 5322 (2020).

21. 21.

DeLucia, E. H., Drake, J. E., Thomas, R. B. & Gonzalez-Meler, M. Forest carbon use efficiency: is respiration a constant fraction of gross primary production? *Global Change Biol.* **13**, 1157–1167 (2007).

22. 22.

Fernández-Martínez, M. et al. Nutrient availability as the key regulator of global forest carbon balance. *Nat. Clim. Change* **4**, 471–476 (2014).

23. 23.

Kennedy, D. et al. Implementing plant hydraulics in the community land model, version 5. *J. Adv. Model. Earth Syst.* **11**, 485–513 (2019).

24. 24.

Manzoni, S. et al. Reviews and syntheses: carbon use efficiency from organisms to ecosystems – definitions, theories, and empirical evidence. *Biogeosciences* **15**, 5929–5949 (2018).

25. 25.

Eyring, V. et al. Earth System Model Evaluation Tool (ESMValTool) v2.0 – an extended set of large-scale diagnostics for quasi-operational and comprehensive evaluation of Earth system models in CMIP. *Geosci. Model Dev.* **13**, 3383–3438 (2020).

26. 26.

Reichstein, M. et al. On the separation of net ecosystem exchange into assimilation and ecosystem respiration: review and improved algorithm. *Global Change Biol.* **11**, 1424–1439 (2005).

27. 27.

Nelson, J. A., Carvalhais, N., Migliavacca, M., Reichstein, M. & Jung, M. Water-stress-induced breakdown of carbon–water relations: indicators from diurnal FLUXNET patterns. *Biogeosciences* **15**, 2433–2447 (2018).

28. 28.

Nelson, J. et al. Coupling water and carbon fluxes to constrain estimates of transpiration: the TEA algorithm. *J. Geophys. Res. Biogeosci.* **123**, 3617–3632 (2018).

29. 29.

Musavi, T. et al. The imprint of plants on ecosystem functioning: a data-driven approach. *Int. J. Appl. Earth Obs. Geoinf.* **43**, 119–131 (2015).

30. 30.

Musavi, T. et al. Potential and limitations of inferring ecosystem photosynthetic capacity from leaf functional traits. *Ecol. Evol.* **6**, 7352–7366 (2016).

31. 31.

Fleischer, K. et al. Low historical nitrogen deposition effect on carbon sequestration in the boreal zone. *J. Geophys. Res. Biogeosci.* **120**, 2542–2561 (2015).

32. 32.

Flechard, C. R. et al. Carbon–nitrogen interactions in European forests and semi-natural vegetation. Part I: Fluxes and budgets of carbon, nitrogen and greenhouse

gases from ecosystem monitoring and modelling. *Biogeosciences* **17**, 1583–1620 (2020).

33. 33.

Migliavacca, M. et al. Semiempirical modeling of abiotic and biotic factors controlling ecosystem respiration across eddy covariance sites. *Global Change Biol.* **17**, 390–409 (2011).

34. 34.

Santoro, M. et al. The global forest above-ground biomass pool for 2010 estimated from high-resolution satellite observations. *Earth Syst. Sci. Data* **13**, 3927–3950 (2021).

35. 35.

Besnard, S. et al. Quantifying the effect of forest age in annual net forest carbon balance. *Environ. Res. Lett.* **13**, 124018 (2018).

36. 36.

Migliavacca, M. et al. Seasonal and interannual patterns of carbon and water fluxes of a poplar plantation under peculiar eco-climatic conditions. *Agric. For. Meteorol.* **149**, 1460–1476 (2009).

37. 37.

Gilmanov, T. G. et al. Productivity, respiration, and light-response parameters of world grassland and agroecosystems derived from flux-tower measurements. *Rangel. Ecol. Manag.* **63**, 16–39 (2010).

38. 38.

Wutzler, T. et al. Basic and extensible post-processing of eddy covariance flux data with REddyProc. *Biogeosciences* **15**, 5015–5030 (2018).

39. 39.

Mahecha, M. D. et al. Global convergence in the temperature sensitivity of respiration at ecosystem level. *Science* **329**, 838–840 (2010).

40. 40.

Migliavacca, M. et al. Influence of physiological phenology on the seasonal pattern of ecosystem respiration in deciduous forests. *Global Change Biol.* **21**, 363–376 (2015).

41. 41.

Reichstein, M. et al. Modeling temporal and large-scale spatial variability of soil respiration from soil water availability, temperature and vegetation productivity indices. *Global Biogeochem. Cycles* **17**, 1104 (2003).

42. 42.

Knauer, J. et al. Towards physiologically meaningful water-use efficiency estimates from eddy covariance data. *Global Change Biol.* **24**, 694–710 (2018).

43. 43.

Medlyn, B. E. et al. Reconciling the optimal and empirical approaches to modelling stomatal conductance. *Global Change Biol.* **17**, 2134–2144 (2011).

44. 44.

Knauer, J., El-Madany, T. S., Zaehle, S. & Migliavacca, M. bigleaf—an R package for the calculation of physical and physiological ecosystem properties from eddy covariance data. *PloS ONE* **13**, e0201114 (2018).

45. 45.

Knohl, A. & Buchmann, N. Partitioning the net CO₂ flux of a deciduous forest into respiration and assimilation using stable carbon isotopes. *Global Biogeochem. Cycles* **19**, GB4008 (2005).

46. 46.

Zhou, S., Yu, B., Huang, Y. & Wang, G. The effect of vapor pressure deficit on water use efficiency at the subdaily time scale. *Geophys. Res. Lett.* **41**, 5005–5013 (2014).

47. 47.

Verhoef, A., De Bruin, H. A. R. & Van Den Hurk, B. J. J. M. Some practical notes on the parameter kB⁻¹ for sparse vegetation. *J. Appl. Meteorol.* **36**, 560–572 (1997).

48. 48.

Thom, A. S. in *Vegetation and the Atmosphere* (ed. Monteith, J. L.) 57–109 (Academic Press, 1975).

49. 49.

Thom, A. S. Momentum, mass and heat exchange of vegetation. *Q. J. R. Meteorolog. Soc.* **98**, 124–134 (1972).

50. 50.

Gentine, P., Entekhabi, D., Chehbouni, A., Boulet, G. & Duchemin, B. Analysis of evaporative fraction diurnal behaviour. *Agric. For. Meteorol.* **143**, 13–29 (2007).

51. 51.

Husson, F., Le, S. & Pages, J. *Exploratory Multivariate Analysis by Example Using R* (CRC Press, 2010).

52. 52.

Kraemer, G., Camps-Valls, G., Reichstein, M. & Mahecha, M. D. Summarizing the state of the terrestrial biosphere in few dimensions. *Biogeosciences* **17**, 2397–2424 (2020).

53. 53.

Dray, S. On the number of principal components: a test of dimensionality based on measurements of similarity between matrices. *Comput. Stat. Data Anal.* **52**, 2228–2237 (2008).

54. 54.

Dray, S. & Dufour, A.-B. The ade4 package: implementing the duality diagram for ecologists. *J. Stat. Softw.* **22**, 20 (2007).

55. 55.

Peres-Neto, P. R., Jackson, D. A. & Somers, K. M. Giving meaningful interpretation to ordination axes: assessing loading significance in principal component analysis. *Ecology* **84**, 2347–2363 (2003).

56. 56.

Richman, M. B. A cautionary note concerning a commonly applied eigenanalysis procedure. *Tellus B* **40B**, 50–58 (1988).

57. 57.

Friedman, J. H. Greedy function approximation: a gradient boosting machine. *Ann. Statist.* **29**, 1189–1232 (2001).

58. 58.

Peters, J., Bühlmann, P. & Meinshausen, N. Causal inference by using invariant prediction: identification and confidence intervals. *J. R. Stat. Soc. B* **78**, 947–1012 (2016).

59. 59.

Haavelmo, T. The probability approach in econometrics. *Econometrica* **12**, 1–115 (1944).

60. 60.

Breiman, L. Random Forests. *Mach. Learn.* **45**, 5–32 (2001).

61. 61.

Hastie, T. J. & Tibshirani, R. J. *Generalized Additive Models* Vol. 43 (CRC Press, 1990).

62. 62.

Wood, S. N. Fast stable restricted maximum likelihood and marginal likelihood estimation of semiparametric generalized linear models. *J. R. Stat. Soc. B* **73**, 3–36 (2011).

63. 63.

Zaehle, S. & Friend, A. D. Carbon and nitrogen cycle dynamics in the O-CN land surface model: 1. Model description, site-scale evaluation, and sensitivity to parameter estimates. *Global Biogeochem. Cycles* **24**, GB1005 (2010).

64. 64.

Zaehle, S. et al. Carbon and nitrogen cycle dynamics in the O-CN land surface model: 2. Role of the nitrogen cycle in the historical terrestrial carbon balance. *Global Biogeochem. Cycles* **24**, GB1006 (2010).

65. 65.

Zaehle, S., Friedlingstein, P. & Friend, A. D. Terrestrial nitrogen feedbacks may accelerate future climate change. *Geophys. Res. Lett.* **37**, L01401 (2010).

66. 66.

Raddatz, T. J. et al. Will the tropical land biosphere dominate the climate–carbon cycle feedback during the twenty-first century? *Clim. Dyn.* **29**, 565–574 (2007).

67. 67.

Mauritsen, T. et al. Developments in the MPI-M Earth system model version 1.2 (MPI-ESM1.2) and its response to increasing CO₂. *J. Adv. Model. Earth Syst.* **11**, 998–1038 (2019).

68. 68.

Krinner, G. et al. A dynamic global vegetation model for studies of the coupled atmosphere-biosphere system. *Global Biogeochem. Cycles* **19**, GB1015 (2005).

69. 69.

Friedlingstein, P. et al. Global carbon budget 2019. *Earth Syst. Sci. Data* **11**, 1783–1838 (2019).

70. 70.

Fleischer, K. et al. Amazon forest response to CO₂ fertilization dependent on plant phosphorus acquisition. *Nat. Geosci.* **12**, 736–741 (2019).

71. 71.

Meyerholt, J. & Zaehle, S. Controls of terrestrial ecosystem nitrogen loss on simulated productivity responses to elevated CO₂. *Biogeosciences* **15**, 5677–5698 (2018).

72. 72.

Zaehle, S. et al. Evaluation of 11 terrestrial carbon-nitrogen cycle models against observations from two temperate free-air CO₂ enrichment studies. *New Phytol.* **202**, 803–822 (2014).

73. 73.

Zaehle, S., Ciais, P., Friend, A. D. & Prieur, V. Carbon benefits of anthropogenic reactive nitrogen offset by nitrous oxide emissions. *Nat. Geosci.* **4**, 601–605 (2011).

74. 74.

Wickham, H. *ggplot2: Elegant Graphics for Data Analysis* (Springer-Verlag, 2016).

75. 75.

Whittaker, R. H. *Communities and Ecosystems* 2nd edn (MacMillan Publishing Co., 1975).

76. 76.

Ricklefs, R. E. *The Economy of Nature* 6th ed. Ch. 5 (W. H. Freeman, 2008).

77. 77.

Liu, Y., Schwalm, C. R., Samuels-Crow, K. E. & Ogle, K. Ecological memory of daily carbon exchange across the globe and its importance in drylands. *Ecol. Lett.* **22**, 1806–1816 (2019).

Acknowledgements

This work has received funding from the European Union’s Horizon 2020 research and innovation programme under the Marie Skłodowska-Curie grant agreement no. 721995. M.M. and M. Reichstein acknowledge the Alexander Von Humboldt Foundation for funding with the Max Planck Research Prize 2013 to M. Reichstein. This work used eddy covariance data acquired and shared by the FLUXNET community, including these networks: AmeriFlux, AfriFlux, AsiaFlux, CarboAfrica, CarboEuropeIP, CarboItaly, CarboMont, ChinaFlux, Fluxnet-Canada, GreenGrass, ICOS, KoFlux, LBA, NECC, OzFlux-TERN, Swiss FluxNet, TCOS-Siberia and USCCC. The ERA-Interim reanalysis data were provided by ECMWF and processed by LSCE. The FLUXNET eddy covariance data processing and harmonization was carried out by the European Fluxes Database Cluster, the AmeriFlux Management

Project and the Fluxdata project of FLUXNET, with the support of the CDIAC and the ICOS Ecosystem Thematic Center, and the OzFlux, ChinaFlux and AsiaFlux offices. R.C. and J. Peters were supported by the VILLUM FONDEN (18968) and J. Peters in addition by the Carlsberg Foundation; P.R. acknowledges funding support from the US National Science Foundation (NSF) Long-Term Ecological Research (DEB-1831944) and Biological Integration Institutes (NSF-DBI-2021898); N.B. acknowledges funding from various SNF projects, including ICOS-CH (20FI21_148992, 20FI20_173691), the ETH Board and ETH Zurich (TH-1006-02); and T.F.K. acknowledges support from the Reducing Uncertainties in Biogeochemical Interactions through Synthesis and Computation Scientific Focus Area (RUBISCO SFA), which is sponsored by the Regional and Global Model Analysis (RGMA) Program of the Office of Biological and Environmental Research (BER) in the US Department of Energy Office of Science. OzFlux is supported by the Australian Government's Terrestrial Ecosystem Research Network (TERN, www.tern.org.au). We thank K. Morris and S. Paulus for comments on the draft, K. Blakeslee for English editing and G. Bohrer for sharing nitrogen data for his site.

Funding

Open access funding provided by Max Planck Society.

Author information

Author notes

1. Mirco Migliavacca

Present address: European Commission, Joint Research Centre (JRC), Ispra, Italy

2. Jürgen Knauer

Present address: Hawkesbury Institute for the Environment, Western Sydney University, Penrith, New South Wales, Australia

Affiliations

1. Max Planck Institute for Biogeochemistry, Jena, Germany

Mirco Migliavacca, Talie Musavi, Miguel D. Mahecha, Jacob A. Nelson, Silvia Calderaru, Nuno Carvalhais, Tarek S. El-Madany, Ulisse Gomarasca, Mathias Göckede, Martin Jung, Jens Kattge, David Martini, Daniel E. Pabon-Moreno, Ulrich Weber, Sönke Zaehle & Markus Reichstein

2. German Centre for Integrative Biodiversity Research (iDiv), Halle-Jena-Leipzig, Germany

Mirco Migliavacca, Miguel D. Mahecha, Jens Kattge & Markus Reichstein

3. Remote Sensing Center for Earth System Research, Leipzig University, Leipzig, Germany

Miguel D. Mahecha & Guido Kraemer

4. Helmholtz Centre for Environmental Research – UFZ, Leipzig, Germany

Miguel D. Mahecha

5. CSIRO Oceans and Atmosphere, Canberra, Australian Capital Territory, Australia

Jürgen Knauer

6. Department of Environmental Science, Policy and Management, University of California, Berkeley, Berkeley, CA, USA

Dennis D. Baldocchi & Trevor F. Keenan

7. Department of Forest Engineering, ERSAF Research Group, University of Cordoba, Cordoba, Spain

Oscar Perez-Priego

8. Department of Mathematical Sciences, University of Copenhagen, Copenhagen, Denmark

Rune Christiansen & Jonas Peters

9. Environment and Sustainability Institute, University of Exeter, Penryn, UK

Karen Anderson

10. Department of Ecology, University of Innsbruck, Innsbruck, Austria

Michael Bahn & Georg Wohlfahrt

11. Faculty of Land and Food Systems, Vancouver, British Columbia, Canada

T. Andrew Black

12. Department of Geography, University of Colorado, Boulder, CO, USA

Peter D. Blanken

13. Université de Lorraine, AgroParisTech, INRAE, UMR Silva, Nancy,
France

Damien Bonal

14. Department of Environmental Systems Science, ETH Zurich, Zurich,
Switzerland

Nina Buchmann & Sebastian Wolf

15. Fundación Centro de Estudios Ambientales del Mediterráneo
(CEAM), Paterna, Spain

Arnaud Carrara

16. Departamento de Ciências e Engenharia do Ambiente, Universidade
Nova de Lisboa, Caparica, Portugal

Nuno Carvalhais

17. European Commission, Joint Research Centre (JRC), Ispra, Italy

Alessandro Cescatti

18. Landscape Ecology & Ecosystem Science (LEES) Lab, Center for
Global Change and Earth Observations, and Department of
Geography, Environmental and Spatial Science, Michigan State
University, East Lansing, MI, USA

Jiquan Chen

19. School of Life Sciences, University of Technology Sydney, Ultimo,
New South Wales, Australia

Jamie Cleverly

20. Terrestrial Ecosystem Research Network, College of Science and Engineering, James Cook University, Cairns, Queensland, Australia

Jamie Cleverly

21. Climate Change Unit, Environmental Protection Agency of Aosta Valley, Aosta, Italy

Edoardo Cremonese, Gianluca Filippa & Marta Galvagno

22. Department of Atmospheric and Oceanic Sciences, University of Wisconsin-Madison, Madison, WI, USA

Ankur R. Desai

23. O'Neill School of Public and Environmental Affairs, Indiana University, Bloomington, IN, USA

Martha M. Farella

24. Research Group Plant and Ecosystems (PLECO), Department of Biology, University of Antwerp, Wilrijk, Belgium

Marcos Fernández-Martínez & Ivan A. Janssens

25. Institute of Photogrammetry and Remote Sensing, TU Dresden, Dresden, Germany

Matthias Forkel

26. Department of Biology, Virginia Commonwealth University, Richmond, VA, USA

Christopher M. Gough

27. Department of Environmental Engineering, Technical University of Denmark (DTU), Kongens Lyngby, Denmark

Andreas Ibrom

28. Institute for Agro-Environmental Sciences, National Agriculture and Food Research Organization, Tsukuba, Japan

Hiroki Ikawa

29. Earth and Environmental Science Area, Lawrence Berkeley National Laboratory, Berkeley, CA, USA

Trevor F. Keenan

30. Bioclimatology, Faculty of Forest Sciences and Forest Ecology, University of Goettingen, Goettingen, Germany

Alexander Knohl

31. Centre of Biodiversity and Sustainable Land Use (CBL), University of Goettingen, Goettingen, Germany

Alexander Knohl

32. Research Institute for Global Change, Institute of Arctic Climate and Environment Research, Japan Agency for Marine-Earth Science and Technology (JAMSTEC), Yokohama, Japan

Hideki Kobayashi

33. Image Processing Laboratory (IPL), Universitat de València, València, Spain

Guido Kraemer

34. Department of Forest Ecosystems and Society, Oregon State University, Corvallis, OR, USA

Beverly E. Law

35. Centre for Tropical, Environmental, and Sustainability Sciences, James Cook University, Cairns, Queensland, Australia

Michael J. Liddell

36. College of Earth and Environmental Sciences, Lanzhou University, Lanzhou, China

Xuanlong Ma

37. Institute for Atmospheric and Earth System Research/Physics, Faculty of Science, University of Helsinki, Helsinki, Finland

Ivan Mammarella

38. CSIRO Land and Water, Floreat, Western Australia, Australia

Craig Macfarlane

39. Consiglio Nazionale delle Ricerche, Istituto per la BioEconomia (CNR – IBE), Sesto Fiorentino, Italy

Giorgio Matteucci

40. Facoltà di Scienze e Tecnologie, Libera Universita' di Bolzano, Bolzano, Italy

Leonardo Montagnani

41. Forest Services of the Autonomous Province of Bozen-Bolzano, Bolzano, Italy

Leonardo Montagnani

42. Department of Earth and Environmental Sciences (DISAT), University of Milano-Bicocca, Milan, Italy

Cinzia Panigada & Micol Rossini

43. Department for Innovation in Biological, Agro-Food and Forest Systems (DIBAF), University of Tuscia, Viterbo, Italy

Dario Papale

44. Hawkesbury Institute for the Environment, Western Sydney University, Penrith, New South Wales, Australia

Elise Pendall, Peter B. Reich & Ian J. Wright

45. CSIC, Global Ecology Unit CREAF-CSIC-UAB, Barcelona, Spain

Josep Penuelas

46. CREAF, Barcelona, Spain

Josep Penuelas

47. Department of Biology, Indiana University, Bloomington, IN, USA

Richard P. Phillips

48. Department of Forest Resources, University of Minnesota, Saint Paul, MN, USA

Peter B. Reich

49. Institute for Global Change Biology and School for Environment and Sustainability, University of Michigan, Ann Arbor, MI, USA

Peter B. Reich

50. Department of Earth and Planetary Sciences, Weizmann Institute of Science, Rehovot, Israel

Eyal Rotenberg & Dan Yakir

51. Southwest Watershed Research Center, USDA Agricultural Research Service, Tucson, AZ, USA

Russell L. Scott

52. INRAE, UMR EcoFoG, CNRS, Cirad, AgroParisTech, Université des Antilles, Université de Guyane, Kourou, France

Clement Stahl

53. Department of Biological Sciences, Macquarie University, Sydney, New South Wales, Australia

Ian J. Wright

54. Michael-Stifel-Center Jena for Data-driven and Simulation Science, Friedrich-Schiller-Universität Jena, Jena, Germany

Markus Reichstein

Contributions

M.M., M. Reichstein, M.D.M. and T.M. conceived the study. M.M. and T.M. performed the majority of the analysis. R.C. and J. Peters designed and coded the causality analysis. J.A.N. provided the transpiration partitioning data. J. Knauer and S.Z. performed the land surface model runs. N.C. and U.W. processed the above-ground biomass data. O.P.-P. provided support with data analysis and discussions. M.M. wrote the first draft. All of the authors participated in intensive discussions on the manuscript and the revision phase, and contributed to writing the final manuscript. In addition, many site principal investigators contributed with additional data for their site.

Corresponding authors

Correspondence to Mirco Migliavacca or Markus Reichstein.

Ethics declarations

Competing interests

The authors declare no competing interests.

Additional information

Peer review information *Nature* thanks J. Hans C. Cornelissen, Diego Miralles and the other, anonymous, reviewer(s) for their contribution to the peer review of this work.

Publisher's note Springer Nature remains neutral with regard to jurisdictional claims in published maps and institutional affiliations.

Extended data figures and tables

[Extended Data Fig. 1 Map of the 203 FLUXNET sites used in this analysis.](#)

Colours represent different plant functional types according to the IGBP classification. IGBP classes are: CSH (close shrublands); DBF (deciduous broadleaved forest), DNF (deciduous needleleaf forests), EBF (evergreen broadleaved forest), ENF (evergreen needleleaf forest), GRA (grasslands), MF (mixed forest), OSH (open shrublands), SAV (savannah), and WET (wetlands). The map was generated with the ggplot2 R package⁷⁴. The shape files used to create the maps were downloaded from <https://github.com/ngageoint/geopackage-js>.

[Extended Data Fig. 2 FLUXNET sites used in the analysis plotted in the precipitation–temperature space.](#)

The background represent climate space of the major biomes according to Whittaker⁷⁵ and further modifications⁷⁶. Biomes are defined as function of the mean annual temperature and mean annual precipitation (MAP). The figure is modified from Liu et al.,⁷⁷ using the code available in git (<https://github.com/kunstler/BIOMEplot>).

Extended Data Fig. 3 Distribution of the selected FLUXNET sites within the climate types.

Climate types were defined according to Köppen-Geiger classification as follow: Tropical (Aw, Af, Am), Dry (BSh, BSk, BWh), Temperate (Cfb), Sub-Tropical (Cfa, Csa, Csb, Cwa), Temperate/Continental Hot (Dfa, Dfb, Dwa, Dwb, Dwc), Arctic (ET)], and Boreal (Dfc, Dsc).

Extended Data Fig. 4 Results of the relative importance analysis conducted with the Random Forest and partial dependence.

See ‘Predictive variable importance’ in Methods. The slopes of the partial dependence plot indicate the sensitivity of the response (PCs) to the specific predictor. The out-of-bag cross-validation leads to predictive explained variance of 56.76% for PC1, 30.24% for PC2, and 20.41% for PC3. The portion of unexplained variance might be related to missing leaf traits predictor such as leaf mass per area or phenological traits. The partial dependence plots of all variables are shown: top panels for PC1 (a–e), middle panels for PC2 (f–l), and bottom panels for PC3 (m–q). The blue lines represent the locally estimated scatterplot (LOESS) smoothing of the partial dependence. Tick marks in the x axis represent the minimum, maximum and deciles of the variable distribution.

Extended Data Fig. 5 Map of FLUXNET sites colour-coded for the value of PC1 and PC2.

a, PC1. **b**, PC2. The map of the PC1 shows the areas of the globe with high productivity (positive values of PC1 in the temperate areas, Eastern North America, Eastern Asia, and Tropics), and areas characterized by lower productivity (Semi-arid regions, high latitude and Mediterranean ecosystems). The map of the PC2 shows the gradient of evaporative fraction and the spatial patterns of water use efficiency. This PC2 runs from sites with a high evaporative fraction (i.e. available energy is dissipated preferentially to evaporated or transpired water), high surface conductance, and low water use efficiency (positive PC2 values), to water limited sites

(i.e. low evaporative fraction where available energy is mainly dissipated by sensible heat) that also show higher water-use efficiency (negative PC2 values). The maps were generated with the ggplot2 R package⁷⁴. The shape files used to create the maps were downloaded from <https://github.com/ngageoint/geopackage-js>.

Extended Data Fig. 6 Biplot resulting from the principal component analysis.

Plot as in Fig. 1. In panel a, points are colour-coded by grass vs. non-grass classes. In panel b, the points are colour-coded according to the logarithm of vegetation height. From these results we conclude that there is not a clear cluster in the biplot for grass and non-grass vegetation. In fact, in Extended Data Fig. 6a, the sites do not cluster according to the designation to grasslands or not, but there is a clear gradient as a function of the vegetation height (Extended Data Fig. 6b).

Extended Data Fig. 7 Comparing observed and modelled global ecosystem functional trade-offs.

PCA for a subset of 48 FLUXNET sites mainly distributed in temperate and boreal regions and 2 different land surface models (Supplementary Table 1). The left column is FLUXNET, the centre column is OCN, and the right column is JSBACH. Panels a, b, c: the biplot resulting from the PCA. Panels d, e, f, bar plot of the loading of each ecosystem functional property to each principal component. Orange bars represent the loadings that are selected as significant and with high contribution (Supplementary Information 2). Panels g, h, i report the variance explained by each principal component. EFP acronym list: apparent carbon-use efficiency (aCUE), evaporative fraction (EF), amplitude of EF (EF_{amp}), maximum evapotranspiration (ET_{max}), gross primary productivity at light saturation (GPP_{sat}), maximum surface conductance (G_{smax}), maximum net ecosystem productivity (NEP_{max}), maximum and mean basal ecosystem respiration (Rb_{max} and Rb , respectively), and growing season underlying water-use efficiency (uWUE). Note that the PCA results for FLUXNET (panels a, d,

g) are different from Fig. 1 because here we use the subset of 48 sites used for the modelling analysis.

Extended Data Fig. 8 Pairwise relationship between some key ecosystem functional properties derived from FLUXNET, and modelled with JSBACH and OCN.

$n = 48$ sites; see Supplementary Table 1. The grey areas represent the 95% confidence interval of the linear and nonlinear regression. Overall the correlation between modelled functions is larger than in the observations. Acronym list: evaporative fraction (EF), amplitude of EF (EF_{ampl}), gross primary productivity at light saturation (GPP_{sat}), maximum surface conductance (G_s), maximum net ecosystem productivity (NEP_{max}), basal ecosystem respiration (R_b), and growing season underlying water-use efficiency (uWUE).

Extended Data Fig. 9 Representation of the 2D ecosystem functional properties space derived from FLUXNET observations and land surface model runs (OCN, JSBACH).

The points represent the principal component (PC) value calculate for each site. The contour lines are computed using a 2D kernel density estimates. The contour lines show the area occupied by ecosystem functional properties and its boundary that, according to the results of the analysis, are set by vegetation characteristics (PC1), water availability, abiotic limitations, and vegetation height (PC2), and above-ground biomass, foliar nitrogen and atmospheric aridity (PC3). The areas computed for FLUXNET are wider than for the models, particularly for PC2 and PC3. This means that ecosystem functional properties as simulated by models are more constrained than for the observations.

Extended Data Fig. 10 Evaluation of above-ground biomass satellite products against FLUXNET observation.

$n = 71$. We evaluated the three above-ground biomass (AGB, t DM ha⁻¹) products derived from the GlobBiomass dataset as reported in the Method section. From the product at its original resolution (100 x 100 m) we extracted the 95th percentile of the estimated AGB in 5 by 5 grid cell windows (AGB5x5, panel a with all sites, and panel b with the grasslands excluded) centered around the location of the FLUXNET sites used for the evaluation. Further, we extracted the median in 3 by 3 and 5 by 5 grid cells centered around the location of the FLUXNET site (panels c and d). Total above-ground biomass observations were gathered from the BADM dataset downloaded from the AMERIFLUX network and from the FLUXNET LaThuile release. Only data with the clear indication of the unit of AGB expressed in dry matter (t DM ha⁻¹) were retained for the analysis. Results show that the median of the 5 by 5 grid cell window (panel c) is the best extraction method to characterize AGB at the FLUXNET sites, and therefore retained for further analysis. Adjusted determination coefficient (R^2), linear regression function, and *p-value* calculated with the F-test are also reported.

Supplementary information

Supplementary Information 2

Significance test of the PCA and information redundancy: We report the number of significant axes to be retained in the PCA analysis and summarize the results of the statistical analysis in Table S2.

Reporting Summary

Supplementary Information 3

Invariant causal regression models and causal variable importance. This section contains theoretical concepts and a detailed description of the methods used in the causality analysis, and additional results.

Supplementary Table 1

List of FLUXNET sites used in the analysis. Coordinates (latitude and longitude), plant functional type (IGBP class), Köppen Geiger class, nitrogen content (N%), maximum leaf area index (LAI_{max}), maximum vegetation height (H_c), and above-ground biomass from the GlobBiomass dataset (AGB) are reported.

Supplementary Table 4

Evaluation of land surface model performances. We report an additional evaluation of the land surface model outputs.

Rights and permissions

Open Access This article is licensed under a Creative Commons Attribution 4.0 International License, which permits use, sharing, adaptation, distribution and reproduction in any medium or format, as long as you give appropriate credit to the original author(s) and the source, provide a link to the Creative Commons license, and indicate if changes were made. The images or other third party material in this article are included in the article's Creative Commons license, unless indicated otherwise in a credit line to the material. If material is not included in the article's Creative Commons license and your intended use is not permitted by statutory regulation or exceeds the permitted use, you will need to obtain permission directly from the copyright holder. To view a copy of this license, visit <http://creativecommons.org/licenses/by/4.0/>.

Reprints and Permissions

About this article

Cite this article

Migliavacca, M., Musavi, T., Mahecha, M.D. *et al.* The three major axes of terrestrial ecosystem function. *Nature* **598**, 468–472 (2021).
<https://doi.org/10.1038/s41586-021-03939-9>

- Received: 30 October 2019
- Accepted: 20 August 2021
- Published: 22 September 2021
- Issue Date: 21 October 2021
- DOI: <https://doi.org/10.1038/s41586-021-03939-9>

Share this article

Anyone you share the following link with will be able to read this content:

[Get shareable link](#)

Sorry, a shareable link is not currently available for this article.

[Copy to clipboard](#)

Provided by the Springer Nature SharedIt content-sharing initiative

This article was downloaded by **calibre** from <https://www.nature.com/articles/s41586-021-03939-9>

| [Section menu](#) | [Main menu](#) |

- Article
- [Published: 13 October 2021](#)

Convergent somatic mutations in metabolism genes in chronic liver disease

- [Stanley W. K. Ng¹](#),
- [Foad J. Rouhani^{1,2}](#),
- [Simon F. Brunner](#) [ORCID: orcid.org/0000-0002-5935-6189¹](#),
- [Natalia Brzozowska¹](#),
- [Sarah J. Aitken](#) [ORCID: orcid.org/0000-0002-1897-4140^{3,4,5}](#),
- [Ming Yang⁶](#),
- [Federico Abascal](#) [ORCID: orcid.org/0000-0002-6201-1587¹](#),
- [Luiza Moore](#) [ORCID: orcid.org/0000-0001-5315-516X¹](#),
- [Efterpi Nikitopoulou⁶](#),
- [Lia Chappell¹](#),
- [Daniel Leongamornlert](#) [ORCID: orcid.org/0000-0002-3486-3168¹](#),
- [Aleksandra Iovicic¹](#),
- [Philip Robinson](#) [ORCID: orcid.org/0000-0002-6237-7159¹](#),
- [Timothy Butler](#) [ORCID: orcid.org/0000-0001-5803-1035¹](#),
- [Mathijs A. Sanders^{1,7}](#),
- [Nicholas Williams](#) [ORCID: orcid.org/0000-0003-3989-9167¹](#),
- [Tim H. H. Coorens](#) [ORCID: orcid.org/0000-0002-5826-3554¹](#),
- [Jon Teague¹](#),
- [Keiran Raine](#) [ORCID: orcid.org/0000-0002-5634-1539¹](#),
- [Adam P. Butler¹](#),
- [Yvette Hooks¹](#),
- [Beverley Wilson¹](#),
- [Natalie Birtchnell¹](#),

- [Huw Naylor](#) ORCID: [orcid.org/0000-0001-8264-8596²](https://orcid.org/0000-0001-8264-8596),
- [Susan E. Davies⁴](#),
- [Michael R. Stratton](#) ORCID: [orcid.org/0000-0001-6035-153X¹](https://orcid.org/0000-0001-6035-153X),
- [Iñigo Martincorena](#) ORCID: [orcid.org/0000-0003-1122-4416¹](https://orcid.org/0000-0003-1122-4416),
- [Raheleh Rahbari](#) ORCID: [orcid.org/0000-0002-1839-7785¹](https://orcid.org/0000-0002-1839-7785),
- [Christian Frezza](#) ORCID: [orcid.org/0000-0002-3293-7397⁶](https://orcid.org/0000-0002-3293-7397),
- [Matthew Hoare](#) ORCID: [orcid.org/0000-0001-5990-9604^{3,8}](https://orcid.org/0000-0001-5990-9604) &
- [Peter J. Campbell](#) ORCID: [orcid.org/0000-0002-3921-0510^{1,9}](https://orcid.org/0000-0002-3921-0510)

Nature volume **598**, pages 473–478 (2021)

- 8622 Accesses
- 220 Altmetric
- [Metrics details](#)

Subjects

- [Genetics research](#)
- [Genomics](#)
- [Liver diseases](#)
- [Metabolic diseases](#)
- [Mutation](#)

Abstract

The progression of chronic liver disease to hepatocellular carcinoma is caused by the acquisition of somatic mutations that affect 20–30 cancer genes^{1,2,3,4,5,6,7,8}. Burdens of somatic mutations are higher and clonal expansions larger in chronic liver disease^{9,10,11,12,13} than in normal liver^{13,14,15,16}, which enables positive selection to shape the genomic landscape^{9,10,11,12,13}. Here we analysed somatic mutations from 1,590 genomes across 34 liver samples, including healthy controls, alcohol-related liver disease and non-alcoholic fatty liver disease. Seven of the 29 patients with liver disease had mutations in *FOXO1*, the major transcription

factor in insulin signalling. These mutations affected a single hotspot within the gene, impairing the insulin-mediated nuclear export of FOXO1.

Notably, six of the seven patients with *FOXO1*^{S22W} hotspot mutations showed convergent evolution, with variants acquired independently by up to nine distinct hepatocyte clones per patient. *CIDEB*, which regulates lipid droplet metabolism in hepatocytes^{17,18,19}, and *GPAM*, which produces storage triacylglycerol from free fatty acids^{20,21}, also had a significant excess of mutations. We again observed frequent convergent evolution: up to fourteen independent clones per patient with *CIDEB* mutations and up to seven clones per patient with *GPAM* mutations. Mutations in metabolism genes were distributed across multiple anatomical segments of the liver, increased clone size and were seen in both alcohol-related liver disease and non-alcoholic fatty liver disease, but rarely in hepatocellular carcinoma. Master regulators of metabolic pathways are a frequent target of convergent somatic mutation in alcohol-related and non-alcoholic fatty liver disease.

Access options

Subscribe to Journal

Get full journal access for 1 year

\$199.00

only \$3.90 per issue

[Subscribe](#)

All prices are NET prices.

VAT will be added later in the checkout.

Tax calculation will be finalised during checkout.

Rent or Buy article

Get time limited or full article access on ReadCube.

from \$8.99

[Rent or Buy](#)

All prices are NET prices.

Additional access options:

- [Log in](#)
- [Access through your institution](#)
- [Learn about institutional subscriptions](#)

Fig. 1: Convergent *FOXO1* mutations in chronic liver disease.

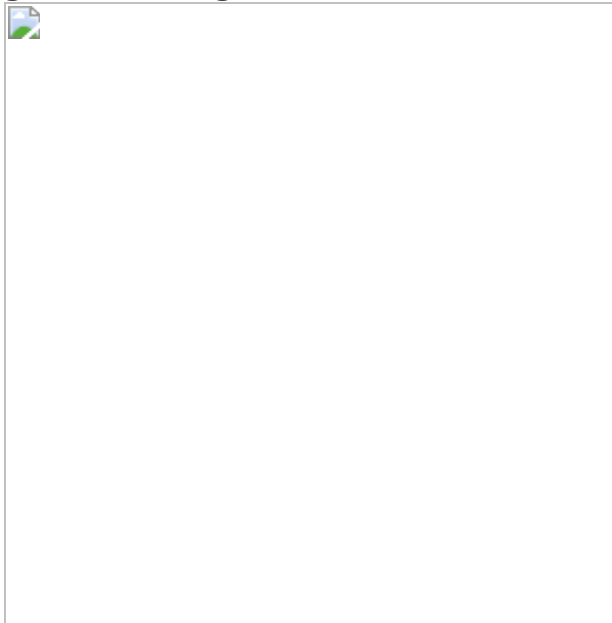


Fig. 2: Somatic mutations of *FOXO1* lead to impaired nuclear export and insulin resistance in vitro.



Fig. 3: Convergent *CIDEB* and *GPAM* mutations in chronic liver disease.

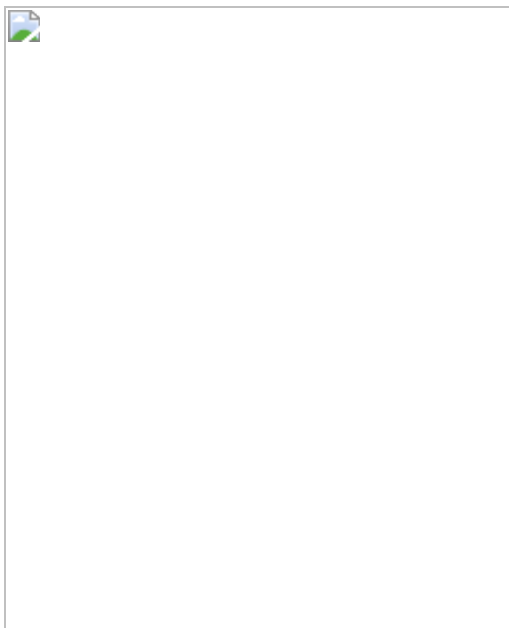
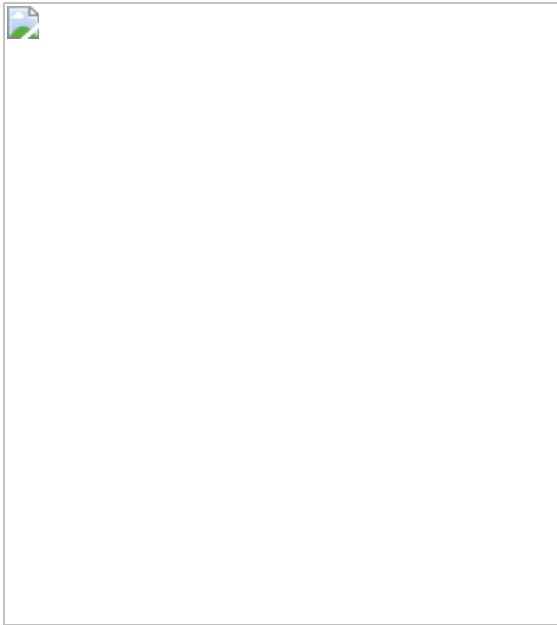


Fig. 4: Other genomic analyses.



Data availability

WGS data in the form of BAM files across samples reported in this study have been deposited in the European Genome-Phenome Archive (accession number [EGAD00001006255](#)). RNA-sequencing data have been deposited in the European Nucleotide Archive (<https://www.ebi.ac.uk/ena/browser/home>) with accession number [ERP123192](#).

Code availability

Detailed methods and custom R scripts for the analysis of clinical features, telomere lengths and metabolomics data are available in the [Supplementary Code](#). Other packages used in the analysis are listed below: R: v.3.5.1, Perl: v.5.3.0, Python: v.3.8.5, MATLAB: v.R2019b, BWA-MEM: v.0.7.17 (<https://sourceforge.net/projects/bio-bwa/>), cgpCaVEMan: v.1.11.2/1.13.14/1.15.1 (<https://github.com/cancerit/CaVEMan>), cgpPindel: v.2.2.2/2.2.4/2.2.5/3.2.0/3.3.0 (<https://github.com/cancerit/cgpPindel>), Brass: v.5.4.1/6.0.5/6.1.2/6.2.0/6.3.4 (<https://github.com/cancerit/BRASS>), ASCAT NGS: v.4.0.1/ 4.1.2/4.2.1 (<https://github.com/cancerit/ascatNgs>), JBrowse: v.1.16.1 (<https://jbrowse.org/>), cgpVAF: v.2.4.0 (<https://github.com/cancerit/vafCorrect>), alleleCount: v.4.1.0

(<https://github.com/cancerit/alleleCount>), SigProfiler: v.1.0.0-GRCh37 (<https://github.com/AlexandrovLab>), HDP: v.0.1.5 (<https://github.com/nicolaroberts/hdp>), dNdScv: v.0.0.1 (<https://github.com/im3sanger/dndscv>), Telomerecat: v.3.4.0 (<https://github.com/jhrf/telomerecat>), STAR: v.2.7.6a (<https://github.com/alexdobin/STAR>), Picard-tools: v.2.20.7 (<https://broadinstitute.github.io/picard/>), Samtools: v.1.12 (<http://www.htslib.org/>), TrimGalore: v.0.6.4 (<https://github.com/FelixKrueger/TrimGalore>), GATK: v.4.1.4.1 (<https://gatk.broadinstitute.org/hc/en-us>), GSEA: v.3.0 (<https://www.gsea-msigdb.org/gsea/index.jsp>), XGBoost: v.0.82.1 (<https://xgboost.readthedocs.io/en/latest/>), NDP.view2 (<https://www.hamamatsu.com/eu/en/product/type/U12388-01/index.html>), label.switching: v.1.8 (<https://cran.r-project.org/web/packages/label.switching/index.html>), philanthropy: v.0.3.0 (<https://cran.r-project.org/web/packages/philanthropy/index.html>), MCMCglmm: v.2.29 (<https://cran.r-project.org/web/packages/MCMCglmm/index.html>), Magick: v.2.0 (<https://cran.r-project.org/web/packages/magick/index.html>), Pheatmap: v.1.0.12 (<https://cran.r-project.org/web/packages/pheatmap/index.html>), Thermo Fisher software Tracefinder: v.5.0 (<https://www.thermofisher.com/uk/en/home/industrial/mass-spectrometry/liquid-chromatography-mass-spectrometry-lc-ms/lc-ms-software/lc-ms-data-acquisition-software/tracefinder-software.html>), CellProfiler: v.4.0.3 (<https://cellprofiler.org/>), PerkinElmer Harmony: v.4.9 (<https://www.perkinelmer.com/category/cellular-imaging-software>).

References

1. 1.

The Cancer Genome Atlas Research Network. Comprehensive and integrative genomic characterization of hepatocellular carcinoma. *Cell* **169**, 1327–1341 (2017).

2. 2.

Schulze, K. et al. Exome sequencing of hepatocellular carcinomas identifies new mutational signatures and potential therapeutic targets. *Nat. Genet.* **47**, 505–511 (2015).

3. 3.

Totoki, Y. et al. Trans-ancestry mutational landscape of hepatocellular carcinoma genomes. *Nat. Genet.* **46**, 1267–1273 (2014).

4. 4.

Fujimoto, A. et al. Whole-genome sequencing of liver cancers identifies etiological influences on mutation patterns and recurrent mutations in chromatin regulators. *Nat. Genet.* **44**, 760–764 (2012).

5. 5.

Letouzé, E. et al. Mutational signatures reveal the dynamic interplay of risk factors and cellular processes during liver tumorigenesis. *Nat. Commun.* **8**, 1315 (2017).

6. 6.

Guichard, C. et al. Integrated analysis of somatic mutations and focal copy-number changes identifies key genes and pathways in hepatocellular carcinoma. *Nat. Genet.* **44**, 694–698 (2012).

7. 7.

Fujimoto, A. et al. Whole-genome mutational landscape and characterization of noncoding and structural mutations in liver cancer. *Nat. Genet.* **48**, 500–509 (2016).

8. 8.

Pinyol, R. et al. Molecular characterization of hepatocellular carcinoma in patients with non-alcoholic steatohepatitis. *J. Hepatol.* **75**, 865–878 (2021).

9. 9.

Nault, J. C. et al. Telomerase reverse transcriptase promoter mutation is an early somatic genetic alteration in the transformation of premalignant nodules in hepatocellular carcinoma on cirrhosis. *Hepatology* **60**, 1983–1992 (2014).

10. 10.

Torrecilla, S. et al. Trunk mutational events present minimal intra- and inter-tumoral heterogeneity in hepatocellular carcinoma. *J. Hepatol.* **67**, 1222–1231 (2017).

11. 11.

Zhu, M. et al. Somatic mutations increase hepatic clonal fitness and regeneration in chronic liver disease. *Cell* **177**, 608–621 (2019).

12. 12.

Kim, S. K. et al. Comprehensive analysis of genetic aberrations linked to tumorigenesis in regenerative nodules of liver cirrhosis. *J. Gastroenterol.* **54**, 628–640 (2019).

13. 13.

Brunner, S. F. et al. Somatic mutations and clonal dynamics in healthy and cirrhotic human liver. *Nature* **574**, 538–542 (2019).

14. 14.

Blokzijl, F. et al. Tissue-specific mutation accumulation in human adult stem cells during life. *Nature* **538**, 260–264 (2016).

15. 15.

Yizhak, K. et al. RNA sequence analysis reveals macroscopic somatic clonal expansion across normal tissues. *Science* **364**, eaaw0726 (2019).

16. 16.

Brazhnik, K. et al. Single-cell analysis reveals different age-related somatic mutation profiles between stem and differentiated cells in human liver. *Sci. Adv.* **6**, eaax2659 (2020).

17. 17.

Barneda, D. et al. The brown adipocyte protein CIDEA promotes lipid droplet fusion via a phosphatidic acid-binding amphipathic helix. *Elife* **4**, e07485 (2015).

18. 18.

Sun, Z. et al. Perilipin1 promotes unilocular lipid droplet formation through the activation of Fsp27 in adipocytes. *Nat. Commun.* **4**, 1594 (2013).

19. 19.

Li, J. Z. et al. Cideb regulates diet-induced obesity, liver steatosis, and insulin sensitivity by controlling lipogenesis and fatty acid oxidation. *Diabetes* **56**, 2523–2532 (2007).

20. 20.

Hammond, L. E. et al. Mitochondrial glycerol-3-phosphate acyltransferase-1 is essential in liver for the metabolism of excess acyl-CoAs. *J. Biol. Chem.* **280**, 25629–25636 (2005).

21. 21.

Wendel, A. A., Cooper, D. E., Ilkayeva, O. R., Muoio, D. M. & Coleman, R. A. Glycerol-3-phosphate acyltransferase (GPAT)-1, but not GPAT4, incorporates newly synthesized fatty acids into triacylglycerol and diminishes fatty acid oxidation. *J. Biol. Chem.* **288**, 27299–27306 (2013).

22. 22.

Jeon, S. & Carr, R. Alcohol effects on hepatic lipid metabolism. *J. Lipid Res.* **61**, 470–479 (2020).

23. 23.

Friedman, S. L., Neuschwander-Tetri, B. A., Rinella, M. & Sanyal, A. J. Mechanisms of NAFLD development and therapeutic strategies. *Nat. Med.* **24**, 908–922 (2018).

24. 24.

Clugston, R. D. et al. Altered hepatic lipid metabolism in C57BL/6 mice fed alcohol: a targeted lipidomic and gene expression study. *J. Lipid Res.* **52**, 2021–2031 (2011).

25. 25.

Puri, P. et al. A lipidomic analysis of nonalcoholic fatty liver disease. *Hepatology* **46**, 1081–1090 (2007).

26. 26.

Meister, G. et al. Identification of novel argonaute-associated proteins. *Curr. Biol.* **15**, 2149–2155 (2005).

27. 27.

Rheinbay, E. et al. Analyses of non-coding somatic drivers in 2,658 cancer whole genomes. *Nature* **578**, 102–111 (2020).

28. 28.

Yaffe, M. B. et al. The structural basis for 14-3-3:phosphopeptide binding specificity. *Cell* **91**, 961–971 (1997).

29. 29.

Saline, M. et al. AMPK and AKT protein kinases hierarchically phosphorylate the N-terminus of the FOXO1 transcription factor,

modulating interactions with 14-3-3 proteins. *J. Biol. Chem.* **294**, 13106–13116 (2019).

30. 30.

Kleiner, D. E. et al. Design and validation of a histological scoring system for nonalcoholic fatty liver disease. *Hepatology* **41**, 1313–1321 (2005).

31. 31.

Ishak, K. et al. Histological grading and staging of chronic hepatitis. *J. Hepatol.* **22**, 696–699 (1995).

32. 32.

Ellis, P. et al. Reliable detection of somatic mutations in solid tissues by laser-capture microdissection and low-input DNA sequencing. *Nat. Protoc.* **16**, 841–871 (2021).

33. 33.

Jones, D. et al. cgpCaVEManWrapper: simple execution of CaVEMan in order to detect somatic single nucleotide variants in NGS data. *Curr. Protoc. Bioinformatics* **56**, 15.10.1–15.10.18 (2016).

34. 34.

Yoshida, K. et al. Tobacco smoking and somatic mutations in human bronchial epithelium. *Nature* **578**, 266–272 (2020).

35. 35.

Papastamoulis, P. `label.switching`: an R package for dealing with the label switching problem in MCMC outputs. *J. Stat. Softw.* **69**, Code Snippet 1 (2015).

36. 36.

Nik-Zainal, S. et al. The life history of 21 breast cancers. *Cell* **149**, 994–1007 (2012).

37. 37.

Martincorena, I. et al. Universal patterns of selection in cancer and somatic tissues. *Cell* **171**, 1029–1041 (2017).

38. 38.

Raine, K. M. et al. cgpPindel: identifying somatically acquired insertion and deletion events from paired end sequencing. *Curr. Protoc. Bioinformatics* **52**, 15.7.1–15.7.12 (2015).

39. 39.

Campbell, P. J. et al. Identification of somatically acquired rearrangements in cancer using genome-wide massively parallel paired-end sequencing. *Nat. Genet.* **40**, 722–729 (2008).

40. 40.

Stephens, P. J. et al. Massive genomic rearrangement acquired in a single catastrophic event during cancer development. *Cell* **144**, 27–40 (2011).

41. 41.

Sohlenius-Sternbeck, A. K. Determination of the hepatocellularity number for human, dog, rabbit, rat and mouse livers from protein concentration measurements. *Toxicol. Vitr.* **20**, 1582–1586 (2006).

42. 42.

Lipscomb, J. C., Fisher, J. W., Confer, P. D. & Byczkowski, J. Z. In vitro to in vivo extrapolation for trichloroethylene metabolism in humans. *Toxicol. Appl. Pharmacol.* **152**, 376–387 (1998).

43. 43.

Bergstrom, E. N. et al. SigProfilerMatrixGenerator: a tool for visualizing and exploring patterns of small mutational events. *BMC Genomics* **20**, 685 (2019).

44. 44.

Alexandrov, L. B. et al. The repertoire of mutational signatures in human cancer. *Nature* **578**, 94–101 (2020).

45. 45.

Drost, H.-G. Philentropy: information theory and distance quantification with R. *J. Open Source Softw.* **3**, 765 (2018).

46. 46.

Qiao, W. et al. PERT: a method for expression deconvolution of human blood samples from varied microenvironmental and developmental conditions. *PLoS Comput. Biol.* **8**, (2012).

47. 47.

Farmacy, J. H. R. et al. Telomerecat: a ploidy-agnostic method for estimating telomere length from whole genome sequencing data. *Sci. Rep.* **8**, 1300 (2018).

48. 48.

Hadfield, J. D. MCMC methods for multi-response generalized linear mixed models: the MCMCglmm R package. *J. Stat. Softw.* **33**, v033i02 (2010).

49. 49.

Hoare, M. et al. NOTCH1 mediates a switch between two distinct secretomes during senescence. *Nat. Cell Biol.* **18**, 979–992 (2016).

50. 50.

Liao, Y., Smyth, G. K. & Shi, W. FeatureCounts: an efficient general purpose program for assigning sequence reads to genomic features. *Bioinformatics* **30**, 923–930 (2014).

51. 51.

Robinson, M. D., McCarthy, D. J. & Smyth, G. K. edgeR: a Bioconductor package for differential expression analysis of digital gene expression data. *Bioinformatics* **26**, 139–140 (2009).

Acknowledgements

This work was supported by a Cancer Research UK Grand Challenge Award (C98/A24032) and the Wellcome Trust. S.W.K.N. holds an EMBO Long Term Fellowship (ALTF 721-2019). S.F.B. was supported by the Swiss National Science Foundation (P2SKP3-171753 and P400PB-180790). M.A.S. is supported by a Rubicon fellowship from NWO (019.153LW.038). The Cambridge Human Research Tissue Bank is supported by the NIHR Cambridge Biomedical Research Centre. M.H. is supported by a CRUK Clinician Scientist Fellowship (C52489/A19924) and a CRUK Accelerator Award (C18873/A26813). P.J.C. was supported by a Wellcome Senior Clinical Fellowship until 2020 (WT088340MA).

Author information

Affiliations

1. Cancer Genome Project, Wellcome Sanger Institute, Hinxton, UK

Stanley W. K. Ng, Foad J. Rouhani, Simon F. Brunner, Natalia Brzozowska, Federico Abascal, Luiza Moore, Lia Chappell, Daniel Leongamornlert, Aleksandra Iovicic, Philip Robinson, Timothy Butler, Mathijs A. Sanders, Nicholas Williams, Tim H. H. Coorens, Jon Teague, Keiran Raine, Adam P. Butler, Yvette Hooks, Beverley Wilson, Natalie Birtchnell, Michael R. Stratton, Iñigo Martincorena, Raheleh Rahbari & Peter J. Campbell

2. Department of Surgery, Addenbrooke's Hospital, Cambridge, UK

Foad J. Rouhani & Huw Naylor

3. CRUK Cambridge Institute, Cambridge, UK

Sarah J. Aitken & Matthew Hoare

4. Department of Pathology, Addenbrooke's Hospital, Cambridge, UK

Sarah J. Aitken & Susan E. Davies

5. MRC Toxicology Unit, University of Cambridge, Cambridge, UK

Sarah J. Aitken

6. MRC Cancer Unit, University of Cambridge, Cambridge, UK

Ming Yang, Eftherpi Nikitopoulou & Christian Frezza

7. Department of Hematology, Erasmus University Medical Center, Rotterdam, The Netherlands

Mathijs A. Sanders

8. Department of Medicine, University of Cambridge, Addenbrooke's Hospital, Cambridge, UK

Matthew Hoare

9. Stem Cell Institute, University of Cambridge, Cambridge, UK

Peter J. Campbell

Contributions

P.J.C., M.H. and S.W.K.N. designed the experiments. S.W.K.N. performed mutation calling and computational analyses including visualization of results for mutation calling; identification of SNV clusters and the inference

of phylogenetic relationships between them; assignment of indels and *FOXO1* hotspot mutations to SNV clusters; clone size estimation and comparisons; mutational signature extraction; identification of protein-coding and non-coding drivers; telomere length estimation; processing and normalization of RNA-sequencing data; gene set enrichment analysis; and estimation of the liver-wide mass of driver-mutation-bearing hepatocytes. S.W.K.N. developed software for the refinement of indel calling, phylogenetic inference and visualization of clonal structure, and clone size estimation, visualization and mapping to histological images. P.J.C. assisted with the filtering of structural variants, performed statistical inference of factors that affect telomere length using mixed effects models and supervised all statistical analyses. N. Brzozowska performed telomere length estimation. F.A. and I.M. provided support for running variants of dNdScv. M.R.S. advised on mutational signature extraction. T.H.H.C. provided support for running beta-binomial-based variant filtering. M.A.S. provided support and advice for performing LCM-specific variant-filtering algorithms for SNV and structural variant calls. D.L. and T.B. provided insights into indel filtering associated with homopolymers and problematic genomic loci. F.J.R., S.F.B., Y.H., B.W. and N. Birtchnell performed tissue sectioning, fixing, staining and histology image generation. S.F.B. also performed LCM and submission for WGS, and was responsible for the initial development of source code for producing diagnostic plots to facilitate the manual determination of clonal relationships, and the visualization of phylogenetic tree structures. P.R., A.I. and T.B. provided wet laboratory support. N.W., J.T., K.R. and A.P.B. provided technical support for computational analyses. M.H. and F.J.R. provided biological samples used in this study, and the associated clinical annotations were curated with assistance from S.J.A. and S.E.D. S.J.A. and S.E.D. analysed histology sections of background liver and HCC from all patients in the study, and L.M. supervised microdissection of tissue samples for sequencing. M.H. coordinated all validation experiments relating to *FOXO1* hotspot mutations using HCC cell lines, with additional support from H.N. M.Y., E.N. and C.F. performed analysis of metabolites from HCC cell lines. L.C. and R.R. performed processing and quality control of RNA-sequencing samples and data. P.J.C., S.W.K.N. and M.H. drafted the manuscript with input and guidance from M.R.S. and I.M., and updated the paper after contributions from all authors.

Corresponding authors

Correspondence to Matthew Hoare or Peter J. Campbell.

Ethics declarations

Competing interests

A patent has been filed by CRUK's technology transfer office, with support from that of Wellcome Sanger Institute (named inventors: S.W.K.N., M.H. and P.J.C.), covering the use of somatic mutations in liver tissue for stratifying diagnosis and treatment of patients with metabolic diseases.

Additional information

Peer review information *Nature* thanks the anonymous reviewers for their contribution to the peer review of this work. Peer reviewer reports are available.

Publisher's note Springer Nature remains neutral with regard to jurisdictional claims in published maps and institutional affiliations.

Extended data figures and tables

[Extended Data Fig. 1 Mutations in *ACVR2A*.](#)

a, Distribution of somatic mutations in *ACVR2A* according to genomic location. Pie charts show fraction of sequencing reads reporting the mutant allele in each microdissection. **b**, Two microdissections in different patients showing structural variants generating copy loss of *ACVR2A*. Black points represent corrected read depth along the chromosome. Lines and arcs represent structural variants, coloured by the orientation of the joined ends (purple, deletion-type orientation; brown, tandem-duplication-type orientation; turquoise, head-to-head inverted; green, tail-to-tail inverted).

Extended Data Fig. 2 Mutations in *TNRC6B* and *NEAT1*.

a, Distribution of somatic mutations in *CLCN5* according to genomic location. Pie charts show fraction of sequencing reads reporting the mutant allele in each microdissection. **b**, Distribution of somatic mutations in the long non-coding RNA, *NEAT1*, according to genomic location. Pie charts show fraction of sequencing reads reporting the mutant allele in each microdissection.

Extended Data Fig. 3 Structural variants affecting *FOXO1* and *GPAM*.

a, A chromothripsis event affecting chromosome 13 in one of the microdissections from PD37907, a patient with NAFLD. Black points represent corrected read depth along the chromosome. Lines and arcs represent structural variants, coloured by the orientation of the joined ends (purple, deletion-type orientation; brown, tandem-duplication-type orientation; turquoise, head-to-head inverted; green, tail-to-tail inverted). The structural variant that breaks *FOXO1* is highlighted, and would be predicted to break the gene within the first intron, preserving the first coding exon but deleting the remaining coding exons. **b**, A tandem duplication upstream of *GPAM* in a microdissection from PD37110, a patient with ARLD. *GPAM* is left intact, but the tandem duplication starts 20kb upstream of the gene.

Extended Data Fig. 4 Multiple independent acquisitions of *FOXO1* mutations in PD37239.

The clone map from Fig. 1b is shown, laid onto an H&E-stained section. On the left of the figure, raw sequencing data from representative samples with and without *FOXO1* mutations are shown, with their physical locations on the H&E section shown by the arrows. In the sequencing data, reads mapping to the forward strand of the reference genome are in pink; the reverse strand in blue. Base calls that do not match the reference genome are shown as coloured squares. The locations of the S22W and R21L mutations are marked with arrows. The scatterplots arranged around the

H&E section represent VAF plots of mutations in pairs of samples. The colours of the x and y axis titles match the clone map colours of the H&E section. Individual mutations called in either sample are shown in orange, according to their VAF, with the *FOXO1* S22W mutation shown in dark green. In clonally related pairs of samples, most of the mutations are shared by both samples, evident as a cloud of mutations with non-zero VAF. In clonally unrelated samples, the mutations line the x and y axes, with the one exception being the *FOXO1* mutation, indicating that it is independently acquired in the two clones.

Extended Data Fig. 5 Further examples of *FOXO1* mutations in patients with chronic liver disease.

a–c, Phylogenetic trees and clone maps are shown for PD37234 (**a**), PD37105 (**b**) and PD37245 (**c**). The left panel shows the phylogenetic tree, with coloured branches showing independently acquired mutations. Solid lines indicate that nesting is in accordance with the pigeonhole principle; dashed lines indicate that nesting is in accordance with the pigeonhole principle, assuming that hepatocytes represent < 100% of cells. The right panel shows the clones from the phylogenetic tree mapped onto an H&E-stained photomicrograph of the liver, with *FOXO1*-mutant clones coloured to match the tree.

Extended Data Fig. 6 Somatic mutations of *FOXO1* impair its phosphorylation and nuclear export.

a, HepG2 cells were transfected with the indicated wild-type or mutant constructs of *FOXO1* fused with a C-terminal GFP. Cells were counterstained with DAPI to highlight the nucleus, and imaged after overnight serum starvation conditions (left) and after 15 min of exposure to 100 nM insulin (right). Studies were performed in triplicate. **b**, HepG2 cells, expressing ectopic eGFP-tagged wild-type or mutant *FOXO1* constructs as indicated and treated for 15 min with vehicle or insulin (100nM), were analysed for the indicated proteins by immunoblotting. Molecular weight markers (kDa) indicated. Studies were performed in

triplicate. Uncropped versions of the blots are shown in [Supplementary Fig. 4](#).

Extended Data Fig. 7 Nuclear–cytoplasmic ratios for wild-type and mutant FOXO1-GFP constructs in HCC cell lines.

a, b, Wide-field view of Hep3B (**a**) and PLC/PRF5 (**b**) cells pseudocoloured on a blue-to-red scale by the nuclear-cytoplasmic ratio of FOXO1-GFP. Cells were imaged under conditions of serum starvation (left), after exposure to insulin 100nM for 15 min (middle) or foetal calf serum (FCS) for 15 min (right).

Extended Data Fig. 8 RNA sequencing from cell lines transduced with either wild-type or mutant FOXO1-GFP constructs.

a, Heat map showing gene expression levels for genes in the ‘Canonical Glycolysis’ gene set from GO (GO:0061621). The order of genes on the x axis is determined by the level of significance (and direction of change) and the order of samples on the y axis is by condition (*FOXO1* status and insulin status). **b**, Heat map showing gene expression levels for genes in the ‘Cell cycle, mitotic’ gene set from Reactome (R-HSA-69278). The order of genes on the x axis is determined by the level of significance (and direction of change) and the order of samples on the y axis is by condition (*FOXO1* status and insulin status). **c–e**, Enrichment plots for the ‘FO XO-mediated transcription of oxidative stress, metabolic and neuronal genes’ gene set of Reactome (9615017) (**c**); ‘Lipid catabolic process’ gene set of GO (0016042) (**d**); and ‘Apoptotic process’ gene set of GO (0006915) (**e**). In each, the top panel reflects the cumulative enrichment score as the gene set is traversed from most up-regulated to most down-regulated in the presence of *FOXO1*-mutant constructs. The bottom panel in each shows the ranking of each gene in the gene set across all genes measured.

Extended Data Fig. 9 CIDEB mutations in patients with chronic liver disease.

a, Distribution of somatic mutations in *CIDEB*. Amino acid residues are coloured by type, with observed mutations in chronic liver disease shown above the wild-type protein sequence. **b**, Phylogenetic trees and clone maps are shown for one of the Couinaud segments of PD48367 with *CIDEB* mutations. The left panel shows the phylogenetic tree, with coloured branches showing independently acquired driver mutations. Solid lines indicate that nesting is in accordance with the pigeonhole principle; dashed lines indicate that nesting is in accordance with the pigeonhole principle, assuming that hepatocytes represent < 100% of cells. The right panel shows the clones from the phylogenetic tree mapped onto an H&E-stained photomicrograph of the liver, with mutant clones coloured to match the tree.

Extended Data Fig. 10 GPAM mutations in patients with chronic liver disease.

a, Distribution of somatic mutations in *GPAM* according to genomic location. Pie charts show fraction of sequencing reads reporting the mutant allele in each microdissection. **b**, Phylogenetic trees and clone maps are shown for a biopsy from PD37111 with *GPAM* mutations. The left panel shows the phylogenetic tree, with coloured branches showing independently acquired driver mutations. Solid lines indicate that nesting is in accordance with the pigeonhole principle; dashed lines indicate that nesting is in accordance with the pigeonhole principle, assuming that hepatocytes represent < 100% of cells. The right panel shows the clones from the phylogenetic tree mapped onto an H&E-stained photomicrograph of the liver, with mutant clones coloured to match the tree.

Extended Data Fig. 11 Properties of clones and patients with driver mutations.

a, Stacked bar chart showing the estimated cumulative liver mass carrying driver mutations, extrapolated from samples analysed in each patient. The calculations assume a total liver mass of 1500g for each patient. Bars are coloured for each of the 6 recurrently mutated genes identified in the study, and patient codes on the x axis are coloured for disease status. **b**, Estimated clone size for the 4 most frequently mutated genes compared to wild-type

clones. The points are overlaid on box-and-whisker plots where the median is marked with a heavy black line and the interquartile range in a thin black box. The whiskers denote mark the full range of the data or 25th/75th centile plus 1.5x the interquartile range (whichever is smaller). The p values are two-sided, derived from Wilcoxon rank-sum tests and have not been corrected for multiple hypothesis testing. Sample sizes are n = 25 mutant clones for *FOXO1*; n = 17 mutant clones for *CIDEB*; n = 15 mutant clones for *GPAM*; and n = 32 mutant clones for *ACVR2A*. **c**, Scatter plot showing the distribution of ages of patients in the cohort by whether they carried clones with mutations in the specified genes or not. The p values are two-sided, derived from Wilcoxon rank-sum tests and have not been corrected for multiple hypothesis testing. Sample sizes were n = 7 *FOXO1* mutant versus n = 22 *FOXO1* wild-type; n = 6 *CIDEB* mutant versus n = 23 *CIDEB* wild-type; and n = 7 *GPAM* mutant versus n = 22 *GPAM* wild-type. **d**, Stacked bar charts showing the proportion of patients with or without type 2 diabetes by whether they carried driver mutations in each gene. The p values are two-sided, derived from Fisher's exact tests and have not been corrected for multiple hypothesis testing. Sample sizes were as for **c**. **e**, Stacked bar charts showing the distribution of the NAFLD Activity Score (NAS) by whether they carried driver mutations in each gene, with low scores denoting a low degree of histological abnormality. The p values are two-sided, derived from chi-squared tests for trend and have not been corrected for multiple hypothesis testing. Sample sizes were as for **c**.

Extended Data Fig. 12 Analysis of telomere lengths.

a, Scatter plot showing the distribution of telomere lengths for samples grouped by disease status, and ranked from lowest to highest age within each disease category. **b**, Posterior distributions of the effect size of clone size (per log₁₀(μm^2)), age (per decade of life) and disease state (NAFLD and ARLD versus normal) on telomere lengths. Density plots are shown from the MCMC sampler, coloured by decile. Posterior 'p values' are calculated from the posterior samples of the MCMC chain and are two-sided and not corrected for multiple hypothesis testing. **c**, Telomere lengths layered onto two representative phylogenetic trees from patients with ARLD. Branches are coloured on a yellow-to-blue scale according to telomere lengths of the sample with the highest VAF assigned to that

branch. The internal nodes are estimated using maximum likelihood and colours are interpolated along each branch.

Extended Data Fig. 13 Distribution of mutational signatures across the phylogenetic trees within the cohort.

Estimated proportional contributions of each mutational signature to each phylogenetically defined cluster of somatic substitutions. Stacked bar plots show proportional contributions of signatures in normal controls (top), patients with ARLD (middle), and patients with NAFLD (bottom).

Extended Data Fig. 14 Distribution of the new T>A signature across three samples.

a, Signatures for a sample with high rates of the novel signature (PD37240). The left panel shows phylogenetic trees with each branch coloured by the proportion of mutations in that branch assigned to the different mutational signatures. The contribution from the new signature is coloured purple. The middle panel shows the overlay of clones onto an H&E-stained liver section. Clones are coloured on a grey-to-purple scale according to the proportion of mutations attributed to the novel signature. The right panel shows observed mutation spectra for representative clones with low (top) or high (bottom) burden of the novel signature, laid out as for Fig. 4b. Purple arrows indicate parts of the mutation spectrum that are characteristic of the new mutational signature. **b, c**, In one patient with NAFLD, we had three samples from 2008 (not shown as the signature was absent), 2011 (**b**) and 2013 (**c**), with the relative contribution of the signature increasing over time. The photomicrograph of the H&E section in **c** was captured after the microdissections were excised, hence the white gaps in the tissue.

Supplementary information

Supplementary Information

This file contains Supplementary Notes 1 and 2, Supplementary Methods including further details on indel calling and mutational signature extraction

not included in the main Methods section, Supplementary References and Supplementary Figures 1–6.

Reporting Summary

Supplementary Tables

This file contains Supplementary Tables 1–9 and a Supplementary Table Guide.

Supplementary Data

This file contains the Supplementary Code: HTMLs of Jupyter notebooks outlining key statistical analyses presented in the manuscript, including analysis of clinical variables, telomere lengths and metabolomics data.

Peer Review File

Rights and permissions

Reprints and Permissions

About this article

Cite this article

Ng, S.W.K., Rouhani, F.J., Brunner, S.F. *et al.* Convergent somatic mutations in metabolism genes in chronic liver disease. *Nature* **598**, 473–478 (2021). <https://doi.org/10.1038/s41586-021-03974-6>

- Received: 17 June 2020
- Accepted: 31 August 2021
- Published: 13 October 2021

- Issue Date: 21 October 2021
- DOI: <https://doi.org/10.1038/s41586-021-03974-6>

Share this article

Anyone you share the following link with will be able to read this content:

[Get shareable link](#)

Sorry, a shareable link is not currently available for this article.

[Copy to clipboard](#)

Provided by the Springer Nature SharedIt content-sharing initiative

This article was downloaded by **calibre** from <https://www.nature.com/articles/s41586-021-03974-6>

| [Section menu](#) | [Main menu](#) |

- Article
- [Published: 29 September 2021](#)

Sensory processing during sleep in *Drosophila melanogaster*

- [Alice S. French¹](#),
- [Quentin Geissmann](#) [ORCID: orcid.org/0000-0001-6546-4306²](#),
- [Esteban J. Beckwith³](#) &
- [Giorgio F. Gilestro](#) [ORCID: orcid.org/0000-0001-7512-8541¹](#)

[Nature](#) volume **598**, pages 479–482 (2021)

- 6951 Accesses
- 1 Citations
- 378 Altmetric
- [Metrics details](#)

Subjects

- [Consciousness](#)
- [Sleep](#)

Abstract

During sleep, most animal species enter a state of reduced consciousness characterized by a marked sensory disconnect. Yet some processing of the external world must remain intact, given that a sleeping animal can be awoken by intense stimuli (for example, a loud noise or a bright light) or by

soft but qualitatively salient stimuli (for example, the sound of a baby cooing or hearing one's own name^{1,2,3}). How does a sleeping brain retain the ability to process the quality of sensory information? Here we present a paradigm to study the functional underpinnings of sensory discrimination during sleep in *Drosophila melanogaster*. We show that sleeping vinegar flies, like humans, discern the quality of sensory stimuli and are more likely to wake up in response to salient stimuli. We also show that the salience of a stimulus during sleep can be modulated by internal states. We offer a prototypical blueprint detailing a circuit involved in this process and its modulation as evidence that the system can be used to explore the cellular underpinnings of how a sleeping brain experiences the world.

Access options

Subscribe to Journal

Get full journal access for 1 year

\$199.00

only \$3.90 per issue

[Subscribe](#)

All prices are NET prices.

VAT will be added later in the checkout.

Tax calculation will be finalised during checkout.

Rent or Buy article

Get time limited or full article access on ReadCube.

from \$8.99

[Rent or Buy](#)

All prices are NET prices.

Additional access options:

- [Log in](#)
- [Access through your institution](#)
- [Learn about institutional subscriptions](#)

Fig. 1: Sleeping *D. melanogaster* react to salient olfactory stimuli.

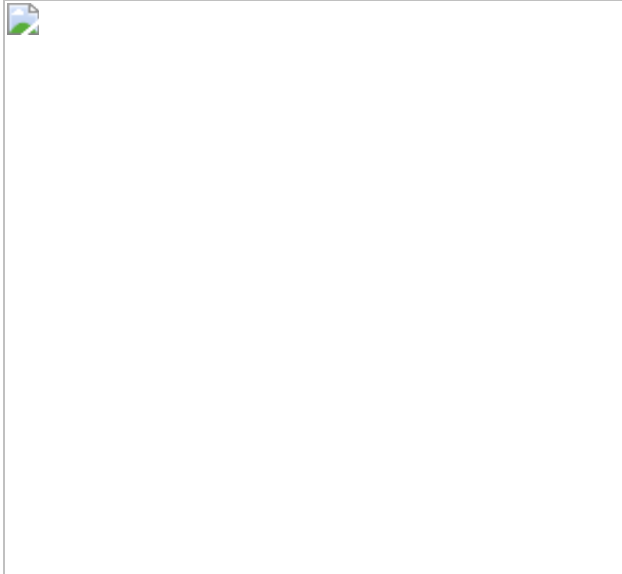


Fig. 2: Subconscious processing of information can be modulated by internal states.

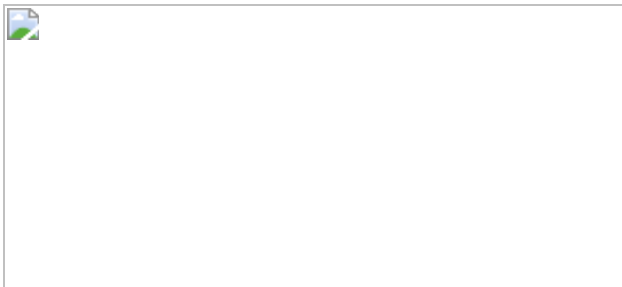


Fig. 3: Genetic manipulation of MBONs and their targets in the FSB modulates waking.

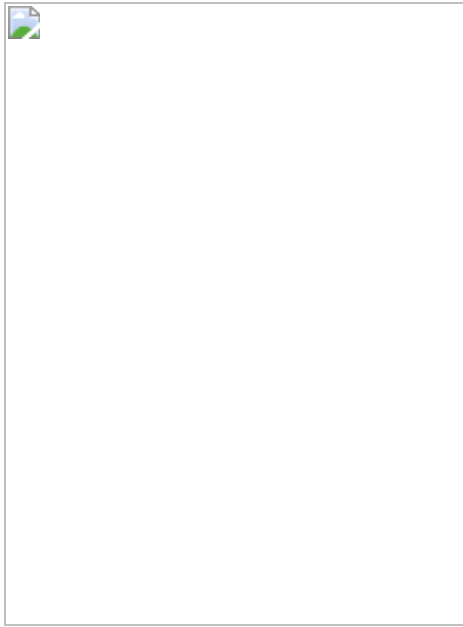
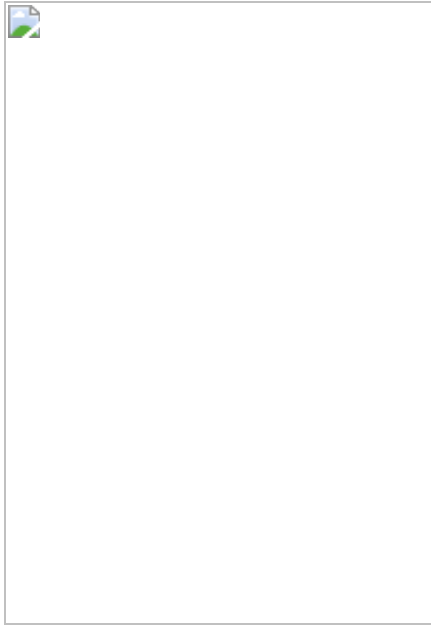


Fig. 4: At least two check points gate waking responses to odours.



Data availability

All raw data used for analysis are made available through the Supplementary Information and through a Zenodo repository (<https://doi.org/10.5281/zenodo.5109970>). Source data are provided with this paper.

Code availability

All scripts used for analysis are made available through the Supplementary Information and through a Zenodo repository (<https://doi.org/10.5281/zenodo.5109970>).

References

1. 1.

Langford, G. W., Meddis, R. & Pearson, A. J. D. Awakening latency from sleep for meaningful and non-meaningful stimuli. *Psychophysiology* **11**, 1–5 (1974).

2. 2.

Buendia, N., Goode, M., Sierra, G. & Segundo, J. P. Responsiveness and discrimination during sleep. *Experientia* **19**, 208–209 (1963).

3. 3.

Oswald, I., Taylor, A. M. & Treisman, M. Discriminative responses to stimulation during human sleep. *Brain* **83**, 440–453 (1960).

4. 4.

Twyver, H. V. & Garrett, W. Arousal threshold in the rat determined by “meaningful” stimuli. *Behav. Biol.* **7**, 205–215 (1972).

5. 5.

Siegel, J. & Langley, T. D. Arousal threshold in the cat as a function of sleep phase and stimulus significance. *Experientia* **21**, 740–741 (1965).

6. 6.

Tannenbaum, P. L. et al. Orexin receptor antagonist-induced sleep does not impair the ability to wake in response to emotionally salient acoustic stimuli in dogs. *Front. Behav. Neurosci.* **8**, 182 (2014).

7. 7.

Beckwith, E. J. & French, A. S. Sleep in *Drosophila* and its context. *Front. Physiol.* **10**, 1167 (2019).

8. 8.

Geissmann, Q. et al. Ethoscopes: an open platform for high-throughput ethomics. *PLoS Biol.* **15**, e2003026 (2017).

9. 9.

Geissmann, Q., Beckwith, E. J. & Gilestro, G. F. Most sleep does not serve a vital function: evidence from *Drosophila melanogaster*. *Sci. Adv.* **5**, eaau9253 (2019).

10. 10.

Knaden, M., Strutz, A., Ahsan, J., Sachse, S. & Hansson, B. S. Spatial representation of odorant valence in an insect brain. *Cell Rep.* **1**, 392–399 (2012).

11. 11.

Joseph, R. M., Devineni, A. V., King, I. F. G. & Heberlein, U. Oviposition preference for and positional avoidance of acetic acid provide a model for competing behavioral drives in *Drosophila*. *Proc. Natl Acad. Sci. USA* **106**, 11352–11357 (2009).

12. 12.

Gao, X. J., Clandinin, T. R. & Luo, L. Extremely sparse olfactory inputs are sufficient to mediate innate aversion in *Drosophila*. *PLoS ONE* **10**, e0125986 (2015).

13. 13.

Chakir, M., Peridy, O., Capy, P., Pla, E. & David, J. R. Adaptation to alcoholic fermentation in *Drosophila*: a parallel selection imposed by environmental ethanol and acetic acid. *Proc. Natl Acad. Sci. USA* **90**, 3621–3625 (1993).

14. 14.

Faville, R., Kottler, B., Goodhill, G. J., Shaw, P. J. & van Swinderen, B. How deeply does your mutant sleep? Probing arousal to better understand sleep defects in *Drosophila*. *Sci. Rep.* **5**, 8454 (2015).

15. 15.

Tamaki, M., Bang, J. W., Watanabe, T. & Sasaki, Y. Night watch in one brain hemisphere during sleep associated with the first-night effect in humans. *Curr. Biol.* **26**, 1190–1194 (2016).

16. 16.

Newman, J. D. Neural circuits underlying crying and cry responding in mammals. *Behav. Brain Res.* **182**, 155–165 (2007).

17. 17.

Ebrahim, I. O., Shapiro, C. M., Williams, A. J. & Fenwick, P. B. Alcohol and sleep I: effects on normal sleep. *Alcohol. Clin. Exp. Res.* **37**, 539–549 (2013).

18. 18.

Masse, N. Y., Turner, G. C. & Jefferis, G. S. X. E. Olfactory information processing in *Drosophila*. *Curr. Biol.* **19**, R700–R713 (2009).

19. 19.

Sayin, S. et al. A neural circuit arbitrates between persistence and withdrawal in hungry *Drosophila*. *Neuron* **104**, 544–558.e6 (2019).

20. 20.

Hattori, D. et al. Representations of novelty and familiarity in a mushroom body compartment. *Cell* **169**, 956–969.e17 (2017).

21. 21.

Seidner, G. et al. Identification of neurons with a privileged role in sleep homeostasis in *Drosophila melanogaster*. *Curr. Biol.* **25**, 2928–2938 (2015).

22. 22.

Wolff, T., Iyer, N. A. & Rubin, G. M. Neuroarchitecture and neuroanatomy of the *Drosophila* central complex: a GAL4-based dissection of protocerebral bridge neurons and circuits. *J. Comp. Neurol.* **523**, 997–1037 (2015).

23. 23.

Ni, J. D. et al. Differential regulation of the *Drosophila* sleep homeostat by circadian and arousal inputs. *eLife* **8**, e40487 (2019).

24. 24.

Modi, M. N., Shuai, Y. & Turner, G. C. The *Drosophila* mushroom body: from architecture to algorithm in a learning circuit. *Annu. Rev. Neurosci.* **43**, 465–484 (2020).

25. 25.

Devineni, A. V., Sun, B., Zhukovskaya, A. & Axel, R. Acetic acid activates distinct taste pathways in *Drosophila* to elicit opposing, state-dependent feeding responses. *eLife* **8**, e47677 (2019).

26. 26.

Ko, K. I. et al. Starvation promotes concerted modulation of appetitive olfactory behavior via parallel neuromodulatory circuits. *eLife* **4**, e08298 (2015).

27. 27.

Keene, A. C. et al. Clock and cycle limit starvation-induced sleep loss in *Drosophila*. *Curr. Biol.* **20**, 1209–1215 (2010).

28. 28.

Lin, C.-C., Riabinina, O. & Potter, C. J. Olfactory behaviors assayed by computer tracking of *Drosophila* in a four-quadrant olfactometer. *J. Vis. Exp.* **114**, e54346 (2016).

29. 29.

Schindelin, J. et al. Fiji: an open-source platform for biological-image analysis. *Nat. Methods* **9**, 676–682 (2012).

30. 30.

Talay, M. et al. Transsynaptic mapping of second-order taste neurons in flies by trans-Tango. *Neuron* **96**, 783-795.e4 (2017).

31. 31.

Feinberg, E. H. et al. GFP reconstitution across synaptic partners (GRASP) defines cell contacts and synapses in living nervous systems. *Neuron* **57**, 353–363 (2008).

32. 32.

Geissmann, Q., Rodriguez, L. G., Beckwith, E. J. & Gilestro, G. F. Rethomics: an R framework to analyse high-throughput behavioural data. *PLoS ONE* **14**, e0209331 (2019).

33. 33.

French, A., Geissmann, Q., Beckwith, E. & Gilestro, G. Sensory processing during sleep in *Drosophila melanogaster*—ethoscope dataset. Zenodo <https://doi.org/10.5281/zenodo.5109970> (2021).

Acknowledgements

We thank all members of the Gilestro laboratory for discussions and intellectual contributions and the fly community for sharing reagents and protocols; special thanks to G. Rubin for sharing unpublished information and to A. Bates for sharing some beautiful drawings on scidraw.io. A.S.F. was supported by the Biotechnology and Biological Sciences Research Council (BBSRC) through grants BB/M003930/1 and BB/R018839/1. E.J.B. was supported by EMBO ALTF 57–2014 and by the People Programme (Marie Curie Actions) of the European Union’s Eighth Framework Programme H2020 under REA grant agreement 705930. Q.G. was supported by a BBSRC DTP scholarship BB/J014575/1. We thank the Imperial College London Advanced Hackspace (ICAH) and the Facility for Imaging by Light Microscopy (FILM) at Imperial College London, partly supported by funding from the Wellcome Trust (grant 104931/Z/14/Z) and BBSRC (grant BB/L015129/1).

Author information

Affiliations

1. Department of Life Sciences, Imperial College London, London, UK
Alice S. French & Giorgio F. Gilestro
2. Department of Microbiology and Immunology, University of British Columbia, Vancouver, British Columbia, Canada
Quentin Geissmann
3. Instituto de Fisiología, Biología Molecular y Neurociencias (IFIBYNE), UBA-CONICET, Buenos Aires, Argentina

Esteban J. Beckwith

Contributions

A.F. and E.J.B. performed all of the experiments. Q.G. wrote the software for the collection and analysis of the data. A.F. and G.F.G. analysed the data. A.F. and G.F.G. devised and planned all of the experiments. All authors contributed to the preparation of the manuscript.

Corresponding author

Correspondence to Giorgio F. Gilestro.

Ethics declarations

Competing interests

The authors declare no competing interests.

Additional information

Peer review information *Nature* thanks the anonymous reviewers for their contribution to the peer review of this work. Peer reviewer reports are available.

Publisher's note Springer Nature remains neutral with regard to jurisdictional claims in published maps and institutional affiliations.

Extended data figures and tables

[Extended Data Fig. 1 Occurrence and length of sleep bouts vary during the day.](#)

a, Schematics of the experimental setup. **b**, Average numbers of puffs per fly per hour in three conditions (0%; 5%; 10% acetic acid. Ns 106, 105, 103

respectively). The top grey bars show how experiments were conducted at eight independent, overlapping intervals. **c**, Mean response per fly at different time point during the day, grouped by concentration of acetic acid. Same dataset as in Fig. [1d](#). **d**, Total distribution of sleep bouts by length, binned at 1-minute intervals during three time points representing different types of sleep (ZT 4-6, ZT 13-15 and ZT18-20). The three grey vertical lines indicate the bins for 5-, 8-, and 12-minutes sleep respectively as chosen for the analysis in Fig. [1c-e](#). In all panels, errors are shown as bootstrapped 95% CI.

[Source data](#)

Extended Data Fig. 2 Changes in internal states affects arousal threshold during sleep.

a, Schematic showing experimental procedures used in **b**, **c** and main Fig. [2a,b](#). **b**, Responses to 5% acetic acid in mock control flies (left) and flies previously intoxicated with vapours of 20% ethanol (right). Ethanol or mock exposure were limited to a 1-hour window between ZT15.5-16.5 and arousal was quantified and shown for ZT18-20. **c**, Quantification of the stimulus-evoked response in rested control flies (left) or flies that were previously deprived of sleep for 12h (right). Sleep deprivation was performed during the subjective night (ZT12-24) and waking to an olfactory stimulus (5% acetic acid) was measured during the subsequent day (ZT0-6). In all panels, errors are shown as bootstrapped 95% CI.

[Source data](#)

Extended Data Fig. 3 Inhibition of MB011B reduces arousal threshold.

a, Waking responses of control flies (MBON-GAL4^{+/+}) and those with temperature inhibited MBONs (MBON-GAL4/Shi^{TS}) to 5% acetic acid between ZT15-24. **b**, 9 h response profile for MB011B Shi^{TS} silencing (light blue) compared to its appropriate parental controls (shades of grey). In all panels, errors are shown as bootstrapped 95% CI.

[Source data](#)

[Extended Data Fig. 4 Activation or inhibition of some MBONs modulates sleep.](#)

a, b, 24h sleep profiles (**a**) and mean sleep amount (**b**) exhibited by flies with inhibited MBON neurons (MBON/Shi^{TS}: blue) or those carrying only the MBON-GAL4 (MBON-GAL4/+: grey solid) or only UAS-Shi^{TS} (UAS-Shi^{TS} /+: grey hashed) transgene over a 24hr baseline day. Ns underneath indicate the number of individual flies and refer to **b** and **a**. **c, d**, 24hr sleep profiles (**c**) and mean sleep amount (**d**) exhibited by flies with activated MBON neurons (MBON/dTRPA1:red) or those carrying only the MBON-GAL4 (MBON-GAL4/+: grey solid) or only UAS-dTRPA1 (UAS-dTRPA1: grey hashed) transgene over a 24hr baseline day. Ns underneath indicate the number of individual flies and refer to **c, d**. In all panels, errors are shown as bootstrapped 95% CI.

[Source data](#)

[Extended Data Fig. 5 Activation or inhibition R23E10 neurons alters behavior.](#)

a, Waking responses of control flies (UAS-Shi^{TS} and UAS-TRPA1) and those with temperature manipulated dFSB neurons (23E10-GAL4/Shi^{TS} and 23E10-GAL4/dTrpa1) to 5% acetic acid, between ZT18-20. Experiment performed at 29 °C. **b**, 24h sleep profile of dFSB inactivation through Shi^{TS} (blue) compared to parental controls (grey). **c**, 24h sleep profile of dFSB forced activation through dTRPA1 (red) compared to parental controls (grey). **d–f**, Walking (**d**), micromovements (**e**) and X-position profiles (**f**) of control flies (UAS-Shi^{TS}: grey hashed, R23E10-GAL4: grey) and those with inhibited dFSB neurons (R23E210-GAL4/UAS-Shi^{TS}) over a 24 h baseline day. **g–i**, Walking (**g**), micromovements (**h**) and X-position profiles (**i**) of control flies (UAS-TRPA1: grey hashed, R23E10-GAL4: grey) and those with activated dFSB neurons (R23E210-GAL4/UAS-TRPA1) over a 24 h baseline day.

Experiments preformed at 29 °C on 2-3 day old male flies in 12h:12h L:D cycle. In all panels, errors are shown as bootstrapped 95% CI.

[Source data](#)

Supplementary information

[Supplementary Table 1](#)

Technical summary of odourants used in Fig. 2

[Reporting Summary](#)

[Peer Review File](#)

[Supplementary Data 1](#)

All raw data and scripts used for analysis

Source data

[Source Data Fig. 1](#)

[Source Data Fig. 2](#)

[Source Data Fig. 3](#)

[Source Data Fig. 4](#)

[Source Data Extended Data Fig. 1](#)

[Source Data Extended Data Fig. 2](#)

[Source Data Extended Data Fig. 3](#)

[Source Data Extended Data Fig. 4](#)

[Source Data Extended Data Fig. 5](#)

Rights and permissions

[Reprints and Permissions](#)

About this article

Cite this article

French, A.S., Geissmann, Q., Beckwith, E.J. *et al.* Sensory processing during sleep in *Drosophila melanogaster*. *Nature* **598**, 479–482 (2021). <https://doi.org/10.1038/s41586-021-03954-w>

- Received: 22 January 2020
- Accepted: 25 August 2021
- Published: 29 September 2021
- Issue Date: 21 October 2021
- DOI: <https://doi.org/10.1038/s41586-021-03954-w>

Share this article

Anyone you share the following link with will be able to read this content:

[Get shareable link](#)

Sorry, a shareable link is not currently available for this article.

[Copy to clipboard](#)

Provided by the Springer Nature SharedIt content-sharing initiative

Flies sense the world while sleeping

- Wanhe Li
- Alex C. Keene

News & Views 29 Sept 2021

This article was downloaded by **calibre** from <https://www.nature.com/articles/s41586-021-03954-w>

| [Section menu](#) | [Main menu](#) |

- Article
- [Published: 01 October 2021](#)

Regulation of prefrontal patterning and connectivity by retinoic acid

- [Mikihito Shibata](#)^{1,na1},
- [Kartik Pattabiraman](#)^{1,2,na1},
- [Belen Lorente-Galdos](#)¹,
- [David Andrijevic](#) ORCID: orcid.org/0000-0002-5703-3837¹,
- [Suel-Kee Kim](#) ORCID: orcid.org/0000-0003-0240-9304¹,
- [Navjot Kaur](#)¹,
- [Sydney K. Muchnik](#)^{1,3},
- [Xiaojun Xing](#)^{1,4},
- [Gabriel Santpere](#)^{1,5},
- [Andre M. M. Sousa](#) ORCID: orcid.org/0000-0003-1740-5066^{1,6,7} &
- [Nenad Sestan](#) ORCID: orcid.org/0000-0003-0966-9619^{1,3,4,8,9,10,11}

Nature volume **598**, pages 483–488 (2021)

- 13k Accesses
- 1 Citations
- 105 Altmetric
- [Metrics details](#)

Subjects

- [Development of the nervous system](#)
- [Diseases of the nervous system](#)
- [Neural circuits](#)

Abstract

The prefrontal cortex (PFC) and its connections with the mediodorsal thalamus are crucial for cognitive flexibility and working memory¹ and are thought to be altered in disorders such as autism^{2,3} and schizophrenia^{4,5}. Although developmental mechanisms that govern the regional patterning of the cerebral cortex have been characterized in rodents^{6,7,8,9}, the mechanisms that underlie the development of PFC–mediodorsal thalamus connectivity and the lateral expansion of the PFC with a distinct granular layer 4 in primates^{10,11} remain unknown. Here we report an anterior (frontal) to posterior (temporal), PFC-enriched gradient of retinoic acid, a signalling molecule that regulates neural development and function^{12,13,14,15}, and we identify genes that are regulated by retinoic acid in the neocortex of humans and macaques at the early and middle stages of fetal development. We observed several potential sources of retinoic acid, including the expression and cortical expansion of retinoic-acid-synthesizing enzymes specifically in primates as compared to mice. Furthermore, retinoic acid signalling is largely confined to the prospective PFC by CYP26B1, a retinoic-acid-catabolizing enzyme, which is upregulated in the prospective motor cortex. Genetic deletions in mice revealed that retinoic acid signalling through the retinoic acid receptors RXRG and RARB, as well as CYP26B1-dependent catabolism, are involved in proper molecular patterning of prefrontal and motor areas, development of PFC–mediodorsal thalamus connectivity, intra-PFC dendritic spinogenesis and expression of the layer 4 marker *RORB*. Together, these findings show that retinoic acid signalling has a critical role in the development of the PFC and, potentially, in its evolutionary expansion.

[Download PDF](#)

Main

The PFC reaches its greatest complexity in anthropoid primates (monkeys and apes), which appear to uniquely have many prefrontal areas that cover the entire anterior two-thirds of the frontal lobe and a well-defined granular layer 4^{10,11}. Previous analyses revealed that the transcriptomic differences between neocortical areas are most prominent in primates during the middle stages of fetal development, corresponding to post-conception weeks (PCW) 13 to 24 (hereafter referred to as ‘mid-fetal’)^{16,17}—a crucial period for neuronal specification and the initial assembly of neocortical neural circuits¹⁸. Thus, we hypothesized that the molecular processes that govern the development and evolutionary diversification of the PFC could be revealed by differential regional gene expression analysis of the primate mid-fetal neocortex.

Fetal frontal upregulation of RA-related genes

Using human BrainSpan RNA-sequencing (RNA-seq) data¹⁷, we screened for genes that are differentially upregulated in the mid-fetal frontal lobe. The mid-fetal data consisted of tissue-level samples ranging in age from PCW 16 to 22, which included four prospective PFC areas (medial, mPFC or MFC; orbital, oPFC or OFC; dorsolateral, dlPFC or DFC; and ventrolateral, vLPFC or VFC) and the primary motor cortex (M1C). Gene expression in these frontal areas was compared to areas within the parietal (primary sensory cortex, S1C; and inferior parietal cortex, IPC), occipital (primary visual cortex, V1C), and temporal lobes (primary auditory cortex, A1C; superior temporal cortex, STC; and inferior temporal cortex, ITC) (Fig. 1a, Extended Data Fig. 1a). We identified 190 protein-coding genes, using stringent criteria, that were specifically upregulated in at least one area within a lobe in comparison with areas from other lobes, including 125 in the frontal lobe, which were able to differentiate the four brain lobes and most areas within them (as observed by principal component analysis (PCA)) (Fig. 1b, Extended Data Fig. 1a,b). Moreover, the first principal component (PC1), which accounts for the highest variability present in the data, corresponded to the anterior–posterior or frontal–temporal axis (Fig. 1b). Gene Ontology (GO) analysis of the frontally upregulated genes identified an enrichment of genes associated with categories such as ‘response to retinoic acid’, ‘synapse organization/assembly’ and ‘axon development/guidance’ (Fig. 1c,d, Supplementary Tables 1, 2), suggesting that these genes may have a role in frontal lobe patterning and circuit development. Many of the same frontal-lobe-enriched and retinoic acid (RA)-related genes were upregulated in the mid-fetal macaque frontal cortex using a PsychENCODE dataset¹⁹ (Extended Data Fig. 1c,d). We also observed prominent frontal enrichment of many of the same genes during the early fetal period (Extended Data Figs. 1, 2). Closer analysis of the spatiotemporal profile of the fetal frontally upregulated genes revealed the enrichment to be largely transient, with mainly conserved and some divergent expression patterns between human and macaque (Extended Data Fig. 4b).

Fig. 1: Predicted RA-signalling-associated genes are upregulated in human mid-fetal prospective frontal areas.

 **figure1**

a, Diagram of the analysed eleven areas of the human mid-fetal brain from the four lobes. **b**, PCA of genes specifically enriched in at least one area within a lobe. Ellipses are centred on the mean of the points of a given area and the size of the axes corresponds to their standard deviation on each component. **c**, GO terms associated with frontally upregulated genes and their unadjusted *P* value. Black text is used to highlight relevant GO terms. **d**, PC loadings with labelled genes being upregulated in the PFC (black dots) and M1C (grey dots). Genes highlighted in blue are associated with RA signalling and genes with red or green outlines are predicted ASD or SCZ risk genes, respectively. For reproducibility information, see [Methods](#).

Analysing only the RNA-seq data that encompassed the five mid-fetal frontal areas¹⁷, predicted RA-signalling-associated genes—such as *CBLN2*, *RXRG*, *CDH8*, *MEIS2* and *RBPI*—were among the genes upregulated in the PFC compared to the M1C (Fig. **1d**, Supplementary Table **2**; see our accompanying study²⁰), whereas the RA-

degrading enzyme CYP26B1 was upregulated in the M1C (Fig. 1d), consistent with previous microarray-based findings²¹. We also identified multiple predicted autism spectrum disorder (ASD) (group 1–3; <https://gene.safari.org/>) and schizophrenia (SCZ) (score of 3 or higher from <http://szdb.org/>) risk genes that were upregulated in the mid-fetal frontal cortex (Fig. 1d, Supplementary Table 2).

Mid-fetal PFC-enriched gradient of RA

RA is a diffusible biologically active derivative of vitamin A that is involved in neural tube patterning, neurogenesis, cell differentiation and synaptic function^{12,13,22,23,24,25,26,27}. Moreover, alterations in RA signalling have been implicated in the pathophysiology of ASD^{28,29,30} and SCZ^{14,31,32}. Given the enrichment of RA-related genes among the upregulated fetal frontal genes, we assessed the concentration of RA in different areas of the human and macaque mid-fetal neocortex, and in the neonatal mouse neocortex (approximately equivalent developmental ages), using an enzyme-linked immunosorbent assay (ELISA). We found that there was a PFC-enriched anterior–posterior gradient of RA concentration in the human and macaque mid-fetal neocortex, with homologous mPFC exhibiting the highest concentration within each species (Fig. 2). Overall, RA concentrations were significantly higher in prospective primate PFC areas compared to more posterior areas. Comparison across the three species identified higher concentrations of RA both in the mPFC and in all four PFC areas overall in humans as compared to the other two species (Fig. 2), as well as in macaques compared to mice (Fig. 2). Notably, the ITC—an association area within the temporal lobe that is thought to exhibit unique features and connectivity in humans³³—had a higher concentration of RA among non-frontal areas in humans (Fig. 2), with a two-fold increase in RA concentration in humans compared to macaques.

Fig. 2: PFC-enriched anterior–posterior gradient of RA.

 **figure2**

RA concentrations in human (post-conception weeks (PCW) 16, 18, 19 and 21), macaque (four post-conception day (PCD) 110 brains) and mouse (four PD 1 brains) cortical areas ($n = 3\text{--}4$ for each sample area). One-way ANOVA with post-hoc Dunnett's adjustment or two-tailed unpaired *t*-test: **** $P < 1 \times 10^{-4}$, *** $P = 0.0005$ (macaque PFC versus mouse PFC), ** $P = 0.005$ (human non-PFC minus ITC versus human ITC), * $P = 0.01$ (human PFC versus macaque PFC), * $P = 0.04$ (human ITC versus macaque ITC). Centre value, average; error bars, s.e.m. The dashed red line in the macaque graph represents the human RA concentrations. A single assay was done for each brain sample. dmPFC, dorsomedial PFC; ENT, entorhinal cortex; PIR, piriform cortex; RSP, retrosplenial cortex; SSs, secondary somatosensory area; VISp, primary visual cortex; vmPFC, ventromedial PFC.

Expanded RA synthesis in the primate cortex

The observed enrichment and primate-specific lateral expansion of RA levels in the fetal PFC led us to systematically examine the spatiotemporal expression of RA-synthesizing enzymes (ALDH1A1–ALDH1A3) and RA-degrading enzymes (CYP26A1, CYP26B1 and CYP26C1^{27,28}) in human, macaque and mouse (for full descriptions, see [Supplementary Results](#)). In brief, we observed several potential sources of RA in the fetal cortex, including conserved expression of ALDH1A1 in the meninges and midbrain axons, and ALDH1A3 in the mPFC²⁶. We also observed primate-specific expression of ALDH1A1 in astrocytes and frontal subplate neurons, and lateral frontal expression of *ALDH1A1* and *ALDH1A3* (Extended Data Fig. 6). These primate-specific expression patterns were complementary to the increase in and

lateral expansion of RA in the mid- and late-fetal primate PFC and the lateral extension of PFC in anthropoid primates^{10,11}.

Frontal RA signalling is mediated by RARB and RXRG

Given the fetal frontal cortical upregulation of both RA and RA synthesizing enzymes, we further assessed the expression of RA-dependent receptors and RA-responsive downstream genes in the developing human, macaque and mouse cortex. In addition to *RXRG*, which is upregulated in the human mid-fetal PFC²¹ (Extended Data Fig. 1c), several genes that encode RA receptors were also detected in the developing human, macaque and mouse cortex or cultured human primary mid-fetal cortical neurons (Extended Data Figs. 5, 8, 9, 15b). Of these, only RARB and RXRG exhibited a higher anterior to lower posterior gradient of expression (Extended Data Figs. 8, 9a).

The RARB–RXRG heterodimer has previously been shown to mediate RA signalling in the adult mouse cortex and striatum, and is required for learning, locomotion and dopamine signalling^{34,35}. To assess whether RARB and RXRG are required for RA signalling activity in the developing mouse frontal cortex, we generated constitutive *Rarb* and *Rxrg* double-knockout (dKO) mice (Extended Data Fig. 9d), which—consistent with previous findings^{34,35}—are viable. Using a *RARE-lacZ* reporter line³⁶ in which *lacZ* is under the transcriptional control of an RA response element, we identified a significant reduction of RA signalling in the mPFC of dKO mice at postnatal day (PD) 0 compared to control mice (Fig. 3a, Extended Data Fig. 10a). In addition, we found a less extensive reduction of RA signalling in the anterior cingulate area (ACA) and retrosplenial area (Extended Data Fig. 10a). Furthermore, expression of frontally enriched RA-regulated genes, *Cbln2*²⁰ and *Meis2*, which are induced by RA in human and chimpanzee cerebral organoids and repressed by RA receptor antagonists in human cortical neurons (Fig. 1d, Extended Data Figs. 11b, 15d), was reduced in the dKO mice (Extended Data Fig. 10b). Together, these findings indicate that RARB and RXRG mediate RA signalling in the developing mouse mPFC.

Fig. 3: Reduced RA signalling in the PFC of mice lacking *Rarb* and *Rxrg* leads to the downregulation of genes involved in synapse and axon development.

 **figure3**

a, β -Galactosidase histochemical staining in *Rarb*^{+/+}*Rxrg*^{+/+} (wild type; WT); *RARE-lacZ* (blue) and *Rarb*^{-/-}*Rxrg*^{-/-} (dKO); *RARE-lacZ* (orange) brains at PD 0. Two-tailed Student's *t*-test (WT versus dKO): *** $P = 1 \times 10^{-6}$ (left), 3×10^{-4} (right). Centre value, average; error bars, s.e.m. ($n = 3$ per genotype). Scale bars, 200 μm ; 50 μm (inset). **b**, First two principal components calculated from the expression of differentially expressed protein-coding genes between WT and dKO littermates in at least one of the three frontal cortex areas (mPFC, MOs and OFC). **c**, GO terms associated with differentially expressed genes showing their *z*-score and unadjusted *P* values. The *z*-score represents the proportion of upregulated versus downregulated genes in the dKO compared to the WT that are associated with each GO term. Dark blue, *z*-score < -5 ; light blue, *z*-score -5 to 0; orange, *z*-score > 0 . The size of the bubbles is proportional to the total number of differentially expressed genes associated with the given GO term. Black text is used to highlight relevant GO terms. **d**, Quantification of excitatory synapses marked by DLG4 (PSD95) in the mPFC, MOs, OFC, MOp and SSp regions of PD 0 WT and dKO mice brains. Two-tailed Student's *t*-test: ** $P = 6 \times 10^{-4}$ (mPFC); 2×10^{-3} (MOs). Centre value, average; error bars, s.e.m. ($n = 3$ per genotype). For reproducibility information, see [Methods](#).

RARB and RXRG regulate frontal connectivity

To understand the functional importance of RA signalling through the RARB–RXRG heterodimer in the developing cortex, we performed RNA-seq analysis of different regions of the PD 0 mouse frontal cortex (mPFC; secondary motor cortex (MOs) and the adjacent parts of the primary motor cortex (MOp); and OFC) microdissected from dKO and wild-type littermates. We identified 4,768 differentially expressed protein-coding genes between the two genotypes in at least one of the areas, with the highest number of differentially expressed genes in the mPFC (Extended Data Fig. [12a](#), Supplementary Table [3](#)). PCA based on the expression of these differentially expressed genes separated the wild-type and dKO mice along PC1, with the mPFC showing the greatest distance between wild type and dKO, further supporting the notion that the mPFC is most affected by the reduction in RA signalling (Fig. [3b](#)).

The GO enrichment analysis revealed that terms associated with genes that are overexpressed in the wild-type compared to the dKO frontal cortex were highly related to the process of synaptogenesis and cellular components related to synapses and axons, whereas the genes that are overexpressed in the dKO were related to the regulation of the cell cycle (Fig. [3c](#), Extended Data Fig. [12c,d](#)). In addition, when analysing differentially expressed genes in individual regions of the frontal cortex, only genes overexpressed exclusively in the wild-type mPFC were associated with the cellular components, axons and synapses (Extended Data Fig. [12c,d](#)). Several of the genes overexpressed in wild-type mice that are related to axon guidance and synapse development exhibited an anterior enrichment in wild-type neonatal mouse cortex (Extended Data Fig. [13a](#), Supplementary Table [4](#)). We also observed a significant enrichment of homologous genes specifically upregulated in the human mid-fetal frontal lobe among the genes that were downregulated exclusively in the frontal cortex and mPFC of the dKO mice (Extended Data Fig. [12b,e](#)). Overall, these results suggest a possible role for RA signalling in the regulation of synaptogenesis and axon development, specifically in the mPFC.

We analysed the role of RA in synaptogenesis by quantifying synaptic puncta in multiple regions of the PD 0 cortex in dKO mice compared to wild-type littermate controls. We identified a significant reduction in DLG4 (also known as PSD95)-positive excitatory post-synaptic densities in the dKO mPFC and MOs compared to wild-type, but not in the OFC, primary motor area (MOp) and primary somatosensory area (SSp) (Fig. [3d](#), Extended Data Fig. [13b](#)). Similarly, we identified a significant decrease in synaptophysin (SYP) and DLG4 co-immunolabelled puncta in deep layers of the mPFC (Extended Data Fig [13c](#)) and a decrease in number of all and mushroom dendritic spines in mPFC pyramidal neurons labelled by the retrograde viral tracer *AAVrg-Cag-Gfp* (Extended Data Fig. [14e](#)). Of note, there was no difference observed in the dendritic complexity of mPFC upper-layer neurons (Extended Data Fig. [14e](#)). In addition, treating human primary cortical neurons with RA induced the expression of *DLG4* (*PSD95*) mRNA, and DLG4 (*PSD95*) and SYP co-immunolabelled synaptic puncta, whereas applying the RA receptor inhibitor

AGN193109 had the opposite effect (Extended Data Fig. 15e–j). Similarly, treatment with RA-soaked beads induced the expression of DLG4 (PSD95) in both human and chimpanzee cerebral organoids (Extended Data Fig. 11b,c). We assessed the role of RA signalling in regulating the expression of the gene encoding synaptic organizer CBLN2 and local connectivity in our accompanying study²⁰.

We investigated the role of RA signalling in long-range connections from the mPFC using diffusion tensor imaging (DTI). We identified a reduction in long-range connections between the mPFC and thalamus in dKO compared to wild-type mice at PD 5 (Fig. 4a,b). There was no observable difference in connections between the left and right mPFC at PD 5 (Fig. 4a,c). Owing to the limitations of the technique and the developmental stage, we were unable to study the connections between the mPFC and striatum or basolateral amygdala (BLA) using DTI. Anterograde lipophilic axon-tracing experiments starting from the mPFC or the mediodorsal thalamus (MD) at PD 21 similarly identified a reciprocal reduction in PFC–MD connectivity, as well as a reduction in the number of fibres in the internal capsule (Fig. 4d,e, Extended Data Fig. 13d). To more fully examine mPFC connectivity in dKO mice, we used a retrograde viral tracer to study inputs into the PD 30 mPFC. We identified reduced inputs from the MD and anterior insula in dKO mice, whereas no obvious changes were identified in inputs from the contralateral mPFC, MOs or MOp, internal capsule, claustrum, piriform cortex, amygdala and ventral hippocampus (Extended Data Fig. 14a–d). Finally, we assessed for changes in dopaminergic innervation of the mPFC and found no significant difference between wild type and dKO (Extended Data Fig. 16f).

Fig. 4: Altered mPFC–MD connectivity in mice lacking *Rarb* and *Rxrg*.

 **figure4**

a, Representation of the number of streamlines generated as a connectivity measurement between the cortical areas, thalamus and internal capsule (IC) at PD 5 using DTI. **b**, Visualization and quantification of streamlines between the mPFC and the thalamus in WT and dKO brains. Two-tailed unpaired *t*-test: $**P = 1 \times 10^{-3}$. Centre value, average; error bars, s.e.m. ($n = 5$ per genotype). **c**, Quantification of select corticothalamic, corticocortical and corticospinal streamlines. Two-tailed unpaired *t*-test: $P = 0.2$ (SSp–Th), 0.3 (mPFC–mPFC), 0.5 (SSp–SSp) and 0.5 (corticospinal). Error bars, s.e.m. ($n = 5$). **d**, **e**, DiI placement in the mPFC (**d**) and medial thalamus (**e**) in WT and dKO brains at PD 21 with labelled processes in the MD (**d**; inset), and mPFC (**e**; inset). Two-tailed Student's *t*-test: $*P = 9 \times 10^{-3}$, $**P = 3 \times 10^{-3}$. Centre value, average; error bars, s.e.m. ($n = 3$ per genotype). AU, arbitrary units. Scale bars, 1 mm; 100 μ m (inset).

Although there is reduced RA activity in the outer shell of the striatum in the dKO brain (Extended Data Fig. 10a), we found that fibres traverse through the medial aspect of the striatum, suggesting that alterations in RA signalling in the lateral striatum do not affect the guidance of reciprocal mPFC–MD connectivity. RA signalling has previously been implicated in thalamic development³⁷, so we assessed whether other thalamocortical connections were altered in the dKO mice at PD 5 using DTI. There was no observable difference in thalamocortical connectivity with the MOp, primary auditory area (AUDp) or SSp (Fig. 4a,c, Extended Data Fig. 16b) or in the formation of barrel fields in the SSp (Extended Data Fig. 16c). Given that *Aldh1a3* is expressed in the ACA²⁶, we also examined whether thalamocortical innervation was altered in the ACA and found no difference in the number of streamlines (Fig. 4a, Extended Data Fig. 16b). The corticospinal tract (CST) and connections across the corpus callosum between the left and right mPFC, SSp and MOp in the dKO showed no difference in the number of streamlines in dKO compared to wild type (Fig. 4a,c, Extended Data Fig. 16b). Furthermore, scalar indexes, which describe the microstructural integrity of white matter, were similar between wild-type and dKO mice in the corpus callosum, anterior commissure and internal capsule (Extended Data Fig. 16a). In addition, the width of the CST at PD 30 was slightly increased in the dKO mice (Extended Data Fig. 16d). The reduction of connections between the mPFC and thalamus was not due to cell death in the mPFC (Extended Data Fig. 16e). In summary, deletion of *Rarb* and *Rxrg* leads to a reduction of RA signalling specifically in the mPFC, as well as a selective reduction of reciprocal mPFC–MD connectivity.

RA signalling has previously been shown to be involved in the regulation of proliferation, cell cycle timing and cortical laminar development^{22,23,24}, which could underlie our findings. Thus, we assessed whether the constitutive deletion of *Rarb* and *Rxrg* leads to changes in cortical size and laminar organization. The volume of the brain, cortex and frontal cortex at PD 5 were not significantly different when measured by magnetic resonance imaging (MRI) (Extended Data Fig. 17a). We also quantified the number of neurons using the upper-layer markers CUX1 and POU3F2 (BRN2), layer 4 marker RORB, and deep-layer markers BCL11B (CTIP2) and TBR1, and found no difference between wild type and dKO in the mPFC, MOs or visual cortex (Extended Data Fig. 17b). We did find a modest reduction in RORB-labelled neurons in the motor cortex (Extended Data Fig. 17b). Of note, the mouse mPFC lacks a granular layer 4 and had minimal RORB-labelled cells.

Ectopic RA expands MD connectivity

MD innervation of the primate frontal cortex is expanded laterally compared to rodents, with the primate PFC areas having a more prominent layer 4^{10,11}. Thus, we investigated whether the expansion of RA signalling is sufficient to increase and laterally extend MD innervation and alter layer 4 development in the mouse neonatal

frontal cortex by genetically deleting the RA-degrading enzyme CYP26B1 in mice (Extended Data Fig. 18a). Consistent with previous findings in humans²¹ and mice²⁴, whole-mount and serial tissue section *in situ* hybridization revealed that *Cyp26b1* is upregulated in the prospective motor cortex (MOs and MOp) and anterior insula compared to the mPFC and OFC, defined by high expression of *Cbln2*, and SSp, defined by *Rorb* (Fig. 5a,b, Extended Data Fig. 18b). Although mice with constitutive deletion of *Cyp26b1* died perinatally, it has previously been shown that genetic deletion of *Cyp26b1* in mice resulted in the expansion of RA signalling in multiple organs prenatally³⁸ and post-natally in the mouse mPFC²⁴. To investigate the possible role of CYP26B1 in restricting RA signalling to the mouse medial frontal cortex, we generated *Cyp26b1* KO mice that also contained the *RARE-lacZ* transgene. The lack of *Cyp26b1* resulted in the spreading of RA signalling dorsolaterally toward the MOs and MOp regions of the *RARE-lacZ* reporter mouse line at post-conceptional day (PCD) 18 (Fig. 5c). This increase was not robustly observed in more posterior regions (Extended Data Fig. 18c).

Fig. 5: Increased RA signalling promotes mPFC–medial thalamic connectivity.

 **figure5**

a, Lateral (top) and coronal (bottom) views of whole-mount in situ hybridization (ISH) of the PD 0 mouse cortex with pseudo-colour merge of *Cbln2*, *Cyp26b1* and *Rorb*. OB, olfactory bulb. **b**, Expression of *Cyp26b1* in the PD 0 mouse brain using ISH. *Cyp26b1* expression shows a gradient from the insula (AI) to the MOs (insets). Arrows

indicate *Cyp26b1* expression at the insula and MOs. Scale bar, 200 µm. AMY, amygdala; GP, globus pallidus; HIP, hippocampus; IG, indusium griseum; IN, insula. **c**, β-Galactosidase histochemical staining of the mPFC of *Cyp26b1*^{+/+} (WT); *RARE-lacZ* and *Cyp26b1*^{-/-} (KO); *RARE-lacZ* mouse brains at PCD 18. Relative signal intensity was quantified in the boxed area compared with anterior mPFC expression (mPFC, MOs and MOp). Two-tailed Student's *t*-test (WT versus *Cyp26b1* KO): ****P* = 1 × 10⁻⁴, 6 × 10⁻⁵ (mPFC, MOp), ***P* = 4 × 10⁻⁴; 1 × 10⁻³ (MOs, MOp), **P* = 4 × 10⁻³, 2 × 10⁻² (mPFC, MOp). Error bars, s.e.m. (*n* = 3 per genotype). **d, e**, Representative images and quantification of DiI labelling in PCD 18 frontal MOp/MOs (**d**) and medial thalamus (**e**) after DiI was placed in the MD thalamus or mPFC of WT and *Cyp26b1* KO brains. Two-tailed Student's *t*-test: ****P* = 4 × 10⁻⁴, **P* = 0.03. Error bars, s.e.m. (*n* = 3 per genotype and condition). Scale bars: 200 µm. **f**, Representative image and quantification of expression of *Rorb* in WT and KO mice in PCD 18 primordial motor cortex divided into 5 bins (1–5). Two-tailed Student's *t*-test (WT versus *Cyp26b1* KO): ****P* = 2 × 10⁻⁴, **P* = 0.01. Centre value, average; error bars, s.e.m. (*n* = 3 per genotype).

Next, we used the *Cyp26b1* KO mice to study the effects of the expansion of RA signalling into the dorsolateral frontal cortex by inserting a crystal of 1,1'-dioctadecyl-3,3,3',3'-tetramethylindocarbocyanine perchlorate (DiI) into the medial thalamus of fixed post-mortem wild-type and KO brains, which were collected at PCD 18 owing to the perinatal lethality of the KO mice. Histological analysis revealed that wild-type littermates had occasional thalamocortical axons within the medial and dorsolateral frontal white matter and cortex at this age. By contrast, KO mice showed precocious and robust innervation of both the medial and the dorsolateral frontal cortex by the axons originating from the medial thalamus (Fig. 5d, Extended Data Fig. 19b). When DiI was placed in the motor cortex, KO mice showed an increased signal in the developing thalamus (Fig. 5e, Extended Data Fig. 19c). We also observed a moderately enlarged frontal cortex with grossly normal cytoarchitecture of the cortical wall and cortical plate in the analysed areas of the *Cyp26b1* KO cortex (Extended Data Fig. 20a, b).

Furthermore, we observed an upregulation and expansion in the laminar expression of the layer 4 marker *Rorb* in the motor cortex of neonatal *Cyp26b1* KO mice (Fig. 5f, Extended Data Fig. 19a) and after misexpression of *Aldh1a3* in the dorsolateral fronto-parietal cortex using in utero electroporation (Extended Data Fig. 20c). In summary, we identified that ectopic RA signalling in the perinatal mouse frontal cortex leads to the expansion of medial thalamocortical innervation as well as the increased laminar expression of *Rorb*, which are both characteristics of the lateral granular PFC in anthropoid primates^{10,11}.

Conclusions

We have shown here that RA signalling is required for proper prefrontal gene expression, spinogenesis and long-range connectivity. We propose that the early- and mid-fetal cortical expansion of RA signalling underlies the lateral expansion of PFC areas and MD innervation in primates. As the expansion of the prefrontal and temporal association areas has been proposed to be one of the evolutionary underpinnings of complex cognition^{9,10,11}, it will be important to explore whether RA signalling has a broader role in developmental specification and the expansion of association areas, as well as in disorders affecting cognition (see [Supplementary Discussion](#) for a detailed discussion).

Methods

Data reporting

No statistical methods were used to predetermine sample size. Data collection was performed by independent investigators. Prior to data analysis, all experiments were randomized and analysed by independent blinded observers.

Analysis of human and macaque transcriptomic data

Developing human and macaque brain RNA-seq data (counts file) with the metadata information were obtained from BrainSpan (<https://brainspan.org/>) and PsychENCODE (<http://development.psychencode.org/>; <http://evolution.psychencode.org/>) projects^{17,19}. The timelines of human and macaque development and associated periods were reported in a previous study³⁹.

For human mid-fetal periods 4–6, a total of 73 mRNA samples corresponding to 11 prospective neocortical areas, comprising the pial surface, marginal zone, cortical plate (layers 2–6) and adjacent subplate zone, from windows 3 and 4 (PCW 16–22) were considered for analyses (Extended Data Fig. 1). The human neocortical areas under study are the orbital (oPFC or OFC), dorsolateral (dlPFC or DFC), ventrolateral (vlPFC or VFC), medial (mPFC or MFC) prefrontal cortex and primary motor cortex (M1C) from the frontal lobe; primary somatosensory cortex (S1C) and posterior inferior parietal cortex (IPC) from the parietal lobe; primary auditory cortex (A1C), posterior superior temporal cortex (STC) and inferior temporal cortex (ITC) from the temporal lobe; and primary visual cortex (V1C) from the occipital lobe. A TMM normalization procedure was applied (function normalizeCounts from tweeDEseq package in R) to the expression of 15,724 protein-coding genes that show sufficiently large counts (determined with function filterByExpr from edgeR package in R). To

identify genes that are upregulated in a given brain lobe, we first applied RNentropy⁴⁰, available as a package in R, to determine which genes are differentially expressed among the 11 neocortical areas. Then, we considered a gene to be specifically overexpressed in a given lobe if (1) there is at least one area in this lobe where the gene is significantly upregulated; (2) the gene is not upregulated in any area of the other lobes; and (3) the gene is under-expressed in at least 30% of the areas from the remaining lobes. Similarly, we identified genes that are specifically upregulated in the PFC compared to the M1C, or vice versa, by first running RNentropy pairwise comparisons between M1C and each of the prefrontal areas independently. Then, a gene was considered to be upregulated in PFC if (1) it is upregulated in a prefrontal area in at least one of the comparisons; (2) it is not upregulated in M1C in any of the comparisons; and (3) it is under-expressed in M1C in at least three of the comparisons. A gene was considered to be upregulated in M1C if (1) it is overexpressed in MOp in at least three of the comparisons; (2) it is not upregulated in any PFC area; and (3) it is under-expressed in a prefrontal area in at least one of the comparisons. Principal component analyses were performed using the prcomp function in R by centring the log₂-transformed expression data of the selected genes. Significant GO terms were obtained with the goana function from the limma package in R, reporting the ones with at least 10 genes in the background and at least 5 in the dataset. Frontal lobe, PFC and M1C upregulated genes were characterized for association with RA signalling, autism spectrum disorder (ASD) and schizophrenia (SCZ) using the following criteria. Association with RA signalling was defined both by dysregulation in the PD 0 *Rarb* and *Rxrg* double-knockout frontal cortex RNA-sequencing dataset and by literature review identifying association with RA signalling. Association with ASD was based on <https://gene.safari.org/database/human-gene/>. Association with SCZ was based on a total score of 3 or higher on http://www.szdb.org/gene_rank.php. Information is provided in Supplementary Table 3.

Predicted ages for macaque samples were calculated via the TranscriptomeAge algorithm described previously¹⁹. To perform statistical comparisons, samples from various developmental periods were grouped (periods 4–6, 7–10 and 11–14) and a two-tailed Student's *t*-test was used to compare gene expression levels between brain regions and species.

Animals

All studies using mice (*Mus musculus*) and rhesus macaques (*Macaca mulatta*) were performed in accordance with protocols approved by Yale University's Institutional Animal Care and Use Committee and National Institutes of Health (NIH) guidelines. The animals were housed, and timed-pregnant prenatal and post-natal mouse and monkey brains were obtained in-house at the Yale Animal Resource Center.

Mice were reared in group housing less than five mice per cage at 25 °C and 56% humidity in a 12-h light:12-h dark cycle and provided food and water ad libitum with veterinary care provided by Yale Animal Resource Center. Both sexes were used and randomly assigned for all experiments. Animals were maintained on the C57BL/6J background. The day on which a vaginal plug was observed was designated as PCD 0.5 in mice. For timed pregnancies in monkeys, females were housed with males for three days and the middle day was designated after observation of a vaginal plug and subsequent pregnancy as PCD 1. By this method, the estimated age of a monkey fetus has a maximal variation of ±1 day in its 165-day gestation. All monkeys tested negative for herpes B virus and tuberculosis. *RARE-lacZ* (Tg(*RARE-Hspa1b/lacZ*)12Jrt) mice and timed-pregnant CD-1 mice for in utero electroporation were purchased from Jackson Laboratory and Charles River Laboratories, respectively. Sex of mouse samples in this study was not characterized.

Post-mortem human and macaque tissue

This study was conducted using post-mortem human brain specimens or RNA-seq data generated previously¹⁷ from tissue collections at the Department of Neuroscience at Yale School of Medicine, the Brain and Tissue Bank for Developmental Disorders at the University of Maryland, the Clinical Brain Disorders Branch of the National Institute of Mental Health, the Human Fetal Tissue Repository at the Albert Einstein College of Medicine, the Birth Defects Research Laboratory at the University of Washington (R24HD000836), Advanced Bioscience Resources and the Joint MRC–Wellcome Trust Human Developmental Biology Resource (www.hdbr.org; MR/R006237/1). Tissue was collected after obtaining parental or next of kin consent and with approval by the institutional review boards at each institution from which tissue specimens were obtained, the Yale University and the NIH. Donated deidentified tissue was handled in accordance with ethical guidelines and regulations for the research use of human brain tissue set forth by the NIH (https://oir.nih.gov/sites/default/files/uploads/sourcebook/documents/ethical_conduct/guidelines-biospecimen.pdf) and the WMA Declaration of Helsinki (<https://www.wma.net/policies-post/wma-declaration-of-helsinki-ethical-principles-for-medical-research-involving-human-subjects/>). All available non-identifying information was recorded for each specimen. No obvious signs of neuropathological alterations were observed in any of the human or macaque specimens analysed in this study. The post-mortem interval was defined as hours between time of death and time when tissue samples were fresh-frozen or started to undergo fixation process. We strived to keep warm ischaemia to a minimum and most of the post-mortem interval was composed of cold ischaemic time.

Generation of *Rarb*, *Rxrg* and *Cyp26b1* knockout mice using the CRISPR–Cas9 gene-editing technique

The overall strategy for the generation of *Rarb* and *Rxrg* KO mice follows a previously described protocol using the CRISPR–Cas9 genome editing technique⁴¹. For the construction of the templates of guidance RNAs, two sets of top and bottom strand oligomers (see Supplementary Table 4) directing the double-strand break at targeting sites were annealed and ligated into the BbsI site of a pX330-U6-Chimeric_BB-CBh-hSpCas9 vector⁴², which was purchased from Addgene (plasmid 42230). After amplification of the insert with T7-tagged primers (Supplementary Table 5), guidance RNAs were synthesized by T7 RNA polymerase. The coding region of Cas9 was PCR-amplified using pX330-U6-Chimeric_BB-CBh-hSpCas9 as a template and inserted into the pSP64 Poly(A) vector (Promega, P1241). Vectors were digested and linearized with EcoRI. *Cas9* mRNA was synthesized by SP6 RNA polymerase. Guidance RNAs and *Cas9* mRNA was purified by the MEGAclear Transcription Clean-Up Kit (Ambion, AM1908). *Cas9* mRNA and two guidance RNAs were mixed at a concentration of 10 ng μl^{-1} or 100 ng μl^{-1} in the microinjection buffer (5 mM Tris-HCl pH 7.5; 0.1 M EDTA) and injected into the pronuclei of fertilized eggs from the B6SJLF1/J mouse strain purchased from The Jackson Laboratory. The fertilized eggs were then transferred to the uterus of females of the CD-1 mouse strain, purchased from Charles River Laboratories. The first generation (F_0) mice with recombined alleles were identified by PCR with two primer sets designed outside and inside of the targeted area (Supplementary Table 5, Extended Data Fig. 9d), confirmed by genome DNA sequencing. The germline transmission in the F_1 generation was confirmed by the same sets of PCR primers. For generation of *Rxrg* KO mice, a pair of guidance RNAs flanking whole exon 3 and 4 were designed to delete a large part of the DNA-binding domain⁴³ (Extended Data Fig. 8d). For generation of *Rarb* KO mice, a pair of guidance RNAs was designed to delete the whole of exon 9 and a part of exon 10 (Extended Data Fig. 8d). As a result, α -helical sheets of H4 to H8 in the ligand-binding domain were deleted, and a frameshift occurred in the rest of the C-terminal region, which results in total abolition of receptor activity⁴³. For generation of *Cyp26b1* KO mice, a pair of guidance RNAs was designed to delete the whole of exon 3 and 6, as described previously, to abolish enzymatic activity⁴⁴ (Extended Data Fig. 18a). All primer sequences are listed in Supplementary Table 5.

Human primary neocortical cultures and differentiation

Fresh tissues from prenatal human brain specimens (PCW 8-HSB#765, sex not determined; PCW 20-HSB#781, female; PCW 23-HSB#784, male) were maintained in ice-cold Hibernate-E (Thermo Fisher Scientific, A1247601) and processed within 12 to 18 h post-mortem interval. Primary cortical neural stem cells from PCW 8 cortical tissue were isolated from the dissected neocortical proliferative zones (that is, the ventricular zone and subventricular zone). Primary cortical neural progenitors and

neurons from PCW 20 or PCW 23 cortical tissue were isolated from dissected neocortical walls, including cortical plate zones. In brief, the tissue was mechanically separated into small pieces, incubated with 2 mg ml⁻¹ papain (Brainbits, PAP) for 20 min, and gently triturated to a single-cell suspension with 0.1 mg ml⁻¹ DNase I (STEMCELL Technologies, 07900) in HBSS (Thermo Fisher Scientific, 88284). Cortical neural stem cell expansion and differentiation were performed as previously described⁴⁵. Cells were plated onto poly-l-ornithine/laminin-coated wells at a density of 2×10^5 cells in a 24-well plate (IBIDI) and cultured with DMEM/F12 supplemented with 1× N2 (Thermo Fisher Scientific, 17502048), 1× B27 (Thermo Fisher Scientific, 17504044), 10 ng FGF2 (R&D Systems, 3718-FB) and 1% penicillin–streptomycin (Thermo Fisher Scientific, 15140122). The expanded cortical stem cells were replated onto poly-l-ornithine/laminin-coated wells at a density of 1×10^5 cells in a 24-well plate, and differentiation to neurons was induced two days after plating by FGF2 withdrawal. The isolated cortical neural progenitors and neurons were plated onto poly-l-ornithine/laminin-coated wells at a density of 2×10^5 cells in a 24-well plate (Ibidi) and cultured without FGF2. On day 4 after the FGF2 withdrawal of cortical neural stem cell culture and day 2 of cortical progenitor and neuron culture, the medium was replaced with neurobasal medium (Thermo Fisher Scientific, 21103049) containing 1× N2 (Thermo Fisher Scientific, 17502048), 1× B27 (Thermo Fisher Scientific, 17504044), 10 ng ml⁻¹ BDNF (Abcam, 9794), 10 ng ml⁻¹ GDNF (R&D Systems, 212-GD) and 1% penicillin–streptomycin (Thermo Fisher Scientific, 15140148). After neural differentiation and further maturation (Extended Data Fig. 15a), cortical neurons were exposed to varying doses of all-trans retinoic acid (Sigma-Aldrich, R2625-50MG) or the pan-retinoic acid receptor antagonist AGN193109 (Tocris, 5758) for another 14 days. See Extended Data Fig. 15a for a summary.

Human and chimpanzee cerebral organoid culture

All human and chimpanzee cell lines were authenticated by morphology or genotyping, and tested negative for mycoplasma contamination, checked monthly using the MycoAlert Mycoplasma Detection Kit (Lonza). For maintenance of human (cell line: HSB311 #36 (refs. 46,47)) and chimpanzee (cell line: 3651D (ref. 48)) cell lines, induced pluripotent stem (iPS) cells were dissociated to single cells with Accutase (Thermo Fisher Scientific, 00-4555-56) and plated at a density of 1×10^5 cells per cm² in Matrigel (BD)-coated 6-well plates (Falcon) with mTeSR1 (STEMCELL Technologies, 85850) containing 5 μM Y27632, ROCK inhibitor (Sigma-Aldrich, Cat. SCM075). ROCK inhibitor was removed at 24 h after plating, and cells were cultured for another four days before the next passage. Cerebral organoids were generated by directed differentiation protocol as previously described^{45,46,47}. Human and chimpanzee iPS cells were dissociated into single cells using Accutase (Thermo Fisher Scientific, 00-4555-56). Neural induction was directed

by dual SMAD and WNT inhibition using neural induction medium supplemented with 100 nM LDN193189 (STEMCELL Technologies, 72147), 10 µM SB431542 (Selleck Chemicals, S1067) and 2 µM XAV939 (Sigma-Aldrich, X3004-5MG). The dissociated cells were reconstituted with the neural induction medium and plated at 10,000 cells per well in a 96-well v-bottom ultra-low-attachment plate (Sumitomo Bakelite). To increase the cell survival and aggregate formation, 10 µM Y-27632 (Sigma-Aldrich, SCM075) was added for the first day. After 10 days of stationary culture, organoids were transferred to a 6-well ultra-low-attachment plate (Millipore Sigma) and kept on an orbital shaker rotating at a speed of 90 rpm to enhance the nutrient and gas exchanges. From day 18, organoids were cultured with neural differentiation medium supplemented with 1× CD lipid concentrate (Thermo Fisher Scientific, 11905031), 5 µg ml⁻¹ heparin (STEMCELL Technologies, 07980), 20 ng ml⁻¹ BDNF (Abcam, 9794), 20 ng ml⁻¹ GDNF (R&D Systems, 212-GD), 200 µM cAMP (Sigma-Aldrich, 20–198) and 200 µM ascorbic acid (Sigma-Aldrich, A92902) for further neuronal maturation (Extended Data Fig. [10a](#)). On day 133, an RA-soaked bead was attached to each cerebral organoid by embedding with and solidifying the growth-factor-reduced Matrigel (Corning, 354230) and further cultured for 48 h before collection.

Preparation of RA-soaked beads

AG1-X2 Resin (150 or 200 µm in diameter, Bio Rad, 140–1231) were added with 1 M formic acid for 1 h and washed with distilled H₂O (5 × 5 min). Beads were completely dried in a 37 °C incubator overnight. Dried beads were soaked in either 1 mg ml⁻¹ or 5 mg ml⁻¹ of all-trans retinoic acid (Sigma-Aldrich, R2625-50MG) dissolved in DMSO (Sigma-Aldrich, D8418) for 1 h and then washed twice in DMEM (Gibco) before being placed onto human or chimpanzee organoids.

In situ hybridization

Whole-mount and section in situ hybridization was performed as described previously^{[49](#)}. Antisense digoxigenin (DIG)-labelled RNA probes were synthesized using DIG RNA Labeling Mix (Roche, 11277073910). Human and mouse *ALDH1A1* (Clone ID 2988388 and 6477503, respectively), *ALDH1A3* (Clone ID 6208628 and 6515355, respectively), *RXRG* (Clone ID 4635470 and 5707723, respectively), *RARB* (Clone ID 30341884 and 30608242, respectively) and mouse *Rorb* (Clone ID 5358124), *Cbln2* (Clone ID 6412317), *Cyp26b1* (Clone ID 6400154) cDNAs were purchased from GE Healthcare for template preparation. Mouse *Meis2* DNA was a gift from J. Rubenstein. For macaque in situ hybridization, human probes were used because of high similarity between human and macaque transcripts (97.7% identity in *ALDH1A1*; 95.4% identity in *ALDH1A3*; 97.7% in *RXRG*; and 98.8% in *RARB*).

Sections were obtained from PCW 21, 22 human brains and PCD 110, 140 macaque brains. In situ hybridization were repeated using these two sets. Images were taken using an Aperio CS2 HR Scanner (Leica) and processed by Aperio ImageScope (v.12.4.3.5008, Leica). In Fig. 5a, *Cbln2*, *Cyp26b1* and *Rorb* expression data were merged by converting colour whole-mount in situ hybridization into black-and-white images, then merged as separate RGB channels. Images were aligned manually by N.S. In Fig. 5f, Extended Data Fig. 19a, the cortical plate was divided into five equal bins and *Rorb* intensity in each bin was quantified using ImageJ (v.2.0.0-rc-69/1.52p).

ELISA

Eleven neocortical areas were dissected from four fresh frozen post-mortem human mid-fetal brains (PCW 16, 18, 18 and 19) and four fresh frozen macaque brains (all four PCD 110) as described previously¹⁹. Twelve neocortical areas were dissected from three fresh mouse brains at PD 1, based on Paxinos⁵⁰ and the Allen Mouse Brain Atlas⁵¹ (<https://mouse.brain-map.org/static/atlas>). Each human and macaque brain sample was further microdissected into three pieces and weighed. Each piece was independently homogenized using a Dounce homogenizer in three to four volumes of homogenizing buffer (isopropanol:ethanol 2:1; 1 mg ml⁻¹ butylated hydroxytoluene), followed by centrifugation at 10,000 rpm for 10 min at 4 °C. Supernatant was used for the determination of both protein concentration by Pierce BCA Protein Assay Kit (Thermo Fisher Scientific, 23227), and RA concentrations using an ELISA colorimetric detection kit according to the manufacturer's instructions (MyBioSource, MBS705877). This kit could not distinguish all-*trans* retinol, all-*trans* retinal or all-*trans* retinoic acid). Thus, the concentration of RA was the concentration of all forms.

Quantitative PCR with reverse transcription

Total RNA was isolated from freshly microdissected cortices after removal of the olfactory bulb and striatum (Extended Data Fig. 9a, b) using Trizol (Thermo Fisher Scientific, 15596026). cDNAs were prepared using SuperScript II (Thermo Fisher Scientific, 18064022) from three independent wild-type cerebral hemispheres.

Quantitative PCR with reverse transcription was performed as described previously⁵² using the 7000HT Sequence Detection System (Applied Biosystems). At least three replicates per transcript were used for every reaction. The copy number of transcripts was normalized against the housekeeping TATA-binding protein (TBP) transcript level. For *Rxra*, *Rxrb*, *Rxrg*, *Rara*, *Rarb*, *Rarc* and *Tbp* primer sets, the correlation (R_2) was higher than 0.98, and the slope was -3.1 to -3.6 in each standard curve. Primers to detect the expression of the genes above were designed in a single exon. Primer sequences are listed in Supplementary Table 5.

β-Galactosidase histochemical staining

Brains were dissected from PD 0 *RARE-lacZ* mouse pups and drop-fixed in 4% paraformaldehyde for 2 h at 4 °C, followed by embedding in OCT compound (Thermo Fisher Scientific, 23-730-572). Brains were sectioned at 20 µm by cryostat (Leica CM3050S) after they were frozen. β-Galactosidase staining followed the protocol described previously⁵³. We used Red-gal (Sigma-Aldrich, RES1364C-A102X) for the chromogenic reaction. The intensity of β-galactosidase staining was quantified using ImageJ (v.2.0.0-rc-69/1.52p).

Nissl staining

Post-mortem brains were immersion fixed in 4% paraformaldehyde overnight at 4 °C, cryoprotected in 30% sucrose, embedded in OCT compound (Thermo Fisher Scientific, 23-730-572) and snap-frozen in dry ice chilled isopentane (2-methylbutane). Brains were sectioned at 15–20 µm by cryostat (Leica, CM3050S) after they were frozen. After PBS wash, sections were dehydrated using an increasing concentration of ethanol, followed by Cresyl violet, wash, and a second ethanol dehydration. Sections were cover-slipped with Permount (Thermo Fisher Scientific, 15820100).

Immunohistochemistry

Human (PCW 12, PCW 16, PCW 19, PCW 20, PCW 21, PCW 22, PCW 24, newborn, and adult (42, 47 and 79 years old; post-mortem interval (PMI) 5–15 h)), macaque (PCD 40, PCD 76, PCD 114, PCD 140, adult (4.5, 8 and 11 years old; PMI under 1 h)) and mouse (PD 0 and adult (4 months)) brain tissue samples, the cultured human cortical neurons and the cerebral organoids were fixed in 4% paraformaldehyde at 4 °C and cryoprotected in graded concentrations of sucrose (15%, 20%, 30%). Brain tissues and cerebral organoids were embedded in OCT compound (Thermo Fisher Scientific, 23-730-572) and snap-frozen in dry ice chilled isopentane (2-methylbutane). Embedded samples were sectioned at 15–20 µm for mouse brain and cerebral organoids, and 50 µm for macaque and human brain by cryostat (Leica, CM3050S). Tissue sections were mounted and dried overnight.

For the immunohistochemistry of mouse brain in Extended Data Fig. [16d–f](#), sections were treated with or without R-Buffer AG pH 6.0 (Electron Microscopy Sciences, 62707-10) for antigen retrieval, followed by washing in PBS (3 × 5 min) and incubation in blocking buffer (5% (v/v) normal donkey serum (Jackson ImmunoResearch Laboratories, 017-000-121), 1% (w/v) bovine serum albumin, (Sigma-Aldrich, A9647-100G), and 0.3% (v/v) Triton X-100 in PBS) for 1 h at room temperature. Sections were incubated for 24–48 h at 4 °C with diluted primary

antibodies in blocking buffer. Sections were then washed in PBS (3×5 min) incubated with fluorescent secondary antibodies for 2 h at room temperature. After washing in PBS (3×5 min), Tissue was cover-slipped with Vectashield (Vector Laboratories, H-1000). For the immunohistochemistry of human, macaque and mouse brain sections in Extended Data Figs. 4d, e, 7b, antigen retrieval was performed using R-Buffer A pH 6.0 (Electron Microscopy Sciences, 62706-10) for post-natal tissue or R-Buffer AG pH 6.0 (Electron Microscopy Sciences, 62707-10) for prenatal tissue. Sections were incubated in 1% hydrogen peroxide/PBS to quench endogenous peroxidase activity. Sections were washed in PBS (3×10 min) and incubated in blocking solution containing 5% (v/v) normal donkey serum (Jackson ImmunoResearch Laboratories, 017-000-121), 1% (w/v) bovine serum albumin (Sigma-Aldrich, A9647-100G), and 0.3% (v/v) Triton X-100 in PBS for 1 h at room temperature. Primary antibodies were diluted in blocking solution and incubated with tissues sections overnight at 4°C . Sections were washed with PBS (3×10 min) before being incubated with the appropriate biotinylated or fluorescent secondary antibodies (Jackson ImmunoResearch Labs) for 1.5 h at room temperature. All secondary antibodies were raised in donkey and diluted at 1:250 in blocking solution. Sections were subsequently washed in PBS and incubated with avidin–biotin–peroxidase complex (Vectastain ABC Elite kit; Vector Laboratories) for 1 h at room temperature. Finally, sections were washed in PBS (3×15 min) and signals were developed using a DAB Peroxidase (HRP) Substrate Kit (Vector Laboratories, NC9276270) according to the manufacturer’s protocol. Following washes in PBS, sections were dried, dehydrated and cover-slipped with Permount (Thermo Fisher Scientific, 15820100). For immunofluorescence, sections were washed in PBS with 0.3% (v/v) Triton X-100 and treated with the Autofluorescence Eliminator Reagent (Millipore, 2160) according to the manufacturer’s instructions, and cover-slipped with Vectashield (Vector Laboratories, H-1000). For the immunocytochemistry shown in Extended Data Fig. 15, the fixed primary cortical neurons were washed in PBS (3×15 min) and incubated with 0.3% (v/v) Triton X-100 and 10% (v/v) donkey serum (Jackson ImmunoResearch Laboratories, 017-000-121) in PBS for 40 min. For the immunohistochemistry shown in Extended Data Fig. 11a, b, the cerebral organoid sections were washed in PBS (3×15 min) and incubated with 0.5% (v/v) Triton X-100 and 10% (v/v) donkey serum (Jackson ImmunoResearch Laboratories, 017-000-121) in PBS for 2 h. Primary cortical neurons and the organoid sections were incubated with primary antibodies in 10% (v/v) donkey serum at 4°C overnight. Samples were then washed in PBS (3×5 min), and incubated with fluorescent secondary antibodies for 2 h at room temperature in 10% (v/v) donkey serum. All sections and tissues processed for immunofluorescence were cover-slipped with Vectashield (Vector Laboratories, H-1000), after washing in PBS (3×5 min).

The sources of primary antibodies were anti-ALDH1A1 (1:500, Abcam, 52492), anti-BCL11B/CTIP2 (1:500, Abcam, ab18465), anti-cleaved caspase3 (1:500; Cell

Signaling, 9611), anti-CUX1 (1:500, Santa Cruz Biotechnology, sc-13024), anti-GFAP (1:2,000, Sigma-Aldrich, G3893), anti-NR4A2 (1:100, R&D systems, AF2156), anti-GAD1 (1:50, R&D systems, AF2086), anti-NRGN (1:50, R&D systems, AF7947), anti-PAX6 (1:200; R&D Systems, AF8150), anti-POU3F2/BRN2 (1:500, Sigma-Aldrich, SAB2702086), anti-DLG4/PSD95 (1:500; Invitrogen, 51-6900), anti-SYP (1:2,000, Sigma-Aldrich, SAB4200544), anti-L1CAM (1:500; Millipore-Sigma, ABT143), anti-RORB (1:500, Novus Biologicals, NBP1-82532), anti-SATB2 (1:200, Abcam, ab92446), anti-SOX2 (1:200, R&D Systems MAB2018), anti-TBR1 (1:200, Abcam, ab31940), anti-TH (1:1,000, Immunostar, 22941), and anti-TUBB3 (1:400; TuJ1 clone, Abcam, 18207). Secondary antibodies: Alexa Fluor 488-, 594-, or 647-conjugated AffiniPure Donkey anti-IgG (1:200; Jackson ImmunoResearch). For all microscopic analysis, images were acquired using an Aperio CS2 HR Scanner (Leica), ApoTome.2 microscope (Zeiss), LSM510 META (Zeiss), LSM800 or LSB880 confocal microscope (Zeiss) and assembled in Aperio ImageScope 12.4.3.5008 (Leica), Zeiss ZEN2009, ImageJ (v.2.0.0-rc-69/1.52p), Adobe Photoshop (v.12.0 x64), and Adobe Illustrator (v.23.1.1).

Western blotting

Five prospective neocortical areas (mPFC, dlPFC, vIPFC, oPFC and M1C) were dissected from fresh frozen brains of human and macaque, and three neocortical areas (mPFC, MOs/p, and OFC) from fresh mouse brains. Dissected tissues were lysed by sonication in RIPA buffer with protease inhibitors (Sigma-Aldrich, 11836153001). Following centrifugation at 10,000g, supernatant protein concentrations were quantified using the Pierce BCA Protein Assay Kit (Thermo Fisher Scientific, 23227). Supernatants were mixed with 4× Laemmli Sample Buffer (Bio Rad, 1610747), boiled, and electrophoresed on NuPage Bis-Tris gels (Thermo Fisher Scientific), followed by protein transfer to PVDF membranes (Bio Rad, 1620174). Blotted membranes were incubated in blocking buffer (TBS/5% milk) for 1 h and then transferred to blocking buffer with primary antibodies diluted at 1:1,000 at 4 °C overnight. Membranes were then washed in TBS/0.1% Tween20 (3 × 5 min), and incubated with secondary antibodies conjugated with HRP. Secondary antibodies were diluted at 1:1,000. After washing with TBS/0.1% Tween20 (3 × 5 min), protein bands were visualized using SuperSignal West Pico Chemiluminescent Substrate (Thermo Fisher Scientific, 34580). The sources of primary antibodies were anti-ALDH1A3 (1:2,000, Novus Biologicals, NBP2-15339) and anti-GAPDH (1:5,000, Abcam, 9485). Of note, two bands were identified using anti-ALDH1A3 antibody, a 56-kDa band likely to be ALDH1A3 and a 54 kDa band likely to be ALDH1A1.

Droplet digital PCR for quantification of gene expression

An aliquot of the total RNA that was extracted from meninges (human: PCW 19, 19 and 20; macaque: PCD 80, 80 and 110) or primary neural cultures were used for secondary validation through droplet digital PCR (ddPCR) analysis. Two hundred nanograms of total RNA was used for cDNA synthesis using SuperScript III First-strand synthesis Supermix (Thermo Fisher Scientific, 18018400) and subsequently diluted with nuclease-free water. ddPCR was carried out using the Bio-Rad QX100 system. After each PCR reaction mixture consisting of ddPCR master mix and custom primers/probe set was partitioned into 15,000–20,000 droplets, parallel PCR amplification was carried out. End-point PCR signals were quantified and Poisson statistics were applied to yield the target copy number quantification of the sample. A two-colour PCR reaction was used for the normalization of gene expression by the housekeeping gene *TBP*. All pre-designed assays used in validation can be found in Supplementary Table 5. For each region, the gene expression was compared between species by one-way ANOVA followed by Dunnett's multi comparison test.

Quantification of post-synaptic and presynaptic puncta marked by immunostaining

For each region of both wild-type and dKO mice, using the 488-nm or 594-nm channels to detect synaptophysin (SYP) immunolabelling, DLG4 (PSD95) immunolabelling and DAPI nuclear counterstain, seven serial optical sections at 0.8- μm intervals over a total depth of 5 μm were imaged and the 2nd, 4th and 6th images were eliminated from further analysis to avoid overlap in counting⁵⁴. The area of each image is 0.079 mm². The number of SYP- and PSD95-immunolabelled puncta on each image was counted using ImageJ (v.2.0.0-rc-69/1.52p) using the automated Analyze Particles function using a threshold of 985 to 4,095, determined based on multiple wild-type and dKO images. At least two sections from each mouse were selected for counting, and at least three mice for each genotype were used. The total number and volume of SYP- and DLG4 (PSD95)-immunolabelled puncta and TuJ1 (anti-TUBB3 antibody) or MAP2 in cultured neurons were analysed with 20 z-stack (0.49 μm intervals) images per each 8 fields for each condition and the total number of DLG4 (PSD95)-immunolabelled puncta and TuJ1 immunolabelled neurons in cerebral organoids were analysed with 5 z-stack images using Volocity (v.6.3.1) and Spotfire (v.11.2.0) software.

Retrograde neuronal tracing with adeno-associated viruses

In brief, wild-type ($n = 4$) and *Rarb;Rxrg* dKO ($n = 4$) mice were anaesthetized by injecting ketamine/xylazine solution and head-fixed in the stereotactic frame. Mice were injected with burenorphine 30 min before the surgery. After lubricating the eyes and shaving the fur, an incision of less than 1 mm was made. A craniotomy was made with the round 0.5-mm drill bit at the desired co-ordinates (mPFC: ML \pm 0.35, AP 1.5,

DV 2.5 from bregma). Using a 0.5- μ l Hamilton neuros syringe, we injected 50 nl of *AAVrg-Cag-Gfp* (Addgene, 37825-AAVrg) into the mPFC. To prevent the virus from spreading along the injecting tract, the needle was held in place for at least 10 min. After injections, the skin was sutured and mice were returned to the cage. After surgery, mice were injected with meloxicam for 48 h. Three weeks later, the mice were euthanized and brains were collected. The brains were coronally sectioned on a vibratome to obtain 70- μ m thick sections. After staining the sections with anti-GFP antibody (1:500, Abcam, ab13970) and DAPI the sections were imaged with an LSM 800 microscope (ZEISS). The intensity and density of labelling was quantified on a scale of 0 to 3 with 0 being no labelling, 1 being weak or sparse cellular labelling (less than 10%), 2 being strong and less than 50% of cell labelled, and 3 being dense labelling. This discrete approach of quantification was used owing to variability in injection site.

Quantification of dendritic spines and arborization from viral tracing sections

The contralateral mPFC to the injection site was used for this analysis; wild type ($n = 4$) and *Rarb;Rxrg* dKO ($n = 4$). For Sholl analysis, the images of entire neurons were acquired at 20 \times magnification. For spine counts, z-stack images across entire dendritic thickness with 29–33 images per stack were obtained. The z-stack images were opened in Reconstruct (v.1.1.0.0)⁵⁵, which is publicly available at <https://www.bu.edu/neural/Reconstruct.html>, and a new series was recreated that enabled us to move across different stacks across z-planes in the same image. Whole dendrite was subdivided into segments of 10 μ m and number of spines across whole thickness were traced for length and breadth of each spine. After tracing, the length and breadth of the spines their ratio was used to determine the spine subtype as described before⁵⁶. After the analysis for each class of spine, standard deviation and P values were calculated using two-way ANOVA with Sidak's multiple comparison method. For Sholl analysis, z-stack images were opened in ImageJ (v.2.0.0-rc-69/1.52p) and dendritic arbors were manually traced using the NeuronJ plugin⁵⁷. Dendritic complexity was then quantified and plotted using the Sholl Analysis option.

Plasmid construction

For construction of expression vectors, full-length cDNAs (mouse *Aldh1a3*, Clone ID 6515355, purchased from GE Healthcare) were inserted into pCAGIG vector (pCAGIG was obtained from Addgene (plasmid 11159).

In utero electroporation

In utero electroporation was performed as previously described⁵². Plasmid DNA (4 µg µl⁻¹) was injected into the lateral ventricle of embryonic mice at E13.5–E14.5 and transferred into the cells of the ventricular zone by electroporation (five 50-ms pulses of 40 V at 950-ms intervals). Brains were dissected at PD 0. Brains and tissue sections of electroporated mice were analysed for GFP expression after fixation with 4% paraformaldehyde for 12 h at 4 °C.

Mouse RNA-seq data generation and analysis

Post-mortem mouse brains were dissected at PD 0 in ice-cold sterile PBS, fresh frozen, and stored at –80 °C. Brains were incubated in RNAlater-Ice at –20 °C for 12–16 h prior to further dissection. mPFC, MOs, and OFC were microdissected based on Paxinos⁵⁰ and the Allen Mouse Brain Atlas⁵¹ (<https://mouse.brain-map.org/static/atlas>) and RNA was isolated using RNeasy Plus Micro kit with additional on-column DNase step (Qiagen, 74134). RNA quality and amount were quantified using the High Sensitivity RNA Screen Tape Assay (Agilent, 5067-5579), and the concentration was standardized to 10 ng µl⁻¹. The SMART-seq v4 Ultra Low Input Kit (Takara Bio, 634890) was used to create cDNA, and the concentration was quantified using Quant-iT PicoGreen dsDNA Assay Kit (Thermo Fisher Scientific, P11496). Nextera XT DNA library Preparation Kit (Illumina, FC-131-1024) was used to create cDNA libraries for sequencing. Libraries were normalized and sequenced at the Yale Center for Genomic Analysis (YGCA) using the NovaSeq with 100-bp paired end reads. Reads from each library were mapped against the mouse assembly GRCm38 using STAR v.2.6.0a (gtf and fasta files downloaded from Ensembl version 94; parameters: --readFilesIn \$j1 \$j2 --outSAMattributes All --outFilterMultimapNmax 1 --outSAMstrandField intronMotif --outFilterIntronMotifs RemoveNoncanonical --quantMode TranscriptomeSAM --outFilterMismatchNoverLmax 0.1 --alignSJoverhangMin 8 --alignSJDBoverhangMin 1 --outSAMunmapped Within --outFilterType BySJout). Counts were obtained using featureCounts v1.6.2 with -p parameter.

To compare the gene expression patterns of three wild-type versus three *Rarb* and *Rxrg* dKO mice, a TMM procedure was applied (function normalizeCounts from tweedDEseq package in R) to the expression of 15,085 protein-coding genes that show sufficiently large counts (determined with function filterByExpr from edgeR package in R). We assessed differentially expressed genes in each brain region (mPFC, OFC and MOs) running RNentropy independently among wild-type and dKO mice per region. Genes overexpressed in a given condition are those that are both significantly upregulated in that condition and significantly downregulated in the opposite condition according to RNentropy. The same criterion was applied for the identification of downregulated genes. Genes with an inconsistent pattern of expression between regions were excluded. Principal component analyses were performed using the

prcomp function in R by centring the log₂-transformed expression data of the selected genes. Significant GO terms were obtained with the goana function from the limma package in R and plotted using the function GOBubble from the GOpot package in R. Fisher test enrichments calculated for RA-related genes (RA synthesis: *Rdh10*, *Rdh5*, *Aldh1a1/Raldh1*, *Aldh1a2/Raldh2*, *Aldh1a3/Raldh3*, *Adh1*, *Adh5*, *Adh7*; RA degradation: *Cyp26a1*, *Cyp26b1*, *Cyp26c1*; RA receptors: *Rara*, *Rarb*, *Rarg*, *Rxra*, *Rxrb*, *Rxrg*; RA binding: *Ttr*, *Rlbp1*, *Rbp1*, *Rbp2*, *Rbp3*, *Rbp4*, *Fabp5*), genes overexpressed in individual lobes of the mid-fetal human cortex based on Fig. 1, and neuropsychiatric-disease related genes (downloaded from ref. ³⁰) in up- and downregulated genes. Genes associated with the GO terms: ‘axon guidance’, ‘axon guidance receptor’, ‘axon development’ and ‘ephrin’ were manually screened for anterior-to-posterior gradient using developingmouse.brain-map.org⁵⁸, gensat.org⁵⁹ and a previous report⁶⁰. Mouse RNA-seq data were deposited into the NCBI Gene Expression Omnibus (GEO) database (accession number GSE142851).

Diffusion-weighted MRI and tractography

Five PD 5 post-mortem dKO homozygotes and five wild-type C57BL/6 mouse brains were drop-fixed in 4% paraformaldehyde solution in 0.1 M PBS for 48 h. They were subsequently transferred to 0.1 M PBS and just before imaging to Fomblin (Sigma-Aldrich, 317926). The diffusion-weighted images were acquired on a Bruker BioSpin 9.4 T MRI (Bruker) using a standard 3D Stejskal-Tanner spin-echo sequence with 30 different angles of diffusion sensitization at a *b* value of 1,000 s mm⁻² and the following parameters: repetition time = 2,000 ms; echo time = 25.616 ms; diffusion encoding duration = 4 ms. The in-plane resolution was 0.11 mm and slice thickness was 0.22 mm. Overall scanning time was around 24 h.

Image processing and tractography

Cerebral cortical regions of interest (ROI) and thalamus were manually defined according to Paxinos⁵⁰ and the Allen Mouse Brain Atlas⁵¹ (<https://mouse.brain-map.org/static/atlas>) by D.A. and K.P. without prior knowledge of the experimental groups. Image preprocessing was done with Advanced Normalization Tools (ANTs, v.2.2.0.0.dev297-gf23cb). The reconstruction of axonal pathways was performed with MRtrix3⁶¹ software (v.3.0.0-65-g91788533) using constrained spherical deconvolution⁶² and probabilistic tracking (iFOD2) with a FOD amplitude cut-off of 0.1. The thalamus was used as a seeding point and each cortical ROI was used as a termination mask. To evaluate the integrity of the major white matter tracts between the groups, both internal capsules, anterior commissure and corpus callosum were manually delineated according to Paxinos⁵⁰ and the Allen Mouse Brain Atlas⁵¹ (<https://mouse.brain-map.org/static/atlas>) by D.A. and K.P. without prior knowledge of

the experimental groups. Values of the fractional anisotropy (FA), apparent diffusion coefficient (ADC), radial (RD) and axial (AD) diffusivity were calculated using underlying scalar maps derived by MRtrix3.

Anterograde tracing of axons

For anterograde tracing of axons between mPFC and thalamus, brains were collected at either PCD 18 or P21, and fixed overnight in 4% paraformaldehyde at 4 °C. Brains were then hemidissected. A crystal of 1,1'-dioctadecyl-3,3,3',3'-tetramethylindocarbocyanine perchlorate (DiI, Sigma-Aldrich, 24364) was inserted into the mPFC, MD nucleus of the thalamus, or medial thalamus under the stereomicroscope. The size of the crystal is around 200 µm. Brains were then placed in 1% paraformaldehyde in PBS and left for 14 days at 37 °C. Following DiI diffusion, the brains were sectioned coronally on a vibrating microtome (Leica) at 80-µm thickness and stained with DAPI. Sections were mounted onto glass and immediately sealed in VECTASHIELD Hardset Antifade Mounting Medium (Vector Laboratories, H-1400). Slides were analysed under a ApoTome.2 microscope (Zeiss) and intensity was quantified using ImageJ (v.2.0.0-rc-69/1.52p).

Processing, analysis and image visualization

To allow robust visualization and analysis, images depicting DiI tracing or immunohistochemistry using antibody against PSD95 (DLG4) have been inverted and/or pseudo-coloured, as in Figs. 4, 5. In addition, background was removed for *in situ* hybridization experiments and images were pseudo-coloured and superimposed in Fig. 5, Extended Data Figs. 4, 7, 9, 10 using Adobe Photoshop.

Reporting summary

Further information on research design is available in the [Nature Research Reporting Summary](#) linked to this paper.

Data availability

The mouse RNA-seq data are available at the NCBI GEO under the accession number [GSE142851](#).

References

1. 1.

Fuster, J. M. *The Prefrontal Cortex* (Elsevier, 2015).

2. 2.

Amaral, D. G. et al. Neuroanatomy of autism. *Trends Neurosci.* **31**, 137–145 (2008).

3. 3.

Willsey, A. J. et al. Coexpression networks implicate human midfetal deep cortical projection neurons in the pathogenesis of autism. *Cell* **155**, 997–1007 (2013).

4. 4.

Tan, H.-Y. et al. Dysfunctional and compensatory prefrontal cortical systems, genes and the pathogenesis of schizophrenia. *Cereb. Cortex* **17**, i171–i181 (2007).

5. 5.

Giraldo-Chica, M. et al. Prefrontal-thalamic anatomical connectivity and executive cognitive function in schizophrenia. *Biol. Psychiatry* **83**, 509–517 (2018).

6. 6.

Fukuchi-Shimogori, T. & Grove, E. A. Neocortex patterning by the secreted signaling molecule FGF8. *Science* **294**, 1071–1074 (2001).

7. 7.

Cholfin, J. A. & Rubenstein, J. L. R. Frontal cortex subdivision patterning is coordinately regulated by *Fgf8*, *Fgfl7*, and *Emx2*. *J. Comp. Neurol.* **509**, 144–155 (2008).

8. 8.

O’Leary, D. D. & Sahara, S. Genetic regulation of arealization of the neocortex. *Curr. Opin. Neurobiol.* **18**, 90–100 (2008).

9. 9.

Geschwind, D. H. & Rakic, P. Cortical evolution: judge the brain by its cover. *Neuron* **80**, 633–647 (2013).

10. 10.

Preuss, T. M. Do rats have prefrontal cortex? The Rose–Woolsey–Akert program reconsidered. *J. Cogn. Neurosci.* **7**, 1–24 (1995).

11. 11.

Petrides, M. et al. The prefrontal cortex: comparative architectonic organization in the human and the macaque monkey brains. *Cortex* **48**, 46–57 (2012).

12. 12.

Durston, A. J. et al. Retinoic acid causes an anteroposterior transformation in the developing central nervous system. *Nature* **340**, 140–144 (1989).

13. 13.

Marshall, H. et al. Retinoic acid alters hindbrain Hox code and induces transformation of rhombomeres 2/3 into a 4/5 identity. *Nature* **360**, 737–741 (1992).

14. 14.

Lamantia, A. S. Forebrain induction, retinoic acid, and vulnerability to schizophrenia: insights from molecular and genetic analysis in developing mice. *Biol. Psychiatry* **46**, 19–30 (1999).

15. 15.

Maden, M. Retinoic acid in the development, regeneration and maintenance of the nervous system. *Nat. Rev. Neurosci.* **8**, 755–765 (2007).

16. 16.

Pletikos, M. et al. Temporal specification and bilaterality of human neocortical topographic gene expression. *Neuron* **81**, 321–332 (2014).

17. 17.

Li, M. et al. Integrative functional genomic analysis of human brain development and neuropsychiatric risks. *Science* **362**, eaat7615 (2018).

18. 18.

Silbereis, J. C. et al. The cellular and molecular landscapes of the developing human central nervous system. *Neuron* **89**, 248–268 (2016).

19. 19.

Zhu, Y. et al. Spatiotemporal transcriptomic divergence across human and macaque brain development. *Science* **362**, eaat8077 (2018).

20. 20.

Shibata M. et al. Hominini-specific regulation of *CBLN2* increases prefrontal spinogenesis. *Nature* <https://doi.org/10.1038/s41586-021-03952-y> (2021).

21. 21.

Johnson, M. B. et al. Functional and evolutionary insights into human brain development through global transcriptome analysis. *Neuron* **62**, 494–509 (2009).

22. 22.

Siegenthaler, J. A. et al. Retinoic acid from the meninges regulates cortical neuron generation. *Cell* **139**, 597–609 (2009).

23. 23.

Haushalter, C. et al. Retinoic acid controls early neurogenesis in the developing mouse cerebral cortex. *Dev. Biol.* **430**, 129–141 (2017).

24. 24.

Larsen, R. et al. The thalamus regulates retinoic acid signaling and development of parvalbumin interneurons in postnatal mouse prefrontal cortex. *eNeuro* **6**, ENEURO.0018-19.2019 (2019).

25. 25.

Aoto, J. et al. Synaptic signaling by all-trans retinoic acid in homeostatic synaptic plasticity. *Neuron* **60**, 308–320 (2008).

26. 26.

Smith, D. et al. Retinoic acid synthesis for the developing telencephalon. *Cereb. Cortex* **11**, 894–905 (2001).

27. 27.

Dmetrichuk, J. M. et al. Retinoic acid induces neurite outgrowth and growth cone turning in invertebrate neurons. *Dev. Biol.* **294**, 39–49 (2006).

28. 28.

Moreno-Ramos, O. A. et al. Whole-exome sequencing in a south American cohort links ALDH1A3, FOXN1 and retinoic acid regulation pathways to autism spectrum disorders. *PLoS ONE* **10**, e0135927 (2015).

29. 29.

Xu, X. et al. Excessive UBE3A dosage impairs retinoic acid signaling and synaptic plasticity in autism spectrum disorders. *Cell Res.* **28**, 48–68 (2018).

30. 30.

Kumar, S. et al. Impaired neurodevelopmental pathways in autism spectrum disorder: a review of signaling mechanisms and crosstalk. *J. Neurodev. Disord.* **11**, 10 (2019).

31. 31.

Goodman, A. B. Three independent lines of evidence suggest retinoids as causal to schizophrenia. *Proc. Natl Acad. Sci. USA* **95**, 7240–7244 (1998).

32. 32.

Reay, W. R. et al. Polygenic disruption of retinoid signalling in schizophrenia and a severe cognitive deficit subtype. *Mol. Psychiatry* **25**, 719–731 (2018).

33. 33.

Rilling, J. K. Comparative primate neurobiology and the evolution of brain language systems. *Curr. Opin. Neurobiol.* **28**, 10–14 (2014)

34. 34.

Chiang, M. Y. et al. An essential role for retinoid receptors RAR β and RXR γ in long-term potentiation and depression. *Neuron* **21**, 1353–1361 (1998).

35. 35.

Krezel, W. et al. Impaired locomotion and dopamine signaling in retinoid receptor mutant mice. *Science* **279**, 863–867 (1998).

36. 36.

Rossant, J. et al. Expression of a retinoic acid response element–*hsplacZ* transgene defines specific domains of transcriptional activity during mouse embryogenesis. *Genes Dev.* **5**, 1333–1344 (1991).

37. 37.

Wilde, J. J. et al. Diencephalic size is restricted by a novel interplay between GCN5 acetyltransferase activity and retinoic acid signaling. *J. Neurosci.* **37**, 2565–2579 (2017).

38. 38.

Yashiro, K. et al. Regulation of retinoic acid distribution is required for proximodistal patterning and outgrowth of the developing mouse limb. *Dev. Cell* **6**, 411–422 (2004).

39. 39.

Kang, H. J. et al. Spatiotemporal transcriptome of the human brain. *Nature* **478**, 483–489 (2011).

40. 40.

Zambelli, F. et al. RNentropy: an entropy-based tool for the detection of significant variation of gene expression across multiple RNA-Seq experiments. *Nucleic Acids Res.* **46**, e46 (2018).

41. 41.

Wang, H. et al. One-step generation of mice carrying mutations in multiple genes by CRISPR/cas-mediated genome engineering. *Cell* **153**, 910–918 (2013).

42. 42.

Cong, L. et al. Multiplex genome engineering using CRISPR/Cas systems. *Science* **339**, 819–823 (2013).

43. 43.

Renaud, J. P. et al. Crystal structure of the RAR- γ ligand-binding domain bound to all-*trans* retinoic acid. *Nature* **378**, 681–689 (1995).

44. 44.

MacLean, G. et al. Apoptotic extinction of germ cells in testes of *Cyp26b1* knockout mice. *Endocrinology* **148**, 4560–4567 (2007).

45. 45.

Micali, N. et al. Variation of human neural stem cells generating organizer states in vitro before committing to cortical excitatory or inhibitory neuronal fates. *Cell Rep.* **31**, 107599 (2020).

46. 46.

Xiang, Y. et al. Fusion of regionally specified hPSC-derived organoids models human brain development and interneuron migration. *Cell Stem Cell* **21**, 383–398 (2017).

47. 47.

Pollen, A. A. et al. Establishing cerebral organoids as models of human-specific brain evolution. *Cell* **176**, 743–756 (2019).

48. 48.

Gallego Romero, I. et al. A panel of induced pluripotent stem cells from chimpanzees: a resource for comparative functional genomics. *Elife* **4**, e07103 (2015).

49. 49.

Wilkinson, D. G. & Nieto, M. A. Detection of messenger RNA by in situ hybridization to tissue sections and whole mounts. *Methods Enzymol.* **225**, 361–373 (1993).

50. 50.

Paxinos, G. *Atlas of the Developing Mouse Brain: at E17.5, P0, and P6* (Academic, 2007).

51. 51.

Dong, H. W. *The Allen Reference Atlas: a Digital Color Brain Atlas of the C57BL/6J Male Mouse* (John Wiley & Sons, 2008).

52. 52.

Shibata, M. et al. MicroRNA-9 modulates Cajal-Retzius cell differentiation by suppressing Foxg1 expression in mouse medial pallium. *J. Neurosci.* **28**, 10415–10421 (2008).

53. 53.

Kokubu, H. & Lim, J. X-gal staining on adult mouse brain sections. *Bio Protoc.* **4**, e1064 (2014).

54. 54.

Ippolito, D. M. & Eroglu, C. Quantifying synapses: An immunocytochemistry-based assay to quantify synapse number. *J. Vis. Exp.* **45**, 2270 (2010).

55. 55.

Fiala, J. C. Reconstruct: a free editor for serial section microscopy. *J. Microsc.* **218**, 52–61 (2005).

56. 56.

Risher, W. C. et al. Rapid Golgi analysis method for efficient and unbiased classification of dendritic spines. *PLoS ONE* **9**, e107591 (2014).

57. 57.

Meijering, E. et al. Design and validation of a tool for neurite tracing and analysis in fluorescence microscopy images. *Cytometry A* **58**, 167–176 (2004).

58. 58.

Thompson, C. L. et al. A high-resolution spatiotemporal atlas of gene expression of the developing mouse brain. *Neuron* **83**, 309–323 (2014).

59. 59.

Gong, E. et al. A gene expression atlas of the central nervous system based on bacterial artificial chromosomes. *Nature* **425**, 917–925 (2003).

60. 60.

Elsen, G. E. et al. The protomap is propagated to cortical plate neurons through an *Eomes*-dependent intermediate map. *Proc. Natl Acad. Sci. USA* **110**, 4081–4086 (2013).

61. 61.

Tournier, J.-D. et al. MRtrix: diffusion tractography in crossing fiber regions. *Int. J. Imaging Syst. Technol.* **22**, 53–66 (2012).

62. 62.

Tournier, J. D. et al. Robust determination of the fibre orientation distribution in diffusion MRI: non-negativity constrained super-resolved spherical deconvolution. *Neuroimage* **35**, 1459–1472 (2007).

63. 63.

Miller, J. A. et al. Transcriptional landscape of the prenatal human brain. *Nature* **508**, 199–206 (2014).

64. 64.

Lun, M. P. et al. Spatially heterogeneous choroid plexus transcriptomes encode positional identity and contribute to regional CSF production. *J. Neurosci.* **35**, 4903–4916 (2015).

Acknowledgements

We thank S. Bai and T. Nottoli for technical help in the generation of gene-edited mouse lines; F. Hyder and J. Mihailovic for their assistance with MRI diffusion-weighted sequence design and conducting the MRIs; A. Duque for the use of equipment from MacBrainResource (MH113257); J. Rubenstein for sharing reagents; F. Li and M. Onorati for generating human iPS cells used in this study; Y. Gilad and B. Pavlovic for providing chimpanzee iPS cells; and the members of the N.S. laboratory for comments. This work was supported by the NIH (HG010898, MH106874, MH106934, MH110926 and MH116488) and the Simons Foundation Autism Research Institute (SFARI) 572080 (N.S.). The project that gave rise to these results received the support of a fellowship from the 'La Caixa' Foundation (ID 100010434). The

fellowship code is LCF/BQ/PI19/11690010. Additional support was provided by the NIH T32 fellowship (MH18268) (K.P.), the National Science Foundation Graduate Research Fellowship Program (S.K.M.), the Ministerio de Ciencia e Innovación, Spain (PID2019-104700GA-I00) (G.S.), the Kavli Foundation and the James S. McDonnell Foundation (N.S.).

Author information

Author notes

1. These authors contributed equally: Mikihito Shibata, Kartik Pattabiraman

Affiliations

1. Department of Neuroscience, Yale School of Medicine, New Haven, CT, USA

Mikihito Shibata, Kartik Pattabiraman, Belen Lorente-Galdos, David Andrijevic, Suel-Kee Kim, Navjot Kaur, Sydney K. Muchnik, Xiaojun Xing, Gabriel Santpere, Andre M. M. Sousa & Nenad Sestan

2. Yale Child Study Center, Yale School of Medicine, New Haven, CT, USA

Kartik Pattabiraman

3. Department of Genetics, Yale School of Medicine, New Haven, CT, USA

Sydney K. Muchnik & Nenad Sestan

4. Yale Genome Editing Center, Yale School of Medicine, New Haven, CT, USA

Xiaojun Xing & Nenad Sestan

5. Neurogenomics Group, Research Programme on Biomedical Informatics (GRIB), Hospital del Mar Medical Research Institute (IMIM), DCEXS, Universitat Pompeu Fabra, Barcelona, Spain

Gabriel Santpere

6. Waisman Center, University of Wisconsin–Madison, Madison, WI, USA

Andre M. M. Sousa

7. Department of Neuroscience, University of Wisconsin–Madison, Madison, WI, USA

Andre M. M. Sousa

8. Department of Comparative Medicine, Yale School of Medicine, New Haven, CT, USA

Nenad Sestan

9. Department of Psychiatry, Yale School of Medicine, New Haven, CT, USA

Nenad Sestan

10. Program in Cellular Neuroscience, Neurodegeneration and Repair, Yale School of Medicine, New Haven, CT, USA

Nenad Sestan

11. Kavli Institute for Neuroscience, Yale University, New Haven, CT, USA

Nenad Sestan

Contributions

M.S., K.P. and N.S. designed the research. M.S., K.P. and N.K. performed mouse experiments and analysed the data. B.L.-G. and S.K.M. analysed human and mouse transcriptomic datasets. G.S. analysed the enrichment of binding sites for RA receptors. S.-K.K. performed and analysed primate organoid and human neuronal primary culture experiments. M.S. generated the constructs for mutant mice lines. X.X. performed pronuclear injection. D.A. and K.P. analysed mouse imaging data. M.S. and A.M.M.S. performed post-mortem human and macaque tissues experiments. N.S. conceived the study. M.S., K.P. and N.S. wrote the manuscript. All authors discussed the results and implications and commented on the manuscript at all stages.

Corresponding author

Correspondence to Nenad Sestan.

Ethics declarations

Competing interests

The authors declare no competing interests.

Additional information

Peer review information *Nature* thanks Alex Pollen and the other, anonymous, reviewer(s) for their contribution to the peer review of this work.

Publisher's note Springer Nature remains neutral with regard to jurisdictional claims in published maps and institutional affiliations.

Extended data figures and tables

[Extended Data Fig. 1 Workflow for analysis of mid-fetal RNA-seq data and genes upregulated in individual lobes.](#)

a, Human developmental neocortical RNA-seq dataset and workflow for analysis to identify genes upregulated in each cortical lobe. **b**, Genes upregulated in the frontal, temporal, parietal and occipital lobes in comparison to the other lobes. We identified 190 protein-coding genes that are specifically upregulated, using stringent criteria, in at least one area within a lobe in comparison with areas from other lobes: 125 in the frontal lobe, 46 in the temporal lobe, 17 in the parietal lobe, and 2 in the occipital lobe. The X-axis represents proportion of putative areas in the frontal lobe in which the gene is significantly upregulated according to RNentropy. The Y-axis represents proportion of areas in the other lobes in which the gene is significantly downregulated according to RNentropy. Upregulated genes, the ones delimited by dashed red lines, are labelled. **c, d**, Gene loadings of PC1 from PCA of protein-coding genes that are specifically enriched in one of the four lobes of the mid-fetal human (c) and macaque (d) cortex.

Colours represent the cortical lobe where the gene was found to be specifically upregulated. For reproducibility information, see [Methods](#).

Extended Data Fig. 2 Analysis of genes upregulated in individual cortical lobes during other developmental periods.

a, Analysis of upregulated genes during window 2 (early fetal period, PCW 12-13 specimens in the BrainSpan dataset¹⁷). See Fig. [1a](#) for further explanation. **b**, Number of upregulated genes during late prenatal, and early postnatal stages in individual lobes are significantly reduced compared to earlier stages. **c, d**, Analysis of upregulated genes during window 8 (postnatal year, PY 13-19) and W9 (PY 21-64). See Fig. [1a](#) for further explanation. For reproducibility information, see [Methods](#).

Extended Data Fig. 3 Extended RA-specific GO analysis and spatiotemporal expression of select genes upregulated in the mid-fetal frontal lobe.

a, Analysis for statistically significant enrichment of upregulated genes during developmental and adult stages for GO terms associated with RA. X-axis represents windows analysed, which are defined at the bottom of the figure. **b**, Spatiotemporal expression of select genes upregulated in the mid-fetal frontal lobe from Fig. [1](#) in sixteen neocortical areas across human (red) and macaque (blue) development using BrainSpan ([brainspan.org](#)) and PsychENCODE ([evolution.psychencode.org](#)) RNA-seq data^{17,19}. Thick full lines represent four PFC areas, thick dotted line represents the primary motor cortex (M1C) and thin dotted lines represent the other non-frontal neocortical areas. Vertical grey box demarcates mid-fetal periods analysed in Fig. [1](#). Timeline of human and macaque development and the associated periods designed by Kang et al³⁹ shown below. Predicted ages were calculated using the *TranscriptomeAge* algorithm¹⁹, which aligns our earliest macaque samples (PCD 60) with human early mid-fetal samples. Distinct global patterns of spatiotemporal expression were observed. For example, precocious expression in the frontal lobe/PFC followed by broad expression in all eleven neocortical areas (e.g. *CBLN2*, *BDNF*), transient enrichment in the frontal lobe/PFC (e.g. *WNT11*, *PCDH17*) and

downregulation in non-PFC areas during mid-fetal development (e.g. *MEIS2*).

Extended Data Fig. 4 Expression of RA-synthesizing enzymes in the developing human and macaque cortex.

a, Spatiotemporal expression of genes encoding RA synthesizing enzymes, *ALDH1A1*, 2 and 3, in eleven neocortical areas of human and macaque during prenatal and postnatal development using BrainSpan (brainspan.org) and PsychENCODE (evolution.psychencode.org) RNA-seq data^{17,19}. Red and blue lines indicate human and macaque, respectively, and dotted lines represent the non-PFC expression in the PFC plot. Vertical grey box demarcates mid-fetal developmental periods. Predicted ages, timeline of human and macaque development, and the associated periods are shown below^{19,63}. **b**, Heat map of normalized (z-score) microarray signals computed for genes encoding RA synthesizing enzymes from the BrainSpan human prenatal laser microdissection microarray data⁶³ (brainspan.org). Left columns represent gene name and specific probe. Each column represents regions of the brain labelled above the heat maps. Darker reds represent high expression levels. **c**, Anteroposterior visual representation of human *ALDH1A1* and *ALDH1A3* expression at PCW 16 and 15 respectively from BrainSpan atlas⁵⁸. *ALDH1A1*, 2 and 3 expression in mid-fetal human (PCW 19, 19, 20) (**d**, left) and macaque (PCD 80, 80, 110) (**e**, left) meninges. Immunostaining for ALDH1A1 and TH in human PCW 12 and 22 brains (**d**, right), and in macaque PCD 76 brain (**e**, right). White arrowheads, and open arrowheads indicate ALDH1A1+;TH+ and ALDH1A1+;TH- axons in the subplate, respectively. NCX, neocortex; PU, putamen; NAC, nucleus accumbens; CA, CA subfields of hippocampus. Errors bars: S.D. N = 3. **f**, Anterior to posterior expression of *ALDH1A3* mRNA in human (PCW 21), macaque (PCD 140) and mouse (PD 0) brain. N = 2 for human and macaque, N = 3 for mouse. **g**, Western blot using ALDH1A3 antibody in human (PCW 20), macaque (PCD 114) and mouse (PD 0) frontal cortex areas. In macaque and human, there are two bands that are likely to represent ALDH1A3 (56 kDa) and ALDH1A1 (54 kDa). Experiments were repeated at least two times for each animal species. See Extended Data Fig. [6a](#) for schemas of frontal areas.

Extended Data Fig. 5 Expression of genes encoding RA-synthesizing enzymes in the developing mouse cortex.

Expression of *Aldh1a1*, *Aldh1a2* and *Aldh1a3* at PCD 11.5, 18.5 and PD 4 (a) and *Rara* at PCD 15.5 and PD 4 (b) from the Allen Developing Mouse Brain Atlas⁵⁸ (developingmouse.brain-map.org). c, Expression of RA related genes in the PCD 18.5 choroid plexus (CP). Blue bars represent lateral ventricle CP and orange bars represent fourth ventricle CP. Data from Lun et al⁶⁴. d, Analysis of *Rarb-gfp* mouse line from the GENSAT project⁵⁹ (gensat.org) at PD 7 revealed GFP expression in upper (open arrows) and deep layer (solid arrows) pyramidal neurons in the mPFC at PD 7. Scale bars: 1 mm. FEZ, Frontonasal ectodermal zone; ChPl, Choroid plexus; RMS, Rostral migratory stream; SN, Substantia nigra; VTA, Ventral tegmental area; mPFC, Medial prefrontal cortex; ACA, anterior cingulate area.

Extended Data Fig. 6 Expression of RA-synthesizing enzymes in the developing and adult cortex.

a, Representative images of *ALDH1A1* and *ALDH1A3* *in situ* hybridization of human (PCW 21; N = 2), macaque (PCD 110 and 140; N = 1 each), and mouse (PD 0; N = 3) PFC. Red, black, and open arrowheads indicate *ALDH1A1*-expressing subplate neurons (insets), astrocytes and meninges, respectively. Scale bars: 200 µm (mouse); 2 mm (human and macaque); 100 µm (mouse, lower panel); 500 µm (human and macaque, lower panel). b, ALDH1A1 immunofluorescence (green) and immunohistochemistry (brown). Human: left, solid and open arrowheads indicate TH+;ALDH1A1+ and TH+;ALDH1A1- axons, respectively; middle, solid and open arrowheads indicate subplate neurons and astrocytes, respectively; right, arrowheads indicate GFAP+;ALDH1A1+ astrocytes. Macaque: left, solid and open arrowheads indicate TH+;ALDH1A1+ and TH+;ALDH1A1- axons, respectively; middle, solid and open arrowheads indicate putative excitatory NRGN+;NR4A2+;ALDH1A1+ and inhibitory GAD1+;ALDH1A1- subplate neurons, respectively; right, arrowheads indicate GFAP+;ALDH1A1+ astrocytes. Mouse: left, solid and open arrowheads indicate TH+;ALDH1A1+ and TH+;ALDH1A1- mPFC axons

(inset), respectively; middle, TH+ (red) and ALDH1A1+ (green) midbrain neurons and axons in striatum (STR), lateral septal nucleus (LSR) and cortex (CTX); right, GFAP+;ALDH1A1- astrocytes. N = 3. Scale bars: 20 µm (human, macaque, and mouse left and middle panels); 1 mm (mouse right panel). For reproducibility information, see [Methods](#).

Extended Data Fig. 7 Expression of genes encoding RA-degrading enzymes in the developing human and macaque cortex.

a, Expression of RA degrading enzymes in individual regions of the cerebral cortex of human and macaque during development. Red and blue lines indicate human and macaque, respectively, and dotted lines represent the non-PFC expression in the PFC plot and vice versa. Vertical grey box demarcates mid-fetal developmental periods. Predicted ages, timeline of human and macaque development, and the associated periods are shown below^{19,39}. * Data for *CYP26A1* was not present in Zhu et al¹⁹ and the data analysed individually. The expression level for human and macaque were not normalized and can't be directly compared. **b**, Heat map of normalized (z-score) microarray signals computed for genes encoding RA degrading enzymes from the BrainSpan human prenatal laser microdissection microarray data⁶³ (brainspan.org). Left column represents gene and specific probe. Rows represent regions of the brain. Darker reds represent high expression levels. **c**, Anteroposterior visual representation of human *CYP26A1* and *CYP26B1* expression at PCW 15 respectively from the BrainSpan atlas.

Extended Data Fig. 8 Expression of genes encoding RA receptors in the developing human and macaque cortex.

a, Expression of genes encoding RA receptors in individual regions of the cerebral cortex of human and macaque during prenatal and postnatal development. Red and blue lines indicate human and macaque, respectively, and dotted lines represent the non-PFC expression in the PFC plot and vice versa. Vertical grey box demarcates mid-fetal developmental periods. Predicted ages, timeline of human and macaque development, and the

associated periods are shown below^{19,39}. * Data for *RXRB* was not present in Zhu et al¹⁹ and the data were analysed individually. The expression level for human and macaque were not normalized and cannot be compared. **b**, Heat map of normalized (z-score) microarray signals computed for genes encoding RA receptors from the BrainSpan human prenatal laser microdissection microarray data⁶³ (brainspan.org). Left column represents gene and specific probe. Rows represent regions of the brain. Darker reds represent high expression levels.

Extended Data Fig. 9 *RARB* and *RXRB* are expressed in a moderate anterior-to-posterior gradient in the developing neocortex.

a, Quantitative PCR analysis of *Rara*, *b*, *g* and *Rxra*, *b*, *g* transcripts in the anterior and posterior half of mouse cortex at PD 0. Two-tailed Student's t-test: *** $P = 4e-4$, $1e-4$; N = 3 per condition; Errors bars: S.E.M. **b**, Quantitative PCR analysis of *Rarb* and *Rxrg* transcripts in four sections dissected out of the cortical plate in anterior-posterior direction. Both genes showed an anterior-posterior gradient in expression level. Two-tailed Student's t-test; N = 3 per condition; Errors bars: S.E.M. **c**, Expression of *Rarb* and *Rxrg* in mouse (PD 0), macaque (PCD 140) and human (PCW 21) brains by *in situ* hybridization. Higher magnification images of the regions of anterior cortex. *Rarb* and *Rxrg* transcripts are upregulated in the anterior part of the cortex in all three. Scale bars, 200 μ m (mouse); 2 mm (human); 500 μ m (human, higher magnification). N = 2 for human and macaque, N = 3 for mouse. **d**, Strategies for the generation of *Rarb* and *Rxrg* KO mice using CRISPR-Cas9 technique⁴¹.

Extended Data Fig. 10 RA signal in the neonatal mouse forebrain.

a, β -galactosidase histochemical staining of more posterior regions of *Rarb*^{+/+}; *Rxrg*^{+/+} (WT); *RARE-lacZ* and *Rarb*^{-/-}; *Rxrg*^{-/-} (dKO); *RARE-lacZ* mouse brains at PD 0. Signal intensity in the boxed area (ACA, SSp, RSPA, STR, HIP and VP) was quantified. Note the reduced activity in anteromedial structures including ACA and RSPA (RSP). There is also

reduced expression in HIP and lateral STR, but not the thalamus. Two-tailed Student's t-test; $*P = 9e-3$, $**P = 7e-4$; $3e-3$ (from left), $***P = 2e-4$, $****P = 2e-7$; $1e-5$; $4e-5$; $5e-6$; $6e-6$ (from left). N = 3 per genotype: Errors bars: S.E.M.; Scale bars, 200 μ m. **b**, *Cbln2* and *Meis2* expression in PD 0 WT and dKO mutant brain by *in situ* hybridization at PD 0. Note that *Cbln2* and *Meis2* expression in mPFC was decreased in dKO. Scale bar, 200 μ m. N = 3 per genotype. ACA, Anterior cingulate area; CP, caudoputamen; HIP, Hippocampus; RSPA/RSP, Retrosplenial area; STR, striatum; VP, Ventroposterior thalamus.

Extended Data Fig. 11 RA regulates *CBLN2*, *MEIS2* and *DLG4* (PSD95) expression in human and chimpanzee cerebral organoids.

a, Expression of cortical neural stem/progenitor markers (PAX6 and SOX2), cortical cell type-specific markers (BCL11B, SATB2 and TBR1) and a pan-neuronal marker (MAP2) across the differentiation times show the dorsal cortical identity of the organoids derived from human and chimpanzee induced pluripotent stem cells. Scale bars, 50 μ m. Each experiment used with 3-5 replicate organoids per times and conditions. **b**, *In situ* hybridization for *CBLN2* and *MEIS2*, immunostaining for PSD95/DLG4, and DAPI nucleic acid (nuclear) staining in human and chimpanzee day 135 organoids exposed to low or high concentration RA-soaked bead for 48 h. Scale bars, 500 μ m. One experiment has done with 3-5 replicate organoids per times and conditions. **c**, Proportion of TuJ1 immuno-positive neurons in day 135 cerebral organoids was similar across conditions. The ratio of total number of PSD95+ synaptic puncta to total number of TuJ1+ cells in the day 135 cerebral organoids was significantly increased in RA-soaked bead applied conditions. Two-tailed t-test, compared to the condition without bead (Control, Ctrl), Errors bars: S.E.M. $***P = 5e-4$, $****P < 1e-4$. N=5 (multiple sections for each organoid) per condition.

Extended Data Fig. 12 Additional analysis of RNA-seq experiments.

a, Number of upregulated genes between PD 0 WT and dKO mice per region and phenotype, as well as combinations of regions and phenotypes. **b**, Gene loadings of the first principal component from PCA in Fig. 3. Colours represent the frontal cortex region where the gene was found to be upregulated. **c**, Cellular component GO terms associated with the total list of 4,768 DEx genes found, showing their z-score and nominal P values. Z-score represents the proportion of upregulated versus downregulated genes in the list of DEx genes associated to each GO term (i.e. z-score = (#up - #down) / sqrt (#all DEx associated to the GO term)). Dark blue: z-score <-5; light blue: z-score (-5,0]; orange: z-score >0. Size of the bubbles are proportional to the total number of DEx genes associated to the given GO term. **d**, Cellular component GO terms associated with DEx genes found in all three frontal cortex regions, and DEx genes unique to each region (mPFC, OFC, MOs) and their unadjusted p value. **e**, Enrichment of RA related genes (green), genes upregulated in individual lobes of the mid-fetal human cortex based on Fig. 1 (purple), and psychiatric disease related genes in up- and downregulated genes (pink). DEx genes are separated by genes that are DEx only in the given region (mPFC, OFC, MOs), genes that are DEx in the two given regions (mPFC + OFC, mPFC + MOs, OFC + MOs), genes that are DEx in all three regions (mPFC + OFC + MOs). Circles plotted for significant enrichments (P value <0.05), in darker colour, significance is considering the adjusted p value. Diameter of circle is associated with odds ratio per legend.

Extended Data Fig. 13 Altered synaptic density and axonal projections in *Rxrg* and *Rarb* dKO mice.

a, Example of downregulated genes between PD 0 *Rarb*+/+; *Rxrg*+/+ (WT) and *Rarb*-/-; *Rxrg*-/- (dKO) that displayed an anterior to posterior gradient in PCD 18 mouse embryo (images are from the Allen Developing Mouse Brain Atlas; developingmouse.brain-map.org⁵⁸). Scale bar: 1 mm. **b**, Immunostaining for PSD95/DLG4 in the cortical subregions (mPFC, MOs, OFC, MOp, and SSp) of WT and dKO brain at PD 0. Each region as shown in Fig. 2c. Scale bar: 25 µm. N = 3 per genotype. **c**, Quantification and representative images of co-localized synaptophysin (SYP) and PSD95 puncta in PD 0 WT and dKO mPFC. Two-tailed Student's t-test; *P = 0.01; N = 3 per genotype; Errors bars: S.E.M.; Scale bar: 10 µm. **d**, **e**, DiI

placement in mPFC (**c**) and medial thalamus (**d**) with tracing data in WT and dKO brain at P21. Additional two replicates of experiment shown in Fig. [4d,e](#) are shown. Asterisks: DiI crystal placement. Scale bar: 1 mm.

Extended Data Fig. 14 Analysis of axonal inputs to the mPFC and dendritic spines in *Rarb* and *Rxrg* dKO mice.

Anteroposterior series of PD 30 coronal sections of representative WT (**a**) and dKO (**b**) with retrograde viral tracer *AAVrg-Cag-Gfp* injected into mPFC (green asterisk). Sections were inverted and converted to greyscale. Black regions indicate the presence of viral tracer. High magnification representative images of labelled regions (**c**) and quantification of labelling using 0-3 scale (**d**) (N = 4 for each genotype; see [Methods](#) section for more details). **e**, Quantification of Sholl analysis (Two-way ANOVA with Sidak's multiple comparison method; $P = .440 - >0.999$); Error bars: S.E.M.) and dendritic spines of upper layer neurons in the contralateral mPFC in WT (blue) and dKO (orange) (N = 4 for each genotype). Two-way ANOVA with Sidak's multiple comparison method was applied; * $P = 0.09$; *** $P < 1e-4$; Error bars: S.E.M. Inset shows representative images of dendritic spines. Scale bar: 5 μ m. ACAd, Dorsal anterior cingulate area; AI, Anterior Insula; BLA, Basolateral amygdala; vHPF, ventral hippocampal fields; CLA, claustrum; cl mPFC, Contralateral medial prefrontal cortex; ILA, Infralimbic area; LHA, Lateral habenula; MD, The mediodorsal nucleus of the thalamus; MOs/p, The secondary and primary motor areas. PER, Perirhinal cortex PIR, Piriform cortex PL, Prelimbic area; SSp, Primary somatosensory area; STN, Subthalamic nucleus; VTA, Ventral tegmental area.

Extended Data Fig. 15 RA regulates *CBLN2*, *MEIS2*, and *DLG4* (*PSD95*) expression and synaptogenesis in human fetal neocortical neurons.

a, Schematics of human cortical neuron differentiation and modulation of RA signalling. From PCW 8 neocortical tissue, cortical neural stem cells were isolated and expanded with FGF2 for 20 days. Neural differentiation was initiated by the mitogen withdrawal. After 14 days of differentiation,

cells were treated with varying doses of RA or RA receptor inhibitor (RARi, AGN193109) for another 14 days. From PCW 20 or 23 neocortical tissue, cortical neural progenitors and neurons were isolated and cultured without FGF2. After 16 days of culture, cells were treated with RA or RARi for another 14 days. Gene expression of cell type markers (**b**), RA receptors (**c**) RA regulated genes *CBLN2* and *MEIS2* (**d**) in PCW 8 cortical cells after 28 days of differentiation, measured by ddPCR. One way ANOVA and multiple comparison, compared to vehicle (0.01% DMSO)-treated control. Errors bars: S.E.M. * $P < 0.05$ (*RXRA* expression, RA1.0, $P = 0.0192$, RARi5, $P = 0.0277$; *CBLN2* expression, RARi10, $P = 0.0135$; *MEIS2* expression, RA1.0, $P = 0.0456$), ** $P < 0.01$ (*RARA* expression, RARi10, $P = 0.0039$; *MEIS2* expression, RARi5, $P = 0.0057$, PARi10, $P = 0.0028$), *** $P < 0.001$ (*MEIS2* expression, RA0.5, $P = 0.0003$), **** $P < 0.0001$. N=3 experimental replicates per condition. **e**, TUBB3/TUJ1 and DLG4/PSD95 expression in RA or RARi-treated PCW 8 cortical cells. Scale bar: 50 μ m. **f**, DLG4/PSD95 transcript in PCW 8 cortical cells was significantly increased in RA 1 μ M condition quantified by ddPCR. Two-tailed t-test, compared to the vehicle treatment. Errors bars: S.E.M. ** $P = 0.0083$. N= 8 fields per condition. **g**, The ratio of total DLG4/PSD95+ puncta volume to total TUJ1+ volume in PCW 8 cortical cells was increased in the RA condition and reduced in the RARi condition. Two-tailed t-test, compared to the vehicle treatment. Errors bars: S.E.M. * $P = 0.0152$, *** $P = 0.0001$. **h**, MAP2, synaptophysin (SYP) and DLG4/PSD95 expression in RA or RARi-treated PCW 20 and 23 cortical cells. Scale bar: 50 μ m. **i**, The ratio of total DLG4/PSD95+ puncta volume to total MAP2+ volume in PCW 20 and 23 cortical cells was increased in RA conditions and reduced in RARi conditions. Two-tailed t-test, compared to the vehicle treatment. Errors bars: S.E.M. * $P < 0.05$ (PCW 20-RA2, $P = 0.0221$; PCW 20 -RARi5, $P = 0.0193$; PCW 23 -RA0.5, $P = 0.0192$), ** $P < 0.01$ (PCW 20-RARi10, $P = 0.0018$; PCW 23-RA1, $P = 0.0081$), *** $P = 0.0004$. N = 8 fields per condition. **j**, The ratio of total number of SYP+ and DLG4/PSD95+ colocalized synaptic puncta to total MAP2+ volume in PCW 20 and 23 neocortical cells was increased in RA conditions and reduced in RARi conditions. Two-tailed t-test, compared to the vehicle treatment. Errors bars: S.E.M. * P (PCW 20 - RA0.5, $P = 0.0271$; PCW 20-RA2, $P = 0.0159$; PCW 23-RA1, $P = 0.0289$; PCW 23-RA2, $P = 0.0447$), *** $P = 0.0004$, **** $P < 0.0001$. N= 8 fields per condition.

Extended Data Fig. 16 Analysis of axonal projections and cell death in *Rarb* and *Rxrg* dKO mice.

a, Four scalar indexes which describe microstructural integrity do not differ in the four major white-matter tracts (corpus callosum, anterior commissure, left and right internal capsules) between WT and dKO mice. FA Comparisons: Corpus callosum (two-tailed unpaired t-test, $P = 0.4$); Anterior cingulate (two tailed mann-whitney test, $P = 0.2$); Internal Capsule left (two-tailed unpaired t-test, $P = 0.07$); Internal Capsule right (two-tailed unpaired t test, $P = 0.8$). ADC Comparisons: Corpus callosum (two-tailed unpaired t-test, p value 0.1); Anterior cingulate (two-tailed unpaired t-test, p value 0.1); Internal Capsule left (two-tailed unpaired t-test, p value 0.9); Internal Capsule right (two-tailed unpaired t-test, $P = 0.3$). RD Comparisons: Corpus callosum (two-tailed unpaired t-test, $P = 0.1$); Anterior cingulate (two-tailed unpaired t-test, $P = 0.1$); Internal Capsule left (two tailed mann-whitney test, $P = 0.1$); Internal Capsule right (two-tailed unpaired t-test, $P = 0.3$). AD Comparisons: Corpus callosum (two-tailed unpaired t-test, $P = 0.08$); Anterior cingulate (two-tailed unpaired t-test, $P = 0.1$); Internal Capsule left (two-tailed unpaired t-test, $P = 0.4$); Internal Capsule right (two-tailed unpaired t-test, $P = 0.2$). N=5; Errors bars: S.E.M.

b, Number of streamlines of MOp-thalamus and corticocortical tracts, did not differ between WT and dKO. Two-tailed unpaired t-test for MOp-MOp, MOp-Th, and AUDp-th ($P = 0.1$, 0.07, and 0.6, respectively). Two-tailed Mann-Whitney test for ACA-Th ($P = 0.3$). N = 5 per genotype; Errors bars: S.E.M.

c, Barrel formation was examined by Nissl staining at PD 5 in WT and dKO. N = 3 per genotype. **d**, Representative images and quantification of corticospinal tract (CST) width using L1CAM expression at PD 5 in WT and dKO. The width of the corticospinal tract (shown in brackets) is slightly increased in dKO. Two-tailed Student's t-test: * $P = 0.02$; N = 5 per genotype; Errors bars: S.E.M.

e, Representative images and quantification of of apoptotic cells in the mPFC detected by cleaved caspase3 (actCASP3) between WT and dKO. Two-tailed Student's t-test: WT vs. dKO; NS; N = 5 per genotype; Errors bars: S.E.M.; Scale bars: 500 μ m; 200 μ m (b,f); 1 mm (c); 100 μ m (d).

f, Representative images and quantification of tyrosine hydroxylase (TH) immunolabelled axons in WT and dKO mouse frontal cortex at PD 5 (N = 4). Rectangles represent regions analysed. Clockwise starting from left-most: mPFC, MOs, OFC. Errors bars: S.E.M.

Extended Data Fig. 17 Analysis of neocortical layers and tissue volume in *Rarb* and *Rxrg* dKO mice.

a, Representative images and quantification of total volume of the brain (left), cerebral neocortex (middle), anterior one-third of the neocortex (right) of WT littermates and *Rarb;Rxrg* dKO at PD 5. Two-tailed unpaired t-test for total volume of the brain and anterior one-third of the neocortex. Two-tailed Mann-Whitney test for volume of cerebral neocortex. $P = 0.3$, 0.1, 0.6. N = 5. Errors bars: S.E.M. **b**, Number of immune-positive cells expressing cortical layer markers POU3F2/BRN2, CUX1, RORB, BCL11B/CTIP2, TBR1 in WT and dKO mouse mPFC, MOs, and primary visual cortex (VISp) at PD 5 (N = 3). (Unpaired t-test: WT vs. dKO * $P = 0.03$; Errors bars: S.E.M.). RORB expression in mouse PFC was too faint to quantify. Below each graph is a representative image of each marker. Scale bar: 200 μ m.

Extended Data Fig. 18 RA signal in posterior cortical regions of *Cyp26b1* KO mice.

a, Strategy for the generation of *Cyp26b1*-/- (*Cyp26b1* KO) mice using CRISPR-Cas9 gene editing technique⁴¹. **b**, *Cyp26b1* expression in PD 0 mice cortex by *in situ* hybridization. The colorimetric staining was purposefully extended compared to the experiment in Fig. 5a to better visualize low expressing locations. **c**, β -Galactosidase staining of more posterior regions of control *Cyp26b1*+/+; *RARE-lacZ* (Ctrl) and *Cyp26b1*-/-; *RARE-lacZ* (KO) mouse brains at PCD 18. Scale bar: 500 μ m. Intensity of signal in the boxed areas (ACA, MO, SSp) was quantified. Increase in RA signalling in *Cyp26b1* KO brains is less significant in posterior regions. Two-tailed Student's t-test: Ctrl vs. *Cyp26b1* KO: * $P = 0.01$; 0.04; 9e-3; 7e-3; 6e-3; 0.02; 0.02; ** $P = 4e-3$; 1e-3; 4e-3; 4e-3, N = 3 per genotype; Errors bars: S.E.M.; Scale bars: 200 μ m.

Extended Data Fig. 19 *Rorb* expression and medial thalamocortical projections in neonatal *Cyp26b1* KO mice.

a, Additional two replicates of *Rorb* expression in WT and *Cyp26b1* KO brains from Fig. 5f are shown. Scale bar: 100 μ m. **b**, DiI was placed in the medial thalamus of WT and *Cyp26b1* KO brains, and signal was detected in the PFC. Additional two replicates of experiment in Fig. 5d are shown. N = 3 per genotype and condition. Arrowheads: Thalamocortical innervation of the medial and dorsolateral frontal cortex. Asterisks: DiI crystals placed. Scale bar: 400 μ m. **c**, DiI was placed in the frontal motor cortex of WT and *Cyp26b1* KO brains, and signal was detected in the medial thalamus. Additional two replicates of experiment in Fig. 5e are shown. N = 3 per genotype and condition. Of note, owing to restriction related to Covid-19, PD 0 brains were left 2 months in cold room after 3 weeks in 37 degree. Scale bar: 400 μ m.

Extended Data Fig. 20 Ectopic RA signalling leads to enlargement of the lateral region of the frontal cortex and upregulation of *Rorb*.

a, Representative image and quantification of the ratio of brain width at anterior and posterior cortex to total brain length at PCD 18 in *Cyp26b1* KO brain compared WT. Two-tailed Student's t-test: WT vs. *Cyp26b1* KO: ***P = 3e-4; N = 4 per genotype; Errors bars: S.E.M. **b**, Nissl staining reveals that the cortical wall and cortical plate are grossly normal when analysed in the mPFC and SSp of *Cyp26b1* KO. N = 3 per genotype. **c**, Representative image and quantification of *Rorb* expression after electroporation of either control pCAG-IRES-*Gfp* or pCAG-*Aldh1a3*-IRES-*Gfp* expression vector plasmid in the dorso-lateral fronto-parietal wall at PCD 14. Brains were dissected out at PD 5. Boxed region represents region of higher magnification to the right. GFP expression as a marker of misexpressing cells are shown in lower panels. *Rorb* signal intensity in the boxed area in the cortex was quantified. Two-tailed Student's t-test: ***P = 2e-4; N = 4 per genotype; Errors bars: S.E.M.; Scale bars: 500 μ m (**a**); 200 μ m (**b**); 1 mm (**c**); 40 μ m and 500 μ m (**d**).

Supplementary information

Supplementary Text

This file contains additional results and discussion.

Reporting summary

Supplementary Figure 1

Original picture of western blot gel from Extended Data 4g.

Supplementary Table 1

Gene ontogeny of mid-fetal frontal lobe enriched genes

Supplementary Table 2

Annotation of mid-fetal prospective PFC and M1C enriched genes

Supplementary Table 3

List of differentially expressed genes from wild-type and *Rarb;Rxrg* dKO PD 0 frontal cortex. obtained using RNentropy72. In brief, the analysis is done in two steps: (i) a global sample specificity test is computed based on their specificity with a background distribution, adjusting their *P* values with a Benjamini–Hochberg procedure; (ii) the expression in each sample of the significant genes that passed the default global threshold in step (i) are then compared with the expression in the remaining samples with a local sample specificity test, obtaining unadjusted *P* values. In this table, those results are summarized per phenotype.

Supplementary Table 4

List and annotation of PD 0 mouse differentially expressed or human PFC enriched genes related to axon development

Supplementary Table 5

List of relevant primers and sgRNA

Rights and permissions

[Reprints and Permissions](#)

About this article

Cite this article

Shibata, M., Pattabiraman, K., Lorente-Galdos, B. *et al.* Regulation of prefrontal patterning and connectivity by retinoic acid. *Nature* **598**, 483–488 (2021). <https://doi.org/10.1038/s41586-021-03953-x>

- Received: 31 December 2019
- Accepted: 25 August 2021
- Published: 01 October 2021
- Issue Date: 21 October 2021
- DOI: <https://doi.org/10.1038/s41586-021-03953-x>

Share this article

Anyone you share the following link with will be able to read this content:

[Get shareable link](#)

Sorry, a shareable link is not currently available for this article.

[Copy to clipboard](#)

Provided by the Springer Nature SharedIt content-sharing initiative

Further reading

- **Hominini-specific regulation of CBLN2 increases prefrontal spinogenesis**

- Mikihito Shibata
- , Kartik Pattabiraman
- , Sydney K. Muchnik
- , Navjot Kaur
- , Yury M. Morozov
- , Xiaoyang Cheng
- , Stephen G. Waxman
- & Nenad Sestan

Nature (2021)

The genetic symphony underlying evolution of the brain's prefrontal cortex

- Jenelle L. Wallace
- Alex A. Pollen

News & Views 01 Oct 2021

Regulators of human brain evolution

- Katherine Whalley

Research Highlight 19 Oct 2021

This article was downloaded by **calibre** from <https://www.nature.com/articles/s41586-021-03953-x>

- Article
- [Published: 01 October 2021](#)

Hominini-specific regulation of *CBLN2* increases prefrontal spinogenesis

- [Mikihito Shibata](#)¹,
- [Kartik Pattabiraman](#)^{1,2},
- [Sydney K. Muchnik](#)^{1,3},
- [Navjot Kaur](#)¹,
- [Yury M. Morozov](#)¹,
- [Xiaoyang Cheng](#)^{4,5,6},
- [Stephen G. Waxman](#) [ORCID: orcid.org/0000-0001-5718-7177](#)^{4,5,6} &
- [Nenad Sestan](#) [ORCID: orcid.org/0000-0003-0966-9619](#)^{1,2,3,7,8,9,10}

[Nature](#) volume 598, pages 489–494 (2021)

- 4881 Accesses
- 2 Citations
- 71 Altmetric
- [Metrics details](#)

Subjects

- [Evolution](#)
- [Neuroscience](#)

Abstract

The similarities and differences between nervous systems of various species result from developmental constraints and specific adaptations^{1,2,3,4}. Comparative analyses of the prefrontal cortex (PFC), a cerebral cortex region involved in higher-order cognition and complex social behaviours, have identified true and potential human-specific structural and molecular specializations^{4,5,6,7,8}, such as an exaggerated PFC-enriched anterior-posterior dendritic spine density gradient⁵. These changes are probably mediated by divergence in spatiotemporal gene regulation^{9,10,11,12,13,14,15,16,17}, which is particularly prominent in the midfetal human cortex^{15,18,19,20}. Here we analysed human and macaque transcriptomic data^{15,20} and identified a transient PFC-enriched and laminar-specific upregulation of cerebellin 2 (CBLN2), a neurexin (NRXN) and glutamate receptor- δ GRID/GluD-associated synaptic organizer^{21,22,23,24,25,26,27}, during midfetal development that coincided with the initiation of synaptogenesis. Moreover, we found that species differences in level of expression and laminar distribution of *CBLN2* are, at least in part, due to Hominini-specific deletions containing SOX5-binding sites within a retinoic acid-responsive *CBLN2* enhancer. In situ genetic humanization of the mouse *Cbln2* enhancer drives increased and ectopic laminar *Cbln2* expression and promotes PFC dendritic spine formation. These findings suggest a genetic and molecular basis for the anterior-posterior cortical gradient and disproportionate increase in the Hominini PFC of dendritic spines and a developmental mechanism that may link dysfunction of the NRXN–GRID–CBLN2 complex to the pathogenesis of neuropsychiatric disorders.

Access options

Subscribe to Journal

Get full journal access for 1 year

\$199.00

only \$3.90 per issue

[Subscribe](#)

All prices are NET prices.

VAT will be added later in the checkout.

Tax calculation will be finalised during checkout.

Rent or Buy article

Get time limited or full article access on ReadCube.

from \$8.99

[Rent or Buy](#)

All prices are NET prices.

Additional access options:

- [Log in](#)
- [Access through your institution](#)
- [Learn about institutional subscriptions](#)

Fig. 1: Phylogenetic, transcriptomic and regulatory characterization of developmental PFC upregulation of *CBLN2*.

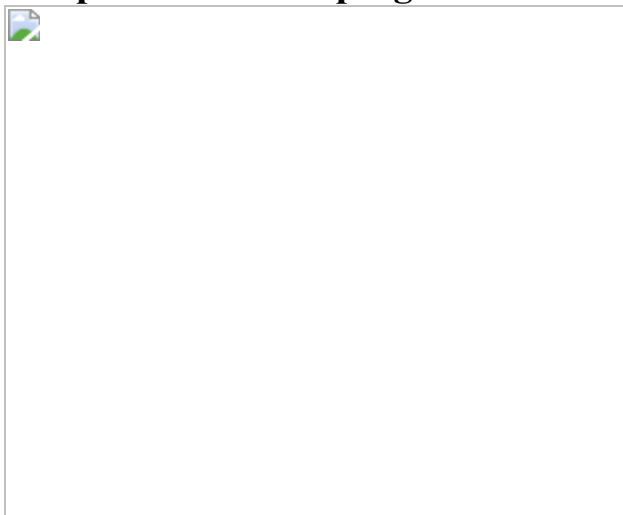


Fig. 2: SOX5 represses *CBLN2* through Hominini-specific regulatory deletions.

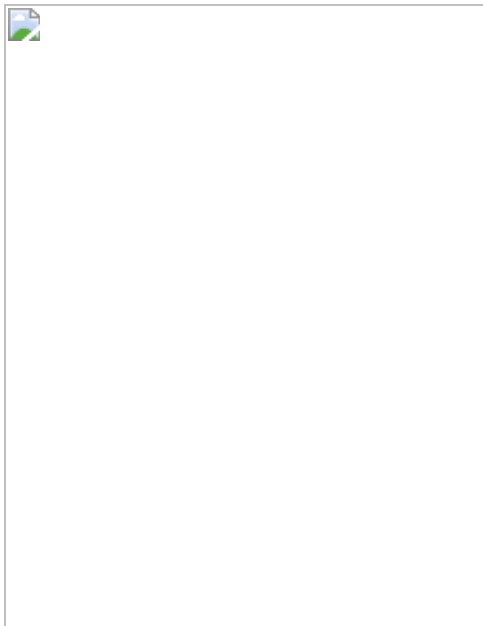


Fig. 3: In situ genetic humanization of the mouse *Cbln2* enhancer drives upregulation and ectopic laminar *Cbln2* expression in the neonatal frontal cortex.

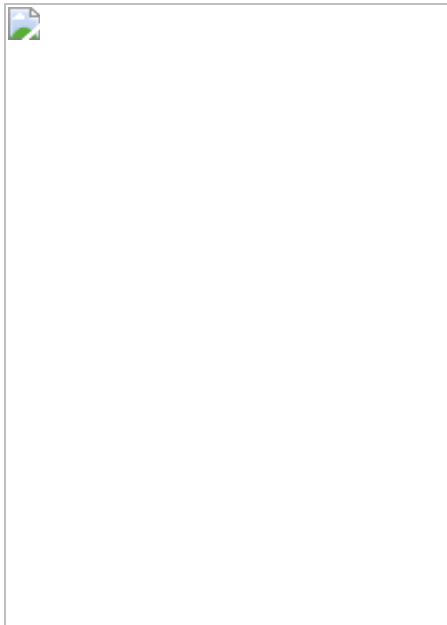
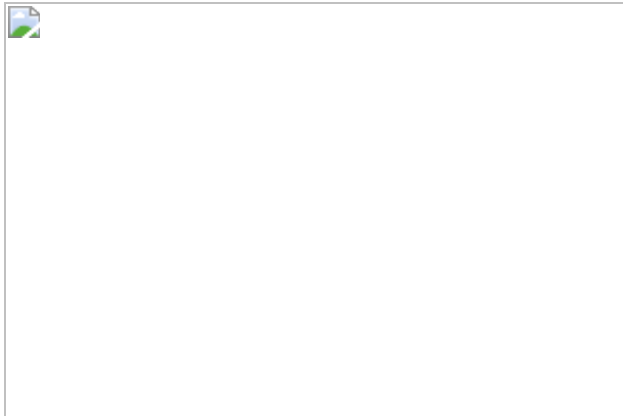


Fig. 4: Increased density of dendritic spines in the mPFC of h*Cbln2* E2 mice.



Code availability

All software and code used in this study are publicly available.

References

1. 1.

Finlay, B. L. & Darlington, R. B. Linked regularities in the development and evolution of mammalian brains. *Science* **268**, 1578–1584 (1995).

2. 2.

Barton, R. A. & Harvey, P. H. Mosaic evolution of brain structure in mammals. *Nature* **405**, 1055–1058 (2000).

3. 3.

Krubitzer, L. & Kaas, J. The evolution of the neocortex in mammals: how is phenotypic diversity generated? *Curr. Opin. Neurobiol.* **15**, 444–453 (2005).

4. 4.

Passingham, R. E. & Wise, S. P. *The Neurobiology of the Prefrontal Cortex: Anatomy, Evolution, and the Origin of Insight* (Oxford Univ.

Press, 2015).

5. 5.

Elston, G. N. et al. Specializations of the granular prefrontal cortex of primates: implications for cognitive processing. *Anat. Rec. A Discov. Mol. Cell. Evol. Biol.* **288**, 26–35 (2006).

6. 6.

Semendeferi, K. et al. Spatial organization of neurons in the frontal pole sets humans apart from great apes. *Cereb. Cortex* **21**, 1485–1497 (2011).

7. 7.

Kwan, K. Y. et al. Species-dependent posttranscriptional regulation of NOS1 by FMRP in the developing cerebral cortex. *Cell* **149**, 899–911 (2012).

8. 8.

Gabi, M. et al. No relative expansion of the number of prefrontal neurons in primate and human evolution. *Proc. Natl Acad. Sci. USA* **113**, 9617–9622 (2016).

9. 9.

Caceres, M. et al. Elevated gene expression levels distinguish human from non-human primate brains. *Proc. Natl Acad. Sci. USA* **100**, 13030–13035 (2003).

10. 10.

Khaitovich, P. et al. Regional patterns of gene expression in human and chimpanzee brains. *Genome Res.* **14**, 1462–1473 (2004).

11. 11.

Uddin, M. et al. Sister grouping of chimpanzees and humans as revealed by genome-wide phylogenetic analysis of brain gene expression profiles. *Proc. Natl Acad. Sci. USA* **101**, 2957–2962 (2004).

12. 12.

Konopka, G. et al. Human-specific transcriptional networks in the brain. *Neuron* **75**, 601–617 (2012).

13. 13.

Bauernfeind, A. L. et al. Evolutionary divergence of gene and protein expression in the brains of humans and chimpanzees. *Genome Biol. Evol.* **7**, 2276–2288 (2015).

14. 14.

Sousa, A. M. M. et al. Molecular and cellular reorganization of neural circuits in the human lineage. *Science* **358**, 1027–1032 (2017).

15. 15.

Zhu, Y. et al. Spatiotemporal transcriptomic divergence across human and macaque brain development. *Science* **362**, eaat8077 (2018).

16. 16.

Pollen, A. A. et al. Establishing cerebral organoids as models of human-specific brain evolution. *Cell* **176**, 743–756 (2019).

17. 17.

Kanton, S. et al. Organoid single-cell genomic atlas uncovers human-specific features of brain development. *Nature* **574**, 418–422 (2019).

18. 18.

Johnson, M. B. et al. Functional and evolutionary insights into human brain development through global transcriptome analysis. *Neuron* **62**,

494–509 (2009).

19. 19.

Pletikos, M. et al. Temporal specification and bilaterality of human neocortical topographic gene expression. *Neuron* **81**, 321–332 (2014).

20. 20.

Li, M. et al. Integrative functional genomic analysis of human brain development and neuropsychiatric risks. *Science* **362**, eaat7615 (2018).

21. 21.

Urade, Y. et al. Precerebellin is a cerebellum-specific protein with similarity to the globular domain of complement C1q B chain. *Proc. Natl Acad. Sci. USA* **88**, 1069–1073 (1991).

22. 22.

Hirai, H. et al. Cbln1 is essential for synaptic integrity and plasticity in the cerebellum. *Nat. Neurosci.* **8**, 1534–1541 (2005).

23. 23.

Uemura, T. et al. Trans-synaptic interaction of GluR δ 2 and neurexin through Cbln1 mediates synapse formation in the cerebellum. *Cell* **141**, 1068–1079 (2010).

24. 24.

Matsuda, K. et al. Cbln1 is a ligand for an orphan glutamate receptor δ 2, a bidirectional synapse organizer. *Science* **328**, 363–368 (2010).

25. 25.

Yasumura, M. et al. Glutamate receptor delta1 induces preferentially inhibitory presynaptic differentiation of cortical neurons by interacting

with neurexins through cerebellin precursor protein subtypes. *J. Neurochem.* **121**, 705–716 (2012).

26. 26.

Wei, P. et al. The Cbln family of proteins interact with multiple signaling pathways. *J. Neurochem.* **121**, 717–729 (2012).

27. 27.

Seigneur, E. & Sudhof, T. C. Genetic ablation of all cerebellins reveals synapse organizer functions in multiple regions throughout the brain. *J. Neurosci.* **38**, 4774–4790 (2018).

28. 28.

Elston, G. N. Pyramidal cells of the frontal lobe: all the more spinous to think with. *J. Neurosci.* **20**, RC95 (2000).

29. 29.

Jacobs, B. et al. Regional dendritic and spine variation in human cerebral cortex: a quantitative golgi study. *Cereb. Cortex* **11**, 558–571 (2001).

30. 30.

Bianchi, S. et al. Synaptogenesis and development of pyramidal neuron dendritic morphology in the chimpanzee neocortex resembles humans. *Proc. Natl Acad. Sci. USA* **110**, 10395–10401 (2013).

31. 31.

Molliver, M. E. et al. The development of synapses in cerebral cortex of the human fetus. *Brain Res.* **50**, 403–407 (1973).

32. 32.

Voigt, T. et al. Synaptophysin immunohistochemistry reveals inside-out pattern of early synaptogenesis in ferret cerebral cortex. *J. Comp. Neurol.* **330**, 48–64 (1993).

33. 33.

Rakic, P. et al. Concurrent overproduction of synapses in diverse regions of the primate cerebral cortex. *Science* **232**, 232–235 (1986).

34. 34.

Shibata, M. et al. Regulation of prefrontal patterning and connectivity by retinoic acid. *Nature* <https://doi.org/10.1038/s41586-021-03953-x> (2021).

35. 35.

Kang, H. J. et al. Spatiotemporal transcriptome of the human brain. *Nature* **478**, 483–489 (2011).

36. 36.

Lambert, N. et al. Genes expressed in specific areas of the human fetal cerebral cortex display distinct patterns of evolution. *PLoS ONE* **6**, e17753 (2011).

37. 37.

Miller, J. A. et al. Transcriptional landscape of the prenatal human brain. *Nature* **508**, 199–206 (2014).

38. 38.

ENCODE Project Consortium et al. An integrated encyclopedia of DNA elements in the human genome. *Nature* **489**, 57–74 (2012).

39. 39.

Chiang, M. Y. et al. An essential role for retinoid receptors RAR β and RXR γ in long-term potentiation and depression. *Neuron* **21**, 1353–1361 (1998).

40. 40.

Krezel, W. et al. Impaired locomotion and dopamine signaling in retinoid receptor mutant mice. *Science* **279**, 863–867 (1998).

41. 41.

Kwan, K. Y. et al. SOX5 postmitotically regulates migration, postmigratory differentiation, and projections of subplate and deep-layer neocortical neurons. *Proc. Natl Acad. Sci. USA* **105**, 16021–16026 (2008).

42. 42.

Shim, S. et al. Cis-regulatory control of corticospinal system development and evolution. *Nature* **486**, 74–79 (2012).

43. 43.

Clarke, R. A. & Eapen, V. Balance within the neurexin trans-synaptic connexus stabilizes behavioral control. *Front. Hum. Neurosci.* **8**, 52 (2014).

44. 44.

State, M. W. & Sestan, N. The emerging biology of autism spectrum disorders. *Science* **337**, 1301–1303 (2012).

45. 45.

Sudhof, T. C. Synaptic neurexin complexes: a molecular code for the logic of neural circuits. *Cell* **171**, 745–769 (2017).

46. 46.

Willsey, A. J. et al. Coexpression networks implicate human midfetal deep cortical projection neurons in the pathogenesis of autism. *Cell* **155**, 997–1007 (2013).

47. 47.

Gulsuner, S. et al. Spatial and temporal mapping of de novo mutations in schizophrenia to a fetal prefrontal cortical network. *Cell* **154**, 518–529 (2013).

48. 48.

Lewis, D. A. & Mirenda, K. Transcriptome alterations in schizophrenia: disturbing the functional architecture of the dorsolateral prefrontal cortex. *Prog. Brain Res.* **158**, 141–152 (2006).

49. 49.

Dy, P., Han, Y. & Lefebvre, V. Generation of mice harboring a Sox5 conditional null allele. *Genesis* **46**, 294–299 (2008).

50. 50.

Mathelier, A. et al. JASPAR 2016: a major expansion and update of the open-access database of transcription factor binding profiles. *Nucleic Acids Res.* **44**, D110–D115 (2016).

51. 51.

Khan, A. et al. JASPAR 2018: update of the open-access database of transcription factor binding profiles and its web framework. *Nucleic Acids Res.* **46**, D260–D266 (2018).

52. 52.

Shim, S. et al. Regulation of EphA8 gene expression by TALE homeobox transcription factors during development of the mesencephalon. *Mol. Cell. Biol.* **27**, 1614–1630 (2007).

53. 53.

Wang, H. et al. One-step generation of mice carrying mutations in multiple genes by CRISPR/Cas-mediated genome engineering. *Cell* **153**, 910–918 (2013).

54. 54.

Liu, P. et al. A highly efficient recombineering-based method for generating conditional knockout mutations. *Genome Res.* **13**, 476–484 (2003).

55. 55.

Cong, L. et al. Multiplex genome engineering using CRISPR/Cas systems. *Science* **339**, 819–823 (2013).

56. 56.

Wilkinson, D. G. & Nieto, M. A. Detection of messenger RNA by in situ hybridization to tissue sections and whole mounts. *Methods Enzymol.* **225**, 361–373 (1993).

57. 57.

Hunt, C. A. et al. PSD-95 is associated with the postsynaptic density and not with the presynaptic membrane at forebrain synapses. *J. Neurosci.* **16**, 1380–1388 (1996).

58. 58.

Essrich, C. et al. Postsynaptic clustering of major GABA_A receptor subtypes requires the γ2 subunit and gephyrin. *Nat. Neurosci.* **1**, 563–571 (1998).

59. 59.

Ippolito, D. M. & Eroglu, C. Quantifying synapses: an immunocytochemistry-based assay to quantify synapse number. *J. Vis.*

Exp. **45**, 2270 (2010).

60. 60.

Fiala, J. C. Reconstruct: a free editor for serial section microscopy. *J. Microsc.* **218**, 52–61 (2005).

61. 61.

Risher, W. C. et al. Rapid Golgi analysis method for efficient and unbiased classification of dendritic spines. *PLoS ONE* **9**, e107591 (2014).

62. 62.

Kaur, N. et al. Neural stem cells direct axon guidance via their radial fiber scaffold. *Neuron* **107**, 1197–1211 (2020).

63. 63.

Meijering, E. et al. Design and validation of a tool for neurite tracing and analysis in fluorescence microscopy images. *Cytometry A* **58**, 167–176 (2004).

64. 64.

Hinrichs, A. S. et al. The UCSC Genome Browser database: update 2006. *Nucleic Acids Res.* **34**, D590–D598 (2006).

65. 65.

Robinson, J. T. et al. Integrative genomics viewer. *Nat. Biotechnol.* **29**, 24–26 (2011).

66. 66.

Kent, W. J. et al. The human genome browser at UCSC. *Genome Res.* **12**, 996–1006 (2002).

67. 67.

Rosenbloom, K. R. et al. ENCODE data in the UCSC Genome Browser: year 5 update. *Nucleic Acids Res.* **41**, D56–D63 (2013).

68. 68.

Shibata, M. et al. MicroRNA-9 regulates neurogenesis in mouse telencephalon by targeting multiple transcription factors. *J. Neurosci.* **31**, 3407–3422 (2011).

69. 69.

Morozov, Y. M., Ayoub, A. E. & Rakic, P. Translocation of synaptically connected interneurons across the dentate gyrus of the early postnatal rat hippocampus. *J. Neurosci.* **26**, 5017–5027 (2006).

70. 70.

Morozov, Y. M., Mackie, K. & Rakic, P. Cannabinoid type 1 receptor is undetectable in rodent and primate cerebral neural stem cells but participates in radial neuronal migration. *Int. J. Mol. Sci.* **21**, 1–19 (2020).

71. 71.

Thompson, C. L. et al. A high-resolution spatiotemporal atlas of gene expression of the developing mouse brain. *Neuron* **83**, 309–323 (2014).

Acknowledgements

We thank S. Bai, T. Nottoli and X. Xing for technical help with generating transgenic mice and genetically humanized mice; A. Sousa for providing tissue; B. Lorente-Galdos and G. Santpere for helping with data analysis; A. Duque for using equipment from MacBrainResource (MH113257); V. Lefebvre for providing floxed *Sox5* mice; and the members of the Sestan laboratory for comments. This work was supported by the National

Institutes of Health (HG010898, MH106874, MH106934, MH110926 and MH116488) and the Simons Foundation Autism Research Institute (SFARI) (572080; to N.S.). Additional support was provided by the National Institutes of Health T32 fellowship (MH18268 to K.P.), the National Science Foundation Graduate Research Fellowship Program (to S.K.M.), the Kavli Foundation and the James S. McDonnell Foundation (to N.S.).

Author information

Affiliations

1. Department of Neuroscience, Yale School of Medicine, New Haven, CT, USA

Mikihito Shibata, Kartik Pattabiraman, Sydney K. Muchnik, Navjot Kaur, Yury M. Morozov & Nenad Sestan

2. Yale Child Study Center, New Haven, CT, USA

Kartik Pattabiraman & Nenad Sestan

3. Department of Genetics, Yale School of Medicine, New Haven, CT, USA

Sydney K. Muchnik & Nenad Sestan

4. Department of Neurology, Yale School of Medicine, New Haven, CT, USA

Xiaoyang Cheng & Stephen G. Waxman

5. Center for Neuroscience and Regeneration Research, Yale University, New Haven, CT, USA

Xiaoyang Cheng & Stephen G. Waxman

6. Rehabilitation Research Center, Veterans Affairs Connecticut Healthcare Center, West Haven, CT, USA

Xiaoyang Cheng & Stephen G. Waxman

7. Department of Comparative Medicine, Yale School of Medicine, New Haven, CT, USA

Nenad Sestan

8. Department of Psychiatry, Yale School of Medicine, New Haven, CT, USA

Nenad Sestan

9. Program in Cellular Neuroscience, Neurodegeneration and Repair, New Haven, CT, USA

Nenad Sestan

10. Kavli Institute for Neuroscience, Yale University, New Haven, CT, USA

Nenad Sestan

Contributions

M.S., K.P. and N.S. designed the research. M.S. and K.P. performed the overall experiments and analysed the data. S.K.M. analysed the RNA sequencing, ChIP sequencing and genomic sequence data. M.S. generated the transgenic and knock-in mice. N.K. performed retrograde neuronal tracing with the AAV and analysed the data. Y.M.M. performed and analysed the electron microscopy experiments. X.C. and S.G.W. performed and analysed the preliminary electrophysiological analysis. N.S. conceived the study. M.S., K.P. and N.S. wrote the manuscript. All authors discussed the results and implications and commented on the manuscript at all stages.

Corresponding author

Correspondence to Nenad Sestan.

Ethics declarations

Competing interests

The authors declare no competing interests.

Additional information

Peer review information *Nature* thanks Alex Pollen and the other, anonymous, reviewer(s) for the peer review of this work.

Publisher's note Springer Nature remains neutral with regard to jurisdictional claims in published maps and institutional affiliations.

Extended data figures and tables

[Extended Data Fig. 1 Spatiotemporal expression of *CBLN2* in the human and macaque neocortex.](#)

a–c, Spatiotemporal expression of *CBLN2* expression in the human and macaque cerebral cortex during development base on BrainSpan (brainspan.org) and PsychENCODE (development.psychencode.org, evolution.psychencode.org) human and macaque RNA-seq data^{15,20}. The RNA-seq data consisted of tissue-level samples comprising the pial surface, marginal zone, cortical plate (layers 2–6) and adjacent subplate zone, of eleven prospective neocortical areas. Red and blue lines indicate human and macaque PFC *CBLN2* expression, respectively, and dotted lines represent the non-PFC *CBLN2* expression. Vertical grey box demarcates mid-fetal developmental periods. Predicted ages, timeline of human and macaque development and the associated periods are shown below. Visual representation of *CBLN2* in human cortex with heatmaps of regional expression in human and macaque below during period 4–6 (**b**) and period 12–13 (**c**). Darker reds represent high expression levels. **d**, Anteroposterior visual representation of human *CBLN2* expression at PCW 21 from the

BrainSpan human prenatal laser microdissection microarray data (brainspan.org)³⁷.

Extended Data Fig. 2 Expression profile of *CBLN1,3,4* genes related to dendrite and synapse development and *CBLN2* binding partners in macaque and human.

a, Developmental trajectory of *CBLN2* expression compared to the expression of key genes related to dendrite development (i.e., *MAP1A* and *CAMK2A*) and synapse development genes (i.e., *SYP*, *SYPL1*, *SYPL2* and *SYN1*). The lists of genes related to synapse and dendrite development were previously complied and analyzed for their expression trajectories by Kang et al.³⁵. **b**, Developmental trajectory of *CBLN2* expression compared to the expression of genes encoding *CBLN2* binding partners (i.e., *GRID1*, *GRID2*, *NRXN1*, *NRXN2* and *NRXN3*). Left and right panels show gene expression in human and macaque, respectively. Gene expression in PFC and non-PFC are indicated by solid and dashed line, respectively. Vertical grey box highlights the mid-fetal developmental periods. Predicted ages, timeline of human and macaque development and the associated periods are shown below. Gene expression values are represented as log₂(RPKM+1). For all of these plots, the shading around the lines represents the 95% confidence interval. Abbreviations are as described in Fig. 1 legend.

Extended Data Fig. 3 Mouse *Cbln2* expression at multiple stages and *Cbln2* E2 transgenic lines.

a, b, Visualization of *Cbln2* expression in wholemount (**a**) and sagittal sections (**b**) at PCD 11.5, 13.5, 15.5 18.5 and PD 4, 14 from Allen Brain Atlas developing mouse brain atlas (developingmouse.brain-map.org)⁷¹. Arrowheads highlight early rostral expression, UL, upper layer; L5, layer 5; SP, subplate. **c**, β -Galactosidase activity in two additional mouse brains from independent transgenic mouse carrying *Cbln2* E2 conjugated with *lacZ* reporter at PCD 17. See Fig. 1c for the third replicate. FP, frontal pole; OB, olfactory bulb. Scale bars, 1 mm.

Extended Data Fig. 4 Comparative analysis of *CBLN2* E2 deletions across mammals.

a, Schematic representation of *CBLN2* E2 from mouse and primate species including apes (human, common chimpanzee, bonobo, gorilla, orangutan and gibbon), old world monkey (Rhesus macaque), new world monkey (marmoset) and prosimians (tarsier and lemur). HSD1, HSD2 and I3 are shaded. Putative RAR-RXR tandem binding sites indicated as red lines and putative SOX5-binding sites as blue lines. **b**, Sequence alignments of HSD1, HSD2 and I3 from macaque, mouse, and rat. Putative SOX5 binding sites are shown in red boxes. **c**, Sequence alignments of HSD1 and HSD2 from primates shown in **a**.

Extended Data Fig. 5 Conservation of *CBLN2* E2 and deleted regions across species.

Phylogenetic tree of selected chordates including placental and non-placental mammals with information about presence of the *CBLN2/Cbln2* gene and *CBLN2* E2/*Cbln2* E2. The last three columns describe the presence of HSD1, HSD2 and I3. The mouse E2 sequence was searched in each most updated animal genome browser at UCSC genome browser (as of December 22, 2019). E2 conservation criteria are: 1) identity over 80%; and 2) alignment length over 600 bp compared with mouse E2 (1005 bp).

Extended Data Fig. 6 SOX5 directly suppresses RXRG-RARB responsive human, chimpanzee, gorilla and mouse *Cbln2* E2 enhancer.

a, Luciferase assay in Neuro-2a cell line from luciferase reporters conjugated to chimpanzee and gorilla wild *CBLN2* E2. Two-tailed Student's t-test; *P = 0.01; ***P = 9e-5 (Chimpanzee), 1e-5 (Gorilla); NS, not significant. Error bars; S.E.M.; N = 3 per condition. **b**, Overexpression of human *SOX5* exerts a similar effect to mouse *Sox5* on human and mouse *Cbln2* E2 reporters. Two-tailed Student's t-test; *P = 5e-3; ***P = 4e-5; ****P = 2e-6; 2e-6, 1e-6 (Human SOX5 + mouse *Cbln2* E2); NS, not significant; Error bars, S.E.M.; N = 3 per condition. **c**, *Cbln2* expression is

upregulated in *Sox5* conditional knockout brain at PD 0. Additional two replicates (Repl #2 and 3) not shown in Fig. 2d are shown. Scale bar, 200 μm (left); 100 μm (right). **d**, Constructs used for luciferase assay and generation of transgenic animals shown in e, f. **e**, Transgenic mouse brain at PCD 17 carrying *Cbln2* E2 ($N = 3$) or *Cbln2* E2 Fr1-*lacZ* reporters ($N = 3$). *Cbln2* expression in the PFC is indicated by arrowheads. Endogenous *Cbln2* expression is also shown for comparison ($N = 4$). Scale bar, 200 μm . **f**, Luciferase assay for *Cbln2* E2 and *Cbln2* E2-Fr1. Two-tailed Student's t-test; ** $P = 1\text{e-}4$ (*Cbln2* E2), $2\text{e-}4$ (*Cbln2* E2-Fr1); *** $P = 8\text{e-}5$; NS, not significant; Error bars: S.E.M.; $N = 3$ per condition.

Extended Data Fig. 7 Humanized *Cbln2* E2 knock-in mouse shows increased *Cbln2* expression in neonatal neocortex.

a, Positions of single-guide RNAs (sgRNA1 and 2) to introduce double-strand breaks in the genomic DNA and targeting vector to replace WT mouse *Cbln2* E2 region with that of human *CBLN2* E2 (humanized h*Cbln2* E2) are shown. **b**, Genotyping strategy for F1 mice. Germline transmission in the F1 generation was confirmed by nested PCR using the primer set of mP3/mP4, followed by hP1/P2 as indicated in a. Two founders #13 and #25 were obtained. **c**, Mice in the following generation were genotyped by PCR with hP1/P2 and mP1/mP2. An example of genotyping for F2 of line #13 mice is shown (c). **d**, Comparison of *Cbln2* expression between WT *Cbln2* E2 (*Mm;Mm*) and h*Cbln2* E2 (*Hs;Hs*) neocortex at PD 0 using quantitative reverse transcription-PCR. RNA was extracted from the neocortex following the removal of hippocampus, olfactory bulb and subpallial regions. Two-tailed Student's t-test; * $P = 0.007$; Error bars: S.E.M.; $N = 5$ per genotype. Genotyping were repeated at least two times in b and c.

Extended Data Fig. 8 Additional replicates.

Additional replicates from Fig. 3. **a, b**, The neocortex of the humanized h*Cbln2* E2 knock-in prenatal and neonatal mice exhibits upregulated *Cbln2* in both upper and deeper layers compared to mice carrying WT *Cbln2* E2. Additional two replicates (Repl #2 and 3) not shown in Fig. 3a are shown for PND 16 and PND18. Scale bars, 200 μm (left); 100 μm (right). All analysis and three replicates for PD1. Neocortex was divided into six equal

bins spanning from pia to ventricular zone, and *Cbln2* signal intensity was quantified for each bin and compared between WT and h*Cbln2* E2 (*Hs;Hs*). Two-tailed Student's t-test; *P = 0.02 (PCD18), 0.02, 0.04 (PD1), **P = 1e-3 (PCD18), 1e-3, 3e-3, 3e-3 (PD1), ***P = 1e-4, 2e-4 (PCD18); N = 3 per genotype. Scale bars, 100 μm . **c**, Expression of the upper layer marker, *Cux2*, and SOX5 in adjacent tissue sections were detected by *in situ* hybridization and immunostaining, respectively. Scale bars, 100 μm . N = 3.

[Extended Data Fig. 9 Expression of Sox5 in the developing mouse and human neocortex.](#)

a, Double immunofluorescent staining for SOX5 and BCL11B in PD 0 and PD 7 mouse neocortex. N = 3 per condition. Scale bar, 100 μm . **b**, SOX5 expression in the PFC and non-PFC areas of the cerebral cortex of human and macaque across development. Red and blue lines indicate human and macaque, respectively. Vertical grey box demarcates mid-fetal developmental periods. For all of those plots, the shading around the lines represents the 95% confidence interval. Predicted ages, timeline of human and macaque development and the associated periods are shown below.

[Extended Data Fig. 10 Quantification of excitatory and inhibitory postsynaptic puncta.](#)

a-d, PD 0 WT and h*Cbln2* E2 mPFC L2-3 and L5 (BCL11B-immunopositive) immunostained for PSD-95/DLG4 or GPHN. Density of PSD-95/DLG4+ excitatory and GPHN+ inhibitory postsynaptic puncta in PD 0 and PD 60 mPFC, primary somatosensory area (SSp), and primary visual area (VISp) of WT (blue), h*Cbln2* E2 (orange), and *Sox5* cKO mice (green). Two-tailed Student's test; *P = 0.018; ***P = 4e-4, 1e-4 (b, WT vs. humanized h*Cbln2* E2 L2-3, and L5, respectively), 1e-4, 7e-5, 4e-4, 2e-4 (d, WT vs. humanized h*Cbln2* E2 L2-3 and L5, respectively; WT vs. *Sox5* cKO L2-3 and L5, respectively); ***P < 1e-5. Error bars: S.E.M.; N = 5 per PD 0 genotype; N = 3 per PD 60 genotype. Scale bar, 25 μm .

[Extended Data Fig. 11 Analysis of dendritic spines and dendritic complexity.](#)

a–c, Quantification of Sholl analysis and representative images (inset) of Golgi stained dendrites and dendritic spines per 10 µm in layer 2-3 and 5 of mPFC (**a**), SSp (**b**) and VISp (**c**) in WT *Cbln2* E2 and humanized hCbln2 E2. Two-way ANOVA with Sidak's multiple comparison method was applied; *P = 0.04; **P = 1e-3, ****P < 0001; Error bars: S.E.M.; N = 16 (WT *Cbln2* E2), and 16 (humanized hCbln2 E2) of PD 60 brains (N = 3). Scale bars: 5 mm. **d, e**, Quantification and representative images of juxtaposed synaptophysin (SYP) and DLG4/PSD-95 immunolabelled puncta in upper (UL) and deep layer (DL) mPFC of WT *Cbln2* E2 and humanized hCbln2 E2. Two-tailed Student's t-test was applied * P = 0.03; Error bars: S.E.M. (N = 3); Scale bar: 10 mm. **f**, Electron microscopy (EM) image shows dendrite emitting spine with postsynaptic density (PSD) and spine apparatus (SA) (left) in PD 60 humanized hCbln2 E2 mouse. 3D reconstruction (right) of the dendrite with numerous spines showing spine heads and synaptic contacts (red). Double arrow points to the spine shown in EM image. Thin spines without head (TS) and not innervated thin extensions (arrow) are also detected. Abbreviation: M, mitochondria. Sixteen-representable dendrite fragments were traced in the serial images (see [Methods](#)). **g**, Quantification of percentage of innervated spines in mPFC of WT *Cbln2* E2 and humanized hCbln2 E2. Two-tailed Student's t-test was applied. NS, Not significant. Error bars: S.E.M. (N = 3).

Supplementary information

[Supplementary Fig. 1](#)

Full image of ChIP-PCR assays from Figure 2c in PD 0 mouse neocortex using anti-RNA polymerase II (anti-POL2), IgG, and anti-SOX5 and *Cbln2* E1 and E2 primers with relevant marker sizes defined.

[Reporting Summary](#)

[Supplementary Table 1](#)

Comparative analysis of the transcription factor binding sites in *CBLN2* E2.

Supplementary Table 2

List and sequence of relevant primers.

Supplementary Table 3

Statistics for all comparisons in Figure 1a.

Rights and permissions

Reprints and Permissions

About this article

Cite this article

Shibata, M., Pattabiraman, K., Muchnik, S.K. *et al.* Hominini-specific regulation of *CBLN2* increases prefrontal spinogenesis. *Nature* **598**, 489–494 (2021). <https://doi.org/10.1038/s41586-021-03952-y>

- Received: 31 December 2019
- Accepted: 25 August 2021
- Published: 01 October 2021
- Issue Date: 21 October 2021
- DOI: <https://doi.org/10.1038/s41586-021-03952-y>

Share this article

Anyone you share the following link with will be able to read this content:

[Get shareable link](#)

Sorry, a shareable link is not currently available for this article.

[Copy to clipboard](#)

Provided by the Springer Nature SharedIt content-sharing initiative

Further reading

- [Regulation of prefrontal patterning and connectivity by retinoic acid](#)

- Mikihito Shibata
- , Kartik Pattabiraman
- , Belen Lorente-Galdos
- , David Andrijevic
- , Suel-Kee Kim
- , Navjot Kaur
- , Sydney K. Muchnik
- , Xiaojun Xing
- , Gabriel Santpere
- , Andre M. M. Sousa
- & Nenad Sestan

Nature (2021)

- [The genetic symphony underlying evolution of the brain's prefrontal cortex](#)

- Jenelle L. Wallace
- & Alex A. Pollen

Nature (2021)

[The genetic symphony underlying evolution of the brain's prefrontal cortex](#)

- Jenelle L. Wallace
- Alex A. Pollen

News & Views 01 Oct 2021

Regulators of human brain evolution

- Katherine Whalley

Research Highlight 19 Oct 2021

This article was downloaded by **calibre** from <https://www.nature.com/articles/s41586-021-03952-y>.

| [Section menu](#) | [Main menu](#) |

- Article
- [Published: 08 September 2021](#)

The EDS1–PAD4–ADR1 node mediates *Arabidopsis* pattern-triggered immunity

- [Rory N. Pruitt](#) [ORCID: orcid.org/0000-0002-4134-8156](#)¹ na1,
- [Federica Locci](#) [ORCID: orcid.org/0000-0001-5443-0717](#)² na1,
- [Friederike Wanke](#) [ORCID: orcid.org/0000-0001-6080-8800](#)³,
- [Lisha Zhang](#) [ORCID: orcid.org/0000-0002-8203-2369](#)¹,
- [Svenja C. Saile](#) [ORCID: orcid.org/0000-0003-2258-3166](#)³,
- [Anna Joe](#)¹,
- [Darya Karelina](#)⁴,
- [Chenlei Hua](#)¹,
- [Katja Fröhlich](#) [ORCID: orcid.org/0000-0002-9491-5927](#)¹,
- [Wei-Lin Wan](#)¹ nAff11,
- [Meijuan Hu](#)⁵,
- [Shaofei Rao](#)⁵ nAff12,
- [Sara C. Stolze](#) [ORCID: orcid.org/0000-0002-1421-9703](#)⁶,
- [Anne Harzen](#)⁶,
- [Andrea A. Gust](#) [ORCID: orcid.org/0000-0003-0466-2792](#)¹,
- [Klaus Harter](#)³,
- [Matthieu H. A. J. Joosten](#)⁷,
- [Bart P. H. J. Thomma](#) [ORCID: orcid.org/0000-0003-4125-4181](#)^{7,8},
- [Jian-Min Zhou](#) [ORCID: orcid.org/0000-0002-9943-2975](#)⁵,
- [Jeffery L. Dangl](#) [ORCID: orcid.org/0000-0003-3199-8654](#)⁹,
- [Detlef Weigel](#)⁴,
- [Hiroyuki Nakagami](#) [ORCID: orcid.org/0000-0003-2569-7062](#)⁶,
- [Claudia Oecking](#)³,

- [Farid El Kasmi](#) [ORCID: orcid.org/0000-0002-4634-7689³](#),
- [Jane E. Parker](#) [ORCID: orcid.org/0000-0002-4700-6480^{2,8}](#) &
- [Thorsten Nürnberg](#) [ORCID: orcid.org/0000-0002-7804-7170^{1,10}](#)

Nature volume **598**, pages 495–499 (2021)

- 8090 Accesses
- 165 Altmetric
- [Metrics details](#)

Subjects

- [Pattern recognition receptors in plants](#)
- [Plant signalling](#)

Abstract

Plants deploy cell-surface and intracellular leucine rich-repeat domain (LRR) immune receptors to detect pathogens¹. LRR receptor kinases and LRR receptor proteins at the plasma membrane recognize microorganism-derived molecules to elicit pattern-triggered immunity (PTI), whereas nucleotide-binding LRR proteins detect microbial effectors inside cells to confer effector-triggered immunity (ETI). Although PTI and ETI are initiated in different host cell compartments, they rely on the transcriptional activation of similar sets of genes², suggesting pathway convergence upstream of nuclear events. Here we report that PTI triggered by the *Arabidopsis* LRR receptor protein RLP23 requires signalling-competent dimers of the lipase-like proteins EDS1 and PAD4, and of ADR1 family helper nucleotide-binding LRRs, which are all components of ETI. The cell-surface LRR receptor kinase SOBIR1 links RLP23 with EDS1, PAD4 and ADR1 proteins, suggesting the formation of supramolecular complexes containing PTI receptors and transducers at the inner side of the plasma membrane. We detected similar evolutionary patterns in LRR receptor protein and nucleotide-binding LRR genes across *Arabidopsis* accessions; overall higher levels of variation in LRR receptor proteins than in LRR

receptor kinases are consistent with distinct roles of these two receptor families in plant immunity. We propose that the EDS1–PAD4–ADR1 node is a convergence point for defence signalling cascades, activated by both surface-resident and intracellular LRR receptors, in conferring pathogen immunity.

Access options

Subscribe to Journal

Get full journal access for 1 year

\$199.00

only \$3.90 per issue

[Subscribe](#)

All prices are NET prices.

VAT will be added later in the checkout.

Tax calculation will be finalised during checkout.

Rent or Buy article

Get time limited or full article access on ReadCube.

from \$8.99

[Rent or Buy](#)

All prices are NET prices.

Additional access options:

- [Log in](#)
- [Access through your institution](#)
- [Learn about institutional subscriptions](#)

Fig. 1: RLCK-VII-7 subfamily members are required for LRR-RP-mediated immunity.

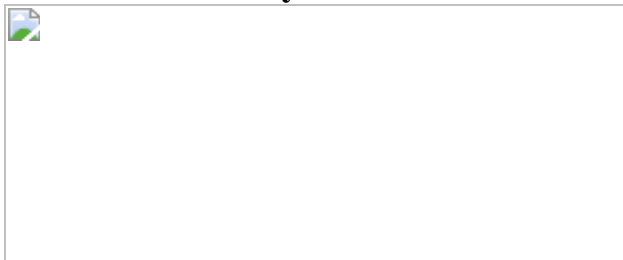


Fig. 2: PAD4, EDS1 and ADR1 helper NLRs are positive regulators of LRR-RP signalling.

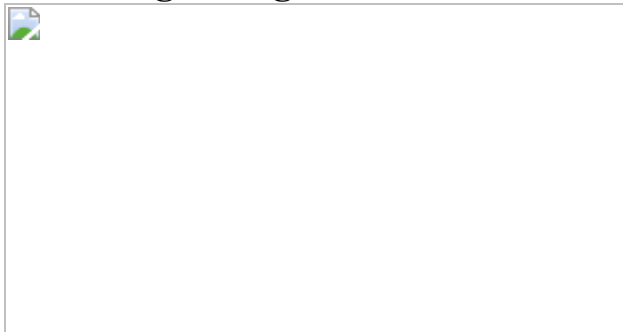
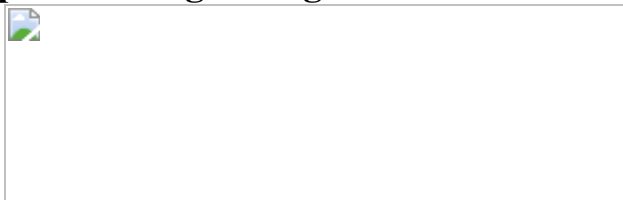


Fig. 3: SOBIR1 associates with EDS1, PAD4 and ADR1 hNLRs to form a potential signalling node.



Data availability

All data are available within this article and its Supplementary Information. Proteomics data are available via the ProteomeXchange Consortium with the identifier [PXD026120](#). MS data were searched against a combined database containing protein sequences from *A. thaliana* TAIR10_pep_20101214 (https://www.arabidopsis.org/download/index-auto.jsp?dir=%2Fdownload_files%2FProteins%2FTAIR10_protein_lists). Genomics data from *A. thaliana* accessions were obtained from the 1001 Genomes project (<https://1001genomes.org/data-center.html>) and mapped to the TAIR10 assembly of the genome (<https://arabidopsis.org>). Original gel blots are shown in Supplementary Fig. 1. Statistical analyses for all

quantitative data are provided in Supplementary Tables [1](#), [2](#) and [5](#). [Source data](#) are provided with this paper.

References

1. 1.

Jones, J. D. & Dangl, J. L. The plant immune system. *Nature* **444**, 323–329 (2006).

2. 2.

Lu, Y. & Tsuda, K. Intimate association of PRR- and NLR-mediated signaling in plant immunity. *Mol. Plant Microbe Interact.* **34**, 3–14 (2021).

3. 3.

Wan, W. L., Fröhlich, K., Pruitt, R. N., Nürnberger, T. & Zhang, L. Plant cell surface immune receptor complex signaling. *Curr. Opin. Plant Biol.* **50**, 18–28 (2019).

4. 4.

Monteiro, F. & Nishimura, M. T. Structural, functional, and genomic diversity of plant NLR proteins: an evolved resource for rational engineering of plant immunity. *Annu. Rev. Phytopathol.* **56**, 243–267 (2018).

5. 5.

Lapin, D., Bhandari, D. D. & Parker, J. E. Origins and immunity networking functions of EDS1 family proteins. *Annu. Rev. Phytopathol.* **58**, 253–276 (2020).

6. 6.

Feehan, J. M., Castel, B., Bentham, A. R. & Jones, J. D. Plant NLRs get by with a little help from their friends. *Curr. Opin. Plant Biol.* **56**, 99–108 (2020).

7. 7.

Yuan, M. et al. Pattern-recognition receptors are required for NLR-mediated plant immunity. *Nature* **592**, 105–109 (2021).

8. 8.

Ngou, B. P. M., Ahn, H. K., Ding, P. & Jones, J. D. G. Mutual potentiation of plant immunity by cell-surface and intracellular receptors. *Nature* **592**, 110–115 (2021).

9. 9.

Wan, W. L. et al. Comparing *Arabidopsis* receptor kinase and receptor protein-mediated immune signaling reveals BIK1-dependent differences. *New Phytol.* **221**, 2080–2095 (2019).

10. 10.

Rao, S. et al. Roles of receptor-like cytoplasmic kinase VII members in pattern-triggered immune signaling. *Plant Physiol.* **177**, 1679–1690 (2018).

11. 11.

Zhang, L. et al. Distinct immune sensors for fungal endopolygalacturonases in closely related Brassicaceae. *Nat. Plants*, <https://doi.org/10.1038/s41477-021-00982-2> (2021).

12. 12.

Fan, L. et al. Genotyping-by-sequencing-based identification of *Arabidopsis* pattern recognition receptor RLP32 recognizing proteobacterial translation initiation factor IF1. Preprint at <https://doi.org/10.1101/2021.03.04.433884> (2021).

13. 13.

Böttcher, C. et al. The multifunctional enzyme CYP71B15 (PHYTOALEXIN DEFICIENT3) converts cysteine-indole-3-acetonitrile to camalexin in the indole-3-acetonitrile metabolic network of *Arabidopsis thaliana*. *Plant Cell* **21**, 1830–1845 (2009).

14. 14.

Mishina, T. E. & Zeier, J. The *Arabidopsis* flavin-dependent monooxygenase FMO1 is an essential component of biologically induced systemic acquired resistance. *Plant Physiol.* **141**, 1666–1675 (2006).

15. 15.

Böhm, H. et al. A conserved peptide pattern from a widespread microbial virulence factor triggers pattern-induced immunity in *Arabidopsis*. *PLoS Pathog.* **10**, e1004491 (2014).

16. 16.

Sun, X. et al. Pathogen effector recognition-dependent association of NRG1 with EDS1 and SAG101 in TNL receptor immunity. *Nat. Commun.* **12**, 3335 (2021).

17. 17.

Lapin, D. et al. A coevolved EDS1–SAG101–NRG1 module mediates cell death signaling by TIR-domain immune receptors. *Plant Cell* **31**, 2430–2455 (2019).

18. 18.

Cui, H. et al. A core function of EDS1 with PAD4 is to protect the salicylic acid defense sector in *Arabidopsis* immunity. *New Phytol.* **213**, 1802–1817 (2017).

19. 19.

Wagner, S. et al. Structural basis for signaling by exclusive EDS1 heteromeric complexes with SAG101 or PAD4 in plant innate immunity. *Cell Host Microbe* **14**, 619–630 (2013).

20. 20.

Bhandari, D. D. et al. An EDS1 heterodimer signalling surface enforces timely reprogramming of immunity genes in *Arabidopsis*. *Nat. Commun.* **10**, 772 (2019).

21. 21.

Joglekar, S. et al. Chemical activation of EDS1/PAD4 signaling leading to pathogen resistance in *Arabidopsis*. *Plant Cell Physiol.* **59**, 1592–1607 (2018).

22. 22.

Saile, S. C. et al. Two unequally redundant “helper” immune receptor families mediate *Arabidopsis thaliana* intracellular “sensor” immune receptor functions. *PLoS Biol.* **18**, e3000783 (2020).

23. 23.

Reuter, L. et al. Light-triggered and phosphorylation-dependent 14-3-3 association with NONPHOTOTROPIC HYPOCOTYL 3 is required for hypocotyl phototropism. Preprint at <https://doi.org/10.1101/2021.04.09.439179> (2021).

24. 24.

Koenig, D. et al. Long-term balancing selection drives evolution of immunity genes in *Capsella*. *eLife* **8**, e43606 (2019).

25. 25.

Guo, Y. L. et al. Genome-wide comparison of nucleotide-binding site-leucine-rich repeat-encoding genes in *Arabidopsis*. *Plant Physiol.* **157**, 757–769 (2011).

26. 26.

1001 Genomes Consortium. 1,135 Genomes reveal the global pattern of polymorphism in *Arabidopsis thaliana*. *Cell* **166**, 481–491 (2016).

27. 27.

Cao, J. et al. Whole-genome sequencing of multiple *Arabidopsis thaliana* populations. *Nat. Genet.* **43**, 956–963 (2011).

28. 28.

Lin, Z. J., Liebrand, T. W., Yadeta, K. A. & Coaker, G. PBL13 is a serine/threonine protein kinase that negatively regulates *Arabidopsis* immune responses. *Plant Physiol.* **169**, 2950–2962 (2015).

29. 29.

Thomma, B. P., Nürnberg, T. & Joosten, M. H. Of PAMPs and effectors: the blurred PTI–ETI dichotomy. *Plant Cell* **23**, 4–15 (2011).

30. 30.

Gust, A. A., Pruitt, R. & Nürnberg, T. Sensing danger: key to activating plant immunity. *Trends Plant Sci.* **22**, 779–791 (2017).

31. 31.

Felix, G., Duran, J. D., Volko, S. & Boller, T. Plants have a sensitive perception system for the most conserved domain of bacterial flagellin. *Plant J.* **18**, 265–276 (1999).

32. 32.

Kunze, G. et al. The N terminus of bacterial elongation factor Tu elicits innate immunity in *Arabidopsis* plants. *Plant Cell* **16**, 3496–3507 (2004).

33. 33.

Jehle, A. K. et al. The receptor-like protein ReMAX of *Arabidopsis* detects the microbe-associated molecular pattern eMax from *Xanthomonas*. *Plant Cell* **25**, 2330–2340 (2013).

34. 34.

Bai, Y. et al. Functional overlap of the *Arabidopsis* leaf and root microbiota. *Nature* **528**, 364–369 (2015).

35. 35.

Albert, M. et al. Regulation of cell behaviour by plant receptor kinases: pattern recognition receptors as prototypical models. *Eur. J. Cell Biol.* **89**, 200–207 (2010).

36. 36.

Jin, L. & Mackey, D. M. Measuring callose deposition, an indicator of cell wall reinforcement, during bacterial infection in *Arabidopsis*. *Methods Mol. Biol.* **1578**, 195–205 (2017).

37. 37.

Willmann, R., Haischer, D. J. & Gust, A. A. Analysis of MAPK activities using MAPK-specific antibodies. *Methods Mol. Biol.* **1171**, 27–37 (2014).

38. 38.

Chinchilla, D. et al. A flagellin-induced complex of the receptor FLS2 and BAK1 initiates plant defence. *Nature* **448**, 497–500 (2007).

39. 39.

El Kasmi, F. et al. Signaling from the plasma-membrane localized plant immune receptor RPM1 requires self-association of the full-length protein. *Proc. Natl Acad. Sci. USA* **114**, E7385–E7394 (2017).

40. 40.

Grefen, C. & Blatt, M. R. A 2in1 cloning system enables ratiometric bimolecular fluorescence complementation (rBiFC). *Biotechniques* **53**, 311–314 (2012).

41. 41.

Mehlhorn, D. G., Wallmeroth, N., Berendzen, K. W. & Grefen, C. 2in1 vectors improve in planta BiFC and FRET analyses. *Methods Mol. Biol.* **1691**, 139–158 (2018).

42. 42.

Chen, H. et al. Firefly luciferase complementation imaging assay for protein–protein interactions in plants. *Plant Physiol.* **146**, 323–324 (2008).

43. 43.

Liebrand, T. W. et al. Receptor-like kinase SOBIR1/EVR interacts with receptor-like proteins in plant immunity against fungal infection. *Proc. Natl Acad. Sci. USA* **110**, 10010–10015 (2013).

44. 44.

Nakagawa, T. et al. Development of series of gateway binary vectors, pGWBs, for realizing efficient construction of fusion genes for plant transformation. *J. Biosci. Bioeng.* **104**, 34–41 (2007).

45. 45.

Karimi, M., Inzé, D. & Depicker, A. GATEWAY vectors for *Agrobacterium*-mediated plant transformation. *Trends Plant Sci.* **7**, 193–195 (2002).

46. 46.

Glöckner, N. et al. Three-fluorophore FRET enables the analysis of ternary protein association in living plant cells. Preprint at <https://doi.org/10.1101/722124> (2020).

47. 47.

Rappaport, J., Ishihama, Y. & Mann, M. Stop and go extraction tips for matrix-assisted laser desorption/ionization, nanoelectrospray, and LC/MS sample pretreatment in proteomics. *Anal. Chem.* **75**, 663–670 (2003).

48. 48.

Cox, J. & Mann, M. MaxQuant enables high peptide identification rates, individualized p.p.b.-range mass accuracies and proteome-wide protein quantification. *Nat. Biotechnol.* **26**, 1367–1372 (2008).

49. 49.

Tyanova, S., Temu, T. & Cox, J. The MaxQuant computational platform for mass spectrometry-based shotgun proteomics. *Nat. Protoc.* **11**, 2301–2319 (2016).

50. 50.

Deutsch, E. W. et al. The ProteomeXchange consortium in 2020: enabling ‘big data’ approaches in proteomics. *Nucleic Acids Res.* **48**, D1145–D1152 (2020).

51. 51.

Perez-Riverol, Y. et al. The PRIDE database and related tools and resources in 2019: improving support for quantification data. *Nucleic Acids Res.* **47**, D442–D450 (2019).

52. 52.

Li, H. & Durbin, R. Fast and accurate short read alignment with Burrows–Wheeler transform. *Bioinformatics* **25**, 1754–1760 (2009).

53. 53.

Li, H. et al. The Sequence Alignment/Map format and SAMtools. *Bioinformatics* **25**, 2078–2079 (2009).

54. 54.

Wang, G. et al. A genome-wide functional investigation into the roles of receptor-like proteins in *Arabidopsis*. *Plant Physiol.* **147**, 503–517 (2008).

55. 55.

Shiu, S. H. et al. Comparative analysis of the receptor-like kinase family in *Arabidopsis* and rice. *Plant Cell* **16**, 1220–1234 (2004).

56. 56.

Kurup, S. et al. Marking cell lineages in living tissues. *Plant J.* **42**, 444–453 (2005).

Acknowledgements

This work was supported by Deutsche Forschungsgemeinschaft (DFG) grants Nu 70/15-1 and ERA-CAPS-Grant SICOPID Nu 70/16-1 to T.N.; grant CRC-1101 to K.H., C.O., D.W., F.E.K. and T.N., and grant CRC-1403-414786233 to J.E.P. S. C. Saile was supported by the Reinhard Frank Stiftung (Project ‘helperless plant’). F.L., J.E.P., H.N., D.K. and D.W. were supported by the Max Planck Society. We thank S. Harter, M. Fechter, B. Löffelhardt and V. Scholz for assistance with cloning and genotyping; B. Kemmerling for statistical data evaluation; E. Chae for annotation information of NLRs; and P. Schulze-Lefert for the *Lysobacter* strain Root690.

Author information

Author notes

1. Wei-Lin Wan

Present address: Department of Biological Sciences, National University of Singapore, Singapore, Singapore

2. Shaofei Rao

Present address: State Key Laboratory for Managing Biotic and Chemical Threats to the Quality and Safety of Agro-products, Institute of Plant Virology, Ningbo University, Ningbo, China

3. These authors contributed equally: Rory N. Pruitt, Federica Locci

Affiliations

1. Department of Plant Biochemistry, Centre of Plant Molecular Biology (ZMBP), University of Tübingen, Tübingen, Germany

Rory N. Pruitt, Lisha Zhang, Anna Joe, Chenlei Hua, Katja Fröhlich, Wei-Lin Wan, Andrea A. Gust & Thorsten Nürnberger

2. Department of Plant–Microbe Interactions, Max Planck Institute for Plant Breeding Research, Cologne, Germany

Federica Locci & Jane E. Parker

3. Department of Plant Physiology, Centre of Plant Molecular Biology (ZMBP), University of Tübingen, Tübingen, Germany

Friederike Wanke, Svenja C. Saile, Klaus Harter, Claudia Oecking & Farid El Kasmi

4. Department of Molecular Biology, Max Planck Institute for Developmental Biology, Tübingen, Germany

Darya Karelina & Detlef Weigel

5. State Key Laboratory of Plant Genomics, Institute of Genetics and Developmental Biology, Innovation Academy for Seed Design, Chinese Academy of Sciences, Beijing, China

Meijuan Hu, Shaofei Rao & Jian-Min Zhou

6. Proteomics Group, Max Planck Institute for Plant Breeding Research,
Cologne, Germany

Sara C. Stolze, Anne Harzen & Hirofumi Nakagami

7. Laboratory of Phytopathology, Wageningen University, Wageningen,
Netherlands

Matthieu H. A. J. Joosten & Bart P. H. J. Thomma

8. Cluster of Excellence on Plant Sciences (CEPLAS), Cologne
University, Cologne, Germany

Bart P. H. J. Thomma & Jane E. Parker

9. Department of Biology, Howard Hughes Medical Institute, University
of North Carolina at Chapel Hill, Chapel Hill, NC, USA

Jeffery L. Dangl

10. Department of Biochemistry, University of Johannesburg,
Johannesburg, South Africa

Thorsten Nürnbergger

Contributions

R.N.P., M.H.A.J.J., B.P.H.J.T., J.L.D., F.E.K., J.E.P. and T.N. conceived and conceptualized the study. R.N.P., W.-L.W., M.H., S.R. and A.A.G. generated materials used in this study. R.N.P., K.F. and W.-L.W. performed the ethylene assays. R.N.P. and W.-L.W. performed the ROS assays. R.N.P., F.L., L.Z. and S. C. Saile performed co-IPs and western blots. R.N.P. performed the pathoassays. R.N.P., F.L. and C.H. performed the MAPK assays. A.J. performed the callose assays. R.N.P. and F.L. performed the RT-qPCR assays. S. C. Saile and F.E.K. performed the split-YFP assays. M.H. and J.-M.Z. performed the split firefly luciferase assays and analysed

the data. F.W., C.O. and K.H. performed the FRET-FLIM assays and confocal microscopy and analysed the data. D.K. and D.W. performed the genetic analysis. Co-IP–MS experiments were designed by F.L., H.N. and J.E.P., executed by F.L. and A.H., and analysed by F.L., S. C. Stolze, H.N. and J.E.P. Statistical analysis was performed by R.N.P., F.L., S. C. Stolze and F.W. T.N. wrote the original draft of the paper. R.N.P., F.L., A.A.G., M.H.A.J.J., B.P.H.J.T., J.L.D., D.W., J.E.P. and T.N. reviewed and edited the paper.

Corresponding authors

Correspondence to Jane E. Parker or Thorsten Nürnberg.

Ethics declarations

Competing interests

The authors declare no competing interests.

Additional information

Peer review information *Nature* thanks Gitta Coaker and the other, anonymous, reviewer(s) for their contribution to the peer review of this work. Peer reviewer reports are available.

Publisher's note Springer Nature remains neutral with regard to jurisdictional claims in published maps and institutional affiliations.

Extended data figures and tables

[Extended Data Fig. 1 LRR-RP-mediated ethylene responses are dependent on RLCK-VII-7 kinases PBL30 and PBL31.](#)

a, RLCK-VII mutant screen for positive regulators of LRR-RP signalling. $n \geq 6$, each from 3 leaf pieces. Exact n values are shown in the graph. Data

are from 2 independent experiments. Two-sided Wilcoxon rank sum pairwise tests with continuity correction were used to analyse significant differences between elicitor-treated Col-0 and the indicated mutant ($*P \leq 0.05$, $**P \leq 0.01$). **b**, Elicitor-induced ethylene production in Col-0 and RLCK-VII-7 mutants. $n = 14$, each from 3 leaf pieces. Data are from 3 independent experiments. Statistical differences between Col-0 and the indicated mutants were analysed using a Kruskal–Wallis test with a post hoc two-sided Steel-Dwass test ($*P \leq 0.05$, $**P \leq 0.01$, $***P \leq 0.0001$). Centre line: median, bounds of box: 25th and 75th percentiles, whiskers: 1.5 * IQR (IQR: the interquartile range between the 25th and the 75th percentile). Exact P values for all experiments are provided in Supplementary Table 5.

[Source data](#)

[Extended Data Fig. 2 PBL31 activity in RLP23 signalling requires its kinase activity.](#)

a, Ethylene accumulation in *pbl30 pbl31 pbl32* complemented with wild-type PBL31-HA (PBL31) or the kinase-dead variant PBL31^{K201A}-HA (PBL31^{K201A}). Bars indicate mean ethylene response \pm s.e.m. For PBL31^{K201A}, $n = 6$; for all others, $n = 9$. A two-sided Welch's t -test was used to analyse significant differences between Col-0 and the indicated line for the given elicitor treatment ($**P \leq 0.01$, $***P \leq 0.0001$). Exact P values are provided in Supplementary Table 5. The experiment was repeated 3 times with similar results. **b**, PBL31 has autokinase activity that is abolished in the PBL31^{K201A} mutant. Recombinant PBL31 and PBL31^{K201A} were subjected to SDS–PAGE followed by anti-His protein blot. PBL31^{K201A} runs near the predicted position for the tagged protein (57.4 kDa). The wild-type version migrates more slowly, consistent with it being auto-phosphorylated. Phosphorylation of the wild-type PBL31 was confirmed by treatment with calf intestinal phosphatase, which increased the migration rate of PBL31 but not PBL31^{K201A}. The experiment was repeated 2 times with similar results. **c**, Anti-HA protein blot with material from plants used in **a**. For gel source data, see Supplementary Fig. 1.

Source data

Extended Data Fig. 3 Immune responses of RLCK-VII-7 mutants treated with LRR-RP-recognized and LRR-RK-recognized elicitors.

a, b, Elicitor-induced ROS production is impaired in *pbl30 pbl31 pbl32*. **a**, Total elicitor-induced ROS production over 30 min in Col-0, *pbl30 pbl31*, and *pbl30 pbl31 pbl32*. $n = 48$ leaf pieces from 3 independent experiments. For all panels *pbl30 pbl31* is in orange, *pbl30 pbl31 pbl32* is in pink. For **a, c, h**, statistical differences between Col-0 and the indicated mutants were analysed using a Kruskal–Wallis test with a post hoc two-sided Steel-Dwass test ($*P \leq 0.05$, $**P \leq 0.01$, $***P \leq 0.0001$). **b**, Mean ROS production over time. Solid line, mean; shaded band, s.e.m.; $n = 16$ leaf pieces. **c**, Nlp20-induced callose deposition in Col-0 is dependent on PBL30 and PBL31. $n \geq 12$ images from at least 3 leaves; exact n values are indicated on the graph. **d**, Nlp20-induced expression of *PAD3*, *CYP71A13*, and *FMO1* is impaired in *pbl30 pbl31 pbl32* plants. Bars indicate mean expression relative to *EF-1 α* 6 h after mock or elicitor treatment determined by qRT–PCR. $n = 8$ biological replicates from 3 independent experiments. A two-sided Wilcoxon rank sum test with continuity correction was used to analyse significant differences between Col-0 and *pbl30 pbl31 pbl32* for the given elicitor treatment ($*P \leq 0.05$, $**P \leq 0.01$). **e**, Relative fresh weight of 12 d-old Col-0 and *pbl30 pbl31 pbl32* seedlings grown in the presence of flg22 or elf18. No significant differences were observed between Col-0 and *pbl30 pbl31 pbl32* growth for any treatment ($P > 0.05$, two-sided Wilcoxon rank sum test with continuity correction). $n = 8$ biological replicates comprising 2 seedlings; for *pbl30 pbl31 pbl32* treated with elf18, $n = 7$. **f**, MAP kinase activation in Col-0 and *pbl30 pbl31 pbl32* treated with nlp20 or flg22 was analysed by immunoblot assay. Ponceau S-stained RUBISCO large subunit serves as a loading control. For gel source data, see Supplementary Fig. 1. **g**, Elicitor-induced defence against infection is impaired in *pbl30 pbl31* and *pbl30 pbl31 pbl32*. Leaves were infiltrated with the indicated elicitor and challenged with *Pst* DC3000 infection after 24 h. Bacterial colonization was assessed at Day 0 and Day 3. $n = 6$ (Day 0) or 12 (Day 3) biological replicates comprising 2 leaf discs. Bars with different letters indicate significant differences of $P \leq 0.05$ (Kruskal–Wallis

test with post hoc two-sided Steel-Dwass test). No statistical differences were observed for Day 0. CFU, colony forming units. **h**, RLCK-VII-7 kinases are not required for an ETI response to *Pst* DC3000 *AvrRps4* or *Pst* DC3000 *AvrRpt2*. $n = 8$ (Day 0) or 12 (Day 3) biological replicates comprising 2 discs; for *pbl30 pbl31 pbl32* infected with *Pst* DC3000 *AvrRpt2* (Day 3), $n = 10$. Growth on *eds1* plants served as control. For box plots in **a**, **c**, centre line: median, bounds of box: 25th and 75th percentiles, whiskers: 1.5 * IQR. For **d**, **e**, **g**, **h** bars indicate mean \pm s.e.m. Experiments in **b**, **c**, **e–h** were repeated at least three times with similar results. Exact *P* values for all quantitative experiments are provided in Supplementary Table 5.

Source data

Extended Data Fig. 4 PTI responses are partially dependent on PAD4 and EDS1.

a, Elicitor-induced ethylene production in *pad4*, *eds1*, *sag101*, EDS1 and EDS1^{LLIF} lines. $n = 14$, each from 3 leaf pieces. Data are from 3 independent experiments. Statistical differences between Col-0 and the indicated mutants were analysed using a Kruskal–Wallis test with a post hoc two-sided Steel-Dwass test (* $P \leq 0.05$, ** $P \leq 0.01$, *** $P \leq 0.0001$). Centre line: median, bounds of box: 25th and 75th percentiles, whiskers: 1.5 * IQR. **b**, Nlp20-induced ethylene production is not dependent on EDS1 and PAD4 putative lipase activity. The *eds1 pad4* is complemented with wild-type proteins (EDS1 PAD4) or variants harbouring mutations in their putative α/β-hydrolase catalytic residues (EDS1^{SDH} PAD4^S)¹⁹. $n = 4$, each from 3 leaf pieces. Statistical differences between Col-0 and the indicated mutants were analysed by two-sided Welch’s pairwise tests (** $P \leq 0.01$). For **b–e**, bars indicate mean \pm s.e.m. **c**, Thaxtomin A pretreatment enhances nlp20-induced ethylene responses in Col-0 but not in *pad4* or *pbl30 pbl31 pbl32* mutants. $n = 4$, each from 3 leaf pieces. Statistical differences between water- and thaxtomin A-treated samples were analysed using a Kruskal–Wallis test with a post hoc two-sided Steel-Dwass test (* $P \leq 0.05$). **d**, Expression of *PAD3*, *CYP71A13* and *FMO1* 6 h after elicitor or mock treatment, determined by qRT–PCR. $n = 8$ biological replicates from 3 independent experiments. A two-sided Wilcoxon rank sum test with

continuity correction was used to analyse significant differences between Col-0 and *pad4* for the given elicitor treatment ($*P \leq 0.05$, $**P \leq 0.01$). **e**, Relative fresh weight of 12 d-old Col-0 and *pad4* seedlings grown in the presence of flg22 or elf18. No significant differences were observed between Col-0 and *pad4* growth for any treatment (two-sided Wilcoxon rank sum test with continuity correction). $n = 8$ biological replicates comprising 2 seedlings; for Col-0 treated with elf18, $n = 7$. **f**, MAP kinase activation in Col-0 and *eds1 pad4 sag101* treated with nlp20 or flg22 was analysed by immunoblot assay. Ponceau S-stained RUBISCO large subunit serves as a loading control. For gel source data, see Supplementary Fig. 1. Experiments in **b–f** were performed at least three times with similar results. Exact P values for all quantitative experiments are provided in Supplementary Table 5.

[Source data](#)

[Extended Data Fig. 5 Transcript and protein levels of immune-related genes in Col-0 and *pad4*.](#)

a, Background levels of a set of immune-related genes in naive Col-0 and *pad4*. Relative expression was determined by qRT–PCR. Expression was normalized to *EF-1 α* transcript and set relative to Col-0. $n = 8$ biological replicates from 3 independent experiments. Centre line: median, bounds of box: 25th and 75th percentiles, whiskers: 1.5 * IQR. No significant differences were identified between Col-0 and *pad4* ($P > 0.05$, two-sided Wilcoxon rank sum test with continuity correction). Exact P values are provided in Supplementary Table 5. **b**, Protein levels of FLS2, BAK1, MPK3, MPK4, and MPK6 are similar in Col-0 and *pad4* plants. Leaves were taken from three 6-week-old plants (labelled 1-3) and endogenous protein levels were evaluated by protein blot. Ponceau S-stained RUBISCO large subunit serves as a loading control. For gel source data, see Supplementary Fig. 1. The experiment was repeated at least three times with similar results.

[Source data](#)

Extended Data Fig. 6 ADR1 helper NLRs are positive regulators of LRR-RP signalling.

a, Elicitor-induced ethylene production in helper NLR mutants. $n = 13$, each from 3 leaf pieces. Data are from 3 independent experiments. Col-0 is grey, *adr1 triple* is pink, *nrg1 double* is orange, and *helperless* is blue for all panels. For **a–c, f**, statistical differences between Col-0 and the indicated mutant for the given elicitor treatment were analysed using a Kruskal–Wallis test with post hoc two-sided Steel-Dwass test ($*P \leq 0.05$, $**P \leq 0.01$, $***P \leq 0.0001$). **b**, Total elicitor-induced ROS production over 30 min. $n = 48$ leaf discs from 3 independent experiments. **c**, Nlp20-induced callose deposition is reduced in *adr1 triple* and *helperless* mutants. $n \geq 12$ images from at least 3 leaves. For Col-0 nlp20, $n = 14$ images; for *adr1 triple* mock, $n = 15$; for all others $n = 16$. **d**, Representative immunoblot for MAP kinase activation in Col-0 and *helperless* treated with nlp20 or flg22. Ponceau S-stained RUBISCO large subunit serves as a loading control. For gel source data, see Supplementary Fig. 1. **e**, Relative fresh weight of 12 d-old Col-0 and *helperless* seedlings grown in the presence of flg22 or elf18 ($n = 8$ biological replicates comprising 2 seedlings). No statistical differences between Col-0 and *helperless* were identified for each elicitor treatment ($P > 0.05$, two-sided student's *t*-test). **f**, Elicitor-induced defence against infection is impaired in *adr1 triple* and *helperless* mutants. Leaves were infiltrated with the indicated elicitor and challenged with *Pst* DC3000 24 h after infiltration. Bacterial colonization was assessed at Day 0 and Day 3. $n = 6$ (Day 0) or $n = 12$ (Day 3) biological replicates comprising 2 leaf discs. Bars with different letters indicate significant differences of $P \leq 0.05$ (Kruskal–Wallis test with post hoc two-sided Steel-Dwass test). No statistical differences were observed for Day 0. CFU, colony forming units. For box plots in **a–c**, centre line: median, bounds of box: 25th and 75th percentiles, whiskers: 1.5 * IQR. For **e, f**, bars indicate mean \pm s.e.m. Experiments in **c–f** were performed at least three times with similar results. Exact *P* values for all quantitative experiments are provided in Supplementary Table 5.

[Source data](#)

Extended Data Fig. 7 Co-immunoprecipitation, split-YFP and split-luciferase complementation assays suggest that SOBIR1 is associated with multiple downstream signalling components.

a, PBL31, ADR1, EDS1, and PAD4 associate with SOBIR1 in a nlp20-independent manner. The indicated proteins were transiently expressed in *Nicotiana benthamiana*. Leaves treated with nlp20 or water (mock) for 10 min were subjected to co-immunoprecipitation with GFP-trap beads. The proteins were not co-immunoprecipitated with a GFP-fused membrane protein (LTI6b⁵⁶). The experiment was performed twice with similar results. **b**, Pull-down of GFP and SOBIR1-GFP transiently co-expressed with ADR1-HA, ADR1-L1-HA or ADR1-L2-HA. Plants transiently expressing the different proteins were subjected to co-immunoprecipitation using GFP-trap beads and subsequently analysed by protein blot using tag-specific antisera. ADR1-L1-HA and ADR1-L2-HA were co-immunoprecipitated at least three times with similar results; ADR1-HA was tested once. **c**, BiFC between SOBIR1 and the ADR1 isoforms confirms constitutive interaction of SOBIR1 with ADR1-L1 and ADR1-L2 at the plasma membrane. Scale bar indicates 20 μ m. The experiment was performed at least three times with similar results. **d**, Protein levels of the transiently expressed proteins in BiFC experiments shown in panel **c**. **e**, Split luciferase complementation assays confirm the interaction of SOBIR1 and ADR1-L1. Bars indicate mean relative luciferase activity \pm s.e.m.: $n = 8$ leaf discs from 4 leaves. The experiment was performed three times with similar results. **f**, Protein levels of the transiently expressed proteins in split luciferase experiments shown in panel **e**. Co-expression of the SOBIR1 and PBL31 constructs led to cell death and low protein abundance. The experiment was performed twice with similar results. For gel source data, see Supplementary Fig. 1.

[Source data](#)

Extended Data Fig. 8 FRET-FLIM analysis demonstrates association of PBL31-GFP with SOBIR1, ADR1-L1 and EDS1.

a, b, Representative confocal images show co-localization of **(a)** SOBIR1-GFP or **(b)** PBL31-GFP with RFP fusions of ADR1, ADR1-L1, ADR1-L2, EDS1, PAD4, SAG101, **(a)** PBL31, or **(b)** SOBIR1 at the PM in transiently transformed *N. benthamiana* leaf cells. Plots show the GFP and RFP fluorescence intensity distribution across the PM in the indicated regions (white bars). Scale bars indicate 10 μ m. This experiment was repeated three times with similar results. **c**, FRET-FLIM reveals spatial proximity of PBL31-GFP with ADR1-L1-RFP, EDS1-RFP, EDS1-RFP + PAD4-HA, PAD4-RFP + EDS1-HA and SOBIR1-RFP. Membrane-associated protein NPH3^{S744A} serves as control. $n \geq 11$ measurements from at least 3 biological replicates. Exact n values are shown below the boxes. Statistical differences in fluorescent lifetime from PBL31-GFP were analysed using a Kruskal–Wallis test with post hoc two-sided Steel–Dwass test ($*P \leq 0.05$, $**P \leq 0.01$, $***P \leq 0.0001$). Exact P values are provided in Supplementary Table 5. Centre line: median, bounds of box: 25th and 75th percentiles, whiskers: 1.5 * IQR.

[Source data](#)

[Extended Data Fig. 9 SOBIR1 specifically co-purifies with YFP-PAD4 in Arabidopsis leaves in mock and nlp20-triggered conditions.](#)

a, b, *Arabidopsis pad4-1/sag101-3* plants complemented with *pPAD4::YFP-gPAD4* (YFP-PAD4) or *pSAG101::gSAG101-YFP* (SAG101-YFP) or *35S::YFP* (YFP) in wild-type Col-0 background were used for immunoprecipitation (IP) assays. Volcano plots show normalized abundances (LFQ, log2 scale) of proteins detected in mass-spectrometry (MS) analyses after IP of total protein extracts from 4.5-week-old *Arabidopsis pad4-1/sag101-3* complementation lines or YFP control line infiltrated with **a**, nlp20 for 10 min, **(b, upper panels)** DMSO (Mock) for 3 h, and **(b, lower panels)** nlp20 for 3 h. Red dots indicate proteins enriched in YFP-PAD4 vs YFP samples ($\log_2(\text{YFP-PAD4 vs YFP}) \geq 1$, left) and YFP-PAD4 vs SAG101-YFP samples ($\log_2(\text{YFP-PAD4 vs SAG101-YFP}) \geq 1$, right), using permutation-based FDR = 0.05. Graphs represent significantly enriched peptides from four independent experiments ($n = 4$ per genotype per treatment). As shown for 10 min treatments (Fig. 3b),

specific enrichment of the two functional Col-0 EDS1 isoforms (EDS1a and EDS1b) was detected in both YFP-PAD4 and SAG101-YFP samples, with EDS1b preferentially enriched following YFP-PAD4 pull-down. **c**, Representative immunoblot analyses to check test protein quality for IP quality in lines used for MS/MS analyses. Total protein extracts (IP inputs) from YFP-PAD4, SAG101-YFP and YFP lines infiltrated with DMSO (mock) or nlp20 for 10 min. Inputs were subsequently immunoprecipitated using GFP-trap agarose beads and analysed by mass spectrometry. The analyses were repeated four times for both 10 min and 3 h treatments with similar results ($n = 8$ per genotype per treatment). **d, e**, Nlp20 treatment triggered immune responses at early (10 min) and late (3 h) time points in samples used for IP MS/MS analyses. **d**, Total protein extracts from Col-0, YFP-PAD4, SAG101-YFP and YFP lines infiltrated with DMSO (mock) and nlp20 for 10 min were analysed on immunoblots using an anti-p44/42-ERK antibody. The identity of individual phosphorylated (p)-MAPKs, as determined by their mobility, is indicated by arrows. The analysis was repeated four times with similar results ($n = 4$ samples per genotype per treatment). For gel source data, see Supplementary Fig. 1. **e**, *PAD3* transcript levels were determined by qRT–PCR at 3 h after mock (DMSO) or nlp20 treatment of the indicated genotypes. Relative expression was normalized to *UBQ5* and set to Col-0 mock samples. Bars indicate mean expression \pm s.e.m. ($n = 12$ biological replicates from 4 independent experiments). Statistical differences between Col-0 and the indicated genotypes were analysed using Kruskal–Wallis with post hoc two-sided pairwise comparisons using Wilcoxon rank sum test with a Benjamini–Hochberg correction (* $P \leq 0.05$, ** $P \leq 0.01$). Exact P values are provided in Supplementary Table 5.

Source data

Extended Data Fig. 10 Classification of LRR-RPs, LRR-RKs and NLRs according to genetic conservation in *Arabidopsis* accessions.

a, Reads from 80 *Arabidopsis* accessions were mapped to the reference genome of Col-0. Genes were categorised as being conserved, having complex patterns of variation or exhibiting presence/absence

polymorphisms according to the distribution of large-scale polymorphisms across all accessions as inferred from stringent read mappings. Criteria for categorization are detailed in the Methods. The numbers of genes falling into each category are provided in the corresponding bars. **b**, LRR-RP genes classified as in **a**. Genes encoding known immune receptors are indicated in bold.

[Source data](#)

Supplementary information

[Supplementary Figure 1](#)

This file contains all uncropped blots and gel images.

[Reporting Summary](#)

[Peer Review File](#)

[Supplementary Table 1](#)

MS/MS and statistical analysis for GFP, YFP-PAD4, and SAG101-YFP treated for 10 min.

[Supplementary Table 2](#)

MS/MS and statistical analysis for GFP, YFP-PAD4, and SAG101-YFP treated for 3 h.

[Supplementary Table 3](#)

Arabidopsis lines used in this study.

[Supplementary Table 4](#)

Quantitative reverse transcription-PCR (qRT-PCR) primers used in this study.

Supplementary Table 5

Statistical summary.

Source data

Source Data Fig. 1

Source Data Fig. 2

Source Data Fig. 3

Source Data Extended Data Fig. 1

Source Data Extended Data Fig. 2

Source Data Extended Data Fig. 3

Source Data Extended Data Fig. 4

Source Data Extended Data Fig. 5

Source Data Extended Data Fig. 6

Source Data Extended Data Fig. 7

Source Data Extended Data Fig. 8

Source Data Extended Data Fig. 9

Source Data Extended Data Fig. 10

Rights and permissions

[Reprints and Permissions](#)

About this article

Cite this article

Pruitt, R.N., Locci, F., Wanke, F. *et al.* The EDS1–PAD4–ADR1 node mediates *Arabidopsis* pattern-triggered immunity. *Nature* **598**, 495–499 (2021). <https://doi.org/10.1038/s41586-021-03829-0>

- Received: 11 December 2020
- Accepted: 16 July 2021
- Published: 08 September 2021
- Issue Date: 21 October 2021
- DOI: <https://doi.org/10.1038/s41586-021-03829-0>

Share this article

Anyone you share the following link with will be able to read this content:

[Get shareable link](#)

Sorry, a shareable link is not currently available for this article.

[Copy to clipboard](#)

Provided by the Springer Nature SharedIt content-sharing initiative

| [Section menu](#) | [Main menu](#) |

- Article
- [Published: 20 September 2021](#)

Activation of TIR signalling boosts pattern-triggered immunity

- [Hainan Tian¹ na1](#),
- [Zhongshou Wu](#) [ORCID: orcid.org/0000-0001-6687-1675^{1,2} na1](#),
- [Siyu Chen^{1,3,4} na1](#),
- [Kevin Ao^{1,2}](#),
- [Weijie Huang¹](#),
- [Hoda Yaghmaiean¹](#),
- [Tongjun Sun](#) [ORCID: orcid.org/0000-0002-0263-3448¹](#),
- [Fang Xu^{1,2,5}](#),
- [Yanjun Zhang](#) [ORCID: orcid.org/0000-0002-7475-103X^{2,6}](#),
- [Shucui Wang](#) [ORCID: orcid.org/0000-0001-7619-2385⁴](#),
- [Xin Li](#) [ORCID: orcid.org/0000-0002-6354-2021^{1,2}](#) &
- [Yuelin Zhang](#) [ORCID: orcid.org/0000-0002-3480-5478¹](#)

[Nature](#) volume **598**, pages 500–503 (2021)

- 7331 Accesses
- 26 Altmetric
- [Metrics details](#)

Subjects

- [Pattern recognition receptors in plants](#)
- [Plant immunology](#)
- [Plant signalling](#)

Abstract

Plant immune responses are mainly activated by two types of receptor. Pattern recognition receptors localized on the plasma membrane perceive extracellular microbial features, and nucleotide-binding leucine-rich repeat receptors (NLRs) recognize intracellular effector proteins from pathogens¹. NLRs possessing amino-terminal Toll/interleukin-1 receptor (TIR) domains activate defence responses via the NADase activity of the TIR domain^{2,3}. Here we report that activation of TIR signalling has a key role in pattern-triggered immunity (PTI) mediated by pattern recognition receptors. TIR signalling mutants exhibit attenuated PTI responses and decreased resistance against pathogens. Consistently, PTI is compromised in plants with reduced NLR levels. Treatment with the PTI elicitor flg22 or nlp20 rapidly induces many genes encoding TIR-domain-containing proteins, which is likely to be responsible for activating TIR signalling during PTI. Overall, our study reveals that activation of TIR signalling is an important mechanism for boosting plant defence during PTI.

Access options

Subscribe to Journal

Get full journal access for 1 year

\$199.00

only \$3.90 per issue

[Subscribe](#)

All prices are NET prices.

VAT will be added later in the checkout.

Tax calculation will be finalised during checkout.

Rent or Buy article

Get time limited or full article access on ReadCube.

from \$8.99

[Rent or Buy](#)

All prices are NET prices.

Additional access options:

- [Log in](#)
- [Access through your institution](#)
- [Learn about institutional subscriptions](#)

Fig. 1: Overexpression of *SNIPER1* leads to attenuated flg22- and nlp20-induced immunity.

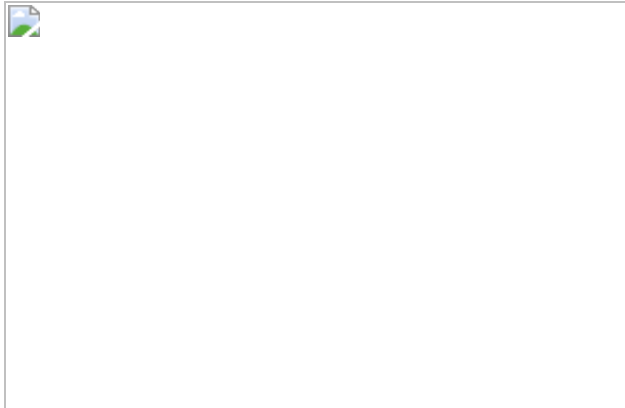
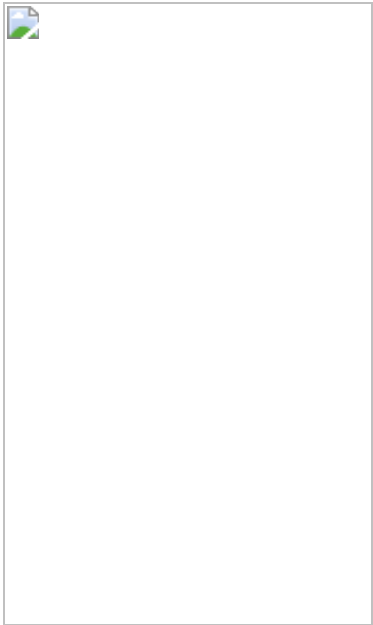


Fig. 2: Contributions of TIR signalling components to flg22- and nlp20-induced immunity.



Fig. 3: PCRK1/2 and PBL19/20 are required for nlp20-induced immunity.



Data availability

All data are included within the article or the Supplementary Information. Statistical analyses are provided in Supplementary Table 5. The RNA-seq data used for analysing nlp20-induced gene expression were from the National Center for Biotechnology Information ([GSE133053](#)). Full versions of all gels and blots are provided in Supplementary Fig. 1. [Source data](#) are provided with this paper.

References

1. 1.

Zhou, J. M. & Zhang, Y. Plant immunity: danger perception and signaling. *Cell* **181**, 978–989 (2020).

2. 2.

Wan, L. et al. TIR domains of plant immune receptors are NAD⁺-cleaving enzymes that promote cell death. *Science* **365**, 799–803 (2019).

3. 3.

Horsefield, S. et al. NAD⁺ cleavage activity by animal and plant TIR domains in cell death pathways. *Science* **365**, 793–799 (2019).

4. 4.

Monaghan, J. & Zipfel, C. Plant pattern recognition receptor complexes at the plasma membrane. *Curr. Opin. Plant Biol.* **15**, 349–357 (2012).

5. 5.

Liebrand, T. W., van den Burg, H. A. & Joosten, M. H. Two for all: receptor-associated kinases SOBIR1 and BAK1. *Trends Plant Sci.* **19**, 123–132 (2014).

6. 6.

Gomez-Gomez, L. & Boller, T. FLS2: an LRR receptor-like kinase involved in the perception of the bacterial elicitor flagellin in *Arabidopsis*. *Mol. Cell* **5**, 1003–1011 (2000).

7. 7.

Felix, G., Duran, J. D., Volko, S. & Boller, T. Plants have a sensitive perception system for the most conserved domain of bacterial flagellin. *Plant J.* **18**, 265–276 (1999).

8. 8.

Böhm, H. et al. A conserved peptide pattern from a widespread microbial virulence factor triggers pattern-induced immunity in *Arabidopsis*. *PLoS Pathog.* **10**, e1004491 (2014).

9. 9.

Albert, I. et al. An RLP23–SOBIR1–BAK1 complex mediates NLP-triggered immunity. *Nat. Plants* **1**, (2015).

10. 10.

Liang, X. & Zhou, J.-M. Receptor-like cytoplasmic kinases: central players in plant receptor kinase-mediated signaling. *Annu. Rev. Plant Biol.* **69**, 267–299 (2018).

11. 11.

Wu, Z. et al. Plant E3 ligases SNIPER 1 and SNIPER 2 broadly regulate the homeostasis of sensor NLR immune receptors. *EMBO J.* **39**, e104915 (2020).

12. 12.

Ngou, B. P. M., Ahn, H.-K., Ding, P. & Jones, J. D. Mutual potentiation of plant immunity by cell-surface and intracellular receptors. *Nature* **592**, 110–115 (2021).

13. 13.

Yuan, M. et al. Pattern-recognition receptors are required for NLR-mediated plant immunity. *Nature* **592**, 105–109 (2021).

14. 14.

Zhang, Y. et al. Control of salicylic acid synthesis and systemic acquired resistance by two members of a plant-specific family of transcription factors. *Proc. Natl Acad. Sci. USA* **107**, 18220–18225 (2010).

15. 15.

Hartmann, M. et al. Flavin monooxygenase-generated *N*-hydroxypipelicolic acid is a critical element of plant systemic immunity. *Cell* **173**, 456–469 (2018).

16. 16.

Sun, T. et al. ChIP-seq reveals broad roles of SARD1 and CBP60g in regulating plant immunity. *Nat. Commun.* **6**, 10159 (2015).

17. 17.

Bonardi, V. et al. Expanded functions for a family of plant intracellular immune receptors beyond specific recognition of pathogen effectors. *Proc. Natl Acad. Sci. USA* **108**, 16463–16468 (2011).

18. 18.

Palma, K. et al. Autoimmunity in *Arabidopsis* acd11 is mediated by epigenetic regulation of an immune receptor. *PLoS Pathog.* **6**, e1001137 (2010).

19. 19.

Yi, H. & Richards, E. J. Phenotypic instability of *Arabidopsis* alleles affecting a disease *Resistance* gene cluster. *BMC Plant Biol.* **8**, 36 (2008).

20. 20.

Wan, W. L. et al. Comparing *Arabidopsis* receptor kinase and receptor protein-mediated immune signaling reveals BIK1-dependent differences. *New Phytol.* **221**, 2080–2095 (2019).

21. 21.

Li, F. et al. Modulation of RNA polymerase II phosphorylation downstream of pathogen perception orchestrates plant immunity. *Cell Host Microbe* **16**, 748–758 (2014).

22. 22.

Aarts, N. et al. Different requirements for EDS1 and NDR1 by disease resistance genes define at least two R gene-mediated signaling pathways in *Arabidopsis*. *Proc. Natl Acad. Sci. USA* **95**, 10306–10311 (1998).

23. 23.

Tian, W. et al. A calmodulin-gated calcium channel links pathogen patterns to plant immunity. *Nature* **572**, 131–135 (2019).

24. 24.

Yu, X. et al. The receptor kinases BAK1/SERK4 regulate Ca^{2+} channel-mediated cellular homeostasis for cell death containment. *Curr. Biol.* **29**, 3778–3790 (2019).

25. 25.

Yoshioka, K. et al. The chimeric *Arabidopsis* CYCLIC NUCLEOTIDE-GATED ION CHANNEL11/12 activates multiple pathogen resistance responses. *Plant Cell* **18**, 747–763 (2006).

26. 26.

Zhao, C. et al. A mis-regulated cyclic nucleotide-gated channel mediates cytosolic calcium elevation and activates immunity in *Arabidopsis*. *New Phytol.* **230**, 1078–1094 (2021).

27. 27.

Kong, Q. et al. Two redundant receptor-like cytoplasmic kinases function downstream of pattern recognition receptors to regulate activation of SA biosynthesis. *Plant Physiol.* **171**, 1344–1354 (2016).

28. 28.

Rao, S. et al. Roles of receptor-like cytoplasmic kinase VII members in pattern-triggered immune signaling. *Plant Physiol.* **177**, 1679–1690 (2018).

29. 29.

Sreekanta, S. et al. The receptor-like cytoplasmic kinase PCRK1 contributes to pattern-triggered immunity against *Pseudomonas*

syringae in *Arabidopsis thaliana*. *New Phytol.* **207**, 78–90 (2015).

30. 30.

Pruitt, R. N. et al. *Arabidopsis* cell surface LRR immune receptor signaling through the EDS1-PAD4-ADR1 node. Preprint at <https://doi.org/10.1101/2020.11.23.391516> (2020).

31. 31.

Wang, Z.-P. et al. Egg cell-specific promoter-controlled CRISPR/Cas9 efficiently generates homozygous mutants for multiple target genes in *Arabidopsis* in a single generation. *Genome Biol.* **16**, 144 (2015).

32. 32.

Liu, Y., Huang, X., Li, M., He, P. & Zhang, Y. Loss-of-function of *Arabidopsis* receptor-like kinase BIR1 activates cell death and defense responses mediated by BAK1 and SOBIR1. *New Phytol.* **212**, 637–645 (2016).

33. 33.

Xu, F. et al. Two N-terminal acetyltransferases antagonistically regulate the stability of a nod-like receptor in *Arabidopsis*. *Plant Cell* **27**, 1547–1562 (2015).

34. 34.

Glazebrook, J., Rogers, E. E. & Ausubel, F. M. Isolation of *Arabidopsis* mutants with enhanced disease susceptibility by direct screening. *Genetics* **143**, 973–982 (1996).

35. 35.

Feys, B. J. et al. *Arabidopsis* SENESCENCE-ASSOCIATED GENE101 stabilizes and signals within an ENHANCED DISEASE SUSCEPTIBILITY1 complex in plant innate immunity. *Plant Cell* **17**, 2601–2613 (2005).

36. 36.

Wu, Z. et al. Differential regulation of TNL-mediated immune signaling by redundant helper CNLs. *New Phytol.* **222**, 938–953 (2019).

37. 37.

Century, K. S., Holub, E. B. & Staskawicz, B. J. NDR1, a locus of *Arabidopsis thaliana* that is required for disease resistance to both a bacterial and a fungal pathogen. *Proc. Natl Acad. Sci. USA* **92**, 6597–6601 (1995).

38. 38.

Torres, M. A., Jones, J. D. & Dangl, J. L. Pathogen-induced, NADPH oxidase-derived reactive oxygen intermediates suppress spread of cell death in *Arabidopsis thaliana*. *Nat. Genet.* **37**, 1130–1134 (2005).

39. 39.

Li, X., Zhang, Y., Clarke, J. D., Li, Y. & Dong, X. Identification and cloning of a negative regulator of systemic acquired resistance, SNI1, through a screen for suppressors of *npr1-1*. *Cell* **98**, 329–339 (1999).

40. 40.

Wu, F.-H. et al. Tape-*Arabidopsis* Sandwich - a simpler *Arabidopsis* protoplast isolation method. *Plant Methods* **5**, 16 (2009).

41. 41.

Zhang, Y. et al. TurboID-based proximity labeling reveals that UBR7 is a regulator of N NLR immune receptor-mediated immunity. *Nat. Commun.* **10**, (2019).

42. 42.

Zhang, J. et al. Receptor-like cytoplasmic kinases integrate signaling from multiple plant immune receptors and are targeted by a *Pseudomonas syringae* effector. *Cell Host Microbe* **7**, 290–301 (2010).

43. 43.

Xiang, T. et al. BAK1 is not a target of the *Pseudomonas syringae* effector AvrPto. *Mol. Plant Microbe Interact.* **24**, 100–107 (2011).

44. 44.

Zhang, R. et al. A high quality *Arabidopsis* transcriptome for accurate transcript-level analysis of alternative splicing. *Nucleic Acids Res.* **45**, 5061–5073 (2017).

45. 45.

Patro, R., Duggal, G., Love, M. I., Irizarry, R. A. & Kingsford, C. Salmon provides fast and bias-aware quantification of transcript expression. *Nat. Methods* **14**, 417–419 (2017).

46. 46.

Soneson, C., Love, M. I. & Robinson, M. D. Differential analyses for RNA-seq: transcript-level estimates improve gene-level inferences. *F1000Research* **4** (2015).

47. 47.

Love, M. I., Huber, W. & Anders, S. Moderated estimation of fold change and dispersion for RNA-seq data with DESeq2. *Genome Biol.* **15**, 550 (2014).

48. 48.

Durinck, S., Spellman, P. T., Birney, E. & Huber, W. Mapping identifiers for the integration of genomic datasets with the R/Bioconductor package biomaRt. *Nat. Protoc.* **4**, 1184 (2009).

Acknowledgements

We thank J. Parker, J. Dangl, J.-M. Zhou, K. Yoshioka and H. Cui for sharing mutant seeds and pathogen strains; L. Tian for help with the high-performance liquid chromatography analysis and biochemical assays; and T. Nuernberger and J. Parker for insightful discussions. This study was financially supported by grants to X.L. and Yuelin Zhang from the Natural Sciences and Engineering Research Council (NSERC) Discovery programme of Canada, NSERC-CREATE-PROTECT, and the Canadian Foundation for Innovation, a grant to Yanjun Zhang from the National Natural Science Foundation of China (31828008), scholarships to H.T., S.C., W.H. and Z.W. from the Chinese Scholarship Council, and scholarships to K.A. from the Alexander Graham Bell Canada Graduate Scholarship Doctoral Program, and the University of British Columbia Four-Year Fellowship programme.

Author information

Author notes

1. These authors contributed equally: Hainan Tian, Zhongshou Wu, Siyu Chen

Affiliations

1. Department of Botany, University of British Columbia, Vancouver, British Columbia, Canada

Hainan Tian, Zhongshou Wu, Siyu Chen, Kevin Ao, Weijie Huang, Hoda Yaghmaiean, Tongjun Sun, Fang Xu, Xin Li & Yuelin Zhang

2. Michael Smith Laboratories, University of British Columbia, Vancouver, British Columbia, Canada

Zhongshou Wu, Kevin Ao, Fang Xu, Yanjun Zhang & Xin Li

3. Key Laboratory of Molecular Epigenetics of MOE & Institute of Genetics and Cytology, Northeast Normal University, Changchun, China

Siyu Chen

4. Laboratory of Plant Molecular Genetics & Crop Gene Editing, School of Life Sciences, Linyi University, Linyi, China

Siyu Chen & Shucai Wang

5. The Key Laboratory of Plant Development and Environmental Adaptation Biology, Ministry of Education, School of Life Sciences, Shandong University, Qingdao, China

Fang Xu

6. Institute of Plant Genetics and Developmental Biology, College of Chemistry and Life Sciences, Zhejiang Normal University, Jinhua, China

Yanjun Zhang

Contributions

H.T. and S.C. together carried out the genetic analysis of the *SNIPER1*-overexpression lines, the TIR signalling mutants and the RLCK mutants. H.T. carried out the overexpression analysis of the TIR genes. Z.W. carried out the analyses on protein–protein interactions, quantification of expression levels of the three TIR genes, and test of the effect of *SNIPER1* overexpression on the accumulation of PTI signalling components. K.A. generated *eds1-24* and performed bioinformatic analyses. W.H. and Yanjun Zhang assisted with SA analysis. F.X. made the ZZ–TEV–FLAG-tagged EDS1 and PAD4 constructs. H.Y. and T.S. generated the combined RLCK mutants. Yuelin Zhang, H.T., Z.W., S.W. and X.L. wrote the manuscript with contributions from all authors.

Corresponding authors

Correspondence to Xin Li or Yuelin Zhang.

Ethics declarations

Competing interests

The authors declare no competing interests.

Additional information

Peer review information *Nature* thanks Gitta Coaker and the other, anonymous, reviewer(s) for their contribution to the peer review of this work. Peer reviewer reports are available.

Publisher's note Springer Nature remains neutral with regard to jurisdictional claims in published maps and institutional affiliations.

Extended data figures and tables

Extended Data Fig. 1 Overexpression of *SNIPER1* leads to reduced expression of *SARD1* and *FMO1*, lower SA accumulation, increased *Pto DC3000 hrcC* growth, but has no effect on MAPK activation and ROS production during PTI.

(a, b) Relative expression levels of *SARD1* (a) and *FMO1* (b) in WT and *OX-SNIPER1* lines (L4 and L5) treated with 10 mM MgCl₂ (mock) or *Pto DC3000 hrcC* for 12 h. Bars represent mean ± s.d. (n = 3 biologically independent samples). **(c, d)** Free SA (c) and SAG (d) levels in the indicated genotypes treated with 10 mM MgCl₂ (mock) or *Pto DC3000 hrcC* (OD₆₀₀ = 0.05) for 12 h. Bars represent mean ± s.d. (n = 3 biologically independent samples). **(e)** Growth of *Pto DC3000 hrcC* in the indicated genotypes. Bars represent mean ± s.d. (n = 4 plants). **(f, g, i, j)** flg22 and nlp20-induced MAPK activation in the indicated genotypes. Seedlings were treated with 0.1 µM flg22 (f, g) or 0.1 µM nlp20 (i, j). MAPK activation

was analyzed by immunoblotting with the anti-pERK antibody. Equal loading is confirmed by Ponceau staining of Rubisco. The signals of phosphorylated MPK6 and MPK3 in samples treated with flg22 (**g**) or nlp20 (**j**) detected by western blots were normalized to the loading control. The intensity of MPK6 or MPK3 bands after elicitors treatment in WT plants was set as 1. Bars represent mean ± s.d. (n = 4 different experiments for (**g**), n = 3 different experiments for (**j**)). (**h, k**) ROS production in the indicated genotypes after treatment with 0.1 µM flg22 (**h**) or 1 µM nlp20 (**k**) measured as luminescence. The values show the peak of luminescence units through all the time points. Bars represent mean ± s.d. (n = 8 leaf disks from different plants). (**l, m**) SAG levels in the indicated genotypes treated with H₂O, 1 µM nlp20 (**l**) or 1 µM flg22 (**m**). Samples were collected for SAG measurement 24 h after 1 µM nlp20, or 9 h after 1 µM flg22 treatment. Bars represent mean ± s.d. (n = 3 biologically independent samples). All data were analyzed by one-way ANOVA with Tukey's test. Exact P values are provided in Supplementary Table 5. The experiments were repeated at least three times with similar results.

Source data

Extended Data Fig. 2 Overexpression of *SNIPER1* does not affect the accumulation of FLS2, BAK1, SOBIR1, RLP23, BIK1, PBL19 or PCRK2, as opposed to SNC1.

(**a, b**) FLS2 and BAK1 protein levels in WT and OX-SNIPER1 lines #4 and #5. Total proteins were extracted from four-week-old soil-grown *Arabidopsis* plants and analyzed by western blot using anti-FLS2 (**a**) or anti-BAK1 (**b**) antibodies. Equal loadings are shown by Ponceau S staining of a non-specific band. The relative bands intensity (n = 3 biologically independent samples) are shown below (normalized to loading control, the protein levels in Col-0 was arbitrarily set at 1). (**c-h**) Immunoblot analysis of protein levels of SOBIR1-3FLAG, RLP23-ZZ-TEV-FLAG, BIK1-3FLAG, PBL19-3FLAG, PCRK2-3FLAG and SNC1-3FLAG in *N. benthamiana* leaves co-expressed with HA-SNIPER1. GFP-HATurboID was used as a negative control. Equal loading is shown by Ponceau S staining of a non-specific band. Numbers underneath (n = 3 biologically independent samples) indicate the relative intensity of bands of SOBIR1-

3FLAG (**c**), RLP23-ZZ-TEV-FLAG (**d**), BIK1-3FLAG (**e**), PBL19-3FLAG (**f**), PCRK2-3FLAG (**g**) and SNC1-3FLAG (**h**).

Extended Data Fig. 3 Analysis of interactions between RPP4NB/SOBIR1/RLP23/BIK1/PCRK2/PBL19 and SNIPER1^{H129Y} by TurboID-based proximity labeling method.

3 × FLAG-tagged NB domain of RPP4 (RECOGNITION OF PERONOSPORA PARASITICA 4) (RPP4NB) or SOBIR1 (**a**), BIK1/RLP23 (**b**), and PCRK2/PBL19 (**c**) were transiently expressed in *N. benthamiana* together with SNIPER1^{H129Y}-HATurboID or GFP-HATurboID. SNIPER1^{H129Y} is a dominant-negative mutant of SNIPER1 that does not affect binding to its substrate but lost its E3 ligase activity, which is used to stabilize the protein interactions with the substrates. The 3 × FLAG-tagged RPP4NB was used as a positive control in the experiment. The 3 × FLAG-tagged proteins were immunoprecipitated with anti-FLAG beads and detected using an anti-FLAG antibody. The biotinylated proteins were detected using HRP-Streptavidin. The experiment was repeated twice with similar results.

Extended Data Fig. 4 Expression of *SARD1/FMO1*, SA accumulation, expression of *FLS2/BAK1/BIK1/RLP23/SOBIR1* and growth of *Pto DC3000 hrcC* in TIR signaling mutants.

(**a, b**) Relative expression levels of *SARD1* (**a**) and *FMO1* (**b**) in WT, *eds1-24*, *pad4-1*, *adr1 triple*, *sag101-1* and *nrg1 triple* mutant plants after treatment with 10 mM MgCl₂ (mock) or *Pto DC3000 hrcC* (OD₆₀₀ = 0.05) for 12 h. Bars represent mean ± s.d. (n = 3 biologically independent samples). (**c, d**) SA (**c**) and SAG (**d**) induction in TIR signaling mutants. Plants of the indicated genotypes were treated with *Pto DC3000 hrcC* (OD₆₀₀ = 0.05). Samples were collected for SA and SAG measurements 12 h after inoculation of *Pto DC3000 hrcC*. Bars represent mean ± s.d. (n = 3 biologically independent samples). (**e**) Growth of *Pto DC3000 hrcC* in plants of the indicated genotypes. Bars represent mean ± s.d. (n = 4 plants). (**f, g**) Relative expression levels of *SARD1* (**f**) and *FMO1* (**g**) in the

indicated genotypes upon flg22 treatment. Bars represent mean ± s.d. (n = 3 biologically independent samples). (h, i) Relative expression levels of *SARD1* (h) and *FMO1* (i) in the indicated genotypes upon nlp20 treatment. Bars represent mean ± s.d. (n = 3 biologically independent samples). (j) Expression levels of *FLS2*, *BAK1* and *BIK1* in WT and *eds1-24* treated with H₂O or flg22. Bars represent mean ± s.d. (n = 3 biologically independent samples). (k) Expression levels of *RLP23*, *SOBIR1*, *BAK1* and *BIK1* in WT and *eds1-24* treated with H₂O or nlp20. Bars represent mean ± s.d. (n = 3 biologically independent samples). (l, m) SAG induction in TIR signaling mutants. Plants of the indicated genotypes were treated with 1 μM flg22 (l) or 1 μM nlp20 (m). Samples were collected for SAG measurements 24 h after treatment with 1 μM nlp20, or 9 h after treatment with 1 μM flg22. Bars represent mean ± s.d. (n = 3 biologically independent samples). For gene expression analysis in (f-k), total RNA was isolated from *Arabidopsis* seedlings 4 h after spraying with 1 μM elicitor (flg22 or nlp20) or H₂O. The expression of each gene in the mock or H₂O-treated WT plants was set as 1. Data in (a-i and l-m) were analyzed by one-way ANOVA with Tukey's test. Exact P values are provided in Supplementary Table 5. Data in (j, k) were analyzed using two-tailed Student's t-test. Exact P values are provided in Supplementary Table 5. All experiments were repeated three times with similar results.

[Source data](#)

[Extended Data Fig. 5 flg22 and nlp20-induced MAPK activation and ROS production in WT and TIR signaling mutants.](#)

(a) flg22-induced MAPK activation in WT, *eds1-24* and *adr1 triple* mutants. 12-day-old seedlings were treated with 0.1 μM flg22. MAPK activation was analyzed by immunoblotting with the anti-pERK antibody. Equal loading was confirmed by Ponceau staining of Rubisco. The experiment was repeated twice with similar results. (b) ROS production in the indicated genotypes after treatment with 0.1 μM flg22 measured as luminescence. The values show the peak of luminescence units through all the time points. Bars represent mean ± s.d. (n = 7 leaf disks from different

plants). Data were analyzed by one-way ANOVA with Tukey's test. Exact *P* values are provided in Supplementary Table 5. The experiment was repeated twice with similar results. (c, d) nlp20-induced MAPK activation in the indicated genotypes treated with 0.1 μM nlp20. MAPK activation was analyzed by immunoblotting with the anti-pERK antibody. Equal loading was confirmed by Ponceau staining of Rubisco. The phosphorylated MPK6 and MPK3 10 min after treatment with nlp20 were quantified in (d). Bars represent mean ± s.d. (*n* = 4 different experiments). The band intensity of MPK6 or MPK3 after elicitors treatment in WT plants was set as 1. Data were analyzed by one-way ANOVA with Tukey's test. Exact *P* values are provided in Supplementary Table 5. (e) ROS production in the indicated genotypes after treatment with 1 μM nlp20 measured as luminescence. The values show the peak of luminescence units through all the time points. Bars represent mean ± s.d. (*n* = 9 leaf disks from different plants). Data were analyzed by one-way ANOVA with Tukey's test. Exact *P* values are provided in Supplementary Table 5. The experiment was repeated three times with similar results.

[Source data](#)

Extended Data Fig. 6 Growth of *Hpa* Noco2 on the distal leaves of TIR signaling mutants.

Three-week-old soil-grown plants of the indicated genotypes were pretreated with H₂O or 1 μM nlp20 and sprayed with *Hpa* Noco2 spores (50,000 spores/ml) 24 h later. Disease ratings showing the relative growth of *Hpa* Noco2 are as described in the Methods. The experiment was repeated three times with similar results.

[Source data](#)

Extended Data Fig. 7 nlp20-induced defense responses in wild-type and *ndr1-1* mutant plants.

(a) MAPK activation in WT and *ndr1-1* plants treated with 0.1 μM nlp20. MAPK activation was analyzed by immunoblotting using the anti-pERK antibody. Equal loading was confirmed by Ponceau staining of Rubisco.

Quantification of the phosphorylated MPK6 and MPK3 was shown on the right. Bars represent mean ± s.d. (n = 4 different experiments). The band intensity of MPK6 or MPK3 after nlp20 treatment in WT plants was set as 1. Data were analyzed by two-tailed student's t-test. Exact P values are provided in Supplementary Table 5. (b) ROS production in WT and *ndrl-1* treated with 1µM nlp20 measured as luminescence. The values show the peak of luminescence units through all the time points. Bars represent mean ± s.d. (n = 9 leaf disks from different plants). Data were analyzed by two-tailed student's t-test. Exact P values are provided in Supplementary Table 5. The experiment was repeated three times with similar results. (c) Levels of free SA in WT and *ndrl-1* treated with H₂O or 1 µM nlp20 for 24 h. Bars represent mean ± s.d. (n = 3 biologically independent samples). Data were analyzed by one-way ANOVA with Tukey's test. Exact P values are provided in Supplementary Table 5. The experiment was repeated three times with similar results. (d) Growth of *Hpa* Noco2 on the local leaves of the indicated plants. Three-week-old soil-grown plants were pretreated with H₂O or 1 µM nlp20 and sprayed with *Hpa* Noco2 spores (50,000 spores/ml) 24 h later. Disease ratings showing the relative growth of *Hpa* Noco2 are as described in the Methods. The experiment was repeated twice with similar results.

Source data

Extended Data Fig. 8 Induction of SA accumulation and the pSARD1::Luc reporter gene expression by overexpression of three TIR genes and up-regulation of the TIR genes by nlp20 and flg22 or in cngc20-4 and cpr22 mutants.

(a, b) Levels of free SA (a) and SAG (b) in *N. benthamiana* leaves after infiltration of *Agrobacterium* (OD₆₀₀ = 0.4) carrying EV (empty vector), the TIR genes *At4g11170*, *At3g04220* or *At2g32140*. Samples were collected 24h and 36 h post infiltration, before cell death was visible. Bars represent mean ± s.d. (n = 3 biologically independent samples). (c) Induction of the *pSARD1::Luc* reporter gene by overexpression of *At4g11170*, *At3g04220* or *At2g32140* in *Arabidopsis* protoplasts. Bars represent mean ± s.d. (n = 3 biologically independent samples) of the firefly luciferase activities in

Arabidopsis protoplasts co-transformed with the indicated constructs. Empty vector (EV) control was set to 1. (d, e) Induction of the indicated TIR genes by nlp20 (d) or flg22 (e). 10-day-old plate-grown WT plants were transplanted to H₂O 1 day before for recovery and then pretreated with H₂O or 100 μM GdCl₃ for 1 h. Samples were collected 1 h after treatment with 1 μM nlp20 or flg22. Bars represent mean ± s.d. (n = 3 biologically independent samples). (f, g) Induction of the indicated TIR genes by nlp20 (f) or flg22 (g) in WT and the *rbohd* mutant. Samples were collected 1 h after treatment with 0.1 μM nlp20 or flg22. Bars represent mean ± s.d. (n = 3 biologically independent samples). (h, i) Induction of the indicated TIR genes by nlp20 (h) or flg22 (i) in WT and *eds1-24*. 10-day-old WT and *eds1-24* seedlings were transplanted to H₂O 1 day before for recovery and then supplied with 1 μM nlp20 or flg22. Samples were collected 1 h after supplying with nlp20 or flg22. Bars represent mean ± s.d. (n = 3 biologically independent samples). (j, k) Expression levels of the indicated TIR genes in *cngc20-4* (j) and *cpr22* (k) mutant plants. Total RNA was isolated from 12-d-old plate-grown seedlings. Bars represent mean ± s.d. (n = 3 biologically independent samples). For (d–i), the expression of each gene in the H₂O-treated WT plants was set as 1. Data in (c) were analyzed by one-way ANOVA with Tukey's test. Exact P values are provided in Supplementary Table 5. Data in (a, b, d–k) were analyzed using two-tailed Student's t-test. Exact P values are provided in Supplementary Table 5. The experiments in (a, b, d–k) were repeated twice with similar results. The experiment in (c) was repeated three times with similar results.

Source data

Extended Data Fig. 9 flg22 or nlp20-induced immune responses in *pckl1/2 pbl19/20* quadruple mutant plants.

(a) Growth of *Hpa* Noco2 on the local leaves of WT, *pckl1/2*, *pckl1/2 pbl19*, and *pckl1/2 pbl19/20* quadruple mutant lines (#33 and #47) after 1 μM nlp20 treatment. Disease ratings showing the relative growth of *Hpa* Noco2 are as described in the Methods. The experiment was repeated three times with similar results. (b) Growth of *Pto* DC3000 in the leaves of four-week-old WT and *pckl1/2 pbl19/20* quadruple mutant lines (#33 and #47)

pre-treated with H₂O or 1 μM nlp20. The treated leaves were infiltrated with *Pto* DC3000 (OD₆₀₀=0.001) 24 h post treatment with nlp20. Samples were taken 3 days after *Pto* DC3000 inoculation. Bars represent mean ± s.d. (n = 8 plants). The reduction of bacterial titer after nlp20 treatment in each genotype was regarded as nlp20-induced protection, which was compared among the WT and the mutants. The experiment was repeated three times with similar results. (c) Levels of SAG in four-week-old soil-grown plants of the indicated genotypes treated with H₂O or 1 μM nlp20 for 24 h. Bars represent mean ± s.d. (n = 3 biologically independent samples). The experiment was repeated three times with similar results. (d, e) nlp20-induced MAPK activation in the indicated genotypes. 12-day-old seedlings were treated with 0.1 μM nlp20. MAPK activation was analyzed by immunoblotting with the anti-pERK antibody (d). Equal loading is confirmed by Ponceau staining of Rubisco. Quantifications of the phosphorylated MPK6 and MPK3 were shown in (e). Bars represent mean ± s.d. (n = 4 different experiments). (f) nlp20-induced ROS production in the indicated genotypes. Leaf strips were treated with 1 μM nlp20 and production of ROS was measured as luminescence. The values show the peak of luminescence units through all the time points. Bars represent mean ± s.d. (n = 8 leaf disks from different plants). The experiment was repeated three times with similar results. (g, h) Induction of *SARD1* (g) and *FMO1* (h) in the indicated genotypes by nlp20. Total RNA extracted from 12-day-old plate-grown plants treated with 1 μM nlp20 for 4 h. The expression of each gene in H₂O-treated WT was set as 1. Bars represent mean ± s.d. (n = 3 biologically independent samples). The experiment was repeated twice with similar results. (i, j) flg22-induced MAPK activation in the indicated genotypes. 12-day-old seedlings were treated with 0.1 μM flg22. MAPK activation was analyzed by immunoblotting with the anti-pERK antibody. Equal loading is confirmed by Ponceau staining of Rubisco. Quantifications of the phosphorylated MPK6 and MPK3 10 min after treatment with flg22 were shown in (j). Bars represent mean ± s.d. (n = 4 different experiments). (k) ROS production in the indicated genotypes after treatment with 0.1 μM flg22 measured as luminescence. The values show the peak of luminescence units through all the time points. Bars represent mean ± s.d. (n = 8 leaf disks from different plants). The experiment was repeated three times with similar results. (l, m) Relative expression levels of *SARD1* (l)

and *FMO1* (**m**) in the indicated genotypes. Total RNA was isolated from 12-day-old plate-grown seedlings 4 h after spraying with H₂O or 1 μM flg22. The expression of each gene in the H₂O -treated WT plants was set as 1. Bars represent mean ± s.d. (n = 3 biologically independent samples). Experiments were repeated twice with similar results. (**n**) Free SA and SAG levels in four-week-old plants of the indicated genotypes after treatment with H₂O or 1 μM flg22 for 9 h. Bars represent mean ± s.d. (n = 3 biologically independent samples). The experiment was repeated three times with similar results. (**o**) Growth of *Pto* DC3000 in the leaves of four-week-old plants of the indicated genotypes after treatment with H₂O or 1 μM flg22. Bars represent mean ± s.d. (n = 6 plants). The reduction of bacterial titer after flg22 treatment in each genotype was regarded as flg22-induced protection, which was compared among different genotypes. The experiment was repeated three times with similar results. The data in (**b**, **c**, **e–h**, **j–o**) were analyzed by one-way ANOVA with Tukey's test. Exact P values are provided in Supplementary Table 5.

[Source data](#)

[Extended Data Fig. 10 Analysis of the interactions between SOBIR1 and PBL19/EDS1/PAD4/ADR1 by TurboID-based proximity labeling method.](#)

Agrobacterium carrying the indicated constructs were infiltrated into *N. benthamiana* leaves for protein expression. Immunoprecipitation of PBL19-3FLAG (**a**), ADR1-3FLAG (**b**), EDS1-ZZ-TEV-FLAG (**c**), and PAD4-ZZ-TEV-FLAG (**d**) was carried out with anti-FLAG beads. The FLAG-tagged proteins were detected by western blot using an anti-FLAG antibody. The biotinylated proteins were detected by western blot using HRP-Streptavidin. The experiments were repeated at least twice with similar results.

Supplementary information

[Supplementary Fig. 1](#)

This file contains the uncropped blots.

Reporting Summary

Peer Review File

Supplementary Tables

This file contains Supplementary Tables 1–4.

Supplementary Table 5

This file contains a statistical summary.

Source data

Source Data Fig. 1

Source Data Fig. 2

Source Data Fig. 3

Source Data Extended Data Fig. 1

Source Data Extended Data Fig. 4

Source Data Extended Data Fig. 5

Source Data Extended Data Fig. 6

Source Data Extended Data Fig. 7

Source Data Extended Data Fig. 8

Source Data Extended Data Fig. 9

Rights and permissions

Reprints and Permissions

About this article

Cite this article

Tian, H., Wu, Z., Chen, S. *et al.* Activation of TIR signalling boosts pattern-triggered immunity. *Nature* **598**, 500–503 (2021).
<https://doi.org/10.1038/s41586-021-03987-1>

- Received: 27 December 2020
- Accepted: 01 September 2021
- Published: 20 September 2021
- Issue Date: 21 October 2021
- DOI: <https://doi.org/10.1038/s41586-021-03987-1>

Share this article

Anyone you share the following link with will be able to read this content:

[Get shareable link](#)

Sorry, a shareable link is not currently available for this article.

[Copy to clipboard](#)

Provided by the Springer Nature SharedIt content-sharing initiative

This article was downloaded by **calibre** from <https://www.nature.com/articles/s41586-021-03987-1>

| [Section menu](#) | [Main menu](#) |

- Article
- [Published: 06 October 2021](#)

A pan-serotype dengue virus inhibitor targeting the NS3–NS4B interaction

- [Suzanne J. F. Kaptein](#) ORCID: [orcid.org/0000-0002-7935-0219¹](https://orcid.org/0000-0002-7935-0219),
- [Olivia Goethals²](#),
- [Dominik Kiemel³](#),
- [Arnaud Marchand⁴](#),
- [Bart Kesteleyn⁵](#),
- [Jean-François Bonfanti](#) ORCID: [orcid.org/0000-0002-2107-8857^{6 nAff11}](https://orcid.org/0000-0002-2107-8857),
- [Dorothée Bardiot⁴](#),
- [Bart Stoops⁵](#),
- [Tim H. M. Jonckers⁵](#),
- [Kai Dallmeier](#) ORCID: [orcid.org/0000-0002-8117-9166¹](https://orcid.org/0000-0002-8117-9166),
- [Peggy Geluykens^{5 nAff12}](#),
- [Kim Thys⁵](#),
- [Marjolein Crabbe⁵](#),
- [Laurent Chatel-Chaix](#) ORCID: [orcid.org/0000-0002-7390-8250^{3 nAff13}](https://orcid.org/0000-0002-7390-8250),
- [Max Münster³](#),
- [Gilles Querat⁷](#),
- [Franck Touret](#) ORCID: [orcid.org/0000-0002-4734-2249⁷](https://orcid.org/0000-0002-4734-2249),
- [Xavier de Lamballerie⁷](#),
- [Pierre Raboisson^{5 nAff14}](#),
- [Kenny Simmen⁵](#),
- [Patrick Chalton^{4,8}](#),

- [Ralf Bartenschlager](#) ORCID: [orcid.org/0000-0001-5601-9307^{3,9}](https://orcid.org/0000-0001-5601-9307),
- [Marnix Van Loock](#) ORCID: [orcid.org/0000-0003-4151-4588²](https://orcid.org/0000-0003-4151-4588) &
- [Johan Neyts](#) ORCID: [orcid.org/0000-0002-0033-7514^{1,10}](https://orcid.org/0000-0002-0033-7514)

Nature volume **598**, pages 504–509 (2021)

- 6191 Accesses
- 1 Citations
- 736 Altmetric
- [Metrics details](#)

Subjects

- [Dengue virus](#)
- [Target identification](#)

A [Publisher Correction](#) to this article was published on 20 October 2021

This article has been [updated](#)

Abstract

Dengue virus causes approximately 96 million symptomatic infections annually, manifesting as dengue fever or occasionally as severe dengue^{1,2}. There are no antiviral agents available to prevent or treat dengue. Here, we describe a highly potent dengue virus inhibitor (JNJ-A07) that exerts nanomolar to picomolar activity against a panel of 21 clinical isolates that represent the natural genetic diversity of known genotypes and serotypes. The molecule has a high barrier to resistance and prevents the formation of the viral replication complex by blocking the interaction between two viral proteins (NS3 and NS4B), thus revealing a previously undescribed

mechanism of antiviral action. JNJ-A07 has a favourable pharmacokinetic profile that results in outstanding efficacy against dengue virus infection in mouse infection models. Delaying start of treatment until peak viraemia results in a rapid and significant reduction in viral load. An analogue is currently in further development.

Access options

Subscribe to Journal

Get full journal access for 1 year

\$199.00

only \$3.90 per issue

[Subscribe](#)

All prices are NET prices.

VAT will be added later in the checkout.

Tax calculation will be finalised during checkout.

Rent or Buy article

Get time limited or full article access on ReadCube.

from \$8.99

[Rent or Buy](#)

All prices are NET prices.

Additional access options:

- [Log in](#)
- [Access through your institution](#)
- [Learn about institutional subscriptions](#)

Fig. 1: Identification of a molecular target of JNJ-A07.

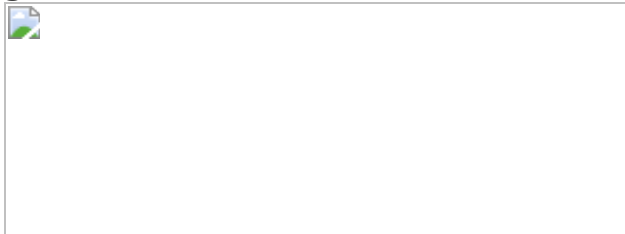


Fig. 2: In vivo efficacy of JNJ-A07 on viraemia and survival in a prophylactic setting.

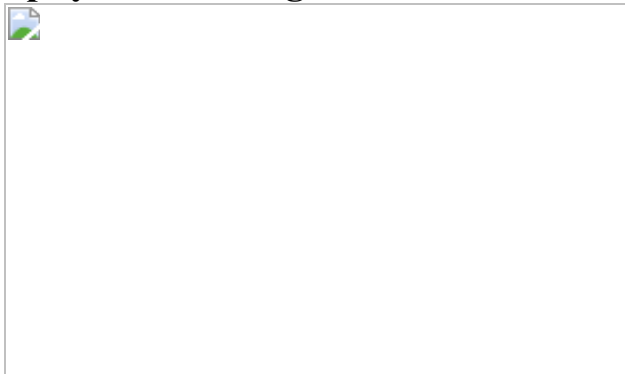
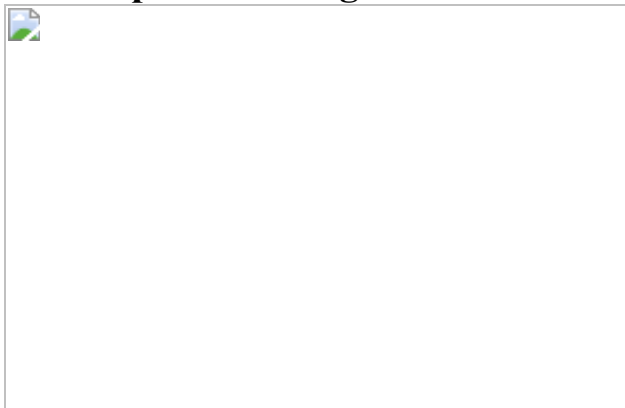


Fig. 3: In vivo efficacy of JNJ-A07 on the kinetics of DENV replication in a therapeutic setting.



Data availability

The genome sequence of DENV-2 RL is deposited at GenBank (accession [MW741553](#)). The synthesis and chemical characterization of all compounds described in this paper is provided as [Supplementary Information](#) ([Supplementary Methods](#)). The uncropped images of the western blots shown in Fig. 1, Extended Data Figs. 5 and 6 are presented in [Supplementary Figs. 1–6](#). All data supporting the findings of this study

are available within the Article, the source data or the [Supplementary Information](#). [Source data](#) are provided with this paper.

Code availability

A custom script⁴³ was used to derive the amino acid composition of each sample for all coding sequences per DENV genotype, which was not specifically developed for this research but for all similar analyses. The code for the custom script is deposited as part of the pipeline VirVarSeq but is individually accessible on the Open Source software platform SourceForge at <https://sourceforge.net/projects/virtools/?source=directory>. The code for this specific variant detection script is ‘codon_table.pl’. Graphs and figures were generated using Microsoft PowerPoint, GraphPad Prism (v.9.0.0) or Adobe Illustrator (v.25.4.1); the software is made available by KU Leuven through a group licence. In some figures, basic templates obtained from the Servier Medical Art library (<https://smart.servier.com/>) were used.

Change history

- [**20 October 2021**](#)

[A Correction to this paper has been published:](#)
<https://doi.org/10.1038/s41586-021-04123-9>

References

1. 1.
Dengue and Severe Dengue. *World Health Organization*, <https://www.who.int/news-room/fact-sheets/detail/dengue-and-severe-dengue> (15 April 2019).
2. 2.

Bhatt, S. et al. The global distribution and burden of dengue. *Nature* **496**, 504–507 (2013).

3. 3.

Ayukekbong, J. A., Oyero, O. G., Nnukwu, S. E., Mesumbe, H. N. & Fobisong, C. N. Value of routine dengue diagnosis in endemic countries. *World J. Virol.* **6**, 9–16 (2017).

4. 4.

Paixão, E. S., Teixeira, M. G. & Rodrigues, L. C. Zika, chikungunya and dengue: the causes and threats of new and re-emerging arboviral diseases. *BMJ Glob. Health* **3**, e000530 (2018).

5. 5.

Simmons, C. P., Farrar, J. J., van Nguyen, V. & Wills, B. Dengue. *N. Engl. J. Med.* **366**, 1423–1432 (2012).

6. 6.

Messina, J. P. et al. The current and future global distribution and population at risk of dengue. *Nat. Microbiol.* **4**, 1508–1515 (2019).

7. 7.

Duong, V. et al. Asymptomatic humans transmit dengue virus to mosquitoes. *Proc. Natl Acad. Sci. USA* **112**, 14688–14693 (2015).

8. 8.

ten Bosch, Q. A. et al. Contributions from the silent majority dominate dengue virus transmission. *PLoS Pathog.* **14**, e1006965 (2018).

9. 9.

Halstead, S. B. Pathogenesis of dengue: dawn of a new era. *F1000Research* **4**, 1353 (2015).

10. 10.

Katzelnick, L. C. et al. Antibody-dependent enhancement of severe dengue disease in humans. *Science* **358**, 929–932 (2017).

11. 11.

Dengue vaccine: WHO position paper—July 2016. *Wkly Epidemiol. Rec.* **91**, 349-364 (2016).

12. 12.

Wilder-Smith, A. et al. Deliberations of the strategic advisory group of experts on immunization on the use of CYD-TDV dengue vaccine. *Lancet Infect. Dis.* **19**, e31–e38 (2019).

13. 13.

Dengue vaccine: WHO position paper—September 2018. *Wkly Epidemiol. Rec.* **93**, 457–476 (2018).

14. 14.

Low, J. G., Gatsinga, R., Vasudevan, S. G. & Sampath, A. In *Dengue and Zika: Control and Antiviral Treatment Strategies. Advances in Experimental Medicine and Biology* (eds Hilgenfeld, R. & Vasudevan, S. G.) 319–332 (Springer, 2018).

15. 15.

Whitehorn, J. et al. Dengue therapeutics, chemoprophylaxis, and allied tools: state of the art and future directions. *PLoS Negl. Trop. Dis.* **8**, e3025 (2014).

16. 16.

Bardiot, D. et al. Discovery of indole derivatives as novel and potent dengue virus inhibitors. *J. Med. Chem.* **61**, 8390–8401 (2018).

17. 17.

Schmid, M. A. & Harris, E. Monocyte recruitment to the dermis and differentiation to dendritic cells increases the targets for dengue virus replication. *PLoS Pathog.* **10**, e1004541 (2014).

18. 18.

Touret, F. et al. Phylogenetically based establishment of a dengue virus panel, representing all available genotypes, as a tool in dengue drug. *Antiviral Res.* **168**, 109–113 (2019).

19. 19.

Płaszczyca, A. et al. A novel interaction between dengue virus nonstructural protein 1 and the NS4A-2K–4B precursor is required for viral RNA replication but not for formation of the membranous replication organelle. *PLoS Pathog.* **15**, e10077362019 (2019).

20. 20.

Chatel-Chaix, L. et al. A combined genetic–proteomic approach identifies residues within dengue virus NS4B critical for interaction with NS3 and viral replication. *J. Virol.* **89**, 7170–7186 (2015).

21. 21.

Moquin, S. A. et al. NITD-688, a pan-serotype inhibitor of the dengue virus NS4B protein, shows favorable pharmacokinetics and efficacy in preclinical animal models. *Sci. Transl. Med.* **13**, eabb2181 (2021).

22. 22.

Clapham, H. E., Tricou, V., Van Vinh Chau, N., Simmons, C. P. & Ferguson, N. M. Within-host viral dynamics of dengue serotype 1 infection. *J. R. Soc. Interface* **11**, 20140094 (2014).

23. 23.

Sim, S. et al. Tracking dengue virus intra-host genetic diversity during human-to-mosquito transmission. *PLoS Negl. Trop. Dis.* **9**, e0004052 (2015).

24. 24.

Simmons, C. P. et al. Recent advances in dengue pathogenesis and clinical management. *Vaccine* **33**, 7061–7068 (2015).

25. 25.

Nguyen, N. M. et al. Host and viral features of human dengue cases shape the population of infected and infectious *Aedes aegypti* mosquitoes. *Proc. Natl Acad. Sci. USA* **110**, 9072–9077 (2013).

26. 26.

Simmons, C. P. et al. Therapeutics for dengue: recommendations for design and conduct of early-phase clinical trials. *PLoS Negl. Trop. Dis.* **6**, e1752 (2012).

27. 27.

Low, J. G., Ooi, E. E. & Vasudevan, S. G. Current status of dengue therapeutics research and development. *J. Infect. Dis.* **215**, S96–S102 (2017).

28. 28.

Unlocking the Potential of Preventive Therapies for Malaria. *World Health Organization*, <https://www.who.int/malaria/media/preventive-therapies/en/> (7 April 2017).

29. 29.

Zou, J. et al. Characterization of dengue virus NS4A and NS4B protein interaction. *J. Virol.* **89**, 3455–3470 (2015).

30. 30.

Miller, S., Sparacio, S. & Bartenschlager, R. Subcellular localization and membrane topology of the dengue virus type 2 non-structural protein 4B. *J. Biol. Chem.* **281**, 8854–8863 (2006).

31. 31.

Chatel-Chaix, L. et al. Dengue virus perturbs mitochondrial morphodynamics to dampen innate immune responses. *Cell Host Microbe* **20**, 342–356 (2016).

32. 32.

Zmurko, J., Neyts, J. & Dallmeier, K. Flaviviral NS4B, chameleon and jack-in-the-box roles in viral replication and pathogenesis, and a molecular target for antiviral intervention. *Rev. Med. Virol.* **25**, 205–223 (2015).

33. 33.

Umareddy, I., Chao, A., Sampath, A., Gu, F. & Vasudevan, S. G. Dengue virus NS4B interacts with NS3 and dissociates it from single-stranded RNA. *J. Gen. Virol.* **87**, 2605–2614 (2006).

34. 34.

Janssen Pharmaceuticals & KU Leuven. Preparation of mono- or di-substituted derivatives as dengue viral replication inhibitors. Patent WO/2016/050841 (2016).

35. 35.

Janssen Pharmaceuticals & KU Leuven. Preparation of mono- or di-substituted derivatives as dengue viral replication inhibitors. Patent WO/2016/050831 (2016).

36. 36.

Janssen Pharmaceuticals & KU Leuven. Preparation of substituted indoline derivatives as dengue viral replication inhibitors. Patent

WO/2017/167951 (2017).

37. 37.

Novartis. *N*-substituted tetrahydrothienopyridine derivatives as antiviral agents and their preparation. Patent WO/2019/244047 (2019).

38. 38.

Fischl, W. & Bartenschlager, R. High-throughput screening using dengue virus reporter genomes. *Methods Mol. Biol.* **1030**, 205–219 (2013).

39. 39.

Aubry, F. et al. Single-stranded positive-sense RNA viruses generated in days using infectious subgenomic amplicons. *J. Gen. Virol.* **95**, 2462–2467 (2014).

40. 40.

Kum, D. B. et al. A yellow fever–Zika chimeric virus vaccine candidate protects against Zika infection and congenital malformations in mice. *NPJ Vaccines* **3**, 56 (2018).

41. 41.

De Burghgraeve, T. et al. 3',5'Di-*O*-trityluridine inhibits in vitro flavivirus replication. *Antiviral Res.* **98**, 242–247 (2013).

42. 42.

Kaptein, S. J. F. et al. A derivate of the antibiotic doxorubicin is a selective inhibitor of dengue and yellow fever virus replication in vitro. *Antimicrob. Agents Chemother.* **54**, 5269–5280 (2010).

43. 43.

Verbist, B. M. et al. VirVarSeq: a low-frequency virus variant detection pipeline for Illumina sequencing using adaptive base-calling accuracy filtering. *Bioinformatics* **31**, 94–101 (2015).

44. 44.

Münster, M. et al. A reverse genetics system for Zika virus based on a simple molecular cloning strategy. *Viruses* **10**, E368 (2018).

45. 45.

Zmurko, J. et al. The viral polymerase inhibitor 7-deaza-2'-C-methyladenosine is a potent inhibitor of in vitro Zika virus replication and delays disease progression in a robust mouse infection model. *PLoS Negl. Trop. Dis.* **10**, e0004695 (2016).

46. 46.

Jaki, T. & Wolfsegger, M. J. Estimation of pharmacokinetic parameters with the R package PK. *Pharm. Stat.* **10**, 284–288 (2011).

Acknowledgements

This work was supported by a Seeding Drug Discovery Strategic Award from the Wellcome Trust (grant 089328/Z/09 and grant 106327/Z/14) and received funding from the Flanders Agency Innovation & Entrepreneurship (VLAIO O&O grants IWT 150863 and HBC.2019.2906). Part of this research work was performed using the ‘Caps-It’ research infrastructure (project ZW13-02) that was financially supported by the Hercules Foundation (FWO) and Rega Foundation, KU Leuven. We thank M. Flament, R. Pholien, C. De Keyzer, C. Vanderheydt, E. Maas, S. Claes and the staff at the Rega animal facility at KU Leuven; E. Peeters, S. De Bruyn, N. Verheyen, C. Van Hove, E. Coesmans, B. De Boeck, A. Beckers, P. Gyseberg, T. Loomans and K. Allaerts at Janssen Pharmaceutica; and J. Fortin, F. Doublet and P. Muller at Janssen-Cilag for technical assistance.

Author information

Author notes

1. Jean-François Bonfanti

Present address: Galapagos, Romainville, France

2. Peggy Geluykens

Present address: Charles River Beerse, Discovery, Beerse, Belgium

3. Laurent Chatel-Chaix

Present address: Institut National de la Recherche Scientifique, Centre Armand-Frappier Santé Biotechnologie, Quebec, Quebec, Canada

4. Pierre Raboisson

Present address: Aligos, Leuven, Belgium

Affiliations

1. Laboratory of Virology and Chemotherapy, Department of Microbiology, Immunology and Transplantation, Rega Institute for Medical Research, KU Leuven, Leuven, Belgium

Suzanne J. F. Kaptein, Kai Dallmeier & Johan Neyts

2. Janssen Global Public Health, Janssen Pharmaceutica, Beerse, Belgium

Olivia Goethals & Marnix Van Loock

3. Department of Infectious Diseases, Molecular Virology, Heidelberg University, Heidelberg, Germany

Dominik Kiemel, Laurent Chatel-Chaix, Max Münster & Ralf Bartenschlager

4. Cistim Leuven, Leuven, Belgium

Arnaud Marchand, Dorothée Bardiot & Patrick Chaltin

5. Janssen Research & Development, Janssen Pharmaceutica, Beerse, Belgium

Bart Kesteleyn, Bart Stoops, Tim H. M. Jonckers, Peggy Geluykens, Kim Thys, Marjolein Crabbe, Pierre Raboisson & Kenny Simmen

6. Janssen Infectious Diseases Discovery, Janssen-Cilag, Val de Reuil, France

Jean-François Bonfanti

7. Unité des Virus Émergents (UVE), Aix-Marseille Univ, IRD 190 Inserm 1207, IHU Méditerranée Infection, Marseille, France

Gilles Querat, Franck Touret & Xavier de Lamballerie

8. Centre for Drug Design and Discovery (CD3), KU Leuven, Leuven, Belgium

Patrick Chaltin

9. German Center for Infection Research, Heidelberg Partner Site, Heidelberg, Germany

Ralf Bartenschlager

10. Global Virus Network (GVN), Baltimore, MD, USA

Johan Neyts

Contributions

S.J.F.K. and J.N. planned, coordinated and executed the experimental virology work at KU Leuven. O.G. and M.V.L. planned, coordinated and executed the experimental virology work at Janssen Pharmaceutica. P.G. executed the experimental virology work at Janssen Pharmaceutica. D.K.,

L.C.-C., M.M. and R.B. planned, coordinated and executed the experimental virology work at Heidelberg University. D.B. planned, coordinated and executed the medicinal chemistry work at Cistim. K.D. did experimental work at KU Leuven and advised on the design of experiments. K.T. performed whole-genome sequence analysis at Janssen Pharmaceutica. M.C. performed the statistical analyses at Janssen Pharmaceutica. G.Q., F.T. and X.d.L. planned, coordinated and executed the experimental work at UVE. B.K., J.-F.B., T.H.M.J. and P.R. planned, coordinated and executed the medicinal chemistry work at Janssen Pharmaceutica. B.S. planned and coordinated the pharmacokinetics and pharmacodynamics work at Janssen Pharmaceutica. A.M. and P.C. coordinated and guided the experimental medicinal chemistry work at CD3. P.C. and J.N. designed and initiated the project. K.S. and M.V.L. initiated the project at Janssen Pharmaceutica. J.N., P.C., A.M., S.J.F.K., O.G., R.B., M.V.L. and K.S. secured funding from external organizations. S.J.F.K., O.G., M.V.L. and J.N. wrote the manuscript with contributions from K.S., D.K. and R.B., and comments from all authors.

Corresponding authors

Correspondence to Marnix Van Loock or Johan Neyts.

Ethics declarations

Competing interests

S.J.F.K., O.G., A.M., B.K., J.-F.B., D.B., B.S., T.H.M.J., K.D., P.R., K.S., P.C., M.V.L. and J.N. have filed a patent application claiming the discovery of this class of antiviral molecules as DENV replication inhibitors (WO/2017/167951). The other authors declare no competing interests.

Additional information

Peer review information *Nature* thanks Brett Lindenbach, R. Guy and the other, anonymous, reviewer(s) for their contribution to the peer review of this work. Peer reviewer reports are available.

Publisher's note Springer Nature remains neutral with regard to jurisdictional claims in published maps and institutional affiliations.

Extended data figures and tables

Extended Data Fig. 1 Dose-response curves of the antiviral activity of JNJ-A07 against DENV-2 on various cell types.

a-f, The antiviral effect (% Inhibition viral RNA replication, % Inhibition eGFP expression, or % Inhibition of infected cells) is depicted by white dots. The effect of JNJ-A07 on cell growth is depicted by grey dots. Assays were performed on Vero cells (**a** and **c**), Huh-7 hepatoma cells (**b**), C6/36 mosquito cells (**d**), human monocytic leukemia THP-1 cells expressing the DC-SIGN receptor (**e**), and immature dendritic cells (imDCs) (**f**). Cells were infected with either the DENV-2/16681/eGFP strain (**a-b, e**), DENV-2/16681 (**f**) or the DENV-2 RL strain (**c-d**). Data represent mean values \pm s.d. from two (for Vero and C6/36 cells using DENV-2 RL, and for imDCs using DENV-2/16681), three (for THP-1/DC-SIGN cells using DENV-2/16681), and at least five (for Vero and Huh-7 cells using DENV-2/16681) independent experiments.

Source data

Extended Data Fig. 2 JNJ-A07 is highly specific for DENV.

a, Antiviral activity of JNJ-A07 against various of RNA and DNA viruses. CHIKV, chikungunya virus; HadV, human adenovirus; HBV, hepatitis B virus; HCV, hepatitis C virus; HIV, human immunodeficiency virus; hRV, human rhinovirus; IVA, influenza virus A; IVB, influenza virus B; RSV, respiratory syncytial virus; rVSV, recombinant vesicular stomatitis virus; VACV, vaccinia virus; JEV, Japanese encephalitis virus; WNV, West Nile virus; YFV, yellow fever virus; ZIKV, Zika virus. ND, not determined. **b**, NS4B sequence alignment of related flaviviruses. The NS4B protein sequence of DENV-2/16681 was aligned with corresponding sequences from JEV strain JEV CNS769 Laos 2009 (GenBank KC196115), tick-borne encephalitis virus strain Oshima 5.10 polyprotein gene (GenBank

MF374487), WNV isolate R94224 CDC polyprotein gene (GenBank MF004388), YFV isolate Bolivia 88 1999 polyprotein gene (GenBank MF004382) and ZIKV strain HPF 2013 (GenBank KJ776791) using Clustal Omega Version 2.1. Post-processing was conducted with Jalview 2.11.1.3. The DENV NS4B topology model was added manually based on Miller et al.³⁰. Black arrowheads are pointing at locations associated with compound-resistance.

[Source data](#)

Extended Data Fig. 3 Time-of-drug-addition and in vitro resistance selection.

a, Experimental setup of the time-of-drug-addition assay (TOA). **b**, TOA and in vitro kinetics of DENV-2 replication. In vitro DENV RNA replication in the absence of compound is depicted by the red curve. Onset of intracellular viral replication is at 10 h post-infection (p.i.), as shown in the inset. The inhibitory effect of JNJ-A07 on DENV replication when added at different time points p.i. is depicted by the blue curves (0.0001 μ M, light blue; 0.001 μ M, dark blue). The broad-spectrum RNA virus inhibitor 7-deaza-2'-C-methyladenosine (7DMA) served as positive control (black curve with white circles). Data (mean \pm s.d.) from at least three independent experiments. **c**, Experimental approach of in vitro resistance selection. **d-e**, The dynamics of appearance of mutations was studied using whole genome sequencing. JNJ-A07 selected for mutations in NS4B, which were not present in the wild-type (WT) viruses that were passaged along without any drug pressure, of two independently selected resistant strains. Results for the A and B sample are shown in **(d-e)**, respectively. Each coloured line shows the dynamics of appearance of a certain mutation during passaging of the virus in presence of JNJ-A07; the mutation is depicted in the same colour. Whole genome sequencing was performed on DENV variants harvested at every 5th passage (P) and at the end of the experiment (i.e., passage 43). One passage represents a one-week time span. The dotted line represents the cut off (15%) for the detection of variants compared with WT in the virus population. The increasing EC₅₀ values, as determined by microscopic evaluation of virus-induced CPE, are depicted below the graphs. **f**, Mutations in DENV NS4B identified at end point after

in vitro resistance selection using JNJ-A07 and Analogue 1. **g**, Natural occurrence of the NS4B mutations in clinical isolates.

[Source data](#)

Extended Data Fig. 4 Replication properties of resistant subgenomic replicons and DENV strains.

a, Schematic representation of the subgenomic DENV-2/16681 reporter replicon sgDVs-R2A³⁸. **b**, Effect of resistance mutations in NS4B on replication fitness. Resistance mutations identified in Extended Data Fig. 3 were introduced into sgDVs-R2A. A replication-deficient replicon containing an inactivating mutation in the NS5 RNA-dependent RNA polymerase domain (GND) served as negative control. Huh-7 cells were transfected with in vitro transcribed RNA of WT or mutant sgDVs-R2A and lysed at the time points given at the top right and Renilla luciferase activity was measured as marker of replication. Relative light units (RLU) were normalized to the 4 h value, reflecting transfection efficiency. Plotted are the mean ± s.d. from at least three independent experiments, each carried out with independent RNA preparations. **c**, In vitro growth kinetics of resistant DENV (blue bars) compared to WT DENV (grey bars) on Vero E6 cells for the A sample. The virus titer in the supernatant was determined by plaque assay. **d**, In vitro growth kinetics of resistant DENV (blue bars) compared to WT DENV (grey bars) on C6/36 cells for the A sample. Viral RNA load in the supernatant was determined by RT-qPCR. **e**, Infectious virus on day 11 p.i. in the supernatant of C6/36 cells infected with resistant DENV (blue bars) or WT DENV (grey bars) for the A sample, as determined by plaque assay. **f**, In vitro growth kinetics of resistant DENV (dark blue bars) compared to WT DENV (light grey bars) on C6/36 cells for the B sample. Viral RNA load in the supernatant collected on day 1–10 p.i. was determined by RT-qPCR. Data are from a single experiment (**d-f**) or mean values ± s.d. from three independent experiments (**c**). LOD, limit of detection; LLOQ, lowest limit of quantification.

[Source data](#)

Extended Data Fig. 5 Impact of JNJ-A07 on the interaction between NS3 and various NS4B species.

a, Experimental design to study the impact of JNJ-A07 on the interaction between NS3 and WT or mutant NS4B. **b**, Captured protein complexes were analyzed by Western blot. A representative Western blot is shown. **c-d**, Western blot analysis to determine the NS3-NS4B interaction strength. The uncropped images of **b-d** are presented in [Supplementary Fig. 1-3](#). Numbers on the left are molecular weights (kDa). GAPDH served as loading control for cell lysates (input). **e-g**, Signal intensities (from three independent blots) of NS3, NS4A-2K-NS4B, 2K-NS4B and NS4B were normalized to WT NS4A-2K-NS4B-HA^{Ct} in DMSO-treated control cells. Protein ratios (mean ± s.e.m.) were calculated for each sample. Repeated measures one-way ANOVA with subsequent Dunnett's multiple comparisons test was used for statistical analysis. *ns*, not significant. **h-j**, Protein intensities (mean ± s.e.m.; three independent experiments) for WT (**h**) and compound-resistant NS4B-mutants V91A (**i**) and T108I (**j**), normalized to an untreated WT control. For statistical analysis, JNJ-A07-treated samples were compared with the corresponding untreated control (left of the dashed line) using ordinary one-way ANOVA with subsequent Dunnett's multiple comparisons test. **k**, EC₅₀ values (mean ± s.e.m.) for protein ratios in (**e-g**) obtained by fitting four-parameter dose-response curves to the results from each individual experiment. Fold change in EC₅₀ is the ratio between the mean EC₅₀ for WT and the respective mutant constructs. **l**, JNJ-A07 potentially slows down the processing dynamics of the NS4A-2K-NS4B precursor (illustrated by the hourglass icon), which is first cleaved by the NS2B-NS3 protease at the NS4A-2K cleavage site. 2K-NS4B is subsequently processed by the host signal peptidase complex into mature NS4B and 2K.

[Source data](#)

Extended Data Fig. 6 JNJ-A07 does not disrupt existing NS3-NS4B complexes.

a, Experimental setup to study the kinetics of JNJ-A07-induced block of the NS3–NS4B interaction. **b**, Impact of JNJ-A07 on forming or pre-formed NS3–NS4B complexes. Huh-7 T7 NS2B-NS3 cells treated with 0.035 µM JNJ-A07 or equal amounts of DMSO were harvested at 1, 8, or 24 h after drug addition. Lysates were subjected to HA-specific pull-down and analyzed by Western blot (enrichment factor 5). A representative Western blot is shown. Numbers on the left represent molecular weights (kDa). **c**, Experimental setup of the in cellulo assay, in which Huh-7 cells were infected with DENV-2(NS4B-HA*)²⁰ at an MOI of 1. At 48 h p.i., cells were treated for given periods with 500 nM of Analogue 2 or DMSO. **d**, NS3–NS4B complexes were enriched by NS4B-HA* pull-down and total lysates (input) and immune complexes (pull-down) were analysed by Western blot. NS3/NS4B ratios (depicted below the picture) were normalized to non-drug treated samples ($n = 1$). **e**, Experimental setup of the in vitro drug assay to investigate the effect of the drug on established NS3–NS4B complexes. Cell lysates were treated with 1 µM of Analogue 2 or equal amounts of DMSO added to the lysis buffer and incubated for 2 h at different temperatures in order to test complex stability. Subsequently, NS4B-HA^{Ct} pull-down was performed. **f**, Western blot analysis ($n = 1$) analogous to the one shown in (d). The lower protein amount observed with the sample incubated at 37 °C was most likely due to proteolytic degradation in spite of adding protease inhibitors. For uncropped images of the representative blots in (b, d, f), see [Supplementary Fig. 4-6](#). GAPDH (b, f) or β-actin (d) served as loading control for cell lysates (input).

[Source data](#)

[Extended Data Fig. 7 In vivo efficacy of JNJ-A07 on viral RNA and cytokine levels.](#)

a-c, Inhibitory effect of JNJ-A07 on viral RNA levels in spleen (a), kidney (b) and liver (c) on day 3 p.i. from AG129 mice treated twice-daily with 30 (white dots), 10 (light blue dots), 3 (dark blue dots) or 1 (grey dots) mg/kg JNJ-A07, as compared to vehicle-treated mice (red dots). Data are from two independent studies with $n = 8$ per group in each study. **d-g**, IL-18 (d), IFNγ (e), TNF (f), and IL-6 (g) levels in plasma on day 3 p.i. (from one of the viremia studies in Fig. 2b). **h**, Inhibitory effect of JNJ-A07 on viral RNA

levels in plasma on day 3 p.i. in the survival study (also see Fig. 2c). Dosing groups were similar to those in (a-c). Treatment started 1 h before infection. Mice were injected with the Anti-Flavivirus antibody one day before infection. Data are from one study with $n = 10$ per group. **i**, Inhibitory effect of NITD-688 on viral RNA levels on day 3 p.i. in AG129 mice treated twice-daily with 100 (yellow dots), 30 (white dots), 10 (light blue dots) or 3 (dark blue dots) mg/kg NITD-688, as compared to vehicle-treated mice (red dots). Treatment started 1 h before infection. Data are from one study with $n = 8$ per group. Individual data and median values are presented.

Undetermined C_t values were imputed at a C_t value of 40 (which is the LOD), corresponding to $2.6 \log_{10}$ viral RNA copies/mL. Statistical analysis was performed using the two-sided Kruskal-Wallis test (a-c, i) or a Tobit regression model (h). P values were adjusted using the Holm's (a-c), Dunn's (d-g) or Bonferroni's (h-i) multiple comparisons correction method. ns, not significant, as compared to vehicle-treated mice. LLOQ, lowest level of quantification.

Source data

Extended Data Fig. 8 Efficacy of JNJ-A07 in the in vivo kinetics study.

a, Schematic outline of the in vivo kinetics study. Each treatment group was sub-divided in group A and B ($n = 8$, per group) for blood collection on alternating days. **b**, Weight curves (mean values \pm s.d.) of AG129 mice for the different treatment groups during the in vivo kinetics study (two independent studies). Colours of the dots represent the different treatment groups, as specified in (c-g). **c-g**, Inhibitory effect of JNJ-A07 on viremia on various days p.i. in mice treated twice-daily with 30 mg/kg (white dots, $n = 8$), 10 mg/kg (light blue dots, $n = 8$), 3 mg/kg (dark blue dots, $n = 16$), 1 mg/kg (grey dots, $n = 8$), or 0.3 mg/kg (green dots, $n = 8$) JNJ-A07, as compared to vehicle-treated mice (red dots, $n = 16$). Treatment was initiated 1 h before intraperitoneal infection. Data (median \pm s.d.) are from two independent studies. Undetermined C_t values were imputed at a C_t value of 40 (which is the limit of detection), corresponding to $2.6 \log_{10}$ viral RNA copies/mL. The mean AUC value and 95% CI was determined for each

group. In case the CIs did not overlap, groups were considered to differ markedly. LLOQ, lowest level of quantification.

[Source data](#)

Extended Data Table 1 Antiviral activity of analogues of JNJ-A07 and NITD-688 against DENV-2

Extended Data Table 2 Pharmacokinetic properties of JNJ-A07 in mice and rats after intravenous (a) and oral (b) dosing

Supplementary information

[Supplementary Information](#)

This file contains Supplementary Methods and Supplementary Figs. 1–6.

[Reporting Summary](#)

[Peer Review File](#)

Source data

[Source Data Fig. 1](#)

[Source Data Fig. 2](#)

[Source Data Fig. 3](#)

[Source Data Table. 1](#)

[Source Data Extended Data Fig. 1](#)

[Source Data Extended Data Fig. 2](#)

[Source Data Extended Data Fig. 3](#)

[**Source Data Extended Data Fig. 4**](#)

[**Source Data Extended Data Fig. 5**](#)

[**Source Data Extended Data Fig. 6**](#)

[**Source Data Extended Data Fig. 7**](#)

[**Source Data Extended Data Fig. 8**](#)

[**Source Data Extended Data Table 1**](#)

[**Source Data Extended Data Table 2**](#)

Rights and permissions

[Reprints and Permissions](#)

About this article

Cite this article

Kaptein, S.J.F., Goethals, O., Kiemel, D. *et al.* A pan-serotype dengue virus inhibitor targeting the NS3–NS4B interaction. *Nature* **598**, 504–509 (2021). <https://doi.org/10.1038/s41586-021-03990-6>

- Received: 30 June 2020
- Accepted: 01 September 2021
- Published: 06 October 2021
- Issue Date: 21 October 2021
- DOI: <https://doi.org/10.1038/s41586-021-03990-6>

Share this article

Anyone you share the following link with will be able to read this content:

[Get shareable link](#)

Sorry, a shareable link is not currently available for this article.

[Copy to clipboard](#)

Provided by the Springer Nature SharedIt content-sharing initiative

A step towards therapeutics for dengue

- Scott B. Biering
- Eva Harris

News & Views 06 Oct 2021

This article was downloaded by **calibre** from <https://www.nature.com/articles/s41586-021-03990-6>

| [Section menu](#) | [Main menu](#) |

- Article
- [Published: 13 October 2021](#)

Mutant clones in normal epithelium outcompete and eliminate emerging tumours

- [B. Colom](#) [ORCID: orcid.org/0000-0001-6256-6462¹](#),
- [A. Herms¹](#),
- [M. W. J. Hall](#) [ORCID: orcid.org/0000-0003-2904-6902^{1,2}](#),
- [S. C. Dentro](#) [ORCID: orcid.org/0000-0002-0478-9729^{1,3}](#),
- [C. King](#) [ORCID: orcid.org/0000-0003-2543-1993¹](#),
- [R. K. Sood¹](#),
- [M. P. Alcolea](#) [ORCID: orcid.org/0000-0002-8396-6454^{4,5}](#),
- [G. Piedrafita](#) [ORCID: orcid.org/0000-0001-8701-1084^{1,6}](#),
- [D. Fernandez-Antoran](#) [ORCID: orcid.org/0000-0003-1608-570X¹](#) nAff¹⁰,
- [S. H. Ong](#) [ORCID: orcid.org/0000-0002-3629-5387¹](#),
- [J. C. Fowler](#) [ORCID: orcid.org/0000-0001-7546-369X¹](#),
- [K. T. Mahbubani](#) [ORCID: orcid.org/0000-0002-1327-2334⁷](#),
- [K. Saeb-Parsy](#) [ORCID: orcid.org/0000-0002-0633-3696⁷](#),
- [M. Gerstung](#) [ORCID: orcid.org/0000-0001-6709-963X^{3,8}](#),
- [B. A. Hall](#) [ORCID: orcid.org/0000-0003-0355-2946⁹](#) &
- [P. H. Jones](#) [ORCID: orcid.org/0000-0002-5904-795X^{1,2}](#)

Nature volume **598**, pages 510–514 (2021)

- 11k Accesses
- 317 Altmetric

- [Metrics details](#)

Subjects

- [Cancer genomics](#)
- [Cancer models](#)

Abstract

Human epithelial tissues accumulate cancer-driver mutations with age^{1,2,3,4,5,6,7,8,9}, yet tumour formation remains rare. The positive selection of these mutations suggests that they alter the behaviour and fitness of proliferating cells^{10,11,12}. Thus, normal adult tissues become a patchwork of mutant clones competing for space and survival, with the fittest clones expanding by eliminating their less competitive neighbours^{11,12,13,14}. However, little is known about how such dynamic competition in normal epithelia influences early tumorigenesis. Here we show that the majority of newly formed oesophageal tumours are eliminated through competition with mutant clones in the adjacent normal epithelium. We followed the fate of nascent, microscopic, pre-malignant tumours in a mouse model of oesophageal carcinogenesis and found that most were rapidly lost with no indication of tumour cell death, decreased proliferation or an anti-tumour immune response. However, deep sequencing of ten-day-old and one-year-old tumours showed evidence of selection on the surviving neoplasms. Induction of highly competitive clones in transgenic mice increased early tumour removal, whereas pharmacological inhibition of clonal competition reduced tumour loss. These results support a model in which survival of early neoplasms depends on their competitive fitness relative to that of mutant clones in the surrounding normal tissue. Mutant clones in normal epithelium have an unexpected anti-tumorigenic role in purging early tumours through cell competition, thereby preserving tissue integrity.

Access options

Subscribe to Journal

Get full journal access for 1 year

\$199.00

only \$3.90 per issue

[Subscribe](#)

All prices are NET prices.

VAT will be added later in the checkout.

Tax calculation will be finalised during checkout.

Rent or Buy article

Get time limited or full article access on ReadCube.

from \$8.99

[Rent or Buy](#)

All prices are NET prices.

Additional access options:

- [Log in](#)
- [Access through your institution](#)
- [Learn about institutional subscriptions](#)

Fig. 1: Most oesophageal tumours are lost over time.

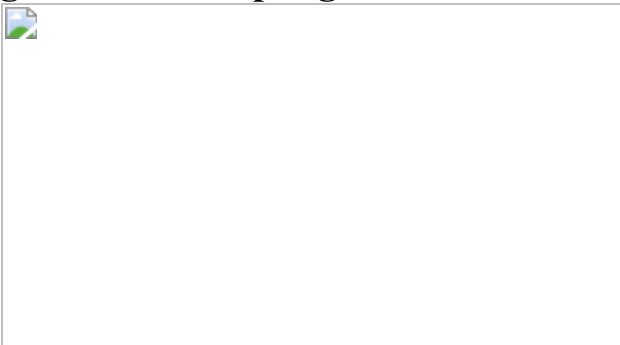


Fig. 2: Sequencing of tumours and adjacent normal tissue.

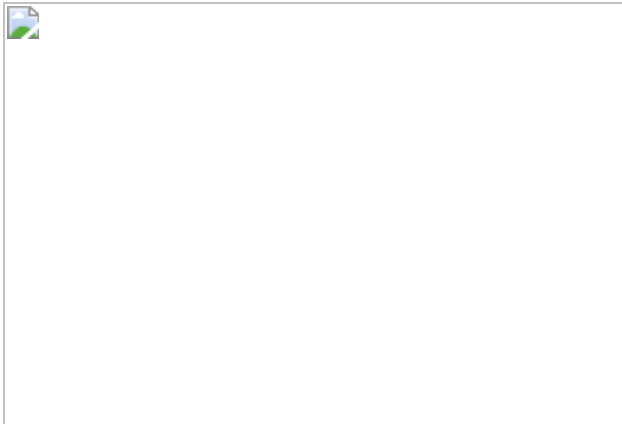
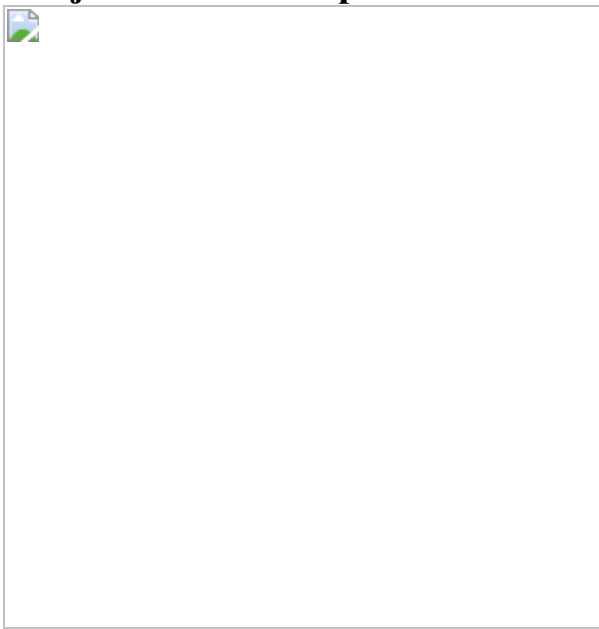


Fig. 3: Elimination of early tumours by expansion of mutant clones in the adjacent normal epithelium.



Data availability

Individual datasets are available in Supplementary Tables 1–11. The targeted DNA sequences from 10-day normal tissue and 10-day and 1-year tumours are available from the European Nucleotide Archive under accession [ERP022921](#). Whole-exome sequences and whole-genome sequences of tumours are available from the European Nucleotide Archive under accessions [ERP015469](#) and [ERP122780](#), respectively. [Source data](#) are provided with this paper.

Code availability

Code is available at https://github.com/michaelhall28/Colom_lesions.

References

1. 1.

Lee-Six, H. et al. The landscape of somatic mutation in normal colorectal epithelial cells. *Nature* **574**, 532–537 (2019).

2. 2.

Martincorena, I. et al. Somatic mutant clones colonize the human esophagus with age. *Science* **362**, 911–917 (2018).

3. 3.

Martincorena, I. et al. High burden and pervasive positive selection of somatic mutations in normal human skin. *Science* **348**, 880–886 (2015).

4. 4.

Suda, K. et al. Clonal expansion and diversification of cancer-associated mutations in endometriosis and normal endometrium. *Cell Rep.* **24**, 1777–1789 (2018).

5. 5.

Yokoyama, A. et al. Age-related remodelling of oesophageal epithelia by mutated cancer drivers. *Nature* **565**, 312–317 (2019).

6. 6.

Moore, L. et al. The mutational landscape of normal human endometrial epithelium. *Nature* **580**, 640–646 (2020).

7. 7.

Yoshida, K. et al. Tobacco smoking and somatic mutations in human bronchial epithelium. *Nature* **578**, 266–272 (2020).

8. 8.

Fowler, J. C. et al. Selection of oncogenic mutant clones in normal human skin varies with body site. *Cancer Discov.* **11**, 340–361 (2021).

9. 9.

Lawson, A. R. J. et al. Extensive heterogeneity in somatic mutation and selection in the human bladder. *Science* **370**, 75–82 (2020).

10. 10.

Vermeulen, L. et al. Defining stem cell dynamics in models of intestinal tumor initiation. *Science* **342**, 995–998 (2013).

11. 11.

Alcolea, M. P. et al. Differentiation imbalance in single oesophageal progenitor cells causes clonal immortalization and field change. *Nat. Cell Biol.* **16**, 615–622 (2014).

12. 12.

Fernandez-Antoran, D. et al. Outcompeting p53-mutant cells in the normal esophagus by redox manipulation. *Cell Stem Cell* **25**, 329–341 (2019).

13. 13.

Colom, B. et al. Spatial competition shapes the dynamic mutational landscape of normal esophageal epithelium. *Nat. Genet.* **52**, 604–614 (2020).

14. 14.

Murai, K. et al. Epidermal tissue adapts to restrain progenitors carrying clonal p53 mutations. *Cell Stem Cell* **23**, 687–699.e688 (2018).

15. 15.

Doupe, D. P. et al. A single progenitor population switches behavior to maintain and repair esophageal epithelium. *Science* **337**, 1091–1093 (2012).

16. 16.

Piedrafita, G. et al. A single-progenitor model as the unifying paradigm of epidermal and esophageal epithelial maintenance in mice. *Nat. Commun.* **11**, 1429 (2020).

17. 17.

Frede, J., Greulich, P., Nagy, T., Simons, B. D. & Jones, P. H. A single dividing cell population with imbalanced fate drives oesophageal tumour growth. *Nat. Cell Biol.* **18**, 967–978 (2016).

18. 18.

Nair, R. R. et al. A role for keratin 17 during DNA damage response and tumor initiation. *Proc. Natl Acad. Sci. USA* **118**, e2020150118 (2021).

19. 19.

Hobbs, R. P. et al. Keratin-dependent regulation of Aire and gene expression in skin tumor keratinocytes. *Nat. Genet.* **47**, 933–938 (2015).

20. 20.

Liu, Z. et al. Keratin 17 activates AKT signalling and induces epithelial-mesenchymal transition in oesophageal squamous cell carcinoma. *J. Proteomics* **211**, 103557 (2020).

21. 21.

Narushima, K. et al. Establishment of a DEN-induced mouse model of esophageal squamous cell carcinoma metastasis. *Esophagus* **14**, 131–137 (2017).

22. 22.

Rubio, C. A., Liu, F. S., Cheifec, G. & Sveander, M. The induction of esophageal tumors in mice: dose and time dependency. *In Vivo* **1**, 35–38 (1987).

23. 23.

McGranahan, N. & Swanton, C. Clonal heterogeneity and tumor evolution: past, present, and the future. *Cell* **168**, 613–628 (2017).

24. 24.

Greaves, M. & Maley, C. C. Clonal evolution in cancer. *Nature* **481**, 306–313 (2012).

25. 25.

Hall, M. W. J., Jones, P. H. & Hall, B. A. Relating evolutionary selection and mutant clonal dynamics in normal epithelia. *J. R. Soc. Interface* **16**, 20190230 (2019).

26. 26.

Martincorena, I. et al. Universal patterns of selection in cancer and somatic tissues. *Cell* **171**, 1029–1041.e1021 (2017).

27. 27.

Martincorena, I., Jones, P. H. & Campbell, P. J. Constrained positive selection on cancer mutations in normal skin. *Proc. Natl Acad. Sci. USA* **113**, E1128–E1129 (2016).

28. 28.

Prasad, V. et al. Haploinsufficiency of *Atp2a2*, encoding the sarco(endo)plasmic reticulum Ca^{2+} -ATPase isoform 2 Ca^{2+} pump, predisposes mice to squamous cell tumors via a novel mode of cancer susceptibility. *Cancer Res.* **65**, 8655–8661 (2005).

29. 29.

Liu, L. H., Boivin, G. P., Prasad, V., Periasamy, M. & Shull, G. E. Squamous cell tumors in mice heterozygous for a null allele of *Atp2a2*, encoding the sarco(endo)plasmic reticulum Ca^{2+} -ATPase isoform 2 Ca^{2+} pump. *J. Biol. Chem.* **276**, 26737–26740 (2001).

30. 30.

Tumbar, T. et al. Defining the epithelial stem cell niche in skin. *Science* **303**, 359–363 (2004).

31. 31.

Brown, S. et al. Correction of aberrant growth preserves tissue homeostasis. *Nature* **548**, 334–337 (2017).

32. 32.

Kon, S. et al. Cell competition with normal epithelial cells promotes apical extrusion of transformed cells through metabolic changes. *Nat. Cell Biol.* **19**, 530–541 (2017).

33. 33.

Shultz, L. D. et al. Human lymphoid and myeloid cell development in NOD/LtSz-scid *IL2R γ ^{null}* mice engrafted with mobilized human hemopoietic stem cells. *J. Immunol.* **174**, 6477–6489 (2005).

34. 34.

Ellis, P. et al. Reliable detection of somatic mutations in solid tissues by laser-capture microdissection and low-input DNA sequencing. *Nat. Protoc.* **16**, 841–871 (2021).

35. 35.

Li, H. Aligning sequence reads, clone sequences and assembly contigs with BWA-MEM. Preprint at <https://arxiv.org/abs/1303.3997> (2013).

36. 36.

Gerstung, M., Papaemmanuil, E. & Campbell, P. J. Subclonal variant calling with multiple samples and prior knowledge. *Bioinformatics* **30**, 1198–1204, (2014).

37. 37.

Alexandrov, L. B. et al. The repertoire of mutational signatures in human cancer. *Nature* **578**, 94–101 (2020).

38. 38.

Rosenthal, R., McGranahan, N., Herrero, J., Taylor, B. S. & Swanton, C. DeconstructSigs: delineating mutational processes in single tumors distinguishes DNA repair deficiencies and patterns of carcinoma evolution. *Genome Biol.* **17**, 31 (2016).

39. 39.

Jones, D. et al. cgPCaVEManWrapper: simple execution of CaVEMan in order to detect somatic single nucleotide variants in NGS data. *Curr. Protoc. Bioinformatics* **56**, 15.10.11–15.10.18 (2016).

40. 40.

Menzies, A. et al. VAGrENT: variation annotation generator. *Curr. Protoc. Bioinformatics* **52**, 15.18.11–15.18.11 (2015).

41. 41.

Scheinin, I. et al. DNA copy number analysis of fresh and formalin-fixed specimens by shallow whole-genome sequencing with identification and exclusion of problematic regions in the genome assembly. *Genome Res.* **24**, 2022–2032 (2014).

42. 42.

Kuilman, T. et al. CopywriteR: DNA copy number detection from off-target sequence data. *Genome Biol.* **16**, 49 (2015).

43. 43.

Nik-Zainal, S. et al. Mutational processes molding the genomes of 21 breast cancers. *Cell* **149**, 979–993 (2012).

44. 44.

Toni, T., Welch, D., Strelkowa, N., Ipsen, A. & Stumpf, M. P. Approximate Bayesian computation scheme for parameter inference and model selection in dynamical systems. *J. R. Soc. Interface* **6**, 187–202 (2009).

45. 45.

Klinger, E., Rickert, D. & Hasenauer, J. pyABC: distributed, likelihood-free inference. *Bioinformatics* **34**, 3591–3593 (2018).

Acknowledgements

We thank E. Choolun, T. Metcalf and staff at the MRC ARES and Sanger RSF animal facilities for technical support. This work was supported by grants from the Wellcome Trust to the Wellcome Sanger Institute (098051 and 296194) and Cancer Research UK Programme Grants to P.H.J. (C609/A17257 and C609/A27326). B.A.H. and M.W.J.H. are supported by the Medical Research Council (Grant-in-Aid to the MRC Cancer unit grant number MC_UU_12022/9 and NIRG to B.A.H., grant number MR/S000216/1). A.H. benefited from the award of an EMBO long term fellowship. M.W.J.H. acknowledges support from the Harrison Watson

Fund at Clare College, Cambridge. B.A.H. acknowledges support from the Royal Society (grant no. UF130039). S.C.D. benefited from the award of an ESPOD fellowship, 2018-21, from the Wellcome Sanger Institute and the European Bioinformatics Institute EMBL-EBI. K.T.M. benefited from the support of the Chan Zuckerberg Initiative. We thank B. Mahler-Araujo and the MRC Metabolic Diseases Unit (MC_UU_00014/5) for the histological analysis of tumour samples. We are grateful to the Cambridge Biorepository for Translational Medicine for access to human tissue. The authors acknowledge the use and/or adaption of diagrams from Servier Medical Art (<https://smart.servier.com>).

Author information

Author notes

1. D. Fernandez-Antoran

Present address: Wellcome Trust–Cancer Research UK Gurdon Institute, University of Cambridge, Cambridge, UK

Affiliations

1. Wellcome Sanger Institute, Hinxton, UK

B. Colom, A. Herms, M. W. J. Hall, S. C. Dentro, C. King, R. K. Sood, G. Piedrafita, D. Fernandez-Antoran, S. H. Ong, J. C. Fowler & P. H. Jones

2. MRC Cancer Unit, University of Cambridge, Hutchison–MRC Research Centre, Cambridge, UK

M. W. J. Hall & P. H. Jones

3. European Molecular Biology Laboratory, European Bioinformatics Institute, Cambridge, UK

S. C. Dentro & M. Gerstung

4. Wellcome-MRC Cambridge Stem Cell Institute, Jeffrey Cheah Biomedical Centre, Cambridge Biomedical Campus, University of Cambridge, Cambridge, UK

M. P. Alcolea

5. Department of Oncology, University of Cambridge, Hutchison–MRC Research Centre, Cambridge, UK

M. P. Alcolea

6. Spanish National Cancer Research Centre (CNIO), Madrid, Spain

G. Piedrafita

7. Department of Surgery and Cambridge NIHR Biomedical Research Centre, Cambridge, UK

K. T. Mahbubani & K. Saeb-Parsy

8. European Molecular Biology Laboratory, Genome Biology Unit, Heidelberg, Germany

M. Gerstung

9. Department of Medical Physics and Biomedical Engineering, University College London, London, United Kingdom

B. A. Hall

Contributions

B.C. and M.P.A. designed experiments. B.C. performed the majority of experiments and data analysis. A.H. and M.P.A. contributed to mouse sample collection and performed preliminary experiments. M.W.J.H. conducted permutation analysis of leukocyte location. G.P. performed initial analysis of immune cell location in tumours and normal areas. D.F.-A. analysed human oesophageal samples. B.C., M.W.J.H., C.K., R.K.S. and

S.H.O. analysed sequencing data. S.C.D. analysed chromosomal copy number alterations under the supervision of M.G. M.W.J.H. developed the mathematical modelling under the supervision of B.A.H. K.T.M., K.S.-P. and J.C.F. collected human samples. B.C., M.W.J.H. and P.H.J. wrote the paper. P.H.J. supervised the research.

Corresponding author

Correspondence to P. H. Jones.

Ethics declarations

Competing interests

The authors declare no competing interests.

Additional information

Peer review information *Nature* thanks Francesca Ciccarelli, James DeGregori and the other, anonymous, reviewer(s) for their contribution to the peer review of this work. Peer reviewer reports are available.

Publisher's note Springer Nature remains neutral with regard to jurisdictional claims in published maps and institutional affiliations.

Extended data figures and tables

[Extended Data Fig. 1 Architecture and dynamics of murine esophageal epithelium.](#)

(a) H&E images and schematic of the mouse esophageal epithelium architecture and dynamics; b = basal cell layer (delineated by white dots), sb = suprabasal layers, str = stroma. Scale-bars: 500 μ m (left image), 50 μ m (inset). Dividing (progenitor) cells are confined to the basal layer. Differentiating cells exit the cell cycle, migrate out of the basal layer,

through the suprabasal layers, and are finally shed into the lumen. (**b–c**) The single progenitor model (see [Supplementary Note](#)). All progenitor cells in the basal layer are functionally equivalent and following division produce either: two progenitors that will persist in the tissue, two differentiating cells that will cease division, stratify and be lost, or one cell of each type. In homeostasis (**b**), the likelihood of the two progenitor and two differentiating cell outcomes is equal. Mutations (**c**) may tip the balance towards a non-neutral behavior, resulting in clonal growth if they favor proliferation of daughter cells. (**d**) Expansion of mutant clones is defined by their relative competitive fitness to adjacent clones. Initially, a fit “winner” mutant progenitor (colored) shows a fate bias towards proliferation and outcompetes its less fit “loser” surrounding cells, resulting in clonal expansion. Eventually, mutant clones begin to collide with each other until surrounded by similarly competitive mutants, at which point their cell fate reverts towards balance and their expansion slows (see [Supplementary Note](#)).

Extended Data Fig. 2 Characterization of Diethyl Nitrosamine (DEN) generated tumors.

(**a, b**) Confocal images of esophagus collected 10 days post-DEN treatment and stained with Dapi and KRT6. Images show top-down (**a, b**) and lateral (**b**) projections and illustrate typical morphological features and expression of KRT6 in tumors (arrowheads) and normal surrounding epithelium. (**c**) Quantification of the mean fluorescence intensity of KRT6 and Dapi in 10 days post-DEN tumors and the adjacent normal epithelium, measured from the images as shown. Two-sided Mann-Whitney test, $n = 48$ tumors from 3 mice. (**d**) Percentage of tumors positive for KRT6 staining. The number of tumors analyzed for each time point is shown between brackets. (**e**) Confocal images of 10-days and 12-months post-DEN tumors showing increased expression of KRT17 (green). Images are representative of 31 and 29 tumors, from 3 and 7 mice, respectively. (**f**) H&E images of esophageal tumors (bottom images) and normal epithelium (top images) from tissues collected at the indicated time points post-DEN treatment. (**g**) Percentage of angiogenic tumors at the indicated time points post-DEN treatment. The number of tumors analyzed at each time point is shown in brackets. (**h, i**) Projected top-down and lateral confocal images of 10 day (**h**) and 9 months

(i) post-DEN tumors immuno-stained for the endothelial cell marker CD31 and KRT6. Images are representative of 18 and 6 tumors, respectively. Scale-bars for panels (a–c), (e–f) and (h–i) are 50 μ m.

[Source data](#)

Extended Data Fig. 3 Collection of 10-day and 1-year esophageal tumors.

(a–b) Mouse esophagus was collected 10-days (**a**) or 1-year (**b**) post-DEN treatment. The esophagus was cut open longitudinally and the epithelium separated from the underlying muscle and stroma. The epithelium was flattened, fixed, stained with KRT6 (grey), mounted and 3D-imaged on a confocal microscope. Tumors were identified from the processed images and manually dissected under a fluorescent microscope and sequenced (see [Methods](#)).

Extended Data Fig. 4 Targeted sequencing of 10 days and 1 year tumors.

(a) Protocol: wild-type mice were treated with DEN for two months and the esophageal tumors collected 10-days or 1-year later. Tumors were then sequenced with a targeted approach (192 gene panel). **(b)** Area of 10-day and 1-year post-DEN tumors ($n = 89$ and 64 tumors from 2 and 9 mice, respectively). Lines show mean \pm s.e.m. **(c)** Mutational spectrum of 10-day and 1-year tumors. The bar plots illustrate the number of mutations in each of the 96 possible trinucleotides. The mutational spectrum of individual tumors is shown in **(d)**. **(e–f)** Percentage of silent, missense, nonsense and splice mutations and indels identified in 10-day or 1-year tumors. Graphs show the values for individual tumors (**e**, each column is a tumor), or the average for all tumors at each time point (**f**). **(g)** Maximum VAF for mutations identified in each tumor at 10 days or 1 year post-DEN ($n = 80$ and 63 tumors, respectively). Colored shadow illustrates VAF > 0.35 , as an estimation for clonality. **(h)** Number of positively selected mutant genes in tumors at 10 days or 1 year post-DEN treatment ($n = 80$ and 63 tumors, respectively). Lines show mean \pm s.e.m (two-tailed Mann-Whitney test). **(i)** Number and type of mutations in the positively selected genes identified by

dN/dS analysis from 10-day or 1-year tumors. (j) Proportion of 10-day and 1-year tumors carrying nonsynonymous mutations in the indicated genes.

[Source data](#)

Extended Data Fig. 5 Whole exome sequencing, whole genome sequencing, and chromosomal alteration of surviving tumors.

(a) Wild-type mice received DEN for two months and the esophagus was collected 9 or 18 months after treatment (n=49 tumors from 16 mice). Tissues were stained for Dapi (blue) and KRT6 (red) and confocal imaged to identify tumors. Scale-bars=2mm (main), 150 μ m (inset). Individual tumors were manually cut under a fluorescent microscope, digested and separated in triplicates. Each triplicate was whole genome amplified (WGA) and whole exome sequenced. To exclude artefactual SNVs generated during WGA, only mutations shared by all three amplified triplicates were considered for further analysis. A total of 32,736 mutations, including silent, missense, nonsense and splice mutations and indels were identified. (b) Cumulative sequencing coverage of the whole exome triplicate samples. (c) Number of synonymous and non-synonymous mutations per tumor, ranked by mutation burden. (d) Distribution of the variant allele fraction (VAF) for the mutations common within triplicates in each tumor. (e) Percentage of silent, missense, nonsense and splice mutations and indels for individual tumors and for all tumors combined. (f) Mutational spectrum of tumors. The bar plots illustrate the percentage of mutations in each of the 96 possible trinucleotides. (g) dN/dS ratios for missense and truncating (nonsense + essential splice site) substitutions indicating genes under significant positive selection in the tumors ($q < 0.05$, calculated with R package dNdScv²⁶). (h) Analysis of chromosomal copy number alterations (CNAs) by whole genome sequencing of 1-year post-DEN tumors (n=64 tumors from 9 mice). Only 2 tumors, MD5924e and MD5928e, exhibited CNAs. (i) Summary of chromosomal alterations found by whole exome sequencing data of 9 or 18 months post-DEN tumors (n=49 tumors from 16 mice). Only alterations present in all 3 whole genome amplified triplicates (j) were considered valid calls. 8140nT2 (top) is a representative example of a tumor without chromosomal alterations. 2 tumors, n2T1 and n34_T1, showed small alterations.

Source data

Extended Data Fig. 6 Early tumors are not eliminated by tumor cell apoptosis, abnormal proliferation or the immune system.

(a) Representative confocal image of a 10-day post-DEN esophageal epithelium immuno-stained for activated Caspase 3⁺ (Yellow) and KRT6 (red). No apoptotic cells were detected in the tumors (arrowhead) ($n = 23$ tumors, 2 mice). Scale-bar: 20 μ m. **(b)** Protocol: wild-type mice were treated with DEN for two months and the tissues collected ten days later. Mice received EdU 1h before tissue collection. **(c)** Representative confocal images showing EdU incorporation (1h pulse) in tumors (dotted line) and the surrounding normal epithelium ($n = 22$ tumors, 3 mice). Scale-bars: 20 μ m. **(d)** *In vivo* label-retaining assay using *Rosa26^{M2rtTA}/TetO-HGFP* transgenic mice to measure the rate of progenitor cell division (see [Methods](#)). **(e)** Protocol: *Rosa26^{M2rtTA}/TetO-HGFP* mice received DEN for one month followed by DEN+Doxo for another month. Tissues were collected at times 0, 10 and 30 days after Doxy/DEN withdrawal. **(f–g)** Representative confocal images (**f**) and quantification (**g**) of the histone-green fluorescent protein (H2BGFP) intensity in esophageal tumors (dotted lines) and the surrounding normal epithelium at the indicated time points post-Doxy withdrawal. Scale bars: 50 μ m. Graph shows median (central box line), 25th–75th percentiles (box) and 5th–95th percentiles (whiskers). Two-tailed Mann-Whitney test ($n = 10$ images per group). **(h)** Confocal images depicting CD45⁺ (immune) cells (green) within a 10-days post-DEN tumor (white dotted line) and its adjacent normal epithelium. **(i–j)** Correlation between the size of tumors and the number of CD45⁺ cells within them (**i**) and the number of CD45⁺ cells in the tumor and the normal epithelium (**j**). Lines show the two-tailed Pearson correlations: $R^2=0.5039$ (**i**), and $R^2=0.1464$ (**j**), with 95% confidence interval (dotted lines). **(k)** Number of CD45⁺ cells per area of tumor or normal esophageal epithelium at 10- or 30-days post-DEN treatment. Graph shows median (central box line), 25th–75th percentiles (box), 5th–95th percentiles (whiskers) and outliers (dots). Two tailed Wilcoxon matched-pairs test, $n = 53$ and 50 images, respectively. **(l)** Permutation analysis of leukocyte location within tumors, based on the

experimental measurements obtained from (**h**). For each image, the location of CD45⁺ cells (black dots) was left intact while the location of the tumor (colored circles) was randomly shuffled (blue shows original location, red shows shuffled “phantom” tumors), and the number of immune cells in contact with the tumor was counted. This was repeated 1000 times to produce the expected distribution. (**m**) Calculated (within the original location) vs. experimentally observed number of CD45⁺ cells in 10- or 30-days post-DEN tumors. (**n**) Distribution of the average number of CD45⁺ cells in 10- or 30-days post-DEN tumors, obtained from the permutation analysis in (**l**). Red dotted line shows the experimentally observed average number of CD45⁺ cells within tumors at the indicated time-points. Statistics are two-tailed permutation tests ([Methods](#)). (**o**) Protocol: Wild-type and immunocompromised NOD Cg-Prkdcscid Il2rgtm1Wjl SzJ (Scid-NOD-IL2r) mice were treated with DEN for two months and the tissues collected 10 or 30 days post-DEN withdrawal. (**p**) Tumor density in mice collected 10-days ($n = 4$) or 30-days ($n = 5$ and 4, respectively) post-DEN treatment. Mean \pm s.e.m (two-tailed Mann-Whitney test).

[Source data](#)

[**Extended Data Fig. 7 Mutational landscape of normal esophageal epithelium at 10 days post-DEN treatment.**](#)

(**a**) Protocol: wild-type mice were treated for two months with DEN. 10 days after DEN withdrawal, normal epithelial samples matching the size of the tumors (Extended Data Fig. [4b](#)) were collected and sequenced with a targeted approach (192 gene panel). (**b**) Number of mutations per sample, including essential splice, frameshift, missense, nonsense and silent mutations ($n = 81$ samples from 2 mice). (**c**) Percentage of mutation types identified in normal epithelium and tumors collected 10 days post-DEN treatment. (**d**) Mutational spectrum of 10-day post-DEN tumors and normal epithelium. The bar plots illustrate the number of mutations in each of the 96 possible trinucleotides. (**e**) Dots show the value of the mutation with maximum VAF identified in each sample ($n = 81$ samples). Lines are mean \pm s.e.m. (**f**) dN/dS ratios for missense and truncating (nonsense + essential splice site) mutations of positively selected genes (dN/dS >1) (only

significant genes are shown, $q < 0.05$ calculated with R package dNdScv²⁶). (g) Number and type of mutations in the positively selected genes identified by dN/dS. (h) Estimated percentage of 10 days post-DEN normal epithelium carrying non-synonymous mutations in the positively selected genes. Range indicates upper and lower bound estimates.

Source data

Extended Data Fig. 8 Expansion of highly competitive clones in normal tissue eliminates early tumors.

(a) Cartoon illustrating the elimination of tumors due to competition with the highly competitive *DN-Maml1* clones. Following the generation of tumors by DEN treatment, *DN-Maml1* clones are induced by BNF and TAM injections. As *DN-Maml1* clones in the normal epithelium expand they eliminate less fit tumors. (b) Qualitative representation of tumor dynamics following *DN-Maml1* induction as compared to non-induced controls (see [Supplementary Note](#)). (c) *In vivo* genetic lineage tracing using *Ahcre^{ERT}/R26^{DNM-GFP/wt}* reporter mice. Upon injection of the drugs tamoxifen (TAM) and β-naphthoflavone (BNF), *Cre*-mediated recombination results in the heritable expression of the highly competitive dominant negative allele of *Maml1* fused to GFP fluorescent protein (*DN-Maml1*), which will then be expressed in all the progeny of the single marked cells, generating clusters of labelled mutant clones. (d) Confocal image (representative of 9 mice) of a DEN-treated *Ahcre^{ERT}/R26^{DNM-GFP/wt}* mouse whole esophageal epithelium, depicting *DN-Maml1* clones (green). Mice were induced ten days after DEN withdrawal and esophagus collected twenty days later (as in Fig. [3b](#)). Scale-bar: 2 mm. (e) Percentage of epithelium covered by *DN-Maml1* clones in induced and non-induced (control) mice ($n = 9$ and 7 mice, respectively). Error-bars are mean ± s.e.m (two-tailed Mann-Whitney test). (f) Number of tumors per mm^2 of esophageal epithelium in control non-induced ($n = 7$) and induced ($n=9$) *Ahcre^{ERT}/R26^{DNM-GFP/wt}* mice. Data for the induced mice is show as the number of tumors per mm^2 of whole tissue area and per mm^2 of area not covered by *DN-Maml1* clones (*DN-Maml1*⁻ area). Error-bars are mean±s.e.m. (two-sided Mann-Whitney test). (g) Correlation between the

area covered by *DN-Mam1* clones and the number of tumors in induced and non-induced *Ahcre^{ERT}/R26^{DNM-GFP/wt}* mice. Line shows the Pearson correlation (two-tailed, $R^2 = 0.7526$) with 95% confidence interval (dotted lines). Inset shows the correlation of the induced mice only ($R^2 = 0.4577$).

[Source data](#)

Extended Data Fig. 9 Spatial interaction between mutant clones in mutagenized normal epithelium and tumors.

(a) Confocal images and cartoons of esophageal epithelium from *Ahcre^{ERT}/R26^{DNM-GFP/wt}* mice treated with DEN for 2 months, induced 10-days post-DEN withdrawal and tissues collected 20-days later (as in Fig. 3b). The images show different categories of *DN-Mam1* clones (green) interacting with early tumors (red). **(b)** Percentage of tumors in each category. Number of tumors in each group is shown between brackets ($n = 386$ tumors from 9 mice). **(c)** Top-down confocal images depicting a *DN-Mam1* clone surrounding a tumor (see also Fig. 3e). A smaller tumor surface area at the base is consistent with a process of extrusion by the expanding *DN-Mam1* clone as illustrated in (g). **(d)** In vivo genetic lineage tracing using the multicolor confetti reporter allele in *R26cre^{ERT2}R26^{fConfetti}* mice. Injection of the drug tamoxifen (TAM), results in Cre-mediated inversion and excision recombination events in scattered single cells. This confers heritable expression of one of four fluorescent proteins (YFP, GFP, RFP or CFP) resulting in labelled clones. **(e)** Protocol:

R26cre^{ERT2}R26^{fConfetti} mice were induced with TAM to label Confetti clones, followed by 2-months DEN treatment. Esophagi were collected 10 days or 30 days after DEN withdrawal. **(f)** Confocal images of Confetti clones surrounding early tumors (KRT6, shown in red) in the categories 2-4 as in (a), suggesting that tumor extrusion events may also take place in mutagenized epithelium in the absence of *DN-Mam1* induced clones.

Images are representative of 13 tumors from 8 mice. **(g)** Cartoon illustrating a potential mechanism of tumor extrusion by expanding mutant clones in the normal epithelium. Once the tumor footprint in the basal layer is displaced by expanding mutant clones in the adjacent normal tissue, the tumor will be shed. Scale-bars in panels (a), (c) and (f) are 25 μ m.

Source data

Extended Data Fig. 10 Increasing competitive fitness throughout the epithelium slows down tumor loss. Human esophageal lesions.

(a) A stochastic drift model ([Supplementary Note](#)) fit to the observed number (mean \pm s.e.m) of tumors following DEN treatment. (b) Experimentally observed (black dots) and model predicted (dashed lines) % of tumors eliminated when highly fit mutant clones (such as DN-Maml1) are induced in esophageal epithelium following DEN-treatment. Dashed lines represent models where the induced mutant clones remove tumors they encounter (blue) or where tumor loss is independent of clones in the surrounding tissue (red) ([Supplementary Note](#)). (c) Cartoon illustrating the predicted effects of DBZ administration. When clones in the normal surrounding epithelium have a higher competitive fitness than the tumors, the probability that tumors will be eliminated from the tissue may be higher (left) than when administration of DBZ levels the competition between the clones and tumors (right). (d) Qualitative representation of tumor dynamics following DBZ vs. control treatment. (e) Protocol: wild-type mice were treated with DEN for two months. Ten days post-DEN withdrawal mice received DBZ or vehicle control. Tissues were harvested two weeks later. (f–g) Experimental (f) and simulated (g, [Supplementary Note](#)) tumors per mm² of esophageal epithelium in DBZ and vehicle control treated mice ($n = 5$ mice/group). Lines in (f) are mean \pm s.e.m (two-tailed Mann-Whitney test). Black dots in (g) show experimental data. (h–i) Numerical example (see [Supplementary Note](#)) of the model showing increased proportion of tumors resistant to displacement by mutant clones (h) and the decrease in tumor density following DEN-treatment (i). Experimental data depicts mean \pm s.e.m. (j) Images of human (top) and mouse (bottom) esophagus. Dotted lines delineate lesions. (k) Confocal images of human normal (top) and neoplastic (bottom) esophageal epithelium stained with KRT6 (red) and Topro3 (nuclei, blue). Scale-bars: 100 μ m. Simulations in (a, g, h and i) show the mean and range between the minimum-maximum outputs of the model run with the accepted parameters from Approximate Bayesian Computation ([Methods](#)).

[Source data](#)

Supplementary information

[Supplementary Note](#)

This document sets out the theory and mathematical modelling of tumour dynamics in Sections 1–7. Section 1 discusses previous results on the growth and competition of mutant clones in normal oesophageal epithelium. Section 2 describes a previously proposed stochastic model of tumour dynamics. Section 3 describes the elimination of tumours by highly competitive mutant clones in the surrounding normal epithelium. Section 4 shows how reducing the competitive imbalance between tumours and highly fit mutant clones in the normal tissue affects tumour survival. Section 5 describes the selection pressure on tumours from competition with surrounding clones in the normal epithelium. In Section 6, we substitute simple mathematical equations into the model to numerically illustrate the principles described in the previous sections. Section 7 is a summary of our conclusions.

[Reporting Summary](#)

[Peer Review File](#)

[Supplementary Tables](#)

This file contains Supplementary Tables 1–11. Supplementary Table 1 lists the area (in μm^2) and number of tumours measured at different time points after DEN treatment. Supplementary Table 2 displays the targeted sequencing data of isolated tumours from 10-day post-DEN-treated mouse oesophageal epithelium. Supplementary Table 3 displays the targeted sequencing data of isolated tumours from 1-year post-DEN-treated mouse oesophageal epithelium. Supplementary Table 4 shows the dN/dS results from targeted sequencing data of isolated tumours from 10-day post-DEN-treated mouse oesophageal epithelium. Supplementary Table 5 shows the dN/dS results from targeted sequencing data of isolated tumours from 1-

year post-DEN-treated mouse oesophageal epithelium. Supplementary Table 6 shows the whole-exome sequencing results of 9- and 18-month post-DEN tumours. Supplementary Table 7 displays the dN/dS results for whole-exome sequencing of 9- and 18-month post-DEN tumours. Supplementary Table 8 displays the HGFP mean intensity in tumours and surrounding normal oesophageal epithelium. Supplementary Table 9 shows the targeted sequencing data of normal oesophageal epithelium from 10-day post-DEN-treated mice. Supplementary Table 10 displays the dN/dS results from targeted sequencing data of normal oesophageal epithelium from 10-day post-DEN-treated mice. Supplementary Table 11 lists the parameters for the mathematical model.

Supplementary Video 1

The video illustrates the mouse oesophageal epithelium at 1 month post-DEN treatment. The video initially shows the entire tissue before zooming in on a tumour.

Supplementary Video 2

The video shows small capillary circling a tumour in the mouse oesophageal epithelium collected 10 days post-DEN treatment, illustrating the early steps of angiogenesis.

Supplementary Video 3

The video shows a developed vasculature surrounding an established tumour in the mouse oesophageal epithelium, collected 9 months post-DEN treatment.

Source data

Source Data Fig. 1

Source Data Fig. 2

[**Source Data Fig. 3**](#)

[**Source Data Extended Data Fig. 2**](#)

[**Source Data Extended Data Fig. 4**](#)

[**Source Data Extended Data Fig. 5**](#)

[**Source Data Extended Data Fig. 6**](#)

[**Source Data Extended Data Fig. 7**](#)

[**Source Data Extended Data Fig. 8**](#)

[**Source Data Extended Data Fig. 9**](#)

[**Source Data Extended Data Fig. 10**](#)

Rights and permissions

[Reprints and Permissions](#)

About this article

Cite this article

Colom, B., Herms, A., Hall, M.W.J. *et al.* Mutant clones in normal epithelium outcompete and eliminate emerging tumours. *Nature* **598**, 510–514 (2021). <https://doi.org/10.1038/s41586-021-03965-7>

- Received: 03 August 2020
- Accepted: 26 August 2021
- Published: 13 October 2021

- Issue Date: 21 October 2021
- DOI: <https://doi.org/10.1038/s41586-021-03965-7>

Share this article

Anyone you share the following link with will be able to read this content:

[Get shareable link](#)

Sorry, a shareable link is not currently available for this article.

[Copy to clipboard](#)

Provided by the Springer Nature SharedIt content-sharing initiative

This article was downloaded by **calibre** from <https://www.nature.com/articles/s41586-021-03965-7>

| [Section menu](#) | [Main menu](#) |

- Article
- [Published: 29 September 2021](#)

Mechanism for Cas4-assisted directional spacer acquisition in CRISPR–Cas

- [Chunyi Hu¹](#) ✉nal,
- [Cristóbal Almendros^{2,3}](#) ✉nal,
- [Ki Hyun Nam](#) [ORCID: orcid.org/0000-0003-3268-354X⁴](#),
- [Ana Rita Costa](#) [ORCID: orcid.org/0000-0001-6749-6408^{2,3}](#),
- [Jochem N. A. Vink^{2,3}](#),
- [Anna C. Haagsma^{2,3}](#),
- [Saket R. Bagde¹](#),
- [Stan J. J. Brouns](#) [ORCID: orcid.org/0000-0002-9573-1724^{2,3}](#) &
- [Ailong Ke](#) [ORCID: orcid.org/0000-0001-5957-7822¹](#)

[Nature](#) volume **598**, pages 515–520 (2021)

- 4097 Accesses
- 38 Altmetric
- [Metrics details](#)

Subjects

- [Bacteriology](#)
- [Cryoelectron microscopy](#)
- [DNA metabolism](#)
- [Multienzyme complexes](#)

Abstract

Prokaryotes adapt to challenges from mobile genetic elements by integrating spacers derived from foreign DNA in the CRISPR array¹. Spacer insertion is carried out by the Cas1–Cas2 integrase complex^{2,3,4}. A substantial fraction of CRISPR–Cas systems use a Fe–S cluster containing Cas4 nuclease to ensure that spacers are acquired from DNA flanked by a protospacer adjacent motif (PAM)^{5,6} and inserted into the CRISPR array unidirectionally, so that the transcribed CRISPR RNA can guide target searching in a PAM-dependent manner. Here we provide a high-resolution mechanistic explanation for the Cas4-assisted PAM selection, spacer biogenesis and directional integration by type I-G CRISPR in *Geobacter sulfurreducens*, in which Cas4 is naturally fused with Cas1, forming Cas4/Cas1. During biogenesis, only DNA duplexes possessing a PAM-embedded 3'-overhang trigger Cas4/Cas1–Cas2 assembly. During this process, the PAM overhang is specifically recognized and sequestered, but is not cleaved by Cas4. This ‘molecular constipation’ prevents the PAM-side prespacer from participating in integration. Lacking such sequestration, the non-PAM overhang is trimmed by host nucleases and integrated to the leader-side CRISPR repeat. Half-integration subsequently triggers PAM cleavage and Cas4 dissociation, allowing spacer-side integration. Overall, the intricate molecular interaction between Cas4 and Cas1–Cas2 selects PAM-containing prespacers for integration and couples the timing of PAM processing with the stepwise integration to establish directionality.

Access options

Subscribe to Journal

Get full journal access for 1 year

\$199.00

only \$3.90 per issue

[Subscribe](#)

All prices are NET prices.
VAT will be added later in the checkout.
Tax calculation will be finalised during checkout.

Rent or Buy article

Get time limited or full article access on ReadCube.

from \$8.99

[Rent or Buy](#)

All prices are NET prices.

Additional access options:

- [Log in](#)
- [Access through your institution](#)
- [Learn about institutional subscriptions](#)

Fig. 1: PAM-spacer acquisition and the dual-PAM prespacer-bound GsCas4/Cas1–Cas2 structure.

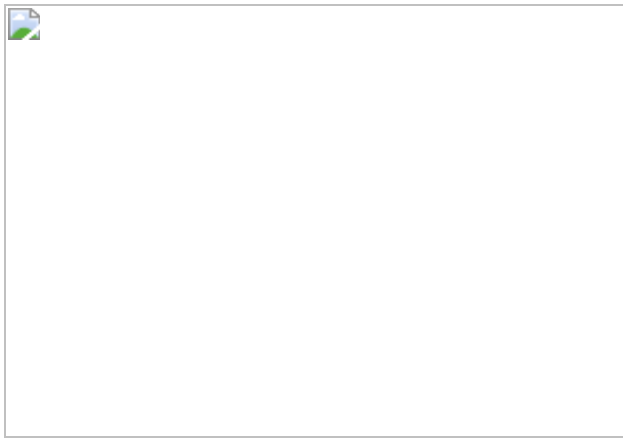


Fig. 2: Cas4-mediated PAM recognition delays overhang cleavage.

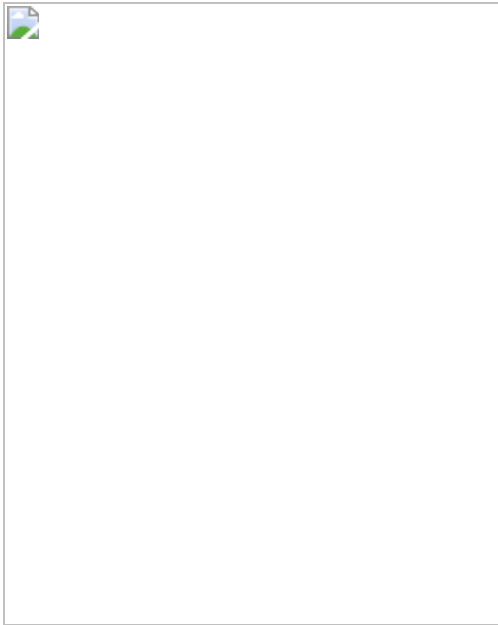


Fig. 3: Mechanistic insights from the single-PAM prespacer-bound GsCas4/Cas1–Cas2 structure.

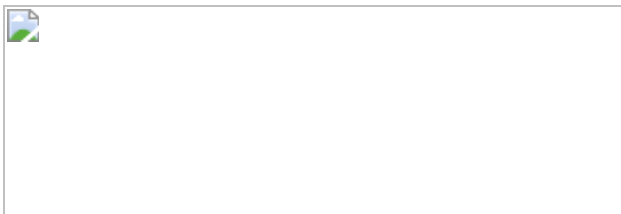
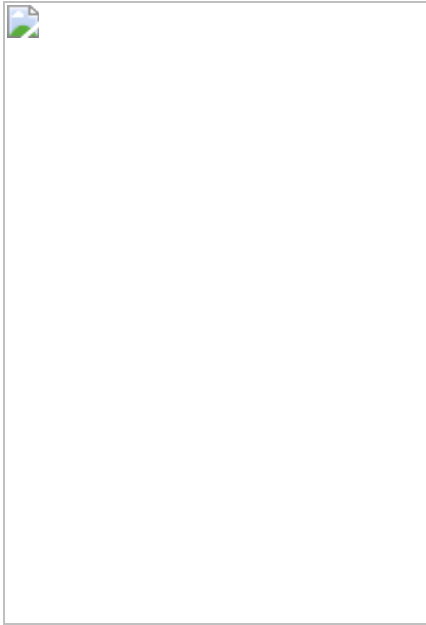


Fig. 4: Structural basis for integration-coupled PAM cleavage by Cas4.



Data availability

The cryo-EM density maps that support the findings of this study have been deposited in the Electron Microscopy Data Bank (EMDB) under accession numbers [EMD-23839](#) (PAM/PAM prespacer bound), [EMD-23840](#) (PAM/non-PAM prespacer bound), [EMD-23843](#) (full-integration complex), [EMD-23845](#) (half-integration complex, Cas4 still blocking the PAM side), [EMD-23849](#) (half-integration complex, Cas4 dissociated) and [EMD-23847](#) (sub-complex). The coordinates have been deposited in the Protein Data Bank (PDB) under accession numbers [7MI4](#) (PAM/PAM prespacer-bound), [7MI5](#) (PAM/non-PAM prespacer-bound), [7MI9](#) (full integration), [7MIB](#) (half integration, Cas4 still blocking the PAM side), [7MID](#) (sub-complex). MiSeq sequencing data that support analysis of in vivo prespacer integration have been deposited in the European Nucleotide Archive (ENA) under accession number [PRJEB41616](#). Plasmids used in this study are available upon request.

References

1. 1.
Barrangou, R. et al. CRISPR provides acquired resistance against viruses in prokaryotes. *Science* **315**, 1709–1712 (2007).
2. 2.
Yosef, I., Goren, M. G. & Qimron, U. Proteins and DNA elements essential for the CRISPR adaptation process in *Escherichia coli*. *Nucleic Acids Res.* **40**, 5569–5576 (2012).
3. 3.
Nuñez, J. K. et al. Cas1–Cas2 complex formation mediates spacer acquisition during CRISPR–Cas adaptive immunity. *Nat. Struct. Mol. Biol.* **21**, 528–534 (2014).
4. 4.

Nuñez, J. K., Lee, A. S., Engelman, A. & Doudna, J. A. Integrase-mediated spacer acquisition during CRISPR–Cas adaptive immunity. *Nature* **519**, 193–198 (2015).

5. 5.

Mojica, F. J., Diez-Villasenor, C., Garcia-Martinez, J. & Almendros, C. Short motif sequences determine the targets of the prokaryotic CRISPR defence system. *Microbiology* **155**, 733–740 (2009).

6. 6.

Marraffini, L. A. & Sontheimer, E. J. Self versus non-self discrimination during CRISPR RNA-directed immunity. *Nature* **463**, 568–571 (2010).

7. 7.

Vink, J. N. A. et al. Direct visualization of native CRISPR target search in live bacteria reveals cascade DNA surveillance mechanism. *Mol. Cell* **77**, 39–50.e10 (2020).

8. 8.

Nuñez, J. K., Harrington, L. B., Kranzusch, P. J., Engelman, A. N. & Doudna, J. A. Foreign DNA capture during CRISPR–Cas adaptive immunity. *Nature* **527**, 535–538 (2015).

9. 9.

Wright, A. V. & Doudna, J. A. Protecting genome integrity during CRISPR immune adaptation. *Nat. Struct. Mol. Biol.* **23**, 876–883 (2016).

10. 10.

Wright, A. V. et al. Structures of the CRISPR genome integration complex. *Science* **357**, 1113–1118 (2017).

11. 11.

Budhathoki, J. B. et al. Real-time observation of CRISPR spacer acquisition by Cas1–Cas2 integrase. *Nat. Struct. Mol. Biol.* **27**, 489–499 (2020).

12. 12.

Xiao, Y., Ng, S., Nam, K. H. & Ke, A. How type II CRISPR-Cas establish immunity through Cas1–Cas2-mediated spacer integration. *Nature* **550**, 137–141 (2017).

13. 13.

Kim, S. et al. Selective loading and processing of prespacers for precise CRISPR adaptation. *Nature* **579**, 141–145 (2020).

14. 14.

Li, M., Wang, R., Zhao, D. & Xiang, H. Adaptation of the *Haloarcula hispanica* CRISPR–Cas system to a purified virus strictly requires a priming process. *Nucleic Acids Res.* **42**, 2483–2492 (2014).

15. 15.

Liu, T. et al. Coupling transcriptional activation of CRISPR-Cas system and DNA repair genes by Csa3a in *Sulfolobus islandicus*. *Nucleic Acids Res.* **45**, 8978–8992 (2017).

16. 16.

Shiimori, M., Garrett, S. C., Graveley, B. R. & Terns, M. P. Cas4 nucleases define the PAM, length, and orientation of DNA fragments integrated at CRISPR loci. *Mol. Cell* **70**, 814–824.e6 (2018).

17. 17.

Kieper, S. N. et al. Cas4 facilitates PAM-compatible spacer selection during CRISPR adaptation. *Cell Rep.* **22**, 3377–3384 (2018).

18. 18.

Almendros, C., Nobrega, F. L., McKenzie, R. E. & Brouns, S. J. J. Cas4–Cas1 fusions drive efficient PAM selection and control CRISPR adaptation. *Nucleic Acids Res.* **47**, 5223–5230 (2019).

19. 19.

Lemak, S. et al. Toroidal structure and DNA cleavage by the CRISPR-associated [4Fe-4S] cluster containing Cas4 nuclease SSO0001 from *Sulfolobus solfataricus*. *J. Am. Chem. Soc.* **135**, 17476–17487 (2013).

20. 20.

Lemak, S. et al. The CRISPR-associated Cas4 protein Pcal_0546 from *Pyrobaculum calidifontis* contains a [2Fe-2S] cluster: crystal structure and nuclease activity. *Nucleic Acids Res.* **42**, 11144–11155 (2014).

21. 21.

Zhang, J., Kasciukovic, T. & White, M. F. The CRISPR associated protein Cas4 is a 5' to 3' DNA exonuclease with an iron–sulfur cluster. *PLoS ONE* **7**, 0047232 (2012).

22. 22.

Lee, H., Dhingra, Y. & Sashital, D. G. The Cas4–Cas1–Cas2 complex mediates precise prespacer processing during CRISPR adaptation. *eLife* **8**, e44248 (2019).

23. 23.

Lee, H., Zhou, Y., Taylor, D. W. & Sashital, D. G. Cas4-dependent prespacer processing ensures high-fidelity programming of CRISPR arrays. *Mol. Cell* **70**, 48–59.e5 (2018).

24. 24.

Xiao, Y., Luo, M., Dolan, A. E., Liao, M. & Ke, A. Structure basis for RNA-guided DNA degradation by Cascade and Cas3. *Science* **361**, aat0839 (2018).

25. 25.

Shah, S. A., Erdmann, S., Mojica, F. J. & Garrett, R. A. Protospacer recognition motifs: mixed identities and functional diversity. *RNA Biol.* **10**, 891–899 (2013).

26. 26.

Jia, N. et al. Structures and single-molecule analysis of bacterial motor nuclease AdnAB illuminate the mechanism of DNA double-strand break resection. *Proc. Natl Acad. Sci. USA* **116**, 24507–24516 (2019).

27. 27.

Nuñez, J. K., Bai, L., Harrington, L. B., Hinder, T. L. & Doudna, J. A. CRISPR immunological memory requires a host factor for specificity. *Mol. Cell* **62**, 824–833 (2016).

28. 28.

Ramachandran, A., Summerville, L., Learn, B. A., DeBell, L. & Bailey, S. Processing and integration of functionally oriented spacers in the *Escherichia coli* CRISPR system depends on bacterial host exonucleases. *J. Biol. Chem.* **295**, 3403–3414 (2020).

29. 29.

Levy, A. et al. CRISPR adaptation biases explain preference for acquisition of foreign DNA. *Nature* **520**, 505–510 (2015).

30. 30.

Modell, J. W., Jiang, W. & Marraffini, L. A. CRISPR–Cas systems exploit viral DNA injection to establish and maintain adaptive immunity. *Nature* **544**, 101–104 (2017).

31. 31.

Makarova, K. S. et al. Evolutionary classification of CRISPR–Cas systems: a burst of class 2 and derived variants. *Nat. Rev. Microbiol.* **18**, 67–83 (2020).

32. 32.

Hudaiberdiev, S. et al. Phylogenomics of Cas4 family nucleases. *BMC Evol. Biol.* **17**, 232 (2017).

33. 33.

Pourcel, C. et al. CRISPRCasdb a successor of CRISPRdb containing CRISPR arrays and *cas* genes from complete genome sequences, and tools to download and query lists of repeats and spacers. *Nucleic Acids Res.* **48**, D535–D544 (2020).

34. 34.

Pruitt, K. D., Tatusova, T. & Maglott, D. R. NCBI reference sequence (RefSeq): a curated non-redundant sequence database of genomes, transcripts and proteins. *Nucleic Acids Res.* **33**, D501–D504 (2005).

35. 35.

Benson, D. A. et al. GenBank. *Nucleic Acids Res.* **46**, D41–D47 (2018).

36. 36.

Sayers, E. W. et al. Database resources of the National Center for Biotechnology Information. *Nucleic Acids Res.* **37**, D5–D15 (2009).

37. 37.

Arndt, D. et al. PHASTER: a better, faster version of the PHAST phage search tool. *Nucleic Acids Res.* **44**, W16–W21 (2016).

38. 38.

Mitchell, A. L. et al. MGnify: the microbiome analysis resource in 2020. *Nucleic Acids Res.* **48**, D570–D578 (2020).

39. 39.

Chen, I. A. et al. IMG/M: integrated genome and metagenome comparative data analysis system. *Nucleic Acids Res.* **45**, D507–D516 (2017).

40. 40.

Paez-Espino, D. et al. IMG/VR v.2.0: an integrated data management and analysis system for cultivated and environmental viral genomes. *Nucleic Acids Res.* **47**, D678–D686 (2019).

41. 41.

Soto-Perez, P. et al. CRISPR–Cas system of a prevalent human gut bacterium reveals hyper-targeting against phages in a human virome catalog. *Cell Host Microbe* **26**, 325–335.e325 (2019).

42. 42.

Group, N. H. W. et al. The NIH Human Microbiome Project. *Genome Res.* **19**, 2317–2323 (2009).

43. 43.

Pasolli, E. et al. Extensive unexplored human microbiome diversity revealed by over 150,000 genomes from metagenomes spanning age, geography, and lifestyle. *Cell* **176**, 649–662.e620 (2019).

44. 44.

Altschul, S. F., Gish, W., Miller, W., Myers, E. W. & Lipman, D. J. Basic local alignment search tool. *J. Mol. Biol.* **215**, 403–410 (1990).

45. 45.

Fu, L., Niu, B., Zhu, Z., Wu, S. & Li, W. CD-HIT: accelerated for clustering the next-generation sequencing data. *Bioinformatics* **28**, 3150–3152 (2012).

46. 46.

Deveau, H. et al. Phage response to CRISPR-encoded resistance in *Streptococcus thermophilus*. *J. Bacteriol.* **190**, 1390–1400 (2008).

47. 47.

Almendros, C., Guzman, N. M., Diez-Villasenor, C., Garcia-Martinez, J. & Mojica, F. J. Target motifs affecting natural immunity by a constitutive CRISPR–Cas system in *Escherichia coli*. *PLoS ONE* **7**, e50797 (2012).

48. 48.

Lange, S. J., Alkhnbashi, O. S., Rose, D., Will, S. & Backofen, R. CRISPRmap: an automated classification of repeat conservation in prokaryotic adaptive immune systems. *Nucleic Acids Res.* **41**, 8034–8044 (2013).

49. 49.

Alkhnbashi, O. S. et al. CRISPRstrand: predicting repeat orientations to determine the crRNA-encoding strand at CRISPR loci. *Bioinformatics* **30**, i489–i496 (2014).

50. 50.

Guindon, S. et al. New algorithms and methods to estimate maximum-likelihood phylogenies: assessing the performance of PhyML 3.0. *Syst. Biol.* **59**, 307–321 (2010).

51. 51.

Katoh, K. & Standley, D. M. MAFFT multiple sequence alignment software version 7: improvements in performance and usability. *Mol. Biol. Evol.* **30**, 772–780 (2013).

52. 52.

Crooks, G. E., Hon, G., Chandonia, J. M. & Brenner, S. E. WebLogo: a sequence logo generator. *Genome Res.* **14**, 1188–1190 (2004).

53. 53.

McKenzie, R. E., Almendros, C., Vink, J. N. A. & Brouns, S. J. J. Using CAPTURE to detect spacer acquisition in native CRISPR arrays. *Nat. Protoc.* **14**, 976–990 (2019).

54. 54.

Punjani, A., Rubinstein, J. L., Fleet, D. J. & Brubaker, M. A. cryoSPARC: algorithms for rapid unsupervised cryo-EM structure determination. *Nat. Methods* **14**, 290–296 (2017).

55. 55.

Xu, K., Zang, X., Peng, M., Zhao, Q. & Lin, B. Magnesium lithospermate B downregulates the levels of blood pressure, inflammation, and oxidative stress in pregnant rats with hypertension. *Int. J. Hypertens.* **2020**, 6250425 (2020).

Acknowledgements

This work is supported by the Netherlands Organization for Scientific Research (NWO) VICI grant (VI.C.182.027) to S.J.J.B. and the National Institutes of Health (NIH) grant (GM118174) to A.K. This work made use of the Cornell Center for Materials Research Shared Facilities which are supported through the NSF MRSEC program (DMR-1719875). We thank S. N. Kieper, R. Miojevic, M. Ramos, G. Schuler and K. Spoth for helpful discussions, advice and technical assistance.

Author information

Author notes

1. These authors contributed equally: Chunyi Hu, Cristóbal Almendros

Affiliations

1. Department of Molecular Biology and Genetics, Cornell University, Ithaca, NY, USA

Chunyi Hu, Saket R. Bagde & Ailong Ke

2. Department of Bionanoscience, Delft University of Technology, Delft, The Netherlands

Cristóbal Almendros, Ana Rita Costa, Jochem N. A. Vink, Anna C. Haagsma & Stan J. J. Brouns

3. Kavli Institute of Nanoscience, Delft, The Netherlands

Cristóbal Almendros, Ana Rita Costa, Jochem N. A. Vink, Anna C. Haagsma & Stan J. J. Brouns

4. Department of Life Science, Pohang University of Science and Technology, Pohang, Republic of Korea

Ki Hyun Nam

Contributions

A.K., S.J.J.B., C.H. and C.A. designed the research. C.H. is responsible for biochemistry and cryo-EM reconstructions; C.A., J.N.A.V., A.R.C. and A.C.H. are responsible for in vivo and bioinformatics analyses; K.H.N. and C.H. are responsible for structure building and refinement; and S.R.B. assisted with cryo-EM work. A.K. and C.H. wrote the manuscript with input from S.J.J.B., J.N.A.V. and A.R.C.

Corresponding authors

Correspondence to Stan J. J. Brouns or Ailong Ke.

Ethics declarations

Competing interests

The authors declare no competing interests.

Additional information

Peer review information *Nature* thanks Martin Jinek, Lennart Randau and Malcolm White for their contribution to the peer review of this work.

Publisher's note Springer Nature remains neutral with regard to jurisdictional claims in published maps and institutional affiliations.

Extended data figures and tables

Extended Data Fig. 1 Reconstitution and characterization of the *GsuCas4/Cas1-Cas2* complex.

a. Active site substitution in Cas4 nuclease center (H48G, D100A) reduced *in vivo* spacer acquisition efficiency dramatically. Left three panels display the WebLogo of PAM code from spacers integrated by each Cas4/1-2 variant. Rightmost panel displays the number of deep-sequencing reads that confirm spacer integration. **b-d.** *GsuCas4/1* purification analyzed by SDS-PAGE, coloring from the Fe-S cluster, and SEC profile, respectively. **e,f.** Affinity purification of *GsuCas2*, SDS-PAGE, and SEC analysis, respectively. **g.** GST pull-down experiments revealing the physical interaction between *GsuCas4/1* and *GsuCas2*, with or without prespacer present. **h.** Metal ion dependency in PAM cleavage reaction. **i.** Biochemistry showing Cas4/1-2 specifically cleaves the PAM-embedded 3'-overhang in prespacer. **j.** PAM-cleavage specificity is lost over time,

presumably due to Fe-S oxidation in Cas4. **k.** SEC profile of *GsuCas4/Cas1-Cas2*, alone or programmed with different prespacer substrates. PAM-containing prespacers drive high-order complex formation. **l.** Cryo-electron micrographs of three different complexes, with corresponding preliminary 2D averages to investigate sample quality.

Extended Data Fig. 2 In-depth analysis of the dual-PAM prespacer bound *GsuCas4/Cas1-Cas2* structure.

a. Comparison between the current 3.2 Å cryo-EM reconstruction with the previous negative staining reconstruction of the *B. hal* Cas4/1-2 complex (EMDB 20131)²². **b-d.** Pairwise alignment between *GsuCas4/Cas1-Cas2/pespacer* and *EcoCas1-Cas2/pespacer*^{8,31} (PDB 5DS4), *EfaCas1-Cas2/pespacer*¹² (PDB 5XVN), and *EfaCas1-Cas2/full-integration*¹² (PDB 5XVO), respectively. Alignments details are noted on the figure panel. Inset: the C-terminal tail of Cas2 plays similar roles in *G. sul* and *E. fae* structures in mediating edge-stacking with both Cas2 and Cas1. **e.** PAM was processed similarly in 22-bp or 26-bp mid-duplex containing prespacer by *GsuCas4/Cas1-Cas2*. **f.** SEC profile was similar when the two different prespacers were used to assemble the complex. **g.** Validation that prespacers containing a 22-bp mid-duplex are actively acquired *in vivo*. N=3 biologically independent assays were evaluated by PCR detection as shown, as well as relative percentages of expanded and non-expanded bands. Data presented as mean ± s.e.m.

Extended Data Fig. 3 Flow-chart of the cryo-EM single particle reconstruction of the dual-PAM prespacer bound *GsuCas4/Cas1-Cas2*.

a. Cryo-EM reconstruction workflow for the dual-PAM prespacer bound Cas4/1-2 complex. **b.** Cryo-EM density of the dual-PAM prespacer bound Cas4/1-2 complex, colored according to local resolution (top). The viewing direction distribution plot (middle) and FSC curves (bottom) for data processing. **c.** Representative EM densities for Cas2, Cas4, and Cas1, superimposed with their corresponding structural model.

Extended Data Fig. 4 In-depth GsuCas4/Cas1-Cas2 interface analysis and structure-guided mutagenesis attempt to switch PAM specificity.

a. Overall dual-PAM structure. Insets: zoom-ins of interface between Cas4 and the two neighboring Cas1s. Cas4 connects to the non-catalytic Cas1 through a 20-amino acid fusion linker (colored in yellow), which mediates the dynamic docking and dissociation of Cas4. **b.** Surface electrostatic potential. Left inset: Cas2 contacts to the mid-duplex; Right inset: Cas1 end-stacking to the mid-duplex. Residues responsible for guiding the 3'-overhang are also shown. Cas1-Cas2 was found to specify a 22-bp mid-duplex rather than a 26-bp mid-duplex as defined by the integration assay; an additional two base-pairs are unwound from each end, and the mid-duplex is end-stacked by the N-terminal domain of the catalytic Cas1s on opposite ends. The 22-bp specification and the limited end-unwinding activity was previously observed in *Efa*Cas1-Cas2^{11,12}. **c.** Cas1-Cas2 and Cas4-Cas2 interfaces. Top inset: the highly conserved C-terminus of Cas2 inserting into a hydrophobic pocket in Cas1, stabilizing complex formation. Bottom inset: the ceiling helix of Cas4 (aa 39–50) makes extensive polar contacts with a helix in Cas2 (aa 42–53). **d.** SEC, SDS-PAGE, and urea-PAGE analyses of the prespacer-bound complex used in cryo-EM analysis. They reveal the molecular weight, protein integrity, and prespacer integrity, respectively. For example, urea-PAGE reveals the PAM-overhang is not cleaved inside the Cas4/1-2 complex. **e.** Modeling the impact on PAM recognition by introducing the equivalent residues of E18 and S191 in *P. fur* Cas4 into *G. sul* Cas4 (E18Y and S191A substitutions). Specific atom changes in A-to-G switching (N6O substitution and N2 amine addition) are highlighted in colored balls. The steric clashes (lightening arrows) to *Pfu*PAM (3'-GGN in the 3'-overhang) are expected to be partially relieved when substitutions are in place. **f.** Impact of E18Y and S191A substitutions on PAM cleavage activity. **g.** *In vivo* spacer acquisition assay results for the wild type and PAM-specificity Cas4 mutants. While E18Y/S191A Cas4 showed compromised *Gsu*-PAM (TTN) prespacer integration, it was able to support integration of *Pfu*-PAM (CCN) containing prespacers *in vivo*. $N = 3$ biological independent assays were analyzed by PCR and the band

quantification revealed integration efficiency. Data presented as mean \pm s.e.m.

Extended Data Fig. 5 In-depth analysis of the structure and sequence conservation in Cas4.

a. Superposition of *GsuCas4* with a standalone Cas4^{19,20}, and the nuclease domains in helicase-nuclease fusion proteins AddAB³², AdnAB²⁶, RecBCD³³, and eukaryotic Dna2³⁴. The caging of the ssDNA substrate and the arrangement of the Fe-S cluster and the catalytic triad are conserved themes. Interestingly, the Cas4 structure aligns poorly with the RecB nuclease in RecBCD; it agrees better with the RecB-like fold in RecC instead. **b, c.** Sequence alignment of *GsuCas4*, *GsuCas1*, and *PfuCas4* with their close homologs. Based on the structural analysis, we marked the residues important for subunit interaction, substrate binding, catalysis and Fe-S cluster formation. **d.** Quality of the purified *GsuCas4* mutants that carry the PAM-recognition residues from *PfuCas4*. These mutants were used in the structure-guided PAM-switching experiments in Extended Data Fig. 4.

Extended Data Fig. 6 Cryo-EM single particle reconstruction of the single-PAM prespacer bound *GsuCas4/Cas1-Cas2*.

a. Flow-chart of the cryo-EM single particle reconstruction process that led to the reconstruction of two major snapshots. Left: Asymmetrical PAM/Non-PAM prespacer bound Cas4/1-2 complex. Right: That of the sub complex lacking (Cas4/1)₂ on the non-PAM side. **b.** Cryo-EM density of the two reconstructions colored according to local resolution (top); viewing direction distribution plot (middle); and FSC curves (bottom). **c.** Superposition of the PAM side and non-PAM side densities showing that Cas4 density is largely missing at the non-PAM side, and the non-PAM 3'-overhang is largely disordered. Only the first four nucleotides of the non-PAM 3'-overhang can be traced in the density, along a similar path as in the PAM-side.

Extended Data Fig. 7 *In vitro* assays to distinguish integration directionality.

a, b. Biochemistry showing that *GsuCas4/1-2* is unable to integrate prespacer into the linear form of leader-repeat DNA. **c.** Successful prespacer integration into a leader-repeat containing plasmid by Cas4/1-2. **d.** The leader-repeat sequence cloned into the plasmid. We cleaved the leader-repeat sequence via the EcoRI and XhoI sites after the integration assay to further resolve the integration directionality on urea-PAGE. **e.** Schematic diagram explaining how the integration directionality can be resolved based on the fluorescent ssDNA sizes. **f.** Integration profile in urea-PAGE when both overhangs are integration-ready (7-nt long). Results showed that from the leader-repeat point of view, integration preferentially initiates from the leader-side, as the spacer-side integration trails after the leader-side integration in the time-course experiment. From the prespacer point of view, the integration directionality is scrambled. Each integration band contains two overlapping fluorescent signals. **g.** Native PAGE showing that in the concentration-gradient experiment, complex formation between Cas4/1-2 and prespacer takes place in a stepwise and PAM-dependent fashion.

Extended Data Fig. 8 In-depth analysis of the mechanistic coupling between half-integration and PAM cleavage by Cas4.

a. Time-course experiment showing ExoI trims PAM and non-PAM overhangs differently. The non-PAM 3'-overhang was trimmed to within one nucleotide of the preferred length, 7 nt. The PAM-side 3'-overhang was protected by the footprint of Cas4 in the same reaction. **b.** Time-course experiment resolving the order of events from prespacer processing to full integration. Using the Cas4/1-2 (left set) and Cas4/1-2 plus ExoI (middle set) lanes as controls, the right set of experiment shows ExoI trimming triggers the integration of the non-PAM overhang into the leader-proximal target DNA. This is followed by the stimulation of PAM cleavage, and then the full integration from PAM-overhang to spacer-side target. **c.** Temperature-dependency of PAM cleavage and spacer-side integration. **d.** Side-by-side comparison of PAM cleavage at 50 °C, prespacer alone or

programmed to the half-integrated state. **e**. Quantification of the cleaved band in **c**. and **d**. revealing the elevated PAM cleavage and full integration when leader-side integration already took place. Data were collected from $N = 3$ biologically independent experiments and presented with mean \pm s.e.m. Statistical significance was assessed by two-tailed t-test, with the exact P values displayed. **f**. Salt-dependency of PAM cleavage and full integration. **g–i**. Optimization of full integration reaction by defining its time course, Cas2-dependency, and pH-dependency, respectively. **j**. Defining pH-dependency of PAM cleavage by Cas4. **k**. SEC analysis of the Cas4/1-2 complex programmed with the half-integration product mimic. Samples in the integrated complex peak was used for cryo-EM data collection and single particle reconstruction. **l**, Schematics of the half-integration product mimic annealed from oligonucleotides. **m**. Urea-PAGE analysis of the SEC peak in **k**. revealing that Cas4/1-2 further catalyzed the full-integration reaction after binding to the half-integration mimic.

Extended Data Fig. 9 Cryo-EM single particle reconstruction of GsuCas4/Cas1-Cas2 programmed with a half-integration mimic.

a. Workflow of cryo-EM data processing. **b**. Overall cryo-EM density showing resolution distribution, viewing direction distribution plot, and FSC curves of three different snapshots. Left: half-integration, Cas4 disappeared; Middle: full-integration; Right: half-integration, Cas4 still blocking PAM-side.

Extended Data Fig. 10 In-depth analysis of the three snapshots captured from GsuCas4/Cas1-Cas2 programmed with a half-integration mimic.

a. Superposition of cryo-EM reconstructions to reveal the structural differences among three functional states. **b**. Orientation view of the full integration snapshot for additional interface analysis. The entire leader-repeat DNA is contacted in a quasi-symmetric fashion at the following four regions. **c**. Contacts from the two Cas1 subunits to the spacer-repeat DNA. The spacer-side DNA density is degenerate and DNA bending is not

significant. The leader-recognition α -helix in the catalytic Cas1 is not inserted into the minor groove of the spacer-side DNA. **d.** The backbone of the central dyad of CRISPR repeat is contacted by the positive charges and a proline-rich motif on the ridge of the Cas2 dimer. **e.** Immediately adjacent to the catalytic loop, the linker connecting Cas4 to Cas1 is involved in DNA contact. A conserved PRPI motif is exposed upon Cas4 dissociation and is involved in DNA minor groove contact. **f.** The 4-bp leader region immediately upstream of the CRISPR repeat is favorably recognized and significantly bent upwards by the DNA minor groove insertion of a glycine-rich α -helix in Cas1. As previously revealed, this recognition leads to strong leader-proximal preference at the first half-integration reaction^{10,11,12}. A pair of inverted repeats is found at the border region of the CRISPR repeat. This inverted repeat is recognized at the major groove region by the catalytic Histidine-containing loop in Cas1¹². **g.** Overall structure of the “Half-integration, Cas4 still blocking PAM-side” snapshot. This represents an early state, when Cas4 is still engaged in PAM recognition and the spacer-side leader-repeat is not allowed to enter into the integration site. **h.** The low-resolution EM density defines that the leader-repeat DNA preferentially contact a positively charged patch in Cas1. It should be noted that we are not able to define which specific DNA contact activates Cas4. This will require even higher temporal and spatial resolutions to resolve.

Extended Data Table 1 Cryo-EM data collection, refinement and validation statistics

Supplementary information

Supplementary Figure 1

This file contains the uncropped gels shown in Figs 1, 3, 4 and Extended Data Figs 1, 2, 4, 7, 8.

Reporting Summary

Supplementary Tables

This file contains Supplementary Tables 1, 2, which contain lists of plasmids, primers and reagents used in the study.

Video 1

| Mechanism for Cas4-assisted prespacer biogenesis. This video illustrates the mechanism of Cas4-assisted prespacer biogenesis process. The animation made use of Pymol to interpolate structural transitions from one functional state to the next.

Video 2

| Mechanism for Cas4-assisted directional spacer integration.

Rights and permissions

Reprints and Permissions

About this article

Cite this article

Hu, C., Almendros, C., Nam, K.H. *et al.* Mechanism for Cas4-assisted directional spacer acquisition in CRISPR–Cas. *Nature* **598**, 515–520 (2021). <https://doi.org/10.1038/s41586-021-03951-z>

- Received: 22 December 2020
- Accepted: 25 August 2021
- Published: 29 September 2021
- Issue Date: 21 October 2021
- DOI: <https://doi.org/10.1038/s41586-021-03951-z>

Share this article

Anyone you share the following link with will be able to read this content:

[Get shareable link](#)

Sorry, a shareable link is not currently available for this article.

[Copy to clipboard](#)

Provided by the Springer Nature SharedIt content-sharing initiative

This article was downloaded by **calibre** from <https://www.nature.com/articles/s41586-021-03951-z>

| [Section menu](#) | [Main menu](#) |

- Article
- [Published: 15 September 2021](#)

Structural insights into hepatitis C virus receptor binding and entry

- [Ashish Kumar¹](#),
- [Reafa A. Hossain¹](#),
- [Samantha A. Yost](#) [ORCID: orcid.org/0000-0002-8286-2530²](#),
- [Wei Bu³](#),
- [Yuanyuan Wang¹](#),
- [Altaira D. Dearborn¹](#),
- [Arash Grakoui^{4,5}](#),
- [Jeffrey I. Cohen³](#) &
- [Joseph Marcotrigiano](#) [ORCID: orcid.org/0000-0001-7670-7836¹](#)

[Nature](#) volume **598**, pages 521–525 (2021)

- 4272 Accesses
- 106 Altmetric
- [Metrics details](#)

Subjects

- [Hepatitis C virus](#)
- [X-ray crystallography](#)

Abstract

Hepatitis C virus (HCV) infection is a causal agent of chronic liver disease, cirrhosis and hepatocellular carcinoma in humans, and afflicts more than 70 million people worldwide. The HCV envelope glycoproteins E1 and E2 are responsible for the binding of the virus to the host cell, but the exact entry process remains undetermined¹. The majority of broadly neutralizing antibodies block interaction between HCV E2 and the large extracellular loop (LEL) of the cellular receptor CD81 (CD81-LEL)². Here we show that low pH enhances the binding of CD81-LEL to E2, and we determine the crystal structure of E2 in complex with an antigen-binding fragment (2A12) and CD81-LEL (E2–2A12–CD81-LEL); E2 in complex with 2A12 (E2–2A12); and CD81-LEL alone. After binding CD81, residues 418–422 in E2 are displaced, which allows for the extension of an internal loop consisting of residues 520–539. Docking of the E2–CD81-LEL complex onto a membrane-embedded, full-length CD81 places the residues Tyr529 and Trp531 of E2 proximal to the membrane. Liposome flotation assays show that low pH and CD81-LEL increase the interaction of E2 with membranes, whereas structure-based mutants of Tyr529, Trp531 and Ile422 in the amino terminus of E2 abolish membrane binding. These data support a model in which acidification and receptor binding result in a conformational change in E2 in preparation for membrane fusion.

Access options

Subscribe to Journal

Get full journal access for 1 year

\$199.00

only \$3.90 per issue

[Subscribe](#)

All prices are NET prices.

VAT will be added later in the checkout.

Tax calculation will be finalised during checkout.

Rent or Buy article

Get time limited or full article access on ReadCube.

from \$8.99

[Rent or Buy](#)

All prices are NET prices.

Additional access options:

- [Log in](#)
- [Access through your institution](#)
- [Learn about institutional subscriptions](#)

Fig. 1: Ribbon diagrams of the tCD81-LEL-eE2(Δ HVR1)-2A12, eE2-2A12 and tCD81-LEL X-ray crystal structures.

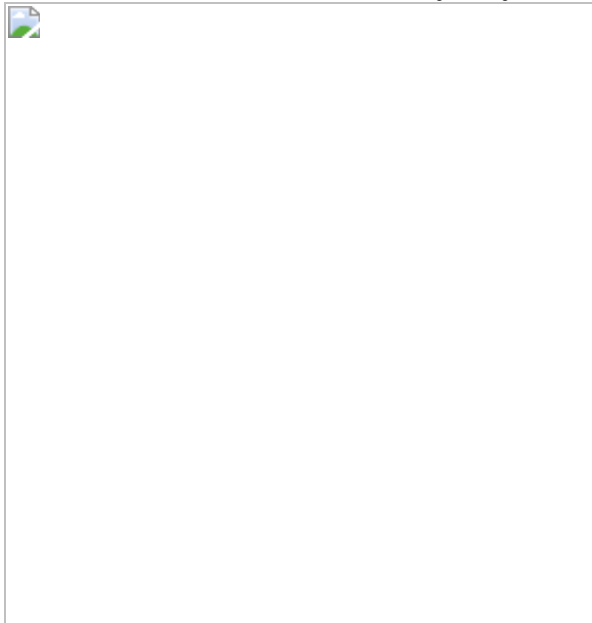


Fig. 2: Ribbon diagrams of the conformational variation in E2 and CD81-LEL.

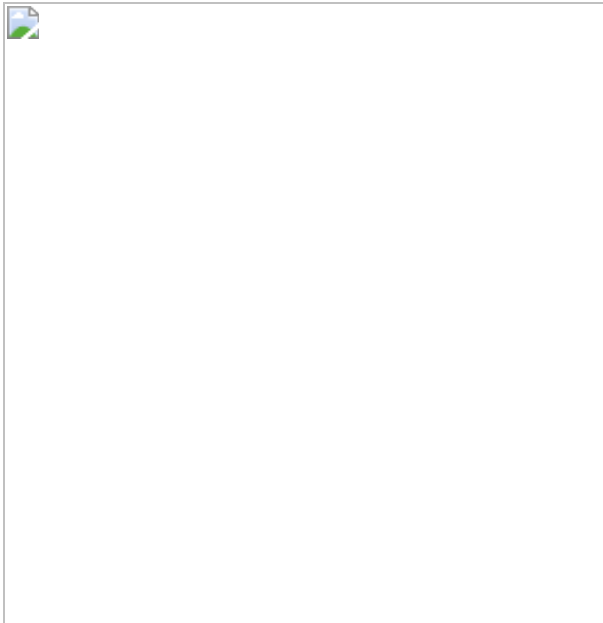


Fig. 3: Neutralizing antibodies compete directly with CD81 for E2 binding.

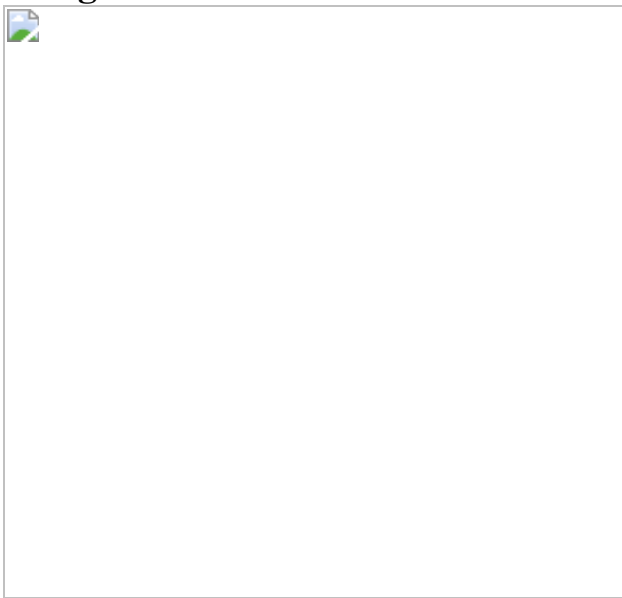
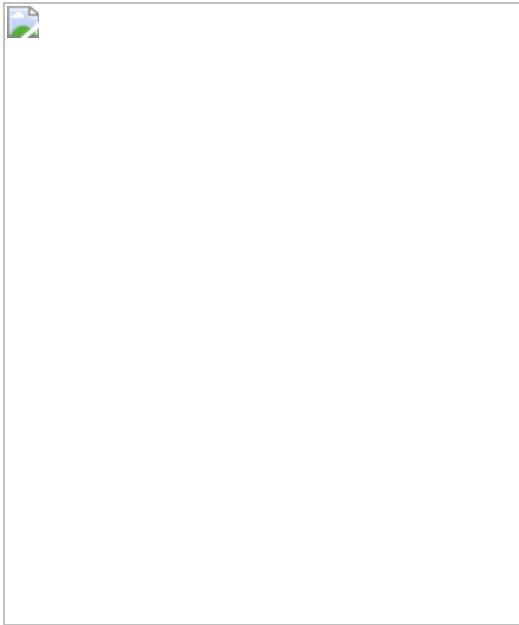


Fig. 4: Proximity and interaction of eE2 with membranes.



Data availability

The coordinates and structure factors for eE2–2A12, tCD81-LEL and tCD81-LEL–eE2(Δ HVR1)–2A12 have been deposited into the RCSB PDB (<https://www.rcsb.org>) under accession numbers [7MWW](#), [7MWS](#) and [7MWX](#), respectively.

References

1. 1.

Gerold, G., Moeller, R. & Pietschmann, T. Hepatitis C virus entry: protein interactions and fusion determinants governing productive hepatocyte invasion. *Cold Spring Harb. Perspect. Med.* **10**, a036830 (2020).

2. 2.

Tzarum, N., Wilson, I. A. & Law, M. The neutralizing face of hepatitis C virus E2 envelope glycoprotein. *Front. Immunol.* **9**, 1315 (2018).

3. 3.

Tscherne, D. M. et al. Time- and temperature-dependent activation of hepatitis C virus for low-pH-triggered entry. *J. Virol.* **80**, 1734–1741 (2006).

4. 4.

Rothwangl, K. B., Manicassamy, B., Uprichard, S. L. & Rong, L. Dissecting the role of putative CD81 binding regions of E2 in mediating HCV entry: putative CD81 binding region 1 is not involved in CD81 binding. *Virol. J.* **5**, 46 (2008).

5. 5.

Drummer, H. E., Wilson, K. A. & Poumbourios, P. Identification of the hepatitis C virus E2 glycoprotein binding site on the large extracellular loop of CD81. *J. Virol.* **76**, 11143–11147 (2002).

6. 6.

Drummer, H. E., Boo, I., Maerz, A. L. & Poumbourios, P. A conserved Gly436-Trp-Leu-Ala-Gly-Leu-Phe-Tyr motif in hepatitis C virus glycoprotein E2 is a determinant of CD81 binding and viral entry. *J. Virol.* **80**, 7844–7853 (2006).

7. 7.

Owsianka, A. M. et al. Identification of conserved residues in the E2 envelope glycoprotein of the hepatitis C virus that are critical for CD81 binding. *J. Virol.* **80**, 8695–8704 (2006).

8. 8.

Zhao, Z. et al. A neutralization epitope in the hepatitis C virus E2 glycoprotein interacts with host entry factor CD81. *PLoS One* **9**, e84346 (2014).

9. 9.

Higginbottom, A. et al. Identification of amino acid residues in CD81 critical for interaction with hepatitis C virus envelope glycoprotein E2. *J. Virol.* **74**, 3642–3649 (2000).

10. 10.

Flint, M. et al. Diverse CD81 proteins support hepatitis C virus infection. *J. Virol.* **80**, 11331–11342 (2006).

11. 11.

Allander, T., Forns, X., Emerson, S. U., Purcell, R. H. & Bukh, J. Hepatitis C virus envelope protein E2 binds to CD81 of tamarins. *Virology* **277**, 358–367 (2000).

12. 12.

Khan, A. G. et al. Structure of the core ectodomain of the hepatitis C virus envelope glycoprotein 2. *Nature* **509**, 381–384 (2014).

13. 13.

Kitadokoro, K. et al. CD81 extracellular domain 3D structure: insight into the tetraspanin superfamily structural motifs. *EMBO J.* **20**, 12–18 (2001).

14. 14.

Cunha, E. S. et al. Mechanism of structural tuning of the hepatitis C virus human cellular receptor CD81 large extracellular loop. *Structure* **25**, 53–65 (2017).

15. 15.

Dearborn, A. D. & Marcotrigiano, J. Hepatitis C virus structure: defined by what it is not. *Cold Spring Harb. Perspect. Med.* **10**, a036822 (2020).

16. 16.

Susa, K. J., Rawson, S., Kruse, A. C. & Blacklow, S. C. Cryo-EM structure of the B cell co-receptor CD19 bound to the tetraspanin CD81. *Science* **371**, 300–305 (2021).

17. 17.

Flyak, A. I. et al. HCV broadly neutralizing antibodies use a CDRH3 disulfide motif to recognize an E2 glycoprotein site that can be targeted for vaccine design. *Cell Host Microbe* **24**, 703–716 (2018).

18. 18.

Kong, L. et al. Hepatitis C virus E2 envelope glycoprotein core structure. *Science* **342**, 1090–1094 (2013).

19. 19.

Flyak, A. I. et al. An ultralong CDRH2 in HCV neutralizing antibody demonstrates structural plasticity of antibodies against E2 glycoprotein. *eLife* **9**, e53169 (2020).

20. 20.

Tzarum, N. et al. Genetic and structural insights into broad neutralization of hepatitis C virus by human VH1-69 antibodies. *Sci. Adv.* **5**, eaav1882 (2019).

21. 21.

Zimmerman, B. et al. Crystal structure of a full-length human tetraspanin reveals a cholesterol-binding pocket. *Cell* **167**, 1041–1051 (2016).

22. 22.

Rajesh, S. et al. Structural basis of ligand interactions of the large extracellular domain of tetraspanin CD81. *J. Virol.* **86**, 9606–9616 (2012).

23. 23.
Vasiliauskaite, I. et al. Conformational flexibility in the immunoglobulin-like domain of the hepatitis C virus glycoprotein E2. *mBio* **8**, e00382-17 (2017).
24. 24.
Lomize, M. A., Pogozheva, I. D., Joo, H., Mosberg, H. I. & Lomize, A. L. OPM database and PPM web server: resources for positioning of proteins in membranes. *Nucleic Acids Res.* **40**, D370–D376 (2012).
25. 25.
Kielian, M. Mechanisms of virus membrane fusion proteins. *Annu. Rev. Virol.* **1**, 171–189 (2014).
26. 26.
Boo, I. et al. Distinct roles in folding, CD81 receptor binding and viral entry for conserved histidine residues of hepatitis C virus glycoprotein E1 and E2. *Biochem. J.* **443**, 85–94 (2012).
27. 27.
Sharma, N. R. et al. Hepatitis C virus is primed by CD81 protein for low pH-dependent fusion. *J. Biol. Chem.* **286**, 30361–30376 (2011).
28. 28.
White, J. M. & Whittaker, G. R. Fusion of enveloped viruses in endosomes. *Traffic* **17**, 593–614 (2016).
29. 29.
Li, H. F., Huang, C. H., Ai, L. S., Chuang, C. K. & Chen, S. S. Mutagenesis of the fusion peptide-like domain of hepatitis C virus E1 glycoprotein: involvement in cell fusion and virus entry. *J. Biomed. Sci.* **16**, 89 (2009).

30. 30.

Yost, S. A., Whidby, J., Khan, A. G., Wang, Y. & Marcotrigiano, J. Overcoming challenges of hepatitis C virus envelope glycoprotein production in mammalian cells. *Methods Mol. Biol.* **1911**, 305–316 (2019).

31. 31.

Adams, P. D. et al. PHENIX: building new software for automated crystallographic structure determination. *Acta Crystallogr. D* **58**, 1948–1954 (2002).

32. 32.

Emsley, P. & Cowtan, K. Coot: model-building tools for molecular graphics. *Acta Crystallogr. D* **60**, 2126–2132 (2004).

33. 33.

Emsley, P. & Crispin, M. Structural analysis of glycoproteins: building N-linked glycans with Coot. *Acta Crystallogr. D* **74**, 256–263 (2018).

34. 34.

Chen, V. B. et al. MolProbity: all-atom structure validation for macromolecular crystallography. *Acta Crystallogr. D* **66**, 12–21 (2010).

35. 35.

Madeira, F. et al. The EMBL-EBI search and sequence analysis tools APIs in 2019. *Nucleic Acids Res.* **47**, W636–W641 (2019).

36. 36.

Baker, N. A., Sept, D., Joseph, S., Holst, M. J. & McCammon, J. A. Electrostatics of nanosystems: application to microtubules and the ribosome. *Proc. Natl Acad. Sci. USA* **98**, 10037–10041 (2001).

37. 37.

Dolinsky, T. J., Nielsen, J. E., McCammon, J. A. & Baker, N. A. PDB2PQR: an automated pipeline for the setup of Poisson-Boltzmann electrostatics calculations. *Nucleic Acids Res.* **32**, W665–W667 (2004).

38. 38.

DeLano, W. L. *The PyMOL molecular graphics system.* <http://www.pymol.org> (Schrödinger, 2002).

39. 39.

Keller, S. et al. High-precision isothermal titration calorimetry with automated peak-shape analysis. *Anal. Chem.* **84**, 5066–5073 (2012).

40. 40.

Zhao, H., Piszczeck, G. & Schuck, P. SEDPHAT—a platform for global ITC analysis and global multi-method analysis of molecular interactions. *Methods* **76**, 137–148 (2015).

Acknowledgements

We acknowledge A. Khan, M. Miller, M. Paskel and L. Tuberty for technical assistance; D. Wu and G. Piszczeck for help with the ITC measurements; C. Rice for reagents and advice; and F. Jiang for his dedication to science and friendship. This work was supported by the Intramural Research Programs of the National Institute of Allergy and Infectious Diseases (J.I.C. and J.M.) and NIH grants R01AI136533, R01AI124680, R01AI126890 and U19AI159819 to A.G. Use of the Advanced Photon Source was supported by the US Department of Energy, Office of Science, Office of Basic Energy Sciences, under contract numbers W-31-109-Eng-38 (SER-CAT) and DE-AC02-06CH11357 (LRL-CAT). SER-CAT is supported by its member institutions, and equipment grants (S10_RR25528 and S10_RR028976) from the National Institutes of Health.

Author information

Affiliations

1. Structural Virology Section, Laboratory of Infectious Diseases, National Institute of Allergy and Infectious Diseases, National Institutes of Health, Bethesda, MD, USA

Ashish Kumar, Reafa A. Hossain, Yuanyuan Wang, Altaira D. Dearborn & Joseph Marcotrigiano

2. Center for Advanced Biotechnology and Medicine, Rutgers, The State University of New Jersey, Piscataway, NJ, USA

Samantha A. Yost

3. Medical Virology Section, Laboratory of Infectious Diseases, National Institute of Allergy and Infectious Diseases, National Institutes of Health, Bethesda, MD, USA

Wei Bu & Jeffrey I. Cohen

4. Division of Infectious Diseases, Department of Medicine, Emory University School of Medicine, Atlanta, GA, USA

Arash Grakoui

5. Emory Vaccine Center, Division of Microbiology and Immunology, Yerkes National Primate Research Center, Emory University, Atlanta, GA, USA

Arash Grakoui

Contributions

A.K., R.A.H., S.A.Y. and Y.W. purified the proteins and determined crystallization conditions. A.K., R.A.H., S.A.Y., W.B., A.D.D., J.I.C. and

J.M. collected, processed and analysed the results. A.G. provided the antibody hybridoma. All authors helped to write and edit the manuscript.

Corresponding author

Correspondence to Joseph Marcotrigiano.

Ethics declarations

Competing interests

A.K., W.B., A.D., J.I.C, and J.M., are named as inventors on a patent application describing the data presented in this paper, which has been filed by the National Institutes of Health.

Additional information

Peer review information *Nature* thanks Yorgo Modis and the other, anonymous, reviewer(s) for their contribution to the peer review of this work.

Publisher's note Springer Nature remains neutral with regard to jurisdictional claims in published maps and institutional affiliations.

Extended data figures and tables

[Extended Data Fig. 1 Sequence divergence between human and tamarin CD81.](#)

a, Sequence alignment (light blue and black font) of full-length human and tamarin CD81 (Accession numbers: Human NM_004356, Tamarin CAB89875.1). The CD81-LEL (black font) has five divergent residues (green and yellow highlights represent nonidentical and similar amino acids, respectively). **b**, Ribbon diagram of tamarin CD81-LEL (blue) bound to eE2(Δ HVR1) (red and CD81-binding loop green) with side chains of the

five, diverging CD81 residues (blue sticks) and proximal residues in eE2 (red sticks).

Extended Data Fig. 2 Thermodynamic characterization of tamarin and human CD81-LEL interaction with eE2.

a–d, ITC for the titration of tCD81-LEL (**a, b**) or hCD81-LEL (**c, d**) into eE2 at pH 7.5 (**a, c**) and pH 5.0 (**b, d**). Thermogram (upper panel), integrated heats and error bars (middle panel), and fit residuals (lower panel) are shown for each. The measurements were performed at 20 °C and analysed with an A + B ⇌ AB heterodimer model. Error bars indicate the error of peak integration over an interpolated baseline with a 68% (1 sigma) confidence interval. Residuals are the *y*-axis difference between the data point and the fitted curve in kcal mol⁻¹.

Extended Data Fig. 3 The asymmetric unit for the tCD81-LEL–eE2(ΔHVR1)–2A12 complex.

a, b, eE2(ΔHVR1) chains C and G (red with extended CD81-binding loop in green), tCD81-LEL chains D and H (blue), 2A12 (wheat) ribbon diagrams in the asymmetric unit of the tCD81-LEL–eE2(ΔHVR1)–2A12 complex from side (**a**) and top (**b**) views. The 90° axis of rotation is indicated. Carbohydrate moieties (yellow heteroatom sticks) are also shown.

Extended Data Fig. 4 Diagram and conservation of HCV E2.

a, Schematic representation of the E2 protein with the CD81-binding loop highlighted in yellow and the asterisks highlighting regions associated with CD81 binding. **b**, Multiple sequence alignment of eE2 from representative strains (as labelled) of the seven genotypes. Conserved residues (cyan highlights) and CD81-binding loop residues (red font) are noted. Asterisks indicate residues ≤4 Å from tamarin CD81 common to both chains C and G (red), chain G only (blue), and chain A only (green). Hypervariable region, antigenic site, and transmembrane are labelled HVR, AS and TM, respectively.

Extended Data Fig. 5 A simulated-annealing $2F_o - F_c$ composite omit map for the eE2(Δ HVR1) CD81-binding loop in the X-ray crystal structure of the complex.

a, b, CD81-binding loop in (a) Chain C and (b) Chain G (green heteroatom sticks), residues as labelled, in a 0.8σ contour level $2F_o - F_c$ composite omit map (blue mesh) calculated from the omission of residues 415–426 and 520–539, and packed against the tCD81-LEL (blue) and eE2(Δ HVR1) (red) ribbon diagrams.

Extended Data Fig. 6 Interface between tCD81-LEL and eE2(Δ HVR1).

Ribbon diagram of tCD81-LEL (blue) and eE2(Δ HVR1) (red) interface, chains C and D, with side chains (blue and red heteroatom sticks, respectively). The labels for tCD81-LEL residues are underlined.

Extended Data Fig. 7 Electrostatic-potential surface maps of E2 and tCD81-LEL.

a–j, Electrostatic-potential surface maps of eE2(Δ HVR1) in complex (a, b), tCD81-LEL–eE2(Δ HVR1) complex (c, d), tCD81-LEL in complex (e, f) and free form (g, h), and full-length eE2 free form (i, j). The surfaces are coloured by electrostatic potential corresponding to +5 kcal/(mol·e) (blue) and –5 kcal/(mol·e) (red) at 298 K calculated at pH 7.5 (a, c, e, g, i) and 5.0 (b, d, f, h, j) as labelled. Panels a, b, i, and j are depicted in the same orientation; panels e–h are depicted in the same orientation. a, b, tCD81-LEL is shown as a transparent, blue ribbon diagram. e, f, The eE2(Δ HVR1)-binding surface is outlined with a dotted line.

Extended Data Fig. 8 Expression, purification and liposome flotation of eE2 mutants.

a, E2-specific western blot of cell culture supernatants showing secreted protein levels of eE2 mutants I422A, Y529A, W531A, and double mutant

Y529A/W531A. Expi293 GnTI⁻ cells were transfected and supernatants (uncleaved eE2 protein) were mixed with reduced 2x sample buffer. 15 ul of supernatant was loaded in each well. E2 2C1 primary antibody was used for western blotting. **b**, Coomassie-stained 4-20% Bis-Tris SDS-PAGE gels of purified eE2 mutant proteins in the presence (Reduced) and absence (Non-reduced) of β-mercaptoethanol. **c**, E2-specific western blot of top fractions from liposome flotation assays, comparing increased loading (as labelled under each blot) of mutants. Protein molecular weight maker (L) and wild-type eE2 is provided as a marker (std). Sample pH, inclusion of tCD81-LEL, and eE2 mutant proteins are labelled.

Extended Data Table 1 Affinity measurements of eE2 to human and tamarin CD81-LEL at neutral and low pH

Extended Data Table 2 Data collection and refinement statistics for eE2–2A12, tCD81-LEL and tCD81-LEL–eE2(ΔHVR1)–2A12 complexes

Extended Data Table 3 Residues making interactions within $\leq 4 \text{ \AA}$

Supplementary information

Supplementary Figure 1

This file contains the uncropped gel source data shown in Fig. 4c.

Reporting Summary

Rights and permissions

Reprints and Permissions

About this article

Cite this article

Kumar, A., Hossain, R.A., Yost, S.A. *et al.* Structural insights into hepatitis C virus receptor binding and entry. *Nature* **598**, 521–525 (2021).
<https://doi.org/10.1038/s41586-021-03913-5>

- Received: 05 May 2020
- Accepted: 13 August 2021
- Published: 15 September 2021
- Issue Date: 21 October 2021
- DOI: <https://doi.org/10.1038/s41586-021-03913-5>

Share this article

Anyone you share the following link with will be able to read this content:

[Get shareable link](#)

Sorry, a shareable link is not currently available for this article.

[Copy to clipboard](#)

Provided by the Springer Nature SharedIt content-sharing initiative

This article was downloaded by **calibre** from <https://www.nature.com/articles/s41586-021-03913-5>

Amendments & Corrections

- **[Author Correction: Transcriptional programs of neoantigen-specific TIL in anti-PD-1-treated lung cancers](#)**

[04 October 2021]

Author Correction •

- Author Correction
- Open Access
- [Published: 04 October 2021](#)

Author Correction: Transcriptional programs of neoantigen-specific TIL in anti-PD-1-treated lung cancers

- [Justina X. Caushi](#)^{1,2,3 nAff1},
- [Jiajia Zhang](#)^{1,2,3 nAff1},
- [Zhicheng Ji](#)^{4 nAff11},
- [Ajay Vaghasia](#)³,
- [Boyang Zhang](#)⁴,
- [Emily Han-Chung Hsue](#)^{3,5,6},
- [Brian J. Mog](#) ORCID: orcid.org/0000-0001-9988-7147^{3,5,6},
- [Wenpin Hou](#) ORCID: orcid.org/0000-0003-0972-2192⁴,
- [Sune Justesen](#)⁷,
- [Richard Blosser](#)^{1,3},
- [Ada Tam](#)^{1,3},
- [Valsamo Anagnostou](#) ORCID: orcid.org/0000-0001-9480-3047^{1,3},
- [Tricia R. Cottrell](#) ORCID: orcid.org/0000-0003-2952-1830^{1,2,3 nAff12},
- [Haidan Guo](#)^{1,2,3},
- [Hok Yee Chan](#)^{1,2,3},
- [Dipika Singh](#)^{1,2,3},
- [Sampriti Thapa](#)^{1,2,3},
- [Arbor G. Dykema](#)^{1,2,3},
- [Poromendro Burman](#)^{1,2,3},
- [Begum Choudhury](#)^{1,2,3},

- [Luis Aparicio](#)^{1,2,3},
- [Laurene S. Cheung](#)^{1,2,3},
- [Mara Lanis](#)^{1,3},
- [Zineb Belcaid](#)^{1,3},
- [Margueritta El Asmar](#)^{1,3},
- [Peter B. Illei](#)³,
- [Rulin Wang](#)³,
- [Jennifer Meyers](#)³,
- [Kornel Schuebel](#)³,
- [Anuj Gupta](#)³,
- [Alyza Skaist](#)³,
- [Sarah Wheelan](#) ORCID: orcid.org/0000-0002-9002-0800³,
- [Jarushka Naidoo](#)^{1,3 nAff13},
- [Kristen A. Marrone](#)^{1,3},
- [Malcolm Brock](#)³,
- [Jinny Ha](#)³,
- [Errol L. Bush](#)³,
- [Bernard J. Park](#)⁸,
- [Matthew Bott](#)⁸,
- [David R. Jones](#)⁸,
- [Joshua E. Reuss](#)^{3 nAff14},
- [Victor E. Velculescu](#) ORCID: orcid.org/0000-0003-1195-438X^{1,3},
- [Jamie E. Chaft](#) ORCID: orcid.org/0000-0002-5838-9982⁸,
- [Kenneth W. Kinzler](#)^{3,5,6},
- [Shibin Zhou](#) ORCID: orcid.org/0000-0003-1941-4425^{3,5,6},
- [Bert Vogelstein](#)^{3,5,6},
- [Janis M. Taube](#)^{1,2,3},
- [Matthew D. Hellmann](#)⁸,
- [Julie R. Brahmer](#)^{1,3},
- [Taha Merghoub](#) ORCID: orcid.org/0000-0002-1518-5111^{8,9,10},
- [Patrick M. Forde](#)^{1,3},
- [Srinivasan Yegnasubramanian](#) ORCID: orcid.org/0000-0003-0744-6606^{1,2,3},
- [Hongkai Ji](#) ORCID: orcid.org/0000-0002-6480-0141⁴,

- [Drew M. Pardoll](#) ^{1,2,3} &
- [Kellie N. Smith](#) [ORCID: orcid.org/0000-0002-6295-8930](#)^{1,2,3}

Nature volume **598**, page E1 (2021)

- 721 Accesses
- 4 Altmetric
- [Metrics details](#)

Subjects

- [CD8-positive T cells](#)
- [Cellular immunity](#)
- [Immunotherapy](#)
- [T-cell receptor](#)
- [Tumour immunology](#)

The [Original Article](#) was published on 21 July 2021

[Download PDF](#)

Correction to: *Nature* <https://doi.org/10.1038/s41586-021-03752-4>
Published online 21 July 2021

In the originally published version of this Article there were three labeling errors in Fig. 1. The cluster names for “CD8-MHCII” and “CD8-proliferating” were switched and the cluster names for “Stem-like memory” and “MAIT” were switched (Fig. 1c). Their positions have now been corrected. In Fig. 1d, a typo in the “*SCL4A10*” gene label has been corrected to “*SLC4A10*.” The legend for Fig. 1c originally referred to the heatmap as displaying the “top-5” most differential genes. This has been corrected to “the top-3” most differential genes. In the eighth paragraph of main text, a typo in the gene name “*LINC02246*” has been corrected to “*LINC02446*.” Further, in Supplementary Table 9, the data point “5” was

missing in the Number of nonsynonymous mutations per exome column for patient NY016-007; this has now been corrected. The original Article has been corrected online.

Author information

Author notes

1. Zhicheng Ji

Present address: Department of Biostatistics and Bioinformatics, Duke University School of Medicine, Durham, NC, USA

2. Tricia R. Cottrell

Present address: Ontario Institute for Cancer Research, Queens University, Kingston, Ontario, Canada

3. Jarushka Naidoo

Present address: Beaumont Hospital Dublin, RCSI University of Medicine and Health Science, Dublin, Ireland

4. Joshua E. Reuss

Present address: Georgetown Lombardi Comprehensive Cancer Center at Georgetown University, Washington, DC, USA

5. These authors contributed equally: Justina X. Caushi, Jiajia Zhang

Affiliations

1. Bloomberg~Kimmel Institute for Cancer Immunotherapy at Johns Hopkins, Baltimore, MD, USA

Justina X. Caushi, Jiajia Zhang, Richard Blosser, Ada Tam, Valsamo Anagnostou, Tricia R. Cottrell, Haidan Guo, Hok Yee Chan, Dipika Singh, Sampriti Thapa, Arbor G. Dykema, Poromendro

Burman, Begum Choudhury, Luis Aparicio, Laurene S. Cheung, Mara Lanis, Zineb Belcaid, Margueritta El Asmar, Jarushka Naidoo, Kristen A. Marrone, Victor E. Velculescu, Janis M. Taube, Julie R. Brahmer, Patrick M. Forde, Srinivasan Yegnasubramanian, Drew M. Pardoll & Kellie N. Smith

2. The Mark Center for Advanced Genomics and Imaging at Johns Hopkins, Baltimore, MD, USA

Justina X. Caushi, Jiajia Zhang, Tricia R. Cottrell, Haidan Guo, Hok Yee Chan, Dipika Singh, Sampriti Thapa, Arbor G. Dykema, Poromendro Burman, Begum Choudhury, Luis Aparicio, Laurene S. Cheung, Janis M. Taube, Srinivasan Yegnasubramanian, Drew M. Pardoll & Kellie N. Smith

3. Sidney Kimmel Comprehensive Cancer Center at Johns Hopkins, Baltimore, MD, USA

Justina X. Caushi, Jiajia Zhang, Ajay Vaghasia, Emily Han-Chung Hsiue, Brian J. Mog, Richard Blosser, Ada Tam, Valsamo Anagnostou, Tricia R. Cottrell, Haidan Guo, Hok Yee Chan, Dipika Singh, Sampriti Thapa, Arbor G. Dykema, Poromendro Burman, Begum Choudhury, Luis Aparicio, Laurene S. Cheung, Mara Lanis, Zineb Belcaid, Margueritta El Asmar, Peter B. Illei, Rulin Wang, Jennifer Meyers, Kornel Schuebel, Anuj Gupta, Alyza Skaist, Sarah Wheelan, Jarushka Naidoo, Kristen A. Marrone, Malcolm Brock, Jinny Ha, Errol L. Bush, Joshua E. Reuss, Victor E. Velculescu, Kenneth W. Kinzler, Shabin Zhou, Bert Vogelstein, Janis M. Taube, Julie R. Brahmer, Patrick M. Forde, Srinivasan Yegnasubramanian, Drew M. Pardoll & Kellie N. Smith

4. Department of Biostatistics, Bloomberg School of Public Health, Johns Hopkins University, Baltimore, MD, USA

Zhicheng Ji, Boyang Zhang, Wenpin Hou & Hongkai Ji

5. Ludwig Center and Howard Hughes Medical Institute at Johns Hopkins, Baltimore, MD, USA

Emily Han-Chung Hsiue, Brian J. Mog, Kenneth W. Kinzler, Shabin Zhou & Bert Vogelstein

6. Lustgarten Pancreatic Cancer Research Laboratory, Sidney Kimmel Comprehensive Cancer Center, Johns Hopkins University, Baltimore, MD, USA

Emily Han-Chung Hsiue, Brian J. Mog, Kenneth W. Kinzler, Shabin Zhou & Bert Vogelstein

7. Immunitrack, Copenhagen, Denmark

Sune Justesen

8. Department of Medicine, Memorial Sloan Kettering Cancer Center and Weill Cornell Medicine, New York, NY, USA

Bernard J. Park, Matthew Bott, David R. Jones, Jamie E. Chaft, Matthew D. Hellmann & Taha Merghoub

9. The Swim Across America and Ludwig Collaborative Laboratory, Immunology Program, Parker Institute for Cancer Immunotherapy at Memorial Sloan Kettering Cancer Center, New York, NY, USA

Taha Merghoub

10. Human Oncology and Pathogenesis Program, Memorial Sloan Kettering Cancer Center, New York, NY, USA

Taha Merghoub

Corresponding authors

Correspondence to Srinivasan Yegnasubramanian, Hongkai Ji, Drew M. Pardoll or Kellie N. Smith.

Rights and permissions

Open Access This article is licensed under a Creative Commons Attribution 4.0 International License, which permits use, sharing, adaptation, distribution and reproduction in any medium or format, as long as you give appropriate credit to the original author(s) and the source, provide a link to the Creative Commons license, and indicate if changes were made. The images or other third party material in this article are included in the article's Creative Commons license, unless indicated otherwise in a credit line to the material. If material is not included in the article's Creative Commons license and your intended use is not permitted by statutory regulation or exceeds the permitted use, you will need to obtain permission directly from the copyright holder. To view a copy of this license, visit <http://creativecommons.org/licenses/by/4.0/>.

[Reprints and Permissions](#)

About this article

Cite this article

Caushi, J.X., Zhang, J., Ji, Z. *et al.* Author Correction: Transcriptional programs of neoantigen-specific TIL in anti-PD-1-treated lung cancers. *Nature* **598**, E1 (2021). <https://doi.org/10.1038/s41586-021-03893-6>

- Published: 04 October 2021
- Issue Date: 21 October 2021
- DOI: <https://doi.org/10.1038/s41586-021-03893-6>

Share this article

Anyone you share the following link with will be able to read this content:

[Get shareable link](#)

Sorry, a shareable link is not currently available for this article.

[Copy to clipboard](#)

Provided by the Springer Nature SharedIt content-sharing initiative

This article was downloaded by **calibre** from <https://www.nature.com/articles/s41586-021-03893-6>

| [Section menu](#) | [Main menu](#) |